Surender Kumar Sharma
Yasir Javed   *Editors*

Magnetic Nanoheterostructures

Diagnostic, Imaging and Treatment

Springer

Nanomedicine and Nanotoxicology

Series Editor

V. Zucolotto, Institute of Physics São Carlos, University of São Paulo, São Carlos, São Paulo, Brazil

More information about this series at

Surender Kumar Sharma · Yasir Javed
Editors

Magnetic Nanoheterostructures

Diagnostic, Imaging and Treatment

🐎 Springer

Editors
Surender Kumar Sharma
Department of Physics
Faculty of Science and Technology
The University of the West Indies
St. Augustine, Trinidad and Tobago

Yasir Javed
Department of Physics
University of Agriculture Faisalabad
Faisalabad, Pakistan

Preface

Nanohybrid systems have raised considerable interest in basic research as well as potential applications due to their broad range of novel and enhanced physical properties. As an important family of materials, nanoheterostructured e.g., core-shell, dumbbell, or dimer architectures have attracted increasing attention. This is due to their unique functionalities, arising from the synergetic combination of interesting physical properties in the same nano-entity, which leads to appealing biomedical applications especially cancer. Early cancer detection is one of the major limitations of currently available techniques, magnetic nanohybrids as contrast agents provide higher relaxation rates and increase the visibility of a portion of the biological systems. There are many reviews available where different magnetic nanoparticles and their applications for magnetic resonance imaging (MRI) and treatment have been discussed in a scattered manner. However, comprehensive data, where different types of magnetic nanohybrids, their structures, magnetism and use for diagnosis, imagining and treatment, is missing.

This book is aimed at highlighting the complexity of the nanoheterostructured especially magnetic metal oxides, ferrites and doped magnetic nanomaterials and their prospective applications for early detection, imaging and treatment of cancer. It will serve as an overview for a wide audience: from beginners and graduate-level students up to advanced specialists in both academic and industrial sectors.

St. Augustine, Trinidad and Tobago   Surender Kumar Sharma

Contents

Chapter 1
Liquid-Phase Synthesis of Multifunctional Nanomaterials: A Recent Update

Gopal Niraula, Navadeep Shrivastava, Kanwal Akhtar, Yasir Javed, J. A. H. Coaquira and S. K. Sharma

Abstract The design of novel materials is a fundamental focal point of material science research. Nanomaterials less than 100 nm in size have attracted significant interest over several decades due to their unique properties led by surface effect and finite size effect. Colloidal chemistry plays a key role in the controlled production of different classes of nanoparticles, thus being a subject of growing interest in several fields of materials, inorganic, physical chemistry, biophysics, and biomedical. Therefore, in this chapter, we sought to present an introductory outline of liquid-phase synthesis, nucleation, and growth mechanism of nanomaterials focusing on the magnetic nanoparticles. As per the broadness of this book, special attention was devoted to nanoparticles based on iron oxide and rare earth compounds, due to their rapid flourishing importance in biomedical field. Therefore, the work presents ideas involved in the most commonly applied methodologies for the liquid-phase synthesis of nanoparticles, such as co-precipitations and hydro/solvothermal techniques, as well as precipitations into nanoreactors based on reverse microemulsions, with a brief survey of the main advances in these fields in recent years. We have thoroughly presented the synthesis routes of several hybrid nanostructures such as magnetic silica/carbon, magnetic luminescence, magneto-plasmonics, and others. At last, the importance of surface modification and further bio-conjugation has been discussed.

G. Niraula
Department of Physics, Federal University of Maranhao, Sao Luis 65080-805, Brazil

N. Shrivastava (✉)
Institute of Physics, Federal University of Goias, Goiânia 74690-900, Brazil
e-mail: enavadeep@gmail.com

K. Akhtar · Y. Javed
Department of Physics, Magnetic Materials Laboratory, University of Agriculture Faisalabad, University Main Rd, Faisalabad 38000, Pakistan

J. A. H. Coaquira
Laboratory of Magnetic Materials, NFA, Institute of Physics, University of Brasilia, Brasilia, DF 70910 900, Brazil

S. K. Sharma (✉)
Department of Physics, the Faculty of Science and Technology, The University of West Indies, St. Augustine, Trinidad and Tobago
e-mail: surender.sharma@sta.uwi.edu; surender76@gmail.com

Introduction

One of the great promises of nanotechnology is the application to biology and
medicine. Nanometer-size protein particles called 'self-assembling peptide nanofiber
scaffold' were used for the regeneration of axonal tissue of a hamster with severe optic
tract. Also, it is used for site-specific or targeted drug delivery applications (Matson
et al. 2011; Ellis-Behnke et al. 2006). Nanoparticles (NPs) selectively coated with
biodegradable polymer can carry the drug in vivo to the desired location such as
tumor cells or around inflammation sites as the polymer degrades. Superparamag-
netic magnetite particles coated with dextran are used as image enhancement agents
to detect small lymph-node metastases of prostate cancer in magnetic resonance
imaging (Sun et al. 2008). Certain nanoparticles integrated on chips, 'laboratory-on-
a-chip,' to work as tags or labels are used as biological tests measuring the presence
or activity of selected substances become quicker, more sensitive, and more flexible
(Jain 2003; Alharbi and Al-sheikh 2014).

Recently, magnetic NPs are an emerging field of study and have gained much atten-
tion among researchers due to their widespread applications in various fields includ-
ing catalysis, data storage, environmental remediation, magnetic fluids, electronic
communication, and biomedicine, etc. (Karatutlu and Sapelkin 2018; Alivisatos
1996). Among different types of magnetic NPs (MNPs), iron oxide NPs (IONPs)
are the most popular and widely used in the field of biomedicine due to their ease of
surface modification, synthesis, and low toxicity. Current studies and literature have
confirmed that magnetic IONPs are frequently used in the treatment of hyperthermia
or as drug carriers in cancer treatment, magnetic resonance imaging (MRI) agents,
bioseparation, gene delivery, biosensors, protein purification, immunoassays, and
cell labeling (Hurley et al. 2016; Ho et al. 2011; Lee et al. 2011; Mazumder et al.
2009; Sun et al. 2010).

Due to the unique properties like superparamagnetism, high coercivity, low Curie
temperature, and high magnetic susceptibility, magnetic iron oxide NPs have a great
importance for the researchers in a broad range of disciplines, including magnetic
fluids, data storage, and catalysis to bio-applications (Hergt et al. 2008; Bertotti
1998; Dias et al. 2017; Aivazoglou et al. 2018). Especially, iron oxide NPs with
appropriate surface chemistry have numerous in vivo applications in biomedical
area such as magnetic resonance imaging (MRI) (Ho et al. 2011; Bae et al. 2012;
Zhang et al. 2017), the deterioration of cancer cells via hyperthermia treatment (Hur-
ley et al. 2016; Hergt et al. 2006; Yang et al. 2015; Carrey et al. 2011), tissue repair,
immunoassay (Mattoussi et al. 2000), detoxification of biological fluids, drug deliv-
ery, and cell separation (Lee et al. 2011; Gao et al. 2004; Kim et al. 2008; Louie et al.
2000; Zhu et al. 2010). In this sense, an accurate choice of the nanomaterial with

adjustable physical and chemical properties plays an important role for such kinds of applications. In this consideration, magnetic NPs became the strong candidates.

The emergence of improved characterization techniques (such as the advances made to transmission electron microscopy) has allowed researchers to probe the precise nature of nanomaterials, enabling the relationships between size, shape, elemental composition, and physical properties of a material to be investigated. As such, the ability to develop 'tunable' nanomaterial syntheses (which can produce a high-quality nanomaterial product with properties pre-determined for a particular application) has emerged as a major research goal for scientists. Within nanoscale research, a number of distinct research branches have emerged, each relating to the study of a particular type of nanomaterial and its applications. It is therefore important to understand the synthesis methods with biocompatibility, coating nucleation and growth of NPs. Many efficient synthetic routes have been developed to produce shape-controlled, highly stable, and monodisperse magnetic NPs. Techniques such as co-precipitation (Salavati-Niasari et al. 2012; Pereira et al. 2012), thermal decomposition (Zhang et al. 2017; Salavati-Niasari et al. 2008; López-Ortega et al. 2015), reverse micelle synthesis (Vestal and Zhang 2003), hydrothermal synthesis (Karatutlu and Sapelkin 2018; Hayashi and Hakuta 2010; Brown et al. 1994), laser pyrolysis (Majidi et al. 2016; Reau et al. 2007), and microwave-assisted synthesis (Karatutlu and Sapelkin 2018; Russo et al. 2012; Tsuji et al. 2005; Bano et al. 2016) have been used to produce high-quality magnetic NPs.

This chapter deals mainly with the synthesis processes of magnetic NPs (and magnetic hybrid NPs) in detail for the sake of the entire book and coating methodologies of such NPs, in view of biomedical applications, along with several illustrative examples. Further, the physics of nucleation and growth of NPs have been provided with few selected illustrations.

Synthesis Methodologies: Role of Chemistry

There are two general approaches to fabricating nanomaterials, commonly known as the 'top-down' and 'bottom-up' methods. The top-down approach uses physical methods and is so-called as it arrives at a nanoscale product by breaking up a bulk material into smaller, nanosized parts. Conversely, the bottom-up approach 'builds' a nanomaterial from atomic or molecular precursors and is considered the chemical approach.

Top-Down Approach

A common top-down approaches to fabricating nanomaterials involve using a high-energy beam to 'etch' nanoscale features and patterns onto a substrate. This etching is achieved using a beam of high-energy particles (photons, ions, or electrons) to achieve

accurate site-specific sputtering and milling of a sample. Patterning of substrates is used extensively by the semiconductor industry when fabricating circuits. This technique is suitable for introducing fine detail onto a surface at the sub-micrometer level, though cannot produce discrete nanomaterial (Stanford et al. 2017; Wang and Xia 2004). Another commonly used top-down technique is ball milling. In ball milling, a powder of bulk material is continually circulated in a cylindrical chamber in the presence of a mixing agent (usually steel or stone balls) which grinds up the powder to produce fine particles. High-energy ball milling has been used to produce NPs with sizes as low as ~9 nm, though the disadvantage of this process is that there is very little control over the final particle shape and size (Prasad Yadav et al. 2012; Piras et al. 2019).

Bottom-Up Approach

The bottom-up approach involves building a nanomaterial in a step-by-step, atomic approach, fueled by the decomposition of a molecular precursor or the generation of atomic species. For example, in the pulsed laser decomposition (PLD) method a target material is irradiated by a laser beam, causing the material to vaporize. The vaporized material can be deposited on a nearby substrate, leading to thin-film growth. PLD allows precise control over the composition and thickness of a thin film, though the PLD apparatus is expensive and not suitable for producing large quantities of material. The solution-based synthesis of nanomaterials has been the subject of significant research interest in recent years, as this approach has the ability to produce a range of nanomaterial products with a high level of size and shape control (Wang and Xia 2004; Charitidis et al. 2014).

Liquid-Phase Synthesis

Over two decades, myriad breakthroughs have emerged following the advent of nano-material research in natural sciences and engineering, due to their unique properties depending upon shape and size. It is well known that reducing the size of materials down to microscale to nanoscale leads to produce nanomaterials with profound and significant changes in its physical, i.e., electrical, magnetic, and thermal properties, and hence could be good candidates in different application, i.e., optoelectronics, magnetic storage memory devices, and biomedical (Karatutlu and Sapelkin 2018; Alivisatos 1996). The designer of such nanomaterial in nanoscale varying with shape and size, depending upon application, is very complex and thus needs proper under-standing of their architecture to synthesis. Usually, bottom-up approach, also referred as solution-phase chemistry that consists of liquid-phase synthesis (LPS hereafter), is used to prepare materials, rather than top-down approach in which bulk materials

Fig. 1.1 Different methods to prepare nanomaterials. Reprinted with permission from Charitidis et al. (2014). Copyright 2014 Manufacturing Review
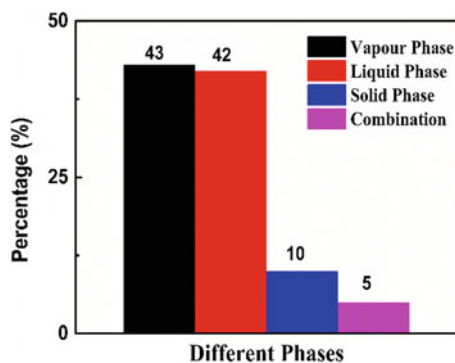
are etched in an aqueous solution for producing NPs or nanostructures, for example, electrochemical etching and mechanical grinding. LPS methods have several advantages over other gas-phase and solid-phase synthesis methods; for instance, LPS helps to controlled size and shape of NMs at low temperature within a short time from minutes to hours, reasonably low cost particularly compared to solid-phase synthesis methods, simple with high mass yield, and surface modifications with functionalization can be achieved in situ, even post-synthesis with respect to the application field (Charitidis et al. 2014; Gutsch et al. 2004; Feng et al. 2015).

Figure 1.1 shows that different ways of preparing nanomaterials and prepared nanomaterial in percentage until date through these ways (Charitidis et al. 2014). NPs obtained by liquid-phase synthesis methods can remain in liquid suspension for further/future use or may be collected by filtering or by spray drying to produce a dry powder. Liquid-phase synthesis methods from a solution of chemical compounds include chemical stain etching, colloidal methods, co-precipitation, electrochemical deposition, direct precipitation, sol–gel processing, microemulsion method, reverse micelle synthesis, hydrothermal synthesis, template methods, polyol method, and laser ablation. Here, we attempt to explain the methods of the most common liquid-phase synthesis as follows.

Precipitation

Co-precipitation was widely studied to prepare magnetic NPs due to its extraordinary advantages, such as gram-scale production and facility. Co-precipitation method based on the hydrolysis of a mixture of Fe^{2+} and Fe^{3+} ions is used to fix the A to B molar ratio in the inverse spinel structure during the preparation of magnetite. Usually, the reaction is performed under an inert (N_2 or Ar) atmosphere using degassed solutions to avoid uncontrollable oxidation of Fe^{2+} into Fe^{3+} (Bandhu et al. 2009), as shown in Fig. 1.2a. In this method, Fe^{2+} and Fe^{3+} ions are generally precipitated in alkaline solutions, such as ammonium hydroxide, potassium hydroxide, or sodium hydroxide. In most cases, the syntheses are performed at 70–80 °C (Ozkaya et al.
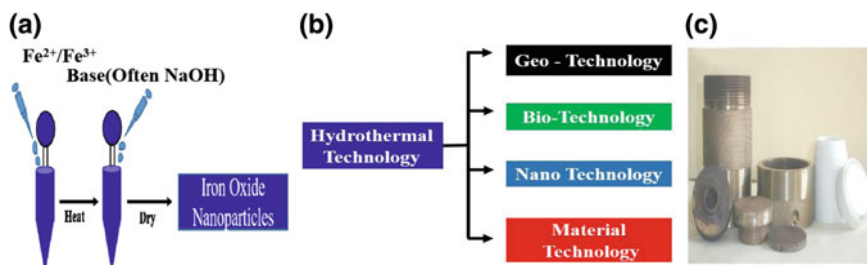
Fig. 1.2 **a** Co-precipitation method of synthesis, **b** application of hydrothermal technology, and **c** most uses autoclave for hydrothermal synthesis. Reprinted with permission from Byrappa and Adschiri (2007), Copyright 2007 Elsevier Ltd. All rights reserved

2009) or higher temperatures. The effects of mixing methods, stirring rate (Valenzuela et al. 2009), digestion time (Gnanaprakash et al. 2007), initial pH, and the presence or absence of a magnetic field (Hu et al. 2009; Vereda et al. 2007) on particle size, morphology, and resulting magnetic properties should take an account as an important factor. Co-precipitation methods performed under various precipitation conditions. For example, when only Fe^{2+} was used for precipitation, then H_2O_2 (Hu et al. 2009; Mizukoshi et al. 2009) or $NaNO_2$ (Nedkov et al. 2006) were adopted to partially oxidize Fe^{2+} into Fe^{3+} in the precipitated product. When only Fe^{3+} was used for precipitation, then Na_2SO_3 (Qu et al. 1999) partially reduces ferric to ferrous ion in the precipitation product. Some co-precipitation methods are performed in the presence of polymers (Pardoe et al. 2001), including polyvinyl alcohol (PVA) and dextran to prevent both agglomeration and/or oxidation of the NPs. All these co-precipitation methods are comparatively complex and require strict control of precipitation conditions.

Recently, several modified co-precipitation methods have been developed; for example, Wu et al. (2011) have synthesized magnetic $NPsFe_3O_4$ nanopowders with an average diameter of 15 nm by ultrasonic-assisted chemical co-precipitation utilizing high purity iron separated from iron ore tailings by an acidic leaching method. The present synthesis method of Fe_3O_4 NPs easily yields SPIONPs without a protecting gas. Pereira et al. (2012) prepared superparamagnetic Fe_3O_4 NPs with sizes of 4.9–6.3 nm, by a one-step aqueous co-precipitation route based on the use of alkanol-amines as the base; the reported methodology provides a simple, versatile, and cost-effective route for the high-yield synthesis of IONPs featuring improved magnetic properties and small particle sizes (Pereira et al. 2012). Currently, the problems of aggregation and biocompatibility of IONPs perhaps hinder the applications in biomedical fields. Therefore, many surfactants and biomolecules have been introduced directly in the co-precipitation process. For instance, Salavati-Niasari et al. (2012) have reported Fe_3O_4 NPs with a size range of 25 nm that were prepared by a facile chemical co-precipitation method; the surfactant octanoic acid was present in the reaction system to improve the dispersity. Liu et al. (2011) have prepared magnetic chitosan-coated Fe_3O_4 NPs by the co-precipitation method under 0.45 T static

magnetic fields, which assisted the glutaraldehyde cross-linking reaction; the water was replaced by 2% chitosan in an acetic acid solution during the reaction process. The resulting NPs were used to immobilize lipase.

Hydro/Solvothermal Synthesis

The word 'hydrothermal' is self-defined, made by hydro plus thermal whose meanings are water plus heat, respectively. Since the last two decades, researchers/technologists of different fields have been attracted toward it to synthesize the NPs. The nanomaterials prepared via this method in the diverse field are shown in Fig. 1.2b.

Several definitions about hydrothermal preparation of materials using autoclave and reagents in solutions at constant pressure and temperature have been mentioned in the past. In conclusion of such several approaches can be summarizing as chemical reactions in solvents contained in sealed vessels in which solvent temperature can be brought to around their critical points (coexistence point of critical temperature and critical pressure) through heating. The process is called 'hydrothermal' synthesis method when water is used as the solvent, whereas the term 'solvothermal process' is used when organics are used as solvents (Byrappa and Adschiri 2007; Rabenau 1985; Morey and Niggli 1913; Byrappa and Yoshimura 2013). Hydrothermal synthesis in supercritical water has advantages for the synthesis of multi-metal-oxide compounds because the reaction rate is enhanced more than 10^3 times that under the conventional hydrothermal conditions owing to the low dielectric constant ($<10^3$) as well as products with high crystallinity (Hayashi and Hakuta 2010; Adschiri et al. 2000). The particle size of metal oxide depends on the hydrolysis rate and solubility of the metal oxide. To achieve the control of the solvent field during nucleation and crystallization of particles, hydrothermal conditions of temperature and pressure can be varied in subcritical and supercritical water. Hydrothermal methods for preparing fine metal-oxide particles in subcritical and supercritical water have been developed using batch reaction and flow reaction systems (Yahya et al. 2001; Hakuta et al. 2004; Sue et al. 2006).

In recent year, the hydro/solvothermal process has gained great success in manufacturing nanomaterials with crystallinity, crystal phase, morphology, and size control, due to its outstanding advantages (Higgins et al. 1998; Maslar et al. 2001). This method is environment friendly and far away from high-cost instrumentation, energy, and precursors than others. Besides for processing nanomaterials, the hydrothermal technique offers special advantages because of the highly controlled diffusivity in a strong solvent media in a closed system. Nanomaterials require control over their physicochemical characteristics, if they are supposed to be used as functional materials. As the size reduced toward the nanometer range, the materials exhibit peculiar and interesting mechanical and physical properties: increased mechanical strength, enhanced diffusivity, higher specific heat, and electrical resistivity compared to their conventional coarse-grained counter-parts due to a quantization effect (Gleiter 1989).

Also, due to mild hydrothermal reaction, temperature (<300 °C) helps to overcome the several encountered found in high-temperature reaction, i.e., poor stoichiometric control due to volatilization of components in other synthesis methods. Moreover, nanomaterials prepared through hydrothermal method help to improve the luminescent properties due to the absence of Schottky defects, mostly present in materials prepared by other high-temperature reactions, for instance Sr, Ta, etc. Thus, varieties of size and morphology have been appeared in NPs synthesized by hydrothermal method. The possibility of hybridization with other synthesis process is another advantage to enhance the kinetics of reaction and to wax the ability to make new material. However, this method includes the need for expensive autoclaves and the impossibility of observing the crystal as it grows if a steel tube is used. The different autoclave for different synthesis is essential as per the interest of nanomaterials. An autoclave that uses at the material laboratory, mostly, is shown in Fig. 1.2c. The laboratory with facility of reliable pressure and temperature is another challenge (Byrappa and Adschiri 2007; Hamann 1981; Song et al. 2016; Cho et al. 1995). The corrosion resistance is major factor to choose the autoclaves because most of the nanomaterials under hydrothermal is prepared by corrosive salt. So autoclave must have the capacity to sustain in highly corrosive solvent at high temperature and pressure for longer time, i.e., hours to several days. The most successful autoclaves using by researcher are stainless steel whose inside is coated with non-reactive material having larger coefficient thermal expansion, called Teflon (also called The Liners), helps to avoid the corrosion (Song et al. 2016; Gogotsi and Yoshimura 1995).

Effect of Time and Temperature on the Size of NPs

There are only some studies about the effect of parameters such as reaction temperature and time on the growth of the NPs. Taniguchi et al. (2009) reported that the average crystalline diameter of sodium oleate-coated iron oxide NPs increased from 8.3 to 10.8 nm with the increase of reaction temperature from 100 to 230 °C under the hydrothermal process. Later, to investigate the effect of the reaction time and temperature on the nanoparticle size, Ozel et al. (2015) prepared the iron oxide NPs with the reaction time 12 h, average size of particles from 14 to 17 nm were obtained, and with increasing reaction time from 12 to 24 h at 150 °C, the size of NPs increased from 16 to 23 nm, respectively. After this, they have studied the effect of increasing temperature at 60 °C, 100 °C, 150 °C, and 180 °C for 12 h and found the size of iron oxide NPs are 12 nm, 14 nm, 16 nm, and 21 nm, respectively. Thus, we can conclude that from above discussion, the size of NPs is time and temperature dependent. Moreover, the magnetic properties such as magnetization and coercivity depend upon the size of NPs; it means that variation of time and temperature on the NPs directly influences to its structural and magnetic properties.

Synthesis of Magnetic NPs by Hydrothermal Method

Several workers have prepared the α-Fe_2O_3 (hematite) phase as NPs under hydrothermal conditions (using both aqueous and non-aqueous solvents) with or without surfactants (Li et al. 2002; Jing and Wu 2004; Zheng et al. 2005). These hematite particles find extensive applications such as catalysts, pigments, recording medium, and sensors. Surfactants like sodium dodecyl sulfonate (SDS), sodium dodecyl benzene sulfonate (DBS), cetyltrimethylammonium bromide (CTAB), and hexadecylpyridinium chloride (HPC) have been used. $FeCl_2$, $FeCl_3$, $FeSO_4$, $Fe(NO_3)_3 \cdot 9H_2O$, or FeC_2O_4, etc., were used as the source of iron. NaOH or *N,N*-dimethylformamide (DMF) was used as a solvent. The experimental temperature ranges from 180 to 250 °C in most of the cases. The typical size of the products varies from 20 to 200 nm depending upon the starting materials (reagents and solvents) and the experimental temperature. Iron oxides of spinel and magnetic structures are very important for their unique magnetic properties, which can be varied systematically through dopants like Co, Ni, Zn, Mn, etc. Cote et al. (2003) have prepared $CoFe_2O_4$ NPs through hydrothermal means within a temperature range 200–400 °C and pressure 25 MPa. A complete mechanism of formation of $CoFe_2O_4$ has been discussed in (Cote et al. 2002). It was found necessary to control the pH and experimental temperature to obtain the desired phase with a size of 100 nm. Wu et al. (2005) have synthesized nanowire arrays of Co-doped magnetite under hydrothermal conditions at 200 °C using ferrous chloride, cobalt chloride, and sodium hydroxide. These nanowires are believed to possess a single magnetic domain which can be regarded as small-wire like magnets. A soft template-assisted hydrothermal route used to prepare single-crystal Fe_3O_4 nanorods with an average diameter of 25 nm and length of 200 nm at 120 °C in 20 h. The formation of these Fe_3O_4 nanorods has been ascribed to ethylenediamine, which plays a crucial role not only as a base source but also as a soft template to form single-crystal Fe_3O_4 nanorods (Byrappa and Yoshimura 2013).

Sattar et al. (2015) have synthesized the $CoFe_2O_4$@$NiFe_2O_4$ core–shell NPs by hydrothermal synthesis method with core diameter of ~18 nm and shell thickness 3 nm as observed by TEM. They found that $CoFe_2O_4$@$NiFe_2O_4$ core–shell nanocomposite is in well-crystalline nature using different techniques. The magnetic properties of this core–shell have been studied via hysteresis loop. The magnetization saturation, coercivity, and retentivity of these NPs are 28.13 emu/g, 867.9 Oe, and 10.77 emu/g; these values were between the magnetic properties of the core ($CoFe_2O_4$) and shell ($NiFe_2O_4$) materials. Both of the saturation magnetization and coercive field are decreased compared with $CoFe_2O_4$. The decreases in the saturation magnetization and coercive field can be explained in terms of the existence of $NiFe_2O_4$ on the surface of $CoFe_2O_4$ NPs (Kolhatkar et al. 2013). Sun et al. (2018a) synthesized of Fe_3O_4@E-SiO_2 core–shell nanostructure with a rough surface. Superparamagnetic Fe_3O_4 nanosphere was first obtained with a hydrothermal process. It was found that $\sim200 \pm 10$ nm in diameter and composed of aggregated Fe_3O_4 NPs. The hysteresis loops with zero remanence and zero coercivity demonstrated that Fe_3O_4 core had a superparamagnetic behavior with the saturation magnetization value of ~72.4 emu/g which could be attributed to its smaller grain size of aggregated Fe_3O_4 NPs than the

critical size for superparamagnetic Fe_3O_4 at $\sim$25 nm (Zhang et al. 2008). After coating by SiO_2, the diameter of the nanosphere increased to $\sim$400 nm with an $\sim$100 nm silica shell. They heated the obtained $Fe_3O_4@SiO_2$ core–shell NPs with polyvinylpyrrolidone (PVP) for 1 h where PVP was adsorbed by the surface of $Fe_3O_4@SiO_2$ with the preservation of morphology of core–shell. This PVP on the surface acts as protecting agent during etching that could be diffuse with pores of SiO_2 shell and become porous. The etched sample had a much larger specific surface area of $\sim$217.8 m^2/g, and its total pore volume increased to $\sim$0.175 cm^3/g which also indicated that the etched sample had a rough surface. Sheng et al. (2014) have developed one-step approach to prepare superparamagnetic NPs with silk fibroin (SF) as the template and coating material, providing a simpler and more feasible way for core–shell $Fe_3O_4@SF$ nanoparticle fabrication by hydrothermal method. The synthesized pure Fe_3O_4 NPs showed irregular morphologies with a size of about 20 nm. However, the increase of SF in the reaction system and the Fe_3O_4 NPs became more regular and finally transformed into nanospheres when the concentration of SF was above 7%. They observed no evident differences in pure Fe_3O_4 and $Fe_3O_4@SF$ NPs, suggesting that the crystalline structure of the NPs was not affected by the SF coating. The Fe_3O_4/SF NPs showed insignificant coercivity, suggesting the superparamagnetic nature of the particles. The potential of $Fe_3O_4@SF$ NPs as a contrast agent was examined by using a 3T MR scanner. An obvious darkening of T_2-weighted MRI was observed with the increasing concentration of Fe, showing a transverse relaxivity (r_2) of 40 mM^{-1} s^{-1}. Thus, their results suggested that SF could be used to control the morphology and size of Fe_3O_4 microspheres. The biocompatibility and transverse relaxivity of the $Fe_3O_4@SF$ core–shell nanomaterial, as well as its easy coupling ability with antibodies, suggest its future in different biomedical applications.

Thermal Decomposition

Thermal decomposition is simple, easier, convenient, and an innovative method to synthesize stable monodispersed NP product. In principle, synthesis strategies can be subdivided into hot-injection approaches, where the precursors are injected into a hot reaction mixture and conventional reaction strategies where a reaction mixture is prepared at room temperature and then heated in a closed or open reaction vessel. Above room temperature, higher monodisperse, narrow size distribution, and highly crystalline magnetic IONPs are obtained from high-temperature thermal decomposition of organometallic or coordinated iron precursors in organic solvents, which display superior properties to those obtained by co-precipitation. It means thermal decomposition helps to overcome some conventional method, for instance co-precipitation (Li et al. 2008; Sun and Zeng 2002). As similar to other method of synthesis, time of reaction, temperature, concentrations of the reactants, stabilizers, capping agents (surfactants), and types of surfactants are factors to be considered to obtain controlled nanometric size (Kino et al. 2008). To date, the thermal decomposition method is mostly used to prepare iron oxide NPs with different shapes as per

application required, such as nanocrystals, nanocubes, and nanospheres, etc. Usually, it is recommended to use of various organic molecules including oleic acid, 1-octadecene, 1-tetradecene, and oleylamine in the reaction process as stabilizers to get monodisperse iron oxide NPs that can slow down the nucleation process and it affects the adsorption of additives on the nuclei and the growing nanocrystals, which may inhibit the growth of the IONPs and favor the formation of small IONPs often below 30 nm. However, the nucleation of IONPs in thermal decomposition involves boiling the solvents, so the accurate shape of the IONPs is not fully reproducible (Lynch et al. 2011). Amara et al. (2012) have offered novel single-step thermal decomposition method to synthesized Fe_3O_4 nanocubes and nanospheres with mixtures of ferrocene and PVP without solvent. Sun and Zeng (2002) have prepared Fe_3O_4 NPs of narrow size distribution which have been synthesized by thermal decomposition of $Fe(acac)_3$ in phenyl ether in the presence of stearyl alcohol, oleic acid, and oleylamine. Park et al. (2005) prepared monodisperse γ-Fe_2O_3 NPs with average diameters from 4 to 16 nm with controlling the molar ratio of metal precursor to surfactant [$Fe(CO)_5$], and oleic acid, respectively. The overall synthetic procedure is similar to seed-mediated growth. These monodisperse NPs were obtained directly without a size-selection process, and the synthetic procedure is highly reproducible. Subsequent chemical oxidation produced monodisperse and highly crystalline iron oxide nanocrystals. This concept of continuous growth without additional nucleation could be applicable to other materials for the incremental, 1-nm size-controlled synthesis of monodisperse NPs. Since several experiments have shown $Fe(CO)_5$ is very expensive and toxic, it is suggested to replace $Fe(CO)_5$ with iron chloride ($FeCl_3$) and iron acetylacetonate [$Fe(acac)_3$]. A growth scheme has been provided in Fig. 1.3.

Kovalenko et al. (2007) reported at first the synthesis of nanocubes by decomposing an iron oleate precursor using a sodium oleate (NaOl) salt along with oleic acid (OA) as ligands. It is well known that oleic acid is one of the most widely employed surfactants for the synthesis of various nanomaterials from metals, semiconductors, and metal oxides. The presence of a carboxylic group with significant affinity to various surfaces together with a nonpolar tail group for sterical hindering is the base for the excellent stabilizing function of this ligand. Commonly used approaches to further tailor the ligand performance of carboxylic acids are those based on the modifications of length or structure of the nonpolar group. They have concluded their synthesis result with various oleic acid salts acting as stabilizers for the size- and shape-controlled synthesis of iron oxide NPs. Their novel shapes for
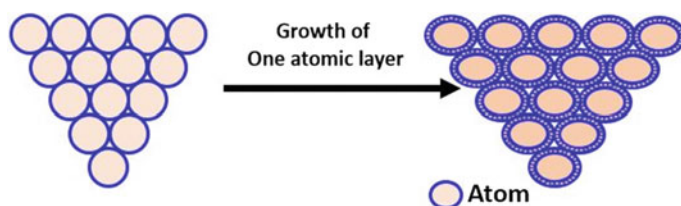
Fig. 1.3 Growth scheme: direct- and atomic-scale controlled synthesis of monodisperse NPs

superparamagnetic iron oxide nanocrystals, such as cubes and bipyramids with different magnetization properties at low temperatures, were demonstrated, enlarging the family of well-defined NP shapes for inverse spinel iron oxides. These results suggest the general applicability of oleic acid salts as stabilizers in well-controlled NP syntheses.

Microwave-Assisted Hydrothermal Method

In the recent years, researcher/scientist have attracted toward microwave-assisted synthesis method and have been successfully applied in various laboratories of nanomaterial synthesis (Nadagouda et al. 2011; Kou and Varma 2012), solid-state chemistry, nanotechnology (Virkutyte and Varma 2011), and organic synthesis (Polshettiwar et al. 2009a), etc., and many more applications, shown in Fig. 1.4a. Recent time has witnessed that the microwave heating technology is emerging as an alternative heat source for rapid volumetric heating with shorter reaction time and higher reaction rate, selectivity, and yield as compared to the conventional heating methods, providing fast chemical reactions and quick material preparation in very short span of time, usually in minutes/seconds, instead of hours or even days usually required by the conventional heating methods, leading to relatively low cost, energy saving, and high efficiency for material production (Galema 1997; Bilecka and Niederberger 2010; Kappe 2004). Beside, having large numbers of advantages of microwave-assisted synthesis, the limitation of such synthesis is rapid heating that requires a reaction component with a large loss tangent, denoted by $\tan \delta$ (such as water, ethylene glycol) than their corresponding reaction media/solvent, phenomena is called selective heating (Baghbanzadeh et al. 2011). So it is always beneficial to use those solvent having high microwave absorbing capacity to get high heating rates, water, and alcohol for example. Also, the poor solubility of organic reactants in aqueous media is another limitation for organic synthesis in water, which usually results in immiscible or biphasic reaction mixtures. However, there were several attempts to
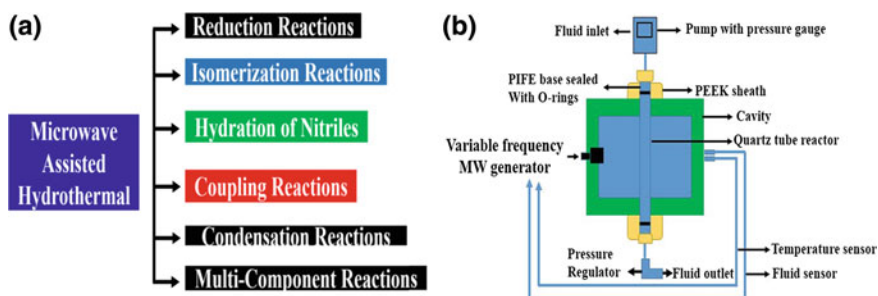
Fig. 1.4 **a** Application of microwave-assisted method, and **b** experimental setup of the present MW-assisted flow reactor system with MW cavity part

Table 1 Loss tangent (tan δ) values at 2.45 GHz and 20 °C and boiling points of different solvents (Gawande et al. 2014)

Solvent	Boiling point	Tan δ
Ethylene glycol	198	1.350
Ethanol	78	0.941
2-propanol	82	0.799
Methanol	65	0.659
1,2 dichlorobenzene	180.5	0.280
N-methyl 2-pyrrolidone	202	0.275
Acetic acid	118	0.174
N,N-dimethylformamide	153	0.161
1,2-dichloroethane	84	0.127
Water	100	0.123
Chlorobenzene	131	0.101
Acetone	57	0.054
Tetrahydrofuran	66	0.047
Toulene	111	0.040
Hexane	68–69	0.020

overcome this problem by using surfactants, mixing with co-solvents, heating of the reaction mixture, or grinding of reactants. Thus, in spite of those limitations, it has great promise in microwave-assisted organic synthesis (MAOS) and in MW-assisted nanomaterial synthesis (Bilecka and Niederberger 2010; Gawande et al. 2014).

Microwave-assisted chemical reactions depend on the ability of the reaction mixture to efficiently absorb MW energy, which often depends on the choice of solvents for the reaction. The ability of a specific solvent or material to convert MW energy into heat is determined by the so-called loss tangent (δ). The concept of dielectric loss tangent was introduced to compare heating efficiencies of microwave in materials with similar characteristics using, which is given by, $\tan \delta = \frac{\varepsilon''}{\varepsilon'}$, where ε'' is the imaginary component of the dielectric and represents the microwave radiation absorption and conversion to heat and ε' is the real component, which signifies the ability of the material to reflect or store an electric field (Baghbanzadeh et al. 2011; Mingos and Baghurst 1991). The solvents used in microwave heating can be classified on the basis of their loss tangent (tan δ): high (tan δ > 0.5), medium (tan δ ≈ 0.1–0.5), and low (tan δ < 0.1) (Kappe 2004). The value of the loss tangent (tan δ) according to solvent is different and briefly tabulated in Table 1.

Microwave Heat Generation and Mechanism

Simply, microwave heating is a process of transferring of electromagnetic energy to thermal energy rather than transfer of heat. The basic principles of microwave chemistry have been discussed in several review papers (Tsuji et al. 2005; Galema

1997; Baghbanzadeh et al. 2011; Mingos and Baghurst 1991; Nüchter et al. 2004; Gabriel et al. 1998). As an example, Gabriel et al. (1998) have provided the theory of the microwave dielectric heating, which consists of two main mechanisms namely dipolar polarization and ionic conduction. Microwaves generally heat any material containing mobile electric charges such as polar molecules or conducting ions in a solvent or in a solid. During the microwave heating, polar molecules such as water molecules strive to orientate with the rapidly changing alternating electric field; thus, heat is induced by the rotation, friction, and collision of molecules (known as dipolar polarization mechanism). Ions also move with the oscillating field, colliding, and generating heat. These collisions of ions with other species in solution generate much more heat than dipolar polarization. The studies on the mechanisms of microwave heating are even complicated by the fact that the rate enhancements of chemical reactions are dependent on many complex factors. Gedye et al. (1988) found the effects of several factors, such as sample volume, solvent, homogeneous and heterogeneous reactions, size of reaction vessel, and power level, on rate enhancements in microwave-assisted organic synthesis. In addition, higher pressure and temperature attained rapidly in MW-assisted processes may help increase the rate of reactions via enhanced homogeneous mixing of the reactants (in water) and decreasing the hydrophobic effects (on water). They proposed that the rate enhancements were caused predominantly by the rapid superheating of the solvent by microwaves. Moreover, they found that the microwave heating rate increased due to the presence of ions in the reaction mixture. In addition to these thermal heating effects, de la Hoz et al.(2005) added the role of 'non-thermal microwave effects' also called 'specific microwave effects' which is arises due to interaction of microwaves with materials in the reaction medium and hence conclude that irradiation on microwave is due to both thermal and non-thermal effects. So it is convoluted to separate discussion in regard to the mechanism of heating factor in microwave.

The reported 'non-thermal microwave effects' include varied activation energy, increased collision efficiency by mutual orientation of polar molecules and possible excitement of rotational or vibrational transitions (Galema 1997; de la Hoz et al. 2005; Perreux and Loupy 2001; Stass et al. 2000). Single-mode microwave reactors, also referred as monomode reactors, having only one reactor vessel can be irradiated, a highly homogenous energy field of high-power intensity is provided, resulting in fast heating rates (Dąbrowska et al. 2018). The simple experimental/instrumental outlook of single-mode microwave reactors is shown in Fig. 1.4b. Such microwave reactor was used for continuous flow reactions, wherein the power was controlled by a temperature feedback module and resonance frequency auto-tracking function (Nishioka et al. 2013; Öhrngren et al. 2012). The continuous flow reactor is capable of operating in a genuine high-temperature/high-pressure process window (310 °C/60 bar) under MW irradiation conditions. The faster heating rate, small reactor volumes, and rapid change in reaction temperature in real time are some of the salient features of this continuous flow MW-assisted organic synthesis (CF-MAOS) system, which aims to be a unique laboratory tool for safe and fast optimization of

reaction conditions and scale-out synthesis. Thus, the fusion of MW and a flow reactor system does offer unique features that can be adapted to organic and inorganic material syntheses (Morschhäuser et al. 2012).

Microwave-Assisted Synthesis of NPs

MW-assisted synthesis of inorganic nanomaterials and the use of nanocatalysts are growing rapidly. Inorganic nanomaterials include diverse classes of functional materials, namely metals, metal oxides, sulfides, phosphates, and halides. Some important examples of NPs are in brief below with the versatility of the MW-assisted approach for accessing a variety of nanomaterials.

α-Fe_2O_3 was synthesized using hydrothermal technique by simply heating the $K_4[Fe(CN)_6]$ in water under MW irradiation condition at 150 °C for three hours. The morphology of these particles appeared like a pine tree and hence the term micropine particle. TEM and ESEM images of the synthesized micropine α-Fe_2O_3 particles show the single-crystal structure. A closer inspection of these particles reveals well-defined and highly ordered branches shown in Fig. 1.5a–e distributed on both the sides. The TEM observations also revealed that the micropine dendrites self-assembled to form a sixfold snowflake-like structure.

There is a crucial role of concentration and time in the formation of different morphology of iron oxide. They observed that decrease in the sharpness of the dendrites, thicker the nanorod branches of dendrite with increasing the concentration of $K_4[Fe(CN)_6]$. However, if we decrease the temperature below 150 °C, we need to extend the time to get similar NPs. Thus, from these results, they suggest that it is possible to control and tune the shape of dendritic nanostructures by controlling the kinetic parameters (temperature and concentration) of the reaction process (Polshettiwar et al. 2009b). Hu et al. (2007) applied a rapid microwave-assisted hydrothermal process to synthesize single-crystalline α-Fe_2O_3 nanorings in solution. Single α-Fe_2O_3 nanoring with a circular shape and an average outer diameter of about 100 nm and inner diameters ranging from 20 to 60 nm were obtained at 220 °C for 25 min. In addition, they also reported the microwave hydrothermal method to

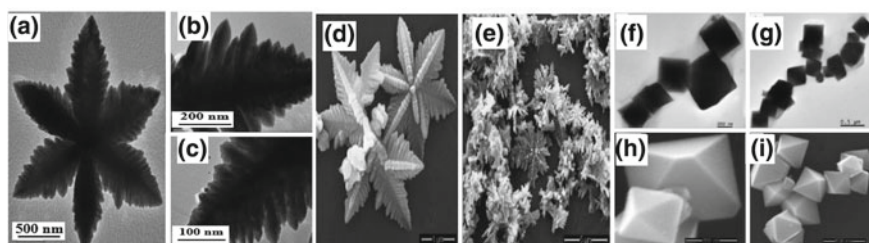**Fig. 1.5** TEM of **a** snowflake and **b, c** pine α-Fe_2O_3, SEM image of α-Fe_2O_3 (**d, e**) and TEM (**f, g**) and FE-SEM (**h, i**) of cobalt oxide. Reprinted with permission from Polshettiwar et al. (2009). Copyright 2009 American Chemical Society

synthesize monodisperse α-Fe$_2$O$_3$ nanocrystals with continuous aspect-ratio tuning and fine shape control. The initial molar ratio of Fe^{3+} to PO$_4^{3-}$ was found to play a crucial role in the final morphology of the α-Fe$_2$O$_3$ products. A variety of morphologies including ellipsoids/spindles with aspect ratios ranging from 1.1 to 6.3, all nanosheets, nanorings, and spheres were obtained with pH of 1.8–2.3 at 220 °C for 10–25 min. MW-assisted hydrothermal heating of K$_3$[Co(CN)$_6$] in water fabricated cobalt oxide in good yield. TEM and SEM studies, shown in Fig. 1.5f–i, revealed the formation of octahedral NPs with sizes ranging from 200 to 500 nm. For an octahedral crystal, every facet is close to an equilateral triangle. All the surfaces are smooth, and there are no defects, with crystallite size 46.21 nm. The effects of substrate concentration and reaction temperature on the morphology of the cobalt oxide NPs were also studied; however, no significant changes were observed in NPs (Polshettiwar et al. 2009b).

Kooti et al. (2011) synthesized maghemite NPs using Fe(acac)$_3$ as an iron precursor, PEG-200 as a size controller, and NaCl as an MW absorber. This mixture was irradiated for 5 min at 1000 W. NPs were imaged by TEM and SEM, revealing an average core size of 13 nm and NP agglomeration. Bano et al. (2016) carried out a MW-assisted green synthesis of superparamagnetic NPs using fruit peel extracts as a biogenic reductant. Mixtures were subjected to MW irradiation at 800-W power in 30-s pulses. Obtained NPs were then surface engineered via carbodiimide (functional group, RN=C=NR) chemistry to functionalize them with PEG-6000 or succinic acid. Size ranged between 17 and 25 nm with an almost spherical morphology. NPs presented a good colloidal stability and water dispersibility and a large r_2 value of 225 mM^{-1} s^{-1}. Synthesized samples were shown to be hemocompatible at concentrations as high as 400 μg/mL. Their utility in photodynamic therapy was assessed in HeLa cells, which showed 23% decreased survival. Sathya et al. (2017) synthesized water-dispersible magnetite NPs by reducing Fe$_2$(SO$_4$)$_3$ using sodium acetate as an alkali, PEG (5–6 kDa) as a capping ligand, and ethylene glycol as a solvent and reductant. Reactants were heated to 200 °C in 10 s in the MW and held at that temperature for different reaction times (from 10 to 600 s). X-ray diffraction (XRD) data showed magnetite crystalline samples with NP core sizes between 9 and 24 nm. The hydrodynamic size of synthesized NPs, measured by dynamic light scattering (DLS), ranged from 35 to 141 nm, increasing with reaction time. Size distribution was narrow for all samples. Nanocluster size increased with reaction time from ~27 nm (10 s reaction time) to ~52 nm (600 s reaction time). Aivazoglou et al. (2018) reported the synthesis of magnetite and maghemite NPs, analyzing the effect of reaction time, MW power, and capping agent on the properties of synthesized NPs. They have carried out separate sets of syntheses. With several syntheses having different MW powers, reaction time with capping and non-capping agents, their average size of NPs ranged from 10.3 to 19.2 nm, with a faceted and crystalline morphology. Their results showed that MW power and reaction time play a pivotal role in controlling NP size and maghemite presence, whereas ammonia concentration is not as relevant. PEG-assisted synthetic route rendered better results in terms of NP size and oxidation resistance. Mohamed and Hessien (2018) have synthesized nickel ferrite NiFe$_2$O$_4$ particles in nanosize scale using microwave-assisted hydrothermal method at 180 °C

for different periods of time (from 2 to 24 h). The prepared samples had an average particle size in the range of from 20 to 40 nm, as observed by using TEM and X-ray diffraction. The nickel ferrite powders were all considered as superparamagnetic materials. The values of coercivity and saturation magnetization were increased by increasing the period of synthesis time.

Polyol Synthesis

The polyol synthesis is reduction reaction method to prepare magnetic NPs with different morphology, also recognized as an inversed sol–gel method (i.e., an oxidation reaction) (Laurent et al. 2008). It designates the liquid-phase synthesis in high-boiling, multivalent alcohols and is mainly directed to NPs. As chemically, ethylene glycol (EG) is very common and simplest reagent in the polyol family. Based on EG, the polyols comprise two main series of molecules: (i) diethylene glycol (DEG), triethylene glycol (TrEG), tetraethylene glycol (TEG), and so on up to polyethylene glycol (PEG) and (ii) propanediol (PDO), butanediol (BD), pentanediol (PD), and so on (Table 2).

In such synthesis process, the polyols not only serve as solvents but also consider as reducing agents, which apply as stabilizers to control particle growth and prevent interparticle aggregation. The high quality of the as-prepared metal particles with uniform size and shape as well as low degree of agglomeration leads toward a great impact of the polyol synthesis. In the typical reaction process, an iron precursor compound is suspended in a liquid polyol. The suspension is stirred and heated to a given temperature that can reach the boiling point of the polyol. Usually, polyols allow for enormous adaptability and flexibility of the polyol synthesis. In principle, the boiling point of the polyols increases with the number of OH functionalities (see on Table 2) and with increasing molecular weight and thus polarity and viscosity

Table 2 Summary of mostly use polyols for the synthesis of materials (Dong et al. 2015)

Polyol	Acronym	Boiling point (°C)
$HO-CH_2-CH_2-OH$	EG	197
$HO-CH_2-CH_2-O-CH_2-CH_2-OH$	DEG	244
$HO-(CH_2-CH_2-O)_2-CH_2-CH_2-OH$	TREG	291
$HO-(CH_2-CH_2-O)_3-CH_2-CH_2-OH$	TEG	314
$HO-(CH_2-CH_2-O)_n-CH_2-CH_2-OH$	PEG	>350
$HO-CH_2-CH_2-CH_2-OH$	PDO	213
$HO-CH_2-CH_2-CH_2-CH_2-OH$	BD	235
$HO-CH_2-CH_2-CH_2-CH_2-CH_2-OH$	PD	242
$HO-CH_2-CH_2(OH)-CH_2-OH$	GLY	290
$C(CH_2OH)_4$	PE	276

of the polyols proportional with increasing molecular weight (Jokerst et al. 2011; Cheng et al. 2011).

Cai and Wan (2007) fabricated monodisperse Fe_3O_4 NPs by using different types of polyols, i.e., ethylene glycol (EG), diethylene glycol (DEG), triethylene glycol (TREG), and tetraethylene glycol (TEG), to reduce $Fe(acac)_3$. Among them, only the TREG results non-agglomerated Fe_3O_4 NPs with uniform shape and narrow size distribution. Their results illustrate that the polyol solvent plays a crucial role to determine the morphology and colloidal stability of the resulting particles. Hachani et al. (2016) have synthesized water-dispersible IONPs successfully via a simple and reproducible polyol synthesis tuning the size and magnetic properties by modifying the solvent, reaction time, and concentration of iron precursor $Fe(acac)_3$. The as-synthesized NPs had a high saturation magnetization (ca. 80 emu g^{-1}) but were not stable as indicated by the hydrodynamic diameter measurements and their precipitation in solution. These unstable IONPs were coated by 3,4-dihydroxyhydrocinnamic acid (IONP-DHCA) which demonstrated long-term stability, even when subjected to various salt concentrations (up to 1 M NaCl). The potential of these novel particles as MRI contrast agents is demonstrated with better relaxivity values when compared to commercial contrast agents. Miguel-Sancho et al. (2011) have synthesized TREG-coated and dimercaptosuccinic acid (DMSA)-coated SPIONs via polyol-mediated synthesis presenting particle size homogeneity (4.8 ± 2 nm) and a good initial particle size distribution, with a mean hydrodynamic size of 15.7 ± 2 nm. The modification of the TREG coating by a multistep process yielded only a moderate increase in stability of the SPION against prolonged exposure to 37 °C (exposure against increased saline concentrations was not tested) but produced a coating with terminal carboxylic groups capable of anchoring a bio-functional antibody, whereas comparatively best results were obtained with DMSA-SPIONs, which yielded a well-dispersed suspension of particles and showed excellent long-term stability, even when subjected to variations in the temperature and saline concentration. Miguel-Sancho and co-workewrs claimed that their methods to modify the surface of the NPs by TREG-coating are relatively easy to implement and use well-established chemistry and procedures and hence have the potential to be applied in a wide variety biomedical application (Miguel-Sancho et al. 2011).

Liquid-Phase Synthesis: Hybrid Nanomaterials

There is rapid progress in the development of novel materials for multimodal imaging applications, drug targeting, biosensing, and several therapies in nanomedicine and have been a area of great interest. Multimodal magnetic nanomaterials could be utilized as diagnostic, surgical, and drug delivery tools, which could help in the diagnosis and treatment of cancer and many other diseases. Owing to their small size, optional functionalization with specific biomarkers (e.g., antibodies, receptors, etc.), and combination of magnetic and fluorescent or plasmonic properties, such

nanocomposites open the unique possibility of controlled target-directed applications (Xie et al. 2017; Yu et al. 2017; Edel et al. 2016; Lim and Gao 2016; Giner-Casares and Liz-Marzán 2014). The novel material development at the microscale to nanoscale has progressed from single-particle synthesis to multi-component assemblies or hierarchical structures, where two or more pre-synthesized nanomaterials are conjugated to extract multifunctionality. These ensembles are termed as nanohybrids. The underlying focus of nanohybrids synthesis is property modulation, which results in an alteration to inherent physicochemical properties, i.e., size, shape, composition, and surface chemistry. Such changes also give rise to novel emerging properties. Size and shape modulation alongside physical or chemical functionalization are used to achieve hierarchical and heterostructures (Paek et al. 2011; Banin et al. 2014; Al-Arbash 2006; Schumacher et al. 2009; Saleh et al. 2014). Such functionalization has altered inherent surface attributes and extracted novel electronic configuration, intrinsic hydrophobicity, dissolution properties, etc., from nanoscale materials. The successes of such manipulations have further encouraged achieving a higher degree of functionality by combining multiple NPs, each possessing unique and novel advantages. For example, nanoscale iron oxide AuNPs, AgNPs, and PtNPs individually possess plasmon resonance and superior charge carrying capability, respectively. However, careful combination of two or more of these materials enhanced their functional performance as observed in the development of the first sets of bimetallic NHs. Silica, gold, and silver NPs (SiNPS, AuNPs, and AgNPs) as well as photoluminescence in the form of fluorescence (semiconductor quantum dots, e.g., CdSe or CdTe (Deng et al. 2012)) or phosphorescence (doped oxide materials, e.g., Y_2O_3), or magnetic moment (e.g., manganese or cobalt oxide NPs) (Vestal and Zhang 2003) have emerged as a broad new research field in the domain of colloids not only for their optical properties, but also for high chemical stability, catalytic use, and size-dependent properties (Hostetler et al. 1998; Sardar et al. 2009; Moon et al. 2010) and thus have gained interest over the decades because of appealing properties, such as catalytic and antibacterial activity which open perspectives in biomedical applications (Xuan et al. 2012; Ding et al. 2012; Pan et al. 2018; Xu et al. 2010). The merits of such NPs are aggregation phenomena can be avoided by protecting agents such as thiols or aminic compounds (Moon et al. 2010). There are many methods for the synthesis of small, monodisperse NPs as well as the control of the shape of such SiNPs, AuNPs, and AgNPs, can be discussed below briefly. Such multifunctional bimetallics were used as magnetic resonance imaging (MRI) agents with added nanoheating capabilities, useful for laser-irradiated drug delivery systems.

Magnetic Silica/Carbon Interface

Silica-Coated IONPs (IONP@Silica)

Silica-coated IONPs (IONP@silica) are a classical and important composite material for both fundamental study and bio-applications. Silica coating helps to enhance the

Table 3 Summary of synthesis method with their merits and demerits

Synthesis method	Merits	Demerits
Stober process	Controllable silica shell and uniform size, high crystallinity	Lack of understanding of its kinetics and mechanism
Microemulsion	Control of particle size, highly homogeneous	Poor yield, time consuming, and more amount of solvents required
Aerosol pyrolysis	Hermitically coated	Complex experimental condition

dispersion in solution because the silica layer could screen the magnetic dipolar attraction between magnetic IONPs and such coating would increase the stability of IONPs and thus protect them in an acidic environment. Since silica contains an abundant silanol groups on its layer, IONP@silica could be easily activated to provide the surface of NPs with various functional groups. Silane has unique properties that easily bind on the surface of IONPs through OH groups. For pragmatic applications, IONP should be coated with a homogeneous silica layer without core-free silica particles, regardless of the size of the NPs. For instance, as a heating source and magnetic guidance, IONPs play an important role in hyperthermia and targeted drug delivery, and the existence of core-free silica particles will lead to a loss in the effective dose of IONPs. The major reason causing uneven heating in hyperthermia and tissue distribution of the targeted drugs can be attributed to the unequal core number and silica shell thickness. Until now, mainly, three different approaches have been explored to designed IONP@silica nanomaterials; they are (a) the Stober process, (b) microemulsion method, and (c) aerosol pyrolysis method as tabulated in Table 3 with their merits and demerits (Zhu et al. 2018).

Generally, the IONPs were homogeneously dispersed in the alcohol, then after added the silane, and finally the water or ammonia aqueous solution was dropped into the mixed solution and IONP@SiO_2 formed. Tetraethoxysilane(TEOS), vinyl-triethoxysilane (VTEOS), and octadecyltrimethoxysilane are the most common used silanes (Zhu et al. 2010; Cao et al. 2013). Lu et al. (2002) have shown that how fer-rofluids can be directly coated with silica shells by the hydrolysis of TEOS. First, they have taken water-based ferrofluid (EMG 340) and diluted with deionized water and 2-propanol. Ammonia solution and various amounts of TEOS were added step-wise to the reaction mixture under stirring. The coating step was allowed to proceed at room temperature for about 3 h under continuous stirring. The coating thickness could be varied by changing the amount of TEOS. Since the iron oxide surface has a strong affinity toward silica, no primer was required to promote the deposition and adhesion of silica. Owing to the negative charges on the silica shells, these coated magnetic NPs are re-dispersible in water without the need of adding other surfac-tants. Xuan et al. (2012) have synthesized monodispersed γ-Fe_2O_3@meso-SiO_2 via Stober process. The size of the magnetic core and the thickness of the shell were con-trolled by tuning the experimental parameters. The magnetic property of the γ-Fe_2O_3 porous core enabled the microspheres to be used as a contrast agent in magnetic res-onance imaging with a high r_2 (76.5 s^{-1} mM^{-1} Fe) relaxivity. The biocompatible

composites possess a large Brunauer-Emmett-Teller (BET) surface area (222.3 m^2 g^{-1}); the composite NPs have been used as a bifunctional agent for both MRI and drug carriers. Pinho et al. (2012) noted that the increase of the silica coating thickness will cause a significant decrease in the r_1 and r_2 relaxivities of their aqueous suspensions. Likewise, Pinho et al. (2010) concluded that the amount of silane used is a key factor for tuning the silica shell thickness, and the adequate silica shell thickness can therefore be tuned to allow for both a sufficiently high response as a contrast agent and adequate grafting of targeted biomolecules. Zhao et al. (2005) have prepared uniform magnetic nanospheres having diameter 270 nm with a magnetic core and a mesoporous silica shell through Stober process. These NPs were double coated with mesoporous silica shell by a simultaneous sol–gel polymerization of TEOS and n-octadecyltrimethoxysilane (n-OTMS).

The microemulsion syntheses, in which micelles or inverse micelles, were used to confine and control the coatings of silica over, core NPs. It is noteworthy that this method requires much effort to separate the core–shell NPs from the large amount of surfactants associated with the microemulsion system. Tartaj and Serna (2003) reported a synthesis of monodisperse air-stable superparamagnetic α-Fe nanocrystals encapsulated in nanospherical silica particles of 50 nm in diameter. The iron oxide NPs are embedded in silica by the reverse microemulsion technique, and the α-Fe is obtained by reduction with hydrogen at 450 °C. Vestal and Zhang (2003) discussed a reverse micelle microemulsion approach which was also reported to coat a layer of silica around spinel ferrite NPs of $CoFe_2O_4$ and $MnFe_2O_4$. Cheng et al. (2012) presented a straightforward synthesis method for magnetically functionalized silica nanotubes, i.e. (Fe_3O_4-CNTs)@SiO_2. First, they prepared Fe_2O_3-CNT@SiO_2 and reduced to Fe_3O_4-CNT@SiO_2 in the presence of Ar at 800 °C for 8 h and finally the obtained Fe_3O_4-CNT@SiO_2 oxidized to γ-Fe_2O_3@SiO_2. The method employs carbon nanotube templates and can be easily scale up to achieve economic and fast production of the material. The material exhibits a considerable magnetization and has a hollow structure which suggests applications with multifunctional character. Their experiments indeed show that local heating is induced by applied alternating magnetic fields which showed the materials' potential for magnetic hyperthermia therapies, as increasing temperature with the application of magnetic field, as shown in Fig. 1.6. However, this heating of nanoparticles in higher field (>50 kA/m) is just to have an idea of change in temperature, not recommended for clinical test. In addition, it can serve as a drug carrier system since a significant amount of rhodamine B was loaded to the material and its release was studied. Interestingly, encapsulated magnetic NPs divide into two differently sized portions, i.e., into particles in the 10 nm and in the 100–200 nm range, respectively. This behavior may be exploited for different magnetic functions since small particles are beneficial when aiming at magnetic hyperthermia while larger particles are needed if an external magnetic field gradient shall exert force for moving particle.

Ding et al. (2012) reported the coating regulations of Fe_3O_4 NPs by the reverse microemulsion method to obtain Fe_3O_4@SiO_2 core–shell NPs. Such regulation produces core–shell NPs with a single core and with different shell thickness and especially can be applied to different sizes of Fe_3O_4 NPs and avoid the formation of
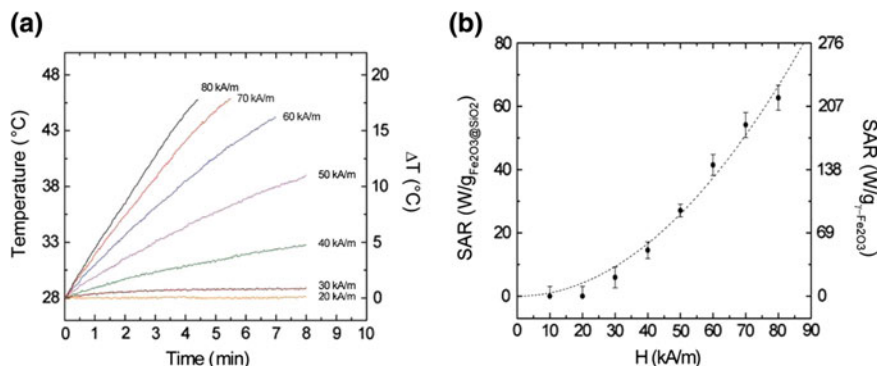
Fig. 1.6 **a** Temperature versus time upon application of AC magnetic fields at various field strengths and a frequency of $f = 120$ kHz and **b** corresponding SAR value for the γ-Fe_2O_3@SiO_2. Reprinted with permission from Chen et al. (2012). Copyright 2012 American Chemical Society

core-free silica particles. They found that the small aqueous domain was suitable to coat ultrathin silica shell, while the large aqueous domain was indispensable for coating thicker shells. To avoid the formation of core-free silica particles, the thicker silica shells were achieved by increasing the content of either TEOS through the equivalently fractionated drops or ammonia with a decreased one-off TEOS. Ye et al. (2012) have synthesized Fe_3O_4@$mSiO_2$ NPs and performed an in-depth study of the effects of surface coating on relaxivities of iron oxide particles for MRI. Tunable relaxivities were obtained by varying the thickness of the $mSiO_2$ coating layer of Fe_3O_4@$mSiO_2$ NPs. It was found that r_1 shows a dramatic decrease accompanied by a smaller decrease in r_2, with an increase in $mSiO_2$ coating thickness. Consequently, Fe_3O_4@$mSiO_2$ NPs exhibit enhanced MRI efficiency, which is ca. 21 times higher than that of the commercial T_2 contrast agents. They studied biocompatibility of obtained NPs and found that Fe_3O_4@$mSiO_2$ NPs have no negative impact on cell viability, which supports the potential application of these particles as a highly efficient and biocompatible MRI T_2 contrast agent.

Carbon-Coated IONPs (IONPs@C)

Carbon has unique chemical, thermal stability, and high electrical conductivity properties. Due to this reason, carbon and its isomer have been used widely in material science as protecting agents.

The carbon coating provides an effective oxidation barrier and prevents corrosion in magnetic core materials. Hydrophilic carbon coating on iron oxide nanoparticle cores endows better dispersibility and stability than those shown by bare IONPs (Bae et al. 2012). Park and Myung (2014) have shown schematic synthesis process regarding the carbon-coated magnetite nanoparticles, as shown in Fig. 1.7. They proposed that, as soon as the crystal seeds of Fe_3O_4 are formed under the synthesis
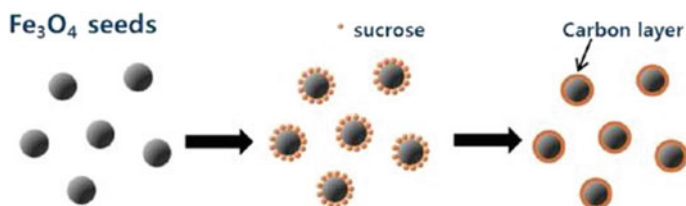
Fig. 1.7 Schematic synthesis of Fe_3O_4@C. Reprinted with permission from Park and Myung (2014). Copyright 2014 American Chemical Society

condition, the seeds are simultaneously encapsulated by sucrose in the solution and carbonization of the sucrose is consequently progressed and finally magnetite covered by carbon layer. As it can be clearly seen in Fig. 1.7, there is no possibility of contact among Fe_3O_4 seeds after the carbonization; particle growth such as carbon-free Fe_3O_4 would be inhibited.

Bae et al. (2012) have synthesized highly water-dispersible carbon-coated core–shell iron oxide NPs for use as contrast agents in MRI. The coated NPs were observed to be spherical in shape, and they showed a uniform size distribution with an average diameter of 90 nm. They found the ratio of two relaxivities, i.e., T_1 and T_2, was close to unity which shows that carbon-coated iron oxide NPs are suitable as both T_1 and T_2 contrast agents in MRI.

Graphene oxide (GO) has recently attracted substantial attention in biomedical field as an effective platform for biological sensing, tissue scaffolds, and in vitro fluorescence imaging. However, the targeting modality and the capability of its in vivo detection have not been explored. In this scenario, to enhance the functionality of GO, Gonzalez-Rodriguez et al. (2019) synthesized GO/Fe_3O_4 NPs with average size of 260 nm having low cytotoxicity and higher r_2/r_1 relaxivity ratios of ~10.7 than of GO as shown in Fig. 1.8.

The pH-sensing capabilities of GO used to detect cancer versus healthy environments in vitro and exhibit fluorescence in the visible for bioimaging. On the other hand, as a drug delivery platform, GO/Fe_3O_4 showed successful fluorescence-tracked transport of hydrophobic doxorubicin non-covalently conjugated to GO with substantial loading and 2.5-fold improved efficacy. With these results, Gonzalez-Rodriguez et al. (2019) concluded that GO/Fe_3O_4 NPs as a novel multifunctional magnetic targeted platform for high efficacy drug delivery traced in vitro by GO fluorescence and in vivo via MRI capable of optical cancer detection.

Magnetic Plasmonic Interface

Plasmonic NPs have unique properties involving surface plasmon resonance phenomena and enabling to achieve the intensive selective absorption or scattering of light that is widely used in sensing, bioassays, diagnostic tools, photothermal and
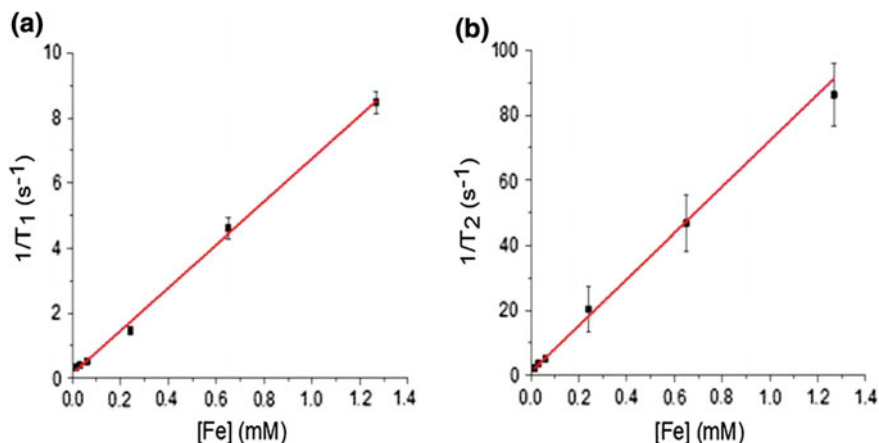
Fig. 1.8 **a** $1/T_1$ versus iron concentration [Fe] of GO-Fe$_3$O$_4$ conjugates and **b** $1/T_2$ versus [Fe] of GO-Fe$_3$O$_4$ conjugates, the bars represent the standard deviation. Reprinted with permission from Gonzalez-Rodriguez et al. (2019). Copyright 2019 Gonzalez-Rodriguez et al.

photodynamic therapy, and other biomedical applications (Xie et al. 2017; Yu et al. 2017; Edel et al. 2016; Lim and Gao 2016; Giner-Casares and Liz-Marzán 2014). Nowadays, a range of synthetic methods is utilized to produce monodisperse, stable suspensions of magnetic plasmonic nanocomposites. Generally, magnetic plasmonic nanomaterials consist of an inner magnetic core and an outer plasmonic layer which are synthesized by chemical co-precipitation, thermal decomposition, and the solvent thermal method, etc., as discussed above in synthesis portion. In principle, one-step route to prepare magnetic plasmonic nanoparticle is Fe$_{3-x}$O$_4$ surface directly coated by an Au/Ag layer. This implies that Au atoms are directly deposited onto Fe$_{3-x}$O$_4$ through the reduction of Au(III) precursors. If the system is reverse, i.e., Au/Fe$_{3-x}$O$_4$, then Fe$_{3-x}$O$_4$ core surface must be appropriately charged to attract the dissolved molecular Au(III) precursors. The schematic view of the formation of magnetic/plasmonic core–shell/satellites is shown in Fig. 1.9a. This method can be accomplished in the absence of surfactant and completed in a one single step, but it does not allow a simple control of the final morphology of the built heterostructures (Nguyen et al. 2018). Pan et al. (2019) proposed an innovative method for the synthesis of magnetic Fe$_3$O$_4$ nanostructures without any capping agents. The synthesis strategy was based on plasmon-driven anti-replacement reaction. The complete synthesis process was completed in several steps. First, fabrication of Au nanoparticles by 1064-nm pulsed laser ablation in water; then after, a mixture solution containing the Au nanoparticles and FeCl$_3$ was irradiated by a laser with a specific wavelength. The plasmonic-driven anti-replacement reaction between Au and Fe^{3+} ions occurs. Finally, the spindle-like single-crystalline Fe$_3$O$_4$ nanocrystals were collected after the reaction. The prepared Au NPs are single crystalline with average diameter of ca. 220 nm, well-defined lattice fringes with an inter-planer spacing of 0.236 nm, which is well consistent with that of the Au(111) crystalline planes. After irradiating
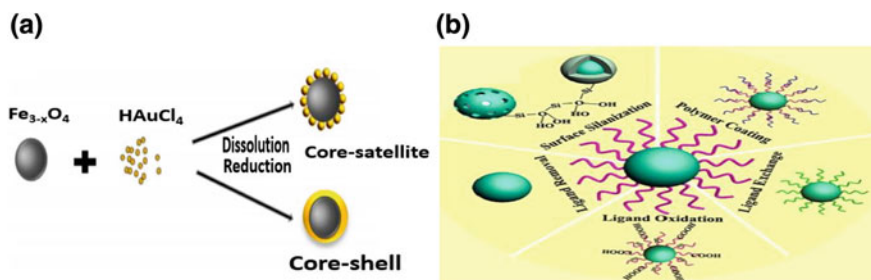
Fig. 1.9 **a** Schematic view of the formation of magnetic/plasmonic core–shell/satellites. Reprinted from Nguyen et al. (2018), Open access, **b** schematic illustration of several strategies used for surface modification of UCNPs, which include inorganic surface silanization, ligand removal, ligand oxidation, ligand exchange, and amphiphilic polymer coating. Reprinted with permission from Sun et al. (2018b). Copyright 2018 Elsevier B.V. All rights reserved

the mixture of $FeCl_3$ and Au NPs by 532 nm laser, spindle-like nanostructures of ca. 100 nm in length and ca. 15 nm in diameter attached on Au NPs were occurred. The spindles accumulate on the surface of Au NPs. The saturation magnetization and coercivity of Fe_3O_4 spindles are 48.7 emu g^{-1} and 218.9 Oe, respectively.

Lee et al. (2012) have been developed a simple but efficient route for the synthesis of spherical Fe_3O_4@Au NPs. The resulting Fe_3O_4@Au NPs have a size of ∼20 nm and strong magnetization via sodium citrate-coated Fe_3O_4 NPs; sodium citrate is used as the sole reducing agent. Cui et al. (2005) presented a synthetic method for the core–shell NPs with a typical size of 50 nm in diameter and practical use of the particles in a solid-phase immunoassay. Zhichuan et al. (2007) described facile synthesis of Au- and Ag-coated Fe_3O_4 NPs with controlled plasmonic and magnetic properties. The plasmonic properties of these core–shell NPs can be fine-tuned by varying the coating thickness and coating material. Bao et al. (2009) reported the synthesis of Fe_2O_3@Au NPs with varying Au shell thickness by reducing $HAuCl_4$ on the surface of α-Fe_2O_3 NPs. Bao et al. (2007) reported that the synthesis of multifunctional core–satellite Fe_3O_4@Au NPs (Type IB) occurs via the chemical bonds of two separate prepared nanomaterials, not via a chemical deposition process. This synthesis can be used for the isolation of a protein, which would still retain strong catalytic activity afterward. The as-prepared bifunctional NPs combine the merits of both gold and Fe_3O_4 NPs and are formed via chemical bonds. Containing approximately 12% gold by weight, the resulting bifunctional NPs maintain excellent magnetic properties.

Magnetic Luminescent Interface

Those materials having the properties of absorption and conversion certain types of energy into radiation of light can be considered as luminescence materials (also

called phosphors). When luminescent particles (organic compounds, polymers, quantum dots, rare earth-based UV-excited or upconversion phosphors) are incorporated into the shells, which could bind with microorganisms (binding with antibodies, antigens, polypeptides, etc.) or tumor tissue, the biocomplex can be localized by irradiation with UV or NIR light. After that due to luminescent and magnetic (optionally) properties, the biocomplex can be cured or removed. Also, drug delivery could be enhanced using magnetic NPs (Wang and Xia 2004; Nyk et al. 2008; Selvan et al. 2010; Yang et al. 2009). Rare earth (RE) ions (including lanthanides plus scandium and yttrium) are trivalent, an important and attractive candidate for several applications due to having better luminescence properties than other materials. It is known that lanthanide (Ln) ions are widely used as emitting species in many phosphors. However, direct excitation of lanthanide ion (Ln^{3+}) is a relatively inefficient process due to the forbidden character of the 4f transitions. So, a doping technique is widely applied to synthesize Ln^{3+}-doped inorganic materials with desirable luminescence. So far, although a series of luminescent materials including fluorescent proteins (Shcherbakova et al. 2015), organic dyes, metal complex (He et al. 2014), semiconductor quantum dots (QDs) (Deng et al. 2012), etc., have been developed for luminescent contrast agents and bio-applications, upconversion NPs (UCNPs) have emerged as more appropriate nanomaterials for bio-applications, for instance biomarkers, drug delivery, cells' labeling, sensitive to magnetic field NPs for the photodynamic therapy (PDT) and photothermal therapy (PPT) (Sun et al. 2010; Mi et al. 2010).

Generally, UCNPs synthesized by the several known methods (i.e., chemical co-precipitation, thermal decomposition, and the hydro/solvent thermal), as they are capped by oleic acid (OA) or oleylamine (OM), which delimit their bio-applications in vitro and in vivo. To be successfully used in biomedical (usually bioimaging and therapy), UCNPs should have good dispersibility and biocompatibility in aqueous solution by using surface modification to provide them with hydrophilic groups such as –COOH, $-NH_2$, –OH for further conjugation with various biomolecules. Recently, several strategies have been reported, including inorganic surface silanization, ligand removal, ligand oxidation, ligand exchange, and amphiphilic polymer coating, as shown in Fig. 1.9b (Sun et al. 2018b). Mou et al. (2017) have successfully synthesized a new Luminescence Resonance Energy Transfer (LRET)-based nanoprobe by using the mesoporous silica-coated lanthanide upconversion $NaYF_4$:Yb, Er@NaGdF$_4$ UCNPs as the luminescence energy donor and Cu^{2+}-responsive rhodamine B derivative DFPP-RhBas energy acceptor, shown in Fig. 1.10. The limit of detection is as low as 54 nM. Meanwhile, a color change from colorless to pink can be observed by naked eye with the addition of Cu^{2+}. The synthetic LRET nanoprobe shows high specificity and selectivity for detecting Cu^{2+}. They synthesized such multifunctional nanoprobe, i.e., UCNPs@mSiO$_2$-P by dissolving UCNPs@mSiO$_2$ with toluene as per requirement. When the mixture was heated to 110 °C, 3-(Triethoxysilyl) propylisothiocyanate was added. The mixture was refluxed under argon for 24 h. After cooling to room temperature, DFPP-RhB was added and the mixture was refluxed for another 24 h. The NPs were washed several times with
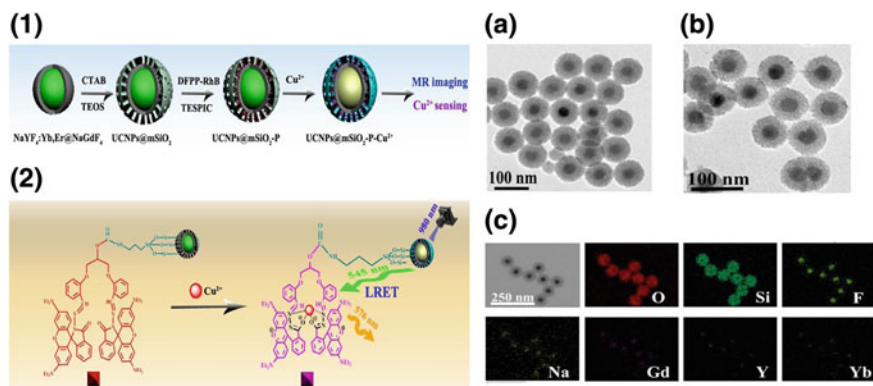
Fig. 1.10 (1) Schematic illustration of synthetic procedure of the nanoprobe UCNPs@mSiO$_2$-P and (2) its interaction with Cu^{2+} ions (2) and TEM images of UCNPs@mSiO$_2$ (A), UCNPs@mSiO$_2$-P (B) dispersed in ethanol. Elemental mappings (O, Si, F, Na, Gd, Y, Yb) of UCNPs@SiO$_2$-P (C) in ethanol. Reprinted with permission from Mou et al. (2017). Copyright 2017 Elsevier B.V. All rights reserved

anhydrous ethanol. As a biomedical test, the effective T_1-weighted MRI enhancement reveals the concentration-dependent brightening effect due to the presence of Gd^{3+} ions. It was successfully applied for magnetic resonance imaging and as an excellent indicator for Cu^{2+} sensing. According to authors, this is the first example of a DFPP-RhB-modified UCL nanostructure for both sensing and imaging application.

Zhang et al. (2013) prepared iron oxide NPs of about 10 nm coated with fluorescent mesoporous silica for neutral progenitor cell MRI. The material demonstrated high magnetic resonance sensitivity and excellent cell labeling efficiency. Zhang et al. (2017) have presented multifunctional core–shell (CoFe$_2$O$_4$@MnFe$_2$O$_4$) nanostructures coated with tetramethylrhodamine-5-carboxamidecadaverine labeled poly(isobutylene-alt-maleic anhydride), PEG via thermal decomposition method and functionalized with folic acid for targeting demonstrated good biocompatibility, high T_2 relaxation values, and long-term fluorescence stability. These fluorescent magnetic nanocomposites have been used to effectively enhance the targeted MRI and fluorescent labeling in vitro and in vivo.

Xu et al. (2010) prepared highly biocompatible luminescent superparamagnetic nanocomposites that consisted of Fe$_3$O$_4$@SiO$_2$-QDs, as shown in Fig. 1.11. First of all, silica shell was coated onto the magnetic particles to form the Fe$_3$O$_4$@SiO$_2$ structure by a hydrolysis sol–gel process and these functional NPs were combined with CdSe/ZnS by thiol coordination. The water-soluble QD solution was then added quickly to the Fe$_3$O$_4$@SiO$_2$-SH solution, and the product was left to stir in a 35 °C water bath for 12 h. Finally, orange particles were separated with a magnet from the solution, and this phenomenon indicated that nanocomposites with magnetic IO particles and fluorescent QDs had been assembled successfully. These NPs acted as a high-efficiency radio frequency (RF) absorber and showed optical ability for cell
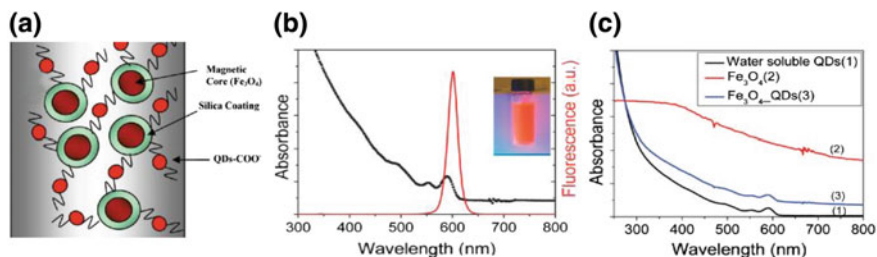
Fig. 1.11 **a** Schematic structure of iron oxide quantum dot, **b** absorption spectrum and fluorescence spectrum of CdSe/ZnS. Insert picture is the orange QD solution under the UV radiation and **c** absorption spectra of different nanomaterials. Reprinted with permission from Xu et al. (2010). Copyright 2010 American Chemical Society

labeling that make it an interesting material for use as a hyperthermia agent in pancreatic cancer therapy. Ortgies et al. (2016) have synthesized fluorescent magnetic nanomaterial with interesting properties to be used in hyperthermia in the combination of magnetic NPs and IR emitting. The nanocomposite allows monitoring of the distribution of the NPs in vivo, which is important for MRI and optical imaging-based tomography and also presents potential for magnetic hyperthermia treatments. de Paula et al. (2017) designed magnetic nanoemulsions loaded with citrate-coated maghemite NPs and chloroaluminum phthalocyanine which have been used as agents for in vitro combined magnetic hyperthermia and photodynamic therapy (at 670 nm wavelength) in the treatment of different cancer cell line models. They found that the use of magnetic hyperthermia resulted in only 15% of the cell viability reduction, while the use of only photodynamic therapy treatment yielded a 52% decrease in the cell viability. Interesting is the total reduction of the cell viability about 70% was achieved by combining the magnetic hyperthermia and photodynamic therapy treatments, and hence, the combined treatment of HPT and PDT represents a promising paradigm for brain cancer intervention, such as glioblastoma.

Shrivastava et al. (2017) have designed magnetic luminescence nanocomposites containing triply-doped $Fe_3O_4/ZnS@LaF_3:xCe^{3+}, xGd^{3+}, yTb^{3+}$ ($x = 5$; $y = 5$, 10, 15 mol%) successfully by a multistep synthesis procedure in which ZnS was used as a spacer between the direct linkage of Fe_3O4 and green $LaF_3:RE^{3+}$ phosphors played its role well. First, they prepared magnetite (Fe_3O_4) through simple hydrothermal method. Then after, certain amount of obtained magnetite dispersed in the mixture of n-propanol and $Zn(O_2CCH_3)_2(H_2O)_2$ in balance condition and stirred 24 h at room temperature. Thereafter, thioacetamide in milli-Q water was added dropwise to the above solution. Such resulting solution was heated at 65 °C under vigorous stirring for 5 h and cooled to get Fe_3O_4/ZnS. Finally, the optical and magnetic $Fe_3O_4/ZnS@LaF3:xCe^{3+}, xGd^{3+}, yTb^{3+}$ ($x = 5$; $y = 5$, 10, and 15 mol%) nanomaterials were prepared by the chitosan-assisted co-precipitation method through a general procedure using a specific amount of Fe_3O_4/ZnS NPs and stoichiometric amounts of $LaCl_36H_2O$, $Ce(NO_3)_3·6H_2O$, $GdCl_36H_2O$, and $TbCl_36H_2O$ precursors. The complete synthesis protocol is shown in Fig. 1.12 (Shrivastava et al. 2017).
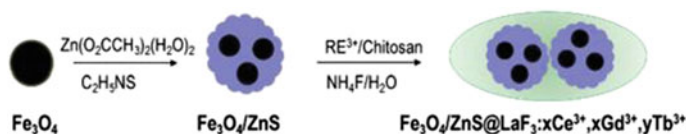
Fig. 1.12 Synthesis scheme for the $Fe_3O_4/ZnS@LaF_3:xCe^{3+}$, xGd^{3+}, yTb^{3+} ($x = 5$, $y = 5$, 10, 15 mol%) bifunctional green emitting magnetic nanocomposites (Shrivastava et al. 2017)

From magnetic and luminescent experimental investigation, they concluded that their magneto-luminescent bifunctional nanocomposite may act as a good candidate for the preparation of emitting layers in magnetic and light-converting molecular devices (MLCMDs) and radiation detection or in downshift applications through magnetic manipulation.

Nucleation and Growth of NPs in Solutions

To understand unique properties and classic laws followed by NPs, many researchers from different areas of physics, chemistry, biology, and material science have been synthesizing the particles in nanoscale. However, complete cognition of different phenomena of magnetic NPs, for instance, finite size effect and surface effect are still remains and area of great interest (Hergt et al. 2006; Nalwa 2004). Finite size effect discusses with superparamagnetism, single/multi-domain and quantum confinement of electron. On the other hand, surface effects result from the symmetry breaking of the crystal structure at the surface of the particle, oxidation, dangling bonds, existence of surfactants, surface strain, or even different chemical and physical structures of internal 'core' and 'surface'—shell parts of the nanoparticle. Due to such well-known effect, the design of magnetic NPs for different biomedical applications is not easily implemented. There are many factors that should be taken into consideration at each and every step of the synthesis which can dramatically change the expected outcome. Both physical and chemical properties of particles can be controlled to fit various applications, so such applications have been surprisingly slow to emerge. This is partially due to the difficulty in the development of reliable and reproducible methods for producing large quantities of un-agglomerated, uniformly sized material. NPs can be produced via vapor and liquid-phase synthesis methods. The problems such as agglomeration and non-uniformity of particle size appeared in vapor phase synthesis can potentially be reduced by following the liquid-phase synthesis route, since various methods of this type yield un-agglomerated and relatively monodisperse ($\sigma < 10\%$) NPs (Murray et al. 2000). The classic studies of La-Mer et al. (LaMer and Dinegar 1950) have shown that the production of monodisperse colloids requires temporal separation between nucleation and nanoparticle growth NPs. Thus, we need to understand the mechanism of nucleation and growth of NPs in solution before start to synthesis that might help to control NPs during synthesis. So we are discussing

the theory of nucleation of NPs in solution and growth mechanism behind it with some examples in the following sections.

Theory of Nucleation

Nucleation refers to the extremely localized building of a distinct thermodynamic phase and represents the first stages during a crystallization process. Usually, the first formation step of the solid phase from the solution is considered as nucleation. More specifically, it is defined as the process by which building blocks (metal atoms in the synthesis of metal nanomaterials) arrange themselves according to their crystalline structure to form a site upon which additional building blocks can deposit over and undergo subsequent growth. In this context, nuclei correspond to infinitesimal clusters consisting of very few atoms of the growth species. The growth process of NPs in solution consists of two phenomena: (i) nucleation followed by (ii) growth of NPs/crystals. To understand the mechanism process to form colloids/NPs from supersaturated and homogeneous medium, La Mer and Dinegar (1950) have been studied the synthesis of uniform colloids/sulfur sol with nucleation and growth mechanism. From this study, he introduced the concept of 'burst nucleation,' which pertains to the formation of a large number of nuclei in a very short period of time, i.e., rapidly, followed by growth without additional nucleation. This allows nuclei to have similar growth histories and, therefore, yield NPs with the same sizes. This concept is referred to as the separation of nucleation and growth stages during the synthesis.

Supersaturation is usually defined as the difference between the chemical potential of the solute molecules in the supersaturated (μ) and saturated (μ_s) states, respectively. In thermodynamic, the chemical potential is also known as the partial molar free energy (Denis et al. 2009; Davey et al. 2015).

$$\Delta\mu = \mu - \mu_s = K_B T \ln S \tag{1.1}$$

where K_B is Boltzmann constant, T is temperature, and S is supersaturation which dimensionless and can be calculated further as taking ratio between concentration of the solute in solution C_i and saturated/equilibrium concentration of the solute C_o, i.e.,

$$S = \frac{C_i}{c_b} \tag{1.2}$$

if $S > 1$, nucleus grows and solid phase formed; if $S < 1$, nucleus dissolves, and if $S = 0$, nucleus and solution are in equilibrium. The supersaturation of growth species comprises the first requirement for the occurrence of homogeneous nucleation. When the concentration of a solute in a solvent exceeds its equilibrium solubility or temperature decreases below the phase transformation point, a new phase appears with the formation of a large number of nuclei in a short space of time. Such NPs thrive

quickly and lower the concentration below nucleation level allowing further growth at the slowest rate by which nucleation and growth have been separated in time. This slow rate of growth leading toward long growth period compared to the nucleation period. When an unknown form of material is crystalized during nucleation, it is 'primary nucleation,' and if nuclei are engendered in the vicinity of solid surface in saturated system, it is referred as 'secondary nucleation' (Coquerel 2014; Mullin 2001). When the burst-nucleated supercritical particles are largely consumed by the secondary aggregation, we can instead assume that these primary particles are captured fast enough by the growing secondary particles so that the effect of their aging on the concentration of solutes can be ignored. Furthermore, the radius of the captured primary particles will be assumed close to the critical radius. The growth rate, obtained from theoretical approach, allowed predicting the diffusion coefficient of sulfur and they claimed that the method under which diffusion coefficient has been calculated is applicable for all colloidal system which was characterized by small particle size distribution. In addition, some qualitative approach was drawn to prepare the monodispersed colloids by both acid decomposition of sodium thiosulfate. This mechanism is applied to prepare several monodispersed particles in homogeneous solution; however, this is not a generalized approach to the synthesis of different systems. Thus, La Mer mechanism of nucleation is suitable for is sulfur sols, and it may not have significance as a general approach to a wide variety of systems (And and Finke 1997; Oskam et al. 2003; Ji et al. 2007).

Classically, the formation of homogeneous nuclei is discussed by thermodynamically. Maris (2006) discussed the concept of Gibbs free energy (G) nucleus formation when the concentration of solute exceeds its supersaturated state. This energy is of the system which would be reduced by isolating solute from solution and is equal to sum of surface free energy μ_s and volume free energy μ_v, also called bulk free energy. The free surface energy μ_s is directly varied by the interfacial tension γ between the solid particle surface and the surrounding solution. When the radius of nuclei increases, interfacial tension also increases, and hence, positive change can be observed in free surface enthalpy. In contrast, volume free energy μ_v is proportional to the negative of volume nucleus. The reduced free energy is considered as driving force for both nucleation and growth. Let C_i, C_o, V_n, and S are the concentration of the solute, equilibrium concentration, atomic volume, and the supersaturation respectively; then, bulk free energy ΔG_v per unit volume of solid phase is dependent on concentration of solute and is given by,

$$\Delta G_v = -\frac{kT}{V_n} \ln \frac{C_i}{C_o} \qquad (1.3)$$

where $S = C_i/C_o$, no nucleation if $S = 0$. When $C_i > C_o$, ΔG_v is negative, and nucleation occurs simultaneously. Let r be the radius of spherical nucleus; then Gibbs free energy or volume energy is given by,

$$\Delta \mu_v = \frac{4}{3}\pi r^3 \Delta G_v \qquad (1.4)$$

And the surface free energy which counterbalanced the reduction energy during the nucleation is given by,

$$\Delta\mu_s = 4\pi r^2 \gamma \qquad (1.5)$$

Thus, total free energy of nanoparticle is the sum of Eqs. (1.2) and (1.3) given by,

$$\Delta G = \frac{4}{3}\pi r^3 \Delta G_v + 4\pi r^2 \gamma \qquad (1.6)$$

Approximately, free surface energy is proportional to the size of nucleus and can be expressed as

$$\Delta\mu_s \approx A_n \approx r^2 \qquad (1.7)$$

whereas volume free energy $\Delta\mu_v$ can be written as

$$\Delta\mu_v \approx V_n \approx r^3 \qquad (1.8)$$

here, where A_n is surface of nucleus and V_n is volume nucleus

From Fig. 1.13a, we can say that newly formed nucleus is stable its radius exceeds critical size r^*. At $r = r^*$, $\frac{d\Delta G}{dr} = 0$ that gives critical free energy ΔG^* called barrier energy which must be overcome for the nucleation, i.e.,

$$R^* = -\frac{2\gamma}{\Delta G_v} \quad \text{and} \quad \Delta G^* = \frac{16\pi \gamma}{3(\Delta G_v)^2} \qquad (1.9)$$
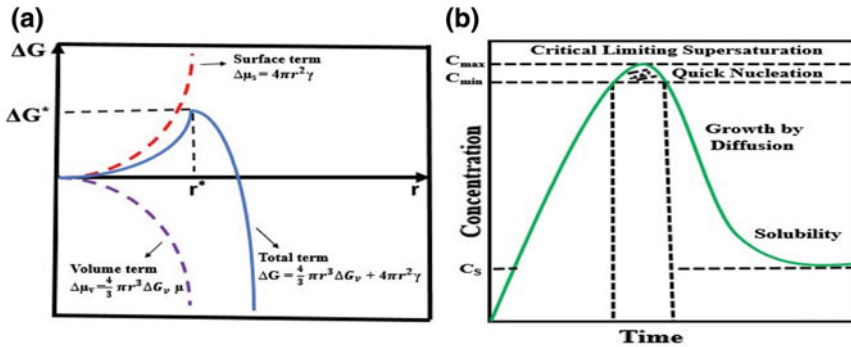
Fig. 1.13 **a** Schematically shows the change of volume free energy, $\Delta\mu_v$, surface free energy, $\Delta\mu_s$, and total free energy, ΔG, as functions of nucleus radius, and **b** processes of nucleation and subsequent growth of nanoparticle in solution. Reprinted with permission from Zhang et al. (2012). Copyright 2012 American Chemical Society

when the nucleus radius smaller than critical radius r^* will dissolve into the solution to reduce the overall free energy, whereas a nucleus larger than r^* is stable and continues to grow bigger to the final crystallized particles. In the synthesis and preparation of NPs or quantum dots by nucleation from supersaturation solution or vapor, this critical size represents the limit how small NPs can be synthesized. To reduce the critical size and free energy, one needs to increase the change of Gibbs free energy, ΔG_v, and reduce the surface energy of the new phase, γ. The Gibbs–Thomson equation shows that the energy barrier for nucleation at the maximum supersaturation (S_m) is proportional to temperature (Zhang et al. 2012; Thanh et al. 2014). Figure 1.13b schematically illustrated the processes of nucleation and subsequent growth. From Fig. 1.13b, as the concentration of solute increases as a function of time, no any nucleation would occur even above the equilibrium solubility. The nucleation occurs only when the supersaturation reaches a certain value above the solubility, which corresponds to the energy barrier (ΔG^*) for the formation of nuclei. After the initial nucleation, the concentration or supersaturation of the growth species decreases and the change of volume in Gibbs free energy reduces. If the concentration decreases below this certain concentration, which corresponds to the critical energy, no more nuclei would form, whereas the growth will proceed until the concentration of growth species reached the equilibrium concentration or solubility.

Growth Mechanism

Let us start with burst nucleation concept as introduced above by LaMer and Dinegar (1950). The model of burst nucleation is appropriate for nanosize particles, typically, crystals consisting of n monomers. For larger particles, nucleated in the initial burst and then grown to dimensions typically over several tens of nanometers in diameter, other growth mechanisms usually broaden the size distribution. We have already mentioned in the above section that there must be two-stage mechanism whereby the nanosized primary particles, burst nucleated and growing in solution, themselves become the singlets and are 'consumed' by the singlet-driven aggregation that results in uniform secondary particles of colloid dimensions clearly shown in Fig. 1.14a–c.

The theoretical model given by LaMer's for the synthesis of monodisperse particles is a concept of separating nucleation and growth and helps to predict the final size distribution of NPs analyzing the actual growth of nuclei. Later, Reiss (1951)
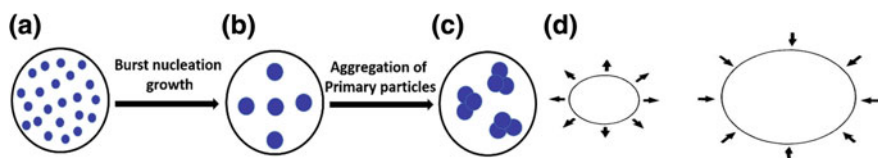
Fig. 1.14 **a** Supersaturated solution, **b** primary particles, and **c** secondary particles, and **d** concept of Ostwald's ripening

developed a growth model known as 'growth by diffusion' in which the growth rate of spherical particles depends solely on the monomer flux supplied to the particles. Reiss deduced that if the diffusional growth is only dependent on the monomer flux, smaller particles will then grow faster in the presence of larger particles, leading to a size focusing (narrowing of size distribution). However, this is a very simplified mechanism since it does not include other effects such as aggregation, coalescence, or dissolution (Ostwald's ripening). Sugimoto (1987) extended Reiss's model qualitatively by including dissolution effects obtaining a size-dependent growth rate by considering the Gibbs–Thomson equation. When the concentration of solutes/monomer's falls below certain nucleation level, called super-saturation, nucleation stops, but the growth of NPs is continuing. Usually, in NPs, large surface area of NPs creates higher surface energy which may play an important role in the particle growth. This growth of NPs placed in two mechanisms: diffusion to the surface and surface reaction.

Let us consider r be the radius of particles, J be the total flux of monomers passing through spherical surface having radius x, D is the diffusion coefficient, and C is the concentration at distance x, and then total flux of monomers is given by Fick's first law,

$$J = 4\pi D x^2 \frac{dC}{dx} \tag{1.10}$$

Let C_b be the bulk concentration of monomers in solution, C_i be the concentration of the monomers at solid/liquid interface, and δ be the distance between particle surface to bulk concentration of monomers in solution, also called thickness of diffusion layer, and J is the constant over diffusion layer at steady state; then, it can be written as,

$$J = \frac{4\pi D r(r + \delta)}{\delta}(C_b - C_i) \tag{1.11}$$

Integrating (1.15) from $r + \delta$ to r, we get

$$J = 4\pi D r(C_b - C_i) \tag{1.12}$$

This flux can be equated to the consumption rate of the monomer species at the surface of the particle. That is,

$$J = 4\pi D r^2 k(C_i - C_r) \tag{1.13}$$

where k is rate of surface reaction which is independent of particle size. But in solution, it is difficult to find out the C_i, so it must be eliminated using the above two equations.

Now if the growth process is controlled by diffusion of growth species from bulk solution to particle surface, then growth rate is given by,

$$\frac{\mathrm{d}r}{\mathrm{d}t} = \frac{Dv(C_b - C_r)}{r} \tag{1.14}$$

where v is the molar volume of the bulk crystal and C_r is the concentration on the surface of solid particle. The growth controlled by diffusion promotes the formation of uniformly particles size.

But, when the diffusion of growth species from the bulk to the growth surface is sufficiently rapid, i.e., the concentration on the surface is the same as that in the bulk, the growth rate controlled by surface process and the rate is given by,

$$\frac{\mathrm{d}r}{\mathrm{d}t} = kv(C_b - C_r) \tag{1.15}$$

There are two mechanisms which consist of surface reaction process, i.e., mono-nuclear growth and poly-nuclear growth. In mono-nuclear growth, the growth of species is incorporated with layer by layer; i.e., next layer growth will be placed only after the first layer growth is completed so that more time required to diffuse on the surface. Conversely, poly-nuclear growth of species will occur when surface concentration is high by which growth of next layer can be started before completed the growth of first layer and growth rate is linear with time. According to William et al., growth of NPs consists of these all three mechanism according to their size. The mono-nuclear growth is occurred in small nuclei, poly-nuclear growth may be predominant if the nuclei become bigger, and diffusion is predominant in case of larger particles. Thus according to the growth condition of the NPs, different mechanisms may be the predominant.

Thus, in summary, the crystal growth process in solution mainly consists of nucleation and growth, which are affected by the intrinsic crystal structure and the external conditions including the kinetic energy barrier, temperature, time, capping molecules, and so forth. The formation of nanostructures after nucleation in solution relates to two primary mechanisms: the aggregation growth process and the Ostwald's ripening process. Crystal growth by aggregation can occur by random aggregation and oriented aggregation, and Ostwald's ripening process involves the growth of larger crystals at the expense of smaller ones (LaMer and Dinegar 1950; Reiss 1951; Sugimoto 1987; Yin et al. 2009).

Ostwald's Ripening

Ostwald's ripening, also referred as 'coarsening', is a final stage of first-order phase transformations following nucleation and growth stages and is often observed in synthesis of NPs (Mantzaris 2005), two-phase mixtures composed of second phase in matrix (Voorhees 1992), binary alloys (Porter and Easterling 1992), clusters on surfaces (Zinke-Allmang et al. 1992), oil–water emulsions, and during epitaxial growth (Taylor 2003). Ostwald's ripening represents (for instance, shown in Fig. 1.14d) the

spontaneous and continuous evolution of precipitated NPs/clusters, during which smaller NPs/clusters of atoms/molecules transfer mass to bigger clusters. According to Ostwald, the driving force for the process is the increased solubility of the smaller particles due to surface tension between the precipitate and the solute. In case of, solute is in local equilibrium with the precipitate, then the solubility difference induces a solute concentration gradient and leads to a diffusive flux from the smaller to the larger particles. The objective to introduce the driving force for Ostwald's ripening is the minimization of the interfacial area between the two phases and as such depends intimately on the interface energetics and the system temperature. The driving force for the ripening process is the well-known curvature dependence of the chemical potential which, assuming isotropic surface energy, is

$$\mu = \mu_0 + \gamma \kappa V_m \tag{1.16}$$

where κ is the mean interfacial curvature, μ_0 is the chemical potential of an atom at a flat interface, V_m is the molar volume, and γ is the surface energy. The above equation explains that the flow of atoms will be from high to low curvature regions. This results in the disappearance of surfaces possessing high curvature and an increase in the size scale of dispersed second phase, which is consistent with the necessary decrease in total energy of the two-phase system. Typically, the net effect of Ostwald's ripening is to broaden the size distribution of nucleated particles (Lifshitz and Slyozov 1961; Chakraverty 1967). As ripening takes place in liquid-phase (Stoeva et al. 2002; Smetana et al. 2005; Pan et al. 2013) and gas-phase (Bae et al. 2012; Zhang et al. 2017; Hergt et al. 2006; Yang et al. 2015) fabrication of two NPs and epitaxial growth of quantum dot arrays (Ross et al. 1998, 1999; Tromp et al. 2000), it prevents the highly desirable formation of narrow size distribution of particles. The study of Ostwald's ripening is important not only to understand the fundamental growth of NPs/clusters but also to prepare uniform particles in the closed system for industrial applications where large seed particles will grow at the expense of large amount of small particles. The advantages of such closed system are to keep supersaturation constant during particle growth, and its level can be controlled by changing the size of small particles. The known mechanisms discussed in the literature for narrowing a particle size distribution (PSD) are as follows: (i) digestive ripening (Smetana et al. 2005; Prasad et al. 2002) and (ii) inverse ripening (Rizza et al. 2001, 2007; Ramaswamy et al. 2005). Digestive ripening can be explained by taking into account electric charges on the particle and by including the electrostatic energy in the free energy minimum (Lee et al. 2007; Lee and Hwang 2009). Likewise, inverse ripening has been described in gold inclusions in an amorphous SiO_2 matrix irradiated with MeV gold ions (Rizza et al. 2007; Ramaswamy et al. 2005). A major advance in the theory of Ostwald's ripening was made in a paper by Lifshitz and Slyozov and followed by a related paper by Wagner (LSW) (Desai and Kapral 2009).

Experimental Explanation

Baumgartner et al. (2013) studied the nucleation and growth mechanism of magnetite formed by co-precipitation, which is the concomitant precipitation from ferrous and ferric iron in alkaline aqueous solution. To observed the rapid nucleation and growth, they developed an experimental setup for the precipitation under controlled physicochemical conditions and investigated the early stages of the mineralization by high-resolution cryogenic transmission electron microscopy (cryo-TEM), which allows the imaging of the involved species in their quasi-native hydrated state as present in solution (Pouget et al. 2009; Yuwono et al. 2010). The nucleation and growth process of magnetite formation follows a crystallization pathway involving the intermediate formation of nanometer-sized primary particles that fuse to form the crystalline iron oxide phase. The formation of these primary particles occurred from an unstable initial precursor phase within 2 min after the initial addition of iron chloride to the dilute sodium hydroxide solution. The primary particles showed a surprisingly monodisperse size distribution of around 2 nm and aggregated in branched networks. Within six min, the aggregates locally became denser and spheroidal NPs of 5–15 nm formed from them. With further reaction time, the NPs grew in number and size at the expense of the primary particles. They observed primary particle attachment to the crystals suggesting a secondary nucleation and growth mechanism through coalescence. The size of attached primary particles and respective surface roughness features on the crystals was reduced to around 1.1 nm that indicates their volume decrease in the course of accretion.

Liu et al. (2010) have studied the synthesis and growth mechanism of Ni–Fe alloys nanostructures. They observed that random aggregation of the nuclei formed spherical primary NPs due to the minimization of the surface free energy and the strong magnetic dipole–dipole interaction. These primary nanospheres have many protuberances on their rough surfaces. The subsequent growth is thermodynamically favorable on such geometric curvatures which have higher chemical potentials than geometric plane surfaces. The schematic growth mechanism is shown in Fig. 1.15. In this growth mechanism, it is found that after primary spherical NPs, the subsequent growth is subjected to a low rate because of the depletions of reactant and more
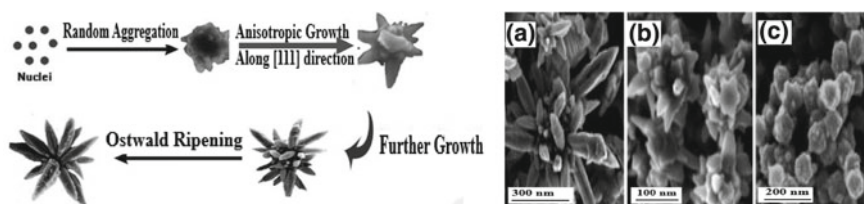
Fig. 1.15 Schematic illustration for the stepwise growth mechanism of the flowerlike Ni–Fe alloy nanostructures. SEM images showing the morphology evolution of the intermediates collected after different hydrothermal reaction times of **a** 3, **b** 4, and **c** 6 h. Reprinted with permission from Liu et al. (2010). Copyright 2010 American Chemical Society
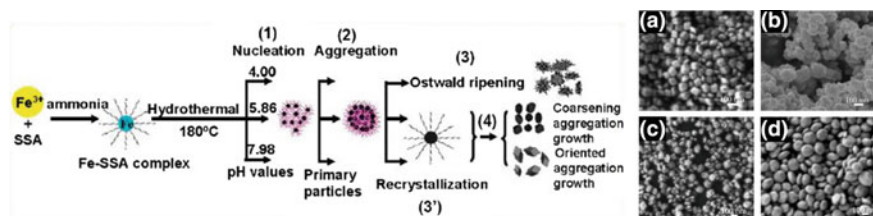
Fig. 1.16 Schematic illustration of the possible mechanism for the formation of the α-Fe₂O₃ nanocrystals: (1–2–3) nucleation Aggregation-Ostwald's ripening growth for nanoaggregates; (1–2–3′–4) nucleation-aggregation recrystallization-aggregation growth (coarsening aggregation and oriented aggregation) for nanospheres, and nanorhombohedra. FE-SEM images of α-Fe₂O₃ samples **a** obtained by only FeCl₃ aqueous solution dissociating without the addition of SSA and ammonia and **b–d** are image of growth with the pH of Fe-SSA complex to 3.10, 5.86, and 7.98. Reprinted with permission from Yin et al. (2009). Copyright 2009 American Chemical Society

pronounced retarding effects by Fe^{3+}. The nanorods grew along the [111] direction to acquire a low magnetic anisotropic energy in the presence of a relatively slow reaction rate. Therefore, many projecting nanorods grow out of the surface of primary nanocores along [111] preferential direction shown in Fig. 1.15b and further grow into Ni–Fe alloy nanorods with various diameters and lengths (Fig. 1.15c). At the last stage, some nanorods continue to grow as the aging time increases, while a number of smaller nanorods disappear, possibly because of 'Ostwald's ripening.' The particles finally develop into a beautiful flowerlike assembly with several nanorods sharing a nanocore.

Yin et al. (2009) reported a facile, 'green,' 5-sulfosalicylic acid dihydrate (SSA)-assisted hydrothermal process for controllable synthesis of α-Fe₂O₃ nanocrystals with different morphologies and proposed the growth mechanism of different α-Fe₂O₃ nanostructures as shown in Fig. 1.16. At a lower pH value (pH 4.10), the relatively stable Fe-SSA complex $[Fe(SSA)]^+$led to the slow release of Fe^{3+} cations in aqueous solution; the nucleation rate is also relatively slow and the as-obtained α-Fe₂O₃ nuclei are small. In contrast, with the increase of the pH value (i.e., pH 5.86, 7.98), the poorer stability of the Fe-SSA complex leads to the relatively rapid release speed of Fe^{3+} ions in the solution, as a result of which nucleation occurred rapidly and large quantities of α-Fe₂O₃ primary nuclei were formed in the solution. Once the small α-Fe₂O₃ nuclei are formed, they are active because of their high surface energy and tend to aggregate growth (Fig. 1.16, step 2, primary aggregation), leading to the formation of larger aggregates to minimize the surface energies. The formed α-Fe₂O₃ primary NPs rotated and rearranged to find a place to minimize the surface energy (ordered primary aggregation, Fig. 1.16, step 2), followed by further recrystallization to form compact bulk crystals through fast simultaneous coarsening aggregation growth for the nanosphere α-Fe₂O₃, and oriented attachment aggregation growth for the α-Fe₂O₃ nanorhombohedra because the SSA may coordinate selectively to the **α**-Fe₂O₃ crystal, hindering the growth of certain crystal surfaces (Fig. 1.16, steps 3 and 4). After the primary aggregation, the larger α-Fe₂O₃ self-aggregates were

formed by aggregation of the smaller primary α-Fe$_2$O$_3$ particles at lower pH value, which were probably driven by the Ostwald ripening process (Fig. 1.16, step 3).

Post-synthesis Chemistry of NPs

Surface Modification and Water Dispersion of NPs

Several reports since the last decade have been suggested that the MNPs were one of the most basic materials in biomedicine. However, they still need to be further modified to obtain high quality. Various strategies for surface modification had been developed. Surface-active groups of MNPs can couple with bioactive substances such as DNA, protein, or antibody, which will broaden their application scopes (Park et al. 2011). The main purposes of surface modification of NPs are: (a) to improve or change the dispersion of MNPs; (b) to improve the surface activity of MNPs; (c) to enhance the physicochemical and mechanical properties; and (d) to improve the biocompatibility of MNPs by preventing any toxic ion leakage from magnetic core into the biological environment and serving as a base for further anchoring of functional groups such as biomarkers, antibodies, and peptides.

Yan and Sun (2014) prepared the carboxylate-functionalized Fe$_3$O$_4$ NPs by a one-step method and subsequently mixed it with HAuCl$_4$ aquatic solution. After that, added NaBH$_4$ to the mixed solution to directly reduce the HAuCl$_4$. Inspired by the experimental results, they put forward a mechanism to synthesize bifunctional Fe$_3$O$_4$@Au nanocomposites, as shown in Fig. 1.17 clearly. Carboxylic acid groups adsorbed AuCl$_4$ under acidic condition, and then, NaBH$_4$ was added to form zero-valent Au which attached to Fe$_3$O$_4$ NPs through the chemistry of the carboxylate group, and gradually, the gold shell was formed around Fe$_3$O$_4$ NPs.

In the architecture of MNPs, fine-tuning of surface modifying materials may have a serious challenge for the pragmatic use of MNPs in clinical applications. The modifying NPs consist of long-chain organic ligands or inorganic/organic polymers, where these ligands or polymers can be introduced: (a) during synthesis (i.e., in situ coating) in which the nucleation of magnetic core and the coating occurs simultaneously in the same reaction solution, (b) after synthesis (post-synthetic coating) in which surface coating materials are introduced after the formation of magnetic cores.
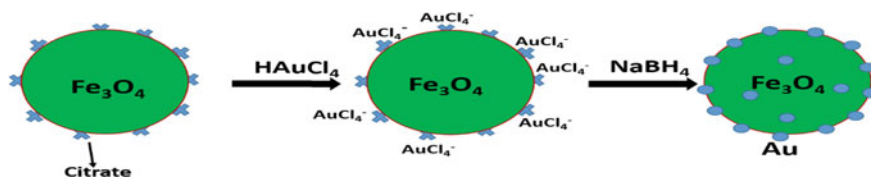
Fig. 1.17 Schematic illustration of the bifunctional Fe$_3$O$_4$@Au nanocomposites. Reprinted with permission from Yan and Sun (2014). Copyright 2014 Elsevier Ltd. All rights reserved
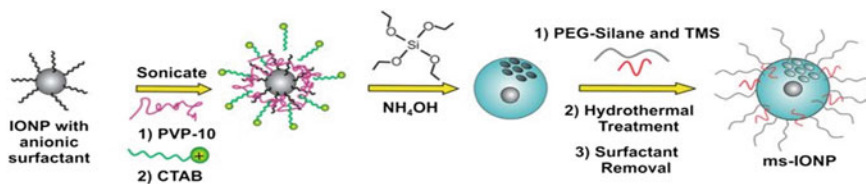
Fig. 1.18 An example of in situ coating of iron oxide NPs (Reprinted with permission from Hurley et al. (2016). Copyright 2016 American Chemical Society)

Either end-grafting or surface encapsulation is followed in both processes in order to link the surface molecules to magnetic cores. In end-grafting, the modifying molecules are clamped on magnetic core by the help of a single capping group at their one end, whereas in surface encapsulation, usually polymers which already carrying multiple active groups are anchored on the surface of magnetic core with multiple connections resulting stronger and more stable coatings. An example of in situ coating of magnetic oxide NPs as shown in Fig. 1.18 (Hurley et al. 2016). It is believed that surface modification of MNPs can dramatically change its magnetic properties in some cases due to the formation of chemical bonds between coating molecules and surface metal ions that could changes the surface spin structure and hence the performance of such MNPs in biomedical applications depending upon coating material is used and how these materials are linked on the magnetic core surface as explained above. Actually, it is difficult to discriminate between surface coating and finite size contributions, the latter being the effect of surface spin canting due to the minimization of magneto-static energy at the surface and observed also in uncoated particles (Kodama 1999). As we know in finite size effect, the canted spins at MNP's surface do not respond to an external applied magnetic field as the bulk spins and give rise to a significant decrease in net magnetization, where this effect becomes dominant in smaller MNPs, since the volume fraction of disordered surface spins is increased. The physical origin of the surface coating effect on magnetic properties is still under research, and different results were reported in several studies for different kinds of magnetic cores and coating materials. For instance, Vestal and Zhang (2003) have investigated the influence of the surface coordination chemistry on the magnetic properties of $MnFe_2O_4$ NPs by capping the 4-, 12-, and 25-nm-sized $MnFe_2O_4$ NPs with a variety of substituted benzenes and substituted benzoic acid ligands and observed an increase in saturation magnetization. Another indirect effect of the surface coating on magnetic properties, which should be mentioned, is to reduce the magnetic interparticle interactions through decreasing the distance between magnetic cores. This is important since strong interparticle interactions can alter the MNPs' overall magnetic properties, i.e., superparamagnetic behavior and diverse it from the isolated one. The surface coating of MNPs plays a crucial role in biomedical applications by fulfilling more than one function at a time.

Bio-conjugation of NPs

Surface functionalization can render NP water solubility, functionality, and stability in physiological environment. After that, NPs are required to conjugate with biomolecules of interest (e.g., small bioactive molecules, peptide, proteins, and nucleic acid) for further biomedical applications. Many conjugation strategies have been developed. Aubin-Tam and Hamad Schifferli (2008) have discussed an initial choice of conjugation is usually determined by a variety of factors such as the NM itself, along with its structure, size, and shape, the type of NM surface ligand, and the presence of available functional end groups, in combination with the type of biomolecule, their size, available functional groups, chemical composition, and of course, what is ultimately required from the composites in practice. Here, some commonly used methods are discussed below.

Direct Absorption

Biological species can interact directly with different kinds of NPs. Conjugates may consist of NMs both with and without attached biomolecule or alternatively a narrow or broad distribution in the ratio or valence of attached biomolecule. The NPs even without additional functionalization have been shown to attach to certain place inside cell (Bruchez et al. 1998). However, the interaction is usually very weak and nonspecific and has limited uses. On the other hand, also the signal generated from nonspecific interaction may interfere with the real measurement. Thereby, the direct absorption of biomolecules by NPs mentioned here refers to the specific attachment of certain biological molecules to NPs with relative strong non-covalent interaction. The general schemes routinely used for the conjugation of peptides to NP materials for direct absorption are shown in Fig. 1.19a. In direct interaction/absorption, such peptide motifs can bind to coordinate with the NP surface with high affinity, and examples include the interaction of free thiols with the surface of AuNPs and the high affinity coordination of polyhistidine tracts with NPs (e.g., QDs) displaying Zn^{2+}-bearing surfaces (Sapsford et al. 2011). Biomolecules with special functional groups can be directly linked to NPs. Depending upon the assembly chemistry utilized, there may also be heterogeneity in the orientation of the attached biomolecules. For example, thiol groups from cytosine amino residue can be used to coordinated peptides or proteins to noble metal NPs and QDs (Mazumder et al. 2009; Hermanson 2008). Zhou et al. (2007) have been used to couple NPs to functional molecules containing a thiol group. This chemistry is particularly convenient for bio-conjugation to antibodies, which have thiols outside of the affinity site so that coupling to NPs does not disrupt specific binding to the targeted molecule. Non-covalent attachments can be sub-grouped into those based on electrostatic interactions along with those based on biological recognition/binding, affinity interactions, or enzyme activity. For instance, negatively charged nucleic acid can be attached to the positively charged surface of
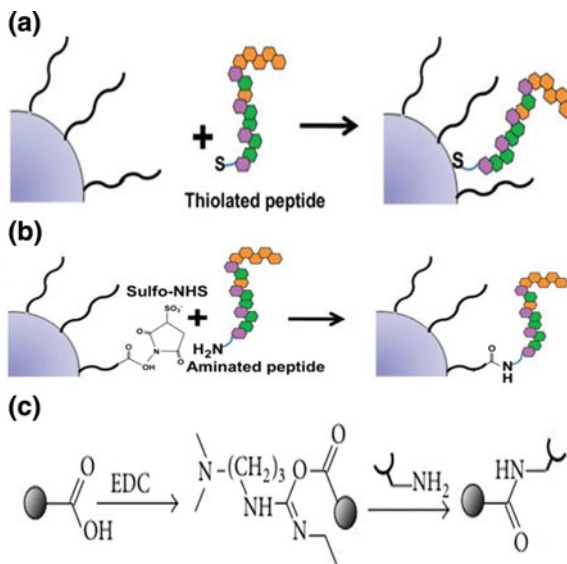
NPs. Proteins, which have a natural positive (or negative) charge under physiochemical environment, can also corroborate to NPs with negative (or positive) charges. Neutral charged proteins could be engineered with charged domain to enhance the adsorption to NP surface. Mattoussi et al. (2000) have developed maltose-binding protein (MBP) and protein G with a positively leucine zipper domain. The engineered proteins can then adhere to the surface of dihydrolipoic acid (DHLA)-capped QDs. As the attachment is mediated by electrostatic interaction, the conjugation is simple dependent on the surface charge of NPs, regardless of the material of NPs. There are, however, some drawbacks with this approach, including sensitive to p^H and salt concentration, high degree of non-specific binding, and required engineering of proteins in some cases.

Covalent Coupling

Covalent bonding through the amine groups present on biomolecules using amide chemistry has been widely exploited to permanently attach proteins, oligonucleotides, and small molecules to the surface of NPs. Covalent coupling allows specific and stable conjugation of biomolecules with NPs. Typically, functional groups on the NPs surface including carboxylic group, amide group, and thiol group can cross-link with biomolecules through various coupling strategies based on the functional groups involved. The general schemes mostly used for the conjugation of peptides to NP materials for covalent coupling is shown in Fig. 1.19b. In covalent chemical coupling, these linkages utilize classical bio-conjugation chemistry such as 1-ethyl-3-dimethylaminopropyl carbodiimide (EDC)-based coupling of amines

to carboxyls or NHS- and maleimide-mediated conjugation to amines and thiols (Sapsford et al. 2011).

Probably, the most commonly coupling methods for bio-conjugation of NPs involve amine functional group. Primary amine can react with carboxylic group to form a 'zero length' amide bonds. The linkage is usually mediated by carbodiimide agents, such as most commonly used EDC. EDC has good solubility in water. This property enables direct application of EDC in aqueous solutions without the addition of any organic compounds. These conditions are suitable for the attachment of bioactive molecules to the carrier surface. During the reaction of EDC with carboxylic group, the active form of intermediate product O-acylisourea ester is formed. The latter reacts with primary amine forming amide bond as shown in Fig. 1.19c. The main advantage of this method is that applied ligand does not need any preliminary modifications usually causing the loss of its activity (Kocbek et al. 2007; Nobs et al. 2004). The conjugation strategy has been applied to coupling of various proteins (e.g., enzyme and antibodies), amine-terminated nucleic acid, small molecules with amine groups, etc., to carboxylic group functionalized NPs (Gao et al. 2004; Agrawal et al. 2006; Liu et al. 2007; Bagalkot et al. 2007; Kell et al. 2008). In some cases, coupling found between amine functionalized NPs and carboxylic groups on biomolecules. More specifically, the coupling efficiency can be enhanced by addition of stabilizing agents such as n-hydroxysuccinimide (NHS) or sulfo-NHS by the formation of a succinimide ester intermediate (Hermanson 2008).

Future of Liquid-Phase Synthesis for Biomedical Applications

In modern research era, colloidal NPs and bottom-up approaches of preparations of NPs have made a big place irrespective of applications. An advance in colloidal NPs synthesis encourages a great future for biomedicals due to several reasons. The physicochemical properties of colloidal NPs (NPs) are influenced by their local environment as, in turn, the local environment influences the physicochemical properties of the NPs. In other words, the local environment around NPs has a profound impact on the NPs, and it is different from bulk due to interaction with the NP surface. The vicinity of NPs can be sensitively influenced by local ions and ligands, with effects already occurring at extremely low concentrations. The local ion concentration hereby affects the colloidal stability of the NPs. This can have subtle effects, now caused by the environment to the performance of the NP, such as for example a buffering effect caused by surface reaction on ultrapure ligand-free NPs, a size quenching effect in the presence of specific ions and a significant impact on fluorophore-labeled NPs acting as ion sensors. On the other hand, the advancement in biomedical, where three aspects of application is important: therapy, diagnosis, and imaging; colloidal NPs are future which is being termed as personalized nanomedicine, which is predicted as future in medical science. A huge literature is available regarding magnetic

and hybrid magnetic NPs as in vivo and several of them are already in practices at clinical level, and some are ready to transform in clinics. This is not an easy task to make perfect biocompatible NPs, and several challenges/risk related to such nanomedicines need to be tackled.

References

Adschiri Tadafumi, Yukiya Hakuta A, Arai K (2000) Hydrothermal synthesis of metal oxide fine particles at supercritical conditions. Ind Eng Chem Res 39:4901–4907. https://doi.org/10.1021/ie0003279

Agrawal A, Zhang C, Byassee T, Ralph A, Tripp A, Nie Shuming (2006) Counting Single Native Biomolecules and Intact Viruses with Color-Coded Nanoparticles. Anal Chem 78:1061–1070. https://doi.org/10.1021/ac051801t

Aivazoglou E, Metaxa E, Hristoforou E (2018) Microwave-assisted synthesis of iron oxide nanoparticles in biocompatible organic environment. AIP Adv 8:048201. https://doi.org/10.1063/1.4994057

Alharbi KK, Al-sheikh YA (2014) Role and implications of nanodiagnostics in the changing trends of clinical diagnosis. Saudi J Biol Sci 21:109–117. https://doi.org/10.1016/j.sjbs.2013.11.001

Alivisatos AP (1996) Semiconductor clusters, nanocrystals, and quantum dots. Science 80:271:933–937. https://doi.org/10.1126/science.271.5251.933

Amara D, Grinblat J, Margel S (2012) Solventless thermal decomposition of ferrocene as a new approach for one-step synthesis of magnetite nanocubes and nanospheres. J Mater Chem 22:2188–2195. https://doi.org/10.1039/c1jm13942h

And CRV, Zhang ZJ (2003) Effects of Surface Coordination Chemistry on the Magnetic Properties of MnFe2O4 Spinel Ferrite Nanoparticles. J Am Chem Soc 125:9828–9833. https://doi.org/10.1021/ja035474n

Aubin-Tam M-E, Hamad-Schifferli K (2008) Structure and function of nanoparticle–protein conjugates. Biomed Mater 3:034001. https://doi.org/10.1088/1748-6041/3/3/034001

Bae H, Ahmad T, Rhee I, Chang Y, Jin S-U, Hong S (2012) Carbon-coated iron oxide nanoparticles as contrast agents in magnetic resonance imaging. Nanoscale Res Lett 7:44. https://doi.org/10.1186/1556-276x-7-44

Bagalkot V, Zhang L, Levy-Nissenbaum E, Jon S, Kantoff PW, Langer R, Farokhzad OC (2007) Quantum dot–aptamer conjugates for synchronous cancer imaging, therapy, and sensing of drug delivery based on bi-fluorescence resonance energy transfer. Nano Lett 7:3065–3070. https://doi.org/10.1021/nl071546n

Baghbanzadeh M, Carbone L, Cozzoli PD, Kappe CO (2011) Microwave-assisted synthesis of colloidal inorganic nanocrystals. Angew Chemie Int Ed 50:11312–11359. https://doi.org/10.1002/anie.201101274

Bandhu A, Mukherjee S, Acharya S, Modak S, Brahma SK, Das D, Chakrabarti PK (2009) Dynamic magnetic behaviour and Mössbauer effect measurements of magnetite nanoparticles prepared by a new technique in the co-precipitation method. Solid State Commun 149:1790–1794. https://doi.org/10.1016/j.ssc.2009.07.018

Banin U, Ben-Shahar Y, Vinokurov K (2014) Hybrid semiconductor-metal nanoparticles: from architecture to function. Chem Mater 26:97–110. https://doi.org/10.1021/cm402131n

Bano S, Nazir S, Nazir A, Munir S, Mahmood T, Afzal M, Ansari FL, Mazhar K (2016) Microwave-assisted green synthesis of superparamagnetic nanoparticles using fruit peel extracts: surface

engineering, T_2 relaxometry, and photodynamic treatment potential. Int J Nanomed 11:3833–3848. https://doi.org/10.2147/ijn.s106553

Bao J, Chen W, Liu T, Zhu Y, Jin P, Wang L, Liu J, Wei Y, Li Y (2007) Bifunctional Au-Fe_3O_4 nanoparticles for protein separation. ACS Nano 1:293–298. https://doi.org/10.1021/nn700189h

Bao F, Yao J-L, Gu R-A (2009) Synthesis of magnetic Fe_2O_3/Au core/shell nanoparticles for bioseparation and immunoassay based on surface-enhanced raman spectroscopy. Langmuir 25:10782–10787. https://doi.org/10.1021/la901337r

Baumgartner J, Dey A, Bomans PHH, Le Coadou C, Fratzl P, Sommerdijk NAJM, Faivre D (2013) Nucleation and growth of magnetite from solution. Nat Mater 12:310–314. https://doi.org/10.1038/nmat3558

Bertotti G (1998) Hysteresis in magnetism: for physicists, materials scientists, and engineers. Academic Press

Bilecka I, Niederberger M (2010) Microwave chemistry for inorganic nanomaterials synthesis. Nanoscale 2:1358. https://doi.org/10.1039/b9nr00377k

Brown PW, Paul W, Constantz B, Society MR (1994) Hydroxyapatite and related materials. CRC, Boca Raton

Bruchez Jr M, Moronne M, Gin P, Weiss S, Alivisatos AP (1998) Semiconductor Nanocrystals as Fluorescent Biological Labels. Science (80-) 281:2013–2016. https://doi.org/10.1126/science.281.5385.2013

Byrappa K, Adschiri T (2007) Hydrothermal technology for nanotechnology. Prog Cryst Growth Charact Mater 53:117–166. https://doi.org/10.1016/j.pcrysgrow.2007.04.001

Byrappa K, Yoshimura M (2013) Handbook of hydrothermal technology. William Andrew

Cai W, Wan J (2007) Facile synthesis of superparamagnetic magnetite nanoparticles in liquid polyols. J Colloid Interface Sci 305:366–370. https://doi.org/10.1016/j.jcis.2006.10.023

Cao Z, Yang L, Ye Q, Cui Q, Qi D, Ziener U (2013) Transition-metal salt-containing silica nanocapsules elaborated via salt-induced interfacial deposition in inverse miniemulsions as precursor to functional hollow silica particles. Langmuir 29:6509–6518. https://doi.org/10.1021/la401468t

Carrey J, Mehdaoui B, Respaud M (2011) Simple models for dynamic hysteresis loop calculations of magnetic single-domain nanoparticles: application to magnetic hyperthermia optimization. J Appl Phys 109:083921. https://doi.org/10.1063/1.3551582

Chakraverty BK (1967) Grain size distribution in thin films—2. Non-conservative systems. J Phys Chem Solids 28:2413–2421. https://doi.org/10.1016/0022-3697(67)90027-3

Charitidis CA, Georgiou P, Koklioti MA, Trompeta A-F, Markakis V (2014) Manufacturing nanomaterials: from research to industry. Manuf Rev 1:11. https://doi.org/10.1051/mfreview/2014009

Chen X, Klingeler R, Kath M, El Gendy AA, Cendrowski K, Kalenczuk RJ, Borowiak-Palen E (2012) Magnetic silica nanotubes: synthesis, drug release, and feasibility for magnetic hyperthermia. ACS Appl Mater Interfaces 4:2303–2309. https://doi.org/10.1021/am300469r

Cheng Y, Zhao L, Li Y, Xu T (2011) Design of biocompatible dendrimers for cancer diagnosis and therapy: current status and future perspectives. Chem Soc Rev 40:2673. https://doi.org/10.1039/c0cs00097c

Cho W-S, Yashima M, Kakihana M, Kudo A, Sakata T, Yoshimura M (1995) Room-temperature preparation of the highly crystallized luminescent $CaWO_4$ film by an electrochemical method. Appl Phys Lett 66:1027–1029

Coquerel G (2014) Crystallization of molecular systems from solution: phase diagrams, supersaturation and other basic concepts. Chem Soc Rev 43:2286–2300. https://doi.org/10.1039/c3cs60359h

Cote LJ, Teja AS, Wilkinson AP, Zhang ZJ (2002) Continuous hydrothermal synthesis and crystallization of magnetic oxide nanoparticles. J Mater Res Res 17:2410–2416. https://doi.org/10.1557/jmr.2002.0352

Cote LJ, Teja AS, Wilkinson AP, Zhang ZJ (2003) Continuous hydrothermal synthesis of $CoFe_2O_4$ nanoparticles. Fluid Phase Equilib 210:307–317. https://doi.org/10.1016/s0378-3812(03)00168-7

Cui Y, Wang Y, Hui W, Zhang Z, Xin X, Chen C (2005) The synthesis of goldmag nano-particles and their application for antibody immobilization. Biomed Microdevices 7:153–156. https://doi.org/10.1007/s10544-005-1596-x

Dąbrowska S, Chudoba T, Wojnarowicz J, Łojkowski W, Dąbrowska S, Chudoba T, Wojnarowicz J, Łojkowski W (2018) Current trends in the development of microwave reactors for the synthesis of nanomaterials in laboratories and industries: a review. Crystals 8:379. https://doi.org/10.3390/cryst8100379

Davey RJ, Back KR, Sullivan RA (2015) Crystal nucleation from solutions–transition states, rate determining steps and complexity. Faraday Discuss 179:9–26. https://doi.org/10.1039/c5fd00037h

de la Hoz A, Díaz-Ortiz A, Moreno A (2005) Microwaves in organic synthesis. Thermal and non-thermal microwave effects. Chem Soc Rev 34:164–178. https://doi.org/10.1039/b411438h

de Paula LB, Primo FL, Pinto MR, Morais PC, Tedesco AC (2017) Evaluation of a chloroaluminium phthalocyanine-loaded magnetic nanoemulsion as a drug delivery device to treat glioblastoma using hyperthermia and photodynamic therapy. RSC Adv 7:9115–9122. https://doi.org/10.1039/c6ra26105a

Deng D, Chen Y, Cao J, Tian J, Qian Z, Achilefu S, Gu Y (2012) High-quality $CuInS_2/ZnS$ quantum dots for in vitro and in vivo bioimaging. Chem Mater 24:3029–3037. https://doi.org/10.1021/cm3015594

Denis M, Puel F, Veesler S (2009) Polymorphism in processes of crystallization in solution: a practical review. Org Process Res Dev 13:1241–1253. https://doi.org/10.1021/op900168f

Desai RC, Kapral R (2009) Lifshitz–Slyozov–Wagner theory. Dynamics of Self-Organized and Self-Assembled Structures. Cambridge University Press, Cambridge, pp 87–95

Dias CSB, Hanchuk TDM, Wender H, Shigeyosi WT, Kobarg J, Rossi AL, Tanaka MN, Cardoso MB, Garcia F (2017) Shape tailored magnetic nanorings for intracellular hyperthermia cancer therapy. Sci Rep 7:14843. https://doi.org/10.1038/s41598-017-14633-0

Ding HL, Zhang YX, Wang S, Xu JM, Xu SC, Li GH (2012) $Fe_3O_4@SiO_2$ core/shell nanoparticles: the silica coating regulations with a single core for different core sizes and shell thicknesses. Chem Mater 24:4572–4580. https://doi.org/10.1021/cm302828d

Dong H, Chen Y-C, Feldmann C (2015) Polyol synthesis of nanoparticles: status and options regarding metals, oxides, chalcogenides, and non-metal elements. Green Chem 17:4107–4132. https://doi.org/10.1039/c5gc00943j

Edel JB, Kornyshev AA, Kucernak AR, Urbakh M (2016) Fundamentals and applications of self-assembled plasmonic nanoparticles at interfaces. Chem Soc Rev 45:1581–1596. https://doi.org/10.1039/c5cs00576k

Ellis-Behnke RG, Liang Y-X, You S-W, Tay DKC, Zhang S, So K-F, Schneider GE (2006) Nano neuro knitting: peptide nanofiber scaffold for brain repair and axon regeneration with functional return of vision. Proc Natl Acad Sci U S A 103:5054–5059. https://doi.org/10.1073/pnas.0600559103

Feng J, Biskos G, Schmidt-Ott A (2015) Toward industrial scale synthesis of ultrapure singlet nanoparticles with controllable sizes in a continuous gas-phase process. Sci Rep 5:15788. https://doi.org/10.1038/srep15788

Gabriel C, Gabriel S, Grant EH, Grant EH, Halstead BSJ, Mingos DMP (1998) Dielectric parameters relevant to microwave dielectric heating. Chem Soc Rev 27:213. https://doi.org/10.1039/a827213z

Galema SA (1997) Microwave chemistry. Chem Soc Rev 26:233. https://doi.org/10.1039/cs9972600233

Gao X, Cui Y, Levenson RM, Chung LWK, Nie S (2004) In vivo cancer targeting and imaging with semiconductor quantum dots. Nat Biotechnol 22:969–976. https://doi.org/10.1038/nbt994

Gawande MB, Shelke SN, Zboril R, Varma RS (2014) Microwave-assisted chemistry: synthetic applications for rapid assembly of nanomaterials and organics. Acc Chem Res 47:1338–1348. https://doi.org/10.1021/ar400309b

Gedye RN, Smith FE, Westaway KC (1988) The rapid synthesis of organic compounds in microwave ovens. Can J Chem 66:17–26. https://doi.org/10.1139/v88-003

Giner-Casares JJ, Liz-Marzán LM (2014) Plasmonic nanoparticles in 2D for biological applications: toward active multipurpose platforms. Nano Today 9:365–377. https://doi.org/10.1016/j.nantod.2014.05.004

Gleiter H (1989) Nanocrystalline materials. Prog Mater Sci 33:223–315. https://doi.org/10.1016/0079-6425(89)90001-7

Gnanaprakash G, Philip J, Jayakumar T, Raj B (2007) Effect of digestion time and alkali addition rate on physical properties of magnetite nanoparticles. J Phys Chem B 111:7978–7986. https://doi.org/10.1021/jp071299b

Gogotsi YG, Yoshimura M (1995) Low-temperature oxidation, hydrothermal corrosion, and their effects on properties of SiC (Tyranno) fibers. J Am Ceram Soc 78:1439–1450. https://doi.org/10.1111/j.1151-2916.1995.tb08835.x

Gonzalez-Rodriguez R, Campbell E, Naumov A (2019) Multifunctional graphene oxide/iron oxide nanoparticles for magnetic targeted drug delivery dual magnetic resonance/fluorescence imaging and cancer sensing. PLoS ONE 14:e0217072. https://doi.org/10.1371/journal.pone.0217072

Gutsch A, Mühlenweg H, Krämer M (2004) Tailor-made nanoparticles via gas-phase synthesis. Small 1:30–46. https://doi.org/10.1002/smll.200400021

Hachani R, Lowdell M, Birchall M, Hervault A, Mertz D, Begin-Colin S, Thanh K (2016) Polyol synthesis, functionalisation, and biocompatibility studies of superparamagnetic iron oxide nanoparticles as potential MRI contrast agents. Nanoscale 8:3278–3287. https://doi.org/10.1039/c5nr03867g

Hakuta Y, Hayashi H, Arai K (2004) Hydrothermal synthesis of photocatalyst potassium hexatitanate nanowires under supercritical conditions. J Mater Sci 39:4977–4980. https://doi.org/10.1023/b:jmsc.0000035349.99273.c7

Hamann SD (1981) Properties of electrolyte solutions at high pressures and temperatures. Phys Chem Earth 13–14:89–111. https://doi.org/10.1016/0079-1946(81)90007-0

Hayashi H, Hakuta Y (2010) Hydrothermal synthesis of metal oxide nanoparticles in supercritical water. Materials 3:3794–3817. https://doi.org/10.3390/ma3073794

He C, Lu K, Lin W (2014) Nanoscale metal-organic frameworks for real-time intracellular ph sensing in live cells. J Am Chem Soc 136:12253–12256. https://doi.org/10.1021/ja507333c

Hergt R, Dutz S, Zeisberger M, Gawalek W (2006) Nanocrystalline iron oxide and Ba ferrite particles in the superparamagnetism-ferromagnetism transition range with ferrofluid applications. J Phys Condens Matter 18:2527–2542. https://doi.org/10.1088/0953-8984/18/38/s01

Hergt R, Dutz S, Röder M (2008) Effects of size distribution on hysteresis losses of magnetic nanoparticles for hyperthermia. J Phys: Condens Matter 20:385214. https://doi.org/10.1088/0953-8984/20/38/385214

Hermanson G (2008) Bioconjugate Techniques 2nd Edition. Elsevier, p 1323

Higgins SR, Eggleston CM, Jordan G, Knauss KG, Boro CO (1998) In-situ observation of oxide and silicate mineral dissolution by hydrothermal scanning force microscopy: initial results for hematite and albite. Mineral Mag A 62:618–619

Al Arbash A, Ahmad Z, Al-Sagheer F (2006) Microstructure and thermomechanical properties of polyimide-silica nanocomposites. J Nanomaterial 2006:Article ID 58648. https://doi.org/10.1155/JNM/2006/58648

Ho D, Sun X, Sun S (2011) Monodisperse magnetic nanoparticles for theranostic applications. Acc Chem Res 44:875–882. https://doi.org/10.1021/ar200090c

Hostetler MJ, Wingate JE, Zhong C-J, Harris JE, Vachet RW, Clark MR, Londono JD, Green SJ, Stokes JJ, Wignall GD, Glish GL, Porter MD, Neal D. Evans A, Murray RW (1998) Alkanethiolate gold cluster molecules with core diameters from 1.5 to 5.2 nm: core and monolayer properties as a function of core size. Langmuir 14:17–30. https://doi.org/10.1021/la970588w

Hu X, Yu JC, Gong J, Li Q, Li G (2007) α-Fe_2O_3 nanorings prepared by a microwave-assisted hydrothermal process and their sensing properties. Adv Mater 19:2324–2329. https://doi.org/10.1002/adma.200602176

Hu D, Wang Y, Song Q (2009) Weakly magnetic field-assisted synthesis of magnetite nano-particles in oxidative co-precipitation (Article in press G Model). Particuology. https://doi.org/10.1016/j.partic.2009.03.005

Hurley KR, Ring HL, Etheridge M, Zhang J, Gao Z, Shao Q, Klein ND, Szlag VM, Chung C, Reineke TM, Garwood M, Bischof JC, Haynes CL (2016) Predictable heating and positive MRI contrast from a mesoporous silica-coated iron oxide nanoparticle. Mol Pharm 13:2172–2183. https://doi.org/10.1021/acs.molpharmaceut.5b00866

Jain K (2003) Nanodiagnostics: application of nanotechnology in molecular diagnostics. Expert Rev Mol Diagn 3:153–161. https://doi.org/10.1586/14737159.3.2.153

Ji X, Song X, Li J, Bai Y, Yang W, Peng X (2007) Size control of gold nanocrystals in citrate reduction: the third role of citrate. J Am Chem Soc 129:13939–13948. https://doi.org/10.1021/ja074447k

Jing Z, Wu S (2004) Synthesis and characterization of monodisperse hematite nanoparticles modified by surfactants via hydrothermal approach. Materials 58:3637–3640. https://doi.org/10.1016/j.matlet.2004.07.010

Jokerst JV, Lobovkina T, Zare RN, Gambhir SS (2011) Nanoparticle PEGylation for imaging and therapy. Nanomedicine 6:715–728. https://doi.org/10.2217/nnm.11.19

Kappe CO (2004) Controlled microwave heating in modern organic synthesis. Angew Chemie Int Ed 43:6250–6284. https://doi.org/10.1002/anie.200400655

Karatutlu A, Sapelkin A (2018) Liquid-phase synthesis of nanoparticles and nanostructured materials. Emerg Appl Nanoparticles Archit Nanostructures 1–28. https://doi.org/10.1016/B978-0-323-51254-1.00001-4

Kell AJ, Stewart G, Ryan S, Peytavi R, Boissinot M, Huletsky A, Bergeron MG, Simard B (2008) Vancomycin-modified nanoparticles for efficient targeting and preconcentration of gram-positive and gram-negative bacteria. ACS Nano 2:1777–1788. https://doi.org/10.1021/nn700183g

Kim J, Kim HS, Lee N, Kim T, Kim H, Yu T, Song IC, Moon WK, Hyeon T (2008) Multifunctional uniform nanoparticles composed of a magnetite nanocrystal core and a mesoporous silica shell for magnetic resonance and fluorescence imaging and for drug delivery. Angew Chemie Int Ed 47:8438–8441. https://doi.org/10.1002/anie.200802469

Kino T, Kuzuya T, Itoh K, Sumiyama K, Wakamatsu T, Ichidate M (2008) Synthesis of chalcopyrite nanoparticles via thermal decomposition of metal-thiolate. Mater Trans 49:435–438. https://doi.org/10.2320/matertrans.mbw200724

Kocbek P, Obermajer N, Cegnar M, Kos J, Kristl J (2007) Targeting cancer cells using PLGA nanoparticles surface modified with monoclonal antibody. J Control Release 120:18–26. https://doi.org/10.1016/j.jconrel.2007.03.012

Kodama R (1999) Magnetic nanoparticles. J Magn Magn Mater 200:359–372. https://doi.org/10.1016/s0304-8853(99)00347-9

Kolhatkar A, Jamison A, Litvinov D, Willson R, Lee T (2013) Tuning the magnetic properties of nanoparticles. Int J Mol Sci 14:15977–16009. https://doi.org/10.3390/ijms140815977

Kooti M, Kooti M, Matturi L (2011) Microwave-assisted fabrication of γ-Fe2O$_3$ nanoparticles from tris (acetylacetonato) iron(III). Int Nano Lett 1:38–42

Kou J, Varma RS (2012) Beet juice-induced green fabrication of plasmonic AgCl/Ag nanoparticles. Chemsuschem 5:2435–2441. https://doi.org/10.1002/cssc.201200477

Kovalenko Maksym V, Bodnarchuk Maryna I, Lechner Rainer T, Hesser Günter, Friedrich Schäffler A, Heiss W (2007) Fatty acid salts as stabilizers in size- and shape-controlled nanocrystal synthesis: the case of inverse spinel iron oxide. J Am Chem Soc 129:6352–6353. https://doi.org/10.1021/ja0692478

LaMer VK, Dinegar RH (1950) Theory, production and mechanism of formation of monodispersed hydrosols. J Am Chem Soc 72:4847–4854. https://doi.org/10.1021/ja01167a001

Laurent S, Forge D, Port M, Roch A, Robic C, Vander Elst L, Muller RN (2008) Magnetic iron oxide nanoparticles: synthesis, stabilization, vectorization, physicochemical characterizations, and biological applications. Chem Rev 108:2064–2110. https://doi.org/10.1021/cr068445e

Lee D-K, Hwang N-M (2009) Thermodynamics and kinetics of monodisperse alloy nanoparticles synthesized through digestive ripening. Scr Mater 61:304–307. https://doi.org/10.1016/j.scriptamat.2009.04.008

Lee D-K, Park S-I, Lee JK, Hwang N-M (2007) A theoretical model for digestive ripening. Acta Mater 55:5281–5288. https://doi.org/10.1016/j.actamat.2007.05.048

Lee JE, Lee N, Kim T, Kim J, Hyeon T (2011) Multifunctional mesoporous silica nanocomposite nanoparticles for theranostic applications. Acc Chem Res 44:893–902. https://doi.org/10.1021/ar2000259

Lee J, Jung Park T, Jae Lee S, Zhou H, Lee J, Youn Park J (2012) Ultrasensitive DNA monitoring by Au-Fe$_3$O$_4$ nanocomplex ultrasensitive DNA monitoring by Au-Fe$_3$O$_4$ nanocomplex. Sens Actuators B 163:224–232. https://doi.org/10.1016/j.snb.2012.01.040

Li GS, Smith RL, Inomata H, Arai K (2002) Preparation and magnetization of hematite nanocrystals with amorphous iron oxide layers by hydrothermal conditions. Mater Res Bull 37:949–955. https://doi.org/10.1016/S0025-5408(02)00695-5

Li Z, Tan B, Allix M, Cooper AI, Rosseinsky MJ (2008) Direct coprecipitation route to monodisperse dual-functionalized magnetic iron oxide nanocrystals without size selection. Small 4:231–239. https://doi.org/10.1002/smll.200700575

Lifshitz IM, Slyozov VV (1961) The kinetics of precipitation from supersaturated solid solutions. J Phys Chem Solids 19:35–50. https://doi.org/10.1016/0022-3697(61)90054-3

Lim WQ, Gao Z (2016) Plasmonic nanoparticles in biomedicine. Nano Today 11:168–188. https://doi.org/10.1016/j.nantod.2016.02.002

Liu Y, Brandon R, Cate M, Peng X, Stony R, Johnson M (2007) Detection of pathogens using luminescent CdSe/ZnS dendron nanocrystals and a porous membrane immunofilter. Anal Chem 79:8796–8802. https://doi.org/10.1021/ac0709605

Liu L, Guan J, Shi W, Sun Z, Zhao J (2010) Facile Synthesis and Growth Mechanism of Flowerlike Ni−Fe Alloy Nanostructures. J Phys Chem C 114:13565–13570. https://doi.org/10.1021/jp104212v

Liu Y, Jia S, Wu Q, Ran J, Zhang W, Wu S (2011) Studies of Fe3O4-chitosan nanoparticles prepared by co-precipitation under the magnetic field for lipase immobilization. Catal Commun 12:717–720. https://doi.org/10.1016/j.catcom.2010.12.032

López-Ortega A, Lottini E, de Fernández CJ, Sangregorio C (2015) Exploring the magnetic properties of cobalt-ferrite nanoparticles for the development of a rare-earth-free permanent magnet. Chem Mater 27:4048–4056. https://doi.org/10.1021/acs.chemmater.5b01034

Louie AY, Hüber MM, Ahrens ET, Rothbächer U, Moats R, Jacobs RE, Fraser SE, Meade TJ (2000) In vivo visualization of gene expression using magnetic resonance imaging. Nat Biotechnol 18:321–325. https://doi.org/10.1038/73780

Lu Y, Yin Y, Mayers BT, Xia Y (2002) Modifying the surface properties of superparamagnetic iron oxide nanoparticles through a sol−gel approach. Nano Lett 2:183–186. https://doi.org/10.1021/nl015681q

Lynch J, Zhuang J, Wang T, LaMontagne D, Wu H, Cao YC (2011) Gas-bubble effects on the formation of colloidal iron oxide nanocrystals. J Am Chem Soc 133:12664–12674. https://doi.org/10.1021/ja2032597

Mahmoud MHH, Hessien MM (2018) Microwave assisted-hydrothermal synthesis of nickel ferrite nanoparticles. Orient J Chem 34:2577–2582. https://doi.org/10.13005/ojc/340546

Majidi S, Zeinali Sehrig F, Farkhani SM, Soleymani Goloujeh M, Akbarzadeh A (2016) Current methods for synthesis of magnetic nanoparticles. Artif Cells Nanomed Biotechnol 44:722–734. https://doi.org/10.3109/21691401.2014.982802

Mantzaris NV (2005) Liquid-phase synthesis of nanoparticles: particle size distribution dynamics and control. Chem Eng Sci 60:4749–4770. https://doi.org/10.1016/j.ces.2005.04.012

Maris HJ (2006) Introduction to the physics of nucleation. Comptes Rendus Phys 7:946–958. https://doi.org/10.1016/j.crhy.2006.10.019

Maslar JE, Hurst WS, Bowers WJ, Hendricks JH, Aquino MI, Levin I (2001) In situ Raman spectroscopic investigation of chromium surfaces under hydrothermal conditions. Appl Surf Sci 180:102–118. doi:0169-4332(20010801)180:1-2<102:ISRSIO>2.0.ZU;2-3

Matson JB, Zha RH, Stupp SI (2011) Peptide self-assembly for crafting functional biological materials. Curr Opin Solid State Mater Sci 15:225–235. https://doi.org/10.1016/j.cossms.2011.08.001

Mattoussi H, Mauro JM, Goldman ER, Anderson GP, Sundar VC, Mikulec FV, Bawendi MG (2000) Self-assembly of CdSe–ZnS quantum dot bioconjugates using an engineered recombinant protein. J Am Chem Soc 122:12142–12150. https://doi.org/10.1021/ja002535y

Mazumder S, Dey R, Mitra MK, Mukherjee S, Das GC (2009) Review: biofunctionalized quantum dots in biology and medicine. J Nanomater 2009:1–17. https://doi.org/10.1155/2009/815734

Mi C, Zhang J, Gao H, Wu X, Wang M, Wu Y, Di Y, Xu Z, Mao C, Xu S (2010) Multifunctional nanocomposites of superparamagnetic (Fe_3O_4) and NIR-responsive rare earth-doped upconversion fluorescent ($NaYF_4$: Yb, Er) nanoparticles and their applications in biolabeling and fluorescent imaging of cancer cells. Nanoscale 2:1141. https://doi.org/10.1039/c0nr00102c

Miguel-Sancho N, Bomatí-Miguel O, Colom GO, Salvador J-P, Marco M-P, Santamaría J, De Bioingeniería Ciber (2011) Development of stable, water-dispersible, and biofunctionalizable superparamagnetic iron oxide nanoparticles. Chem Mater 23:2795–2802. https://doi.org/10.1021/cm1036452

Mingos DMP, Baghurst DR (1991) Tilden lecture. Applications of microwave dielectric heating effects to synthetic problems in chemistry. Chem Soc Rev 20:1. https://doi.org/10.1039/cs9912000001

Mizukoshi Y, Shuto T, Masahashi N, Tanabe S (2009) Preparation of superparamagnetic magnetite nanoparticles by reverse precipitation method: contribution of sonochemically generated oxidants. Ultrason Sonochem 16:525–531. https://doi.org/10.1016/j.ultsonch.2008.12.017

Moon SY, Tanaka S, Sekino T (2010) Crystal growth of thiol-stabilized gold nanoparticles by heat-induced coalescence. Nanoscale Res Lett 5:813–817. https://doi.org/10.1007/s11671-010-9565-6

Morey GW, Niggli P (1913) The hydrothermal formation of silicates, a review. J Am Chem Soc 35:1086–1130. https://doi.org/10.1021/ja02198a600

Morschhäuser R, Krull M, Kayser C, Boberski C, Bierbaum R, Püschner PA, Glasnov TN, Kappe CO (2012) Microwave-assisted continuous flow synthesis on industrial scale. Green Process Synth 1. https://doi.org/10.1515/gps-2012-0032

Mou X, Wang J, Meng X, Liu J, Shi L, Sun L (2017) Multifunctional nanoprobe based on upconversion nanoparticles for luminescent sensing and magnetic resonance imaging. J Lumin 190:16–22. https://doi.org/10.1016/j.jlumin.2017.05.006

Mullin JW (2001) Crystallization. Elsevier, Amsterdam

Murray CB, Kagan CR, Bawendi MG (2000) Synthesis and characterization of monodisperse nanocrystals and close-packed nanocrystal assemblies. Annu Rev Mater Sci 30:545–610. https://doi.org/10.1146/annurev.matsci.30.1.545

Nadagouda MN, Speth TF, Varma RS (2011) Microwave-assisted green synthesis of silver nanostructures. Acc Chem Res 44:469–478. https://doi.org/10.1021/ar1001457

Nalwa HS (2004) Encyclopedia of nanoscience and nanotechnology, vol 1–10. American Scientific Publishers

Nedkov I, Merodiiska T, Slavov L, Vandenberghe RE, Kusano Y, Takada J (2006) Surface oxidation, size and shape of nano-sized magnetite obtained by co-precipitation. J Magn Magn Mater 300:358–367. https://doi.org/10.1016/j.jmmm.2005.05.020

Nguyen T, Mammeri F, Ammar S (2018) Iron oxide and gold based magneto-plasmonic nanostructures for medical applications: a review. Nanomaterials 8:149. https://doi.org/10.3390/nano8030149

Nishioka M, Miyakawa M, Daino Y, Kataoka H, Koda H, Sato K, Suzuki TM (2013) Single-mode microwave reactor used for continuous flow reactions under elevated pressure. Ind Eng Chem Res 52:4683–4687. https://doi.org/10.1021/ie400199r

Nobs L, Buchegger F, Gurny R, Allémann E (2004) Current methods for attaching targeting ligands to liposomes and nanoparticles. J Pharm Sci 93:1980–1992. https://doi.org/10.1002/jps.20098

Nüchter M, Ondruschka B, Bonrath W, Gum A (2004) Microwave assisted synthesis—a critical technology overview. Green Chem 6:128–141. https://doi.org/10.1039/b310502d

Nyk M, Kumar R, Ohulchanskyy TY, Bergey EJ, Prasad PN (2008) High contrast in vitro and in vivo photoluminescence bioimaging using near infrared to near infrared up-conversion in Tm^{3+} and Yb^{3+} doped fluoride nanophosphors. Nano Lett 8:3834–3838. https://doi.org/10.1021/nl802223f

Öhrngren P, Fardost A, Russo F, Schanche J-S, Fagrell M, Larhed M (2012) Evaluation of a non-resonant microwave applicator for continuous-flow chemistry applications. Org Process Res Dev 16:1053–1063. https://doi.org/10.1021/op300003b

Ortgies DH, de la Cueva L, del Rosal B, Sanz-Rodríguez F, Fernández N, Iglesias-de la Cruz MC, Salas G, Cabrera D, Teran FJ, Jaque D, Martín Rodríguez E (2016) In vivo deep tissue fluorescence and magnetic imaging employing hybrid nanostructures. ACS Appl Mater Interfaces 8:1406–1414. https://doi.org/10.1021/acsami.5b10617

Oskam G, Abhinav Nellore R, Lee Penn A, Searson PC (2003) The growth kinetics of TiO_2 nanoparticles from titanium(IV) alkoxide at high water/titanium ratio. J Phys Chem B 107:1734–1738. https://doi.org/10.1021/jp021237f

Ozel F, Kockar H, Karaagac O (2015) Growth of iron oxide nanoparticles by hydrothermal process: effect of reaction parameters on the nanoparticle size. J Supercond Nov Magn 28:823–829. https://doi.org/10.1007/s10948-014-2707-9

Ozkaya T, Toprak MS, Baykal A, Kavas H, Köseoğlu Y, Aktaş B (2009) J Less-Common Metals. Elsevier Pub. Co

Paek S-M, Oh J-M, Choy J-H (2011) A lattice-engineering route to heterostructured functional nanohybrids. Chem Asian J 6:324–338. https://doi.org/10.1002/asia.201000578

Pan J, El-Ballouli AO, Rollny L, Voznyy O, Burlakov VM, Goriely A, Sargent EH, Bakr OM (2013) Automated synthesis of photovoltaic-quality colloidal quantum dots using separate nucleation and growth stages. ACS Nano 7:10158–10166. https://doi.org/10.1021/nn404397d

Pan S, Liu Z, Lu W (2018) Synthesis of naked plasmonic/magnetic Au/Fe_3O_4 nanostructures by plasmon-driven anti-replacement reaction. Nanotechnology 30:6. https://doi.org/10.1088/1361-6528/aaf17c

Pan S, Liu Z, Lu W (2019) Synthesis of naked plasmonic/magnetic Au/Fe_3O_4 nanostructures by plasmon-driven anti-replacement reaction. Nanotechnology 30:065605. https://doi.org/10.1088/1361-6528/aaf17c

Pardoe H, Chua-Anusorn W, St. Pierre TG, Dobson J (2001) Structural and magnetic properties of nanoscale iron oxide particles synthesized in the presence of dextran or polyvinyl alcohol. J Magn Magn Mater 225:41–46. https://doi.org/10.1016/S0304-8853(00)01226-9

Park D-Y, Myung S-T (2014) Carbon-coated magnetite embedded on carbon nanotubes for rechargeable lithium and sodium batteries. ACS Appl Mater Interfaces 6:11749–11757. https://doi.org/10.1021/am502424j

Park J, Lee E, Hwang N-M, Kang M, Kim SC, Hwang Y, Park J-G, Noh H-J, Kim J-Y, Park J-H, Hyeon T (2005) One-nanometer-scale size-controlled synthesis of monodisperse magnetic iron oxide nanoparticles. Angew Chemie Int Ed 44:2872–2877. https://doi.org/10.1002/anie.200461665

Park HJ, McConnell JT, Boddohi S, Kipper MJ, Johnson PA (2011) Synthesis and characterization of enzyme-magnetic nanoparticle complexes: effect of size on activity and recovery. Colloids Surf B Biointerfaces 83:198–203. https://doi.org/10.1016/j.colsurfb.2010.11.006

Pereira C, Pereira AM, Fernandes C, Rocha M, Mendes R, Fernández-García MP, Guedes A, Tavares PB, Grenèche J-M, Araújo JP, Freire C (2012) Superparamagnetic MFe_2O_4 (M = Fe Co, Mn) nanoparticles: tuning the particle size and magnetic properties through a novel one-step coprecipitation route. Chem Mater 24:1496–1504. https://doi.org/10.1021/cm300301c

Perreux L, Loupy AÂ (2001) A tentative rationalization of microwave effects in organic synthesis according to the reaction medium, and mechanistic considerations. Tetrahedron 57:9199–9223. https://doi.org/10.1016/s0040-4020(01)00905-x

Pinho SLC, Pereira GA, Voisin P, Kassem J, Bouchaud V, Etienne L, Peters JA, Carlos L, Mornet S, Geraldes CFGC, Rocha J, Delville M-H (2010) Fine tuning of the relaxometry of γ-Fe_2O_3@SiO_2

nanoparticles by tweaking the silica coating thickness. ACS Nano 4:5339–5349. https://doi.org/10.1021/nn101129r

Pinho SLC, Laurent S, Rocha J, Roch A, Delville M-H, Mornet S, Carlos LD, Vander Elst L, Muller RN, Geraldes CFGC (2012) Relaxometric studies of γ-Fe_2O_3@SiO_2 core shell nanoparticles: when the coating matters. J Phys Chem C 116:2285–2291. https://doi.org/10.1021/jp2086413

Piras CC, Fernández-Prieto S, De Borggraeve WM (2019) Ball milling: a green technology for the preparation and functionalisation of nanocellulose derivatives. Nanoscale Adv 1:937–947. https://doi.org/10.1039/c8na00238j

Polshettiwar V, Nadagouda MN, Varma RS (2009a) Microwave-assisted chemistry: a rapid and sustainable route to synthesis of organics and nanomaterials. Aust J Chem 62:16–26. https://doi.org/10.1071/ch08404

Polshettiwar V, Baruwati B, Varma RS (2009b) Self-assembly of metal oxides into three-dimensional nanostructures: synthesis and application in catalysis. ACS Nano 3:728–736. https://doi.org/10.1021/nn800903p

Porter DA, Easterling KE (1992) Phase transformations in metals and alloys. Springer, US, Boston, MA

Pouget EM, Bomans PHH, Goos JACM, Frederik PM, de With G, Sommerdijk NAJM (2009) The Initial Stages of Template-Controlled $CaCO_3$ Formation Revealed by Cryo-TEM. Science (80-) 323:1455–1458. https://doi.org/10.1126/science.1169434

Prasad BL V., Stoeva SI, Christopher M. Sorensen A, Klabunde KJ (2002) Digestive ripening of thiolated gold nanoparticles: the effect of alkyl chain length. Langmuir 18:7515–7520. https://doi.org/10.1021/la020181d

Prasad Yadav T, Manohar Yadav R, Pratap Singh D (2012) Mechanical milling: a top down approach for the synthesis of nanomaterials and nanocomposites. Nanosci Nanotechnol 2:22–48. https://doi.org/10.5923/j.nn.20120203.01

Qu S, Yang H, Ren D, Kan S, Zou G, Li D, Li M (1999) Magnetite nanoparticles prepared by precipitation from partially reduced ferric chloride aqueous solutions. J Colloid Interface Sci 215:190–192. https://doi.org/10.1006/jcis.1999.6185

Rabenau A (1985) The role of hydrothermal synthesis in preparative chemistry. Angew Chemie Int Ed English 24:1026–1040. https://doi.org/10.1002/anie.198510261

Ramaswamy V, Haynes TE, White CW, MoberlyChan WJ, Roorda S, Aziz MJ (2005) Synthesis of nearly monodisperse embedded nanoparticles by separating nucleation and growth in ion implantation. Nano Lett 5:373–377. https://doi.org/10.1021/nl048077z

Reau A, Guizard B, Mengeot C, Boulanger L, Ténégal F (2007) Large scale production of nanoparticles by laser pyrolysis. Mater Sci Forum 534–536:85–88. https://doi.org/10.4028/www.scientific.net/MSF.534-536.85

Reiss H (1951) The growth of uniform colloidal dispersions. J Chem Phys 19:482–487. https://doi.org/10.1063/1.1748251

Rizza GC, Strobel M, Heinig KH, Bernas H (2001) Ion irradiation of gold inclusions in $SiO2$: Experimental evidence for inverse Ostwald ripening. Nucl Instruments Methods Phys Res Sect B Beam Interact with Mater Atoms 178:78–83. https://doi.org/10.1016/s0168-583x(01)00496-7

Rizza G, Cheverry H, Gacoin T, Lamasson A, Henry S (2007) Ion beam irradiation of embedded nanoparticles: Toward an in situ control of size and spatial distribution. J Appl Phys 101:014321. https://doi.org/10.1063/1.2402351

Ross FM, Tersoff J, Tromp RM (1998) Coarsening of self-assembled Ge quantum dots on Si(001). Phys Rev Lett 80:984–987. https://doi.org/10.1103/physrevlett.80.984

Ross FM, Tromp RM, Reuter MC (1999) Transition states between pyramids and domes during Ge/Si Island growth. Science 286:1931–1934 . https://doi.org/10.1126/science.286.5446.1931

Russo P, Acierno D, Palomba M, Carotenuto G, Rosa R, Rizzuti A, Leonelli C (2012) Ultrafine magnetite nanopowder: synthesis, characterization, and preliminary use as filler of polymethylmethacrylate nanocomposites. J Nanotechnol 2012:1–8. https://doi.org/10.1155/2012/728326

Salavati-Niasari M, Davar F, Mazaheri M (2008) Synthesis of Mn_3O_4 nanoparticles by thermal decomposition of a [bis(salicylidiminato)manganese(II)] complex. Polyhedron 27:3467–3471. https://doi.org/10.1016/j.poly.2008.04.015

Salavati-Niasari M, Mahmoudi T, Amiri O (2012) Easy synthesis of magnetite nanocrystals via coprecipitation method. J Clust Sci 23:597–602. https://doi.org/10.1007/s10876-012-0451-5

Saleh N, Afrooz A, Bisesi J, Aich N, Plazas-Tuttle J, Sabo-Attwood T (2014) Emergent properties and toxicological considerations for nanohybrid materials in aquatic systems. Nanomaterials 4:372–407. https://doi.org/10.3390/nano4020372

Sapsford KE, Tyner KM, Dair BJ, Deschamps JR, Medintz IL (2011) Analyzing Nanomaterial Bioconjugates: A Review of Current and Emerging Purification and Characterization Techniques. Anal Chem 83:4453–4488. https://doi.org/10.1021/ac200853a

Sardar R, Funston AM, Mulvaney P, Murray RW (2009) Gold nanoparticles: past, present, and future. Langmuir 25:13840–13851. https://doi.org/10.1021/la9019475

Sathya A, Kalyani S, Ranoo S, Philip J (2017) One-step microwave-assisted synthesis of water-dispersible Fe_3O_4 magnetic nanoclusters for hyperthermia applications. J Magn Magn Mater 439:107–113. https://doi.org/10.1016/j.jmmm.2017.05.018

Sattar AA, EL-Sayed HM, ALsuqia I (2015) Structural and magnetic properties of $CoFe_2O_4/NiFe_2O_4$ core/shell nanocomposite prepared by the hydrothermal method. J Magn Magn Mater 395:89–96. https://doi.org/10.1016/j.jmmm.2015.07.039

Schumacher M, Ruppel M, Kohlbrecher J, Burkhardt M, Plamper F, Drechsler M, Müller AHE (2009) Smart organic–inorganic nanohybrid stars based on star-shaped poly(acrylic acid) and functional silsesquioxane nanoparticles. Polymer 50:1908–1917. https://doi.org/10.1016/j.polymer.2009.02.010

Selvan ST, Tan TTY, Yi DK, Jana NR (2010) Functional and multifunctional nanoparticles for bioimaging and biosensing. Langmuir 26:11631–11641. https://doi.org/10.1021/la903512m

Shcherbakova DM, Shemetov AA, Kaberniuk AA, Verkhusha VV (2015) Natural photoreceptors as a source of fluorescent proteins, biosensors, and optogenetic tools. Annu Rev Biochem 84:519–550. https://doi.org/10.1146/annurev-biochem-060614-034411

Sheng W, Liu J, Liu S, Lu Q, Kaplan Ac DL, Zhu H (2014) One-step synthesis of biocompatible magnetite/silk fibroin core-shell nanoparticles. J Mater Chem B 2:7394–7402. https://doi.org/10.1039/c4tb01125b

Shrivastava N, Khan LU, Khan ZU, Vargas JM, Moscoso-Londoño O, Ospina C, Brito HF, Javed Y, Felinto MCFC, Menezes AS, Knobel M, Sharma SK (2017) Building block magneto-luminescent nanomaterials of iron-oxide/ZnS@LaF_3: Ce^{3+}, Gd^{3+}, Tb^{3+} with green emission. J Mater Chem C 5:2282–2290. https://doi.org/10.1039/c6tc05053k

Smetana AB, Klabunde KJ, Sorensen CM (2005) Synthesis of spherical silver nanoparticles by digestive ripening, stabilization with various agents, and their 3-D and 2-D superlattice formation. J Colloid Interface Sci 284:521–526. https://doi.org/10.1016/j.jcis.2004.10.038

Song D, Guo G, Jiang J, Zhang L, Ma A, Ma X, Chen J, Cheng Z (2016) Hydrothermal synthesis and corrosion behavior of the protective coating on Mg-2Zn-Mn-Ca-Ce alloy. Prog Nat Sci Mater Int 26:590–599. https://doi.org/10.1016/j.pnsc.2016.11.002

Stanford MG, Lewis BB, Mahady K, Fowlkes JD, Rack PD (2017) Review article: advanced nanoscale patterning and material synthesis with gas field helium and neon ion beams. J Vac Sci Technol B, Nanotechnol Microelectron Mater Process Meas Phenom 35:030802. https://doi.org/10.1116/1.4981016

Stass DV, Woodward JR, Timmel CR, Hore PJ, McLauchlan KA (2000) Radiofrequency magnetic field effects on chemical reaction yields. Chem Phys Lett 329:15–22. https://doi.org/10.1016/s0009-2614(00)00980-5

Stoeva S, Klabunde KJ, Sorensen CM, Dragieva I (2002) Gram-scale synthesis of monodisperse gold colloids by the solvated metal atom dispersion method and digestive ripening and their organization into two- and three-dimensional structures. J Am Chem Soc 124:2305–11. https://doi.org/10.1021/ja012076g

Sue K, Suzuki M, Arai K, Ohashi T, Ura H, Matsui K, Hakuta Y, Hayashi H, Watanabe M, Hiaki T (2006) Size-controlled synthesis of metal oxide nanoparticles with a flow-through supercritical water method. Green Chem 8:634. https://doi.org/10.1039/b518291c

Sugimoto T (1987) Preparation of monodispersed colloidal particles. Adv Colloid Interface Sci 28:65–108. https://doi.org/10.1016/0001-8686(87)80009-x

Sun S, Zeng H (2002) Size-controlled synthesis of magnetite nanoparticles. J Am Chem Soc 124:8204–8205. https://doi.org/10.1021/ja026501x

Sun C, Lee JSH, Zhang M (2008) Magnetic nanoparticles in MR imaging and drug delivery. Adv Drug Deliv Rev 60:1252–1265. https://doi.org/10.1016/j.addr.2008.03.018

Sun P, Zhang H, Liu C, Fang J, Wang M, Chen J, Zhang J, Mao C, Xu S (2010) Preparation and characterization of Fe_3O_4/CdTe magnetic/fluorescent nanocomposites and their applications in immuno-labeling and fluorescent imaging of cancer cells. Langmuir 26:1278–1284. https://doi.org/10.1021/la9024553

Sun W, Yang W, Xu Z, Li Q (2018a) Anchoring Pd nanoparticles on $Fe_3O_4@SiO_2$ core-shell nanoparticles by cross-linked polyvinylpyrrolidone for nitrite reduction. ACS Appl Nano Mater 1:5035–5043. https://doi.org/10.1021/acsanm.8b01149

Sun L, Wei R, Feng J, Zhang H (2018b) Tailored lanthanide-doped upconversion nanoparticles and their promising bioapplication prospects. Coord Chem Rev 364:10–32. https://doi.org/10.1016/j.ccr.2018.03.007

Taniguchi T, Nakagawa K, Watanabe T, Matsushita N, Yoshimura M (2009) Hydrothermal growth of fatty acid stabilized iron oxide nanocrystals. J Phys Chem C 113:839–843. https://doi.org/10.1021/jp8062433

Tartaj P, Serna CJ (2003) Synthesis of monodisperse superparamagnetic Fe/silica nanospherical composites. J Am Chem Soc 125:15754–15755. https://doi.org/10.1021/ja0380594

Taylor P (2003) Ostwald ripening in emulsions: estimation of solution thermodynamics of the disperse phase. Adv Colloid Interface Sci 106:261–285

Thanh NTK, Maclean N, Mahiddine S (2014) Mechanisms of nucleation and growth of nanoparticles in solution. Chem Rev 114:7610–7630. https://doi.org/10.1021/cr400544s

Tromp RM, Ross FM, Reuter MC (2000) Instability-Driven SiGe Island Growth. Phys Rev Lett 84:4641–4644. https://doi.org/10.1103/physrevlett.84.4641

Tsuji M, Hashimoto M, Nishizawa Y, Kubokawa M, Tsuji T (2005) Microwave-assisted synthesis of metallic nanostructures in solution. Chem Eur J 11:440–452. https://doi.org/10.1002/chem.200400417

Valenzuela R, Fuentes MC, Parra C, Baeza J, Duran N, Sharma SK, Knobel M, Freer J (2009) Influence of stirring velocity on the synthesis of magnetite nanoparticles (Fe_3O_4) by the co-precipitation method. J Alloys Compd 488:227–231. https://doi.org/10.1016/j.jallcom.2009.08.087

Vereda F, Juan de Vicente A, Hidalgo-Álvarez R (2007) Influence of a magnetic field on the formation of magnetite particles via two precipitation methods. Langmuir 23:3581–3589. https://doi.org/10.1021/la0633583

Vestal CR, Zhang ZJ (2003) Synthesis and magnetic characterization of Mn and Co spinel ferrite-silica nanoparticles with tunable magnetic core. Nano Lett 3:1739–1743. https://doi.org/10.1021/nl034816k

Virkutyte J, Varma RS (2011) Green synthesis of metal nanoparticles: biodegradable polymers and enzymes in stabilization and surface functionalization. Chem Sci 2:837–846. https://doi.org/10.1039/c0sc00338g

Voorhees PW (1992) Ostwald ripening of two-phase mixtures. Annu Rev Mater Sci 22:197–215. https://doi.org/10.1146/annurev.ms.22.080192.001213

Wang Y, Xia Y (2004) Bottom-up and top-down approaches to the synthesis of monodispersed spherical colloids of low melting-point metals. Nano Lett 4:2047–2050. https://doi.org/10.1021/nl048689j

Watzky MA, Finke RG (1997) Transition metal nanocluster formation kinetic and mechanistic studies. A new mechanism when hydrogen is the reductant: slow, continuous nucleation and

fast autocatalytic surface growth. J Am Chem Soc 119:10382–10400. https://doi.org/10.1021/ja9705102

Werengowska-Ciećwierz K, Wiśniewski M, Terzyk AP, Furmaniak S (2015) The Chemistry of Bioconjugation in Nanoparticles-Based Drug Delivery System. Adv Condens Matter Phys 2015:1–27. https://doi.org/10.1155/2015/198175

Wu M, Xiong Y, Jia Y, Ye J, Zhang K, Chen Q (2005) Co-doped magnetite nanowire arrays prepared hydrothermally. Appl Phys A 81:1355–1358. https://doi.org/10.1007/s00339-005-3289-y

Wu S, Sun A, Zhai F, Wang J, Xu W, Zhang Q, Volinsky AA (2011) Fe_3O_4 magnetic nanoparticles synthesis from tailings by ultrasonic chemical co-precipitation. Mater Lett 65:1882–1884. https://doi.org/10.1016/j.matlet.2011.03.065

Xie T, Jing C, Long Y-T (2017) Single plasmonic nanoparticles as ultrasensitive sensors. Analyst 142:409–420. https://doi.org/10.1039/c6an01852a

Xu Y, Karmakar A, Wang D, Mahmood MW, Watanabe F, Zhang Y, Fejleh A, Fejleh P, Li Z, Kannarpady G, Ali S, Biris AR, Biris AS (2010) Multifunctional Fe_3O_4 cored magnetic-quantum dot fluorescent nanocomposites for rf nanohyperthermia of cancer cells. J Phys Chem C 114:5020–5026. https://doi.org/10.1021/jp9103036

Xuan S, Lee S-F, Lau JT-F, Zhu X, Wang Y-XJ, Wang F, Lai JMY, Sham KWY, Lo P-C, Yu JC, Cheng CHK, Leung KC-F (2012) Photocytotoxicity and magnetic relaxivity responses of dual-porous γ-Fe_2O_3@meso-SiO_2 microspheres. ACS Appl Mater Interfaces 4:2033–2040. https://doi.org/10.1021/am300008x

Yahya RB, Hayashi H, Nagase T, Ebina T, Onodera Y, Saitoh N (2001) Hydrothermal synthesis of potassium hexatitanates under subcritical and supercritical water conditions and its application in photocatalysis. Chem Mater 13:842–847. https://doi.org/10.1021/cm000561p

Yan F, Sun R (2014) Facile synthesis of bifunctional Fe3O4/Au nanocomposite and their application in catalytic reduction of 4-nitrophenol. Mater Res Bull 57:293–299. https://doi.org/10.1016/j.materresbull.2014.06.012

Yang P, Quan Z, Hou Z, Li C, Kang X, Cheng Z, Lin J (2009) A magnetic, luminescent and mesoporous core–shell structured composite material as drug carrier. Biomaterials 30:4786–4795. https://doi.org/10.1016/j.biomaterials.2009.05.038

Yang Y, Liu X, Lv Y, Herng TS, Xu X, Xia W, Zhang T, Fang J, Xiao W, Ding J (2015) Orientation mediated enhancement on magnetic hyperthermia of Fe_3O_4 nanodisc. Adv Funct Mater 25:812–820. https://doi.org/10.1002/adfm.201402764

Ye F, Laurent S, Fornara A, Astolfi L, Qin J, Roch A, Martini A, Toprak MS, Muller RN, Muhammed M (2012) Uniform mesoporous silica coated iron oxide nanoparticles as a highly efficient, non-toxic MRI T_2 contrast agent with tunable proton relaxivities. Contrast Media Mol Imaging 7:460–468. https://doi.org/10.1002/cmmi.1473

Yin W, Chen X, Cao M, Hu C, Wei B (2009) α-Fe_2O_3 nanocrystals: controllable SSA-assisted hydrothermal synthesis, growth mechanism, and magnetic properties. J Phys Chem C 113:15897–15903. https://doi.org/10.1021/jp904413m

Yu R, Liz-Marzán LM, García de Abajo FJ (2017) Universal analytical modeling of plasmonic nanoparticles. Chem Soc Rev 46:6710–6724. https://doi.org/10.1039/c6cs00919k

Yuwono VM, Burrows ND, Soltis JA, Penn RL (2010) Oriented Aggregation: Formation and Transformation of Mesocrystal Intermediates Revealed. J Am Chem Soc 132:2163–2165. https://doi.org/10.1021/ja909769a

Zhang Q, Zhang T, Ge J, Yin Y (2008) Permeable silica shell through surface-protected etching. Nano Lett 8:2867–2871. https://doi.org/10.1021/nl8016187

Zhang R, Khalizov A, Wang L, Hu M, Xu W (2012) Nucleation and growth of nanoparticles in the atmosphere. Chem Rev 112:1957–2011. https://doi.org/10.1021/cr2001756

Zhang L, Wang Y, Tang Y, Jiao Z, Xie C, Zhang H, Gu P, Wei X, Yang G-Y, Gu H, Zhang C (2013) High MRI performance fluorescent mesoporous silica-coated magnetic nanoparticles for tracking neural progenitor cells in an ischemic mouse model. Nanoscale 5:4506. https://doi.org/10.1039/c3nr00119a

Zhang Q, Yin T, Gao G, Shapter JG, Lai W, Huang P, Qi W, Song J, Cui D (2017) Multifunctional Core@Shell magnetic nanoprobes for enhancing targeted magnetic resonance imaging and fluorescent labeling in vitro and in vivo. ACS Appl Mater Interfaces 9:17777–17785. https://doi.org/10.1021/acsami.7b04288

Zhao Wenru, Jinlou Gu, Zhang Lingxia, Hangrong Chen A, Shi J (2005) Fabrication of uniform magnetic nanocomposite spheres with a magnetic core/mesoporous silica shell structure. J Am Chem Soc 127:8916. https://doi.org/10.1021/ja051113r

Zheng Y, Cheng Y, Wang ÃY, Bao F, Biefeld R (2005) Synthesis and shape evolution of a-Fe_2O_3 nanophase through two-step oriented aggregation in solvothermal system. J Cryst Growth 284:221–225. https://doi.org/10.1016/j.jcrysgro.2005.06.051

Zhichuan Xu, Yanglong Hou A, Sun S (2007) Magnetic core/shell Fe_3O_4/Au and Fe_3O_4/Au/Ag nanoparticles with tunable plasmonic properties. J Am Chem Soc 129:8698–8699. https://doi.org/10.1021/ja073057v

Zhou M, Nakatani E, Gronenberg LS, Tokimoto T, Wirth MJ, Hruby VJ, Roberts A, Lynch RM, Ghosh I (2007) Peptide-Labeled Quantum Dots for Imaging GPCRs in Whole Cells and as Single Molecules. Bioconjug Chem 18:323–332. https://doi.org/10.1021/bc0601929

Zhu Y, Ikoma T, Hanagata N, Kaskel S (2010) Rattle-Type Fe_3O_4@SiO_2 hollow mesoporous spheres as carriers for drug delivery. Small 6:471–478. https://doi.org/10.1002/smll.200901403

Zhu N, Ji H, Yu P, Niu J, Farooq M, Akram M, Udego I, Li H, Niu X, Zhu N, Ji H, Yu P, Niu J, Farooq MU, Akram MW, Udego IO, Li H, Niu X (2018) Surface modification of magnetic iron oxide nanoparticles. Nanomaterials 8:810. https://doi.org/10.3390/nano8100810

Zinke-Allmang M, Feldman LC, Grabow MH (1992) Clustering on surfaces. Surf Sci Rep 16:377–463. https://doi.org/10.1016/0167-5729(92)90006-w

Chapter 2
Iron Oxide Magnetic Nanoparticles (NPs) Tailored for Biomedical Applications

Giorgio Zoppellaro

Abstract Many variables need to be considered and implemented in the NP systems when these nanostructured magnetic materials are tailored for biological applications. In this chapter, we discuss the chemical basis that drives the selection of magnetic cores and outer shell compositions, sizes, morphologies, to improve NP stability, low cytotoxicity, and circulation time. Toxicity effects are dissected, with emphasis on metal metabolism and ROS generation. NP biodistribution is analyzed, as well as the possible interactions between NPs with cells, proteins, and redox molecules present in vitro and in vivo experiments that can alter and limit NP functions as contrast agent materials and as vectors in drug delivery.

Keywords Synthetic methods · Magnetic nanoparticles · Nanomaterial's metabolism · Nanomaterial's biodistribution · Medical applications

Introduction

Tailoring the properties of magnetic nanosystems for biomedical applications is a challenging ground of research for chemists, physicists of magnetism, and biochemists (Figuerola et al. 2010; Xie and Jon 2012; Sapsford et al. 2013). Magnetic nanoparticles (NPs) based on paramagnetic metal oxide, especially iron, such as magnetite (Fe_3O_4) or maghemite (γ-Fe_2O_3), have been extensively studied in biomedical applications in the last three decades (Pankhurst et al. 2003; Corchero and Villaverde 2009), because of their effectiveness to act as magnetic probes in medical diagnostic (magnetic resonance imaging, MRI) (Laurent et al. 2008; Maity et al. 2012), in multimodal imaging (Thorek et al. 2006; Xie et al. 2010), as flexible vectors for the transport of pharmaceutical compounds (McCarthy and Weissleder 2008; Basuki et al. 2013; Wang et al. 2013a; Phan et al. 2013) and the potentiality to open doors to new medical therapies (hyperthermia) (Cohen and Shoushan 2013; Kievit and

G. Zoppellaro (✉)
Department of Physical Chemistry, Faculty of Science, Regional Centre of Advanced Technologies and Materials, Palacky University in Olomouc, Slechtitelu 11, 78371 Olomouc, Czech Republic
e-mail: giorgio.zoppellaro@upol.cz; zoppellarogiorgio@gmail.com

Zhang 2011; Le Renard et al. 2010; Kolhatkar et al. 2013). Historically, the large attention devoted to superparamagnetic Fe_3O_4 or γ-Fe_2O_3 core-shell nanoparticles by the material research community has been gated with the application of NPs as contrast agent materials. These metal oxides are easy to obtain and have high magnetic moments (up to 94–96 emu/g for Fe_3O_4 and up to 84–86 emu/g for γ-Fe_2O_3), characteristic that provides large enhancement of the transverse relaxivity (T_2 and T_2*), which give the negative image contrast of the tissues where those materials are located (Mahmoudi et al. 2011a; Tong et al. 2010; Ghosh et al. 2012). Several reviews, especially focusing on the use and efficacy of magnetic nanoparticles in the field of contrast agents, have been recently published (Lee et al. 2012a; Lee and Hyeon 2012; Reddy et al. 2012) and the topic is not treated in detail here. In this chapter, focus is drawn on the synthetic aspects that are keys in materials design for the NP biological applications, discuss the use of biocompatible coating materials to improve circulation time, bioavailability, specificity in cell's targeting, impacts on cell's metabolism, interaction between NPs with proteins and biologically relevant molecules in vivo, biodistribution, and finally discuss the potentiality that emerged from the use of NPs in the modern pharmaceutical and medical diagnostic practices.

The Synthetic Design of Biocompatible NPS: Factors to Consider

To safely act in biological environments, many factors need to be considered and implemented in the NP systems. These variables can be rationalized into (I) chemical selection of magnetic cores and outer shell compositions, including formulation of the encapsulating materials to improve NP stability and delivery, control of (II) morphology (e.g., spherical, rods, cubes, cuboctahedron), (III) NP's hydrodynamic sizes, colloidal properties at various pHs and ionic strengths, and (IV) knowledge of possible interactions between NPs with cells, proteins, and redox molecules present in the bloodstream. Altogether, these variables form the key aspects that determines stability, action and limitations of NPs in vivo and their ability to act as contrast agent and imaging probes, vectors for drug-delivery, and effectiveness in hyperthermia treatments (Lu et al. 2007a). Figure 2.1 shows a schematic representation of a magnetic nanosystem that includes several diverse functionalities, all tailored for biomedical applications.

Figure 2.2 reports drawings of diverse NP architectures, illustrating the creativity-driven design that inspired researchers active in the field of bio-nanotechnology (Phan et al. 2013; Park et al. 2007; Pichon et al. 2011; Gao et al. 2008; Chen et al. 2014; Thomas et al. 2010; Hyeon et al. 2001; Lee et al. 2011a; Wang et al. 2013b; Li et al. 2013a, b; Zoppellaro et al. 2014; Hickey et al. 2014). Figure 2.2a shows iron oxide NPs (γ-Fe_2O_3) that are produced with well-defined sizes by thermal decomposition processes of metal–surfactant complexes, as described in the work of Park et al. (2007). Figure 2.2b shows iron oxide nanocubes (NC16), which are made by
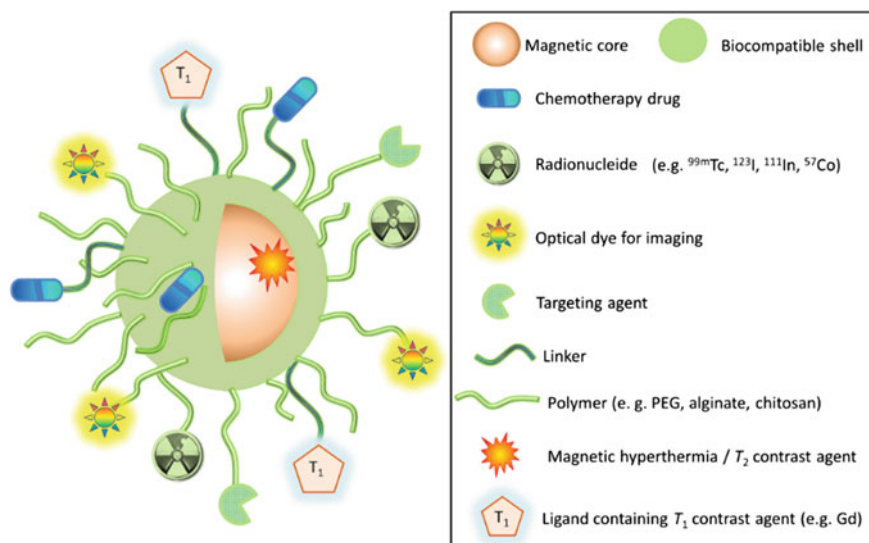
Fig. 2.1 Schematic representation of a magnetic nanoparticle (NP) encoding multi-functional groups at the surface, engineered for biomedical applications. The superparamagnetic core (iron oxide, Fe_3O_4, γ-Fe_2O_3 or composed by mixed metal oxides such as $CoFe_2O_4$, $MnFe_2O_4$, $NiFe_2O_4$) is protected by a canopy (organic, inorganic) of a biocompatible material (shell). The core brings the negative (T_2) image contrast in MRI for medical diagnostics and is used as heating centre for hyperthermia treatments in cancer therapy. Functional groups (optical dyes, targeting agents) and polymeric moieties on the surface are introduced in a way to tailor further the NP function. Dyes lead to combination of T_2 MRI ability with optical imaging capabilities, non-fouling polymers enhance the plasma residence, targeting agents allow to boost specific cell-type recognition, introduction of radionuclides brings dual imaging capabilities (e.g., for SPECT/MRI), and gadolinium-containing ligands are introduced to optimize materials that combine T_1-T_2 MRI imaging. Furthermore, NP can transport therapeutic drugs, passively, using the bloodstream through the enhanced permeability and retention (EPR) effect or actively, by a magnetically driven process, or using specific surface-exposed targeting agents. The drug (and/or the gene therapeutic material) can be introduced into NP by suitable drug-linkers or simply be entrapped by NP through electrostatic and H-bonding interactions between the drug and the material composing the NP shell

two components, the spinel phase and the wüstite phase (face-centered cubic (fcc) Fe_xO ($0.8 < x < 1$) obtained by Pichon et al. (Pichon et al. 2011). Panels (c) and (d) show γ-Fe_2O_3 hollow nanoparticles (c) and $Pt@Fe_2O_3$ yolk-shell nanoparticles (d) obtained by Gao et al. (2008). Panel (e) presents more complex architecture for NPs, obtained from sodium alginate and poly-L-lysine-coated $Fe@SiO_2$ nanoparticles ($Fe@SiO_2@AL/PLL$) prepared from α-$Fe_2O_3@SiO_2$ by Chen et al. (2014). Panel (f) reports the zinc-doped iron oxide nanocrystals (ZnNCs) encapsulated within meso-porous silica by Thomas et al. (2010), panel (g) the magneto-polymersomes assembled with 19.9 nm iron oxide nanoparticles obtained by Hickey et al. (2014), panel (h) MnO@Mn-doped iron oxide [$MnO@(Mn_{0.2}Fe_{0.8})_3O_4$] nanoparticles encoding cross-shape morphology as reported by Phan et al. (2013), panel (i) condensed packing of γ-Fe_2O_3 nanoclusters encaged by alginate chains (MagAlg), used to transport
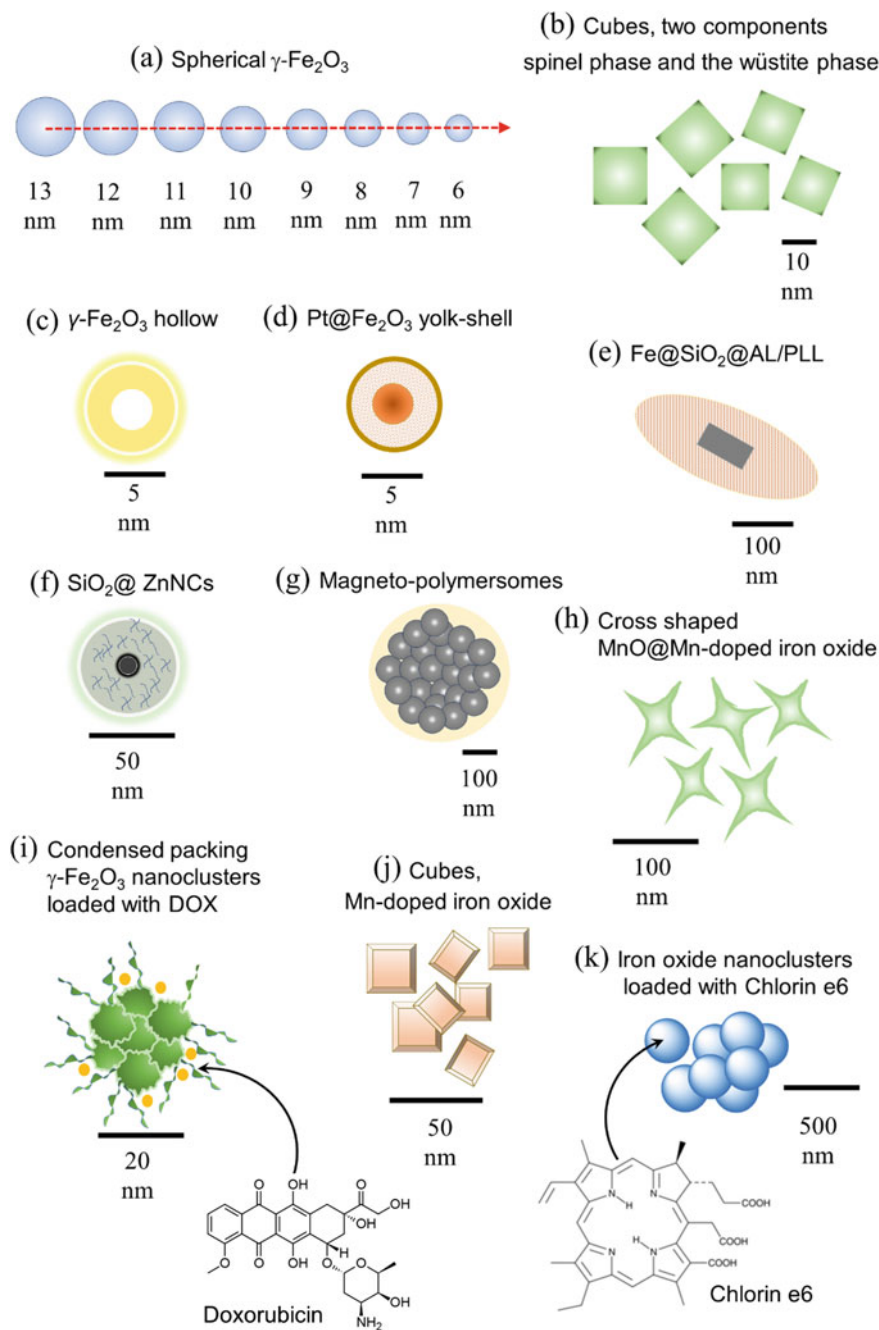
Fig. 2.2 Various morphological organizations and chemical compositions of core-shell metal-oxide nanoparticles used in biomedicine, drawn as cartoons

the anticancer drug doxorubicin (Zoppellaro et al. 2014), panel (j) Mn-doped iron oxide nanoparticles (Phan et al. 2013), and panel (k) PEG-functionalized iron oxide nanoclusters loaded with chlorin e6 (Ce6) obtained by Li et al. (2013b).

Synthetic Methods: Pros and Cons

Different synthetic approaches have been pursued for the synthesis of the superparamagnetic Fe_3O_4 or γ-Fe_2O_3 systems encoding sizes down to 3.2 nm (Figuerola et al. 2010; Laurent et al. 2008; Guardia et al. 2011; Kucheryavy et al. 2013), as well as assembly of mixed metal-oxide systems such as, for example, $CoFe_2O_4$ (sizes from 4.2 to 18.6 nm) (Pereira et al. 2012), ultra-small $CoFe_2O_4$ particles (down to 2.8 nm size) (Peddis et al. 2008), $MnFe_2O_4$ (sizes from 9.3 to 59.5 nm) (Pereira et al. 2012), $Zn_{04}Fe_{2.6}O_4$ (sizes from 18 to 120 nm) (Noh et al. 2012), $NiFe_2O_4$ (12 nm size) (Lee et al. 2006a), $Ni_{08-x}Zn_{0.2}Mg_xFe_2O_4$ (sizes from 36 to 59 nm) (Gabal and Bayoumy 2010). So far, the co-precipitation method from suitable mixtures of inorganic metal salts in water solutions (Figuerola et al. 2010; Laurent et al. 2008; Maity et al. 2012) represents one of the most explored approaches for the NP synthesis. The principal advantage of the co-precipitation route is the easy access to large amounts of NPs (from the laboratory-bench perspectives) but offers, in general, less control over the particle size distribution compared to other methodologies. In this context, alternative routes have been explored to obtain NPs with controlled sizes and shapes and to introduce complex functionalities. These methods can be shortly divided into (i) constraint environment approaches, (ii) hydrothermal synthesis, (iii) sol–gel reactions, (iv) flow injections, and (v) microwave-assisted processes. Other methods, however, can be found in the literature and benefit from a combination of the methodologies (i) to (v) (Laurent et al. 2008). The constraint environment approach (i) takes advantage from the use of amphoteric surfactants to create micellar-type structures in apolar solvents (Liz et al. 1994; Dresco et al. 1999; Santra et al. 2001; Talelli et al. 2009; Gobe et al. 1983; Lee et al. 2005a, 2012b). For example, Talelli et al. (2009) synthesized superparamagnetic iron oxide nanoparticles (SPIONs), which have been encaged into micelles, composed of amphiphilic, thermosensitive, and biodegradable block copolymers of poly(ethylene glycol)-b-poly[N-(2-hydroxypropyl) methacrylamide dilactate] (mPEG-b-p(HPMAm-Lac2)) (Fig. 2.3a). Other examples on the use of constraint environments employed, as confining matrixes, protein cages (Uchida et al. 2006; Fantechi et al. 2014; Kostiainen et al. 2013) (Fig. 2.3b), viral capsids (Douglas et al. 2002; Allen et al. 2007), dendron cages (Strable et al. 2001; Saha et al. 2013; Bulte et al. 2001) (Fig. 2.3c–e), and phospholipid vesicles (De Cuyper and Joniau 1991; Faure et al. 2009). The synthetic method (ii), namely the hydrothermal synthesis, is used to promote the thermal decomposition of iron salt precursors (Park et al. 2007; Hyeon et al. 2001; Kolenko et al. 2014; Kim et al. 2009; Li et al. 2004; Sun and Zeng 2002; Rockenberger et al. 1999), where nature of surfactants, solvents, time, and temperatures is the key variables that allow the finest tuning of the NP's size distribution and material's crystallinity (see also Fig. 2.2a); this method
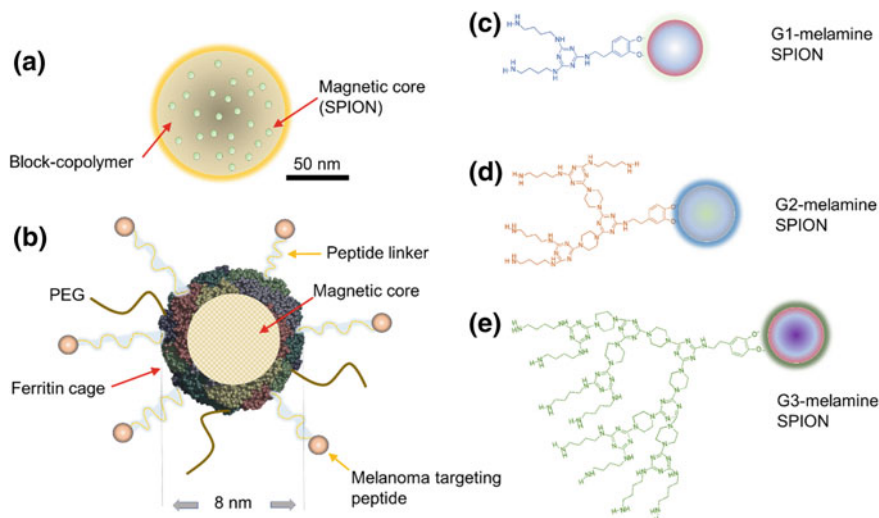
Fig. 2.3 a SPION encaged in micelles (Talelli et al. 2009), **b** cobalt-doped iron oxide highly monodisperse mineralized inside a genetically modified variant of ferritin (HFt) by Fantechi et al. (2014), **c**, **d**, **e** melamine dendron (G1–G3)-iron oxide nanoparticles (G-SPION) synthesized by Saha et al. (2013)

is perhaps the second alternative chosen by many researchers in the field, being the co-precipitation procedure the first choice. The methods (iii), sol–gel reactions, are processes based on the hydroxylation, condensation, and inorganic polymerization of metal-containing precursors in solution at room temperature, which leads to the formation of 3D metal-oxide networks that require further heat treatments for obtaining in the final metal oxide the crystalline phase (Kim et al. 2008a; Lee et al. 2011b). The (iv) flow injection method is an alternative to the constraint environment approach and uses a continuous flow of the reactants into a narrow reaction chamber and allows the engineering of magnetic nanoparticles with very narrow size distribution (Salazar-Alvarez et al. 2006). The (v) microwave-assisted processes (Parsons et al. 2009; Edrissi and Norouzbeigi 2010; Bilecka et al. 2008; Osborne et al. 2012) employ the fast temperature gradients achievable with microwave energy to dramatically shorten the reaction times compared to the previous and more conventional (i)–(iii) synthetic methods and allow the preparation of materials with good quality and in highly reproducible fashion, making easier the translation from laboratory-bench production of NPs to cost-effective preparation of NPs for commercial uses.

However, as recently reported by Pascu et al. (2012), after comparison of the performance and quality of microwave-assisted synthesized iron oxide nanoparticles with those obtained by thermal decomposition process of metal complexes, they demonstrated that the former exhibits a surface reactivity significantly smaller than their thermal decomposition counterparts. This characteristic may pose some limits to the use of this method when the ability of engineering the NP surface with an array of complex functionalities is required. While size, shape, chemical composition,

and crystallinity of the metal oxide core have pivotal impacts on the nanoparticle's magnetic regime (e.g., saturation magnetization, M_s; see Fig. 2.4 for illustrative cases) and performances, especially for hyperthermia treatments, biosensing and imaging (MRI), the chemical nature of the shell becomes often vital in determining the NP biological impact. Thus, the selection of the organic/inorganic materials
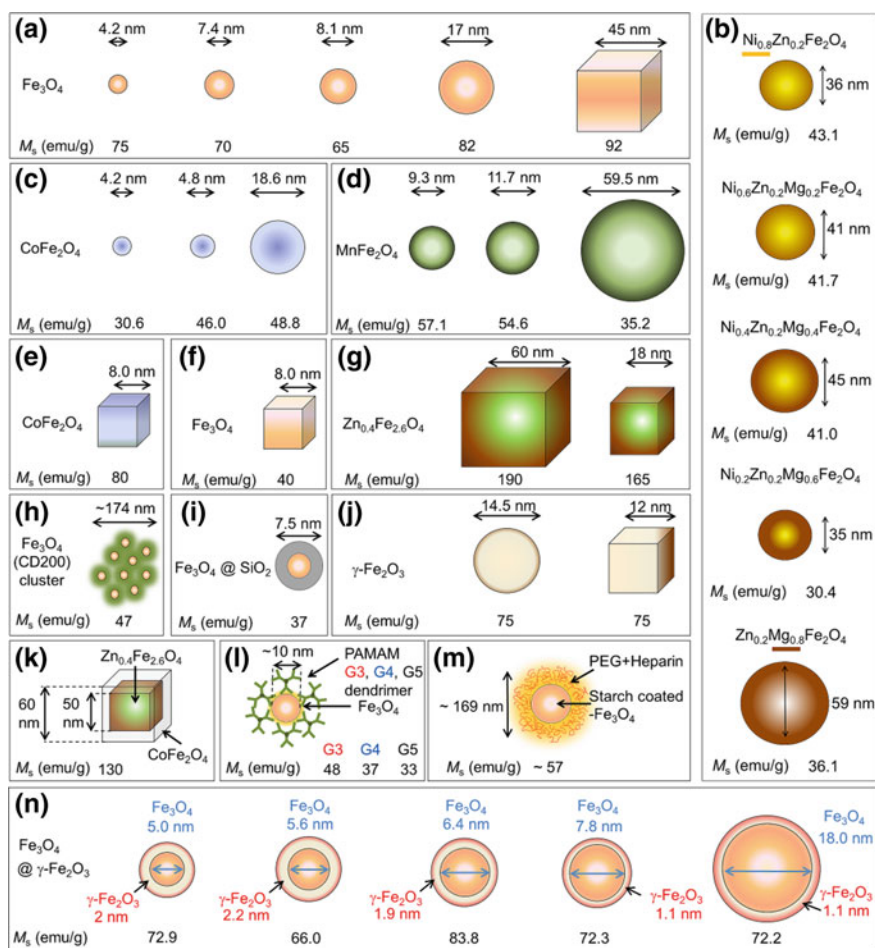
Fig. 2.4 Observed dependence of the mass magnetization (M_s, $T = 300$ K) from the nanoparticle's core chemical composition, size, morphology, and architecture (core-shell) in some illustrative systems as reported in the literature. Data taken from **a** Guardia et al. (2011), **b** Gabal and Bayoumy (2010), **c**, **d** from Pereira et al. (2012), **e** from Song et al. (2004), **f** from Zhen et al. (2011), **g** from Noh et al. (2012), **h** the magnetite-cyclodextrin cluster (CD200) from Yallapu et al. (2011), **i** from Larumbe et al. (2012), **j** from Salazar-Alvarez et al. (2008). **k** Noh et al. (2012), **l** from Nigam et al. (2014), **m** the starch-coated, PEGylated, and heparin-functionalized iron oxide magnetic nanoparticles (DNPH) from Zhang et al. (2013), **n** the core-shell system $Fe_3O_4@\gamma$-Fe_2O_3 from Frison et al. (2013). Note that in (**l**) the term PAMAM stands for polyamidoamine

encaging the magnetic cores represents an important step in the NP design (Boyer et al. 2010). The coating materials, in fact, do not simply grant to the NPs the necessary ferrofluid behavior but should provide protecting layers against a fast-metabolic degradation of the NPs, process that may lead to the emergence of cytotoxicity, thus limiting the NP's ability to function as diagnostic/therapeutic toolbox (Mahmoudi et al. 2010, 2011b, c) (vide infra).

Biologically Compatible Coating Materials for NPs

In core-shell nanoparticles (see Fig. 2.1), the outer-shell material should act in way to decrease (i) the tendency of the nanoparticle to agglomerate into big clusters in solution, phenomenon that may produce, when significant, potentially harmful occlusions of blood vessels after infusion and (ii) they should decrease the rate of the nanoparticle's opsonization, phenomenon that leads to the fast removal of the NPs from the bloodstream by the reticuloendothelial system (RES), also called mononuclear phagocyte system (MPS). Several other properties can be directly linked to the chemical identity and composition of the NP coating materials, such as (i) the maintenance of the nanoparticle's charge (zeta-potential) in physiological ranges of pHs and ionic strengths, (ii) the release of cargo molecules in response to specific pH alterations or temperature alterations in the local environment (thermo-sensitive polymers) (Peppas et al. 2000; Brannon-Peppas and Blanchette 2004; Brazel 2009), (iii) the ability to graft fluorescent molecules for the generation of dual probes where optical and MRI imaging can be combined on a single nanomagnetic platform (Gallagher et al. 2009; Lamanna et al. 2011; Yen et al. 2013), (iv) to generate, for example, mixed Gd-iron oxide nanosystems for enhanced T_1-T_2 MRI agents (Di Corato et al. 2013; Yang et al. 2011), (v) to couple MRI and gene delivery systems (Guo et al. 2012), and (vi) to boost active biosensing and MRI imaging by inclusion of specific biomarkers (e.g., for the in vivo targeting of folate receptors or transferrin receptors in cancer cells) (Choi et al. 2004; Kresse et al. 1998). For those reasons, several types of coating materials (organic and inorganic) have been tested and validated as biocompatible. Among the large number of multifunctional/biocompatible shell variants that can be found in the literature, some have been more extensively studied and those include polyethylene glycol (Fig. 2.5k), polyethylene glycol fumarate chains (Yamaoka et al. 1994; Lee et al. 2007a; Sun et al. 2010; Larsen et al. 2009; Mahmoudi et al. 2009a, b; Cole et al. 2011), alginate (Zoppellaro et al. 2014; Ma et al. 2007; Xu et al. 2006; Chen et al. 2006; Sipos et al. 2003; Dias et al. 2011) (Fig. 2.5g), chitosan (Nicolás et al. 2013; Kim et al. 2008b; Jiang et al. 2002; Lee et al. 2005b; Arias et al. 2012) (Fig. 2.5b), dextran (Kumar et al. 2012; Tassa et al. 2011; Mojica Pisciotti et al. 2014; Nath et al. 2009) (Fig. 2.5d), silica shells (Chen et al. 2014; Kim et al. 2008a; Lu et al. 2007b; Jana et al. 2007; Zhang et al. 2008; Ye et al. 2012; Kunzmann et al. 2011; Malvindi et al. 2014), gold (Lyon et al. 2004; Fan et al. 2013; Tamer et al. 2013), polyvinyl alcohol (Mahmoudi et al. 2009c; Osada and Gong 1998; Petri-Fink et al. 2008), poly(vinylpyrrolidone) (D'Souza et al. 2004; Zhang et al. 2012; Huang
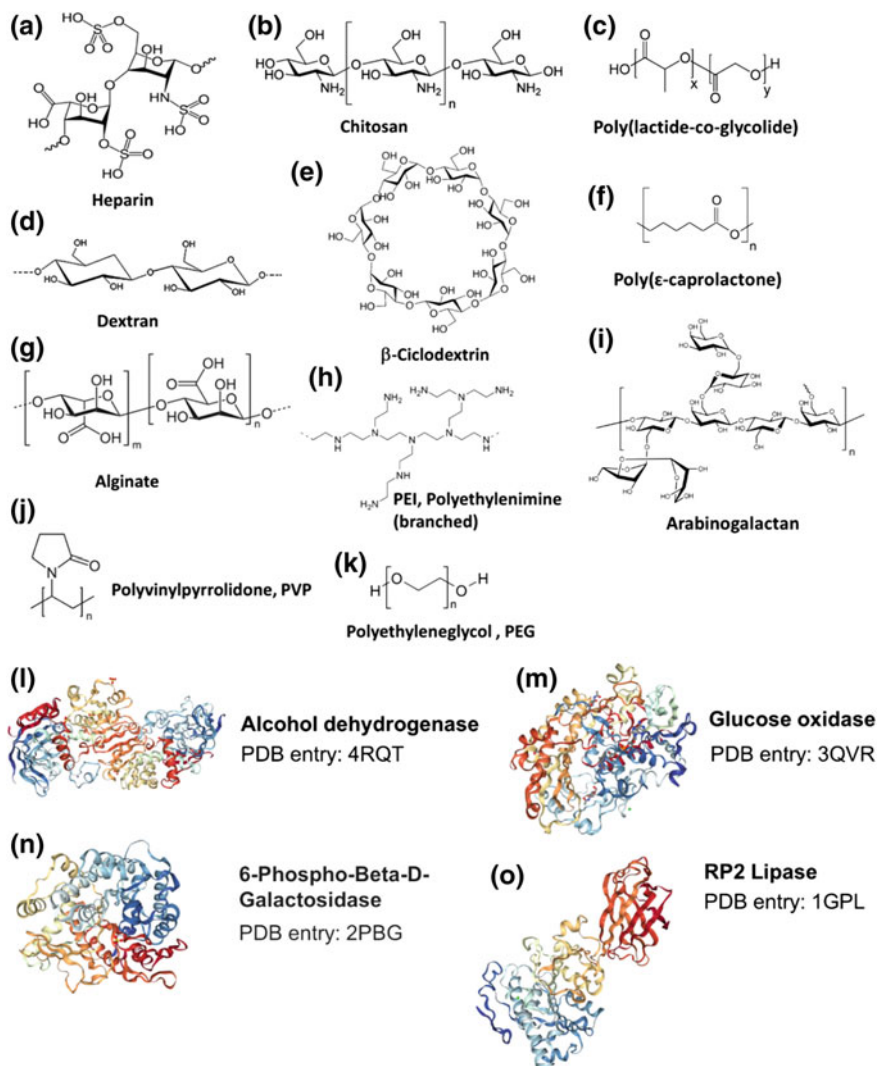
Fig. 2.5 Structural drawings of some of the polymeric biocompatible coating materials and protein molecules used as canopies for the application of the magnetic oxide nanoparticles in biomedical applications

et al. 2010; Lee et al. 2008) (Fig. 2.5j), acrylate-based coatings (Bakandritsos et al. 2010a; Li et al. 2013c), starch (Kim et al. 2003), PEG-modified, cross-linked starch-coating (Cole et al. 2011), polyamine (Lin et al. 2014; El Khoury et al. 2007), PEI (poly(ethyleneimine)) (Thünemann et al. 2006) (Fig. 2.5h), bisphosphonate-PEG moieties (Sandiford et al. 2013) and PEG-derivatized phosphine oxide ligands (Bin

et al. 2007), poly(lactide)-PEG chains (Bakandritsos et al. 2010b), poly(lactide-co-glycolide) chains (Lee et al. 2012c) (Fig. 2.5c), poly(ε-caprolactone) (Flesch et al. 2004, 2005) (Fig. 2.5f), arabinogalactan (Lawaczeck et al. 2004) (Fig. 2.5i), heparin (Lee et al. 2012d) (Fig. 2.5a), β-cyclodextrin (Li et al. 2012) (Fig. 2.5e). Furthermore, several biomolecules (e.g., proteins, enzymes) have been used as well in the form of outer-shell canopies. These biomolecules include alcohol dehydrogenase (core magnetite NPs, 10.6 nm size) (Liao and Chen 2001) (Fig. 2.5l), β-D galactosidase (core magnetite–chitosan NPs, size 30 nm) (Pan et al. 2009) (Fig. 2.5n), glucose oxidase (core magnetite NPs, size 20 nm) (Rossi et al. 2004) (Fig. 2.5m), lipase (core magnetite NPs, size 16 nm) (Mak et al. 2009) (Fig. 2.5o), phosphatase (core magnetite NPs, size 40 nm) (Saiyed et al. 2007), α-amylase (cellulose-coated core magnetite NPs, size up to 22.5 nm) (Namdeo and Bajpai 2009), and casein (magnetite core with size of 15 nm) (Huang et al. 2013). NP preparations based on enzymatic systems, proteins, and nucleic acid are also available from commercial sources (e.g., magnetic beads with immobilized avidin, streptavidin, oligodeoxythimidine). The use of polysaccharides as coating materials (e.g., heparin/heparin sulfate, cyclodextrin, alginate, chitosan) is particularly useful, because these polymers can themselves actively enter in several biological processes, such as cell signaling and adhesion.

For example, heparin is as therapeutic agent, clinically administrated as an anticoagulant for thromboembolic diseases (Jin et al. 1997). Heparan sulfate functions in several key biological processes, including regulation of cell growth and proliferation, angiogenesis, viral invasion, and tumor metastasis (Rabenstein 2002). Chitosan is an efficient delivery vehicle for nucleic acids (gene-transfection), and cyclodextrins is known to solubilize hydrophobic drugs and is used in pharmaceutical formulations for drug delivery, as well as in both food and pharma industry for its ability to sequester cholesterol molecule (Thatiparti et al. 2010). In this context, Vance and Karten (2014) have recently shown the mobilization of lysosomal cholesterol by cyclodextrin in the Niemann–Pick C disease, thus providing the literature data for a promising therapeutic agent in the treatment of NPC patients, for whom no effective treatment is currently available. The NPC is a pathology in which endocytosed cholesterol becomes sequestered in late endosomes/lysosomes (LE/L) due to mutations in either the NPC1 or NPC2 gene. These mutations cause progressive neurodegeneration, as well as liver and lung disease; thus, further studies using unconventional delivery, such as magnetically driven and biocompatible nanoparticles coated with this oligosaccharide (Li et al. 2012), may open novel landscapes for the therapy. Most of core-shell iron oxide nanoparticles based on the aforementioned coatings materials have been found highly biocompatible. The biocompatibility of NPs is generally tested in vitro, following several protocols such as the 3-(4,5-dimethylthiazol-2-yl)-2,5-diphenyltetrazolium bromide (MTT) assay (Mosmann 1983), the comet assay (single-cell gel electrophoresis for measuring deoxyribonucleic acid (DNA) strand breaks in eukaryotic cells, (Liao et al. 2009)), the cell-life cycle assay (Riccardi and Nicoletti 2006), the NBT assay (nitro-blue tetrazolium chloride) for sensitive detection of alkaline phosphatase (Freeman and King 1972), and the lactate dehydrogenase (LDH) assay (Smith et al. 2011). Figure 2.6 shows the biocompatibility

-Acid phosphatase
Lysosomal activity

-MTT / XTT
Mithochondrial metabolism
Respiratory toxicity

-Neutral red
Lysosomal activity
Membrane permeability

ANIMAL CELL

Pinocytotic vesicle — — Mitochondrion

Lysosome

Golgi vesicles — — Golgi Apparatus

Rough
Endoplasmic
Reticulum

— Nucleolus

— Nucleus

-Crystal violet
Cell proliferation
DNA

Smooth ER
(without ribosomes)

— Centrioles

— Microtubules

Cell Membrane — — Cytoplasm

— Ribosome

-LDHe
Membrane permeability

-Glucose
General Physiological cell state

-Sulforhodamine B
Cell proliferation
Total protein synthesis

Fig. 2.6 Biochemical tests used to probe the impact of NPs on the cell's metabolic functions

tests usually employed to address the impact of NPs on the metabolic functions of animal cells.

Ideally, at least two or more different tests should be used, to ascertain good biocompatibility. In addition, the NP screening against several types of cells is becoming a practice highly recommended. Once the cytotoxicity impact has been addressed in vitro, the next step toward the effective application of the magnetic nanosystem in the medical practice requires the careful validation of the NPs by in vivo *studies*. At this stage, it is pivotal to obtain the clear understanding of the NP uptake process in different cells in living organisms, NP metabolism, and biological pathways of NP degradation.

The Cellular Uptake Process of NPs

The uptake process generally relies on the NP's passive transport into bloodstream, by injection of physiological solutions containing the magnetic nanosystem in the living models first (e.g., mice) and finally in healthy patients. The intravenous administration of the ferrofluid nanoparticles is regarded as the most useful methodology that grants a fast reach of the targeted organs and/or tissues, method faster than the other approach employed for delivering these materials (e.g., oral preparations). In oral preparations, the nanoparticles need to travel across the epithelial cells in the gastrointestinal tract and then are transferred (absorption) into the bloodstream; thus, interactions of magnetic nanoparticles with the blood components (cells, proteins,

and small redox molecules) require understanding of their stabilities and possible metabolic pathways, interaction mechanisms with other biomolecules, half-life, and biodistribution. The physical characteristics that determine the biological uptake, metabolism, and cytotoxicity impact of the magnetic nanoparticles are associated directly with the chemical nature of the nanoparticle's surface (surface charge and composition) and their effective dimension (hydrodynamic size) when introduced in the biological environment (Verma and Stellacci 2010; Liu et al. 2013; Soenen et al. 2011a). These are the properties immediately screened by the immune system (Dobrovolskaia et al. 2008). In its simplest picture, the immune system can be described as composed of a variety of cells, such as phagocytes (macrophages, neutrophils, dendritic cells), mast cells, eosinophils, basophils, natural T-killer cells, and protein/enzymatic factors (e.g., cytolytic proteins).

These proteins and cells are strategically distributed in the body, especially in the bloodstream, and they broadly act in way to identify and clear senescent cells, foreigner microorganisms, or unwanted materials. As shown in Fig. 2.7, the bone marrow is the source of numerous immune and blood cells in the healthy adult animals. Table 2.1 collects information on localization and functions of the immune cells. All immune cells originate from hematopoietic stem cells, and then, these differentiate into various immune cell types. Some of these cells mature in the bone marrow itself, and others migrate through the circulatory system and undertake final maturation in other tissues. After intravenous administration, the nanoparticles that are more prone to establish interactions (opsonization) with Ig immunoglobulin proteins (glycoproteins) complement component (C3, C4, and C5) and blood serum proteins are cleared up within minutes from the bloodstream. Immunoglobulins are produced by plasma cells, exocrine, and tissue fluid. They represent ~20% of the total plasma proteins. Differences in the heavy polypeptide chain allow the immunoglobulins to function at
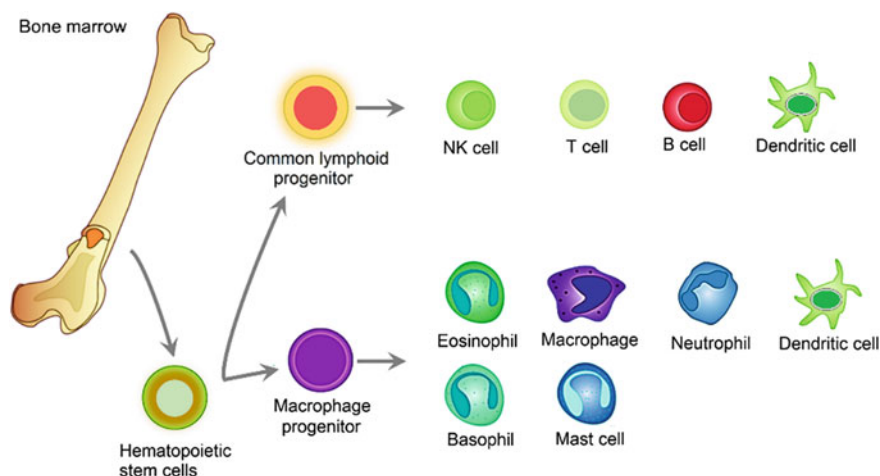
Fig. 2.7 Types of immune cells generated from stem cells in the bone marrow

Table 2.1 Localization and function of various immune cells

	Localization	Function
Mast cell	Connective tissues and mucous membranes	Dilates blood vessel, induces inflammation through release of histamines and heparin. Alerts macrophage and neutrophils
Macrophage	Migrates from blood vessels into tissues	Phagocytic activity, consuming pathogens and cancer cells. Stimulate responses of other immune cells
NK cell	Circulates in blood, migrates in the tissues	Destroy virus-infected cells and tumor cells
Dendritic cell	Located in epithelial tissues (skin, lung, digestive tract). Migrates to lymph nodes when activated	Have antigens on the surface, which trigger adaptive immunity
Monocyte cell White cell[a]	Located in the spleen, migrates through blood vessels to reach infected tissues	Differentiates into macrophages and dendritic cells in response to inflammations
Neutrophil cell	Migrates from blood vessels into tissues	Initial responder at the site of trauma or infection. Releases toxins, recruits other immune cells
Basophil cell	Circulates in blood and migrates from blood vessels into tissues	Defense against parasites. Releases histamines
Eosinophil cell	Circulates in blood and migrates from blood vessels into tissues	Releases toxins, killing bacteria and parasites. Can cause tissue damages

Monocycles circulate in the blooodstream (1-3 days) then move into tissues and differentiate into macrophages and dentric cells

particular stages of the immune response. Five classes of Ig are known, IgA (dimer), IgD (monomer), IgG (monomer), IgE (monomer), IgM (pentamer), and are shown in Fig. 2.8.

Iron oxide and mixed iron/d-block metal oxide nanoparticles are up taken by almost all cells involved in the immune response (Fig. 2.7), including microglia and dendritic cells within the brain. Neutrophils have not been found to uptake small nanoparticles (<30 nm, called ultra-small superparamagnetic iron oxide nanoparticles, USPIO). The recognition/clearance mechanism of the nanoparticles as foreigner
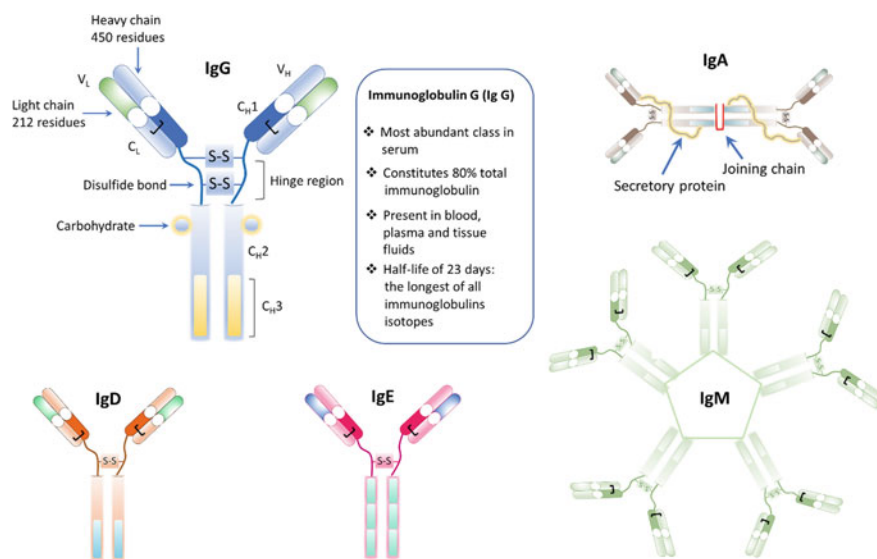
Fig. 2.8 Structural organization of immunoglobulins (IgA, IgD, IgE, IgG, IgM)

material is a complex metabolic process but can be depicted as the spontaneous adsorption of circulating plasma proteins (opsonins) on the nanoparticle's surfaces.

Nanoparticles that fast interact with plasma components (i.e., Ig components) are rapidly cleared by the mononuclear phagocyte system (MPS) (Mahmoudi et al. 2010; Yoo et al. 2010). Phagocytes have many types of receptors on the surface (opsonin, scavenger, toll-like receptors), and once the adhesion process between NPs with any of these proteins, including Ig, occurred, these form recognition sites that alert high activity of monocytes and macrophages, and the process of endocytosis/phagocytosis of the nanoparticles begins, leading to clearance from circulation and transport in organs with high phagocytic activity.

Endocytosis is the major process of trapping and transports the nanosystems across the cell's membrane (McCarthy and Weissleder 2008). It is generally classified into phagocytosis and pinocytosis (Tantra and Knight 2011; Conner and Schmid 2003). Figure 2.9a, b shows an overview of these processes. Phagocytosis is the process that follows recognition of the foreign materials and entraps them through vesicular internalization into phagosome that may fuse with lysosome forming the final phagolysosome (phagosome maturation (Kirchen and Ravichandran 2008). Here, the caged material is either digested or degraded by acidification (where the pH is ~4.6–5.1) and enzymolysis (by, e.g., cathepsin) (Repnik et al. 2012) and the leftover material released into to the cytoplasm. The process is mediated by actin polymerization, which supports the formation of a protrusion in the cell membrane (cup-shape) and allows engulfing the nanoparticle. This route can be inhibited by cytochalasin B (Axline and Reaven 1974). Pinocytosis is present in all types of cells. Here, the nanoparticles are brought across the plasma membrane following

Fig. 2.9 Different endocytic pathways associated with the nanoparticles cell's internalization processes. In **a**, other possible endocytic pathways (e.g., CLIC/GEEC) were not shown for simplicity. The suggested sizes of the various vesicles formed within the processes of phagocytosis, clathrin and caveolin-dependent, macropinocytosis and clathrin/caveolin-independent endocytosis were shown on the top of each internalization path (from ~60 to >1 mm). Panel **b** shows the different pathways of degradation for cationic and anionic nanoparticles entrapped in the phagosomes

first the formation of an invagination in the membrane and then suspended within small vesicles. Internalization by pinocytosis can be divided into receptor-mediated, clathrin-dependent endocytosis (Mousavi et al. 2004), caveolae-dependent endocytosis (Nabi and Le 2003), receptor independent, macropinocytosis (Kerr and Teasdale 2009), and clathrin- and caveolae-independent endocytosis (Pelkmans et al. 2001). In the clathrin-dependent endocytosis after NPs have been engulfed into the vesicles, these structures are pinched off by the GTPase activity of dynamin forming clathrin-coated vesicles, which are then transferred to lysosomes. In the caveolin-dependent endocytic process after binding to this receptor in the plasma membrane, the NPs are engulfed in a vesicle that also need the action of dynamin to be pinched-off. The caveolae vesicle can bypass the lysosome path (fusion with early and late lysosome), and this is the entry strategy into the host cell of many bacteria and viruses so to avoid lysosomal digestion.

As shown by Pelkmans et al. (2001, 2002), the Simian virus 40 (SV40) can use the caveolae path for cell entry, following a two-step transport pathway from plasma membrane caveolae through an intermediate organelle (the caveosome), a pH neutral compartment. Although rich in caveolin-1, these organelles do not contain markers for endosomes, lysosomes, ER, or Golgi and are transferred in the smooth endoplasmic reticulum (ER) in a microtubule-dependent fashion. It is suggested that such materials embedded in ER can leak into the cytosol and enter the nuclei via the nuclear pore complexes, which are large protein systems (nucleoporins) that cross the nuclear envelope and encode size cut-off for cargo transport of ~30 nm (diameter) when nuclear localization signal (NLS) is present or size cut-off of <10 nm in the absence of NLS (Mincer and Simon 2011). The NPs, following this route, can thus access both ER and nuclei. In the macropinocytosis, the NPs are adsorbed in nonspecific way, and such process makes up for larger vesicles (>1 μm) that can either fuse with lysosomes, initiating the NP degradation process, or can even travel back to the cell surface and release the cargo outside the cell.

The clathrin- and caveolin-independent endocytic routes (Damm et al. 2005; Mayor and Pagano 2007) are subjected to a complex and subtle paths of interactions between the material undergoing endocytosis and various lipid molecules, such as cholesterol, DNM2/Dynamin-2, small GTPases, tyrosine kinase, and as reported recently by Chaudhary et al. (Chaudhary et al. 2014), caveolae proteins can act as negative regulators of clathrin-independent endocytosis, providing evidences for multiple levels of crosstalk between these dependent-independent pathways. After intravenous administration, the nanoparticles that are more prone to establish interactions (opsonization) with immunoglobulin (IgG and IgM) complement component (C3, C4, and C5) and blood serum proteins are cleared up rapidly (within minutes) from the bloodstream. Thus, long-circulating nanoparticles are those that must evade the macrophage uptake. Phagocytic cellular uptake increases with particle size (Daldrup-Link et al. 2003). NPs with hydrodynamic dimension (d) of 50 nm $< d <$ 180 nm undergo phagocytosis faster than NPs encoding a size smaller than 50 nm. Cell membranes possess negative charges on the surface and thus cationic nanoparticles are believed to undergo stronger electrostatic interaction with the membranes than negative nanoparticles and, as mentioned earlier, depending on their size, can

feature rapid entry. In addition, positively charged nanoparticles, namely those containing cationic coating materials, may escape endosome confinement through "proton sponge effect". The notion of proton sponge effect was proposed by Boussif et al. (1995), by recognizing that the cationic polymer polyethyleneimine (PEI) could act as nonviral vectors, e.g., for DNA/RNA transfection, as efficiently as lipopolyamines and polyamidoamine polymers which do not require for transfection any extra virus-derived function or lysomotropic additive. They suggested that the unprotonated amine of PEI (and thus, in general, polycations encoding high H-buffering capacity in the pH range of endosomes) can absorb/buffer the protons while they are pumped into the lysosome (Fig. 2.10). This effect can cause the rapture of the lysosome membrane followed by the release of the material previously entrapped into the cytoplasm, through a combination of the osmotic swelling and the polymer swelling emerging from the electrostatic repulsion of the protonated amines.

Similar buffering property/ability has been recently validated also in chitosan and chitosan-DNA polyplexes by Richard et al. (2013). The modulation in the nanoparticle's cell internalization processes as a function of the surface charge has been shown, for example, by Cengelli et al. (2006) via in-depth investigation of the cellular uptake, cytotoxicity, and interactions of various iron oxide systems. They employed dextran-coated SPIO with hydrodynamic size of 30 nm (neutral charge), dextran-coated SPION with larger size, 80–150 nm (neutral charge), and PVA-surface functionalized nanoparticles as native (30 nm, neutral charge), coated with amino PVA (30 nm size, cationic), with carboxylate PVA (30 nm size, anionic) and thiol PVA (30 nm size, anionic). The NP interaction with cells was monitored using brain-derived rat EC219 endothelial cells and murine N9 and N11 microglial cells under various concentrations. The uptake of dextran-coated SPIONs by brain-derived cells was found limited, irrespective of the hydrodynamic size of the SPIONs and the cell activation state (namely in the presence of lipopolysaccharide, LPS-activated
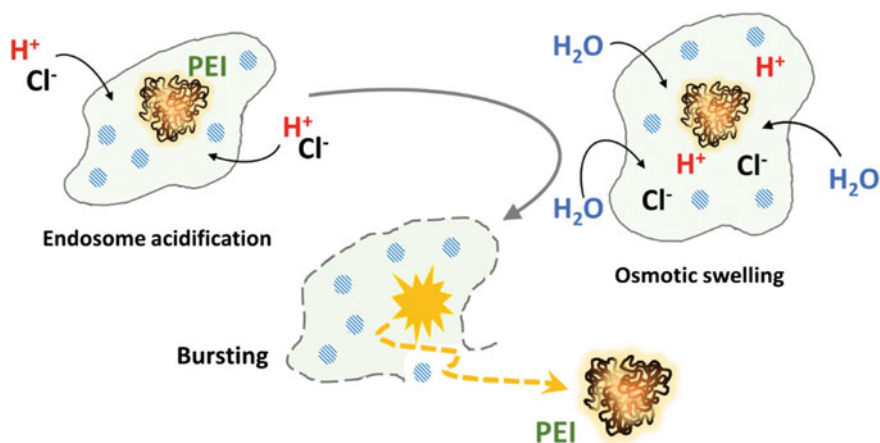
Fig. 2.10 Cationic PEI polyplexes and its endosomal escape by "proton sponge effect"

cells). Furthermore, against dextran-coated SPIO the endothelial cells responded to LPS by increasing nitric oxide (NO) release because of the positive inflammatory stimuli. Native PVA-, carboxylate PVA-, or thiol PVA-SPIONs were not taken up by N11 microglial cells, but the positively charged amino PVA-SPIONs showed internalization in both N11 and EC219 without production of NO, indicative for the absence of inflammatory processes in these cells. The overall cytotoxicity impacts were found, however, very low in all cases. Similarly, He et al. (2010) studied in-depth the cellular uptake of covalently labeled rhodamine B iron oxide nanoparticles with well-controlled size and surface charge, namely negatively charged carboxymethyl chitosan grafted NPs (RhB-CMCNP, zeta-potential from −15 to −25 mV, size from 150 to 500 nm) and positively charged chitosan hydrochloride-grafted NPs (RhB-CHNP, *zeta*-potential from +15 to +25 mV, size from 150 to 300 nm). Cellular uptake assessments were screened against several cell lines, such as in murine peritoneal macrophage, human liver cell line L02, human hepatoma cell line SMMC-7721, human embryonic kidney cell line HEK 293, human adenocarcinoma renal cell line 786-O, human embryonic lung cell line HFL-I, and human lung carcinoma cell line A549. In murine macrophage, it was found that the uptake increased when surface charge increased (either positive or negative). The phagocytic cells favored the uptake of larger particles, and when the absolute values of *zeta* potential were similar, positively charged NPs showed a higher phagocytic uptake compared to negatively charged NPs, irrespectively of the NP composition. For non-phagocytic cells (hepatoma, L02, and human liver, SMMC-7721), less negatively charged RhB-CMCNP and more positively charged RhB-CHNP tended to be more efficiently internalized. Non-phagocytic cells favored the uptake of smaller particles. It is important to note that magnetic iron oxide nanomaterials have been known for long time to express either low or negligible cytotoxicity (Soenen et al. 2011a; Mahmoudi et al. 2011d, 2012) against different types of cells and tissues, from in vitro to in vivo studies. However, various ranges of concentrations have been associated with their low/negligible cytotoxicity impacts and values that depended on the nature of the coating and surface charges, from μgFe/mL to mgFe/mL (Mahmoudi et al. 2012). This observation substantiates why iron oxide nanoparticles have been administrated for over fifty years as iron replacement therapy in patients affected by anemia. Ferumoxyol (SPIO, size 30 nm, coating polyglucose sorbitol carboxymethylether) can be used for this reason in patients affected by chronic renal failure (Landry et al. 2005) and has been tested in such patients under applied dosage up to 510 mg (Landry et al. 2005; Spinowitz et al. 2005). However, the witnessed great variability of concentrations of what has been addressed as safe dosage for iron oxide-based nanomaterials has boosted in the last decade a thorough re-evaluation of the broader biological impact of SPIO nanoparticles (short- and long-term analyses) and finer investigations, especially with an eye to the cell response (behavior) following the nanoparticle cell internalization process.

Generation of Reactive Oxygen Species in Response to NP's Cellular Uptake

From the outset, the capability of iron oxide nanoparticles to be well tolerated arises from the fact that the iron cell homeostasis is a process highly regulated in mammals (Zhang and Enns 2009; De Domenico et al. 2008; Anderson and Shah 2013), which has the ability to prevent the possible oxidative stress (ROS) generated when an excess of this metal is introduced in the body, upon trapping the material into the liver and spleen. The macrophages of the reticuloendothelial system can store iron as part of the process of breaking down hemoglobin from engulfed red blood cells, and they act in the similar way when break down the iron oxide cores, by incorporating back Fe into the hemoglobin pool (being ferritin the major iron storage protein and transferrin (Tf) the primary plasma iron carrier protein). When ROS generation occurs as the result of the local confinement and degradation of NPs in the phagolysosome (or slow degradation by remaining into phagosomes, where pH is 6.0–6.8), cells can defend themselves against damages with an array of enzymes such as alpha-1-microglobulin, superoxide dismutases (SOD), catalases, glutathione peroxidases, lactoperoxidase, and peroxiredoxins or through the action of small antioxidant molecules such as ascorbic acid, tocopherol, uric acid, and glutathione (Fig. 2.11).

In the average healthy adult, about 3000–4000 mg of iron is stored in the body, with the liver containing an average of 0.2 mg of iron per gram (Kohgo et al. 2008). From the currently approved iron oxide nanoparticles for diagnostic MR imaging, a regular adult dose can contain 50–200 mg of iron (namely <4 mg/kg mg). Chronic iron toxicity is known to occur when the concentration of iron within the liver reaches a level of 4 mg of iron per gram of liver (Bonnemain 1998). However, as recently highlighted in some reports, different cell types and tissues can respond very differently toward detoxification of NPs, following the magnetic core degradation, and to the formation of reactive oxygen species (ROS, nitric oxide, NO; hydroxyl radicals, $HO^{\bullet}$; peroxide, H_2O_2), the nanoparticle's toxicity impact can vary significantly in different types of tissues and in different cell lines (Kunzmann et al. 1810; Tran and Webster 2010; Nel et al. 2006; Berry et al. 2004; Naqvi et al. 2010). Gao et al. (2007) demonstrated that magnetic nanoparticles possess an intrinsic peroxidase-like activity and can become active catalysts for the H_2O_2 activation, hence prone to boost the ROS chemistry. Chen et al. (2012) studied the peroxidase-like and catalase-like activity of iron oxide nanoparticles coated with dimercaptosuccinic acid (DMSA) molecules (coded as $D-Fe_2O_3$, 9 nm size, with zeta potential—32.1 ± 3.5 mV, pH 7.4; and $D-Fe_3O_4$, 7.8 nm size, with zeta-potential 29.2 ± 2.6 mV, pH 7.4) and screened the extent of their interaction with hydrogen peroxide (H_2O_2) on human glioma U251 cells, which has been used as model system. Results showed that both types of NPs were internalized into cells and mostly located in lysosomes; both systems could enhance the H_2O_2-induced cell damage dramatically at acid pH, with toxic potency $D-Fe_3O_4 > D-Fe_2O_3$ as the results of the high increase in peroxidase-like activity. However, both NPs did not produce hydroxyl radicals in neutral conditions but rather catalyzed H_2O_2 into H_2O and O_2 directly through catalase-like activity.
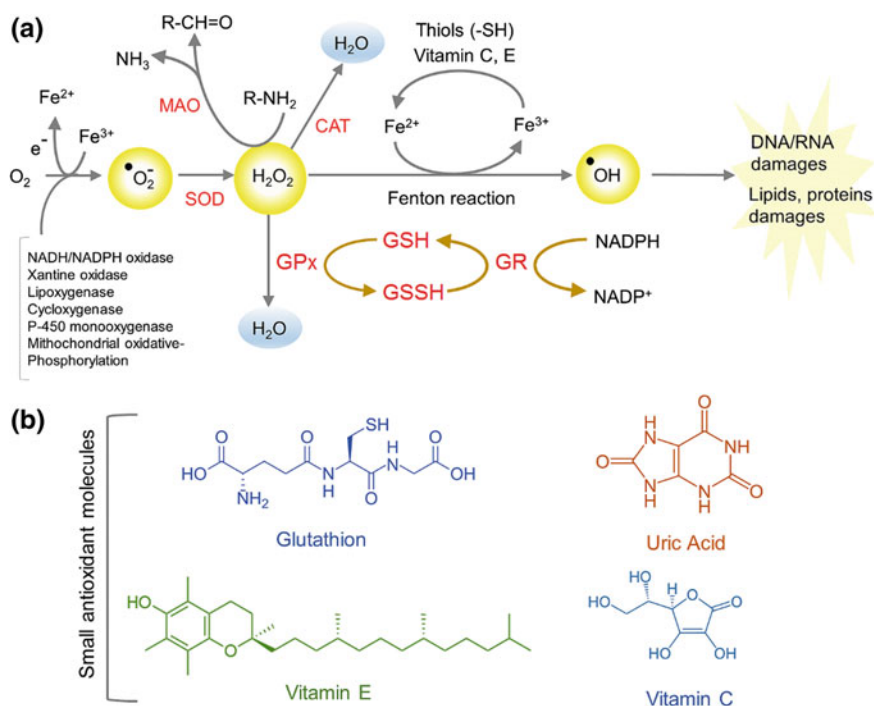
Fig. 2.11 a Formation and removal of reactive oxygen species (ROS). The red labels indicate glutathione peroxidase (GPx), glutathione reductase (GR), superoxide dismutase (SOD), catalase (CAT), monoamine oxidase (MAO), glutathione (GSH), and glutathione disulfide (GSSG). Panel **b** shows the structure of biologically important small antioxidant molecules

Wang et al. (2013c) also studied the free radical generation induced by the interaction between H_2O_2 and iron oxide nanoparticles in bio-micro-environment and in the presence of a physiological amount of biogenic reducing agents (L-cysteine or NADPH). They employed uncoated α-Fe_2O_3 NPs (40 nm size) and γ-Fe_2O_3 NPs (31 nm size) and monitored the reaction at different pH conditions (from 1.2 to 7.2). While in the absence of reductants γ-Fe_2O_3 NPs generated more ·OH radical at low pH (1.2 and 4.2) than α-Fe_2O_3, in the presence of L-cysteine or NADPH more ·OH was induced by α-Fe_2O_3 NPs than γ-Fe_2O_3 NPs suggesting that these physiological reducing agents may mediate the catalytic processes in the homogeneous or heterogeneous Fenton chemistry. However, Huang and co-workers have recently reported that dextran-coated iron oxide-based nanoparticles can surprisingly diminish intracellular peroxide without inducing damages, factor that promoted cellular proliferation rather than cell death (Huang et al. 2009). In-depth studies of the cytotoxicity impact of four different nanoparticles types (dextran-coated Endorem, carboxydextran-coated Resovist, lipid-coated magnetoliposomes (MLs), and citrate-coated very small iron oxide particles (VSOPs)) were performed by Soenen et al. (2011b), probed against a variety of cell types, being C172 neural progenitor cells, PC12 rat pheochromocytoma

cells, and human blood outgrowth endothelial cells. The effect of the NP concentration on cell morphology, cytoskeleton, proliferation, reactive oxygen species (ROS), functionality, viability, and cellular homeostasis revealed that the safe concentration of these nanomagnetic systems can indeed vary significantly; for ML preparations, the biological non-toxic amounts can peak to 67.37 ± 5.98 pg Fe/cell, whereas VSOP preparations were the most toxic particles and only down to 18.65 ± 2.07 pg Fe/cell could be considered safe concentration. Therefore, slight variations in the formulations of the iron oxide nanoparticles can produce considerable differences in the cytotoxic impacts, and the extent of such phenomenon is, at present, difficult to entirely predict.

Biodistribution of NP's Following Cellular Uptake

The averaged and typical biodistribution found in the case iron oxide nanoparticles can be traced down to 80–90% in liver, 5–8% in spleen, and 1–2% in bone marrow. The localization of nanoparticles in specific tissues, such as liver and spleen (Huang et al. 2010; Kunzmann et al. 1810; Jain et al. 2008; Lee et al. 2010; Ma et al. 2008; Daldrup-Link et al. 2011), is not surprising, since these organs are responsible for blood purification and contains tissues expressing the mononuclear phagocyte system. In the liver, uptake occurs predominately in Kupffer macrophage cells, whereas both macrophage action and mechanical filtration processes become responsible for the localization of the nanoparticles in the spleen. It is recognized from recent studies that nanoparticles having a diameter (d) of 10 nm < d < 40 nm are those that seem to encode, in general, a good compromise between cellular uptake (high) and witnessed toxicity (low) for in vivo applications (Soenen et al. 2011a). Big nanoparticles (40 nm–200 nm) can fast localize in the liver (80%) and spleen (20%) with decreased tendency of cellular uptake upon increasing size; nanoparticles very large ($\gg$100 nm) are quickly opsonized and cleared. The effect of nanoparticle size (hydrodynamic, from ~32 to ~118 nm; core size from ~8 to ~65 nm; zeta potential ~12–14 mV) on magnetic resonance imaging (MRI) of hepatic lesions in vivo has been systematically examined recently by Huang et al. (Huang et al. 2010) using polyvinylpyrrolidone (PVP)-coated iron oxide nanoparticles (PVP-IOs). The maximum uptake by mouse macrophage cells (RAW264.7) was observed for those nanoparticles encoding hydrodynamic size of ~102 nm (core size ~37 nm), value that was 1.3, 2.8, and 5.3 times the uptake of nanoparticles with hydrodynamic size of 118, 71, and 32 nm, respectively. Both size and cellular uptake are factors that finally determined the liver MRI contrast enhancement. The authors found that the relatively lower contrast enhancement of smaller nanoparticles was likely attributed to the probable lower uptake into Kupffer cells and their naturally smaller relaxivities, while the outperformance of the nanoparticles with hydrodynamic size of ~102 nm reconciled nicely with the best macrophage engulfment and the close-to-maximum R_2 value (transverse relaxivity). In term of plasma half-life, the large nanoparticles feature in general short-circulation time, in the order of minutes, while small nanoparticles

have much longer plasmatic half-life, e.g. several hours (>36 h). Small NPs (USPIO) exhibit slower uptake by liver and spleen following intravenous administration. NPs smaller than 10 nm undergo faster tissue extravasation than larger nanoparticles (SPIO, >50 nm), they do not undergo renal elimination, which gives an enhanced safety characteristic for patients with renal dysfunctions (Neuwelt et al. 2008), and they have high tendency to be fast internalized in the cells but have also higher probability to promote cytotoxic effects, due to the possibility to pass the nuclei membrane. For example, histological samples from resected brain tumors in patients treated with small iron oxide nanoparticles showed that the extravasated NPs were included in parenchymal cells, demonstrating that their localization was traceable to both intracellular and interstitial (Varallyay et al. 2002). As shown by Weissleder et al. (Weissleder et al. 1990), ultrasmall superparamagnetic iron oxide nanoparticles (USPIO), with size smaller than 10 nm, exhibit blood half-life in rats of 81 min, considerably longer than that of larger superparamagnetic iron oxide preparations such as AMI-25, (SPIO-dextran-coated nanoparticles, with size 120–180 nm) that shows half-life of 6 min. The rate of clearance can generally be reduced upon functionalization of the nanoparticle surfaces with coating materials that resist to the MPS interactions. The polyethylene glycol (PEG) has demonstrated to be one among the most biocompatible coating material for the nanoparticles that provide steric resistance to opsonization and macrophage uptake processes, facilitating prolonged plasma residence (Laurent et al. 2008; Mahmoudi et al. 2011d). This is due to the fact that PEG has uncharged hydrophilic residues combined with high surface mobility leading to high steric exclusion. Zhang et al. (2002) showed that surface modification of SPIO nanoparticles with PEGylated moieties (or with folic acid residues) not only allowed to avoid the macrophage recognition but did also exhibit a level of uptake that depended on the cell type (RAW 264.7 and BT-20). While uncoated nanoparticles could be internalized easily by mouse macrophage cells (RAW 264.7) and quickly (12 pg/cell in a day), the PEG and folic acid modified SPIO avoided the uptake process very well (about 2.3 pg/cell after 1 day). On the other hand, when human breast cancer cells were used (BT-20), the uptake for folic acid and also PEG modified SPIO peaked the value of 75 pg/cell for the latter and 60 pg/cell in the former, after just one day. The results observed for the folic acid modified SPIO against BT-20 are nowadays rather expected. Many kinds of tumors including ovarian, renal, breast, colorectal and neuroendocrine overexpress folate receptors, which are usually absent in most of the normal tissues. The even higher uptake witnessed for PEG-SPIO without the presence in the outer shell of such receptor underlines once more how the cell internalization process of magnetic nanoparticles is profoundly associated to the cell type (and so does the cytotoxicity). As mentioned earlier, PEG coatings can considerably improve the NP circulation time in the blood pool and this factor represents one of the key features to address when the target is the engineering of flexible multifunctional platforms for biomedical application. For example, nanoparticles engineered to transport drugs that encodes long circulation time can generate drug nano-reservoirs from which drugs can be released into the vascular compartment in a controlled fashion and potentially allow tailoring both passive and active targeting. Similarly, magnetic nanostructures used for medical screenings (e.g., imaging) with

long-circulation time provide a clinical window to decrease considerably the amount of magnetic probe needed (thus its potential cytotoxicity impact) to achieve an optimal contrast enhancement, namely increasing the available time-window for screening before contrast agent clearance (Wang et al. 2001). Several derivatives from PEG exhibit such improvement in plasma residence (expressed in terms of half-life, $t_{1/2}$). Some recent examples are (i) the amino-derivative (NP-SAS-PEGNH$_2$, iron oxide core size 12 nm, hydrodynamic size of 38 nm, PBS buffer) prepared by Fang et al. (2009) that has shown to feature negligible macrophages uptake combined with high stability and biocompatibility, due to the presence of a densely packed PEG coating and the strong affinity of SAS to the iron oxide surfaces (triethoxysilylpropylsuccinic anhydride, SAS), (ii) the PEG-modified cross-linked starch-coated iron oxide nanoparticles prepared by Cole et al. (2011) (D20, hydrodynamic size ~168 nm, $t_{1/2}$ 11.75 h), engineered for magnetic brain tumor targeting, and (iii) the bisphosphonate-anchored PEGylation of USPIO by Sandiford et al. (2013) encoding long-circulating time for in vivo multimodal (T1 MRI-SPECT) imaging ($t_{1/2}$ about 3 h). Similar capability to slower down the fast body clearance combined with high biocompatibility is witnessed when other biopolymers such as dextran, poly(vinylpyrrolidone), and chitosan are used for the iron oxide magnetic core. The dextran-based coatings in superparamagnetic iron oxide nanoparticles (SPIO) are used in clinical screenings as contrast agents for magnetic resonance imaging (Wang et al. 2001) (core size 4–6 nm, Fe$_3$O$_4$ for ferucarbotran and ferumoxtran, and Fe$_3$O$_4$/γ-Fe$_2$O$_3$ for ferumoxides, hydrodynamic sizes from 35 to over 160 nm), but following intravenous administration they have a tendency to become extensively coated by plasma proteins and are cleared from blood circulation with half-life of 1–3 h (Simberg et al. 2009). This factor indicates the importance to control or at least envision the possible transient interactions involving NPs and plasma proteins (Davis 2002), because those interactions can influence strongly both toxicological impact as well as performance of the nanosystem in vivo (Lynch and Dawson 2008). Cationic plasma proteins such as kininogen (HMWK) and histidine-proline-rich glycoprotein (HPRG) can recognize and bind the anionic components present on the nanoparticles shells (if any), while immunoglobulins (Y-shaped proteins) and lectins (carbohydrate-binding proteins), which systems that play an important role in innate immunity by recognizing a wide range of pathogens (Fujita et al. 2004), can recognize and then bind the dextran's sugar residues in dextran-coated SPIO. Recently, Karmali et al. (2012) described the design of a novel dextran-based SPIO system capable to overcome the slightly shorter circulation time in plasma of dextran-coated NPs compared to PEG-coated systems, by converting dextran-based magnetic nanoworms made from magnetite cores into stealth hydrogel nanoparticles (with half-life in blood of ~500 min) upon crosslinking with epichlorohydrin (1-chloro-2,3-epoxypropane, size 105 nm, zeta potential of −1.65 mV). The authors noticed that hydrogelation did not reduce the absorption of cationic proteins on the nanoparticle surface, namely no reduction on the surface binding of kininogen, histidine-rich glycoprotein, and protamine sulfate. In addition, hydrogelation did not prevent the activation of plasma kallikrein on the metal oxide surface, hence suggesting that (i) a stealth hydrogel coating did not mask the charge interactions with the iron oxide core and (ii) the total blockade of

plasma protein absorption is not the *conditio sine qua non* for maintaining iron oxide nanoparticles' long-circulating stealth properties.

Tailoring the NPs/Plasma Components Interactions to Achieve Specific Tissue Targeting

The nanoparticle/plasma component interactions, when controlled and tailored, can be used as powerful toolbox for tuning the NP properties in vivo, can aid the design of biocompatible smart delivery systems (e.g., for drugs and gene transfection), can be used as disease marker to enhance the contrast agent's properties following the NP's selective localization in tissues as well as the NP's therapeutic effects. The use of plasma protein (e.g., human serum albumin) as flexible drug carrier for pharmaceutical preparations has been exploited in a number of cases, such the HSA-bound paclitaxel (PTX, Abraxane®), one known chemotherapeutic agent for cancer treatment approved by FDA. HSA is the most abundant plasma protein encoding several functions such as transport of hormone, fatty acids, bilirubin, drugs (Gradishar et al. 2005), and HAS acts in way to buffer pH and maintains osmotic pressure. Xie et al. (2010) took advantage from the loading ability of HAS and used it to co-guest iron oxide nanoparticle surface functionalized with dopamine, which were easily encapsulated into HSA matrices in a way similar to PTX loading (HSA-IONPs). The HSA-IONP nanosystem, further labeled with Cy5.5 dye and ^{64}Cu-DOTA chelates, after injection into subcutaneous U87MG tumor-bearing mouse model not only exhibited an r_2 of 313 mM^{-1}s^{-1} much higher than that of Ferridex (123 mM^{-1}s^{-1}), but also gave high retention rate, good extravasation rate, and low macrophage uptake rate at the tumor area, probably as the result of the increased permeability of the vasculature environment at the tumor site (EPR effect, Fig. 2.12).

The compromised leaky vasculature of a solid tumor combined with its rich vascular character can promote the passive extravasation of the NPs from the blood circulation and their retention in the tumor interstitium, because the lymphatic drainage is poor. In contrast, endothelial cells in normal tissue vessels are densely packed; thus, they form barriers that hinder the NP's vascular permeability. Such morphological differences can be used as driving tool for the NP's selective penetration in the tumor regions (Maeda 2010). Human serum albumin (HAS) and bovine serum albumin (BSA) are proteins similar to each other in many aspects (e.g., both albumins share 76% sequence homology), even though HAS contains only one tryptophan residue rather than two as in BSA (Steinhardt et al. 1971), and indeed, BSA was used successfully by Lee et al. (2009) as coating canopy to assemble a highly biocompatible nanoprobe for the development of "all-in-one" magnetic systems that granted simultaneous delivery and multimodal imaging in the context of cancer-cell-targeted gene silencing (Kami et al. 2011; Medarova et al. 2007). The BSA protein engulfed nicely Mn-doped MEIO NPs (MEIO, magnetism-engineered iron oxide)
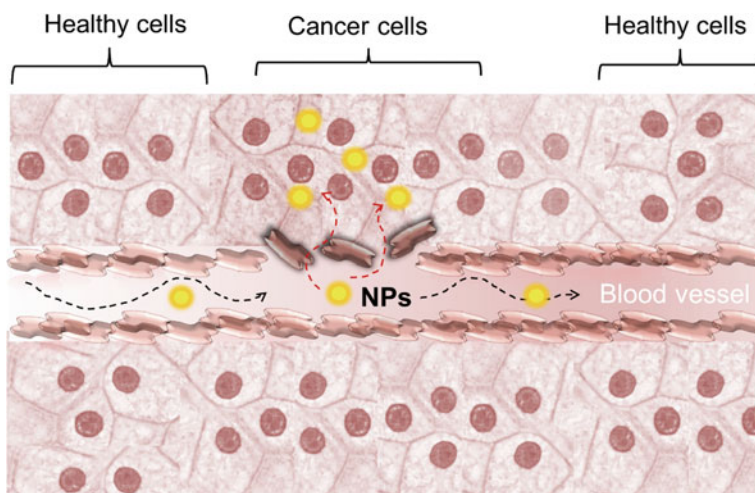
Fig. 2.12 a Enhanced permeability and retention effect (EPR). Differing from normal tissues where endothelial cells are tightly bound to each other, in cancer tissues the vasculature becomes leaky, leading to openings in which NPs can more easily extravasate from the blood vessel. Local concentration of NPs can be boosted by the action of macrophages and by the introduction of targeting ligands or selected proteins on the NP shells

which were coupled to fluorescent dye, siRNA, and a RGD-peptide targeting moiety. The Arg-Gly-Asp (RGD) conjugated nanoparticles could then bind strongly to $\alpha_v\beta_3$ integrin, a transmembrane receptor overexpressed in both endothelial and cancer cells such as breast cancer (MDA-MB-435 cells) and was more easily internalized by cells via receptor-mediated endocytosis, without promoting the endosomal escape of nanoparticles into the cytoplasm. Arginyl-glycyl-aspartic acid (RGD) peptide forms a sequence that is a common element in cellular recognition, and SPION-Tat peptide conjugates have been used since long time to improve intracellular magnetic labeling of different target cells, such as murine lymphocytes, human natural killer (NK) cells, and HeLa cells. The active tumor-specific molecular targeting represents nowadays one of the forefront frontiers in the theranostic applications of magnetic nanoparticles. Simberg et al. (2007) employed the potentiality expressed by the specific affinity approach for clotted plasma proteins as the targeting element for cancer therapy (the mice bearing MDA-MB-435 human breast cancer have been used as model). The nanoparticle's design relied on coating the NP surfaces with a tumor-homing peptide (fluorescein-labeled CREKA (Cys-Arg-Glu-Lys-Ala) grafted onto 50-nm superparamagnetic, amino dextran-functionalized iron oxide nanoparticles. Such NP shell granted a specific affinity for tumor vessels (and tumor stroma). The authors were further able to avoid the RES uptake by decoy macrophages with liposomal clodronate, which prolonged the NP's blood half-life ($t_{1/2}$ ~100 min) and increased the time frame for tumor targeting. In addition, the tumor-targeted nanoparticles cause intravascular clotting in tumor blood vessels and the intravascular clots attracted more nanoparticles into the tumor amplifying the targeting and, potentially, the possibility

of selective therapy (e.g., magnetic hyperthermia). Several other targeting ligands have been tested and validated for their biocompatibility and performances as complements to the outer shell coronas with the aim to tailor the NP's active targeting (Veiseh et al. 2010). Those includes, for example, (i) folic acid or trasferrin receptors grafted onto the shell of iron oxide NPs, as mentioned earlier (Choi et al. 2004; Kresse et al. 1998), (ii) chlorotoxin peptide (4-kDa purified from the *Leiurus quinquestriatus* scorpion) combined with near-IR fluorophore (both conjugated to iron oxide NPs containing polyethylene glycol–grafted chitosan copolymer) for specific targeting of brain tumor as reported by Veiseh et al. (2009), (iii) pan-bombesin analog [β-Ala11, Phe13, Nle14] conjugated to dye-functionalized superparamagnetic iron oxide nanoparticles for selective prostate cancer cells imaging engineered by Martin et al. (2009), (iv) the antibody grafted onto iron oxide nanoparticles (10 nm for the core size) probed by Hadjipanayis et al. for the selective targeting of the epidermal growth factor receptor (EGFR) deletion mutant (EGFRvIII) present on human glioblastoma multiforme (GBM) cells, which exhibited convection-enhanced delivery (CED), therapeutic targeting, and MRI contrast enhancement (Hadjipanayis et al. 2010), and (v) the F3 peptide conjugated dextran-coated iron oxide nanoparticles described by Zhang et al. to selectively target cancer breast epithelial cells (MCF-7) versus normal breast epithelial cells (MCF-10A) (Zhang et al. 2009). Physiological responses triggered by the emergence of pathological alterations in tissues can lead to local accumulation of magnetic iron oxide nanoparticles, hence enhancing the imaging responses (diagnostic), but those effects can also be used to establish the physiological basis to tailor more selective therapies. For example, tissue inflammation (inflammatory processes) can lead to vasodilation, increased permeability of vessels, and migration of leukocytes. During the inflammatory process, cell adhesion molecules are expressed on the cell surface, such as E-selectin on endothelial cells and P-selectin on platelets and endothelium. The number of these receptors increases through redistribution mediated by histamine or thrombin. Rademacher et al. (2009) have used an E-selectin mimetic ligand coupled to PEGylated USPIO nanoparticles that allowed monitoring inflamed muscles in mice, after induction of the inflammatory process by intramuscular injection of Freund's Complete Adjuvant. They observed a significant increase in SPIO accumulation accompanied by a sensible increase in the sensitivity and detection of those inflamed regions, effect that was in fact aided by two overlapping factors (i) the non-specific local accumulation of iron oxides (EPR effect, see Fig. 2.12) and (ii) their improved localization in these areas by using the E-selectin ligands. Other inflamed tissues, e.g., those associated with degenerative disorder of the central nervous system, ischemic stroke, osteomyelitis, can be similarly revealed even at the very early stage in MRI screenings using generic iron oxide NPs, but mainly because of macrophage accumulation into the altered tissues and the preferential accumulation of iron oxide NPs into the macrophages (Stoll and Bendszus 2010; Saleh et al. 2007; Jander et al. 2007; Bierry et al. 2010). As noted by Nighoghossian et al. (Nighoghossian et al. 2007), upon following the inflammatory response after ischemic stroke using ferumoxtran (AMI-227) as contrast agent, they suggested that the enhancement response may not be

clearly related to the subacute lesion volume, namely the extension of tissue alter-
ation, and this contrast agent, which do not contain targeting agents, may underesti-
mate the intensity of the inflammatory response. The dynamic of the post-ischemic
neuroinflammation process includes several cell types, such as granulocytes and T
lymphocytes. These conclusions found support from the work of Jander et al. (2007)
that suggested that the witnessed USPIO enhancement in such lesions may reflect the
infiltration of only a specific macrophage subpopulation. With respect to temporal
pattern and cell types involved, microglia is activated within minutes of ischemia,
while post-ischemic inflammation is dominated by cells of the innate, nonspecific
immune system with local microglia/brain macrophages, and blood-derived mono-
cytes/macrophages (Kleinschnitz et al. 2003). A large number of macrophages and
activated microglia have been found within and around brain tumors and those can
be used as target for SPIO nanoparticles (Fleige et al. 2001; Rosenberg et al. 2012).
The microglia-dependent neuroinflammatory response is strongly connected to the
emergence of pathology such as Alzheimer's disease (AD). Sillerud et al. (2013)
synthesized antibody-conjugated superparamagnetic iron oxide nanoparticles (SPI-
ONs), for use as an in vivo contrast agent for the detection of amyloid-β plaques in
AD and validated the ability of novel anti-AβPP conjugated SPIONs to penetrate the
blood–brain barrier to effectively obtain imaging of plaques. Also, Wadghiri et al.
(2013) engineered bifunctional ultrasmall superparamagnetic iron oxide (USPIO)
nanoparticles, chemically functionalized with Aβ1-42 peptide, which were coupled
to polyethylene glycol (PEG) to improve the permeability for the blood–brain barrier
(BBB), and successfully imaged amyloid plaque deposition in the mouse brain. From
the examples presented so far, it is clear the advancements in the potential medical
applications that have been brought by the employment of nanoprobes based on iron
oxide NPs and how finely the NP's shell architecture can be tailored to grant simul-
taneously biocompatibility, tissue selectivity, and contrast enhancements. From the
clinician perspective, the ability to differentiate abnormal body tissues from those
being healthy, the possibility to address their extension, and to unveil secondary
alterations in the body (e.g., metabolic and functional) using noninvasive techniques
such as MRI provides the grounds to improve anamnesis, before proceeding with
surgical treatments.

The Effective Use of NPs in Medicine

The ability of NPs to obtain contrast enhancement in magnetic resonance imaging
(MRI) has been a pivotal step in the application of NPs in medical diagnostic, and
the phenomenon is linked to the effective magnetic moment (m_s) of the iron oxide-
based nanosystem. Some examples of NP's systems probed in a laboratory-bench
environment to be very effective in MRI imaging have been given already in the
previous sections. The contrast enhancement property is intimately connected to the
elemental composition of the magnetic core, size, and crystallinity (see Fig. 2.4). The
term "contrast" refers to the signal differences obtained between adjacent regions

in the body, having different "characteristics" such as tissues from vessels from bones (Fig. 2.13). Under application of an external magnetic field, paramagnetic and/or ferromagnetic molecules can change the local signal contrast by creating time-varying magnetic fields, which promote diverse spin–lattice (T_1, longitudinal) and spin–spin relaxation (T_2, transverse) of the body water molecules. Based on their diverse relaxation processes, the contrast agents are therefore classified as T_1 and T_2 contrast agents. Commercially available T_1 contrast agents are mostly composed by paramagnetic metal complexes and T_2 contrast agents by iron oxide nanoparticles or mixed iron/d-block metal oxides. Among the iron oxide, NPs developed and sold by the pharma industry for clinical MRI, such as (I) ferumoxsil (400 nm hydrodynamic size, coating with poly[N-(2-aminoethyl)-3-aminopropyl] siloxane, discontinued), (II) ferumoxide (80–200 nm hydrodynamic size, coating with dextran, used and discontinued), (III) ferristene (3500 nm hydrodynamic size, coating with polystyrene (sulfonated styrene-divinylbenzene copolymer), approved and discontinued), (IV) ferumoxytol (30 nm hydrodynamic size, polyglucose sorbitol carboxymethylether, clinical trials), and (V) ferucarbotran (60 nm hydrodynamic size, coating with carboxydextran, approved but discontinued). Despite these NPs exhibited excellent biocompatibilities, the products were discontinued because were found not competitive enough against gadolinium-based MRI. Only one superparamagnetic iron oxide tracer (Sienna+®) remains in use in Europe. This compound is successfully applied in imaging with special equipment (not conventional MRI) of lymph nodes for early detection of breast cancer.

For such reason, other types of magnetic nanosystems and NP architectures, which are not solely based on iron oxide, have been in recent years engineered and preliminary tested. There are several synthetic strategies that have been used for improving the magnetic properties of NPs, and among others, the metal-dopant substitution of metal ferrite NPs and the formation of condensed nano-crystal clusters (CNCs) seem to bear great promises. The term CNCs refers to superstructures of nanocrystallites organized into higher-order colloidal entities in which the crystal planes of each NP adopt the same orientation through epitaxial aggregation. In this structural organization, the overall crystallite size becomes as large as ~50–300 nm, shows single-crystal-like structure throughout almost the whole volume, and behaves as ensembles of smaller independent (5–15 nm) units in which the super-paramagnetism is retained. An example of such morphological organization is given in Fig. 2.14 (Zoppellaro et al. 2014) and the list of some CNC colloids is given in Table 2.2 (Wang et al. 2013b; Zoppellaro et al. 2014; Deng et al. 2005; Zhu et al. 2007; Barick et al. 2009a; Xuan et al. 2009; Xu et al. 2009, 2012a, b, c; Hu et al. 2010; Luo et al. 2011; Xing et al. 2011; Lartigue et al. 2012; Barick et al. 2009b; Ma et al. 2012; Berret et al. 2006; Lee et al. 2006b; Taboada et al. 2009; Yoon et al. 2011; Pothayee et al. 2013; Béalle et al. 2012; Skouras et al. 2011; Meledandri et al. 2011; Martina et al. 2005; Mikhaylov et al. 2011; Peiris et al. 2012a, b; Zhou et al. 2010; Park et al. 2008; Ai et al. 2005; Yang et al. 2007; Paquet et al. 2011; Sanson et al. 2011; Qiu et al. 2010; Lim et al. 2011; Pöselt et al. 2012; Kim et al. 2008c; Bigall et al. 2013), which includes relevant parameters such as size of the clusters and size of the individual components, magnetization saturation (M_s) values, and relaxivity ($1/T_2 = R_2$) indexes.
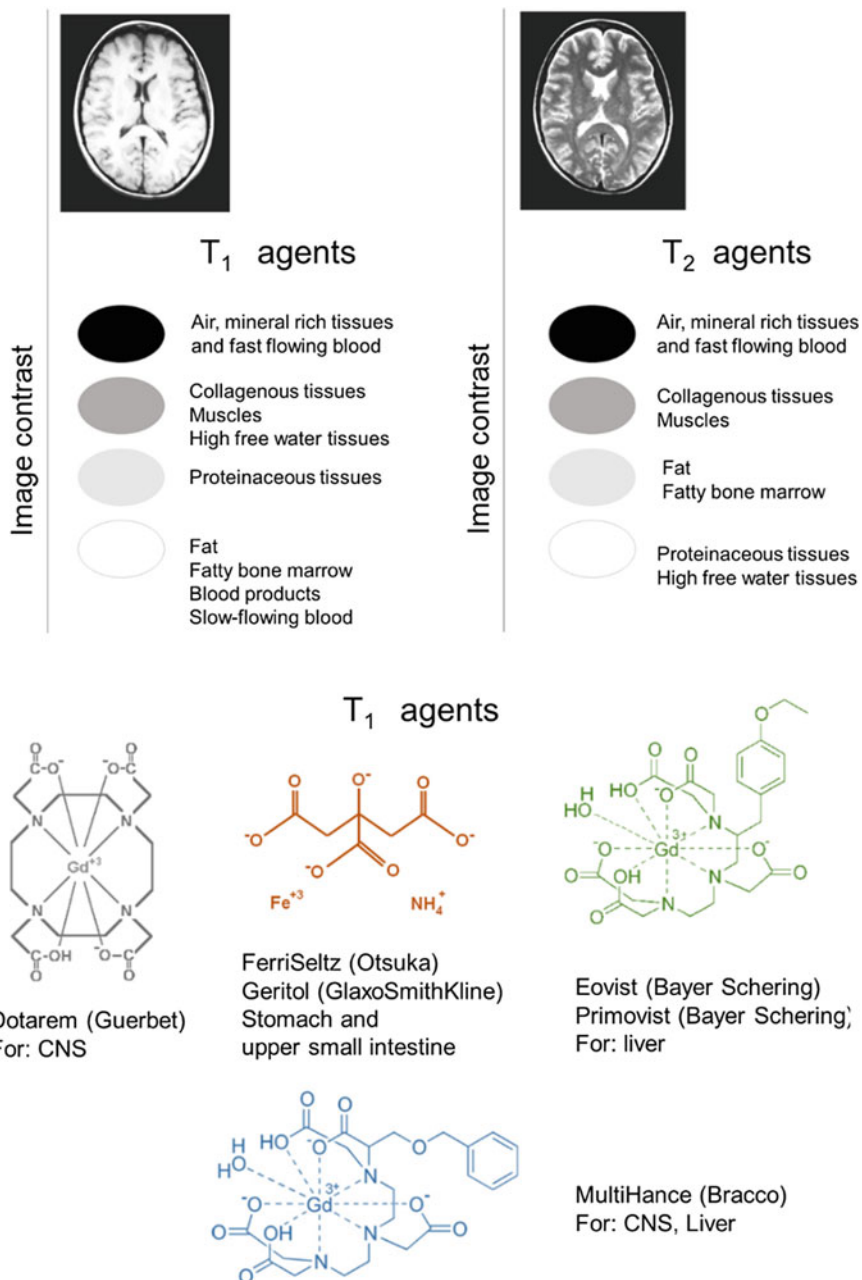
Fig. 2.13 Diverse image contrast obtained during a magnetic resonance imaging experiment, following T_1 or T_2 acquisition procedures. The chemical compounds drawn at the bottom are examples of commercially developed T_1 MRI agents
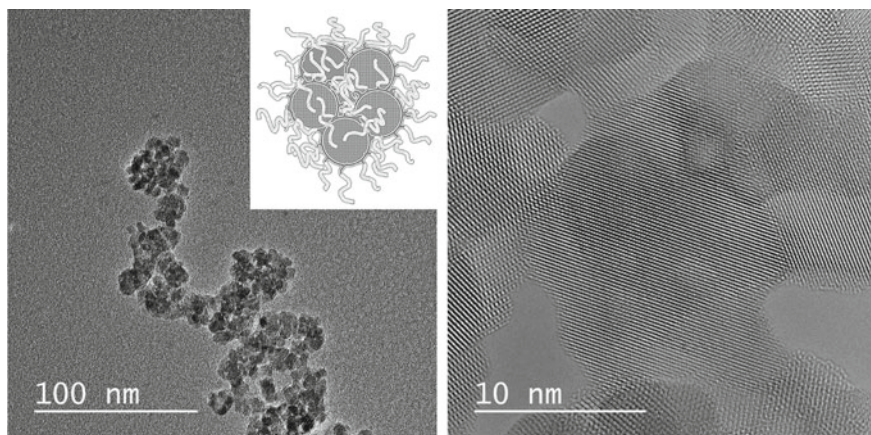
Fig. 2.14 HR-TEM images of CNC iron oxide clusters (MagAlg) loaded with the drug doxorubicin, taken from Zoppellaro et al. (2014), unpublished TEM images

It should be noted that many of these CNC systems can act as carriers for drugs (such as doxorubicin) more efficiently than simpler NPs, due to their higher entrapment efficiencies. As for the metal-doping approach, Lee et al. (2007b) reported a series of metal-doped MEIO nanoparticles (magnetically engineered iron oxide) having spinel structure with general composition MFe_2O_4 where M stands for Mn^{2+}, Fe^{2+}, Co^{2+}, or Ni^{2+} that have been coated with 2,3-dimercaptosuccinic acid (DMSA) molecules in order to grant ferrofluid behavior. These nanosystems, with core size of 12 nm, encoded high M_s values, which decreased along the sequence $MnFe_2O_4$ (110 emu/g) > $FeFe_2O_4$ (101 emu/g) > $CoFe_2O_4$ (99 emu/g) > $NiFe_2O_4$ (85 emu/g). Such high M_s values allowed to improve considerably the negative contrast capabilities (expressed as R_2 and probed under 1.5 T), following the same trends as M_s, with $MnFe_2O_4$ being the most performant (358 mmol^{-1} s^{-1}) > $FeFe_2O_4$ (218 mmol^{-1} s^{-1}) > $CoFe_2O_4$ (172 mmol^{-1} s^{-1}) > $NiFe_2O_4$ (152 mmol^{-1} s^{-1}). Such values certainly represent solid improvements with respect to other known and in clinically tested negative contrast agents, such as ferumoxides (120 mmol^{-1} s^{-1}) (Jung and Jacobs 1995), ferucarbotran (186 mmol^{-1} s^{-1}) (Wang et al. 2001), ferumoxtran (65 mmol^{-1} s^{-1}) (Wang et al. 2001), or CLIO-tat (dextran coating/Fe_3O_4, 62 mmol^{-1} s^{-1}) (Josephson et al. 1999) obtained under the same applied field (1.5 T). The authors, in addition, validated that the effective increase in M_s and R_2 correlated well with the increase in particle sizes, upon synthesizing NPs with smaller dimensions (6 and 10 nm), which were found less effective. The most performant $MnFe_2O_4$ system was tested for its cytotoxicity impact (against HeLa and HepG2 cells), before and after conjugation with Herceptin, and the nanosystem did not exhibit appreciable cytotoxicity impact. Further analyses of the in vitro contrast enhancements on various cell lines with different levels of HER2/neu overexpression (Bx-PC-3, MDA-MB-231, MCF-7, and NIH3T6.7) and then in vivo (implanted NIH3T6.7 cells in the proximal femur

Table 2.2 Morphological characteristics and magnetic properties of iron oxide nanoparticles encoding condensed cluster architectures (CNC)

	Shell	D_{TEM} cluster (nm)	D_{XRD} particle (nm)	D_h (z-avg) (nm)	M_s (Am² kg⁻¹)	r_2 (mmol⁻¹ s⁻¹)	Type of colloid	Ref.
1	Alginate	40	6	83	71.1	243	Co-CNC	Zoppellaro et al. 2014
2	None	200–800	–	–	(a) 81.9[a] (b) 53.2[a] (c) 60.0[a] (d) 61.6[a]		Co-CNC	Deng et al. 2005
3	Poly(vinyl pyrrolidone)	100	5	–	42.8	–	Co-CNC	Zhu et al. 2007
4	Ethylene diamine	40	6	–	64.3	314.6	Co-CNC	Barick et al. 2009a
5	Sodium acrylate/citrate	(a) 6 (b) 60 (c) 120 (d) 170	(a) 6 (b) 7 (c) 8.3 (d) 13.5	–	(a) 36.2 (b) 38.7 (c) 46.5 (d) 67.2	(a) 65.3 (b) – (c) 80.4 (d) 84.6	Co-CNC	Xuan et al. 2009
6	Sodium citrate or poly(ethylene)-imine	200	9.7–11.5	217–277	53–70	124–360	Co-CNC	Xu et al. 2009
7	poly(ethylene)-glycol	30	4.8	47[b]	<35	240	CNC	Hu et al. 2010
8	Sodium citrate, poly(acrylic) acid, poly(glutamic)-acid	200	20–35	>300	80	–	Co-CNC	Xu et al. 2012a
9	poly(glutamic) acid	(a) 140 (b) 220 (c) 230	(a) 9.3 (b) 10.4 (c) 13.7	–	(a) 64 (b) 67 (c) 80	–	Co-CNC	Luo et al. 2011
10	Sodium carboxymethylcellulose	180	10	290	69		Co-CNC	Xing et al. 2011
11	Sodium citrate	30	12	39[c]	65[d]	365	Co-CNC	Lartigue et al. 2012

(continued)

Table 2.2 (continued)

	Shell	D_{TEM} cluster (nm)	D_{XRD} particle (nm)	D_h (z-avg) (nm)	M_s (Am² kg⁻¹)	r_2 (mmol s⁻¹)	Type of colloid	Ref.
12	Poly(acrylic)-acid	(a) 13 (b) 36 (c) 64	(a) 8 (b) 11 (c) 13	(a) 30 (b) 60 (c) 100[b]	(a) 66 (b) 68 (c) 68	(a) 240 (b) 540 (c) 650	Co-CNC	Xu et al. 2012b
13	(a) Soyabean (b) Casein (c) Poly(glutamic)-acid (d) Agarose (e) Chitosan	200	9–13	>300[c]	(a) 27 (b) 50 (c) 57 (d) 66 (e) 74	–	Co-CNC	Xu et al. 2012c
14	Ethylenediamine	40	6	90[b]	64.3	314.6	Co-CNC	Barick et al. 2009b
15	Poly(acrylic)-acid	100	–	>300	27	–	Co-CNC	Ma et al. 2012
16	PTEA-b-PAM[e]	20–50	6.3	60–80	50[c]	160–170	Soft CNC	Berret et al. 2006
17	Immobilized on the surface of SiO₂ nanoparticles	~30	9	46	–	400	Soft CNC	Lee et al. 2006b
18	Entrapped in SiO₂	(a) 70 (b) 80 (c) 160	–	(a) 160[c] (b) 120[c] (c) 300[c]	(a) 2.8 (b) 4.4 (c) 3.7	(a) 148 (b) 164 (c) 326	Soft CNC	Taboada et al. 2009
19	Entrapped in SiO₂	80–90	16	–		700	Soft CNC	Yoon et al. 2011
20	Poly(ethyleneglycol) conjugated to poly(acrylic)-acid	–	–	(a) 50 (b) 105 (c) 140 (d) 180	21.5 (67[d])	(a) 70 (b) 255 (c) 440 (d) 604	Soft CNC	Pothayee et al. 2013

(continued)

Table 2.2 (continued)

	Shell	D_{TEM} cluster (nm)	D_{XRD} particle (nm)	D_h (z-avg) (nm)	M_s (Am² kg⁻¹)	r_2 (mmol s⁻¹)	Type of colloid	Ref.
21	Magnetoliposomes		7–9	240	58 (300 kA/m)	270	Soft CNC (liposomes)	Béalle et al. 2012
22	Magnetoliposomes	100	–	~100ᶜ	–	140	Soft CNC	Skouras et al. 2011
23	Magnetoliposomes	–	13	110	57	270–900ᵈ	Soft CNC	Meledandri et al. 2011
24	Magnetoliposomes	–	8	190	–	130	Soft CNC	Martina et al. 2005
25	Magnetoliposomes	–	6.5	55	–	1286	Soft CNC	Mikhaylov et al. 2011
26	PEG and peptide	100	10	140ᶜ		120	Soft CNC (worm)	Peiris et al. 2012a, b
27	Poly(cyclotriphosphazene-co sulfonyldiphenol)	200	20	–	62.5	124	Worms of co-CNCs	Zhou et al. 2010
28	Dextran	50–80	5	65	74.2ᶠ	116	Soft CNC (worm)	Park et al. 2008
29	Poly(caprolactone)-b-PEG	–	(a) 4 (b) 8 (c) 16	(a) 75 (b) 97 (c) 110ᵇ	–	(a) 169 (b) 318 (c) 471	Soft CNC (micelles)	Ai et al. 2005
30	Poly(lactic acid-co-glycolic acid)-b-PEG	–	–	70ᵇ	40	330	Soft CNC (micelles)	Yang et al. 2007

(continued)

Table 2.2 (continued)

	Shell	D_{TEM} cluster (nm)	D_{XRD} particle (nm)	D_h (z-avg) (nm)	M_s (Am² kg⁻¹)	r_2 (mmol s⁻¹)	Type of colloid	Ref.
31	Polyacrylic-based	45–80	9	53–94[b]	58	245–500	Soft CNC (emulsion)	Paquet et al. 2011
32	Poly(trimethyl carbonate)-b-poly(glutamic)-acid	100–400	6.5	100	–	182	Soft CNC in polymersomes	Sanson et al. 2011
33	Poly(acrylic)-acid, poly(ethyleneimine), silica	120	12	–	65	227	Soft CNC (emulsion)	Qiu et al. 2010
34	Dextran-pyrene	–	12	110[b]	50	320	Soft CNC (micellar)	Lim et al. 2011
35	Poly(ethyleneimine)-b-poly(caprolactone)-b-PEG	–	13	(a) 60 (b) 95[g]	26	(a) 250 (b) 400	Soft CNC (micellar)	Pöselt et al. 2012
36	Polypyrrole	50	8–10	150	20	90	Soft CNC (emulsion)	Wang et al. 2013b
37	poly(lactic acid-co-glycolic acid) and polylysine-PEG	100–200	15	200[g]	–	190	Soft CNC (micelles)	Kim et al. 2008c
38	Poly(maleic anhydride-alt-1-octadecene)	134	8	200[b]	–	236	Soft CNC	Bigall et al. 2013

Note Soft CNC is named those MIONs not assembled through oriented aggregation or direct attachment

[a] Values obtained for 200 nm size particles, expressed in emu/g, with composition (a) (Fe₃O₄) (b) (MnFe₂O₄), (c) (ZnFe₂O₄), (d) (CoFe₂O₄)

[b] By number

[c] Method not reported

[d] Expressed per mass of magnetic material

[e] Poly(trimethylammonium-ethyl acrylate)methylsulfate-b-poly(acrylamide)

[f] Expressed per mass of Fe ions

[g] By volume

regions of a nude mouse) revealed the excellent contrast enhancements of this system. Yon et al. (2011) developed core-shell NP's magnetic materials with a different architecture, Fe@MFe$_2$O$_4$ (Fe as core and iron oxide as shell, core size 16 nm, and hydrodynamic size ~45 nm) having, however, similar DMSA coating material in order to grant to the system's ferrofluid properties. The magnetic responses were found also very high, with Fe@MnFe$_2$O$_4$ (149 emu/g) > Fe@Fe$_3$O$_4$ (142 emu/g) > Fe@CoFe$_2$O$_4$ (133 emu/g) > Fe@FeO(92 emu/g) as well as the contrast proclivity (R_2 obtained at 0.47 T) with similar trend as Ms, namely Fe@MnFe$_2$O$_4$ (356 mmol^{-1} s^{-1}) > Fe@Fe$_3$O$_4$ (260 mmol^{-1} s^{-1}) > Fe@CoFe$_2$O$_4$ (243 mmol^{-1} s^{-1}) > Fe@FeO (188 mmol^{-1} s^{-1}). The biological impact tested for the best performant system (Fe@MnFe$_2$O$_4$) unveiled low cytotoxicity against normal (3T3 fibroblast) and cancer (HCT 116) cells (up to 200 µg/mL metal content). The targeting potential of Fe@MnFe$_2$O$_4$ was addressed upon further conjugation with monoclonal antibodies (to HER2/*neu*) for cellular detection (cancer cells, SkBr3) and demonstrated not only the high contrast ability of this system but also its high sensitivity in MR-based diagnostics, since it enabled the detection of ca. 10 cancer cells in the presence of abundant host cells (measurements on SkBr3 on whole blood). In an earlier work, Jang et al. (2009) synthesized 15-nm-sized Zn^{2+}-doped nanoparticles of (Zn$_x$Mn$_{1-x}$)Fe$_2$O$_4$ and (Zn$_x$Fe$_{1-x}$)Fe$_2$O$_4$ (with $x = 0$, 0.1, 0.2, 0.3, 0.4, and 0.8) and found that they all exhibited high magnetic moments and high transverse relaxivity index, with the (Zn$_{0.4}$Mn$_{0.6}$)Fe$_2$O$_4$ and the (Zn$_{0.4}$Fe$_{0.6}$)Fe$_2$O$_4$ being the most performant systems with R_2 of 860 mmol^{-1} s^{-1} and 678 mmol^{-1} s^{-1}, respectively. These values are much larger than those known for undoped Fe$_3$O$_4$ (276 mmol^{-1}s^{-1}), MnFe$_2$O$_4$ (422 mmol^{-1}s^{-1}), or Feridex. In particular, the 15-nm-sized (Zn$_{0.4}$Mn$_{0.6}$) Fe$_2$O$_4$ nanoparticles that encoded the high M_s value of 175 emu/g was considered an ideal candidates for hyperthermia studies and showed that (84.4%) HeLa cells upon exposure to (Zn$_{0.4}$Mn$_{0.6}$) Fe$_2$O$_4$ nanoparticles died after 10 min of alternating current (AC) magnetic field application (500 kHz AC magnetic field with an amplitude of 3.7 kAm^{-1}), whereas only 13.5% of cells died when treated with Feridex. The hyperthermia effect, namely the ability of magnetic nanoparticles to adsorb alternating current (AC) energy and to convert it into heat following the relaxation of the rotating magnetic moments induced by AC field, represents another forefront application of magnetic nanoparticles for medical therapies and has been thoroughly revised in recent works (Kolhatkar et al. 2013; Laurent et al. 2011; Kobayashi 2011). Beji et al. (2010) also studied Zn-substituted MnFe$_2$O$_4$ nanoparticles with composition Mn$_{0.2}$Zn$_{0.8}$Fe$_2$O$_4$ (uncoated, 8 nm size, M_s of 88 emu/g at room temperature) and monitored the cytotoxicity effect against human endothelial cells (HUVCs). While at very low concentration (1 µg/mL), no toxic effects were observed within 72 h time frame; at higher concentration (100 µg/mL), the cell viability dropped to nearly 40% after only 4 h from inoculation. Novak et al. (2013) used a model invertebrate animal, the *Porcellio scaber*, to study the effect of ingested CoFe$_2$O$_4$ nanoparticles in the presence of digestive juices and provided experimental evidences of the formation of Co^{2+}, Fe^{2+}, and Fe^{3+} ions from the dissolution of CoFe$_2$O$_4$ nanoparticles. The biological impacts on the animals' health were evaluated, showing that Co^{2+} cations were more toxic than both intact nanoparticles and Fe^{n+} cations derived from

their dissolution, and Co^{2+} accumulated in the hepatopancreas. There is no doubt that the doping approach opens a wide-operational window and offers many possibilities for the generation of much more performant MR contrast agents, but there is still the need of more extended analyses on their biological impacts, before they could enter in the day-by-day clinical practice. This is particularly relevant when elements such as cobalt (toxic range >0.129 μg/g), nickel (toxic range >0.55 μg/g), and manganese (toxic range >1.93 μg/g) are included in the preparations, because those are potentially more toxic than iron. Another approach combining the best of two worlds in theranostics includes admixture of T_1 and T_2 agents in combination with drug release. Recently, Santra et al. (2012) reported the assembly of Gd-DTPA encapsulated within the poly(acrylic acid) (PAA) polymer coating of a superparamagnetic iron oxide nanoparticle (IO-PAA), which formed a magnetic nanoprobe (IO-PAAGd-DTPA) where the quenched longitudinal spin–lattice magnetic relaxation (T_1) of GD-DTPA was restored upon release of the gadolinium complex in acid medium. Conjugation of the magnetic probe with folate residues together with the encapsulation of the anticancer drug Taxol evidenced that when HeLa cells where incubated with this composite, the T_1 activation of the probe coincided with the rate of drug release and the correspondent cytotoxic effect in the cell culture studies. The result agrees with the lysosome acidic degradation of the iron oxide core nanoprobe (IO-PAA), effect that can be used to trigger both imaging and therapy (drug release). There are several pharmaceutical preparations currently sold on the market, where anticancer drugs (Fig. 2.15) have been encapsulated in inorganic vehicles to improve circulation time. For example, Genexol-PM® (paclitaxel-loaded polymeric micelles), Doxil® (PEGylated liposomal encapsulating doxorubicin), DaunoXome® (liposome-encapsulated daunorubicin), Myocet® (non-pegylated liposomal doxorubicin citrate), Abraxane® (albumin-bound paclitaxel), and DepoCyt® (liposomal cytarabine). However, to date, no anticancer drug loaded in any of so far developed magnetic NPs has been clinically approved in medical practice (El-Boubbou 2018).
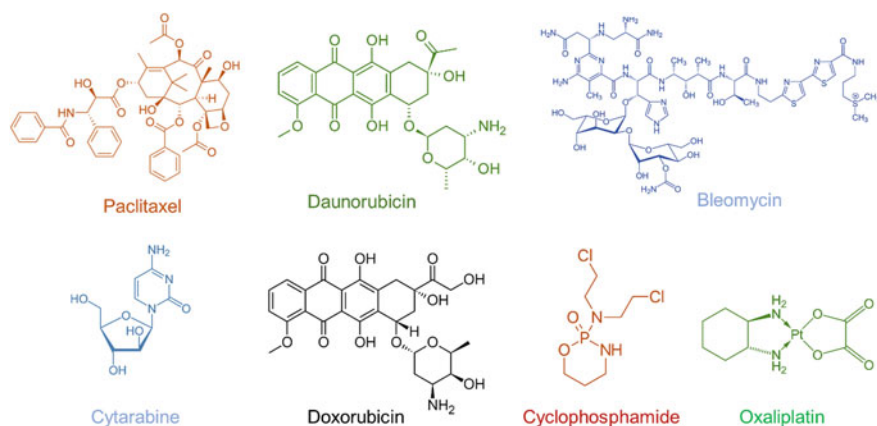
Fig. 2.15 Structure of some important anticancer drugs currently sold on the market

Nevertheless, the use of magnetic NPs in support of clinical screening or as an alternative treatment with respect to more conventional cancer chemotherapies remains a healthy ground of research explored by the pharma industry. For example, NanoTherm® is superparamagnetic iron oxide silane-coated nanoparticles (commercialized by MagForce). These NPs are currently sold for therapeutic treatments against brain cancer and are under clinical testing in patients suffering of prostate and glioblastoma tumors (Johannsen et al. 2007, 2010). Feraheme® (Ferumoxytol injection) is SPION nanoparticles (coating with semi-synthetic poly-glucose sorbitol carboxymethyether) recommended for treatments of iron deficiencies in patients with chronic kidney disease (Helenek et al. 2010; Pai and Garba 2012). Furthermore, the use of Feraheme®, branded as Ferumoxytol®, is under clinical evaluation as a contrast agent material for MR angiography and brain tumor (Provenzano et al. 2009).

Conclusion

Tremendous synthetic, physical, biochemical, and preclinical research efforts have been put forward by the research community and pharma industry into the development of magnetic NP systems, which can be tailored for drug delivery, MRI screenings, and hyperthermia treatments. Besides the potentiality expressed in the theranostic, in terms of flexible design and harmonious combination of properties (and functions) into a single engineered unit, and the widening of our understanding of the impact of nanostructured materials on numerous biochemical functions, several drawbacks hamper their takeover of the nanomedical arena. In fact, a very limited number of NP formulations find their way in the factual clinical applications. Several problems appear to form the basis of such poor translation into clinical practice, which can be rationalized in the following points: (i) moving from lab-bench preparations (mg, g scale) to industrial preparations (kg scale), including the establishment of strict protocols that grants reproducibility, appears harder to set up than expected; (ii) systemic validation of the NP performances, moving from in vitro to in vivo, (iii) systemic validation of their stability profiles, safety profiles, toxicity profiles, pharmacokinetics, clearance by dissecting their metabolic pathways, and (iv) the lack of an ample and detailed database of results obtained from their applications on trial patients.

References

Ai H, Flask C, Weinberg B, Shuai XT, Pagel MD, Farrell D, Duerk J, Gao J (2005) Adv Mater 17:1949–1952

Allen M, Prissel M, Joung JM, Douglas T (2007) Constrained metal oxide mineralization: lessons from ferritin applied to other protein cage architectures. In: Behrens P, Baeuerlein E (eds) Handbook of biomineralization: biomimetic and bioinspired chemistry. Wiley-VCH, Weinheim

Anderson ER, Shah YM (2013) Compr Physiol 3:315–330

Arias JL, Reddy LH, Couvreur PJ (2012) Mat Chem 22:7622–7632

Axline SG, Reaven EPJ (1974) Cell Biol 62:647–659

Bakandritsos A, Papagiannopoulos A, Anagnostou EN, Avgoustakis K, Zboril R, Pispas S, Tucek J, Ryukhtin V, Bouropoulos N, Kolokithas-Ntoukas A, Steriotis TA, Keiderling U, Winnefeld F (2010a) Small 8:2381–2393

Bakandritsos A, Mattheolabakis G, Zboril R, Bouropoulos N, Tucek J, Fatouros DG, Avgoustakis K (2010b) Nanoscale 2:564–572

Barick KC, Aslam M, Prasad PV, Dravid VP, Bahadur D (2009a) J Magn Magn Mater 321:1529–1532

Barick KC, Aslam M, Lin Y-P, Bahadur D, Prasad PV, Dravid VP (2009b) J Mater Chem 19:7023–7029

Basuki JS, Duong HTT, Macmillan A, Erlich RB, Esser L, Akerfeldt MC, Whan RM, Kavallaris M, Boyer C, Davis TP (2013) ACS Nano 7:10175–10189

Béalle G, Di Corato R, Kolosnjaj-Tabi J, Dupuis V, Clément O, Gazeau F, Wilhelm C, Ménager C (2012) Langmuir 28:11834–11842

Beji Z, Hanini A, Smiri LS, Gavard J, Kacem K, Villain F, Grenèche J-M, Chau F, Ammar S (2010) Chem Mater 22:5420–5429

Berret J-F, Schonbeck N, Gazeau F, El Kharrat D, Sandre O, Vacher A, Airiau M (2006) J Am Chem Soc 128:1755–1761

Berry CC, Wells S, Charles S, Aitchison G, Curtis ASG (2004) Biomaterials 25:5405–5413

Bierry G, Jehl F, Neuville A, Lefevre S, Robert P, Kremer S, Dietemann JL (2010) Am J Roentgenol 194:W521–W526

Bigall NC, Wilhelm C, Beoutis M-L, García-Hernandez M, Khan AA, Giannini C, Sánchez-Ferrer A, Mezzenga R, Materia ME, Garcia MA, Gazeau F, Bittner AM, Manna L, Pellegrino T (2013) Chem Mater 25:1055–1062

Bilecka I, Djerdj I, Niederberger M (2008) Chem Commun 7:886–888

Bin NH, Lee IS, Seo H, Park YI, Lee JH, Kim S, Hyeon T (2007) Chem Commun 48:5167–5169

Bonnemain BJ (1998) Drug Target 6:167–174

Boussif O, Lezoualc'h F, Zanta MA, Mergny MD, Scherman D, Demeneix B, Behr JP (1995) Proc Nat Acad Sci (USA) 92:7297–7301

Boyer C, Whittaker MR, Bulmus V, Liu J, Davis TP (2010) NPG Asia Mater 2:23–30

Brannon-Peppas L, Blanchette JO (2004) Adv Drug Deliv Rev 56:1649–1659

Brazel CS (2009) Pharm Res 26:644–656

Bulte JWM, Douglas T, Witwer B, Zhang SC, Strable E, Lewis BK, Zywicke H, Miller B, van Gelderen P, Moskowitz BM, Duncan ID, Frank JA (2001) Nature Biotechnol 19:1141–1147

(a) Cengelli F, Maysinger D, Tschudi-Monnet F, Montet X, Corot C, Petri-Fink A, Hofmann H, Juillerat-Jeanneret L (2006) J Pharm Exp Ther 318:108–116. (b) Cengelli F, Maysinger D, Tschudi-Monnet F, Montet X, Corot C, Petri-Fink A, Hofmann H, Juillerat-Jeanneret L (2006) J Pharm Exp Ther 318:1388

Chaudhary N, Gomez GA, Howes MT, Lo HP, McMahon K-A, Rae JA, Schieber NL, Hill MM, Gaus K, Yap AS, Parton RG (2014) PLoS Biol 12:e10001832

Chen KL, Mylon SE, Elimelech M (2006) Environ Sci Technol 40:1516–1523

Chen Z, Yin J-J, Zhou Y-T, Zhang Y, Song L, Song M, Hu S, Gu N (2012) ACS Nano 6:4001–4012

Chen H, Sulejmanovic D, Moore T, Colvin DC, Qi B, Thompson Mefford O, Gore JC, Alexis F, Hwu SJ, Anker J (2014) n. Chem Mater 26:2105–2112

Choi H, Choi SR, Zhou R, Kung HF, Chen IW (2004) Acad Radiol 11:996–1004

Cohen Y, Shoushan SY (2013) Curr Opin Biotechnol 24:672–681

Cole AJ, David AE, Wang J, Galban CJ, Hill HL, Yang VC (2011) Biomaterials 32:2183–2193

Conner SD, Schmid LS (2003) Nature 422:37–44

Corchero JL, Villaverde A (2009) Trends Biotechnol 27:468–476

Daldrup-Link HE, Rudelius M, Oosterndorp RA, Settles M, Piontek G, Metz S, Rosenbrock H, Keller U, Heinzmann U, Rummeny EJ, Schlegel J, Link TM (2003) Radiology 228:760–767

Daldrup-Link HE, Golovko D, Ruffell B, DeNardo DG, Castaneda R, Ansari C, Rao J, Tikhomirov GA, Wendland MF, Corot C, Coussens LM (2011) Clin Cancer Res 17:5695–5704

Damm E-M, Pelkmans L, Kartenbeck J, Mezzacasa A, Kurzchalia T, Helenius AJ (2005) Cell Biol 168:477–488

Davis ME (2002) Curr Opin Biotechnol 13:128–131

De Cuyper M, Joniau M (1991) Langmuir 7:647–652

De Domenico I, McVey Ward D, Kaplan J (2008) Nat Rev Mol Cell Biol 9:72–81

Deng H, Li X, Peng Q, Wang X, Chen J, Li Y (2005) Angew Chem Int Ed 44:2782–2785

Di Corato R, Gazeau F, Le Visage C, Fayol D, Levitz P, Lux F, Letourneur D, Luciani N, Tillement O, Wilhelm C (2013) ACS Nano 7:7500–7512

Dias AMGC, Hussain A, Marcos AS, Roque ACA (2011) Biotechnol Adv 2011(29):142–155

Dobrovolskaia MA, Aggarwal P, Hall JB, McNeil SE (2008) Mol Pharm 5:487–495

Douglas T, Strable E, Willits D, Aitouchen A, Libera M, Young M (2002) Adv Mater 14:415–418

Dresco PA, Zaitsev VS, Gambino RJ, Chu B (1999) Langmuir 15:1945–1951

D'Souza AJM, Schowen RL, Topp EM (2004) J Contr Release 94:91–100

Edrissi M, Norouzbeigi R (2010) J Nanopart Res 12:1231–1238

El Khoury JM, Caruntu D, O'Connor CJ, Jeong KU, Cheng SZD, Hu J (2007) J Nanopart Res 9:959–964

El-Boubbou K (2018) Nanomedicine (Lond.) 8:953–971

Fan U, Senapati D, Singh AK, Ray PC (2013) Mol Pharm 10:857–866

Fang C, Bhattarai N, Sun C, Zhang M (2009) Small 5:1637–1641

Fantechi E, Innocenti C, Zanardelli M, Fittipaldi M, Falvo E, Carbo M, Shullani V, Di Cesare Mannelli L, Ghelardini C, Ferretti AM, Ponti A, Sangregorio C, Pierpaolo C (2014) ACS Nano 8:4705–4719

Faure C, Meyre ME, Trépout S, Lambert O, Lebraud E (2009) J Phys Chem B 113:8552–8559

Figuerola A, Di Corato R, Manna L, Pellegrino T (2010) Pharmacol Res 62:126–143

Fleige G, Nolte C, Synowitz M, Seeberger F, Kettenmann H, Zimmer C (2001) Neoplasia 3:489–499

Flesch C, Delaite C, Dumas P, Bourgeaut-Lami E, Duguet E (2004) J Polym Sci Part A Polym Chem 42:6011–6020

Flesch C, Bourgeaut-Lami E, Mornet S, Duguet E, Delaite C, Dumas P (2005) J Polym Sci Part A Polym Chem 43:3221–3231

Freeman R, King B (1972) J Clin Path 25:912–914

Frison L, Cernuto G, Cervellino A, Zaharko O, Colonna GM, Guagliardi A, Masciocchi N (2013) Chem Mat 25:4820–4827

Fujita T, Matsushita M, Endo Y (2004) Immunol Rev 198:185–202

Gabal MA, Bayoumy WA (2010) Polyhedron 29:2569–2573

Gallagher JJ, Tekoriute R, O'Reilly J-A, Kerskens C, Gunko YK, Lynch M (2009) J Mater Chem 19:4081–4084

Gao LZ, Zhuang J, Nie L, Zhang JB, Zhang Y, Gu N, Wang TH, Feng J, Yang DL, Perrett S, Yan XY (2007) Nat Nanotechnol 2:577–583

Gao JH, Liang GL, Cheung JS, Pan Y, Kuang Y, Zhao F, Zhang B, Zhang XX, Wu EX, Xu B (2008) J Am Chem Soc 130:11828–11833

Ghosh D, Lee Y, Thomas S, Kohli AG, Yun DS, Belcher AM, Kelly KA (2012) Nat Nanotechnol 7:677–682

Gobe M, Kon-No K, Kandori K, Kitahara AJ (1983) Colloid. Interface Sci 93:293–295

Gradishar WJ, Tjulandin S, Davidson N, Shaw H, Desai N, Bhar P, Hawkin M, O'Shaughnessy J (2005) J Clin Oncol 23:7794–7803

Guardia P, Labarta A, Battle X (2011) J Phys Chem C 115:390–396

Guo Y, Chen W, Wang W, Shen J, Guo R, Gong F, Lin S, Cheng D, Chen G, Shuai X (2012) ACS Nano 6:10646–10657

Hadjipanayis CG, Machaidze R, Kaluzova M, Wang L, Schuette AJ, Chen H, Wu X, Mao H (2010) Cancer Res 70:6303–6312

He C, Hu Y, Yin L, Tang C, Yin C (2010) Biomaterials 13:3657–3666

Helenek MJ, Tokars ML, Lawrence RP (2010) US Patent 7754702 B2

Hickey RJ, Koski J, Meng X, Riggleman RA, Zhang P, Park SJ (2014) ACS Nano 8:495–502

Hu F, MacRenaris KW, Waters EA, Schultz-Sikma EA, Eckermann AL, Meade TJ (2010) Chem Commun 46:73–75

Huang DM, Hsiao JK, Chen YC, Chien LY, Yao M, Chen YK, Ko BS, Hsu SC, Tai LA, Cheng HY, Wang SW, Yang CS, Chen YC (2009) Biomaterials 30:3645–3651

Huang J, Bu L, Xie J, Chen K, Cheng Z, Li X (2010) ACS Nano 4:7151–7160

Huang J, Wang L, Lin R, Wang AY, Yang L, Kuang M, Qian W, Mao H (2013) ACS Appl Mater Interfaces 5:4632–4639

Hyeon T, Lee SS, Park YC, Na HB (2001) J Am Chem Soc 123:12798–12801

Jain TK, Reddy MK, Morales MA, Leslie-Pelecky DL, Labhasetwar V (2008) Mol Pharm 5:316–327

Jana NR, Earhart C, Ying JY (2007) Chem Mater 19:5074–5082

Jander S, Schroeter M, Saleh A (2007) Stroke 38:642–645

Jang J-T, Nah H, Lee J-H, Moon SH, Min GK, Cheon C (2009) Angew Chem Int Ed 48:1234–1238

Jiang X, Ding Y, Ge H, Yuan Y, Yang C (2002) Biomaterials 23:3193–3201

Jin L, Abrahams JP, Skinner R, Petitou M, Pike RN, Carrell RW (1997) Proc Nat Acad Sci (USA) 94:14683–14688

Johannsen M, Gneveckow U, Taymoorian K, Thiesen B, Waldöfner N, Scholz R, Jung K, Jordan A, Wust P, Loening SA (2007) Int J Hyperthermia 23:315–323

Johannsen M, Thiesen B, Wust P, Jordan A (2010) Int J Hyperthermia 26:790–795

Josephson L, Tung C-H, Moore A, Weissleder R (1999) Bioconjugate Chem 10:186–191

Jung CP, Jacobs P (1995) Magn Reson Imaging 13:661–674

Kami D, Takeda S, Itakura Y, Gojo S, Watanabe M, Toyoda M (2011) Int J Mol Sci 12:3705–3722

Karmali PP, Chao Y, Park J-H, Sailor MJ, Ruoslahti E, Esener SE, Simberg D (2012) Mol Pharm 9:539–545

Kerr MC, Teasdale RD (2009) Traffic 10:364–371

Kievit FM, Zhang M (2011) Acc Chem Res 44:853–862

Kim DK, Mikhaylova M, Wang FH, Kehr J, Bjelke B, Zhang Y, Tsakalakos T, Muhammed M (2003) Chem Mater 15:4343–4351

Kim J, Kim H, Lee N, Kim T, Kim H, Yu T, Song I, Moon W, Hyeon T (2008a) Angew Chem Int Ed 47:8438–8441

Kim DH, Kim KN, Kim KM, Lee YKJ (2008b) Biomed Mat Res Part A 88A:1–11

Kim J, Lee JE, Lee SH, Yu JH, Lee JH, Park TG, Hyeon T (2008c) Adv Mater 20:478–483

Kim D, Lee N, Park M, Kim BH, An K, Hyeon T (2009) J Am Chem Soc 131:454–455

Kirchen JM, Ravichandran KS (2008) Nat Rev Mol Cell Biol 9:781–795

Kleinschnitz C, Bendszus M, Frank M, Solymosi L, Toyka KV, Stoll GJ (2003) Cereb Blood Flow Metabolism 23:1356–1361

Kobayashi T (2011) Biotechnology 6:1342–1347

Kohgo Y, Ikuta K, Ohtake T, Torimoto Y, Kato J (2008) Int J Hematol 88:7–15

Kolenko YV, Bañobre-López M, Rodríguez-Abreu C, Carbó-Argibay E, Sailsman A, Piñeiro-Redondo Y, Fátima Cerqueira M, Petrovykh DY, Kovnir K, Lebedev OI, Rivas J (2014) J Phys Chem C 118:8691–8701

Kolhatkar AG, Jamison AC, Litvinov D, Willson RC, Lee TR (2013) Int J Mol Sci 14:15977–16009

Kostiainen MA, Hiekkataipale P, Laiho A, Lemieux V, Seitsonen J, Ruokolainen J, Ceci P (2013) Nat Nanotechnol 8:52–56

Kresse M, Wagner S, Pfefferer D, Lawaczeck R, Elste V, Semmler W (1998) Magn Reson Med 40:236–242

Kucheryavy P, He J, John VT, Maharjan P, Spinu L, Goloverda GZ, Kolesnichenko VL (2013) Langmuir 29:710–716

Kumar K, Nightinga AM, Krishnadasan SH, Kamaly N, Wylenzinska-Arridge M, Zeissler K, Branford WR, Ware E, deMello AJ, deMello JC (2012) J Mater Chem 22:4704–4708

Kunzmann A, Andersson B, Thurnherr T, Krug H, Schynius A, Fadeel B (1810) Biochim Biophys Acta 2011:361–373

Kunzmann A, Andersson B, Vogt C, Feliu C, Ye F, Gabrielsson S, Toprak MS, Buerki-Thurnherr T, Laurent S, Vahter M, Krug H, Muhammed M, Scheynius A, Fadeel B (2011) Toxicol Appl Pharm 253:81–93

Lamanna G, Kueny-Stotz M, Mamlouk-Chaouachi H, Ghobril C, Basly B, Bertin A, Miladi I, Billotey C, Pourroy G, Begin-Colin S, Felder-Flesch D (2011) Biomaterials 32:8562–8573

Landry R, Jacobs PM, Davis R, Shenouda M, Bolton WK (2005) Am J Nephrol 25:400–410

Larsen EKU, Nielsen T, Wittenborn T, Birkedal H, Vorup-Jensen T, Jakobsen MH, Østergaard L, Horsman MR, Besenbacher F, Howard KA, Kjems J (2009) ACS Nano 3:1947–1951

Lartigue L, Hugounenq P, Alloyeau D, Clarke SP, Lévy M, Bacri J-C, Bazzi R, Brougham DF, Wilhelm C, Gazeau F (2012) ACS Nano 6:10935–10949

Larumbe S, Gomez-Polo C, Perez-Landazabal J, Pastor JMJ (2012) Phys Condens Matter 24:1–6

Laurent S, Forge D, Port M, Roch A, Robic C, Vander EL, Muller RN (2008) Chem Rev 108:2064–2110

Laurent S, Dutz S, Häfeli UO, Mahmoudi M (2011) Adv Coll Interf Sci 166:8–23

Lawaczeck R, Menzel M, Pietsch H (2004) Appl Organomet Chem 18:506–513

Le Renard PL, Jordan O, Faes A, Petri-Fink A, Hofmann H, Rufebacht D, Bosman F, Buchegger F, Doelker E (2010) Biomaterials 31:691–705

Lee N, Hyeon T (2012) Chem Soc Rev 41:2575–2589

Lee Y, Lee J, Bae CJ, Park JC, Noh HJ, Park JH, Hyeon T (2005a) Adv Funct Mater 3:503–509

Lee HS, Kim EH, Shao H, Kwak BK (2005b) J Magn Magn Mater 293:102–105

Lee JH, Huh YM, Jun YW, Seo JW, Jang JT, Song HT, Kim S, Cho EJ, Yoon HG, Suh JS, Cheon J (2006a) Nat Med 13:95–99

Lee J-H, Jun Y, Yeon S-I, Shin J-S, Cheon J (2006b) Angew Chem Int Ed 45:8160–8162

Lee H, Yu MK, Park S, Moon S, Min JJ, Jeong YY, Kang HW, Jon S (2007a) J Am Chem Soc 129:12739–12745

Lee J-H, Huh Y-M, Jun Y-W, Seo J-W, Jang J-T, Song H-T, Kim S, Cho EJ, Yoon HG, Suh JS, Cheon J (2007b) Nat Med 13:95–99

Lee HY, Lee SH, Xu C, Xie J, Lee JH, Wu B, Koh AL, Wang X, Sinclair R, Wang SX, Nishimura DG, Biswal S, Sun S, Cho SH, Chen X (2008) Nanotechnology 19:165101

Lee J-H, Lee K, Moon SH, Lee Y, Park TG, Cheon J (2009) Angew Chem Int Ed 48:4174–4179

Lee MJ-E, Veiseh O, Bhattarai N, Sun C, Hansen SJ, Ditzler S, Knoblaugh S, Lee D, Ellenbongen R, Zhang M, Olson JM (2010) PLoS ONE 5:e9536

Lee JH, Jang JT, Choi JS, Moon SH, Noh SH, Kim JW, Kim JG, Kim IS, Park Kl, Cheon J (2011) Nat Nanotechnol 6:418–422

Lee JE, Lee N, Kim T, Kim J, Hyeon T (2011b) Acc Chem Res 44:893–902

Lee D-E, Koo H, Sun I-C, Ryu JH, Kim K, Kwon IC (2012a) Chem Soc Rev 41:2656–2672

Lee N, Choi Y, Lee Y, Park M, Moon WK, Choi SH, Hyeon T (2012b) Nano Lett 12:3127–3131

Lee DJ, Park GY, Oh KT, Oh NK, Kwag DS, Youn YS, Oh YT, Park JW, Lee ES (2012c) Int J Pharm 434:257–263

Lee JH, Jung MJ, Hwang YH, Lee YJ, Lee S, Lee DY, Shin H (2012d) Biomaterials 33:4861–4871

Li Z, Chen H, Bao H, Gao M (2004) Chem Mater 16:1391–1393

Li H, El-Dakdouki MH, Zhu DC, Abela GS, Huang X (2012) Chem Commun 48:3385–3387

Li Y, Ma J, Zhu H, Gao X, Dong H, Shi D (2013a) ACS Appl Mater Interfaces 5:7227–7235

Li Z, Wang C, Cheng L, Gong H, Yin S, Gong Q, Li Y, Liu Z (2013b) Biomaterials 34:9160–9170

Li L, Liu C, Zhang L, Wang T, Yu H, Wang C, Su Z (2013c) Nanoscale 5:2249–2253

Liao MH, Chen DH (2001) Biotechnol Lett 23:1723–1727

Liao W, McNutt MA, Zhu WG (2009) Methods 48:46–53

Lim E-K, Jang E, Kim B, Choi J, Lee K, Suh J-S, Huh Y-M, Haam S (2011) J Mater Chem 21:12473–12478

Lin L-S, Cong Z-H, Cao J-B, Ke K-M, Peng Q-L, Gao J, Yang H-H, Liu G, Chen X (2014) ACS Nano 8:3876–3883

Liu G, Gao J, Ai H, Chen X (2013) Small 9:1533–1545

Liz L, Lopez-Quintela MA, Mira J, Rivas J (1994) J Mater Sci 29:3797–3801

Lu A-H, Salabas EL, Schuth F (2007a) Angew Chem Int Ed 46:1222–1244

Lu CW, Hung Y, Hsiao JK, Yao M, Chung TH, Lin YS, Wu SH, Hsu SC, Liu HM, Mou CY, Yang CS, Huang DM, Chen YC (2007b) Nano Lett 7:149–154

Luo B, Xu S, Luo A, Wang W-R, Wang S-L, Guo J, Lin Y, Zhao D-Y, Wang C-C (2011) ACS Nano 5:1428–1435

Lynch I, Dawson KA (2008) Nano Today 3:40–47

Lyon JL, Fleming DA, Stone MB, Schiffer P, Williams ME (2004) Nano Lett 4:719–723

Ma H, Qi X, Maitani Y, Nagai T (2007) Int J Pharm 333:177–186

Ma HL, Xu YF, Qi XR, Maitani Y, Nagai T (2008) Int J Pharm 354:217–226

Ma W-F, Wu K-Y, Tang J, Li D, Wei C, Guo J, Wang S-L, Wang C-C (2012) J Mater Chem 22:15206–15214

Maeda H (2010) Bioconjug Chem 21:797–802

Mahmoudi M, Simchi A, Imani M, Häfeli UO (2009a) J Phys Chem C 113:8124–8131

Mahmoudi M, Simchi A, Imani M, Milani AS, Stroeve P (2009b) Nanotechnology 20:225104

Mahmoudi M, Simchi A, Imani M (2009c) J Phys Chem C 113:9573–9580

Mahmoudi M, Milani AS, Stroeve P (2010) Int J Biomed Nanosci Nanotechnol 1:164–201

Mahmoudi M, Hosseinkhani H, Hosseinkhani M, Boutry S, Simchi A, Journeay WS, Subramani K, Laurent S (2011a) Chem Rev 11:253–280

Mahmoudi M, Sant S, Wang B, Laurent S, Sen T (2011b) Adv Drug Deliv Rev 63:24–46

Mahmoudi M, Azadmanesh K, Shokrgozar MA, Journeay WS, Laurent S (2011c) Chem Rev 111:3407–3432

Mahmoudi M, Sahraian M, Shokrgozar MA, Laurent S (2011d) ACS Chem Neurosci 2(118):140

Mahmoudi M, Hofmann H, Rothen-Rutishauser B, Petri-Fink A (2012) Chem Rev 112:2323–2338

Maity D, Zoppellaro G, Sedenkova V, Tucek J, Safarova K, Polakova K, Tomankova K, Diwoky C, Stollberger R, Machala L (2012) Zboril. R Chem Commun 48:11398–11400

Mak KH, Lu CY, Kuan IC, Lee SL (2009) ISESCO Sci Technol Vis 5:19–23

Malvindi MA, De Matteis V, Galeone A, Brunetti V, Anyfantis GC, Athanassiou A, Cingolani R, Pompa PP (2014) PLoS ONE 9:e85835

Martin AL, Hickey JL, Ablack AL, Lewis JD, Luyt LG, Gillies ER (2009) J Nanopart Res 12:1599–1608

Martina M-S, Fortin J-P, Ménager C, Clément O, Barratt G, Grabielle-Madelmont C, Gazeau F, Cabuil V, Lesieur S (2005) J Am Chem Soc 127:10676–10685

Mayor S, Pagano RE (2007) Nat Rev Mol Cell Biol 8:603–612

McCarthy JR, Weissleder R (2008) Adv Drug Deliv Rev 60:1241–1251

Medarova Z, Pham W, Farrar C, Petkova V, Moore A (2007) Nat Med 13:372–377

Meledandri CJ, Ninjbadgar T, Brougham DF (2011) J Mater Chem 21:214–222

Mikhaylov G, Mikac U, Magaeva AA, Itin VI, Naiden EP, Psakhye I, Babes L, Reinheckel T, Peters C, Zeiser R, Bogyo M, Turk V, Psakhye SG, Turk B, Vasiljeva O (2011) Nat Nanotechnol 6:594–602

Mincer JS, Simon SM (2011) Proc Nat Acad Sci (USA) 108:351–358

Mojica Pisciotti ML, Lima Jr E, Mansilla MV, Tognoli VE, Troiani HE, Pasa AA, Creczynski-Pasa TB, Silva AH, Gurman P, Colombo L, Goya GF, Lamagna A, Zysler RD (2014) J Biomed Mater Res Part B: Appl Biomater 102:860–868

Mosmann T (1983) J Immunol Meth 65:55–63

Mousavi SA, Malerød L, Berg T, Kjeken R (2004) Biochem J 377:1–16

Nabi R, Le PUJ (2003) Cell Biol 161:673–677

Namdeo M, Bajpai SKJ (2009) Mol Cat B Enzymatic 59:134–139

Nath S, Kaittanis C, Ramachandran V, Dalal NS, Perez JM (2009) Chem Mater 21:1761–1767

(a) Naqvi S, Samim M, Abdin MZ, Ahmed FJ, Maitra AN, Prashant CK, Dinda AK (2010) Int J Nanomed 5:983–989. (b) Soenen SJH, Illyes E, Vercauteren D, Braeckmans K, Majer Z, De Smedt SC, De Cuyper M (2009) Biomaterials 30:6803–6813

Nel A, Xia T, Madler L, Li N (2006) Science 311:622–627

Neuwelt EA, Hamilton BE, Varallyay CG, Rooney VR, Edelman RD, Jacobs PM, Watnick SG (2008) Kidney Int 75:465–474

Nicolás P, Saleta M, Troiani H, Zysler R, Lassalle V, Ferreira ML (2013) Acta Biomater 9:4754–4762

Nigam S, Chandra S, Newgreen DF, Bahadur D, Chen Q (2014) Langmuir 30:1004–1011

Nighoghossian N, Wiart M, Cakmak S, Berthezene Y, Derex L, Cho TH, Nemoz C, Chapuis F, Tisserand GL, Pialat JB, Trouillas P, Froment JC, Hermier M (2007) Stroke 38:303–307

Noh SH, Na W, Jang JT, Lee JH, Lee EJ, Moon SH, Lim Y, Shin JS, Cheon J (2012) Nano Lett 12:3716–3721

Novak S, Drobne D, Golobič M, Zupanc J, Romih T, Gianoncelli A, Kiskinova M, Kaulich B, Pelicon P, Vavpetič P, Jeromel L, Ogrinc N, Makovec D (2013) Environ Sci Technol 47:5400–5408

Osada Y, Gong JP (1998) Adv Mater 10:827–837

Osborne EA, Atkins TM, Gilbert DA, Kauzlarich SM, Liu K, Louie AY (2012) Nanotechnology 23:215602

Pai AB, Garba AO (2012) J Blood Med 3:77–85

Pan CL, Hu B, Li W, Sun Y, Ye H, Zeng XXJ (2009) Mol Cat B Enzymatic 61:208–215

Pankhurst QA, Connolly J, Jones SK, Dobson J (2003) J Phys D Appl Phys 36:R167–R181

Paquet C, de Haan HW, Leek DM, Lin H-Y, Xiang B, Tian G, Kell A, Simard B (2011) ACS Nano 5:3104–3112

Park J, Joo J, Kwon SG, Jang Y, Hyeon T (2007) Angew Chem Int Ed 46:4630–4660

Park J-H, von Maltzahn G, Zhang L, Schwartz MP, Ruoslahti E, Bhatia SN, Sailor M (2008) J Adv Mater 20:1630–1635

Parsons JG, Luna C, Botez CE, Elizalde J, Gardea-Torresdey JL (2009) J Phys Chem Solids 70:555–560

Pascu O, Carenza E, Gich M, Estradé S, Peiró F, Herranz G, Roig A (2012) J Phys Chem C 116:15108–15116

Peddis D, Mansilla MV, Mørup S, Cannas C, Musinu A, Piccaluga G, D'Orazio F, Lucari F, Fiorani D (2008) J Phys Chem B 112:8507–8513

Peiris PM, Toy R, Doolittle E, Pansky J, Abramowski A, Tam M, Vicente P, Tran E, Hayden E, Camann A, Mayer A, Erokwu BO, Berman Z, Wilson D, Baskaran H, Flask CA, Keri RA, Karathanasis E (2012a) ACS Nano 6:8783–8795

Peiris PM, Bauer L, Toy R, Tran E, Pansky J, Doolittle E, Schmidt E, Hayden E, Mayer A, Keri RA, Griswold MA, Karathanasis E (2012b) ACS Nano 6:4157–4168

Pelkmans L, Kartenbeck J, Helenius A (2001) Nat Cell Biol 3:473–483

Pelkmans L, Püntener D, Helenius A (2002) Science 296:535–539

Peppas NA, Huang Y, Torres-Lugo M, Ward JH, Zhang J (2000) Annu Rev Biomed Eng 2:9–29

Pereira C, Pereira AM, Fernandes C, Rocha M, Mendes R, Fernandez-Garcia M, Guedes A, Tavares PB, Greneche JM, Araujo JP, Freire C (2012) Chem Mater 24:1496–1504

Petri-Fink A, Steitz B, Finka A, Salaklang J, Hofmann H (2008) Eur J Pharm Biopharm 68:129–137

Phan VN, Lim E-K, Kim T, Kim M, Choi Y, Kim B, Lee M, Oh A, Jin J, Chae Y, Baik H, Suh J-S, Haam S, Huh Y-M, Lee K (2013) Adv Mater 25:3202–3208

Pichon BP, Gerber O, Lefevre C, Florea I, Fleutot S, Baaziz W, Pauly M, Ohlmann M, Ulhaq C, Ersen O, Pierron-Bohnes V, Panissod P, Drillon M, Begin-Colin S (2011) Chem Mater 23:2886–2900

Pöselt E, Kloust H, Tromsdorf U, Janschel M, Hahn C, Maßlo C, Weller H (2012) ACS Nano 6:1619–1624

Pothayee N, Balasubramaniam S, Pothayee N, Jain N, Hu N, Lin Y, Davis RM, Sriranganathan N, Koretsky AP, Riffle JSJ (2013) Mater Chem B 1:1142–1149

Provenzano R, Schiller B, Rao M, Coyne D, Brenner L, Pereira BJG (2009) Clin J Am Soc Nephrol 4:386–393

Qiu P, Jensen C, Charity N, Towner R, Mao C (2010) J Am Chem Soc 132:17724–17732

Rabenstein DL (2002) Nat Prod Rep 19:312–331

Rademaker KA, Beghein N, Boutry S, Laurent S, Vander Elst L, Muller RN, Jordan BF, Gallez B (2009) Invest Radiol 44:398–404

Reddy LH, Arias J, Nicolas J, Couvreur P (2012) Chem Rev 112:5818–5878

Repnik U, Stoka V, Turk V, Turk B (2012) Biochim Biophys Acta 1824:22–33

Riccardi C, Nicoletti I (2006) Nat Protoc 1:1458–1461

Richard I, Thibault M, De Crescenzo G, Buschmann MD, Lavertu M (2013) Biomacromol 14:1732–1740

Rockenberger J, Scher EC, Alivisatos PA (1999) J Am Chem Soc 121:11595–11596

Rosenberg JT, Sachi-Kocher A, Davidson MW, Grant SC (2012) Contrast Media Mol Imaging 7:121–129

Rossi LM, Quach AD, Rosenzweig Z (2004) Analyt Bioanal Chem 380:606–613

Saha I, Chaffee KE, Duanmu C, Woods BM, Stokes AM, Buck LE, Walkup LL, Sattenapally N, Huggenvik J, Gao Y, Boyd M, Goodson BM (2013) J Phys Chem C 117:1893–1903

Saiyed ZM, Sharma S, Godawat R, Telang SD, Ramchand CN (2007) J Biotechnol 131:240–244

Salazar-Alvarez G, Muhammed M, Zagorodni AA (2006) Chem Eng Sci 61:4625–4633

Salazar-Alvarez G, Qin J, Sepelak V, Bergmann I, Vasilakaki M, Trohidou KN, Ardisson JD, Macedo WAA, Mikhaylova M, Muhammed M, Baró MD, Nogués J (2008) J Am Chem Soc 130:13234–13239

Saleh A, Schroeter M, Ringelstein A, Hartung HP, Siebler M, Mödder U, Jander S (2007) Stroke 38:2733–2737

Sandiford L, Phinikaridou A, Protti A, Meszaros LK, Cui X, Yan Y, Frodsham G, Williamson PA, Gaddum N, Botnar RM, Blower PJ, Green MA, de Rosales RTM (2013) ACS Nano 7:500–512

Sanson C, Diou O, Thévenot J, Ibarboure E, Soum A, Brûlet A, Miraux S, Thiaudière E, Tan S, Brisson A, Dupuis V, Sandre O, Lecommandoux S (2011) ACS Nano 5:1122–1140

Santra S, Tapec R, Theodoropoulou N, Dobson J, Hebard A, Tan W (2001) Langmuir 17:2900–2906

Santra S, Jativa SD, Kaittanis C, Normand G, Grimm J, Perez JM (2012) ACS Nano 6:7281–7294

Sapsford KE, Algar WR, Berti L, Gemmill KB, Casey BJ, Oh E, Stewart MH, Medintz IL (2013) Chem Rev 113:1904–2074

Sillerud LO, Solberg NO, Chamberlein R, Orlando RA, Heidrich JE, Brown DC, Brady CI, Vander Jagt TA, Garwood M, Vander Jagt DL (2013) J Alzheimers Dis 34:349–365

Simberg D, Duza T, Park JH, Essler M, Pilch J, Zhang L, Derfus AM, Yang M, Hoffman RM, Bhatia S, Sailor MJ, Ruoslahti E (2007) Proc Nat Acad Sci 104:932–936

Simberg D, Park JH, Karmali PP, Zhang WM, Merkulov S, McCrae K, Bhatia SN, Sailor M, Ruoslahti E (2009) Biomaterials 30:3926–3933

Sipos P, Berkesi O, Tombacz E, St. Pierre TG, Webb J (2003) J Inorg Biochem 95:55–63

Skouras A, Mourtas S, Markoutsa E, De Goltstein M-C, Wallon C, Catoen S, Antimisiaris SG (2011) Nanomed Nanotechnol Biol Med 7:572–579

Smith SH, Wunder MB, Norris DA, Shellman YG (2011) PLoS ONE 6:e26908

Soenen JS, Rivera-Gil P, Montenegro JM, Parak WJ, De Smedt S, Braeckmans K (2011) Nano Today 6:446–465

Soenen SJH, Himmelreich U, Nuytten N, De Cuyper M (2011b) Biomaterials 32:195–205

Song Q, Zhang ZJ (2004) J Am Chem Soc 126:6164–6168

Spinowitz BS, Schwenk MH, Jacobs PM, Bolton WK, Kaplan MR, Charitan C, Galler M (2005) Kidney Int 68:1801–1807

Steinhardt J, Krijin J, Leidy JC (1971) Biochemistry 10:4005–4015

Stoll G, Bendszus M (2010) Curr Opin Neurol 23:282–286. Nighoghossian N, Wiart M, Berthezene YJ (2008) Neuroimaging 18:349–352

Strable E, Bulte JW, Moskowitz B, Vivekanandan K, Allen M, Douglas T (2001) Chem Mater 13:2201–2209

Sun SH, Zeng H (2002) J Am Chem Soc 124:8204–8205

Sun C, Du K, Fang C, Bhattarai N, Veiseh O, Kievit F, Stephen Z, Lee D, Ellenbogen RG, Ratner B, Zhang M (2010) ACS Nano 4:2402–2410

Taboada E, Solanas R, Rodríguez E, Weissleder R, Roig A (2009) Adv Funct Mater 19:2319–2324

Talelli M, Rijcken CJF, Lammer T, Seevinck PR, Storm G, van Nostrum CF, Hennink WE (2009) Langmuir 25:2060–2067

(a) Tamer U, Gundogdu Y, Boyaci IH, Pekmez K (2013) J Nanopart Res 12:1187–1196 (b) Tamer U, Cetin D, Suludere Z, Boyaci IH, Temiz HT, Yegenoglu H, Daniel P, Dincer I, Elerman Y (2013) Int J Mol Sci 14:6223–6240

Tantra R, Knight A (2011) Nanotoxicology 5:381–392

Tassa C, Shaw SY, Weissleder R (2011) Acc Chem Res 18(44):842–852

Thatiparti TR, Shoffstall AJ, Von Recum HA (2010) Biomaterials 31:2335–2347

Thomas CR, Ferris DP, Lee J-H, Choi E, Cho MH, Kim ES, Stoddart JF, Shin J-S, Cheon J, Zink JI (2010) J Am Chem Soc 132:10623–10625

Thorek DLJ, Chen A, Czupryna J, Tsourkas A (2006) Ann Biomed Eng 34:23–38

Thünemann AF, Schütt D, Kaufner L, Pison U, Möhwald H (2006) Langmuir 22:2351–2357

Tong S, Hou S, Zheng Z, Zhou J, Bao G (2010) Nano Lett 10:4607–4613

Tran N, Webster TJ (2010) J Mater Chem 20:8760–8767

Uchida M, Flenniken ML, Allen M, Willits DA, Crowley BA, Brumfield S, Willis AF, Jackiw L, Jutila M, Joung MJ, Douglas T (2006) J Am Chem Soc 128:16626–16633

Vance JE, Karten BJ (2014) Lip Res 55:1609–1621

Varallyay CG, Nesbit G, Muldoon LL, Nixon RR, Delashaw J, Cohen JI, Petrillo A, Rink D, Neuwelt EA (2002) AJNR Am J Neuroradiol 23:510–590

Veiseh O, Sun C, Fang C, Bhattarai N, Gunn J, Kievit F, Du K, Pullar B, Lee D, Ellenbogen RG, Olson J, Zhang M (2009) Cancer Res 69:6200–6207

Veiseh O, Gunn JW, Zhang M (2010) Adv Drug Deliv Rev 62:284–304

Verma F, Stellacci F (2010) Small 6:12–21

Wadghiri YZ, Li J, Wang J, Hoang DM, Sun Y, Xu H, Tsui W, Li Y, Boutajangout A, Wang A, de Leon M, Wisnieski T (2013) PLoS ONE 8:e57097

(a) Wang XY, Hussain SM, Krestin GP (2001) Eur J Radiol 11:2319–2331. (b) Moghimi SM, Hunter AC, Murray JC (2001) Pharm Rev 53:283–318

Wang C, Xu H, Liang C, Liu Y, Li Z, Yang G, Cheng L, Li Y, Liu Z (2013a) ACS Nano 7:6782–6795

Wang C, Xu H, Liang C, Liu Y, Li Z, Yang G, Cheng L, Li Y, Liu Z (2013b) ACS Nano 7:6782–6795

Wang B, Yin J-J, Zhou X, Kurash I, Chai Z, Zhao Y, Feng W (2013c) J Phys Chem C 117:383–392

Weissleder L, Elizondo G, Wittenberg J, Rabito CA, Bengele HH, Josephson L (1990) Radiology 175:489–493

Xie J, Jon S (eds) (2012) Magnetic nanoparticles-based theranostics. Theranostics 2:3–121

Xie J, Chen K, Huang J, Lee S, Wang J, Gao J, Li X, Chen X (2010) Biomaterials 31:3016–3022

Xing R, Wang X, Zhang C, Wang J, Zhang Y, Song Y, Guo Z (2011) J Mater Chem 21:11142–11149

Xu XQ, Shen H, Xu JR, Xie MQ, Li XJ (2006) Appl Surf Sci 253:2158–2164

Xu F, Cheng C, Xu F, Zhang C, Xu H, Xie X, Yin D, Gu H (2009) Nanotechnology 20:405102

Xu S, Luo Z, Han Y, Guo J, Wang C (2012a) RSC Adv 2:2739–2742

Xu F, Cheng C, Chen D-X, Gu H (2012b) ChemPhysChem 13:336–341

Xu S, Sun C, Guo J, Xu K, Wang C (2012c) J Mater Chem 22:19067–19075

Xuan S, Wang Y-XJ, Yu JC, Cham-Fai Leung K (2009) Chem Mater 21:5079–5087

Yallapu MU, Othman SF, Curtis ET, Gupta BK, Jaggi M, Chauhan SU (2011) Biomaterials 32:1890–1905

Yamaoka T, Tabata Y, Ikada Y (1994) J Pharm Sci 83:601–606

Yang J, Lee C-H, Ko H-J, Suh J-S, Yoon H-G, Lee K, Huh Y-M, Haam S (2007) Angew Chem Int Ed 46:8836–8839

Yang H, Zhuang Y, Sun Y, Dai A, Shi X, Wu D, Li F, Hu H, Yang S (2011) Biomaterials 32:4584–4593

Ye F, Laurent S, Fornara A, Astolfi L, Qin J, Roch A, Martini A, Toprak MS, Muller RN, Muhammed M (2012) Contrast Media Mol Imag 7:460–468

Yen SK, Jańczewski D, Lakshmi JL, Dolmanan SB, Tripathy S, Ho VHB, Vijayaragavan V, Hariharan A, Padmanbhan P, Bhakoo KK, Sundhaharan T, Ahmed S, Zhang Y, Selvan TS (2013) ACS Nano 7:6796–6805

Yonn T-J, Lee H, Shao H, Weissleder R (2011) Angew Chem Int Ed 50:4663–4666

Yoo J-W, Chambers E, Mitragotri S (2010) Curr Pharm Des 16:2298–2307

Yoon T-J, Lee H, Shao H, Hilderbrand SA, Weissleder R (2011) Adv Mater 23:4793–4797

Zhang AS, Enns CA (2009) Hematology 207–214

Zhang Y, Kohler N, Zhang M (2002) Biomaterials 23:1553–1561

Zhang H, Zhong X, Xu JJ, Chen HY (2008) Langmuir 24:13748–13752

Zhang Y, Yang M, Park J-H, Singelyn J, Ma H, Sailor MJ, Ruoslahti E, Ozkan M, Ozkan C (2009) Small 5:1990–1996

Zhang B, Jiang B, Chen Y, Huang H, Xie Q, Kang M, Zhang H, Zhai C, Wu Y (2012) Cont Med Mol Imag 7:35–44

Zhang J, Shin MC, David AE, Zhou J, Lee K, He H, Yang VC (2013) Mol Pharmaceutics 10:3892–3902

Zhen G, Muir BW, Moffat BA, Harbour P, Murray KS, Moubaraki B, Suzuki K, Madsen I, Agron-Olshina N, Waddington L, Mulvaney P, Hartley PG (2011) J Phys Chem C 115:327–334

Zhou J, Meng L, Feng X, Zhang X, Lu Q (2010) Angew Chem Int Ed 49:8476–8479

Zhu Y, Zhao W, Chen H, Shi J (2007) J Phys Chem C 111:5281–5285

Zoppellaro G, Kolokithas-Ntoukas A, Polakova K, Tucek J, Zboril R, Loudos G, Fragogeorgi E, Diwoky C, Tomankova K, Avgoustakis K, Kouzoudis D, Bakandritsos A (2014) Chem. Mat. 26:2062–2074

Chapter 3
Superparamagnetic Composite-Based GO/rGO for the Multimode Biomedical Applications

Hafeez Anwar, Iram Arif and Huma Mushtaq

Abstract Graphene oxide/reduced graphene oxide (GO/rGO)-based nanomaterials are fast emerging materials due to their unique structure and excellent mechanical, optical and electrical properties that can exploit for many important applications. In the present chapter, we will highlight the different types and physical properties of superparamagnetic composite-based GO/rGO, especially for various biomedical applications.

Keywords Superparamagnetic nanocomposites · Go/rGo-based materials · Magnetic resonance imaging · Drug delivery · Gene therapy

Introduction

The most interesting topic of the modern solid state and nanotechnology is nanomagnetism. The whole world is seeking for miniaturization, and it is worth mentioning that there are some phenomenon and effects which appears only at nanoscale in magnetic materials, e.g. in superparamagnetism, new kind of domain walls and spin structures can be observed only at nanoscale. On commercial scale, nanomagnetism sets a new trend and becomes the most demanding phenomenon. For the storage of data, magnetic materials are promising candidates. This ability of magnetic materials will also be increased in future. For other applications such as biosensing, drug delivery, imaging, magnetic materials are used with great interest (Pfannes et al. 2001). Superparamagnetism deals with the inversion of magnetization at nanoscale. To understand these concepts of nanomagnetism, ferromagnetism is rendered research and applications (Benitez et al. 2011).

H. Anwar (✉) · I. Arif · H. Mushtaq
Department of Physics, University of Agriculture, Faisalabad 38040, Pakistan
e-mail: hafeez.anwar@gmail.com

The Superparamagnetism Phenomenon

The superparamagnetism is a phenomenon that mostly occurs in ferromagnetic or ferrimagnetic nanoparticles. At a small scale, i.e. few nanometres, as the temperature changes, magnetic spins can flip direction randomly. This phenomenon is known as the superparamagnetism. The time between two magnetic flips is called the Neel relaxation time, and it occurs below the curie temperature of the material that differentiates it from standard magnetization (Marghussian 2015). In 1930, Frenkel and Doefman first purposed the idea of superparamagnetic behaviour of nanomaterials (Ghazanfari et al. 2016). They predicted that if magnetic materials changed into nanoparticles, then they would exhibit characteristics of superparamagnetic materials. Magnetic spins change its direction mainly due to the changes in temperature. Behaviour of superparamagnetism has appeared in ferro-/ferrimagnetic materials. Most common example of this is iron oxide which is ferromagnetic in bulk form but exhibits superparamagnetic behaviour when size reduced to 20 nm or less. Another factor that can affect the spin flipping is change in Neel relaxation temperature, and all these changes in spins happen in the absence of external magnetic field. The average magnetization appears to be zero and thus become superparamagnetic. Superparamagnetic nanoparticles are stable, when dispersed into an aqueous solution and after applying the coating is formed ferrofluid. Superparamagnetic nanoparticles are widely used in vivo and in vitro for different applications such as drug delivery, magnetic hyperthermia and contrast agent in MRI (Enriquez-Navas and Garcia-Martin 2012).

Importance of Graphene and GO/rGO-Related Materials

Carbon Materials

In Earth's crust, the fifteenth most abundant element is carbon (Briscoe and Dunn 2016). All the celestial objects contain a large amount of carbon which is the basis of all known life. Carbon shows allotropic properties as it exhibits variations in covalent bonding among two carbon atoms. Every allotrope exhibits unique characteristics due to the spatial conformation of carbon atom. There are many allotropes of carbon, e.g. one-dimensional, two-dimensional, three-dimensional. The oldest three-dimensional crystals of carbon are graphite, diamond and amorphous carbon (Falcao and Wudl 2007). In these allotropes, carbon shows different hybridization, i.e. sp^2, sp^3 and mixed sp^2/sp^3 (Zhao et al. 2016). In near past era, several new allotropes have been discovered and researchers are in view to find the new carbon allotropes. In 1985, zero-dimensional fullerene was discovered (Muhammad et al. 2013), in 1996 that discovery got a Nobel Prize in Chemistry (Smalley 1997). In 1991, Sumio Iijima discovered the one-dimensional carbon nanotubes (CNT) in fullerene soot (Paradise and Goswami 2007).

In 2004, the first two-dimensional single carbon sheet has been discovered in which carbon is sp^2 hybridized and it organized in hexagonal lattice similar to honeycomb (Katsnelson 2007). More than fifty years ago, it was declared in the theory that the multi-layered graphite has such single layers of carbon, but the idea was not clear because of the thermodynamic instability, aggregation and decomposition. But in 2004, Andre Geim and Kostya Novoselov in the University of Manchester separate single-atom sheets by micromechanical cleavage overcoming the van der Waals forces between the stacks of carbon sheets (Katsnelson 2007).

In 2010, they got a Nobel Prize in Physics as the graphene shows outstanding results and self-supporting stability (Gerstner 2010). Discovery of graphene considered to be the building block for other carbon allotropes, e.g. fullerene, carbon nanotubes and carbon nanohorns.

Over the last decade, research on such materials opens the new horizon. In near future, it may be possible that new forms of allotropes will be discovered as scientists are interested in the modification of carbon (Fig. 3.1).

Graphene is considered to be best as compared to its predecessor as it shows quantum Hall effect, high electron mobility, optical transparency (97.7%), better thermal conductivity and biocompatibility (Xu et al. 2016). It also provides a larger surface area. Apart from all these properties, zero energy gap highest occupied molecular orbital (HOMO) and the lowest unoccupied molecular orbital (LUMO) are shown by graphene.

There are enormous applications of graphene that have been established in recent past years, including energy storage, photovoltaic, field-effect transistors, biosensing
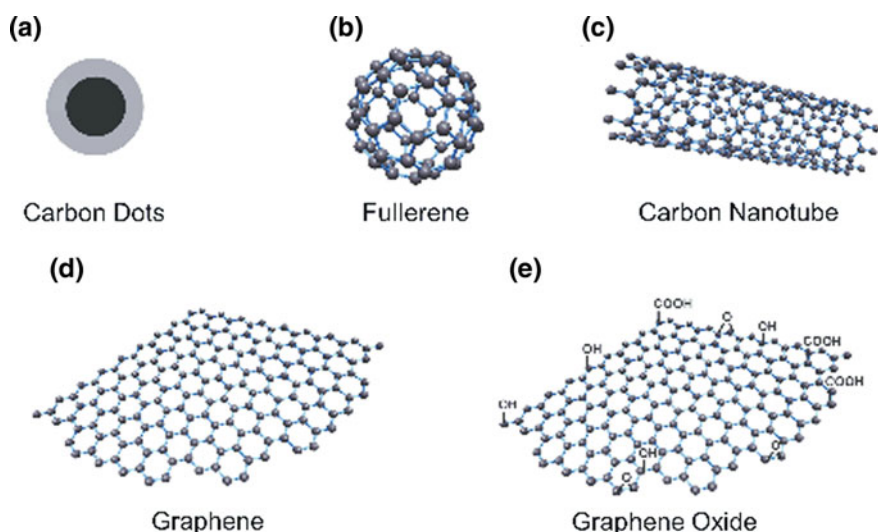
Fig. 3.1 Zero-dimensional carbon nanomaterials, **a** carbon dots and **b** fullerene. One-dimensional carbon nanomaterial, **c** carbon nanotube. Two-dimensional carbon nanomaterial, **d** graphene and **e** graphene oxide

and catalytic applications (Zhu et al. 2010). An intelligent surface engineering of the graphene domain, particularly, graphene oxide (GO) plays an essential role in many applications.

For instance, the solubility (thanks to the abundant *hydrophilic groups on its surface*) and biocompatibility of GO can be greatly enhanced after PEGylation, reducing the inherent toxicity of GO in vitro and in vivo for biological applications. Likewise, the specific high surface area of graphene or reduced graphene oxide (rGO) as well as single-layered GO further provides an outstanding opportunity to integrate them with high loadings of a variety of nanoscale structures, including, but not limited to, metal nanoparticles (NPs) (Pd, Pt, Fe, Au and Ni) or their hybrids (Pd-Au/Ag/Ni/Pt/Fe) and metal oxides.

These graphene-based nanocomposites have shown great potential in biomimetics, catalysis and biomedical applications.

Graphene Oxide (GO) and Reduced Graphene Oxide (rGO)

The graphene sheet covalently decorated with the functional groups having oxygen, e.g. hydroxyls, epoxide and a little amount of carboxyl group (Pei and Cheng 2012). That is the reason for the mixed hybridization of carbon atom, i.e. sp^2/sp^3 hybridization. When the water dispersed on the GO, it has a negative charge which provides stable aqueous suspension.

Nowadays, GO has been prepared as a purified single layer but in 1859 the British Benjamin Brodie first prepared the few layers of GO. However, the reduced graphene oxide (rGO) is produced by the reduction of graphene oxide in diverse ways, including thermal, chemical and UV-assisted methods. As rGO contains quite less amount of oxygen, it is utilized to regain the electric conducting characteristics of graphene oxide.

Sp^2 carbon atoms permit different synthetic routes to be established to attach different functional groups to the graphene and reduced graphene oxide. A variety of oxygenated groups is permitted by rGO to attach with it and modifies the surface of it, because of the difference in the reactivity. This property of rGO leads it to make conjunction with an immense variety of molecules to attach with and provides a platform in the biomedical field.

Superparamagnetic Composites

The most promising candidate among all metal oxides is iron oxide nanoparticles (IONPs). As it enhanced the properties of graphene and its derivatives for various applications, it is very easy to prepare, less expensive, having better chemical stability, non-toxic and provides an active surface for adsorption. There are different types of IONPs, e.g. Fe_3O_4, $Fe_2 O_3$ (iron III oxides), $\alpha\text{-}Fe_2O_3$ (hematite), $\beta\text{-}Fe_2O_3$ (beta

phase) and γ-Fe_2O_3 (maghemite), have been used in the fabrication of magnetic graphene nanocomposites. These are used in the enzyme mimicry, bio-analytical chemistry and molecular imaging in a more suitable way.

It must be noticed that the graphene sheet is unable to become an anchor of IONPs, as it does not have hydrophilic groups attach with it. Therefore, it shows inertness and not capable of loading IONPs. However, graphene oxide (GO) is the most effective and convenient precursor for the loading of IONPs.

Synthesis of GO/rGO

It is interesting to note that the graphene oxide was discovered to measure the molecular weight of the graphite. Brodie used fumes of HNO_3 and mixes it with the graphite in the presence of potassium chlorate (Yap 2015). The frequent oxidations created the sample of graphite oxide (yellow solid) and that was known as the graphic acid based on its dispersion behaviour at different pH values.

In 1958, Hummers used a mixture of $NaNO_3$ and concentrated H_2SO_4 and introduced $KMnO_4$. Hummers' modified method is used widely for the preparation of graphene oxide.

Graphene oxide has been under study because of its chemical structure. Lerf Klinowski model of graphite oxide is very famous and well recognized by the scientist working on graphene oxide (Fig. 3.2).

It is supposed that the surface of graphite oxide having many functional groups attached to it, including hydroxyl (–OH), epoxide (C–O–C) functions, carbonyl (CDO) and carboxylic acid (–COOH) groups. The presence of oxygen creates defects (nanovoids and vacancies) on the surface, and it differs from the pristine graphite because of this.

Graphite oxide composed of carbon, oxygen and hydrogen, and these are observed by using high-resolution transmission electron microscopy (HRTEM) and maintains a carbon/oxygen (C/O) ratio of 1.8 and 2.5; but in the most sample, the C/O ratio is almost 2. Graphene oxide is very important as it is intermediate between graphite and graphene, and we can obtain it by chemical, mechanical and treatments of graphite oxide.

However, graphite oxide has the lamellar structure, and graphene oxide (GO) consists of single layer, double layer or few layers of graphene sheet. These are different in structure but chemically they show the same behaviour and are hydrophilic in nature due to the presence of different functional groups. As a result, the water molecules are introduced between the layers and their hybridization state changes from sp^2 (planar) to sp^3 (tetrahedral).

It is generally believed that in Hummers' modified method, Bronsted acid is present and it makes it a promising candidate for the acid-catalysed reactions. Graphene oxide also acts as the oxidant due to the presence of a large amount of oxygen, and it can oxidize Fe^{2+} to $FeCl_2$ and Fe_2SO_4. In situ deposition of Fe_3O_4 nanoparticles onto rGO nanosheets is the self-reduction from GO to rGO.

(a)

graphite oxide

(b)

thermally treated graphite oxide
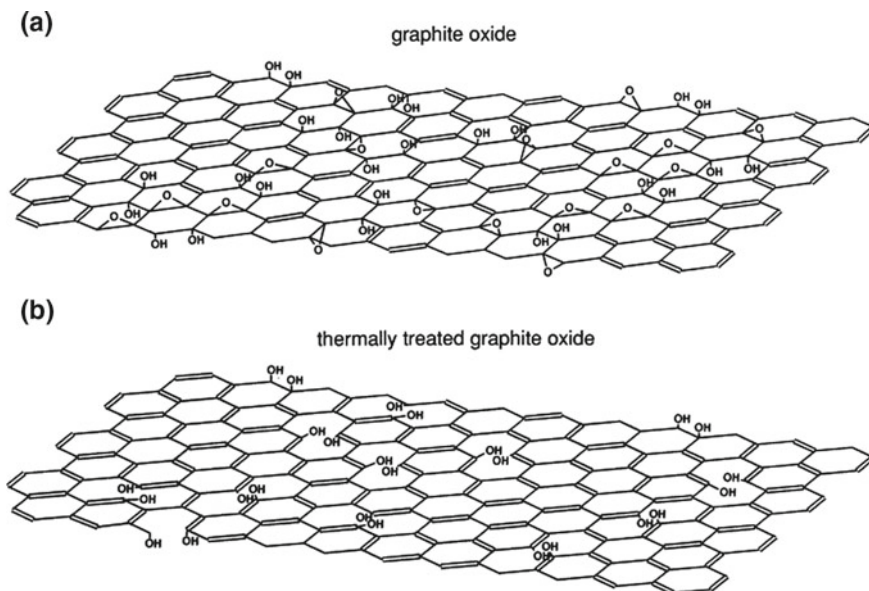
Fig. 3.2 New structural model for **a** as-prepared GO; **b** GO after thermal treatment at 100 °C for 24 h in vacuum

Loading of iron oxide nanoparticles on graphene oxide is the preferred choice for the synthesis of magnetic graphene nanocomposites, and for the synthesis, both routes, i.e. ex situ and in situ routes, are applied.

Synthesis of the graphene oxide is done by Brodie, Staudenmaier or Hummers' method, etc. In these techniques, oxidation of the graphite has been done at distinct stages. In Brodie and Staudenmaier method, potassium chlorate and nitric acid are utilized in a combination of the oxidation of graphite. But in Hummers' method, different chemicals as compared to the method discussed above are used. Potassium permanganate and sulphuric acid are used for the treatment of the graphite. Graphite salts are synthesized by introducing strong acids such as sulphuric acid, nitric acid and hydrogen per chloric acid with graphite. As there are polar oxygen functional groups are present in graphene oxide, so these show hydrophilic property and it may be exfoliated in other solvents. Graphene oxide has good dispersion in water (Zhu et al. 2010).

It is also reported that the graphene oxide can also be prepared by thermal treatment; these methods are cost-effective and more efficient. In electrochemical reduction method, removal of oxygen functional group from graphene oxide has been done. Sodium borohydride with sulphuric acid is used in thermal annealing which provides high purity carbon. Now, the focus of the scientists is chemical reduction and oxidation and tuning of graphene platelets.

Hummers' Method of Synthesis of GO

In Hummers' method, oxidation of graphite has been done to synthesize graphene oxide. For the preparation of graphene oxide, graphene flakes and sodium nitrate are mixed in sulphuric acid and continue the stirring process for two hours under −5 °C and added potassium permanganate slowly. During the addition, it must be kept in mind that temperature does not exceed than 15 °C. After removing an ice bath, the mixture stirred at 35 °C until it turned to pasty brownish and kept it for stirring for two days.

The dilution of the mixture was done with the help of water and that increased the temperature to 98 °C, and it changed colour also, by adding water that solution is more diluted and stirred continuously. To end the reaction, hydrogen per oxide has been used. For removing all impurities, 10% hydrochloric acid was used and after that many times with deionized water. Graphene oxide has been obtained by drying it in vacuum at room temperature and after filtrating the mixture (Fig. 3.3).

Scanning electron microscopy gives information about the structure and morphology of the material. The images of graphite and graphene oxide taken from scanning electron microscopy are shown in figure. The image (a) describes the stacking of graphene sheets, and the image (b) shows that the graphene sheets are exfoliated. In modified Hummers' method, oxidation and exfoliation of graphite are involved because of the thermal treatment of solution (Paulchamy et al. 2015).
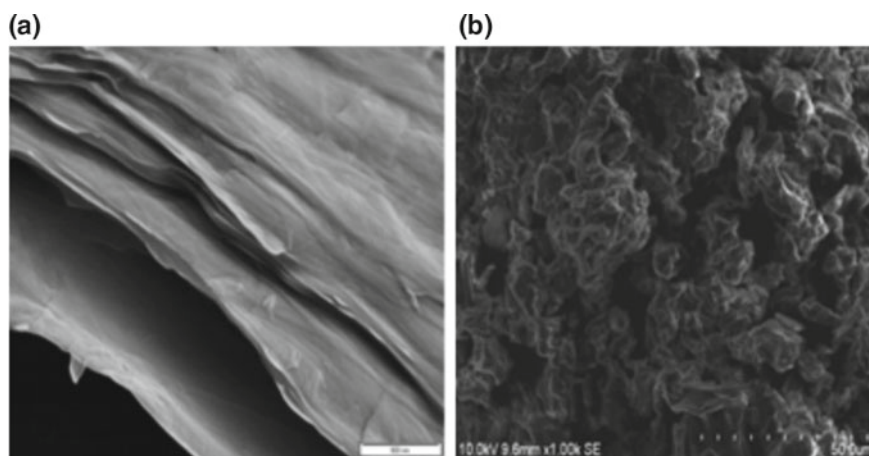
Fig. 3.3 SEM image of **a** graphite **b** graphene oxide

Fabrication of Smart Magnetite/Reduced Graphene Oxide Composite

Due to the extensive use of nanocomposites of magnetite based on graphene oxide or reduced graphene oxide in drug delivery, magnetic resonance imaging and water purification process, these are researched on a large scale. A magnetorheological material consists of iron oxide based on graphene oxide nanocomposites which are fabricated by in situ chemical deposition. When dispersed in silicone oil, the magnetorheology characteristics of the material were measured by using a rotational rheometer at different magnetic fields under steady flow. Particularly, Fe_3O_4/GO has been used as anode in lithium-ion batteries. As reduced graphene oxide also has analogous structure to graphene oxide, and it can also be used as magnetorheological fluid.

The graphene oxide has greater surface area and stability that allows to combine it with Fe_3O_4 to form Fe_3O_4/rGO composites. Fe_3O_4 is used in different biomedical applications because it is less toxic, easy to prepare and show better magnetic characteristics. The in situ synthesis of graphene-based Fe_3O_4 is involved in the chemical deposition, hydrothermal treatment, sol–gel procedure, reduction of iron salt precursors and self-assembly of Fe_3O_4 on GO or rGO sheets. These increased the dispersion stability of Fe_3O_4 and reduced the accumulation of the graphene oxide and reduced graphene oxide sheets (Fig. 3.4).
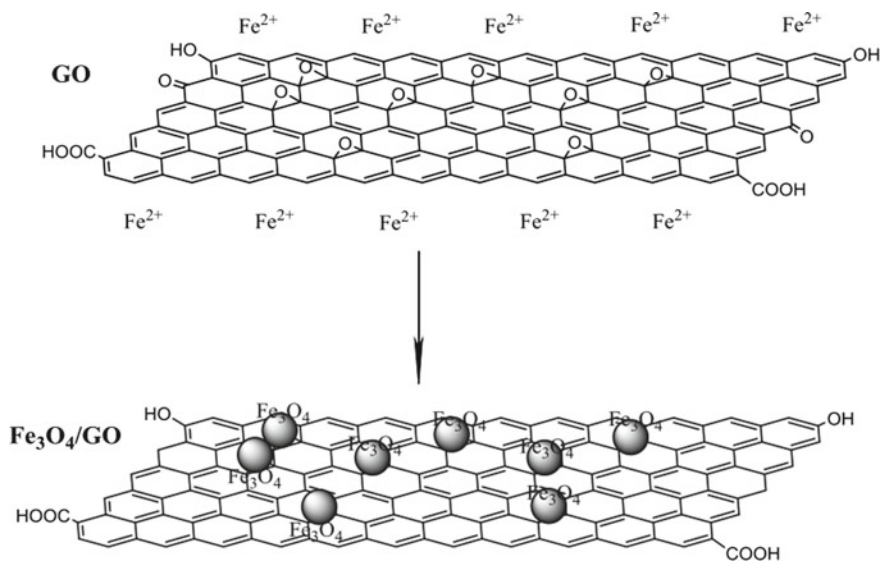
Fig. 3.4 Preparation route to Fe_3O_4/RGO via redox reaction between GO and Fe^{2+} (Hong et al. 2016)
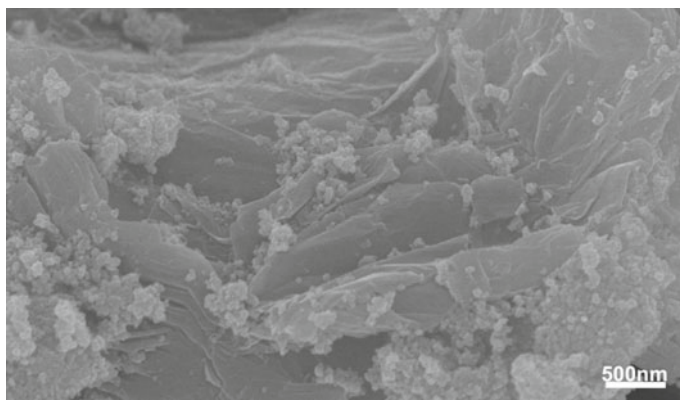
Fig. 3.5   SEM image of Fe$_3$O$_4$/rGO

The structural composition of superparamagnetic Fe$_3$O$_4$/rGO nanocomposites can be observed by using scanning electron microscopy and transmission electron microscopy images. The sedimentation stability was also checked by both testing the density of the Fe$_3$O$_4$/rGO particles and measuring its sedimentation profile (Hong et al. 2016) (Fig. 3.5).

Importance of Magnetic Composites in Biomedicine

The superparamagnetic composites based on graphene oxide or reduced graphene oxide are the most promising candidates for the detection of molecules. As these show greater surface-to-volume ratio and larger rate of transfer of electron, so they considered to be more appropriate in sensors. Sp^2 carbon hybridized domain of carbon, and the oxygen presents in graphene oxide nanohybrids more suitable materials for biomedical applications.

Graphene and its derivatives are very suitable for the destruction of cancerous cells. Nanocomposites of graphene oxide behave as carriers that help anticancer drugs to move to the cells. The extraordinary characteristics of superparamagnetic composites of graphene oxide are attracted the researchers to use these in the drug delivery process and for the magnetic resonance imaging (MRI).

By dispersing magnetic nanoparticles, ferrofluids are prepared. By using external magnetic field, ferrofluids are projected to that part of body where the drug delivery is required, and the same phenomenon is applied for magnetic resonance imaging. Due to this efficient behaviour, magnetic particles gained the special attention of researcher. They are biocompatible and have facile surface modification. As they have come in contact with human body, so it is necessary for them to be biocompatible and does not harm human body. Biocompatibility can be divided into two categories (i) hemocompatibility and (ii) histocompatibility. Hemocompatibility is

necessary when the nanoparticles are in contact with the blood cells. So, the blood aggregation and hemolysis are studied to check that the blood is compatible with the nanoparticles. The surface area, surface charge, hydrophobicity and hydrophilicity of nanoparticles significantly affect blood compatibility. In histocompatibility, nanoparticles are compatible to tissues. Superparamagnetic material shows suitable surface chemistry for many in vivo applications, for example, in tissue repairing, detoxification of biological fluids, hyperthermia and cell separation.

Biomedical Applications of Superparamagnetic Composites Based on GO/rGO

Magnetic Resonance Imaging

The technique which provides image of the organs and internal structure of the body by using magnetic field and pulses of radio waves is known as magnetic resonance imaging (MRI). The person, who is supposed to be examined, comes to the place in MRI scanner, and the part of the body, whose image wants to be observed, kept under the strong magnetic field zone. The presence of hydrogen in human body plays significant role in MRI.

When body is under magnetic field, the protons become excited, and these release radio waves. The radio waves are measured through a receiving coil. The radio signals give the position information by changing the magnetic field using gradient coils. Alternately, switching it on and off creates the characteristic repetitive noise of an MRI scanner. The most promising aspect of MRI in biomedical is the high spatial resolution and better tissue contrast.

Working of MRI is based on minimizing the longitudinal relaxation time (T_1) or the transverse relaxation (T_2) of water protons. Negative (T_2) contrast agents are used in blood pool imaging. On the other hand, (T_1) contrast agents are used as extracellular agents in clinical applications.

MRI is a prevailing technique for finding the location and distributing cells in non-invasive manner. Fe_3O_4 nanoparticles provide inhomogeneity of field due to which signal intensity decreases which in turn decreases the transverse relaxation time. To get the increment in the contrast effect of MRI and stability, Fe_3O_4 nanoparticles have been modified with appropriate functionalities. Superparamagnetic composites based on GO are used in cellular MRI application as T_2 contrast agent. Prussian blue staining analysis shows that Fe_3O_4/GO can adopt by HeLa cells, which depends upon the concentration of Fe_3O_4/GO nanocomposites that incubated in cells. It is also observed that Fe_3O_4/GO shows comparatively improved cellular MRI as compared to Fe_3O_4 only (Chen et al. 2011). Gonzalez-Rodriguez et al. also reported iron oxide–graphene oxide (Fe_3O_4/GO) nanocomposites having the size of 260 nm. Iron oxide (Fe_3O_4) presents in composites provided the superparamagnetic properties that allowed to manipulate the magnetic field required for magnetic drug delivery with
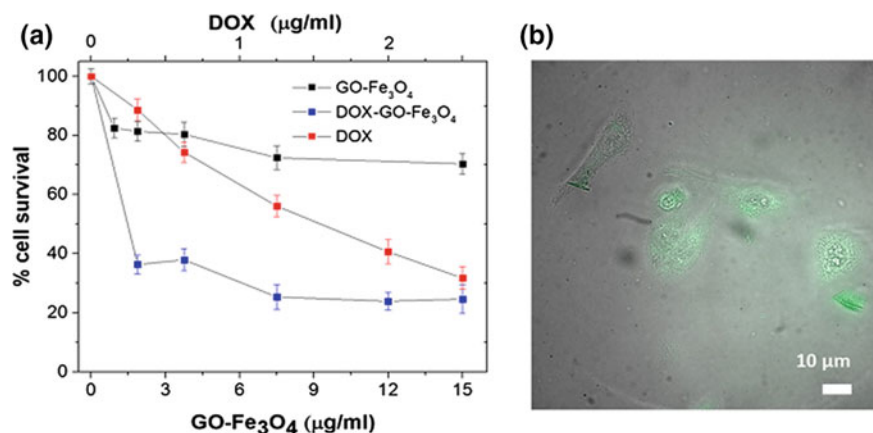
Fig. 3.6 a Cell viability of HeLa cells subject to: GO-Fe$_3$O$_4$ (black squares), DOX-GO-Fe$_3$O$_3$ (blue squares) and DOX (red squares) and **b** GO-Fe$_3$O4 internalization fluorescence imaging in HeLa cells

high relativity (r_2/r_1) ratio ~10.70. The nanohybrids were used for the delivery of hydrophobic doxorubicin. The results showed that prepared nanohybrids have good efficiency in vitro drug delivery 2.5-fold as compared to free drug and in vivo capable of cancer detection by MRI as shown in Fig. 3.6 (Gonzalez-Rodriguez et al. 2019).

Drug Delivery

One of the major applications of GO/rGO-based nanohybrids is their use in drug delivery systems. The advancements in drug delivery systems revolutionized the biomedicine (Hu et al. 2012). Various techniques have been used for better control of delivering and releasing the drugs as compared to the traditional methods. Carbon presents in GO/rGO has sp^2 hybridization lattice configuration, and large surface area of nanoparticles enhances the capacity of loading and delivering of drugs. The electrons present on the surface of two-dimensional GO nanosheet actively interact with the drug specifically aromatic drugs, whereas the functional groups such as carboxyl, epoxide and hydroxyl etc. (Jeong et al. 2008) present in the material alters the nanoparticles by covalent bonding in targeted system (Weaver et al. 2014). GO-based nanohybrids are preferred in drug delivery applications because they have much better adsorption in bloodstream as compared to other materials (Mccallion et al. 2016).

In recent years, various GO/rGO-based nanohybrids are reported for drug loading and delivery applications and provided exceptionally good results (Ahmad et al. 2018). Bao et al. reported the graphene oxide–chitosan (GO/CS) nanosheets with 64

wt% of chitosan which are synthesized by facile amidation process. Graphene oxide–chitosan (GO/CS) nanohybrids were loaded with anticancer drug (camptothecin) that is insoluble in water by hydrophobic interactions and π-π stacking. Results showed that the prepared nanohybrids have excellent biocompatibility and aqueous solubility as well as better loading capacity for camptothecin (Bao et al. 2011). Ma et al. synthesized the graphene oxide–iron oxide nanohybrids composites that are functionalized by polyethylene glycol to attain the stability in solutions. It was loaded by anticancer drug doxorubicin that enables the targeted drug delivery magnetically. The results exhibit that these composites have a good optical absorbance from far visible to near-infrared region and can be used for photothermal ablation of cancer cells that made them a promising candidate in cancer theranostics (Ma et al. 2012). Weaver et al. also reported a controlled drug delivery system in which graphene oxide nanocomposites were doped with polypyrrole and used for the controlled delivery of dexamethasone (anti-inflammatory drug). The electrical stimulation was used for the release of drug from the nanohybrids. The results showed that the drug released efficiency is 2.30 times better than the normal polypyrrole, and the whole process is surface dependent. They also studied the maximum drug delivery by various stimulations, and after 600 stimulations for 0.5 V for 5 s, drug delivery provides linear response over 400 stimulations. It was applied to HCT 116 cancer cells and showed high anticancer effect (Weaver et al. 2014). Yang et al. also reported graphene oxide-based drug delivery system that dual targeting and pH-sensitive. They first prepared iron oxide–graphene oxide (Fe_3O_4/GO) nanocomposites by precipitation technique then used folic acid as a targeting agent for cancer cells that were coupled with iron oxide by using the chemical linkage of (3-aminopropyl) triethoxysilane (APTES) as shown in Fig. 3.7. The anticancer drug, doxorubicin hydrochloride, was loaded with high capacity of 0.387 mg/mg. The results showed that the iron oxide–graphene oxide (Fe_3O_4/GO) nanocomposites have potential applications in targeted anticancer drug delivery.

Photothermal Therapy

Photothermal therapy (PTT) is a medical treatment in which light is used to treat the disease. It has proved itself a promising candidate for the treatment of external infections as well as for various types of cancers like prostate cancer (Lu et al. 2010), epithelial carcinoma (El-Sayed et al. 2006) and breast cancer (Ye et al. 2019). This technique is an extension of photodynamic therapy (PDT) in which sensitizer that is photosensitive mostly infrared exited with a particular band gap. In this excited state, photosensitizer releases the vibrational energy in the form of heat that kills the cancer cells. The major advantage of this kind of treatment is that it does not require oxygen to interact with cancer cells as in photodynamic therapy (PDT) (Kim and Lee 2018). The schematic diagram of photothermal therapy is given in Fig. 3.8 (Yang et al. 2012).

In recent years, various researches reported in which graphene oxide-based nanohybrids were used for photothermal therapy. Sharker et al. reported the reduced graphene oxide nanohybrids which are near-infrared-sensitive and pH-dependent by using electrostatic interaction technique. The rGO nanohybrids are coupled with indocyanine green that not only targeted the cancer cells but also have very low impact
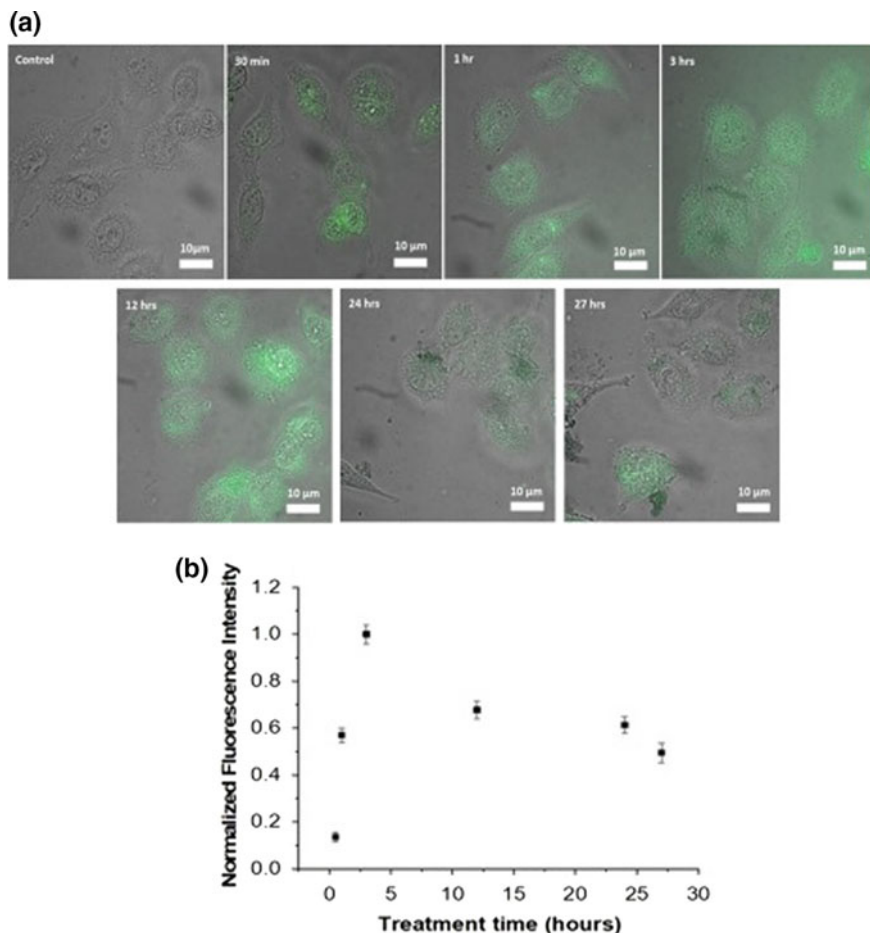
Fig. 3.7 a Images of GO-Fe$_3$O$_4$ fluorescence in HeLa cells at different transfection times and **b** GO internalization over time assessed by average normalized intensity per unit emissive area of GO-Fe$_3$O$_4$ fluorescence in HeLa cells

on normal cells in surroundings. These nanohybrids showed the photothermal heat generation capability in the pH range of 5–7.4 due to quenching mechanism. In near-infrared irradiation, these nanohybrids treated cancer cells (tumours) and healed after the treatment of 18 days (Sharker et al. 2015). Justin et al. also prepared the iron oxide-reduced graphene oxide quantum dots by using green hydrothermal technique that not only converted the graphene oxide nanosheet into the quantum dots but also reduced it. Results showed that the prepared quantum dots radiated in violet at 320 nm and had very low cytotoxicity at low concentration towards the non-cancerous cells. The magnetic hysteresis tests showed the zero-residual magnetization. Their application for photothermal therapy was carried out by rapid increase in temperature up to 50 °C with suspension of 100 µg/ml. The results showed the ablation of cancer
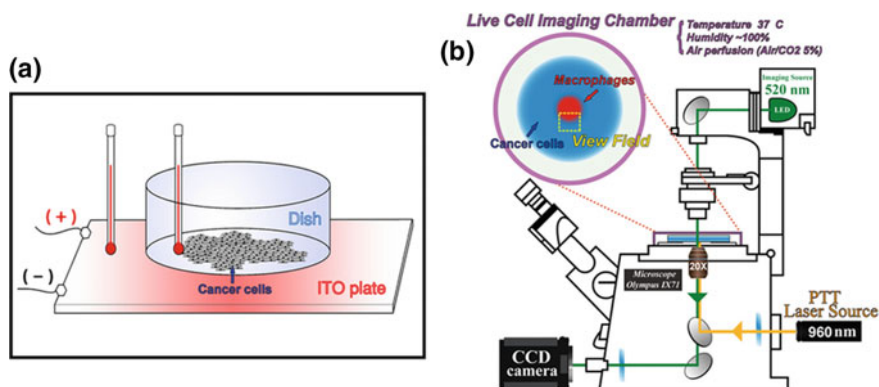
Fig. 3.8 Schematic diagram of thermal destruction and photothermal treatment (PTT) study using real-time phase-contrast imaging system with live cell chamber. **a** The live cell imaging chamber with the cancer cell line on an indium tin oxide (ITO) heating plate is heated to calculate the heating-induced cellular destruction rate. **b** The light source for phase-contrast imaging is a 525-nm-wavelength LED, and the source for the PTT is a 960-nm-wavelength laser

cells (HeLa cells) under near-infrared (NIR) irradiation (Justin et al. 2016). Cheon et al. also reported the reduced graphene oxide nanosheet functionalized by protein (bovine serum albumin) as shown in Fig. 3.9. This was used for the anticancer drug, doxorubicin delivery and photothermal chemotherapy of brain tumour at 60 °C and pH 12. The characterization was carried out by using UV-Vis spectrometer and photoelectron spectrometry. The results showed low cytotoxicity with better efficiency (Cheon et al. 2016).

Ma et al. recently reported the reduced graphene oxide–cadmium sulphide–iron oxide (rGO/CdS/Fe$_3$O$_4$) nanohybrids prepared by solvothermal technique. The characterization was carried out by using XRD, Raman spectroscopy, TEM and FTIR spectroscopy. The live–dead assay technique was used for the cytocompatibility analysis which showed 95% survival of rGO/CdS/Fe$_3$O$_4$ nanohybrids, i.e. these are excellent for cancer treatment (Ma et al. 2019).

Gene Therapy

In recent years, gene therapy has gained enormous importance in biomedical and therapeutic studies. Non-specific in vivo distribution of drug creates serious side effects specifically in neuroblastoma (Ratner et al. 2016), cystic fibrosis and Parkinson's patients; during chemotherapy, it cannot differentiate among the healthy and cancerous cells that lead to lifelong health problems (Sagnella et al. 2018). In gene therapy, a mutated gene of affected cell is replaced by the new genes that resist against the disease caused by mutated genes (Aoyama et al. 2015). The magnetic nanoparticles encapsulate the gene and help it to reach the target cell effectively. There are two major types of gene therapy—somatic gene therapy and germline gene therapy. The germline gene therapy is banned because of the risks attached to
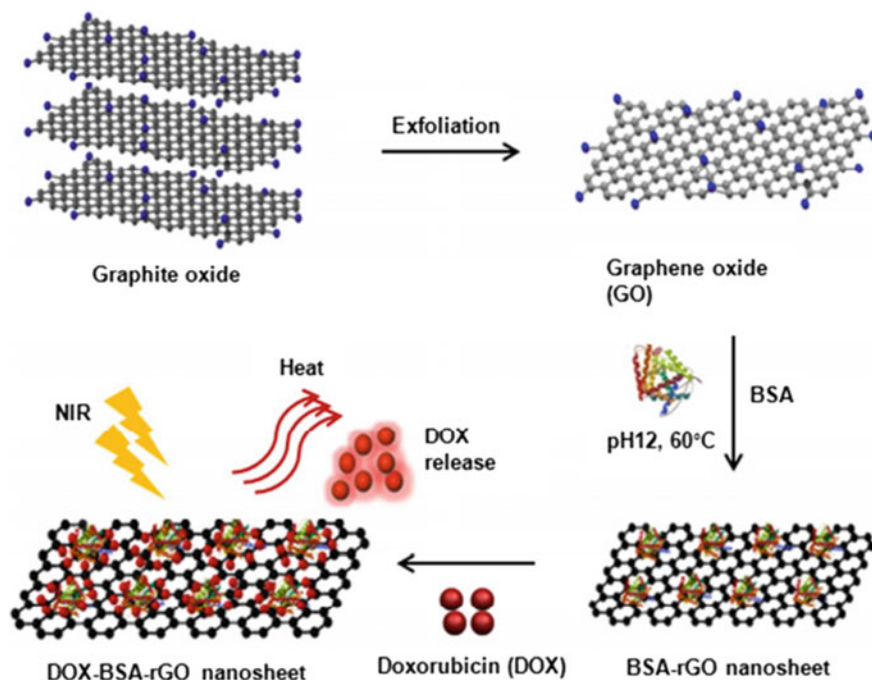
Fig. 3.9 Schematic diagram of the reduced graphene oxide nanosheet functionalized by protein (bovine serum albumin)

it (Glannon 2018). The gene therapy (somatic) is carried out by both viral and non-viral vectors. In viral vectors, gene is directly transferred to DNA very efficiently, but it has its own limitations in the selectivity of gene, whereas in non-viral vectors, core–shell nanoparticles, peptides, micelles have less efficiency as compared to viral vectors but more safe, easily synthesized and economical. Graphene oxide nanohybrids have gained the attention of researchers due to their biocompatibility and gene carrier ability. Various publications have been reported in the past decade. Lerra et al. prepared a nanohybrid based on magnetic iron oxide nanoparticles in combination with graphene oxide (GO/MNPs) by redox reactions and used it for the delivery of doxorubicin in cancer cells (neuroblastoma SH-SY5Y). The schematic diagram of the process is shown in Fig. 3.10.

The results showed that the pH response is better in acidic environment (45% at pH 5) as compared to neutral (28% at pH 7.4) with an increase in the drug release. The presence of GO/MNPs nanohybrids inside the neuroblastoma SH-SY5Y cytoplasm was confirmed by cell internalization studies. The nanohybrids help to control the doxorubicin cytotoxicity level and MNPs allowed remote actuation and enhanced the dose delivery to the target (Glannon 2018).
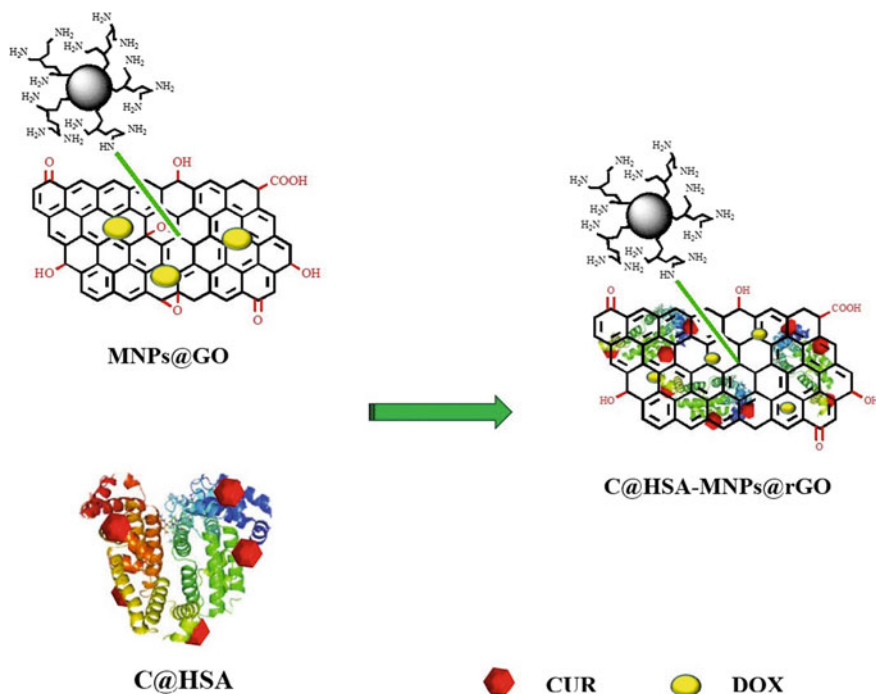
Fig. 3.10 Schematic representation of the synthesis of nanohybrid C@HSA-MNPs@rGO

Conclusion

Application of graphene oxide (GO) and graphene-based superparamagnetic composites in biomedical has become highly attractive research field. A lot of investigations have been done in order to develop various chemical routes for their synthesis to make them compatible with biological systems. It is very important to understand the interaction between graphene-based composites and biological systems in order to employ these in biomedical applications. Functionality of these graphene-based composites depends upon different parameters such as size, surface charge, surface chemistry and lateral dimensions, and these parameters may also affect the biological systems. Although exciting properties of these materials are already being explored, still there is a dire need for research in such a way to open up new avenues for the betterment of mankind, and it is only possible if this field can be converted into a market-oriented research field.

References

Ahmad H, Fan M, Hui D (2018) Graphene oxide incorporated functional materials: a review. Compos B Eng 145:270–280

Aoyama Y, Kobayashi K, Morishita Y, Maeda K, Murohara T (2015) Wnt11 gene therapy with adeno-associated virus 9 improves the survival of mice with myocarditis induced by coxsackievirus B3 through the suppression of the inflammatory reaction. J Mol Cell Cardiol 84:45–51

Bao H, Pan Y, Ping Y, Sahoo NG, Wu T, Li L, Li J, Gan LH (2011) Chitosan-functionalized graphene oxide as a nanocarrier for drug and gene delivery. Small 7:1569–1578

Benitez M, Mishra D, Szary P, Confalonieri GB, Feyen M, Lu A, Agudo L, Eggeler G, Petracic O, Zabel H (2011) Structural and magnetic characterization of self-assembled iron oxide nanoparticle arrays. J Phys: Condens Matter 23:126003

Briscoe J, Dunn S (2016) The future of using Earth-abundant elements in counter electrodes for dye-sensitized solar cells. Adv Mater 28:3802–3813

Chen W, Yi P, Zhang Y, Zhang L, Deng Z, Zhang Z (2011) Composites of aminodextran-coated Fe_3O_4 nanoparticles and graphene oxide for cellular magnetic resonance imaging. ACS Appl Mater Interfaces 3:4085–4091

Cheon YA, Bae JH, Chung BG (2016) Reduced graphene oxide nanosheet for chemo-photothermal therapy. Langmuir 32:2731–2736

El-Sayed IH, Huang X, El-Sayed MA (2006) Selective laser photo-thermal therapy of epithelial carcinoma using anti-EGFR antibody conjugated gold nanoparticles. Cancer Lett 239:129–135

Enriquez-Navas PM, Garcia-Martin ML (2012) Application of inorganic nanoparticles for diagnosis based on MRI. Frontiers of nanoscience. Elsevier, pp 233–245

Falcao EH, Wudl F (2007) Carbon allotropes: beyond graphite and diamond. J Chem Technol Biotechnol: Int Res Process, Environ Clean Technol 82:524–531

Gerstner E (2010) Nobel prize 2010: Andre geim and konstantin novoselov. Nat Phys 6:836

Ghazanfari MR, Kashefi M, Shams SF, Jaafari MR (2016) Perspective of Fe_3O_4 nanoparticles role in biomedical applications. Biochem Res Int 2016:7840161

Glannon W (2018) Genes and future people: Philosophical issues in human genetics. Routledge

Gonzalez-Rodriguez R, Campbell E, Naumov A (2019) Multifunctional graphene oxide/iron oxide nanoparticles for magnetic targeted drug delivery dual magnetic resonance/fluorescence imaging and cancer sensing. PLoS ONE 14:e0217072

Hong CH, Kim MW, Zhang WL, Moon IJ, Choi HJ (2016) Fabrication of smart magnetite/reduced graphene oxide composite nanoparticles and their magnetic stimuli-response. J Colloid Interface Sci 481:194–200

Hu H, Yu J, Li Y, Zhao J, Dong H (2012) Engineering of a novel pluronic F127/graphene nanohybrid for pH responsive drug delivery. J Biomed Mater Res, Part A 100:141–148

Jeong H-K, Lee YP, Lahaye RJ, Park M-H, An KH, Kim IJ, Yang C-W, Park CY, Ruoff RS, Lee YH (2008) Evidence of graphitic AB stacking order of graphite oxides. J Am Chem Soc 130:1362–1366

Justin R, Tao K, Román S, Chen D, Xu Y, Geng X, Ross IM, Grant RT, Pearson A, Zhou G, Macneil S, Sun K, Chen B (2016) Photoluminescent and superparamagnetic reduced graphene oxide–iron oxide quantum dots for dual-modality imaging, drug delivery and photothermal therapy. Carbon 97:54–70

Katsnelson MI (2007) Graphene: carbon in two dimensions. Mater Today 10:20–27

Kim H, Lee D (2018) Near-infrared-responsive cancer photothermal and photodynamic therapy using gold nanoparticles. Polymers 10:961

Lu W, Singh AK, Khan SA, Senapati D, Yu H, Ray PC (2010) Gold nano-popcorn-based targeted diagnosis, nanotherapy treatment, and in situ monitoring of photothermal therapy response of prostate cancer cells using surface-enhanced Raman spectroscopy. J Am Chem Soc 132:18103–18114

Ma X, Tao H, Yang K, Feng L, Cheng L, Shi X, Li Y, Guo L, Liu Z (2012) A functionalized graphene oxide-iron oxide nanocomposite for magnetically targeted drug delivery, photothermal therapy, and magnetic resonance imaging. Nano Res 5:199–212

Ma Y, Yan F, Liu L, Wei W, Zhao Z, Sun J (2019) The enhanced photo-thermal therapy of Surface improved photoactive cadmium sulfide (CdS) quantum dots entrenched graphene oxide nanoflakes in tumor treatment. J Photochem Photobiol, B 192:34–39

Marghussian V (2015) 4—Magnetic properties of nano-glass ceramics. In: Marghussian V (ed) Nano-glass ceramics. William Andrew Publishing, Oxford, pp 181–223

Mccallion C, Burthem J, Rees-Unwin K, Golovanov A, Pluen A (2016) Graphene in therapeutics delivery: problems, solutions and future opportunities. Eur J Pharm Biopharm 104:235–250

Muhammad S, Xu H-L, Zhong R-L, Su Z-M, Al-Sehemi AG, Irfan A (2013) Quantum chemical design of nonlinear optical materials by sp 2-hybridized carbon nanomaterials: issues and opportunities. J Mater Chem C 1:5439–5449

Paradise M, Goswami T (2007) Carbon nanotubes–production and industrial applications. Mater Des 28:1477–1489

Paulchamy B, Arthi G, Lignesh B (2015) A simple approach to stepwise synthesis of graphene oxide nanomaterial. J Nanomed Nanotechnol 6:1

Pei S, Cheng H-M (2012) The reduction of graphene oxide. Carbon 50:3210–3228

Pfannes H-D, Dias Filho J, Magalhães-Paniago R, López J, Paniago R (2001) Mössbauer spectroscopy, superparamagnetism and ferrofluids. Braz J Phys 31:409–417

Ratner N, Brodeur GM, Dale RC, Schor NF (2016) The "neuro" of neuroblastoma: Neuroblastoma as a neurodevelopmental disorder. Ann Neurol 80:13–23

Sagnella SM, Trieu J, Brahmbhatt H, Macdiarmid JA, Macmillan A, Whan RM, Fife CM, Mccarroll JA, Gifford AJ, Ziegler DS (2018) Targeted doxorubicin-loaded bacterially derived nano-cells for the treatment of neuroblastoma. Mol Cancer Ther 17:1012–1023

Sharker SM, Lee JE, Kim SH, Jeong JH, In I, Lee H, Park SY (2015) pH triggered in vivo photothermal therapy and fluorescence nanoplatform of cancer based on responsive polymer-indocyanine green integrated reduced graphene oxide. Biomaterials 61:229–238

Smalley RE (1997) Discovering the fullerenes. Rev Mod Phys 69:723

Weaver CL, Larosa JM, Luo X, Cui XT (2014) Electrically controlled drug delivery from graphene oxide nanocomposite films. ACS Nano 8:1834–1843

Xu Y, Gao Q, Liang H, Zheng K (2016) Effects of functional graphene oxide on the properties of phenyl silicone rubber composites. Polym Testing 54:168–175

Yang T, Choi W, Yoon TH, Jin Lee K, Lee J-S, Hun Han S, Lee M-G, Yim H, Min Choi K, Park M, Jung K-Y, Baek S-K (2012) Real-time phase-contrast imaging of photothermal treatment of head and neck squamous cell carcinoma: an in vitro study of macrophages as a vector for the delivery of gold nanoshells. J Biomed Opt 17:128003

Yap YK (2015) Chemical synthesis and characterization of graphene oxide for use as saturable absorber and broadband polarizer/Yap Yuen Kiat. University of Malaya

Ye H, Wang K, Wang M, Liu R, Song H, Li N, Lu Q, Zhang W, Du Y, Yang W (2019) Bioinspired nanoplatelets for chemo-photothermal therapy of breast cancer metastasis inhibition. Biomaterials 206:1–12

Zhao C-X, Niu C-Y, Qin Z-J, Ren XY, Wang J-T, Cho J-H, Jia Y (2016) H 18 carbon: a new metallic phase with sp^2–sp^3 hybridized bonding network. Sci Rep 6:21879

Zhu Y, Murali S, Cai W, Li X, Suk JW, Potts JR, Ruoff RS (2010) Graphene and graphene oxide: synthesis, properties, and applications. Adv Mater 22:3906–3924

Chapter 4
Gadolinium-Doped Iron Nanostructures Decorated with Novel Drugs for Magnetic Resonance Imaging, Photodynamic, and Photothermal Therapy Applications

Muhammad Fakhar-e-Alam, Arslan Mahmood, Shabab Nasir, Malik Saadullah, M. Waseem Akram and Magnus Willander

Abstract Multidrug drug resistance (MDR) builds many limitations/troubles/problems in magnetic resonance imaging (MRI) and treatment techniques. In this strategy, novel idea of polyethylene glycol/polyacrylic acid (PEG-co-PAA)-decorated gadolinium-doped iron was employed for cancer diagnostics and therapy purposes. In real sense, multifarious/various morphology of Gd-doped Fe-NMPs was found to be useful in versatile format of biomedical applications. Schematic of ongoing experimental strategy illustrates that three efficient photosensitizers, e.g., chlorine e6, Foscan®, and 5-ALA were decorated with Gd-doped iron capsulated with PEG-co-PAA such that their size/morphology consists within range of 100–120 nm of nanospheres. Final form of this nanospheres/nanocapsule plays a vital role through synergistic response of mutual plasmonic reaction of drug decorated nanocapsule. One of the prime

M. Fakhar-e-Alam (✉) · A. Mahmood (✉)
Department of Physics, GC University, Faisalabad 38000, Pakistan
e-mail: fakharphy@gmail.com

A. Mahmood
e-mail: arslan4physics@gmail.com

M. Fakhar-e-Alam
Key Laboratory of Magnetic Materials and Devices & Division of Functional Materials and Nanodevices, Ningbo Institute of Materials Technology and Engineering, Chinese Academy of Sciences, No. 1219 Zhongguan West Road, Ningbo, China

S. Nasir
Department of Zoology, GC University, Faisalabad 38000, Pakistan

M. Saadullah
Department of Pharmaceutical Chemistry, GC University, Faisalabad 38000, Pakistan

M. Waseem Akram
Institute of Fundamental and Frontier Sciences (IFFS), University of Electronic Science and Technology, Chengdu, Sichuan, China

M. Willander
Department of Science and Technology, Linköping University, Campus Norrköping, 601 74 Norrköping, Sweden

© Springer Nature Switzerland AG 2020

focus of this novel experimental approach/review is to trace feasibility of PEG-co-PAA-decorated Gd-doped Fe-NMPs complex with drugs for photothermal therapy, magnetic resonance imaging (MRI) and photodynamic therapy (PDT) application. Current chapter consists of diverse flavor of original results includes SEM and TEM analysis, UV-Visible spectroscopy, NMR analysis of final product of PEG-co-PAA-doped Gd-Fe_3O_4 decorated with effective drugs, and cytotoxic and phototoxic effects of current developed organic–inorganic nanocapsule. The results indicate that PEG-co-PAA-encapsulated Gd-doped Fe-NMPs are very promising nanospecies for T_1-MRI applications. Both the individual Gd-doped Fe-NPs and its conjugated species exhibited significant toxic effects for photodynamic therapy (PDT) and photothermal therapy (PTT) applications as observed in MCF-7/Hela cancer cell model. These results led to the empirical modeling of individual Gd-doped Fe-NPs and its conjugated species with cancer cells by analyzing the statistical data obtained from experiments and thus novel way toward a more practical strategy for the concept of PEG-co-PAA-encapsulated Gd-doped Fe-NMPs and its conjugates as photosensitizers for MRI, PTT and/or PDT.

Introduction

Molecular imaging, as a simple, economical, convincing, comprehensive and well-developed technique, is an emerging and fascinating field of research for early cancer detection. It not only saves human life without significant invasiveness with living tissues/cells, but also it has attracted many young researchers to biomedical science because of unique appealing characteristics. In this context, activatable imaging nanoprobes, that is, designed to amplify or boost the imaging signals in response to the marked/located place only, play a key role in nanomedicine. It has been reported that below 5 nm morphology, the composites of iron nanoparticles (IPs) become T_1-MRI contrast, while above 5 nm its characteristics are shifted to act as T_2-MRI contrast agent (Zeng et al. 2013).

The use of gadolinium-based contrast agents (GBCA) plays a vital role in magnetic resonance imaging (MRI)-based diagnosis as an outcome of T_1 contrast agent or T_2 contrast agent and follow-up of many central nervous system (CNS) disorders. Although free gadolinium metal is proved to be invasive, its chelated forms with eight bonds have been revealed to be adequately safe throughout the diagnostics and treatment protocol. The T_1-based MRI contrast agents, demonstrated by conventional low-molecular-weight Gd-chelates, have enabled well resolved and contrast-enhanced MR imaging for manifold diagnostics application in clinical practice especially tumor detection and characterization as well as vascular imaging (Helm 2010).

The multifunctional nanobiocomposites have attracted great attention in recent years due to their versatile characteristics of magnetic resonance imaging (MRI), cell separation, drug delivery agents, labeling, and as optical probes that led to

their applications in the field of nanobiotechnology and nanomedicine. In this context, gadolinium-doped nanomaterials possess many advantages, such as high fluorescence, quantum yields, low toxicity, long life cycles, and high stability, when compared to quantum dots and organic dyes.

Photodynamic Therapy

Photodynamic therapy (PDT) is one of the alternative methods in tumor treatment. It consists of three components, photosensitizer, cellular oxygen, and light of suitable wavelength. The basic idea of this photochemistry-based treatment modality is that to take a chemical and excite with light. Furthermore, the key point of this treatment modality is that laser light (photon) is used to initiates chemistry and chemistry infects initiates biology (Verma et al. 2007; Solban et al. 2006; Dougherty et al. 1998; Huang 2005). In many studies, the pharmacokinetics of different PS's for killing of malignant cells with and without laser light has been studied in various biological tissues in vivo (Sprague Dawley and Wistar rats)/in vitro (HepG2, Hep2C, RD, HEK293T, foreskin fibroblast, melanocytes), and finally, biological-damaging effects were assessed using neutral red assay (NRA)/MTT assay, reactive oxygen species (ROS) detection, staining of mitochondria, microscopic, and macroscopic analysis of biological cells/tissues and confocal microscopy. Ongoing research suggests that photodynamic therapy (PDT) is an encouraging, minimally invasive treatment modality for premalignant, malignant lesions requiring the interaction of light (UV-Visible). The drug uptake/pharmacokinetics is one of the important factors in field of PDT; the beauty of photosensitizer is that it accumulates preferentially in the tumor (Boyle and Dolphin 1996; Peng et al. 1997a, b, c, d; Wu et al. 2003). Selectivity for eradicating only the tumor area is conferred by the preferential localization of the sensitizer and light to the treatment area.

Advantages of PDT

- Effective
- Noninvasive, well tolerated
- Selective
- Tissue sparing
- Excellent cosmetic results
- Repeated therapy possible
- Outpatient therapy.

Laser Interactions with Tissues

Heat generation is the primarily focusing parameter in the field of biomedical optics research, e.g., absorption of light, light emission, heat generation, and interaction of light with biological cells/tissues like phenomena involved in aforementioned research. Moreover, the generation of heat is unnecessary factor/constituent in PDT as well as optical diagnosis system, because in our research context cell killing via apoptosis or necrosis because of photochemical reactions relatively at low temperature. Clinical applications of laser dosimetry were analyzed with the earliest types of lasers, e.g., He–Ne and diode laser (red light, 630 nm). The first applications to cosmetic surgery were performed and rely on easily available industrial and research lasers. Medical lasers are now developed for the purpose of therapeutically and diagnostic clinical applications for the treatment of different timorous/carcinogenic organs including liver carcinoma, lung carcinoma, cervical cancer, and general surgery fragmenting of kidney and gall stones (Grossweiner et al. 2005). The emission wavelength, power level, and temporal mode of operation are the most constituents/basic factors in field of laser therapy (PDT). Above the threshold dose of light, many other factors, e.g., photocoagulation, carbonization, and photoablation, are involved in field of PDT. We have to cure our suggested tissue/sample from all these undesirable phenomena for experimental accuracy and targeting PDT. But the interaction of light with tissue/cell is not much simple basically it is too much difficult/complex to understand the reality of this complex system. Along with photochemical reactions, many other factors, i.e., heating on the optical and thermal properties of tissues, may enhance the light tissue interaction. The laser tissue interaction is grouped in different categories, i.e., "thermal" and "non-thermal." Induction of laser heating and vaporization mechanism is due to light thermal properties. High power with continuous form of light as well as pulsed lasers may induce the quick response of ejection of material referred to laser ablation phenomena. But in spite of all this context, pressure waves and visible plasmas are responsible for the generation of high-power pulsed lasers because of cavity and resonator configuration of "laser." The ultraviolet excimer laser is capable for the production of "cold laser," on the basis of all background data relevant to configuration and laser characteristics ablation produced/obtained which resulted from photochemical pressure waves induced by photoionization (Grossweiner et al. 2005).

Laser Tissue-Heat Equation

The thermal energy which relates and equilibrate between the different loss contribution and generation of heat after interacting with the tissue/cell can describe in this relationship:

Heat Accumulation = Heat Input − Heat flow − Heat removal by blood flow.

Tissue Heating by Laser Radiation

Laser radiation stimulates biological injury/damage in suggested tissue via photochemical e.g., cell apoptosis/cell necrosis, photothermal, and photomechanical interactions. The type of light (visible) response depends on the tissue's optical and thermal properties, rate of light flux, wavelength, light density as well as pulse duration (Grossweiner et al. 2005).

Optical Transition in Molecules

Colony of atoms combined in molecules oscillates and vibrate in directions determined by the structural analysis of chromophores. It is easier to assess/trace vibrational energy in the context of a small/tiny molecule, its relevant vibrational energy levels, and corresponding assigned type of motion. Very complex vibrations/oscillations and rotations in the context of comparatively heavy molecules must be estimated by means of molecular orbital theory. According to the aforementioned theory, the separation of vibrational energy levels is lower than the electronic levels. Each electronic energy level has the corresponding band of vibrational or vibrionic levels. In some context of atomic motion, the colony of atoms might have/involved in rotatory motion; it is, therefore, the gap/separation of rotational levels is usually smaller than the spacing of vibrionic energy levels which leads to IR spectra. Figure 4.1 depicts the schematic/algorithm of the Jablonski diagram. The ground/lowest state of molecule/chromophore is assigned by "0" state and its corresponding vibrational level implied by S_0. The highest state in the energy level diagram/Jablonski diagram was assigned by S1, S_2, S_3. The length of each vertical adjacent gap/separation indicates photonic energy of each corresponding transition. Commonly, the most excited/highest state and its reside atoms/molecules "hot" molecules are unstable (not in equilibrium) as compared to the environment. During the deexcitation state, the excess vibrational energy might be in the form of radiative (fluorescence/phosphorescence) or non-radiative decay (heat emission). If the probability of decay process existence occurs between allowed transitions (singlet to singlet), the decay process/mechanism must be assigned in the form of fluorescence (FLUOR), which is important for diagnostic point of view. In case of disallowed/forbidden transition decay process (triplet state to singlet state), the emissive energy must be in the form of phosphorescence (PHOSPHOR), acts as keystone for the liberation of reactive oxygen species (ROS)/RNS leads to cell death. It is suggested by many researchers that the fluorescence emission band is focused at longer wavelengths than the longest wavelength absorption bands owing to the energy decay process in the form of heat loss; the given mechanism is assigned by the Stokes shift. The basic theme/essence of the Jablonski diagram concludes with strong evidence that the emissive fluorescence spectrum is not dependent on the exciting wavelength of light and also depends upon the configuration/structural properties
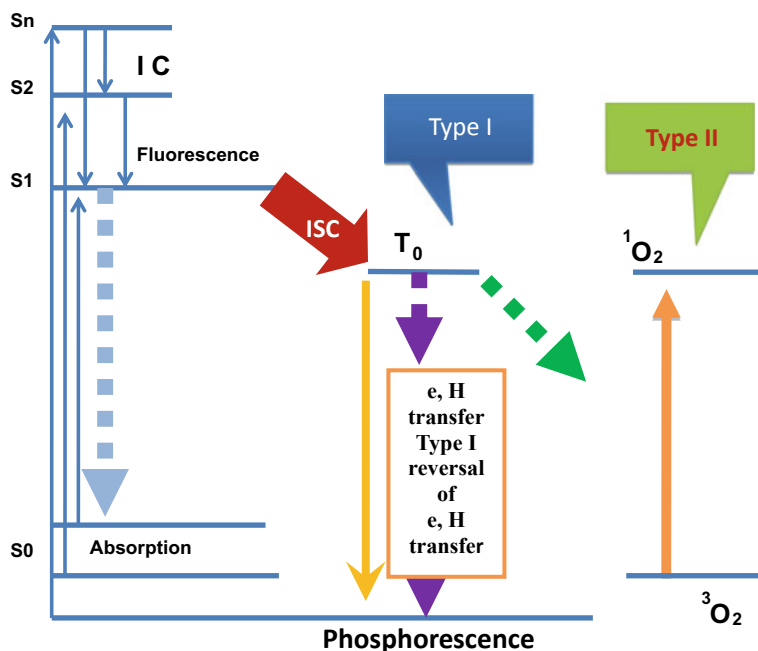
Fig. 4.1 Schematic representation of the Jablonski diagram showing different energy levels S_0, S_1, S_2, S_3, …, Sn (The image is taken from the Ph.D. thesis of Dr. Fakhar-e-Alam "Photosensitizer's Dynamics Studies in Different Biological Samples using Laser Irradiation")

of chromophores/biomolecules. The strong evidence suggested by many research experts is that non-radiative decay commonly takes place in fast consecutive stages. The initial step is of energy-conserving "horizontal" transition within range of high vibrational ($S_n - S_3$, S_2, S_1) which is assigned by internal conversion (IC), another important fate of the fluorescent state is its spontaneous conversion to a triplet state via a change of an electron spin direction, and the process is called the intersystem crossing (ISC) usually represented by wavy/wiggly horizontal curve/line. The probability of ISC becomes into reality in case of heavy atoms and paramagnetic ions, and it is also dependent on structure and environment state. It occurs in stepwise non-radiative decay during singlet to triplet transition. "T" state has longer decay lifetime as compared to "S".

The Science of PDT

The originating of photochemical reactions in phototherapy may lead to the vascular shutdown of malignant/timorous cells, e.g., killing of cancer cells or tissues, and alteration of the immunity/immune system. The basic mechanisms regarded to cell death are described/demonstrated below.

Necrosis

Necrosis is a cell death mechanism via cell blebbing or cell inflammation and mechanical stress/trauma. Most of the targeted/focusing areas of necrosis are the plasma membrane, mitochondria, and lysosomes.

Apoptosis

The mechanism of programmed cell death is assigned by apoptosis, which is characterized by multiple morphological modifications/alterations, e.g., cell shrinkage, nuclear condensation, bleb formation, and basically absence of inflammatory responses of the affected tissue (Richter 2000). Apoptosis is a highly regulated and interdisciplinary controlled process that avoids inflammation and damage to the surrounding tissue. Apoptosis is an indisputable process during normal growth, tissue hemostasis, development of the nervous system, and regulation of the immune system. Disregulation of programmed cell death has been entitled to the pathogenesis of many diseases, including immune deficiency syndrome, neurodegenerative disorders, and vascular injury. It is also characterized by a recognizable pattern of DNA fragmentation complied by the mutation of cells to apoptotic bodies. Mitochondria and DNA are likely focusing areas by damaging point of view in the process of the apoptotic response. Moreover, apoptotic and pathways are implicated in the immunological responses to PDT (Grossweiner et al. 2005).

Vascular Effects

The relationship between the photodamaging effect and drug configuration/structure is still questionable because a drug may localize within the cell after the initial accumulation. However, some evidences obtained by experimental model conducted via animal in vivo/in vitro, and some general drug uptake/response has been suggested

from the background/previous data. Results compiled by experimental model regarding vascular damage have been recorded by using different efficient photosensitizers, e.g., including Photofrin®, 5-aminolevulinic acid (ALA-PpIX), PPDME, and Photogem®. The primary poring part of the cell-damaging effect is endothelial cells of the microvasculature. Hypoxia is basically in favor of type 1 reaction (oxidative products) develops within few minutes after the start of photochemical reactions. Basically, mention response involves three stages:

(1) Initial oxygen consumption, (2) reduction in regional blood supply, and (3) total vascular exclusion (ischemia). Formation of $^1O_2$ or oxidative products, i.e., libration of reactive oxygen species (ROS) leads to cell killing mechanism via vascular blockade of cell, mitochondria-damaging effect or lysosomal injury (cell necrosis/cell apoptosis). The significant vascular damage for hydrophilic agents takes place afterward, unless peak serum levels are attained. Hydrophobic and factors show various patterns in which the vascular damage parallels the serum concentration at the time of illumination. The described cellular effects of PDT on epithelial cells admit release of clotting factors, calcium inflow, and modification of the cytoskeleton.

Types of Reaction

The photochemical reaction resulted in two types:

- Type I reaction
- Type II reaction.

Type I Reaction

The light stimulates the photosensitizer from its ground state to excited singlet states. Then intersystem crossing (ISC) occurs and the photosensitizer decays to a triplet state. Thus, excited sensitizer transfers its excess energy to species in the surrounding medium by a radiationless mechanism and causes the formation superoxide radicals and oxidative products, e.g., ($^1O_2$) or hydroxyl radicals (OH) and H_2O_2. These radicals then destroy the target tissue (Allen et al. 2001; Berlin 2006).

Type II Reaction

Photosensitization of malignancy by most PDT drugs is assigned to the type 2 pathway intermediated by singlet oxygen $^1O_2$. The photochemical mechanism is shown in Fig. 4.2. The photosensitizer localized in the target tissue is stimulated as before to its lowest energy triplet state and then transfers its excess energy to molecular oxygen present in surrounding tissue to form particularly oxidative products e.g., "$^1O_2$" (amount of energy ≈22 kcal/mol, is required). This singlet/toxic oxygen may

Photon+Drug+Oxygen→Singlet   oxygen→Oxidative injury→ cell- death.

Oxidizing Radicals

Type I   Sen⁻ + Substrate⁺

Light

Activated Drug

Cell Death

Or

Drug   **Type II**   ¹O₂

³O₂
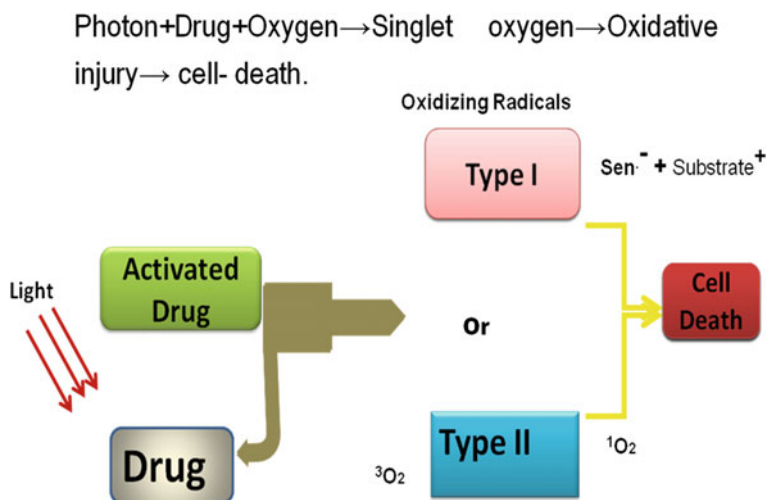
Fig. 4.2 Image represents the oxidative stress cause cell death (the image is taken from the Ph.D. thesis of Dr. Fakhar-e-Alam "Photosensitizer's Dynamics Studies in Different Biological Samples using Laser Irradiation")

destroy target tissue. After the transfer of energy, the photosensitizer returns to its starting point, where it is available to begin the whole process again (Allen et al. 2001; Valenzeno 1987; Dolmans et al. 2003).

Role of Drugs in Photodynamic Therapy

The low dark toxicity of PDT photosensitizers, comparatively high uptake and retention by malignant/tumors, rapid clearance from the normal healthy cells, and effective tumor drug properties are possible requisites of efficient PDT drugs. A desirable treatment protocol, matchable wavelength of light source, and ideal/efficient drug carrier are basic demands for effectivity of PDT drugs (Boyle and Dolphin 1996). Drugs deduced from second-generation photosensitizer are most widely used as famous PDT photosensitizers currently. Dougherty and his coworkers have discussed in their data that the active component in mentioned photosensitizer as a dimeric atoms/molecule comprising of two porphyrin units linked by an ether linkage which was named as dihematoporphyrin ether (DHE). Again DHE comprises mixture of pigments, dimmers, and small amount of oligomers linked by ether and ester bridges (Ferriera et al. 2008). The absorption peak of suggested drug is an important constituent for PDT outcome. Most of the drugs take part in a vital role due to high penetration of visible region of light, e.g., Photofrin® offers the good PDT outcome due to high penetration of light in visible region (630 nm of wavelength) (Atif et al. 2010). The optical absorption of given photosensitizer is typical due to its

strong band near 370 nm and four weak visible bands (Q bands) which lie between 510 and 630 nm. But the rest of the bands, i.e., fluorescence emissions bands, lie between 630 and 680 nm. In addition, 5-ALA have maximum absorption peak at 635 nm of red-light wavelength (Atif et al. 2009). It has been analyzed that ALA is not a photosensitizer it is precursor to PpIX which having therapeutic effectivity. The slow clearance of Photofrin® from serum and skin has been a major motivation/basic need in the search for new PDT drugs for excellent PDT outcome. Basically, a long serum lifetime is not necessarily disadvantageous because in some cases it permits effective laser treatments many weeks after the initial administration of Photofrin®.

Types of Drugs

- **Hydrophilic**

Such compounds which are freely soluble in water at physiological conditions. Compounds with three or more charged peripheral substituents are usually hydrophilic (Prasad 2003; Grossweiner et al. 2005).

- **Hydrophobic**

Such compounds are virtually insoluble in water and alcohol. Molecules without charged substituents are usually hydrophobic (Prasad 2003; Grossweiner et al. 2005).

- **Amphiphilic**

Such compounds have present in their structures both a hydrophobic and hydrophilic region (Grossweiner et al. 2005).

Pharmacokinetics of PDT Drugs

Administration of the photosensitizer is the basic step/factor step in PDT. For systemic administration of photosensitizer in the drug dose is assigned as mg/kg of body weight in vivo and μg/ml in vitro. Hydrophilic drugs, e.g., Photofrin and Npe_6, are administered by intravenous injection through tail vein or cava vein. Aqueous solutions of porphyrins are referred to as concentration-dependent self-aggregation. But the reversible conjugations, e.g., dimmers with irreversible aggregates may consist of larger entities (Korbelik 1996). The exact finding of efficient concentration of PDT drugs in the malignant cell as well as serum is very difficult. Radiolabeling technique along with clear image of biodistribution of Photofrin® (lipophilic PS) in Sprague Dawley rats acts as an animal model which has been studied in our previous published data (Fakhar-e-Alam et al. 2010). A vehicle for drug carrier is required for administration of a hydrophobic agent, e.g., a liposome suspension or an oil-in-water emulsion. Amphiphilic drugs, e.g., BPD-MA, may be administered

either in aqueous medium or via carrier, e.g., nanoparticles (ZnO, Fe_2O_3). Liposomes are usually employed for PDT applications in order to facilitate drug cellular response/uptake. Aqueous vehicles such as Hyskon are employed for topical PDT with ALA (Bellnier and Dougherty 1996). The aqueous solubility of a PDT drug and its interactions with serum proteins and biological membranes are important factors in the pharmacokinetics of drug delivery (Bellnier and Dougherty 1996).

Photosensitizers in Photodynamic Therapy

The pharmacokinetics/uptake and efficacy of mentioned photosensitizers (heme and Porphyrin like photosensitizers) have been proved in the USA, China, and Germany as a PDT drug for the treatment of late stage esophageal cancer (1995) and early stage lung cancer (1998). The mentioned drug (PS) has been in Canada for the treatment of recurrent bladder cancer in Japan for early stage lung, esophageal, gastric and cervical cancer as well as cervical dysplasia in the Netherlands and France for advance esophageal and lung cancers and in Germany for early stage lung cancer. These approvals motivated the inspiration of drug (PS) in the field of clinical PDT. There are marvelous number of clinical trials around the world testing the efficacy of PDT with several new developing photosensitizers as a primary or an adjuvant therapy for the treatment of variety of cancers as well as for local infections, e.g., actinic keratosis (A. K), cutaneous leishmaniasis (CL), and macular degeneration (Jeffes et al. 1997). The member of this porphyrin family acts as an ideal photosensitizer from an experimental as well as clinical point of view due to its photobleaching capability, high uptake in tumors, quick secretion from normal/healthy cells and successful therapeutic results (Mang 2004). The aforementioned drug has been used to treat a variety of malignancy/tumors in the past including choroidal melanomas (Schmidt-Erfurth et al. 1994), lung carcinoma (Furuse et al. 1993), brain tumors (Whelan et al. 1993), and breast cancers (Xue et al. 2001). Currently, Photofrin® has been employed for the successful treatment of human gliomas and in preclinical animal experiments (Whelan et al. 1994). The drug appears to be efficient, reliable, active pain-free, safe, and non-toxic (Xue et al. 2001). Photofrin® is not a single chemical entity. It is a mixture of oligomers formed by ether and ester linkages of up to eight porphyrin units. Molecular formula of Photofrin® can be expressed as $C_{68}H_{74}N_8O_{11}$ for $n = 0$.

The major limitation in the treatment of cancer by the PDT method is quenching of fluorescence by chromophores, blood and normal tissues that hold the data acquisition and recording of the fluorescence radiographically or photographically. Therefore, radioactive labeled porphyrins with gamma emitters of short half-lives were suggested to be better alternative for tumor detection (Bases et al. 1958; Thaller et al. 1983; Fawwaz et al. 1990; Georgakoudi et al. 1997; Dougherty et al. 1998) (Fig. 4.3).

Fig. 4.3 Molecular structure of ALA (second photosensitizer has been evaluated as an inducer of photodamage on different malignant cell line (RD, HepG2, Hep2C, HeLa, etc.))
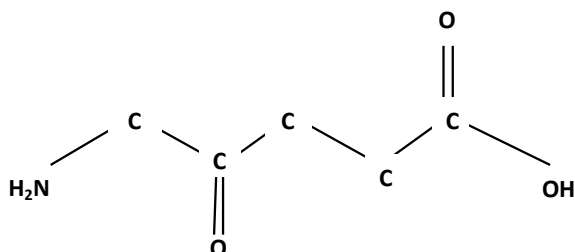
δ-Aminolevulinic acid (ALA, Levulan®) is the biosynthetic precursor of all porphyrins in nature. In the animal pathway, two molecules of ALA condense to form porphobilinogen (PBG), followed by the reaction of four PBG molecules and several decarboxylation steps to form protoporphyrin PpIX (Khursid et al. 2010). ALA is a promising second photosensitizer has been evaluated as an inducer of photodamage on different malignant cell line (RD, HepG2, Hep2C, HeLa, melanocytes). It is a prodrug and acts as a starter in the biosynthesis of heme group. It is the first intermediary in the biosynthesis of protoporphyrin IX (PpIX) and of the heme group. Many researchers proved in their published data that the concentration of PpIX in malignant cell line is higher as compared to normal cell line because in cancerous cells, the excess of low-density lipoproteins (LDL) receptors and enzyme which converts PpIX to heme has been found to be reduced. In experimental studies, optimal concentration of mentioned PS, irradiation time, various combinations of PS and light doses has been traced by investigating effective PDT outcome in research as well as clinical point of view (Atif et al. 2009; Peng et al. 2001). Its molecular structure and HAEM reaction are shown in Figs. 4.4 and 4.5 (Grossweiner et al. 2005).

In literature survey, it has been complied that 5-ALA, i.e., second-generation photosensitizer induces apoptosis in human malignant cell lines after conversion in PpIX, undergoing multiple molecular mechanisms, e.g., mitochondrial and nuclear DNA damage (Khursid et al. 2010), mitochondrial release of cytochrome C (Kriska et al. 2005), apoptosis-inducing factor (AIF) for caspase-independent apoptosis, endoplasmic reticulum stress, decrease in Bcl-2, Bcl-Xl, and activation of caspase-9 and
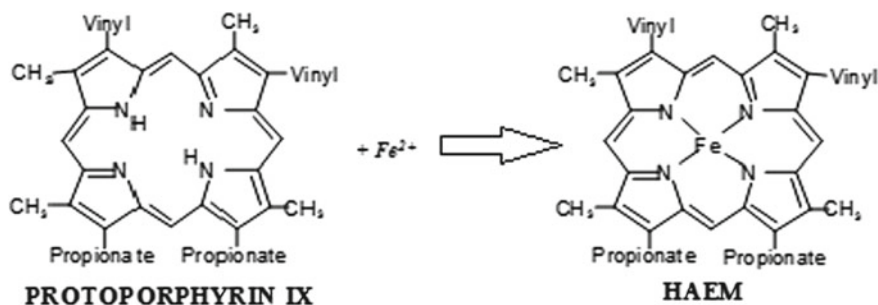
Fig. 4.4 PROTOPORPHYRIN IX" to synthesize the HAEM

Fig. 4.5 Absorption Spectrum of Photogem® (results obtained newly developed materials by Fakhar-e-Alam and Arslan Mahmood)
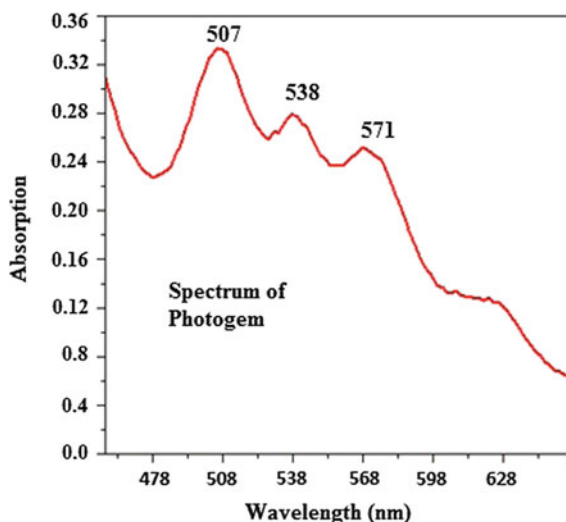
caspase-3 (Grebenová et al. 2003; Furre et al. 2005). Moreover, ALA-PDT causes cytoskeletal changes in human carcinogenic cells (Uzdensky et al. 2005). Some researcher analyzed that mitochondria play a key role in the metabolic pathway to cell death either by mitochondria proteins involved in the cell killing mechanism (cell apoptosis) or by the loss of functionality resulting in ATP depletion. Thus mitochondrial damage is suspected to be the major cause of phototoxicity (Bernardi et al. 1999; Morgan and Oseroff 2001). In one of our studies, we have studied/tested the effectiveness of 5-ALA-PDT for triggering of apoptosis in rhabdomyosarcoma cells and explored the multiple but complex mechanisms involved in this process (Karmakar et al. 2007). The preferential uptake of 5-ALA in the tumor is reported for the intense metabolic activity of carcinogenic cells and to the confined capacity of ferrochelatase to convert porphyrins in heme. ALA-PpIX or other photosensitizer mediated PDT produces oxidative insult to tumor cells, thereby leading to the initiation of cell death mechanisms through necrosis/apoptosis. Our group performed series of experiments for determination of optimization and efficacy of ALA-mediated PDT using different malignant cell lines as an experimental model. Different steps of 5-ALA to HAEM reaction are shown in Fig. 4.4. Furthermore, in our previous study synthesized the "PROTOPORPHYRIN IX," now by using the PROTOPORPHYRIN IX to synthesize the HAEM.

The production of 5-ALA-PpIX has been investigated by many research experts, which are almost 6 h in case of in vivo study (Fakhar-e-Alam et al. 2010). A promising approach in PDT involves the exogenous administration of 5-ALA which is naturally occurring compound present in malignant cells, e.g., mammalian cells that can be metabolized to a porphyrin photosensitizer, PpIX via the heme biosynthetic pathway (Bourre et al. 2008). A significant drawback to ALA-PDT is also included along with tremendous advantage, ALA is zwitterions at physiologic pH resulting

in low lipid solubility and limiting passage through biological barriers, e.g., cellular membranes. To overcome this problem, several chemical approaches have been attempted to improve the accumulation of ALA and also its selectivity in the tumor greater amount as compared to healthy cells with a ratio of 3:1. One approach has been to use more lipophilic ALA derivatives, such as alkyl or ethylene glycol esters, which are potential substrates for cellular esterases (Kloek and Beijersbergen 1996; Berger et al. 2000), or different delivery systems including dendrimers (Battah et al. 2001; Di Venosa et al. 2006; Battah et al. 2006) or liposomes (Casas et al. 2002; Casas and Batlle 2006). For the determination of effectivity of ALA-PDT and drug uptake into different cell lines (malignant) has been explored by many research scholars (Tsai et al. 1999). The potential usefulness of ALA for PDT of tumors has been demonstrated in vivo (Kennedy et al. 1990; Kennedy and Pottier 1992; Messmann et al. 1995) and human studies (Loh et al. 1993; Cairnduff et al. 1994). As a clinical trial, ALA-PDT has been used systematically, e.g., intravenous/intraperitoneal and topical (in the form of cream) in case of nodular BCC and superficial basal cell carcinomas (BCC) (Ikram et al. 2011). Its treatment response in terms of BCC was significant ≈90%, but insignificant achievement has been got in the treatment of nodular BCC, which is ≈45–60%. But the major drawback for ALA uptake is the permeability of cell membrane and active immune system which allows the multidrug resistance (MDR) like characteristics. The mentioned disadvantage has been dissolved by tracing the ALA esters, which having a capability of increased lipophilicity have therefore been accomplished in order to increase the penetration depth of the precursor and efficacy of 5-ALA useful in clinical practice as well as in the field of PDT. Preclinical studies developed the concept that 5-ALA esters induce PpIX more efficiently by applying/practicing the given drug in case of topical applications, than 5-ALA [76, 77]. Discriminate transport/uptake systems usually serve for cationic, zwitterionic, and anionic amino acids in different cell lines specifically in mammalian cell type which has been analyzed by many research scholars (Peng 1996; Rud et al. 2000). It has been reported by many PDT experts that PpIX uptake depends on the levels of key enzymes of porphyrin biosynthesis, e.g., ferrochelatase and porphobilinogen deaminase in the carcinomas/tumors (Christensen 1985). Furthermore, the availability of iron also plays a vital role in the enhancement of PpIX production level in tumor and normal tissue (Kondo et al. 1993; Hinnen et al. 1998). The most advantageous effect/versatility of ALA is that it has been successfully used in the diagnosis and treatment of neoplastic tissue along with local bioinfections. ALA itself is not a photosensitizer (PS), but serves a biological precursor in the heme biosynthesis pathway (Gardner et al. 1991; Peng et al. 1997a, b, c, d). The potential applications of ALA-PDT in the treatment of tumors have been manifested in vivo model (Kennedy and Pottier 1992; Messmann et al. 1995) and human studies (Mlkvy et al. 1998; Soler et al. 2000; Friesen et al. 2002). But along with tremendous advantageous effect of different drugs, not free from drawbacks, i.e., side effects of cutaneous photosensitivity of some PS's are commonly found in the clinical trials of PDT. The advantage of ALA-PDT is that it having less prolonged photosensitivity or cumulative toxicity as compared to other PS's, e.g., Photofrin (Kennedy et al. 1996). ALA can be administered topically as well as orally, but the

most preferable choice for superficial lesions in skin as well as local infection and oral cavity. The developing evidence in topical application of ALA-PDT is an effective as systematically administered 5-ALA, resulting in a significant response rate with excellent healing and little to no scarring of the treated site (Rhodes et al. 1997; Kübler et al. 1998; Gerscher et al. 2000). Matchable statement has been quoted by many research experts that the accumulation of photosensitizer (PS) in tumor cells is so much high as compared to surrounding normal tissue, due to high uptake tumor cells which were selectively destroyed compared to normal cells (Peng et al. 1997a, b, c, d). The effectiveness of PDT depends upon both amount of PpIX production along with its relevant light dose. Time of span for production of intracellular PpIX levels by applying exogenous 5-ALA administration in different cell lines has been investigated by many research scholars (Krieg et al. 2002; Tsai et al. 2004; Zhang and Zhang 2004). Many PDT experts proved experimentally that ALA-PDT is useful not only for cancerous, sometimes it is feasible for the treatment of local infections e.g., cutaneous leishmaniasis (C. L) (Akilov et al. 2007). There are several other mechanisms involved in tissue damage by photodynamic effects. An initial destruction of the vascular system and the intracellular matrix is followed by hypoxia, which leads to the production of reactive oxygen species especially oxidative products with type 1 reaction, resulted in cell death via mitochondria-damaging process/vascular injury. It is assumed that the vascular damage would have less effect in PDT for cutaneous leishmaniasis (CL) as compared to PDT against tumors with their abundant vascularity (Luksiene 2003; Vishwanath and Takashima 2007). ALA, a non-fluorescent drug, has been used as a precursor to the fluorescent photosensitizer protoporphyrin IX (PpIX) which acts as keystone in the field of PDT. Conversion of PpIX happens under irradiation of visible light especially 630 nm of red light, triplet oxygen ($3O_2$) to singlet oxygen ($1O_2$), which initiates the induction of abnormal cell death, the expectation of efficient results of ALA depends upon the accumulation of PpIX into targeting cell/tumoral tissue (Kennedy and Pottier 1992; Dougherty et al. 1998; Collaud et al. 2004). ALA-PDT having great importance not only in the field of research also plays an important role in clinical treatment too, especially in effective treatment of superficial basal cell carcinoma (BCC) (Kopera et al. 1996; Rifkin et al. 1997; Loncaster et al. 2005). Porphyrins act as keystone not only as a prerequisite for heme synthesis, but also in the approach to the treatment or cancer detection by applying various novel techniques one of them is the photodynamic diagnosis (PDD) using fluorescence dye material for detection (Kennedy et al. 1990; Moan and Berg 1992; Gahlen et al. 1999). The metastasis process involves the detachment and infiltration of the cells from original primary tumor. Firstly, the malignant/abnormal cells have to penetrate to blood and lymphatic vessels. The circulating cells can then migrate through the cell wall vessels to surrounding tissues. Secondly, the cell released from primary tumor settle, adhere, proliferate, and induce angiogenesis. Some experts reported that PDT having promising preference over other conventional therapies act as successful candidate for suppression of metastasis (Gomer et al. 1987; Schreiber et al. 2002; Lisnjak et al. 2005). In addition, absorption spectrum of Photogem®.

Role of Nanomaterials in Photodynamic Therapy

Some specific nanomaterial has a great importance in the field of biomedical applications due to its cytotoxic effects. Such compounds possess attractive features for the development of new technology of medical diagnostic procedures and drug delivery system. Nanomaterials interact with proteins and enzymes in human cells mediating through antioxidant defense mechanism leading to reactive oxygen species (ROS) generation, resulting in inflammatory response and destruction of the mitochondria/DNA damage, causing apoptosis or necrosis. Nanowires (ZnO and MnO_2) and nanoparticles (Fe_2O_3) contain several properties to play a dominant role in their enhanced magnetic, electrical, optical, mechanical, and structural effects on human cells (Christofori 2006). The results of the given articles describe that cell toxicity is dose and incubation time dependent. In addition, ZnO nanoparticles with size of 70 nm and 420 nm liberates the significant ROS fluorescence and loss in cell toxicity (82% loss for 70 nm, 72% loss for 420 nm) in human lung epithelial cells via cell membrane leakage, ROS production, reduced GSH levels, increased LDH levels, lipid peroxidation as well as oxidative DNA damage (Ferreira et al. 2006; Soikkeli et al. 2015). Steep response template/pattern was observed with other metal oxides. P. J. Moos et al. are of the opinion, cell toxicity of RKO cells is time and concentration of nanoparticles—cell contact dependent, but independent of the amount of Zn in cell culture media. In addition, nano-sized ZnO (nZnO) particles owing more cytotoxic as compare to micro-sized ZnO (mZnO) nanoparticles in cell lines. The multiple factors are involved in cell death mechanism, e.g., disruption of mitochondria function, loss of mitochondrial function, increase in generation of superoxide's ions, Annexin V staining and robust markers of apoptosis. Moreover, the impact of particle size, structure, and dimension of ultrafine nanoparticles on cell toxicity is still query in recent studies, but the correlation of cytotoxicity with size of macrophages exposed to silica particles was investigated by many researchers (Semelka et al. 2016). It is under debate that the ultrafine nanoparticles dietary metal oxides, e.g., ZnO, have chronic effects on the colon. Ingestion of large amounts of ZnO has been demonstrated by many investigators. Ultrafine nano-oxides can cause gastroduodenal corrosive injury in humans without systemic toxicity. Inhaled ZnO can cause pulmonary toxicity but minimal toxicity to other organs (Kaushik et al. 2008; Ghaghada et al. 2009; ZubairIqbal et al. 2015; Kanal 2016; Tomonori Kanda et al. 2016; Liza and Valappil Mohanan 2016; Frangville et al. 2016). Increased consumption of fine and ultrafine particulate matter is hypothesized to exacerbate inflammatory bowel disease (Fakhar-e-Alam et al. 2017a; Shaheen et al. 2017a, b; Fakhar-e-Alam et al. 2017b). The original finding/real picture is still not clear.

Role of Magnetic Nanoparticles for Photothermal Therapy

Revolution of nanotechnology opens new horizons and contributes significantly in the field of biomedical and clinical applications. Nanotechnology is the emerging field which utilizes the novel materials and device for controlling and development of chemical and physical mechanisms at atomic and microlevel scale with one dimension within range of nanometer scale. Biotechnology deals with metabolic and physiochemical response of biological organisms. The mutual combination of these technologies, e.g., nanobiotechnology, plays a key role for development and employs several cherished tools for quality of life. According to the NIH report, every year 7.6 million out of 68 million causalities happened due to various types of cancer. After the successful development of ultrafine Fe_3O_4 nanoparticles, it will be possible to recognize and treatment of liver cancer, which might be significant contribution for survival of cancer patient life. Photothermal therapy and photodynamic therapy are non-invasive treatment modalities which need desired nanoparticles along with excitation wavelengths of light. The basic idea of photothermal therapy is to take desired drug/nanoparticles and produce hypothermia conditions after successful demonstration of photothermal effect. Initially, the significant biodistribution/pharmacokinetics of photothermal responsible nanoparticles toward targeted site is the key factor. After suitable biodistribution of iron oxide nanoparticles/Gd-doped Fe_3O_4 nanoparticles the optimal wavelength of NIR light, e.g., 808 nm of wavelength required for optimal photothermal reactions. The internal temperature of tissues/organ tends to 106 °C or larger than this temperature then hyperthermia condition reached finally cell killing mechanism convoluted within territory of cancerous/malignant (Soikkeli et al. 2015).

Iron oxide nanoparticles (IONPs) are very exciting materials for liberating hyperthermia and very excellent materials for their wide range of biomedical applications. Current project highlights the basic concept of photothermal therapy, magnetic hyperthermia therapy, photodynamic therapy, and magnetic resonance imaging. This project also elaborates the basic concepts, various therapy approaches (PTT, PDT, magnetic hyperthermia therapy (MHT), chemotherapy and immunotherapy), intrinsic properties, and mechanisms of cell death of IONPs; it also provides a brief overview of recent developments in IONPs, with focus on their therapeutic applications. Much attention is devoted to elaborating the various parameters, intracellular behaviors and limitations of MHT. Bimodal therapies which act alone or in combination with other innovative treatment modalities. Meanwhile, IONPs can be exploited for imaging-guided delivery and multimodal theranostics, 19 where more than one cancer modality is combined, such as PTT, PDT, MHT, chemotherapy, and immunotherapy. Tailored design of magnetic NPs is crucial to determine the effectiveness of NPs for a desired biomedical application (Gu et al. 2015; Semelka et al. 2016). The synthesis, surface functionalization, and tumor targeting strategies of magnetic NPs are discussed elsewhere.

Magnetic Resonance Imaging (MRI)

It is a powerful cancer/local infectious diagnostic technique in which strong powerful magnets, radiowaves, and computers used to construct the detailed pictures of the body. Unlike X-rays, computed tomography (CT) in this type of diagnostic technique MRI does not use any ionizing radiation. Principle of MRI is "water protons in all over the body" when strong magnetic field is applied to targeted area, these water protons are aligned and through computer software the image of internal structure can be drawn under resonance effect. The versatility of this imaging technique is to diagnose any type of cancer, e.g., lung cancer, kidney, head and neck cancer, pancreatic, and liver cancer.

In addition, their aqueous colloidal stability, with low toxicity and excellent self-heating efficacy, makes nanomaterials suitable for the PTT and PDT treatment of cancer, while their luminescent entity can be beneficial to identify the location of magnetic nanoparticles during in vitro cellular imaging. Although most FDA approved MRI contrast agents, such as Gd (III) complexes and some superparamagnetic iron oxide (SPIO) agents, have an excellent research track record due to simple, economical, well-established technique and reliable data providing portable instrumentation, there are some serious acute/invasive problems of kidney/renal dysfunctions and ischemia in patients. In addition, these contrast agents have a tendency to cause nephrogenic systemic kidney disorder (Soikkeli et al. 2015)

The Gd-loaded liposomes have drawn a significant attention in tumor diagnosis as they are efficient MRI contrast agents with significant dispersion stability, optimal size, and high zeta potential for tumor targeting, with favorable imaging properties along enhanced relaxation time. A severe challenge, that limits the potential of Gd as MRI contrast agent, is desirable specificity and efficiency in targeted sites. The stable gadolinium-based contrast agents (GBCAs) are believed to be safe and suitable for MRI, but the controversy of GBCAs as a safe drug still exists, particularly among patients with renal/kidney problems (Semelka et al. 2016). Subsequently, Kanal (2016) reported the short-term and long-term safety issues of intravenous gadolinium-based contrast agents (GBCAs) and their possible solution (Kanal 2016).

Recently, the use of MRI contrast agents is being minimized due to a revolution in the technology, and the applications have shifted to organic radicals (Kanda et al. 2016). Thus, the trend toward organic nitroxide radicals in basic research has accelerated in the last three decades. However, the rapid reduction of nitroxide free radical via hydroxylamine in the presence of natural reductants, such as ascorbic acid, is a serious problem that has not been resolved to date. Consequently, the research is underway to overcome this problem by utilizing the appropriate bonding arrangement of some chelating ligands in the natural reducing agent (Ghaghada et al. 2009).

Well-stabilized form of iron oxide nanoparticles with dextran (DIONPs), a potential candidate for hyperthermia treatment, led to oxidative stress of premalignant/human blood lymphocytes and malignant tissues/cells due to their ultrafine size and magnetic susceptibility, while their individual form may be useful for MRI techniques (Liza and Valappil Mohanan 2016).

Synthesis and modification of PEG derivatives are easily adapted for the coating of metallic and oxidic substrates. A copolymer consisting of a negatively charged poly (acrylic acid) (PAA) is the backbone to which PEG side chains could be grafted. Since Gd-doped iron nanostructures can be stabilized in solution via negative surface charges, as in most colloids, they should readily adsorb to positively charged surfaces via electrostatic interaction. Accordingly, the synthesis of the PEG-co-PAA biopolymer can be carried out in aqueous solution at room temperature as the copolymer spontaneously adsorbs to positively charged surfaces. However, there have been no reports on the combination of magnetic properties with bipolymer conjugated gadolinium-doped iron nanostructures (Frangville et al. 2016).

A novel strategy presented for the preparation of polymer blend of inorganic various morphology involving nanospheres within the range of 25–37 nm of Iron individual and their composite with gadolinium owing/having various morphology, e.g., nanospheres, nanostarts, and nanorods in the presence and absence of novel effective photosensitizers/chemical agents. Co-polymer blend of inorganic and photosensitizers have examples such as PEG-co-PAA-encapsulated Gd-doped Fe-NPs/Chlorine (e6), PEG-co-PAA-encapsulated Gd-doped Fe-NPs/5-ALA, and PEG-co-PAA-encapsulated Gd-doped Fe-NPs/Foscan®. Results provide not only an easy approach to accomplish MRI and treatment analysis of tumor cells, based on the over-expressed intracellular GSH level, but also gives a new insight into the design of activated MRI/NMR nanoprobe along with its multimodal therapeutic applications. In addition, this novel strategy recommends the immune boost up and tumor suppressed scheme which of course big break proves to be as milestone in the field of biomedical research.

Synthesis and Characterization of PEG-co-PAA Blend of Gadolinium-Doped Iron

A hydrophilic route and hydrophobic chemical route were adopted for successful fabrication of PEG-co-PAA blend of Gd-doped iron (Kaushik et al. 2008; Zubair Iqbal et al. 2015). The prime task of this novel approach was getting idea of magnetic resonance imaging (MRI) and photodynamic therapy (PDT) as well as immune therapy using versatile nanocapsule as schematic is shown in Scheme 1. This idea assisted a lot to overcome the deficiency of significant drug nanoparticle ligand along with bipolymeric compound, i.e., PEG-co-PAA blend with Gd-doped iron conjugated with three various efficient photosensitizers (chlorine e6, 5-ALA, and Foscan®). In this experimental technique, very novel and comprehensive synthesis scheme was employed for achieving the various morphology of Gd-doped iron oxide nanoparticles for MRI and PTT applications. In addition, the importance of Au doped TiO2 doped with DOx for PDT mechanism was elaborated. In addition, no such concept of bipolymeric form of organic blend with inorganic form along with drug was used for first time toward biomedical applications.
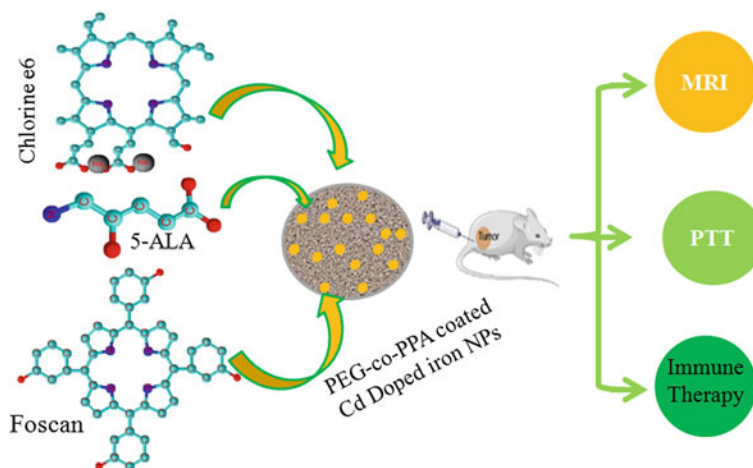
Scheme 1 Graphical flowchart of experimental strategy (prime task of this novel approach was getting idea of magnetic resonance imaging (MRI) and photodynamic therapy (PTT) as well as immune therapy used to treat the cancer) (new develop)

Figure 4.6 depicts the scanning electron (SEM) morphology of Gd-doped Fe nanospheres. SEM analysis shows that the average diameter of both Gd and Fe nanospheres between 25 and 37 nm and which is below 40 nm (indicated by marking some nanospheres) as shown in Fig. 4.7a. The spheres are agglomerated shape and the surface is highly porous. SEM and EDS analysis confirms the desired morphology and Gd–Fe blend in nanostructure pattern. These nanospheres were investigated by energy dispersive spectroscopy (EDS) to determine the elemental composition of these spheres. The EDS analysis shows that Fe is the main constituent and the presence of Gd peaks confirms doping. Other shoulder peaks appeared due to solvothermal constituent's compounds consisting of ferric and ferrous chloride and gadolinium chloride drop-wise solution addition. In addition, the dominant peaks of Fe, Gd were seen in EDS analysis as depicted in Fig. 4.7b. For more details about the morphology of Gd-doped iron NPs, SEM images of said discussed particles are shown in Fig. 4.7c–e, g. In all above SEM images, the nanoparticle size lies between 30 and 50 nm which is fit for biomedical analysis of magnetic resonance imaging, immune therapy as well photodynamic therapy. In recent submitted article by our group, iron composite with black titania, manganese, and organic free radical blend with iron were employed toward MRI and therapeutic applications as MRI contrast agent and PDT and PTT photosensitizing agent.

Gd nanostructures with three different shapes: Nanospheres, nanostar, and nanorod are shown in low magnification TEM image (Fig. 4.7a–c). Figure 4.7a–f shows TEM image of multifarious morphology of gadolinium, e.g., gadolinium nanospheres (Gd NSps), gadolinium nanostars (Gd NSts), gadolinium nanorods (Gd NRds) having scale bar of 50 nm. It is cleared from TEM image that the nanospheres of Gd are about 5–8 nm of size, and similarly, the size of the nanostar in the range of 35–45 nm and nanorods size of about 8–10 nm of diameter and 40–45 nm of nanorod
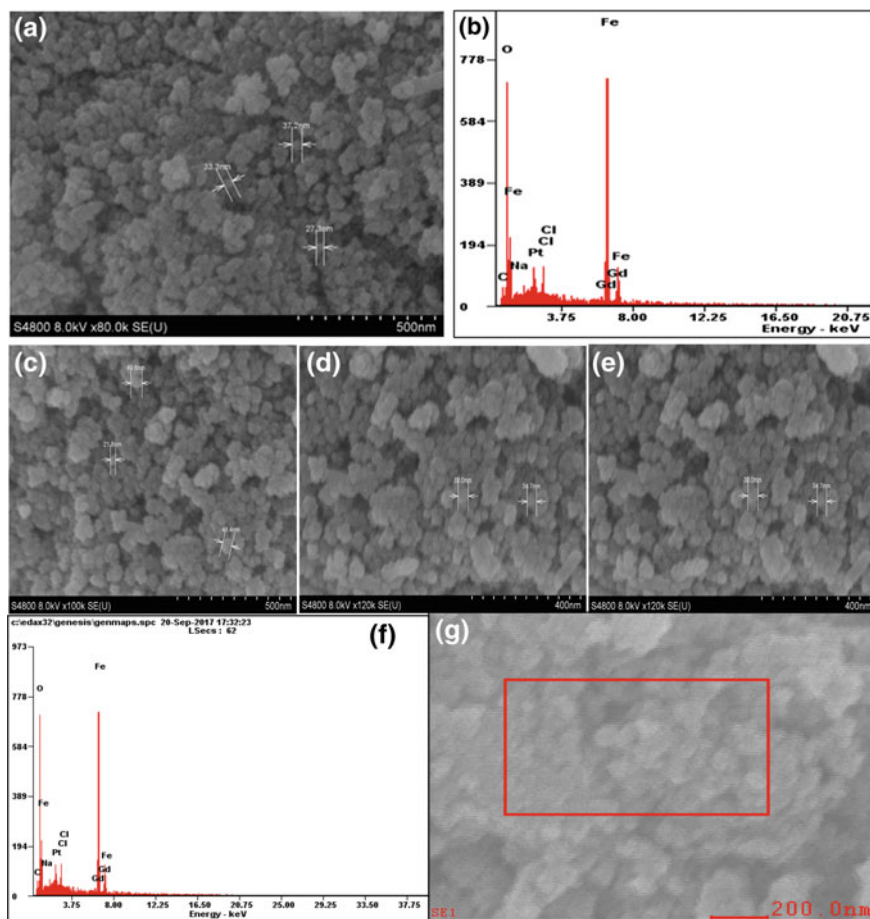
Fig. 4.6 SEM analysis of Gd-doped Fe$_3$O$_4$ (**a**, **c–e**), EDS analysis shown (**b** and **f**) high quality/intensity SEM of Gd-doped iron (Fe$_3$O$_4$) shown (**g**) (data/results obtained newly developed materials by Fakhar-e-Alam)

length. In this experiment, very simple and facile method of hydrothermal approach was employed as described briefly. Combine all above chemicals (FeCl$_3$ · 6H$_2$O 3.45 g, FeCl$_2$ · 4H$_2$O (90%) 3.5 g, oleic acid (90%)-3.5 g, oleylamine (80–90%)-3.3 g and ethanol absolute-2.3 g) into suitable capacity of beaker. For homogenous, perform sonication of 10 min and allow it for 20 min of vigorously magnetic stirring. Now the solution is ready for next step. For the further pursuit of desired nanomaterial, place an updated form of chemical solution in hydrothermal reactor Teflon and the internal empty space of autoclave around Teflon filled with 10 ml ethanol and 5 ml of deionized water. The reaction was continued for 18 h at 180 °C till the few nanometers of iron oxide Nanostructures (Nanospheres) developed. On the next day, put off the oven and wait for cooldown of oven reach to room temperature. After
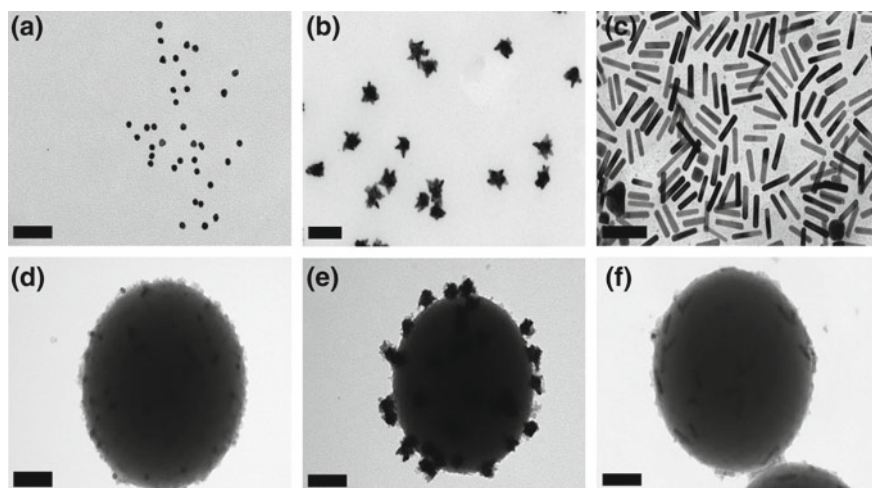
Fig. 4.7 TEM analysis of **a** gadolinium spheres (Gd NSps), **b** gadolinium nanostars (Gd NSts), **c** gadolinium nanorods (Gd NRds), **d** iron (Fe$_3$O$_4$ nanospheres) interfaced gadolinium spheres (Gd NSps), **e** iron (Fe$_3$O$_4$ nanospheres) interfaced gadolinium nanostars (Gd NSts), **f** iron (Fe$_3$O$_4$ nanospheres) interfaced gadolinium nanorods (GdNRds); scale bars 100 nm

thorough examine, the black precipitate can be visualized via naked eye. Wash this prepared form of iron oxide nanospheres with ethanol twice very gently with the help of centrifuge having 11,500 rpm for 10 min at room temperature. Now add 97% of n-hexane C$_6$H$_{14}$ for perfect dispersion and suitable amount of cyclohexane for non-polar chain/mixing mode. Now stored it at room temperature the nanomaterial should be dark brown color. The capping of Gd multifarious morphology on the surface of iron is obvious from TEM image as sown in Fig. 4.8d–f. All these Gd nanostructures are attached/dispersed to the surface of Fe nano-ellipsoids as shown in Fig. 4.7c–e.
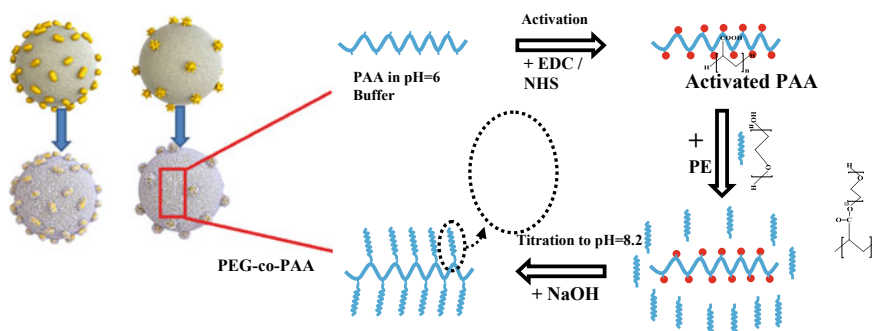
Fig. 4.8 Capsulation of bipolymer blend on surface of Gd-doped iron oxide nanospheres (synthesis scheme new develop)

The optical characterization has been done using UV/VIS/NIR (PerkinElmer Lamda-19 spectrophotometer). It is clear that Iron oxide NPs having sonly one shoulder peak but in case of Iron blend with Gd nanomorphology one shoulder peak between 200 and 300 nm of wavelength is very prominent and second peak which lies between 300 and 400 nm of wavelength tries to develop, which confirms the successful formulation of iron-Gd-doped form. Development of new form of peak toward visible region is a sign of excellent outcome of photodynamic therapy reaction whose wavelength usually lies in the region of visible wavelength. These techniques are especially useful for iron oxide NPs and Gd-doped iron oxide NPs due to actively involvement of biomedical (therapeutic) and diagnostic MRI applications. Size/morphology along with crystallite plays a key role in clinical practice as well as medical novel modalities.

After successful fabrication of desired morphology of Gd-doped iron oxide NPs, the main task was capsulation of PEG-co-PAA on the surface of Gd-doped iron. After successful growth of polymer-coated iron oxide NPs and polymer-coated Gd composite with iron oxide NPs, synthesized nanomaterials were tested for feasibility of PDT, PTT, and MRI applications. For ongoing experiment, multiple 96-well plates were cultured for exploring the feasibility of toxicity occurring in the presence of iron oxide NPs and Gd-doped iron oxide NPs alone and conjugation with three efficient photosensitizers, e.g., chlorine e6, 5-ALA, and Foscan® toward Hela cell line (cervical cancerous model). It is investigated that alone iron oxide NPs are nontoxic/biocompatible in the dark and when conjugated with chlorine e6 and Foscan® show significant toxicity up to 80–90% cell death assessed, which implies that chlorine e6 and Foscan® in the presence of PEG-coated iron oxide NPs not only overcome the possibility of drug accumulation also produced countable toxicity toward cervical carcinoma, cell viability plot depicted in Fig. 4.10a, b (Fakhar-e-Alam et al. 2011a, b, c; Zubair Iqbal et al. 2015; Boix-Garriga et al. 2015; Shaheen 2017a, b; Fakhar-e-Alam et al. 2017a, b).

From Fig. 4.9a, b, the same trend in the loss in cell viability was seen with the difference in 5-ALA relevant cell viability loss. In case of PEG-coated Gd-doped iron NPs, only the steeply tumbling behavior of cell viability loss was noted. When Hela cells were exposed with PEG-coated Gd-doped iron NPs conjugated with chlorine e6 or Foscan®, the trough hump in the cell viability plot was recorded, which implies that initially the critical cell loss was assessed but after a certain uptake, and some Hela cells shows resistance against ligands uptake and start reproduce from dead population factor (Fakhar-e-Alam et al. 2011a, b, c) (Fig. 4.9a MTT assay).

$$\text{Model}_i = P1 * x^2 + P2 * x + P3 \qquad (1)$$

where model has four options as shown in the figure $= \{1, 2, 3, 4\}$, x is PEG-doped iron oxide NPs and $P1$, $P2$, $P3$ are extracted from least square errors method as shown in Table 4.1.
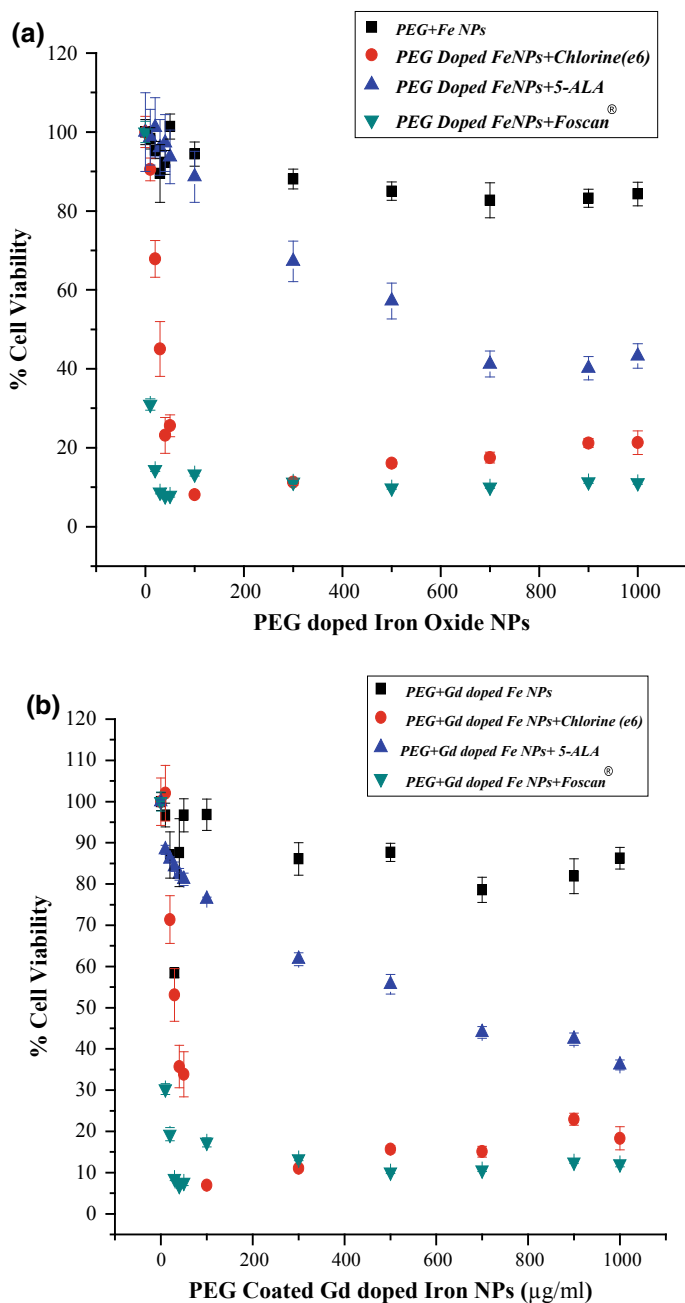
Fig. 4.9 a Cell viability of Hela cell line when labeled with PEG-coated iron oxide NPs by MTT assay. **b** % Cell viability of Hela cell line when labeled with PEG-coated Gd-doped iron oxide NPs by MTT assay

Table 4.1 Number of different constant values used in the model given in Eq. 4.1 and extracted through least square errors method along with the indicators of fitness of the curve

	*P*1	*P*2	*P*3	SSE	R-square	Adjusted R-square	RMSE	P-value
Model1	2.617e−05	−0.03999	98.06	0.335	0.9966	0.9943	0.3342	4.46e−06
Model2	−6.234e−06	0.02203	5.803	1.902	0.9866	0.9776	0.7962	6.79e−05
Model3	7.327e−05	−0.133	101.5	28.91	0.9842	0.9736	3.104	9.44e−05
Model4	1.197e−05	−0.0151	14.7	0.5813	0.9264	0.8774	0.4402	0.002082

Model1 = PEG + FeNPs; Model2 = PEG-doped FeNPs + chlorine (e6); Model3 = PEG-doped FeNPs + ALA; Model4 = PEG-doped FeNPs + Foscan. Data relevant to Fig. 4.6b

Table 4.2 Values of different constants used in the model given in Eq. 4.1 and extracted through least square errors method along with the indicators of fitness of the curve

	*P*1	*P*2	*P*3	SSE	R-square	Adjusted R-square	RMSE	P-value
Model1	4.109e−05	−0.05812	102	35.76	0.8133	0.6888	3.453	0.013984
Model2	−9.807e−06	0.02552	4.435	22.15	0.8571	0.7619	2.717	0.008049
Model3	2.489e−05	−0.06962	82.3	19.68	0.9822	0.9704	2.562	0.000119
Model4	2.201e−05	−0.02908	19.92	2.141	0.9352	0.892	0.8448	0.001611

Model1 = PEG Gd-doped + FeNPs; Model2 = PEG Gd-doped FeNPs + chlorine (e6); Model3 = PEG Gd-doped FeNPs + ALA; Model4 = PEG Gd-doped FeNPs + Foscan. Data relevant to Fig. 4.6b

Model presented is same as described in Eq. 4.1. The model has four options as shown in Fig. 4.6b and Table 4.2, $i = \{1, 2, 3, 4\}$, x is PEG-coated Gd-doped iron oxide NPs and $P1$, $P2$, $P3$ are extracted from least square errors method as shown in Table 4.2 (Figs. 4.10 and 4.11).

By analyzing the data via empirical modeling of statistical approach of experimental data, it is obvious that experimental data and empirical modulated data show very worthy agreement. It is investigated and provides by model, maximal/severe toxicity was recorded in case of PEG-coated iron and PEG-coated Gd-doped iron when conjugated with chlorine e6 or Foscan®. Empirical model fitted curve with experimental plot was shown in Fig. 4.6a, b (Fakhar-e-Alam et al. 2011a, b, c) [131–132]. Some overview of schematic illustration is shown in Fig. 4.12 (Waseem Akram and Fakhare-Alam 2018).

But product may be useful for multimodal applications, i.e., magnetic resonance Imaging (MRI), immune therapy (experiment conducted with normal cells) as well as photodynamic therapy (PDT) in a single uptake which has been already proved by conducting the series of relevant experiments for results confirmation. Single form of nanostructure for trimodal purpose (MRI, immune therapy and PDT) is the novelty of these nanosystems.

For further step of experimental scheme, MCF-7 cells were cultured on suitable conditions and environments (having 10% FBS, 5% CO_2, 37 °C and in the presence of penicillin and streptomycin). Foresaid cells were administered to different concentrations of PEG capped Gd-doped iron NP individual and conjugated with chlorine e6,
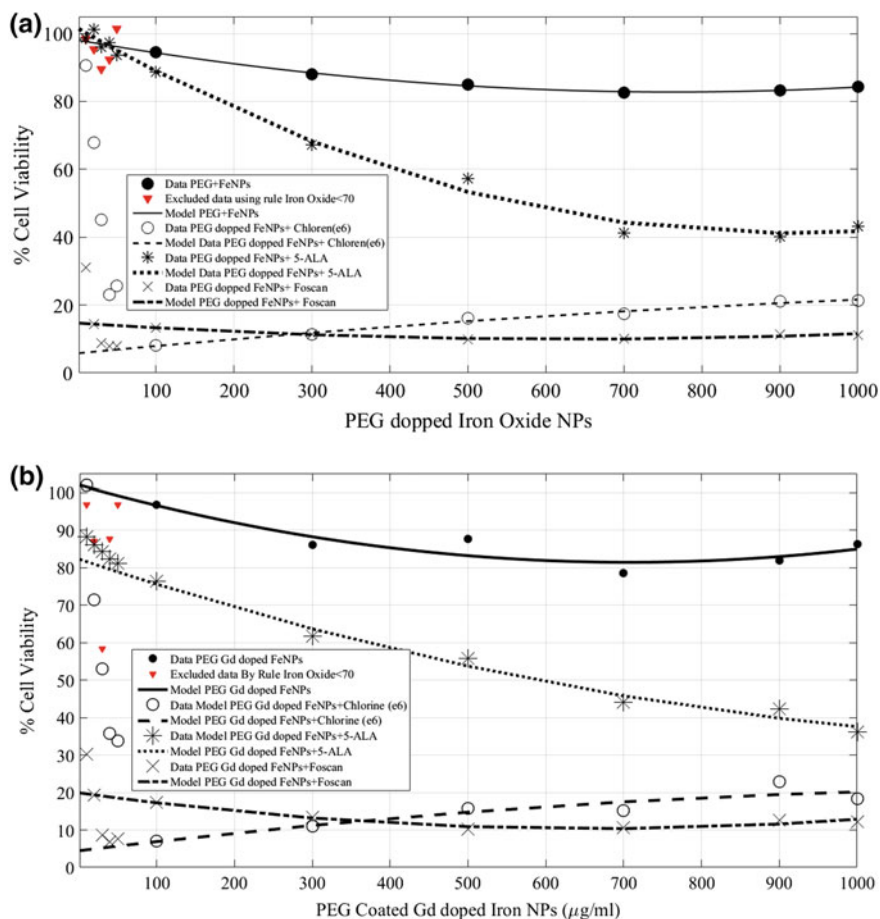
Fig. 4.10 a Empirical modeling of Hela cells when incubated with PEG coated with iron oxide NPs. **b** Empirical modeling of Hela Cells when incubated with PEG coated with Gd-doped iron oxide NPs

Foscan, and 5-ALA. In addition, very outstanding correlation morphology of treated cells was obtained when exposed with chlorine e6 and Foscan® and is depicted in Fig. 4.13c control MCF-cells and MCF-7 cells treated with PEG-capped Gd-doped Iron + 5-ALA shown from Fig. 4.13b, MCF-7 cells treated with PEG-capped Gd-doped iron + chlorine e6 and MCF-7 cells were treated with PEG-capped Gd-doped iron + Foscan® from Fig. 4.13c, d, respectively. Furthermore, iron NPs or Gd-doped iron NPs alone does not evoke significant cell toxicity at recommended/suitable concentrations toward MCF-7 provided that exposed in the dark without any drug labeling agent. This novel experimental strategy will not demonstrate and overcome the problem of cancer diagnostic also useful for treatment modality. It is investigated
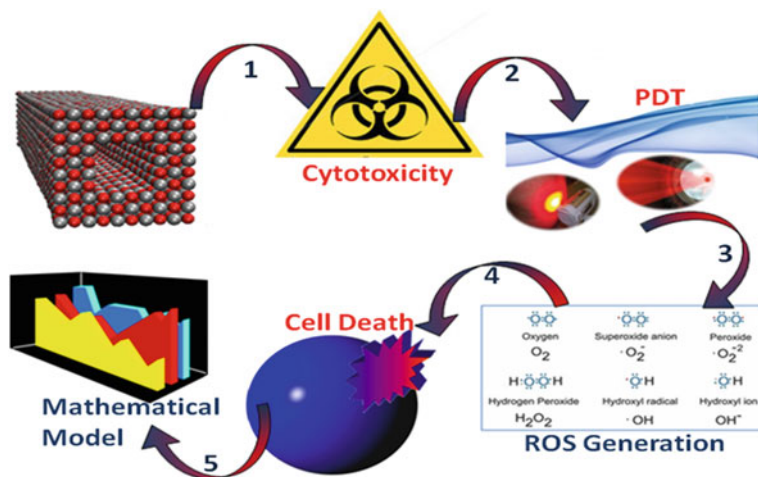
Fig. 4.11 Schematic illustration of iron oxide NPs for photochemical reactions and empirical modeling implementation (new develop)
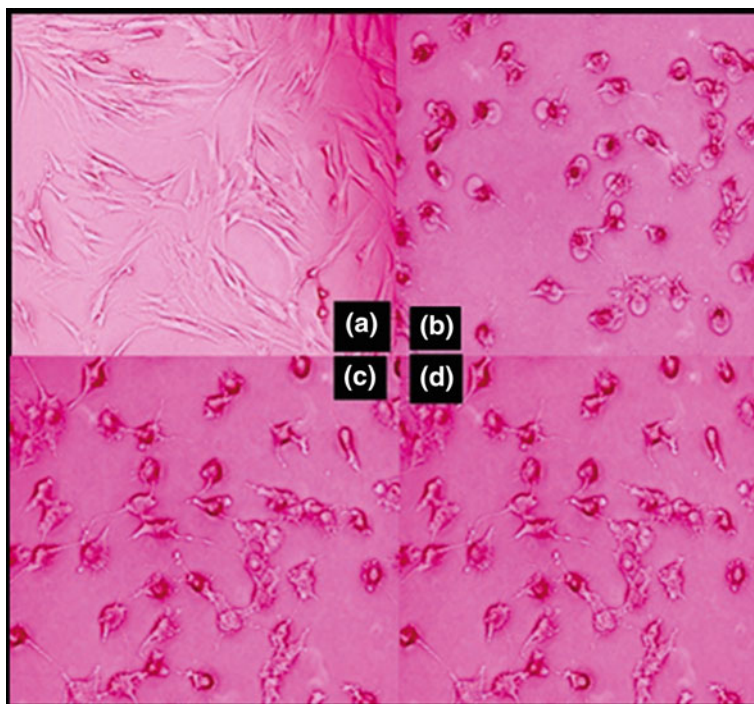
Fig. 4.12 Microscopic view of cancerous cells stained with various concentrations of nanoparticles and drug
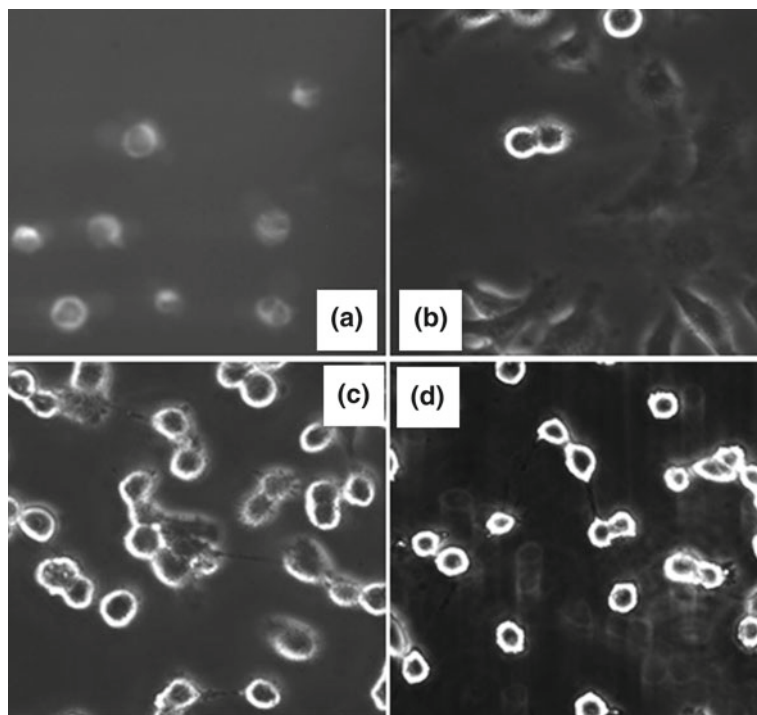
Fig. 4.13 Cell mitochondria stained with mitotracker for ROS analysis (from Fig. 4.14, it is obvious that reactive oxygen species (ROS) fluorescence is being increased after significant chemical reactions which leads to synergisticity of singlet oxygen + free radicals and as resulted of cell death.)

that PEG-coated Gd-doped iron NPs alone should be useful for MRI (MRI contrast agent as T_1 and at low concentration as T_2), but demonstrated the unique properties in addition of two efficient photosensitizers (chlorine e6 and Foscan®).

Toxicity of Gd-doped iron conjugated with chlorine e6 and Foscan® was confirmed by staining mitochondria using mitotracker dye. From Fig. 4.8, it is obvious that reactive oxygen species (ROS) fluorescence is being increased after significant chemical reactions which leads to synergisticity of singlet oxygen + free radicals and as resulted of cell death. In first snapshot very faint/superficial ROS fluorescence were visualized but it increases as far as liberation of reactive oxygen species stimulated as shown in figure (Fig. 4.14b–d). Similar kind of study has already conducted and reported by [136–138]. After careful investigation of cell/tissue analysis and conducting series test of experiment, e.g., cell viability by MTT assay [139–140], cell morphology analysis, ROS fluorescence, mitochondrial membrane potential test, nanoparticle-drug distribution test, and histopathological results of breast tissue analysis, it is confirmed that chlorine e6 and Foscan are very potential candidates for
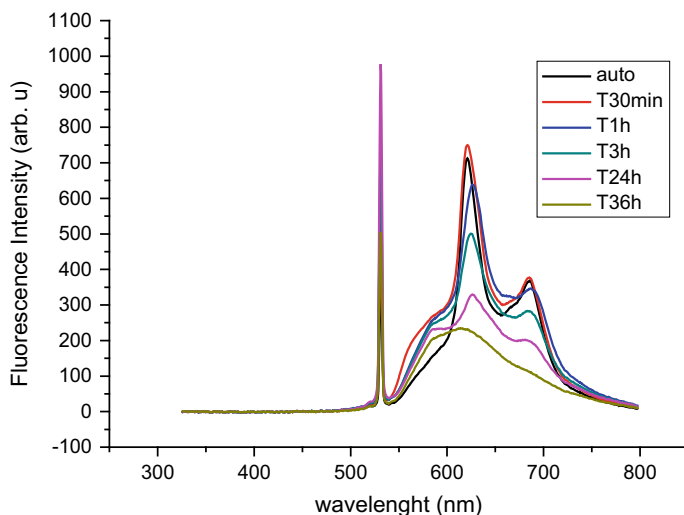
Fig. 4.14 Drug peak in in vivo tissue analysis

breast cancer treatment and very efficient toward MRI applications in the presence of Gd blend with iron oxide nanoparticles.

Three animals (Dawley rats) were quantified for each group of PDT measurement, initially their optimization parameters, i.e., optimal dose/concentration of each relevant nanoparticles alone/complex ligands form of disperse solution, PDT absorption light suitable dose and wavelength selectivity, time of light irradiation, etc. were analyzed for suitability of excellent outcome. The results obtained from the histopathological analysis of the animal model (Fig. 4.15). It is obvious from the results that in case of nanoparticles conjugated with chlorine e6 and Foscan® very acute cell apoptosis/necrosis was attained as 1.15 (b, c and e, f), the detail information regarding control cells and various concentration of PEG-coated iron oxide and PEG-coated Gd-doped iron oxide NPs. Furthermore, precise measurement of PEG-coated iron oxide/Gd-doped iron oxide toward animal study was confirmed by animal γ (gamma) chromatography. This is more reliable and precise form measurement of nanoparticle/drug accumulation study. Our recent published data concluded that many novel materials are useful for MRI and photodynamic therapy applications (Fakhar-e-Alam and Butt 2018; Waseem Akram and Fakhare-Alam 2018). The scientific analogy of conjugations is when any drug nanoparticles ligand is employed for toxicity measurement into mimic model of breast cancer/tissue phantom, there are three possibilities, either nanoparticle-drug complex cancel each other effect or enhance the possible mechanism of toxicity/necrotic producibility or no response/interaction each other effects.

In this case when iron oxide/Gd-doped iron oxide were labeled with chlorine/Foscan their toxicity enhanced but opposite in case of 5ALA, only chlorine
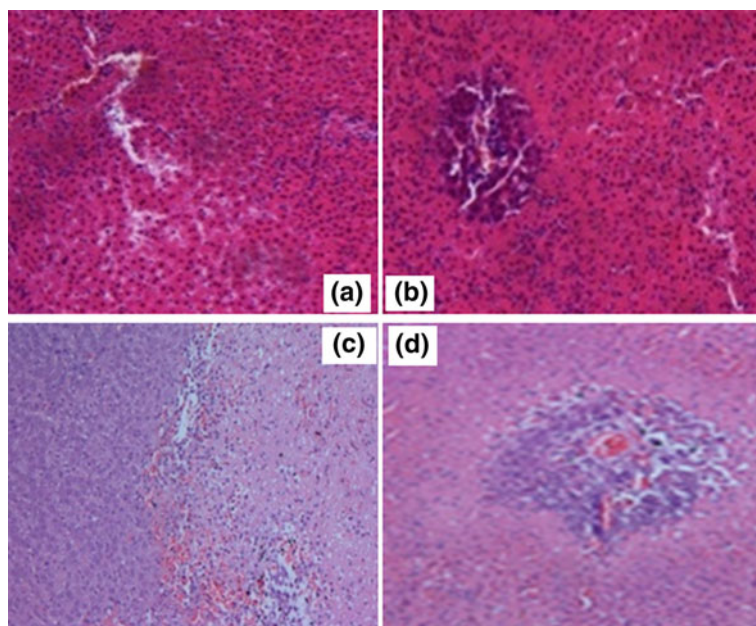
Fig. 4.15 Histopathological analysis of cancerous tissue model (for confirmatory test, four groups of animal models were employed to check the toxicity and phototoxicity effects of optimized parameters of PEG-coated Fe, PEG-coated Fe + 5ALA, and PEG-coated Fe + chlorine e6 and Foscan®)

e6 and Foscan claims significant outcome which may be in the future very helping for overcoming the huge causalities due to breast/cervical cancer.

Magnetic Resonance Measurements with Clinical MRI

The relaxation times (T_1, longitudinal; T_2, transversal) as well as relaxivities (r_1, r_2) of individual and conjugated magnetite nanoparticles (Gd-Fe_3O_4) were examined at different field strengths, i.e., 1.5T. Relaxation times (T1 and T_2) values of MNPs were calculated with the help of a clinical MRI instrument at 1.5T Field. Standard "birdcage" head coil was used throughout the experiments. The temperature in the magnet room was 20.1 °C. The diluted samples (25 mL) were placed in a plastic box filled with water. T_1 and T_2 were calculated for Gd-doped iron nanoparticles with different concentrations (1, 2.5, 5, 7, and 10 mg Gd-Fe_3O_4/L). According to the theory [10 c], the relaxation rates ($1/T_1$, $1/T_2$) are linearly dependent on the iron concentration. Relaxivities r_1 and r_2 were then calculated as the slope of the plot of $1/T_1$ and $1/T_2$ versus Gd concentration in the diluted suspensions of MNPs to compare contrast enhancing effect of different coatings. Results are depicted in Figs. 4.16 and

Fig. 4.16 Gd-doped iron nanoparticles as contrast agent (from high concentration to low concentration)
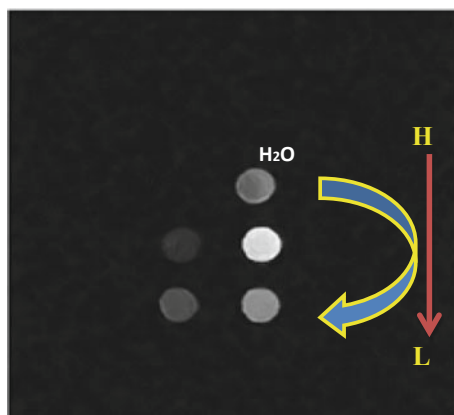
4.17, respectively. Coefficient of determination (R-squared) was calculated to assess the goodness of each curve fit.

The novel photodynamic therapy approach based on PEG-co-PAA-decorated Gd-doped iron oxide nanoparticles pure and PEG-co-PAA-decorated Gd-doped iron oxide nanoparticles conjugated with chlorine e6, 5-ALA, and Foscan are exciting material demonstrate the ability of cell killing properties up to maximum via direct excitation process of two simultaneous therapeutic techniques PDT/PTT. Of course, there are some significant MDR issues which resolve by decorating nanocapsule with PEG-co-PAA which enhance free standing drug distribution toward targeted site of malignancy. It has been explored that even after attempt of manifold treatment modalities (chemotherapy, radiotherapy, phototherapy, and hypothermia therapy) there were some live island of cancerous/malignant tissues were found which liberate tissue mutation finally leads to poor quality of survival of malignant patient
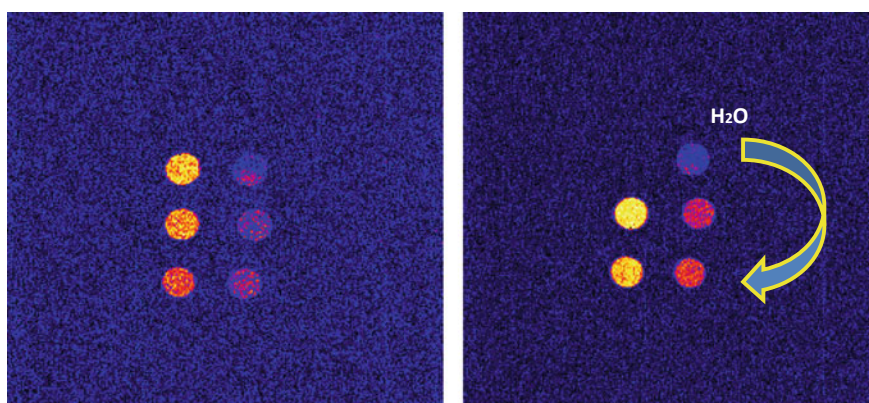
Fig. 4.17 Gd-doped iron nanoparticles as contrast agent from (high concentration to low concentration) (new developed result)
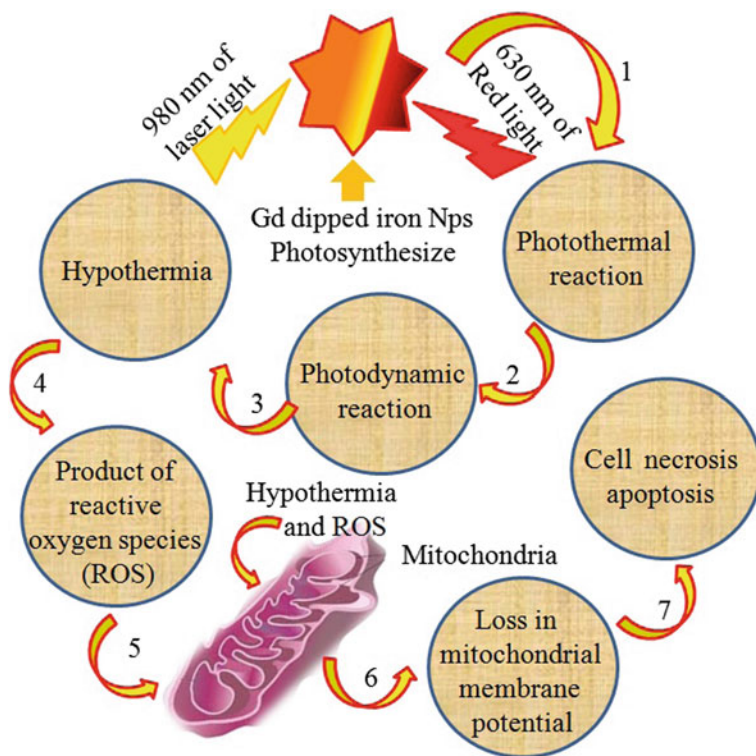
Fig. 4.18 Schematic diagram of PDT and PTT (preferred for the treatment of cancer)

life. To overcome said mentioned problem, new comprehensive form of experimental strategy was introduced for demonstrating the perfect treatment PDT/PTT plan based on synergistic response of Gd-doped iron oxide nanoparticles conjugated with chlorine e6, 5-ALA, and Foscan which can act as MRI contrast agents that act as targeting weapon toward malignant cervical tissues. Prime focus of experimental development is to address and resolve MDR problem, to kill targeted unnecessary tissue island comprehensively, and online MRI contrast agent facility as schematic shown in Fig. 4.13. Given figure shown the comprehensive tissue removal by exposing 980 nm of NIR light via ROS liberation as outcome of hypothermia treatment leads to loss in mitochondrial membrane potential as result of cell death (Fig. 4.18).

Conclusion

Gd-doped nanoparticles such as magnetic nanoparticles were preferred for biomedical applications. Gd-doped iron oxide nanoparticles are the magnetic nanoparticles and are of great importance because of extensive potential in biomedical applications.

For instance, these particles are used for treatment of cancer, by using many fields of biological science like targeted drug delivery, magnetic hyperthermia therapy, MRI as a contrast agent, controlled drug release process, photodynamic therapy, photothermal therapy, biosensor technology, drugs delivery, and X-ray imaging process. All these techniques are more suitable for magnetic nanoparticles. But non-toxic material for human cells like doped iron oxide nanoparticles is mostly preferred for all these techniques. Therefore, here much effort has been focused toward MRI contrast agent along with therapeutic approach. Gd-decorated iron oxide NPs are obtained/developed by employing direct, facile, and economical synthesis approach. Firstly, the obtained product, e.g., polyethylene glycol/polyacrylic acid (PEG-co-PAA)-encapsulated gadolinium-doped iron having multistructural nanomorphology (Gd-doped Fe-NMPs), was found to be useful in versatile format of biomedical applications. Prior to PDT outcome finding the final product of nanocapsule (PEG-co-PAA decorated with Gd-doped iron oxide NPs) was successfully conjugated with three various efficient photosensitizers and confirmed by applying diverse variety of analytic techniques. Histopathological analysis of malignant cells and tissues declared that PEG-co-PAA decorated with Gd-doped iron oxide NPs complex with Foscan® not only produce favorable outcome after overcoming the problem of multidrug resistance (MDR) also excellent nanocapsule for comprehensive treatment of cervical cancer. Our results were justified with variety of techniques, e.g., MTT assay, mitochondrial membrane potential analysis, ROS detection, and histopathological analysis. Secondly, it was proved that Gd-doped iron oxide NPs having excellent characteristics for feasibility of T_1 MRI contrast agent. The combined effect of Gd-doped iron oxide NPs along with Foscan floats the comprehensive idea of photodynamic therapy in our study which produces a synergistic effect; hence, such combined process is more convenient and effective than the individual nanoparticles. Finally, it was realized that experimental results and empirical modulated data having very similar trend cell viability loss/malignant tissue loss Foscan-decorated nanocapsule of Gd-doped iron oxide.

References

Akilov OE, Kosaka S, O'Riordan K, Hasan T (2007) Photodynamic therapy for cutaneous leishmaniasis: the effectiveness of topical phenothiaziniums in parasite eradication and Th1 immune response stimulation. Photochem Photobiol Sci 6(10):1067–1075

Allen CM, Sharman WM, Van Lier JE (2001) Current status of phthalocyanines in the photodynamic therapy of cancer. J Porphyrins Phthalocyanines 5(02):161–169

Atif M, Firdous S, Khurshid A, Noreen L, Zaidi SS, Ikram M (2009) In vitro study of 5-aminolevulinic acid-based photodynamic therapy for apoptosis in human cervical HeLa cell line. Laser Phys Lett 6(12):886

Atif M, Fakhar-e-Alam M, Firdous S, Zaidi SSZ, Suleman R, Ikram M (2010) Study of the efficacy of 5-ALA mediated photodynamic therapy on human rhabdomyosarcoma cell line (RD). Laser Phys Lett 7(10):757

Bases R, Brodie SS, Rubenfeld S (1958) Attempts at tumor localization using CU64-labeled copper porphyrins. Cancer 11(2):259–263

Battah SH, Chee CE, Nakanishi H, Gerscher S, MacRobert AJ, Edwards C (2001) Synthesis and biological studies of 5-aminolevulinic acid-containing dendrimers for photodynamic therapy. Bioconjug Chem 12(6):980–988

Battah S, O'Neill S, Edwards C, Balaratnam S, Dobbin P, MacRobert AJ (2006) Enhanced porphyrin accumulation using dendritic derivatives of 5-aminolaevulinic acid for photodynamic therapy: an in vitro study. Int J Biochem Cell Biol 38(8):1382–1392

Bellnier DA, Dougherty TJ (1996) A preliminary pharmacokinetic study of intravenous Photofrin® in patients. J Clin Laser Med Surg 14(5):311–314

Berger Y, Greppi A, Siri O, Neier R, Juillerat-Jeanneret L (2000) Ethylene glycol and amino acid derivatives of 5-aminolevulinic acid as new photosensitizing precursors of protoporphyrin IX in cells. J Med Chem 43(25):4738–4746

Berlin JC (2006) *Silicon* phthalocyanines for photodynamic therapy. Case Western Reserve University

Bernardi P, Scorrano L, Colonna R, Petronilli V, Di Lisa F (1999) Mitochondria and cell death. Eur J Biochem 264(3):687–701

Boix-Garriga E, Acedo P, Casado A, Villanueva A, Stockert JC, Cañete M, Mora M, Sagrista ML, Nonell S (2015) Poly(D, L-lactide-co-glycolide) nanoparticles as delivery agents for photodynamic therapy: enhancing singlet oxygen release and photototoxicity by surface PEG coating. Nanotechnology 38(26)

Bourre L, Giuntini F, Eggleston IM, Wilson M, MacRobert AJ (2008) 5-Aminolaevulinic acid peptide prodrugs enhance photosensitization for photodynamic therapy. Mol Cancer Ther 7(6):1720–1729

Boyle RW, Dolphin D (1996) Structure and biodistribution relationships of photodynamic sensitizers. Photochem Photobiol 64(3):469–485

Cairnduff F, Stringer MR, Hudson EJ, Ash DV, Brown SB (1994) Superficial photodynamic therapy with topical 5-aminolaevulinic acid for superficial primary and secondary skin cancer. Br J Cancer 69(3):605

Casas A, Batlle A (2006) Aminolevulinic acid derivatives and liposome delivery as strategies for improving 5-aminolevulinic acid-mediated photodynamic therapy. Curr Med Chem 13(10):1157–1168

Casas A, Perotti C, Saccoliti M, Sacca P, Fukuda H, del C Batlle AM (2002) ALA and ALA hexyl ester in free and liposomal formulations for the photosensitisation of tumour organ cultures. Brit J Cancer 86(5):837

Christensen HN (1985) On the strategy of kinetic discrimination of amino acid transport systems. J Membr Biol 84(2):97–103

Christofori G (2006) New signals from the invasive front. Nature 441(7092):7444

Collaud S, Juzeniene A, Moan J, Lange N (2004) On the selectivity of 5-aminolevulinic acid-induced protoporphyrin IX formation. Curr Med Chem Anti-Cancer Agents 4(3):301–316

Di Venosa GM, Casas AG, Battah S, Dobbin P, Fukuda H, MacRobert AJ, Batlle A (2006) Investigation of a novel dendritic derivative of 5-aminolaevulinic acid for photodynamic therapy. Int J Biochem Cell Biol 38(1):82–91

Dolmans DEJGJ, Fukumura D, Jain RK (2003) Photodynamic therapy for cancer. Nat Rev Cancer 3(5):380

Dougherty TJ, Gomer CJ, Henderson BW, Jori G, Kessel D, Korbelik M, Moan J, Peng Q (1998) Photodynamic therapy. JNCI J Nat Cancer Inst 90(12):889–905

Fakhar-e-Alam M, Butt AR et al (2018) Magnesium oxide in nanodimension: model for MRI and multimodal therapy. J Nanomater Article ID 4210920:12 pages. https://doi.org/10.1155/2018/4210920

Fakhar-e-Alam M, Roohi S, Atif M, Firdous S, Amir N, Zahoor R (2010) Labelling and optimization of PHOTOFRIN® with 99mTc. Radiochim Acta Int J Chem Aspects Nucl Sci Technol 98(12):813–818

Fakhar-e-Alam M, Kishwar S, Khan Y, Siddique M, Atif M, Nur O, Willander M (2011a) Tumoricidal effects of nanomaterials in HeLa cell line. Laser Phys 2011(21):1978–1988

Fakhar-e-Alam M, Usman Ali SM, Ibupoto ZH, Atif M, Willander M (2011b) Role of ALA sensitivity in HepG2 cell in the presence of diode laser. Laser Phys 21:2165–2170

Fakhar-e-Alam M, Khan Y et al (2011c) The potential applications of ZnO nanoparticles conjugated with ALA and Photofrin® as a biomarker in HepG2 cells. Laser Phys 2011(21):2156–2164

Fakhar-e-Alam M, Waseem Akram M, Iqbal S, Alimgeer KS, Atif M, Sultana K, Willander M, Wang ZM (2017a) Empirical modeling of physiochemical immune response of zinc oxide nanowires under UV exposure to melanoma and foreskin fibroblast. Sci Rep 7:46603. https://doi.org/10.1038/srep46603

Fakhar-e-Alam M, Waseem Akram M, Iqbal S, Alimgeer KS, Atif M, Sultana K, Willander M, Wang ZM (2017b) Empirical modeling of physiochemical immune response of zinc oxide nanowires under UV exposure to melanoma and foreskin fibroblast. Sci Rep 7:46603. https://doi.org/10.1038/srep46603

Fawwaz R, Bohdiewicz P, Lavallee D, Wang T, Oluwole S, Newhouse J, Alderson P (1990) Use of metalloporphyrins in diagnostic imaging. Nucl Med Biol 17(1):65–72

Ferreira J, Kurachi C, Moriyama LT, Menezes PFC, Perussi JR, Sibata C et al (2006) Laser Phys Lett 3:91

Ferriera J, Menezes PFC, Kurachi C, Sibata C, Allison RR, Bagnato VS (2008) Laser Phys Lett 2008(5):161–166

Frangville C et al (2016) Assembly of double-hydrophilic block copolymers triggered by gadolinium ions: new colloidal MRI contrast agents. Nanoletter 16:4069–4073

Friesen SA, Hjortland GO, Madsen SJ, Hirschberg H, Engebraten O, Nesland JM, Peng Q (2002) 5-Aminolevulinic acid-based photodynamic detection and therapy of brain tumors. Int J Oncol 21(3):577–582

Furre IE, Shahzidi S, Luksiene Z, Møller MT, Borgen E, Morgan J, Tkacz-Stachowska K, Nesland JM, Peng Q (2005) Targeting PBR by hexaminolevulinate-mediated photodynamic therapy induces apoptosis through translocation of apoptosis-inducing factor in human leukemia cells. Can Res 65(23):11051–11060

Furuse K, Fukuoka M, Kato H, Horai T, Kubota K, Kodama N, Kusunoki Y, Takifuji N, Okunaka T, Konaka C (1993) A prospective phase II study on photodynamic therapy with photofrin II for centrally located early-stage lung cancer. The Japan Lung Cancer Photodynamic Therapy Study Group. J Clin Oncol 11(10):1852–1857

Gahlen J, Stern J, Laubach HH, Pietschmann M, Herfarth C (1999) Improving diagnostic staging laparoscopy using intraperitoneal lavage of δ-aminolevulinic acid (ALA) for laparoscopic fluorescence diagnosis. Surgery 126(3):469–473

Gardner LC, Smith SJ, Cox TM (1991) Biosynthesis of delta-aminolevulinic acid and the regulation of heme formation by immature erythroid cells in man. J Biol Chem 266(32):22010–22018

Georgakoudi I, Nichols MG, Foster TH (1997) The mechanism of Photofrin photobleaching and its consequences for photodynamic dosimetry. Photochem Photobiol 65(1):135–144

Gerscher S, Connelly JP, Griffiths J, Brown SB, MacRobert AJ, Wong G, Rhodes LE (2000) Comparison of the pharmacokinetics and phototoxicity of protoporphyrin IX metabolized from 5-aminolevulinic acid and two derivatives in human skin in vivo. Photochem Photobiol 72(4):569–574

Ghaghada KB, Ravoori M, Sabapathy D, Bankson J, Kundra V, Annapragada A (2009) New dual mode gadolinium nanoparticle contrast agent for magnetic resonance imaging. Plos One 4(10):e7628

Gomer CJ, Ferrario A, Murphree AL (1987) The effect of localized porphyrin photodynamic therapy on the induction of tumour metastasis. Br J Cancer 56(1):27

Grebeňová D, Kuželová K, Smetana K, Pluskalová M, Cajthamlová H, Marinov I, Fuchs O, Souček J, Jarolím P, Hrkal Z (2003) Mitochondrial and endoplasmic reticulum stress-induced apoptotic pathways are activated by 5-aminolevulinic acid-based photodynamic therapy in HL60 leukemia cells. J Photochem Photobiol B Biol 69(2):71–85

Grossweiner LI, Grossweiner JB, Gerald Rogers BH (2005) The science of phototherapy: an introduction. Springer, Dordrecht, The Netherlands

Gu M-J, Li K-F, Zhang L-X, Wang H, Liu L-S, Zheng Z-Z, Han N-Y, Yang Z-J, Fan T-Y (2015) In vitro study of novel gadolinium-loaded liposomes guided by GBI-10 aptamer for promising tumor targeting and tumor diagnosis by magnetic resonance imaging. Int J Nanomed 10:5187–5520

Helm L (2010) Optimization of gadolinium-based MRI contrast agents for high magnetic-field applications. Future Med Chem 2(3):385–396. https://doi.org/10.4155/fmc.09.174

Hinnen P, de Rooij FW, Van Velthuysen ML, Edixhoven A, Van Hillegersberg R, Tilanus HW, Wilson JH, Siersema PD (1998) Biochemical basis of 5-aminolaevulinic acid-induced protoporphyrin IX accumulation: a study in patients with (pre) malignant lesions of the oesophagus. Br J Cancer 78(5):679

Huang Z (2005) A review of progress in clinical photodynamic therapy. Technol Cancer Res Treat 4(3):283–293

Ikram M, Khan RU, Firdous S, Atif M, Nawaz M (2011) Photodynamic therapy of non-melanoma skin cancers. Laser Phys 21(2):427–433

Jeffes EW, McCullough JL, Weinstein GD, Fergin PE, Nelson JS, Shull TF, Simpson KR, Bukaty LM, Hoffman WL, Fong NL (1997) Photodynamic therapy of actinic keratosis with topical 5-aminolevulinic acid: a pilot dose-ranging study. Arch Dermatol 133(6):727–732

Kanal E (2016) Gadolinium based contrast agents (GBCA): safety overview after 3, decades of clinical experience. Magn Reson Imaging 2016(34):1341–1345

Kanda T, Nakai Y, Oba H, Toyoda K, Kitajima K, Furui S (2016) Gadolinium deposition in the brain. Magn Reson Imaging 34:1346–1350

Karmakar S, Banik NL, Patel SJ, Ray SK (2007) 5-Aminolevulinic acid-based photodynamic therapy suppressed survival factors and activated proteases for apoptosis in human glioblastoma U87MG cells. Neurosci Lett 415(3):242–247

Kaushik A, Khan R, Solanki PR, Pandey P, Alam J, Ahmad S, Malhota BD (2008) Iron oxide nanoparticlrs-chitosan composite based glucose biosensor. Biosens Bioelectron 24:676–683

Kennedy JC, Pottier RH (1992) New trends in photobiology: endogenous protoporphyrin IX, a clinically useful photosensitizer for photodynamic therapy. J Photochem Photobiol B 14(4):275–292

Kennedy JC, Pottier RH, Pross DC (1990) Photodynamic therapy with endogenous protoporphyrin: IX: basic principles and present clinical experience. J Photochem Photobiol B 6(1–2):143–148

Kennedy JC, Marcus SL, Pottier RH (1996) Photodynamic therapy (PDT) and photodiagnosis (PD) using endogenous photosensitization induced by 5-aminolevulinic acid (ALA): mechanisms and clinical results. J Clin Laser Med Surg 14(5):289–304

Khursid A, Atif M, Firdous S, Zaidi SS, Salman R, Ikram M (2010) Study of the efficacy of 5 ALA-mediated photodynamic therapy on human larynx squamous cell carcinoma (Hep2c) cell line. Laser Phys 20(7):1673–1678

Kloek J, Beijersbergen van Henegouwen GM (1996) Prodrugs of 5-aminolevullinic acid for photodynamic therapy. Photochem Photobiol 64(6):994–1000

Kondo M, Hirota N, Takaoka T, Kajiwara M (1993) Heme-biosynthetic enzyme activities and porphyrin accumulation in normal liver and hepatoma cell lines of rat. Cell Biol Toxicol 9(1):95–105

Kopera D, Cerroni L, Fink-Puches R, Kerl H (1996) Different treatment modalities for the management of a patient with the nevoid basal cell carcinome syndrome. J Am Acad Dermatol 34(5):937–939

Korbelik M (1996) Induction of tumor immunity by photodynamic therapy. J Clin Laser Med Surg 14(5):329–334

Krieg RC, Messmann H, Rauch J, Seeger S, Knuechel R (2002) Metabolic characterization of tumor cell–specific protoporphyrin IX accumulation after exposure to 5-aminolevulinic acid in human colonic cells. Photochem Photobiol 76(5):518–525

Kriska T, Korytowski W, Girotti AW (2005) Role of mitochondrial cardiolipin peroxidation in apoptotic photokilling of 5-aminolevulinate-treated tumor cells. Arch Biochem Biophys 433(2):435–446

Kübler A, Haase T, Rheinwald M, Barth T, Mühling J (1998) Treatment of oral leukoplakia by topical application of 5-aminolevulinic acid. Int J Oral Maxillofac Surg 27(6):466–469

Lisnjak IO, Kutsenok VV, Polyschuk LZ, Gorobets OB, Gamaleia NF (2005) Effect of photodynamic therapy on tumor angiogenesis and metastasis in mice bearing Lewis lung carcinoma. Exp Oncol 27(4):333–335

Liza S, Valappil Mohanan P (2016) Toxicological evaluation of dextran stabilized iron oxide nanoparticles in human peripheral blood lymphocytes. Biointerphases 11(4):04B302. https://doi.org/10.1116/1.4962268

Loh CS, MacRobert AJ, Bedwell J, Regula J, Krasner N, Bown SG (1993) Oral versus intravenous administration of 5-aminolaevulinic acid for photodynamic therapy. Br J Cancer 68(1):41

Loncaster JA, Moore JV, Allan D, Allan E (2005) An ultrasound analysis of the response of Gorlin syndrome-related and sporadic basal cell carcinomas to aminolaevulinic acid photodynamic therapy. Photodiagn Photodyn Ther 2(2):149–155

Luksiene Z (2003) Photodynamic therapy: mechanism of action and ways to improve the efficiency of treatment. Medicina 39(12):1137–1150

Mang TS (2004) Lasers and light sources for PDT: past, present and future. Photodiagn Photodyn Ther 1(1):43–48

Messmann H, Mlkvy P, Buonaccorsi G, Davies CL, MacRobert AJ, Bown SG (1995) Enhancement of photodynamic therapy with 5-aminolaevulinic acid-induced porphyrin photosensitisation in normal rat colon by threshold and light fractionation studies. Br J Cancer 72(3):589

MÍkvy P, Messmann H, Regula J, Conio M, Pauer M, Millson CE, MacRobert AJ, Bown SG (1998) Photodynamic therapy for gastrointestinal tumors using three photosensitizers—ALA induced PPIX, Photofrin and MTHPC. Pilot Study. Neoplasma 45(3):157–161

Moan J, Berg K (1992) Photochemotherapy of cancer. Exp Res Photochem Photobiol 55(6):931–948

Morgan J, Oseroff AR (2001) Mitochondria-based photodynamic anti-cancer therapy. Adv Drug Deliv Rev 49(1–2):71–86

Peng Q (1996) Build-up of esterified aminolevulinic-acid-derivative-induced porphyrin fluorescence in normal mouse skin. J Photochem Photobiol B Biol 34:95–96

Peng Q, Berg K, Moan J, Kongshaug M, Nesland JM (1997a) 5-Aminolevulinic acid-based photodynamic therapy: principles and experimental research. Photochem Photobiol 65(2):235–251

Peng Q, Warloe T, Berg K, Moan J, Kongshaug M, Giercksky KE, Nesland JM (1997a) 5-Aminolevulinic acid-based photodynamic therapy: clinical research and future challenges. Cancer Interdisc Int J Am Cancer Soc 79(12):2282–2308

Peng Q, Warloe T, Berg K, Moan J, Kongshaug M, Giercksky KE, Nesland JM (1997b) 5-Aminolevulinic acid-based photodynamic therapy: clinical research and future challenges. Cancer Interdisc Int J Am Cancer Soc 79(12):2282–2308

Peng Q, Berg K, Moan J, Kongshaug M, Nesland JM (1997) 5-aminolevulinic acid-based photodynamic therapy: principles and experimental research. Photochem Photobiol 65(2):235–251

Peng Q, Warloe T, Moan J, Godal A, Apricena F, Giercksky KE, Nesland JM (2001) Antitumor effect of 5-aminolevulinic acid-mediated photodynamic therapy can be enhanced by the use of a low dose of photofrin in human tumor xenografts. Can Res 61(15):5824–5832

Prasad PN (2003) Introduction to biophotonics, Chap 1, pp 1–593. Wiley Interscience

Rhodes LE, Tsoukas MM, Anderson RR, Kollias N (1997) Iontophoretic delivery of ALA provides a quantitative model for ALA pharmacokinetics and PpIX phototoxicity in human skin. J Invest Dermatol 108(1):87–91

Richter C (2000) Mitochondria as targets for the induction of apoptosis in photodynamic therapy. Photomed Gynecol Reprod 157

Rifkin R, Reed B, Hetzel F, Chen K (1997) Photodynamic therapy using SnET2 for basal cell nevus syndrome: a case report. Clin Ther 19(4):639–641

Rud E, Gederaas O, Høgset A, Berg K (2000) 5-aminolevulinic acid, but not 5-aminolevulinic acid esters, is transported into adenocarcinoma cells by system BETA transporters. Photochem Photobiol 71(5):640–647

Schmidt-Erfurth U, Bauman W, Gragoudas E, Flotte TJ, Michaud NA, Birngruber R, Hasan T (1994) Photodynamic therapy of experimental choroidal melanoma using lipoprotein-delivered benzoporphyrin. Ophthalmology 101(1):89–99

Schreiber S, Gross S, Brandis A, Harmelin A, Rosenbach-Belkin V, Scherz A, Salomon Y (2002) Local photodynamic therapy (PDT) of rat C6 glioma xenografts with Pd-bacteriopheophorbide leads to decreased metastases and increase of animal cure compared with surgery. Int J Cancer 99(2):279–285

Semelka R, Ramalho J, Vakharia A, AlObaidy M, Burke LM, Jay M, Ramalho M (2016) Gadolinium deposition disease: initial description of a disease that has been around for a while. Magn Reson Imag 34:1383–1390

Shaheen F, Aziz MH, Fakhar-e-Alam M et al (2017a) An In vitro study of the photodynamic effectiveness of GO-Ag nanocomposites against human breast cancer cells. Nanomaterials 7(401). https://doi.org/10.3390/nano7110401

Shaheen F, Aziz MH, Fakhar-e-Alam M et al (2017b) An in vitro study of the photodynamic effectiveness of GO-Ag nanocomposites against human breast cancer cells. Nanomaterials; MDPI 7(401). https://doi.org/10.3390/nano7110401

Soikkeli M, Sievänen K, Peltonen J, Kaasalainen T, Timonen M, Heinonen P, Rönkkö S, Lehto VP, Kavakka JS, Heikkinen S (2015) Synthesis and in vitro phantom NMR and MRI studies of fully organic free radicals, TEEPO-glucose and TEMPO-glucose, potential contrast agents for MRI. RSC Adv 5(20):15507–15510. https://doi.org/10.1039/c4ra11455h

Solban N, Rizvi I, Hasan T (2006) Targeted photodynamic therapy. Lasers in surgery and medicine. Offic J Am Soc Laser Med Surg 38(5):522–531

Soler AM, Angell-Petersen E, Warloe T, Tausjø J, Steen HB, Moan J, Giercksky KE (2000) Photodynamic therapy of superficial basal cell carcinoma with 5-aminolevulinic acid with dimethylsulfoxide and ethylendiaminetetraacetic acid: a comparison of two light sources. Photochem Photobiol 71(6):724–729

Tang J, Liu X, Li D, Yang Y, Khan X, Mehmood ur Rehman K Structure and magnetic analyses of hexaferrite $Sr1 - xLaxFe22 + Fe163 + O27$ prepared via the solid-state reaction. J Mater Sci Mater Electron. https://doi.org/10.1007/s10854-018-0291-7

Thaller RA, Lyster DM, Dolphin D (1983) Potential use of radiolabelled porphyrins for tumor scanning. In: Porphyrin photosensitization. Springer, Boston, MA, pp 265–278

Tsai JC, Hsiao YY, Teng LJ, Chen CT, Kao MC (1999) Comparative study on the ALA photodynamic effects of human glioma and meningioma cells. Lasers in surgery and medicine. Offic J Am Soc Laser Med Surg 24(4):296–305

Tsai T, Hong RL, Tsai JC, Lou PJ, Ling IF, Chen CT (2004) Effect of 5-aminolevulinic acid-mediated photodynamic therapy on MCF-7 and MCF-7/ADR cells. Lasers Surg Med 34(1):62–72

Uzdensky A, Kolpakova E, Juzeniene A, Juzenas P, Moan J (2005) The effect of sub-lethal ALA-PDT on the cytoskeleton and adhesion of cultured human cancer cells. Biochim et Biophys Acta (BBA) General Subj 1722(1):43–50

Valenzeno DP (1987) Photomodification of biological membranes with emphasis on singlet oxygen mechanisms. Photochem Photobiol 46(1):147–160

Verma S, Watt GM, Mai Z, Hasan T (2007) Strategies for enhanced photodynamic therapy effects. Photochem Photobiol 83(5):996–1005

Vishwanath M, Takashima A (2007) J Invest Dermatol 127:1546–1549

Waseem Akram M, Fakhare-Alam M et al (2018) Temperature dependent toxic effects of multifarious assembly of magnesium oxide (MgO). In: Nanostructures in a human cervical model in press in scientific report, vol 7

Whelan HT, Schmidt MH, Segura AD, McAuliffe TL, Bajic DM, Murray KJ, Moulder JE, Strother DR, Thomas JP, Meyer GA (1993) The role of photodynamic therapy in posterior fossa brain tumors: a preclinical study in a canine glioma model. J Neurosurg 79(4):562–568

Whelan HT, Kras LH, Ozker K, Bajic D, Schmidt MH, Liu Y, Trembath LA, Uzum F, Meyer GA, Segura AD, Collier BD (1994) Selective incorporation of 111 In-labeled PHOTOFRIN™ by glioma tissuein vivo. J Neurooncol 22(1):7–13

Wu SM, Ren QG, Zhou MO, Peng Q, Chen JY (2003) Protoporphyrin IX production and its photodynamic effects on glioma cells, neuroblastoma cells and normal cerebellar granule cells in vitro with 5-aminolevulinic acid and its hexylester. Cancer Lett 200(2):123–131

Xue LY, Chiu SM, Oleinick NL (2001) Photodynamic therapy-induced death of MCF-7 human breast cancer cells: a role for caspase-3 in the late steps of apoptosis but not for the critical lethal event. Exp Cell Res 263(1):145–155

Zeng L, Ren W, Xiang L, Zheng J, Chen B, Wu A (2013) Multifunctional Fe_3O_4–TiO_2 nanocomposites for magnetic resonance imaging and potential photodynamic therapy. Nanoscale 5(5):2107–2113

Zhang SJ, Zhang ZX (2004) 5-aminolevulinic acid-based photodynamic therapy in leukemia cell HL60. Photochem Photobiol 79(6):545–550

Zubair Iqbal M, Chen T, Ma X, Zhang L, Ren W et al (2015) Silica coated super-paramagnetic iron oxide nanoparticles (SPIONPs): a new type contrast agent of T1 magnetic resonance imaging (MRI). J Mater Chem B 3:5172–5181

Chapter 5
Magnetic Nano- and Microparticles in Life Sciences and Medical Imaging

Daniel Horák

Abstract The rapidly growing interest in biology and medicine is due to ongoing progress in noninvasive in vitro or in vivo diagnosis and imaging or treatment of various diseases, including monitoring of the survival, migration, and fate of transplanted cells over the long-term. This requires the use of contrast agents, drug delivery vehicles, and separation media often based on magnetic nanoparticles and/or microspheres. This chapter is going to describe approaches to their development at the Institute of Macromolecular Chemistry in Prague, the Czech Republic, during the last twenty-five years.

Keywords Magnetic · Nanoparticles · Microparticles · Surface modification · Biomedical applications

Introduction

The rapidly growing interest in medicine is due, in part, to ongoing progress in cell therapy. Its success profoundly depends on noninvasive in vivo monitoring of the survival, migration, homing, and fate of transplanted cells over the long-term. This monitoring requires the use of contrast agents, among which magnetic particles play a special role. Magnetic nano- and microparticles are well-established materials that offer controlled size, ability to be manipulated externally by the magnetic field, and enhancement of contrast in magnetic resonance imaging (MRI) of cells and tissues. Because of the potential benefits of multimodal functionality in biomedical applications, researchers design and fabricate multifunctional magnetic particles. As a result, these particles have additional applications in biology and medicine, including cell labeling, immunomagnetic separation of pathogenic microorganisms from complex mixtures like blood, urine, tissues, foodstuffs, and soil, protein purification, drug delivery, hyperthermia for tumor treatment, the embolization of tumorous vascular system, or in immunoassays for genome analysis. Industrial applications

D. Horák (✉)
Institute of Macromolecular Chemistry, Czech Academy of Sciences, Heyrovského nám. 2, 162 06 Prague 6, Czech Republic
e-mail: horak@imc.cas.cz

of magnetic particles, which are not subject of this review, then include magnetic inks and fluids, recording media, or isolation of environmentally hazardous materials from wastewater. Distinct advantages of magnetic particles include high-speed high-throughput gentle separation, elimination of mechanical damage by centrifugation, the absence of dilution, possibility of reusing, or improved protein and enzyme and pH stability. Generally, magnetic particles consist of ferromagnetic elements, such as iron, cobalt, manganese, zinc, and nickel, included in ferrites (e.g., $ZnFe_2O_4$) or lanthanum manganese perovskites ($La_{1-x}Sr_xMnO_3$) with controllable Curie temperature (Horák et al. 2009). Because the last three elements can induce toxicity (Lanone et al. 2009), they are not good candidates for applications in biomedicine. In contrast, iron-based particles, namely maghemite (γ-Fe_2O_3) and magnetite (Fe_3O_4), are the most appropriate for medical uses because they exhibit minor toxicity and were FDA-approved as MRI contrast agent (Hafeli et al. 2009; Thurman and Serkova 2013; Shubayev et al. 2009). Their additional advantage is that iron participates in human metabolism and is thus well-tolerated by the living organism. After the intracellular uptake, the iron oxide nanoparticles are metabolized in the lysosomes into a soluble, non-superparamagnetic form of iron that becomes a part of the normal iron pool (e.g., ferritin, hemoglobin).

Currently, there are three strategies to fabricate multifunctional magnetic particles. (i) Molecular biofunctionalization involves conjugation with proper ligands such as antibodies, proteins, and dyes to the magnetic particles to exhibit highly selective binding. (ii) Integration of the magnetic particles with other functional nanocomponents, such as quantum dots or metallic nanoparticles. Because they can exhibit several features synergistically and deliver more than one function simultaneously, such multifunctional magnetic nanoparticles could have unique advantages in biomedical applications. (iii) Paramagnetism that exhibits features such as magnetic targeting.

Magnetic particles intended for biomedical applications have to fulfill some specific requirements. (i) Surface of the particles has to be tailored not only to render them with non-toxicity, biocompatibility, non-genotoxicity, and non-immunogenicity, but also to provide suitable functional groups to allow immobilization of antibodies, peptides, and other biomolecules. Possible toxic effects can be significantly reduced if non-toxic precursors and reactants are used in the synthesis. (ii) Size of the magnetic nanoparticles has to be in the range of 10–50 nm. Particles <10 nm undergo efficient renal clearance that drastically reduces their half-life in the bloodstream (Gallo et al. 2013). Particles >50 nm have high value of remanent magnetization, which induces magnetically derived aggregation compromising application in the living organism. (iii) Magnetic nanoparticles have to also form stable aqueous dispersions without agglomeration; such colloids are called ferrofluids. The absence of aggregates is important, because they can clog the arteries, decreasing theranostic efficacy and resulting in embolization, localized hypoxia, necrosis, and hypersensitive reactions (Chandrasekharan et al. 2011). Although there are very many review works on the magnetic nano- and microparticles (Barry 2008; Elaissari and Fessi 2010; Hao et al. 2010; Ho et al. 2011; Thanh 2018; Panagiotopoulos et al. 2015; Park et al. 2009; Strehl et al. 2016; Mahmoudi et al. 2011), this chapter is going to describe

approaches to their development at the Institute of Macromolecular Chemistry in Prague, the Czech Republic, during the last twenty-five years.

A Reductionist View: Going from Microscale to Nanoscale

It is interesting to follow the development of particle sizes during the last forty years. Starting from the 1980s, the particles for ion exchange or gas chromatography were typically with size in hundred-micrometer range. Progress in high-pressure liquid chromatography then shifted the size of packings to 10 µm. Major discovery occurred, when John Ugelstad pioneered a process to manufacture monodisperse magnetic microbeads (1–5 µm) (Ugelstad 1984). With the emergence of nanotechnologies in the 2000s, there was a growing demand for nanoparticles with the size between 1 and 100 nm. This reduction of the particle size led to substantial changes in structure, which in turn greatly influenced the properties of the magnetic materials.

In addition to the size, also the shape matters. Out of many conceivable shapes (rod, wire, tube, membrane, slab, irregular, etc.), the spherical form is essential for practical applications if the best possible hydrodynamic (flow) properties are required. It offers important practical advantages of easy handling both in batch and continuous separation processes. Irregularly shaped particles are much more susceptible to mechanical attrition and breakdown to "fines" than spherical ones. In contrast to conventional particles with a broad particle size distribution, monodisperse particles (or at least with a narrow size distribution) provide a great advantage, because they possess uniform physical, chemical, and biological properties and do not aggregate in liquids so easily as polydisperse particles do. Moreover, the size uniformity guarantees reproducibility in the reactions and enables them to obtain a nice and regular array in microchip applications. Large particles have a disadvantage of a small specific surface area available for the attachment of functional groups or immobilization of biomolecules (including enzymes). This is the reason why microspheres and especially nanoparticles (micrometer size and smaller) are required on the market, because they ensure a sufficiently high specific surface area available for immobilization of reactive groups, enzymes, and other biologically active compounds and boost catalytic activity in phase transfer reactions. However, too small particles may cease to be magnetically responsive.

Principles of Magnetism

Magnetic Properties

Magnetism is a physical phenomenon that arises from the intrinsic properties of electron, namely its movement around the atomic nucleus and spin (Coey 2010).

Each electron in an atom has a magnetic moment that makes it act like a tiny magnet. Vector sum of all magnetic moments of atoms (μ; A m^{-2}) divided by volume (V; m^3) is called magnetization (M; A m^{-1}) as shown in Eq. (5.1):

$$M = \mu/V \qquad (5.1)$$

M depends on temperature and nature of the material and is related to the intensity of magnetic field (H; A m^{-1}) via magnetic susceptibility (χ; dimensionless) (Callister and Rethwisch 2006; Narayan 2009) according to Eq. (5.2):

$$M = \chi \cdot H \qquad (5.2)$$

χ provides information about the degree of the material magnetization in response to a magnetic field. It depends on the temperature according to Curie law in Eq. (5.3):

$$\chi = C/T \qquad (5.3)$$

where C is the material-specific Curie constant and T (K) is the absolute temperature. All materials can be divided into three classes depending on the magnetic ordering, magnitude, and temperature dependence of the magnetic susceptibility (Fig. 5.1) (Callister and Rethwisch 2006).

Diamagnetic ($\chi < 0$) substances have only paired electrons. Applied external magnetic field induces change in their orbital movement and consequently produces small magnetic moments, direction of which is opposite to the applied field. χ is negative and very small (typically -1×10^{-5}).

Paramagnetic ($\chi > 0$) materials have unpaired electrons that are randomly oriented within different atoms inside the matter. When magnetic field is applied, the electrons preferentially align along the field, but their magnetic moments act individually without mutual interactions. χ of the paramagnetic material is positive, ranging from 10^{-5} to 10^{-2}.

Ferro- and ferrimagnetic ($\chi \gg 0$) materials have unpaired electrons, which are parallel to each other and act simultaneously. The mutual alignment of magnetic
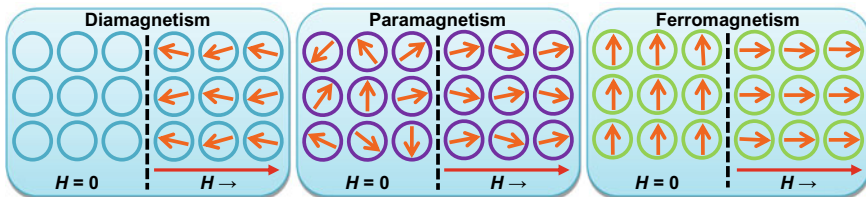
Fig. 5.1 Different types of magnetism. Orange arrows represent the magnetic moments; rings are atoms; $H = 0$ means that magnetic field is absent; $H \rightarrow$ is the presence of external magnetic field; red arrows show direction of applied magnetic field
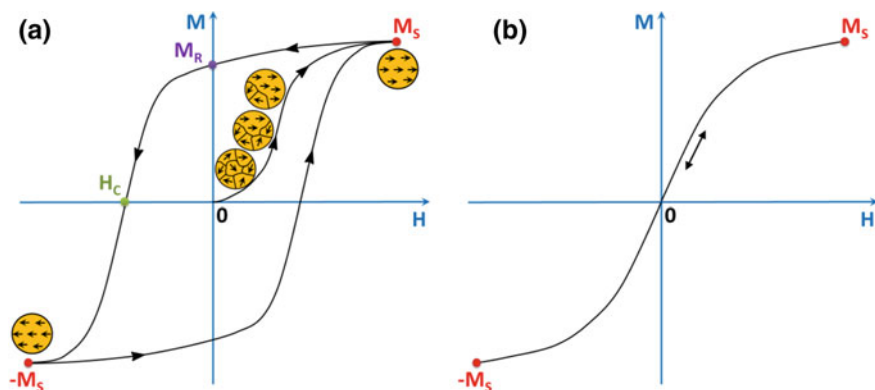
Fig. 5.2 Dependence of magnetization (M) of **a** ferromagnetic and **b** superparamagnetic materials on applied magnetic field (H); yellow circles schematically represent domain wall motion of multi-domain ferromagnet in the magnetic field

moments is preserved even in the absence of H. In contrast to paramagnetic materials, ferro- and ferrimagnetic substances exhibit much higher values of magnetic susceptibility (typically 10^{-2} to 10^6).

Dia- and paramagnetic materials interact with the external magnetic field weakly; therefore, they are not good candidates for applications involving manipulation and sensing through external magnetic field. At macroscopic level, any ferro- and ferrimagnetic materials are composed of small regions, where magnetic moments are uniformly oriented. The regions called magnetic domains are separated by magnetic (Bloch) walls. When external magnetic field is applied, the domains change shape and size by the movement of the Bloch walls. If H is high enough, domains grow, while their magnetic moments align in the direction of field, until the entire space in the substance is occupied (Fig. 5.2a). At this point, material reaches its highest value of magnetization—saturation magnetization (M_s). After removal of external magnetic field, the matter stays magnetized with remanent magnetization (M_r). Ferro- and ferrimagnetic materials have a coercive field (H_c) defined as a magnetic field of opposite sign needed for returning system to the state of $M = 0$. Because reorientation of magnetic domains takes some energy, in alternating magnetic field the magnetization will trace out a *hysteresis loop*. In addition, temperature has a strong impact on the magnetic properties. Thermal motion of atoms neutralizes the coupling forces between neighboring magnetic moments inducing their misalignment (Callister and Rethwisch 2006). As a result, M_s of ferro- and ferrimagnets decreases with increasing temperature and finally drops to zero at point called Curie temperature (T_c; 585 °C for Fe_3O_4) (Narayan 2009). Above this temperature, both ferro- and ferrimagnetic materials are paramagnetic.

As already mentioned above, the size has a crucial impact on the properties of the nanoparticles. Multi-domain structure of a ferromagnet cannot exist, when its size is smaller than a critical value. Because the formation of domain walls requires

energy, which at a certain size overcomes the magnetostatic energy required to orient magnetic moment in parallel direction to external magnetic field, single-domain state is favored. If the external field is removed, the thermal energy of a nanoparticle is sufficient to readily invert the orientation of magnetic moment and magnetization decreases to zero (Jun et al. 2008). Magnetic materials with above-described behavior are called superparamagnetic (Knobel et al. 2008). Superparamagnetic nanoparticles exhibit a net magnetization only when an external magnetic field is applied and relax to the initial state once the field has been removed. Superparamagnetic particles have a high value of M_s, but in contrast to ferromagnetic ones, they do not show hysteresis and $M_r = 0$ (Fig. 5.2b). The superparamagnetic state of iron oxide nanoparticles is observed if their size is <30 nm (Qiao et al. 2009; Ghazanfari et al. 2016). This behavior makes superparamagnetic iron oxide nanoparticles the most suitable candidates for biomedical applications, because they can be manipulated by magnetic field without aggregation induced by internal magnetization after removal of the external magnetic field. Moreover, hysteresis loop enables estimation of the concentration of iron oxide in the composite particles by comparing their saturation magnetization with that of neat iron oxide; the value has to agree with the Fe content found by chemical analysis. Although reported saturation magnetization of, e.g., bulk maghemite, is relatively high ($M_s = 74$ emu/g) (Hasany et al. 2012), real magnetic behavior of γ-Fe_2O_3 nanoparticles evaluated by vibrating sample magnetometer (VSM) is usually lower (e.g., $M_s = 56.5$ emu/g) (Zasońska et al. 2013). This is explained by the fact that the material is not pure maghemite due to various surface effects and imperfections in the crystal structure that are typical for nanoparticles (Goss 1988). The saturation magnetization of silica or polymer-modified γ-Fe_2O_3 nanoparticles is even lower due to the presence of coating.

Magnetic Polymer Nano- and Microspheres

Preparation of Magnetic Nanoparticles

The oldest technique for preparation of magnetic nanoparticles is grinding of bulk magnetite in a ball mill for 500–1000 h in the presence of a surfactant (Papell 1965). Nevertheless, in the past few decades a considerable attention has been paid to the development of the new methods of iron oxide nanoparticle fabrication in order to better control their properties, including morphology, size and its distribution, and availability of the reactive groups on the surface (Jeong et al. 2006).

Coprecipitation

Coprecipitation of stoichiometric amounts of Fe^{2+} and Fe^{3+} salts in the presence of a base (e.g., NaOH or NH_4OH) produces magnetic iron oxide according to Eq. (5.4):

$$2Fe^{3+} + Fe^{2+} + 8OH^- \rightarrow Fe_3O_4 + 4H_2O \qquad (5.4)$$
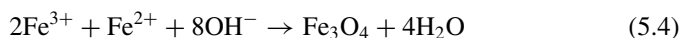
Because magnetite (Fe_3O_4) is chemically unstable in air or water, its controlled oxidation with sodium hypochlorite on maghemite (γ-Fe_2O_3) is preferred, see Eq. (5.5):

$$2Fe_3O_4 + NaOCl \rightarrow 3\gamma\text{-}Fe_2O_3 + NaCl \qquad (5.5)$$
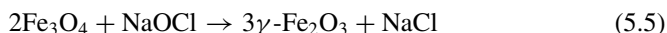
The key step in the formation of a stable magnetite/maghemite colloid consists in the careful removal of all the impurities remaining after the synthesis. Formation of a colloid by purification with water using magnetic separation is called peptization. The method allows preparation of particles with size in the range of 5–20 nm depending on the experimental conditions, such as type of iron salt (chlorides, sulphates, and nitrates), Fe^{2+}/Fe^{3+} molar ratio, pH, ionic strength, and temperature (Wu et al. 2008; Justin et al. 2017). To get an acid colloid, the Fe_3O_4 precipitate is stirred with aqueous perchloric acid ($HClO_4$). Sodium citrate is another electrostatic stabilizer providing negatively charged colloid (ζ-potential ~ −46 mV at pH 7). Tetramethylammonium hydroxide is example of agent providing an anionic colloid. Advantages of the coprecipitation method include preparation of hydrophilic particles with good magnetic properties and low cost of the starting materials. Disadvantage is a wide particle size distribution that results in irregular magnetic behavior.

Sol–Gel Reaction

Sol–gel reaction involves hydrolysis and condensation of metal alkoxides or alkoxide precursors, producing dispersion of oxide nanoparticles termed "sol" that forms three-dimensional oxide network after removal of the solvent by drying, gelling, or by chemical reaction (Hasany et al. 2012). Structure and properties of the produced gel depend on the type of the solvent, temperature, nature and concentration of the metal precursor, pH, and stirring speed (Laurent et al. 2008). The method provides some benefits, such as fabrication of materials with predetermined structure, which depends on experimental conditions, monodispersity, and good control of the particle size in the range of 20–200 nm. Nevertheless, because the method produces gel, it is not suitable for the formation of individual (non-aggregated) particles (Hasany et al. 2012).

Microemulsion

In this method, the iron oxide nanoparticles are synthesized inside nano-sized water droplets (typically ~10 nm in diameter) homogeneously dispersed in a continuous oil phase and stabilized by surfactants (Hasany et al. 2012). Water nano-reactors provide unique microenvironment for particle formation, limiting nucleation and growth (Teja and Koh 2009). Using this method, magnetic particles can be prepared

by two different approaches. First approach involves the addition of reducing or precipitating agent (e.g., hydrazine or NH_3) to the microemulsion of metal salt dissolved in an aqueous phase (Pillai et al. 1995). Second approach uses the dissolution of metal precursor and reducing agent in water phases of individual emulsions that are then mixed. As a result, water droplets containing two different reactants collide and produce nanoparticles (Pillai et al. 1995). The method allows preparation of nanoparticles with controlled particle morphology, size in the range of 4–15 nm, narrow size distribution, and high M_s (Gupta and Gupta 2005). Significant disadvantage of this approach is problem in scaling-up and the presence of impurities (residual surfactants).

Flame Spray Pyrolysis

Flame spray pyrolysis is based on the combustion of aerosols or organic solutions, which contain metal precursors (e.g., nitrates or carbonates), in flame (Teoh et al. 2010). The advantage of this procedure is large-scale production of high-purity nonporous particles with size 5–60 nm (Gupta and Gupta 2005). The main disadvantage is aggregation of the particles and their broad size distribution (Kammler et al. 2001).

Thermal Decomposition

Thermal decomposition of Fe-organic precursors, such as Fe(III) carboxylates (typically oleate, mandelate, or glucuronate), $Fe(CO)_5$, Fe(III) *N*-nitroso-*N*-phenylhydroxylamine, and Fe(III) acetylacetonate, produces magnetic iron oxide nanoparticles in the presence of a stabilizer (e.g., oleic acid or oleylamine) in a high-boiling solvent (e.g., octyl ether or octadec-1-ene) (Hufschmid et al. 2015; Park et al. 2004; Saravanan et al. 2003; Wang et al. 2011; Kostiv et al. 2017). The method allows large-scale preparation of monodisperse magnetic nanoparticles with high crystallinity and precise control of size in the range of 2–30 nm (Hufschmid et al. 2015). Increasing OA concentration decreases the particle size, while with increasing boiling point of the solvent, diameter of Fe_3O_4 nanoparticles increases (Patsula et al. 2014). The main disadvantage consists of usage of high temperature during the synthesis and hydrophobic nature of coating on the particles, which requires post-synthesis modification to make them water-dispersible (Wu et al. 2008). Properties of the iron oxide nanoparticles depend on the reaction temperature and time, type of solvent, iron precursor, and stabilizer and on their initial ratios in the reaction mixture (Roca et al. 2006; Majewski and Thierry 2007). The mechanism of this process involves three steps: (i) thermal decomposition of an iron precursor at elevated temperature followed by formation of poly(iron oxo) clusters serving as building blocks for particles, (ii) short burst nucleation, and (iii) nanoparticle growth at additional temperature increase (Fig. 5.3) (Park et al. 2004; Kwon et al. 2007). Due to the combination of short nucleation time and the presence of the stabilizer, which
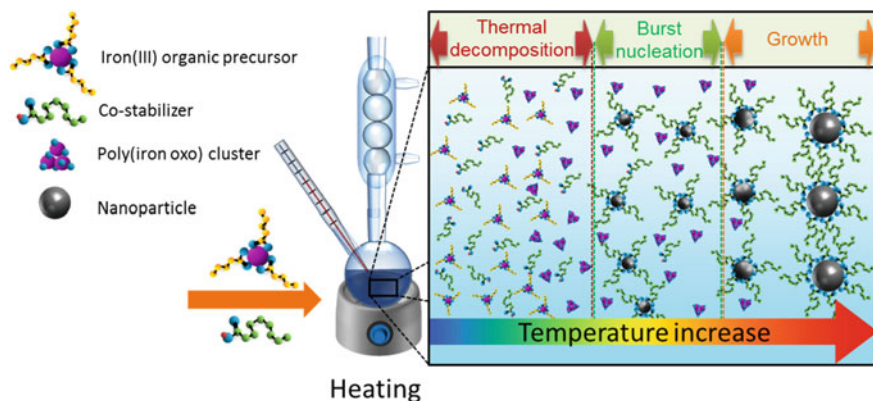
Fig. 5.3 Scheme of iron oxide nanoparticle formation by the thermal decomposition

prevents aggregation of the nuclei and ensures uniform conditions for each particle growth, the resulting particles are monodisperse.

Other Methods

Other methods for the preparation of the magnetic nanoparticles involve electrochemical, (hydro)solvothermal synthesis, sonolysis or biosynthesis (Wu et al. 2008; Laurent et al. 2008). These techniques are generally quite complex, requiring high-cost starting materials and equipment (autoclave for high temperature and pressure) and therefore are less frequently used. Nanoparticles can be made also by biomimetic processes like biomineralization in ferritin or magnetosomes are produced by magnetotactic bacteria. Another technique includes the layer-by-layer method based on the electrostatic attraction between the oppositely charged particles. It produces coated colloids of different shapes, sizes, uniform layers of diverse compositions, and controllable thickness.

Preparation of Magnetic Microspheres

The larger size of magnetic microspheres is more favorable for recovery by collection in an external magnetic field than the nanoparticles. To be able to effectively intercept a 10-μm cell, the microsphere size should be also in the micrometer range.

Magnetic microspheres are prepared in a number of ways usually involving the coating of superparamagnetic particles (most often iron oxides) with synthetic polymers by the solvent evaporation method. Alternatively, conventional supports are "past magnetized" by treatment with magnetic ferrofluid, or magnetic particles are

precipitated in situ in a polymeric matrix, for example, by chemical metal deposition. As far as polymers are concerned, they can be styrene, methyl methacrylate, 2-hydroxyethyl methacrylate (HEMA), glycidyl methacrylate (GMA), or thermoresponsive *N*-isopropylacrylamide (Macková et al. 2013). Surface functionalization of the nano- and microspheres also allows further attachment of biomolecules. Alternatively, magnetite is incorporated into the particles during emulsion polymerization (Horák et al. 2007). Suspension polymerization, typically stabilized by high-molecular-weight poly(vinyl alcohol) (PVA) or poly(*N*-vinylpyrrolidone) (PVP), has an advantage that porous particle can be prepared by the addition of a porogen, e.g., a mixture of cyclohexanol (a thermodynamically good solvent for poly(2-hydroxyethyl methacrylate)—PHEMA) and dodecan-1-ol (a thermodynamically poor solvent) in the organic phase dispersed in water. An important requirement for magnetic polymer nano- and microspheres is that the magnetic material has to be homogeneously distributed and properly encapsulated in the polymer particles to avoid any leakage of iron oxide and its interaction with a surrounding medium and to resist non-specific protein adsorption.

Multistep Swelling and Polymerization

Multistep swelling and polymerization are a complex and tedious procedure to produce robust separated (non-aggregated) monodisperse macroporous polymer microspheres based on monodisperse seeds (Fig. 5.4). Over the other techniques, it has the advantage of being industrializable in large batches, as shown by the continuous commercial success of magnetic polystyrene microspheres prepared according to the Ugelstad pioneering work (Ugelstad 1984). The condition for the successful formation of monodisperse particles is that the number of initial seeds remains fixed during the whole process; subsequently, they only increase in size by swelling based on thermodynamic principles, maintaining monodispersity of initial seeds throughout the whole process. The seeds, e.g., 0.7 μm in size, are typically prepared by emulsifier-free emulsion polymerization of styrene. The swelling time has to be tuned to completely transfer all the swelling (both the pre-swelling and that of monomer) emulsion into the particles.

The synthesis is exemplified on copolymerization of HEMA or GMA and ethylene dimethacrylate (EDMA). Resulting PHEMA is hydrophilic, offering the advantage of biocompatibility and low non-specific protein adsorption (compared with hydrophobic matrices), which are so important in the biomedical field. Moreover, PHEMA has a long history of application as a non-toxic and mechanically stable material (Wichterle and Lim 1960). In contrast, the greatest advantage of poly(glycidyl methacrylate) (PGMA) consists in the presence of easily transformable oxirane groups. Chemical modification is usually performed via ring-opening of the oxirane. Oxirane groups can be hydrolyzed to vicinal diols or directly reacted with miscellaneous substances, e.g., amines, aminopyridines, propanesultone, and phenol (May 1988). By oxidation with sodium periodate, PGMA can be transformed to
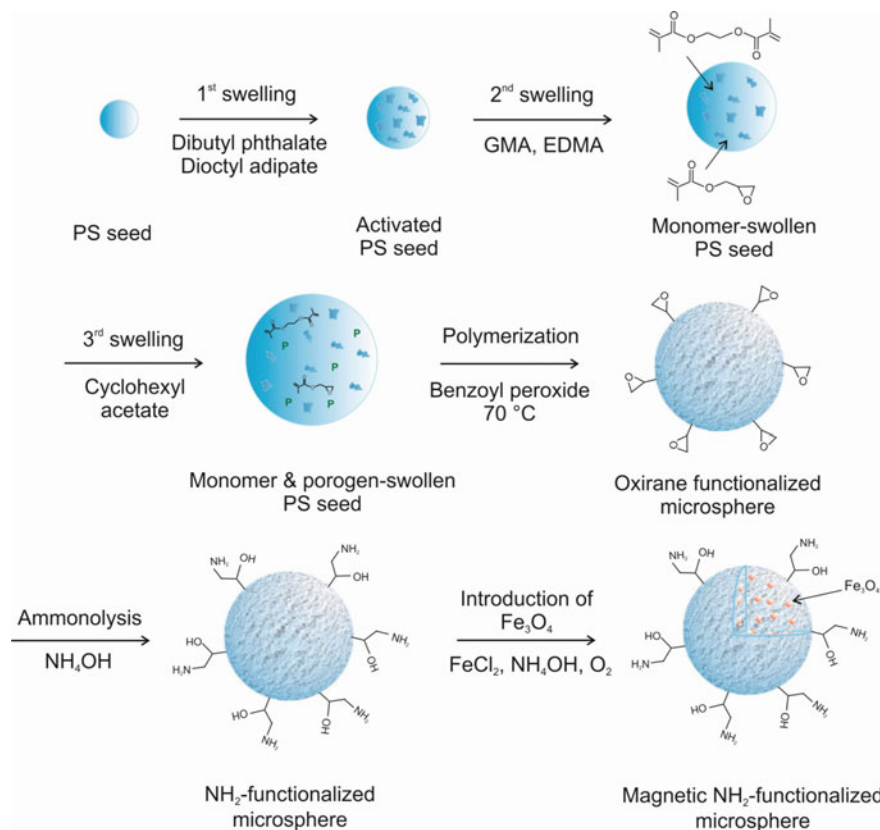
Fig. 5.4 Preparation of monodisperse macroporous PGMA-NH$_2$ microspheres by multi-step swelling polymerization and precipitation of iron oxide inside the pores; GMA—glycidyl methacrylate, EDMA—ethylene dimethacrylate, PS—polystyrene. Reproduced with permission from (Kuan et al. 2014). Copyright 2014, with permission from Elsevier (Mosby, Saunders, Churchill Livingstone, Academic Press)

polymers containing aldehyde groups that easily immobilize proteins and antibodies via a Schiff base linkage.

First, the seeds are activated (pre-swelled) with a highly water-insoluble compound, such as dibutyl phthalate and/or dioctyl adipate, to increase their volume by approximately one thousand times and enable subsequent swelling with the monomers, initiator, and porogen (e.g., cyclohexyl acetate) in the second and third step. This is followed in the fourth step by 2-hydroxyethyl cellulose- and (hydroxypropyl)methylcellulose-stabilized and benzoyl peroxide-initiated suspension polymerization of HEMA (or GMA) and EDMA (Fig. 5.4). The prepared microspheres contain macropores formed by phase separation during the polymerization in the presence of sufficient amount of the porogen (cyclohexyl acetate). To produce magnetic carriers (Horák et al. 2012), magnetite (Fe$_3$O$_4$) is prepared inside the

pores of the macroporous microspheres by the precipitation of a ferrous salt with ammonium hydroxide and oxidation of $Fe(OH)_2$ with oxygen (Fig. 5.4). The precipitation procedure can be repeated to increase the amount of loaded iron oxide. The TEM micrograph of a cross section of a magnetic ammonolyzed poly(glycidyl methacrylate) (PGMA-NH_2) microsphere shows that iron oxide (dark spots) is dispersed mainly within the particle pores (Fig. 5.5a), while atomic force microscopy (AFM) displays three-dimensional topography (Fig. 5.5b).

Solvent Evaporation

Solvent evaporation is the easiest way to encapsulate magnetic particles in a polymer. The resulting microparticles, however, are polydisperse and usually rather large. The magnetic material is dispersed in a polymer solution (typically dichloromethane) and then emulsified with a surfactant until solvent evaporates. 125–250 µm magnetic spherical particles are prepared from a chloroform solution of poly(vinyl butyral) containing magnetite, which is stirred in water with poly(vinyl alcohol) (PVA), sodium dodecyl sulfate, and Pluronic F6800 (ethylene oxide/propylene oxide block copolymer) emulsifiers until chloroform evaporates (Tanyolac and Ozdural 2000). Alternatively, magnetite nanoparticles and model drugs are encapsulated in poly(D,L-lactic-*co*-glycolic acid) (Shubhra et al. 2014).

Sol–Gel Transition of Viscose

Magnetic bead cellulose (MBC; Fig. 5.6) is prepared using sol–gel transition of viscose in the presence of maghemite (γ-Fe_2O_3) nanoparticles (Yan et al. 2013). Cellulose microspheres are highly porous and swollen in water, consisting of about 85% water, which enables penetration of large molecules into the cellulose bulk. With negligible non-specific adsorption of biological substances and the possibility of chemical modification, the cellulose materials are suitable as carriers in biochemical and biological applications (Rittich et al. 2002).

Other Techniques

Other techniques proposed for the preparation of magnetic polymer particles include heterogeneous polymerizations, such as microfluidic-based emulsification and polymerization, (mini)emulsion or suspension polymerization in the presence of iron oxide; inverse emulsion is an option (Qiu et al. 2015). However, it is difficult to increase amount of iron oxide and prevent its localization on the particle surface. Alternatively, magnetic PHEMA or PGMA microspheres are prepared in a simple one-step procedure by cellulose acetate butyrate-stabilized dispersion polymerization in toluene/2-methylpropan-1-ol mixture in the presence of oleic acid-coated iron oxides (Horák et al. 2000; Horák 2001). Advantage of the dispersion polymerization
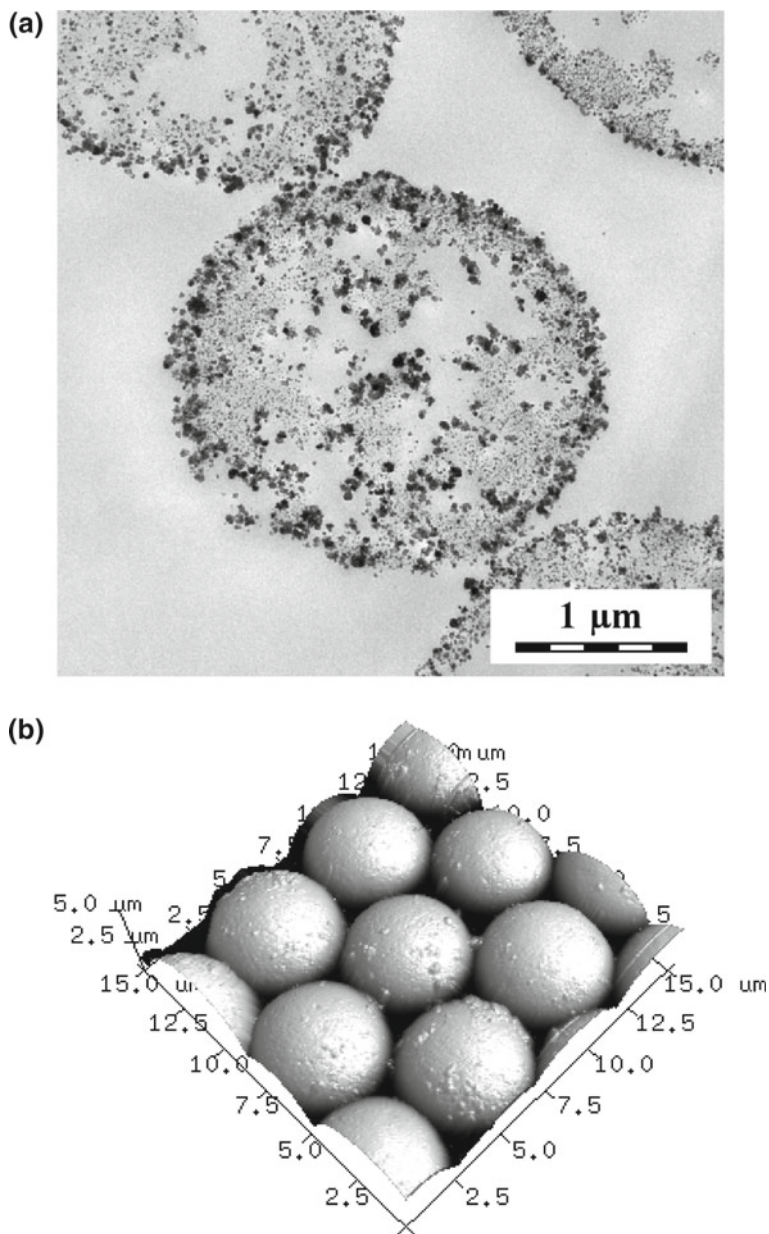
Fig. 5.5 a TEM micrograph of magnetic PGMA-NH$_2$ microsphere cross section and **b** 3D AFM topography. Reproduced with permission from (Horák et al. 2014). Copyright 2014, with permission from John Wiley & Sons (Wiley-Interscience, Wiley-VCH, Wiley-Blackwell)
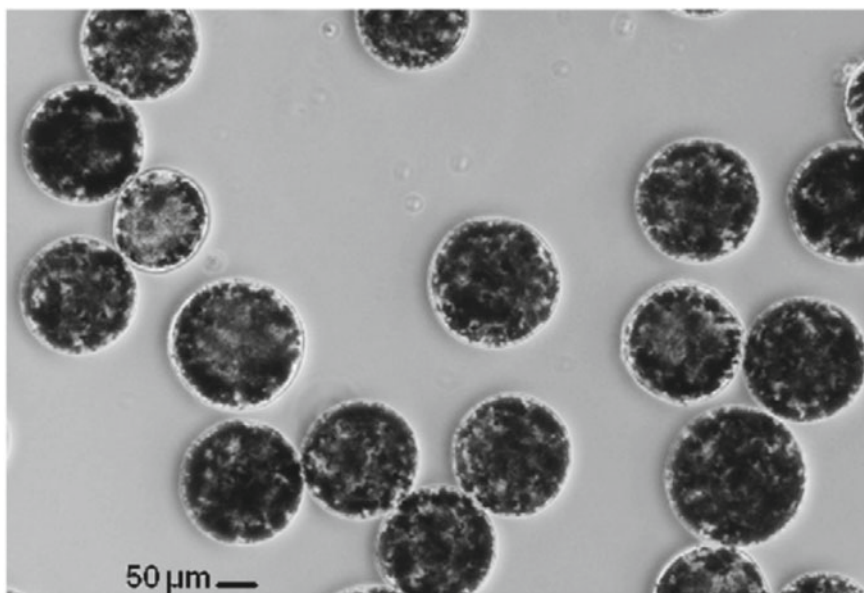
Fig. 5.6 Magnetic macroporous bead cellulose; particle size 125–250 µm. Reproduced with permission from (Rotková et al. 2009). Copyright 2009, with permission from Elsevier (Mosby, Saunders, Churchill Livingstone, Academic Press)

is that it can provide monodisperse particles in the micrometer size range if the reaction conditions are optimized. The size of the particles can be easily tuned by changing the reaction conditions (e.g., kind of stabilizer and initiator and their concentrations). The size of the microspheres also depends on the propan-2-ol/toluene and iron oxide/monomer ratios, monomer concentration, and polymerization temperature.

Surface Modification of the Nano- and Microspheres and Their Interaction with Environment

Coating of the particle surface by a biocompatible shell is a necessary condition to ensure stability in media, prevent aggregation, minimize toxicity, and control interaction of the particles with living cells in a well-defined and controllable way, which enables particle internalization by the cells (Fig. 5.7). For example, a receptor-mediated interaction is realized by immobilization of specific antibodies on the particle surface. Also, polymer coatings can be attractive for cell membrane; such a particle–cell interaction is non-specific. Nanoparticles can adhere to the cell surface or be engulfed into the cells through their membrane (Parton et al. 2007). Increased affinity of the particles to the cell surface is needed for cell labeling applications in regenerative medicine or preparation of drug carriers for cancer treatment. On
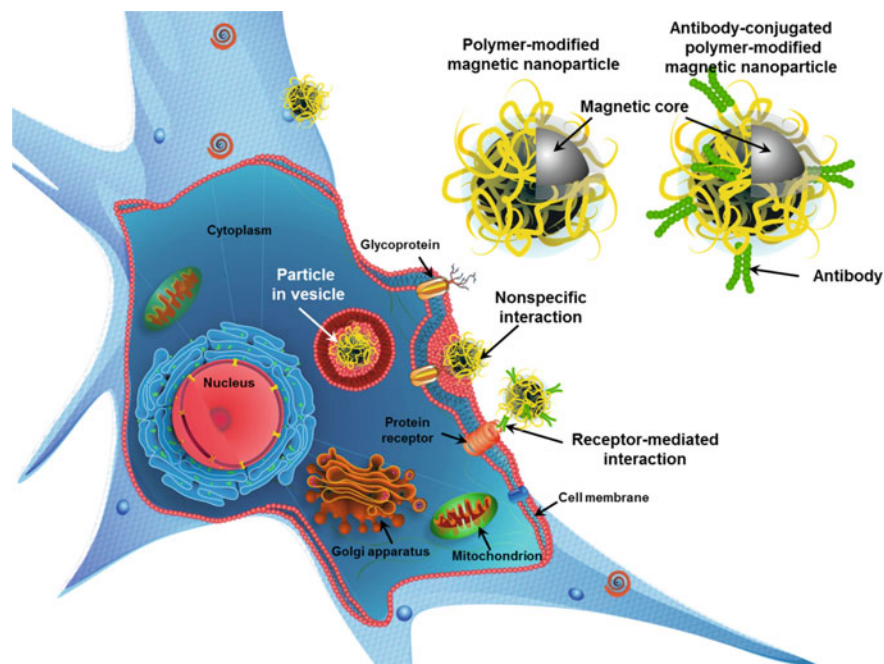
Fig. 5.7 Interactions of magnetic nanoparticles with a living cell

the other hand, low affinity to cell membrane will be beneficial for preparation of long-time circulating contrast agents for MRI of tissues.

Colloidal Stability

Superparamagnetic iron oxide nanoparticles have a large surface-to-volume ratio and high surface energy. To minimize excessive energy, particles naturally tend to aggregate, which makes them useless in biomedical applications. In addition, the neat uncoated nanoparticles are not chemically stable and can be rapidly oxidized in the presence of oxygen losing magnetic properties. Electrostatic stabilization is possible; however, the particles tend to aggregate by changing pH or ionic strength of the medium. Steric stabilization based on coating of the nanoparticle surface with polymers, such as dextran, PVA, poly(ethylene glycol) (PEG), is therefore preferred, providing a physical steric barrier and preventing these undesirable physical and chemical processes in microenvironment. Stability of the particle systems is governed by the balance between different attraction and repulsive forces, i.e., van der Waals attraction, double-layer electrostatic repulsion, and steric interaction (Tadros and Tadros 2006; Kontogeorgis and Kiil 2016). To maintain colloidal stability, the

attraction forces must be as low as possible and the repulsive forces must be sufficient to counteract them. This can be achieved either electrostatically or sterically (Fig. 5.8).

Electrostatic stabilization (using perchlorate, citrate, nitrate or tetramethylammonium ions) is based on the presence of ionic charges on the surface of the particles that results in their mutual repulsion. This effective surface charge determines the distribution of counter and co-ions from the dispersant in the particle surroundings and forces them to move with the particle. Such organization of ions around the particle is called electrical double layer (Tadros and Tadros 2006). Counter-ions located near to the particle surface are strongly bonded and form the Stern layer (Fig. 5.8). Ions located further are loosely bonded and form diffusion layer. The potential at the slipping plane that separates Stern layer from the continuous phase is called ζ-potential and is used as a reference value for the establishment of electrostatic stability of colloids. To achieve maximum stability, ζ-potential should be as large as possible, i.e., the particle colloid is considered to be stable when ζ-potential is > +30 or < −30 mV (Greenwood 2003). The electrostatic repulsion force becomes weaker as the ionic strength of the medium increases. Thus, use of electrostatically stabilized colloids is problematic in biomedical applications that require high ionic strength solutions isotonic with blood.

Steric stabilization of particles is based on the adsorption of nonionic amphiphilic macromolecules on the particle surface. When two particles with adsorbed polymer chains approach each other, the shells interact and two different situations can occur; chains can overlap or undergo compression (Tadros and Tadros 2006). Both these phenomena result in the increased local polymer concentration at the site of interaction, triggering thus strong repulsion. First effect is based on increased osmotic pressure in the overlap area due to the adverse mixing of polymer chains and moves solvent molecules separating the particles. Second effect, compression of the polymer chains, is associated with loss of configurational entropy (Goddard and Gruber 1999). The compressed macromolecules tend to regain their extended conformations and the only way how to attain this is particle disengagement. Sterically stabilized particles are much less sensitive to electrolytes than electrostatically stabilized ones
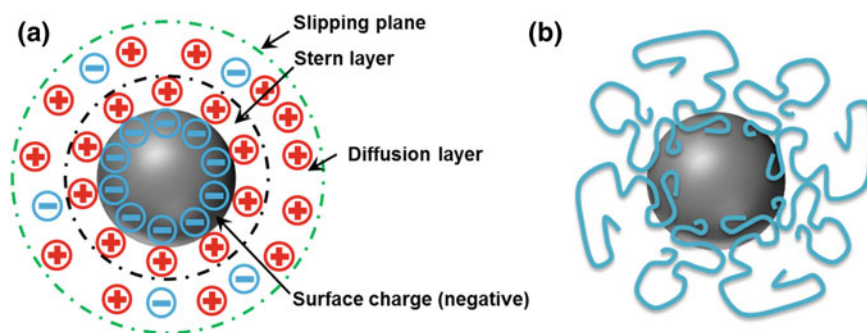
Fig. 5.8 Particles stabilized by **a** electrostatic and **b** steric repulsion
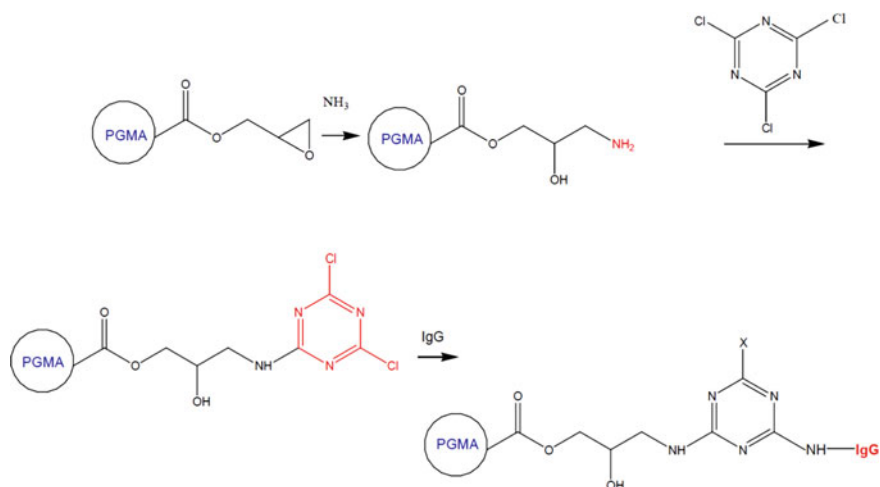
Fig. 5.9 Ammonolysis of PGMA microspheres, activation with 2,4,6-trichloro-1,3,5-triazine and immobilization of antibody; PGMA—poly(glycidyl methacrylate). Reproduced with permission from (Horák and Hochel 2005). Copyright 2005, with permission from De Gruyter

and can be used at a high ionic strength; therefore, they are appropriate for biomedical applications.

Carboxyl and Amino Group-Containing Particles

Very useful is the introduction of functional groups on the particles to make covalent attachment of biomolecules possible. Among them, carboxyl and amino groups play priority. For example, carboxyl groups were obtained by oxidation of PHEMA (or hydrolyzed PGMA) microspheres with potassium permanganate (Horák et al. 2007). Optionally, carboxyl groups can be introduced by hydrolysis of 2-[(methoxycarbonyl)methoxy]ethyl methacrylate (MCMEMA) comonomer in PHEMA microspheres to covalently couple trypsin via EDC/sulfo-NHS chemistry. Amino groups can be conveniently obtained by ammonolysis of PGMA (Fig. 5.9). These newly developed biofunctionalized magnetic microspheres demonstrate the possibility of long-term storage without significant changes, which thus indicates great potential for their successful use in bioapplications (Horák et al. 2012).

Antifouling Properties

The major problem with biomedical applications of the magnetic polymer particles is connected with the undesirable non-specific adsorption of cells and biomolecules,

mainly proteins from cell lysates or complex aqueous media. Therefore, to minimize the adverse nonspecific interactions, it is important to coat the particle surface with various natural or synthetic blocking agents, e.g., albumin crosslinked with glutaraldehyde (Horák et al. 2013), zwitterionic phosphorylcholine (Lewis 2000), sulfobetaine, and carboxybetaine or non-charged polymers, such as poly(ethylene glycol) (Shang et al. 2006) and poly[N-(2-hydroxypropyl) methacrylamide] (Fairbanks et al. 2014). Non-specific protein adsorption on the magnetic PGMA-NH$_2$ microspheres was suppressed by covering them with three generations of a compact amino acid dendritic network (Ser-Lys-Ser/Lys-Ser/Lys-Ser) using peptide chemistry (Fig. 5.10) (Hlídková et al. 2017). The resulting particles did not aggregate under physiological conditions and contained ~1 mmol of NH$_2$/g that was available for further modifications. Alkyne groups accessible for click chemistry were introduced to the dendrimer-coated particles by a reaction with 4-pentynoic acid. The ability to undergo a click reaction was then confirmed by coupling with an ^{125}I-N$_3$-RGDS peptide (Fig. 5.10).
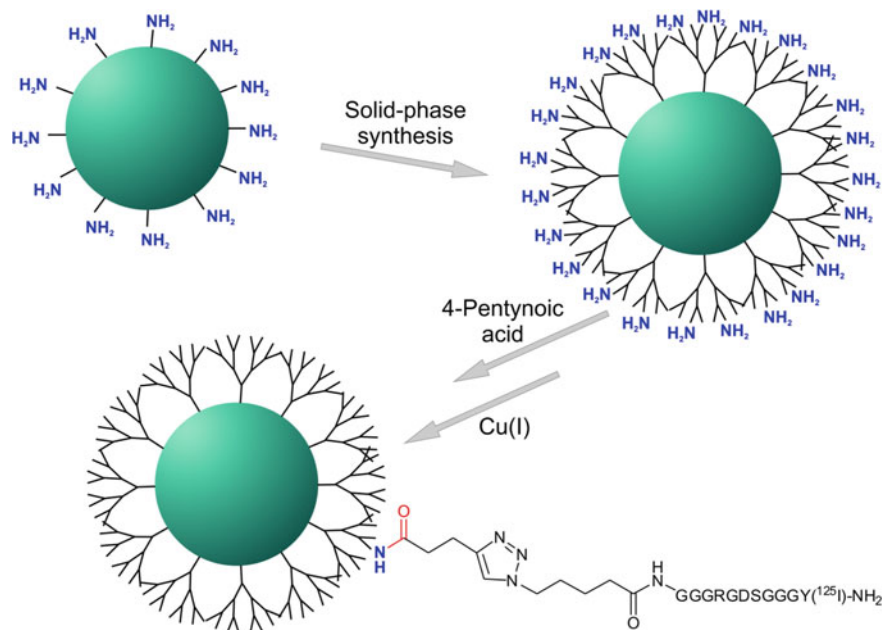
Fig. 5.10 Modification of magnetic PGMA-NH$_2$ microspheres with dendrimer, 4-pentynoic acid, and click reaction with ^{125}I-N$_3$-RGDS peptide. Reproduced with permission from (Hlídková et al. 2017). Copyright 2017, American Chemical Society

Surface Coatings

To achieve the efficient and specific cellular uptake of magnetic nanoparticles requires the nanoparticle surface to be modified with suitable ligands or transfection agents, which also enhances colloid stability and cell interactions and minimizes toxicity. Coatings significantly increase the size of the nanoparticles, which may affect their penetration ability and metabolic clearance rate in the body. Functionalization of the particle surface can be done in situ (during the synthesis) or as a postsynthetic procedure. In both cases, binding of coating molecules to the surface of magnetic cores is generally performed either by end-grafting or by surface encapsulation. Two approaches are used to graft polymer chains onto particles: "grafting-to" and "grafting-from" (Zhao and Brittain 2000). In the "grafting-to" system, end-functionalized polymers react with surface groups of nanoparticles. In the "grafting-from" method (also called surface-initiated polymerization), polymer chains grow in situ from initiators that have been anchored to the surface of the nanoparticles. The latter method allows easy control of the shell thickness and brush density by varying the concentrations of the hydrophilic monomer and initiator during living polymerization. Different modification strategies and coating agents result in the formation of magnetic/composite nanoparticles with different morphology, such as core–shell, multi-core–shell, and strawberry-like (Fig. 5.11) (Horák et al. 2007; Ramimoghadam et al. 2014). However, the majority of biomedical applications require core–shell morphology, where the magnetic core is enclosed in the outer coating layer (Umut 2013).

In contrast to other types of the nanoparticles, surface of iron oxide particles contains a large number of hydroxyl groups that can be easily functionalized (Dave and Chopda 2014). A variety of materials were used for particle modification to make them colloidally stable and biocompatible. These materials include low-molecular organic compounds (citric acid, mannose, bisphosphonates, etc. (Laurent et al. 2008; Borisova et al. 2014), noble metals (Au, Ag, Pt, etc.) (Duan and Wang 2013), silica (Zasońska et al. 2016), or polymers. Polymer coatings can be divided into natural and synthetic ones. From the vast variety of natural polymers, the most commonly used are dextran, chitosan, alginate, heparin, hyaluronic acid, and starch (Uthaman
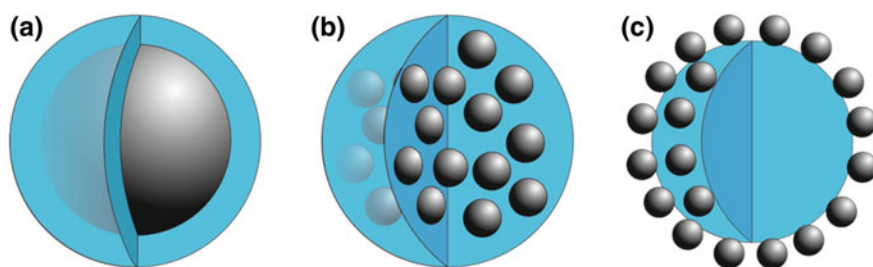
Fig. 5.11 Different morphologies of composite polymer/iron oxide nanoparticles: **a** core–shell, **b** multi-core–shell, and **c** strawberry-like

et al. 2015; Covaliu et al. 2011). From synthetic polymers, great attention is paid to poly(ethylene glycol) (PEG), poly(ethyleneimine), poly(*N*-vinylpyrrolidone), and poly(*N,N*-dimethylacrylamide) (PDMA) (Hlídková et al. 2017; Zasońska et al. 2013; Babič et al. 2009; Zasonska et al. 2012).

Poly(L-Lysine)

Poly(L-lysine) (PLL; preferably of $M_w = 93,800$) is a suitable modification agent of the surface of the nanoparticles with the aim of promoting cellular uptake (Babič et al. 2008). Binding is achieved via the electrostatic attraction of opposite charges of PLL and iron oxide surface.

Poly(Ethylene Glycol)

PEG is polyether synthesized by ionic ring-opening polymerization (Vohlídal 1995; Bailey and Koleske 1976) of oxirane (Fig. 5.12) and is available with different molecular weights and terminal functional groups. This non-ionic polymer is well soluble in water and organic solvents, cheap, non-toxic (biocompatible), provides strong steric hindrances and is also approved by FDA in the USA for clinical applications. There are several strategies for introducing PEG onto the surface of particles, namely physisorption, "grafting-to" and "grafting-from." Although the "grafting-from" strategy enables immobilization of PEG with high grafting density, the "grafting-to" approach is less elaborate and time-consuming.

PEGylated surfaces resist cell and protein adsorption and have a high tolerance to host immune system. Functionalization of proteins and liposomes with PEG significantly increases their half-life in bloodstream, making it the most widely used polymer for the preparation of pharmaceutical formulations (Harris and Zalipsky 1997). Prolonged half-life in blood (invisibility to the reticuloendothelial system) improves the likelihood of reaching target tumor cells, e.g., by enhanced permeability and retention effect. Moreover, PEGylation of magnetic particles significantly reduces their adhesion on glass or poly(dimethylsiloxane) walls. PEGylation of
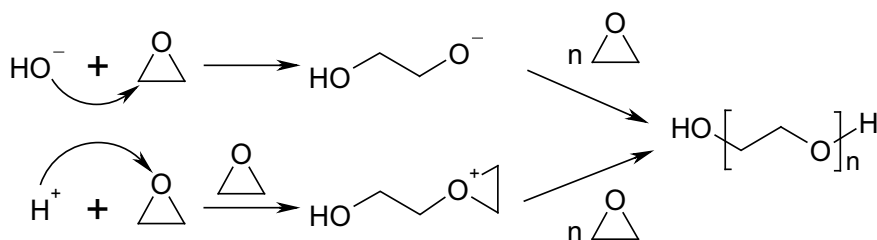
Fig. 5.12 Synthesis of PEG by anion- and cation-initiated ring-opening polymerization of oxirane
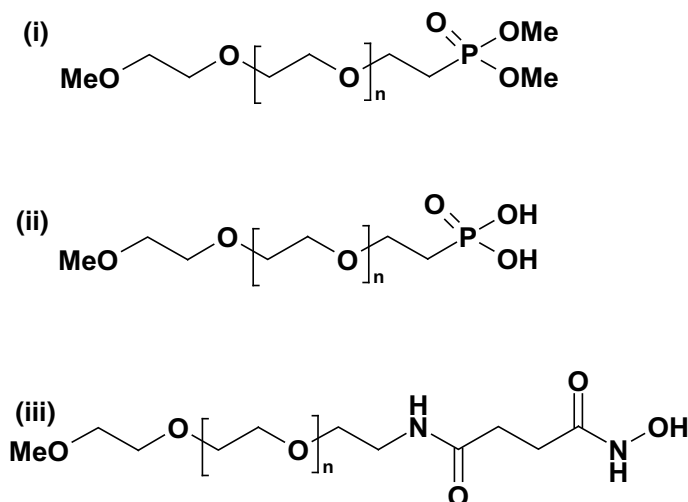
Fig. 5.13 Structure of synthesized PEG derivatives: (i) dimethyl ester of phosphonic acid-terminated-PEG, (ii) phosphonic acid-terminated-PEG, and (iii) hydroxamic acid-terminated-PEG. Reproduced with permission from (Patsula et al. 2014). Copyright 2014, with permission from Springer-Verlag (Kluwer, Humana, Birkhäuser)

hydrophobic Fe_3O_4 particles via a ligand exchange with hydroxamic or phosphonic acid-terminated methyl-PEG (Fig. 5.13) with a strong affinity to iron made phase transfer of the particles into water possible (Patsula et al. 2014).

Conventional approach involves coating of magnetic PHEMA or PGMA microspheres with amino or carboxyl-functionalized poly(ethylene glycol) (PEG) via 1-ethyl-3-(3-dimethylaminopropyl) carbodiimide/N-hydroxysuccinimide (EDC/NHS) chemistry (Fig. 5.14).

Poly(*N*,*N*-Dimethylacrylamide) (PDMA) and Poly(*N*-Propargylacrylamide) (PPRA)

Solution radical polymerization of *N,N*-dimethylacrylamide (DMA) in the presence of maghemite yields PDMA-coated γ-Fe_2O_3 nanoparticles. If the molecular weight of PDMA is <50,000 Da, it is cleared by kidneys (Yang and Kopeček 2015). Magnetic PHEMA microspheres were grafted with PDMA using click reaction to couple chain transfer agent [CTA; 2-azidoethyl ester of 2-(ethylsulfanylthiocarbonylsulfanyl)propionic acid] on propargylamine-modified microspheres, followed by reversible addition–fragmentation chain transfer (RAFT) polymerization of *N,N*-dimethylacrylamide (DMA; Fig. 5.15) (Cao et al. 2016). It is the advantage of controlled radical techniques including also nitroxide-mediated polymerization (NMP) and atom transfer radical polymerization (ATRP) that the synthesis of highly defined polymers is possible. And benefits of the click reactions
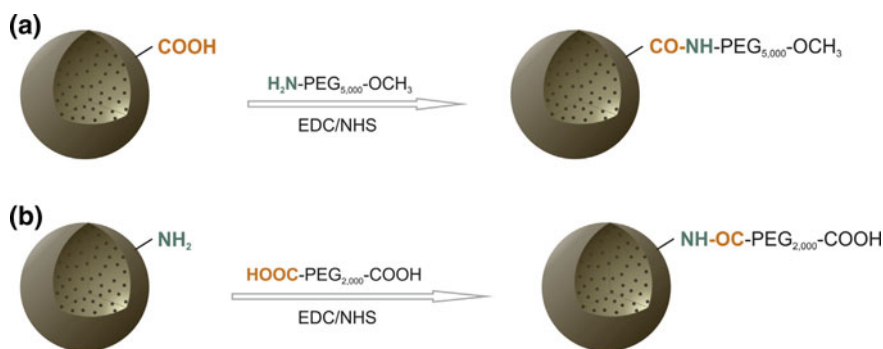
Fig. 5.14 Surface modification of **a** magnetic PHEMA-COOH and **b** magnetic PGMA-NH₂ microspheres with PEG; EDC—1-ethyl-3-(3-dimethylaminopropyl) carbodiimide, NHS—*N*-hydroxysuccinimide. Reproduced with permission from (Horák et al. 2015). Copyright 2015, with permission from Elsevier (Mosby, Saunders, Churchill Livingstone, Academic Press)
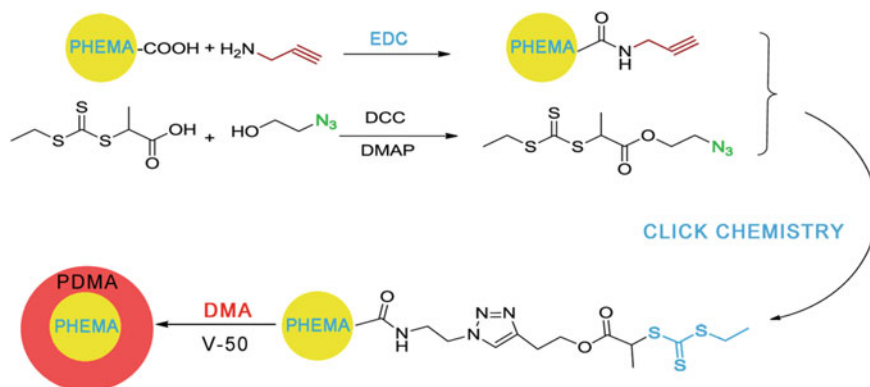
Fig. 5.15 Attachment of azido-activated CTA to magnetic PHEMA-propargylamine microspheres using azido-alkyne click reaction; CTA—chain transfer agent, EDC—*N*-(3-dimethylaminopropyl)-*N*′-ethylcarbodiimide hydrochloride, DCC—*N,N*′-dicyclohexylcarbodiimide, DMAP—4-dimethylaminopyridine, DMA—*N,N*-dimethylacrylamide, V-50—2,2′-azobis(2-methylpropionamidine) dihydrochloride, and PHEMA—poly(2-hydroxyethyl methacrylate). Reproduced with permission from (Cao et al. 2016). Copyright 2016, with permission from John Wiley & Sons (Wiley-Interscience, Wiley-VCH, Wiley-Blackwell)

consist in that they allow mild (typically physiological) reaction conditions and provide high chemical selectivity, which makes it similar to many naturally occurring reactions. They do not require stringent reaction conditions, such as harmful solvents or high temperatures, can be easily performed without extensive purification, and a high chemical yield is ensured due to the stereospecificity of the reaction.

Magnetic PPRA microspheres prepared by the precipitation polymerization of propargylacrylamide (PRA) in a toluene/propan-2-ol medium in the presence of oleic acid-coated Fe₃O₄ enable a click reaction with an azido-end-functionalized peptide
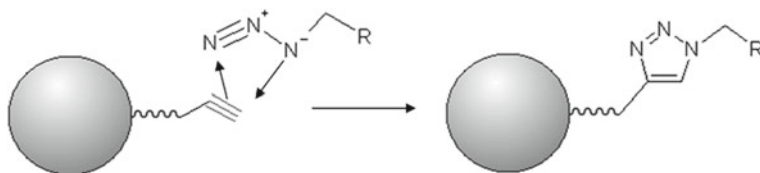
Fig. 5.16 Labeling of magnetic poly(*N*-propargylacrylamide) microspheres; *R* = 4-phenylalanine or GGGRGDSGGY(^{125}I)–NH$_2$ peptide. Reproduced with permission from (Macková et al. 2011). Copyright 2011, with permission from John Wiley & Sons (Wiley-Interscience, Wiley-VCH, Wiley-Blackwell)

[radiolabeled azidopentanoyl–GGGRGDSGGGY [(Pongrac et al. 2016) I)–NH$_2$] and 4-azidophenylalanine using a Cu(I)-catalyzed 1,3-dipolar azide–alkyne cycloaddition reaction in water (Fig. 5.16) (Macková et al. 2011). Also azide-modified proteins, antibodies, oligonucleotides, carbohydrates or cells can be bound to the alkyne-containing microspheres.

Carbohydrates

Dextran or (carboxymethyl)dextran is the most common coating of iron oxides prepared by either their precipitation in a dextran solution or dextran solution is added after alkaline precipitation. Carboxydextran has the advantage of the good affinity of COOH groups to Fe^{2+} ions. Dextran-coated iron oxides were approved by FDA under trade names Resovist® (Bayer-Schering), Sinerem® (Guerbet), Feridex® (AMAG Pharmaceuticals), Combidex® (Radboudumc), or Endorem® (Guerbet) as contrast agents in MRI of tissues, though the companies withdraw the approval. The reason consists in that the radiologists prefer white contrast of Gd complexes to the black iron oxides. Another effective carbohydrate stabilizer preventing particle aggregation is D-mannose (Horák et al. 2007). Recently, increased attention is paid to synthetic carbohydrate-based polymers due to their ability to be recognized by cells (Slavin et al. 2011). They are biocompatible, because they mimic properties of natural carbohydrates (Narain 2011). As an example, poly(3-*O*-methacryloyl-α-*D*-glucopyranose) (PMG) containing glucose units was synthesized by free-radical polymerization of 3-*O*-methacryloyl-1,2:5,6-di-*O*-isopropylidene-α-*D*-glucofuranose (MDG) initiated by 2,2′-azobis(isobutyronitrile) (AIBN) followed by removal of isopropylidene groups by acidic hydrolysis (Fig. 5.17) (Sharma and Mudhoo 2011).

Glycoproteins

One widely used coupling method involves site-specific (oriented) immobilization of glycoproteins (enzymes, hormones, and/or antibodies) through their carbohydrate moieties on hydrazide solid supports (Bílková et al. 2002). Such reactors are suitable
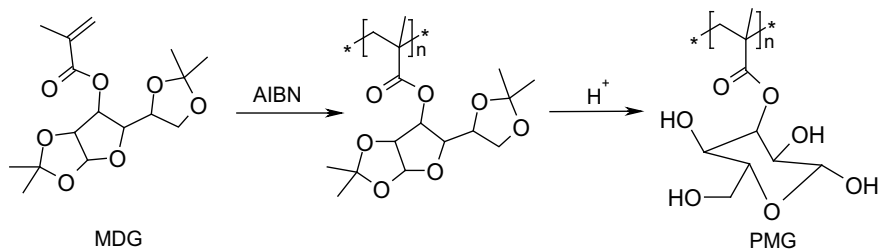
Fig. 5.17 Preparation of poly(3-*O*-methacryloyl-α-*D*-glucopyranose) (PMG) from 3-*O*-methacryloyl-1,2:5,6-di-*O*-isopropylidene-α-*D*-glucofuranose (MDG); AIBN—2,2′-azobis(isobutyronitrile)

for enzymatic oxidation of glycoproteins or for the specific removal of biomolecules. In the case of antibodies, such as immunoglobulin G (IgG), carbohydrate residues are localized on the Fc fragment which is not involved in antigen recognition. As a result, the fragment antigen-binding (so-called Fab) remains sterically available for specific reaction with the antigen as the target molecule (Rao et al. 1998). Hydrazide-containing particles obtained by functionalization of carboxyl group-containing magnetic particles with adipic acid dihydrazide (Svobodová et al. 2018) or reaction of P(HEMA-2-[(methoxycarbonyl)methoxy]ethyl methacrylate) with hydrazine (Fig. 5.18) capture glycoproteins of bacterial origin (*Francisella tularensis*) (Horák et al. 2012). It is an advantage of 2-[(methoxycarbonyl)methoxy]ethyl methacrylate (MCMEMA) monomer that it carries a reactive moiety that subsequently provides carboxyl groups necessary for the attachment of antibodies. Optionally, immunoglobulin G (IgG) was immobilized on PGMA-NH$_2$ microspheres via 2,4,6-trichloro-1,3,5-triazine (Fig. 5.9). Orientally immobilized neuraminidase and galactose oxidase with high storage and operational stability, very good accessibility of active sites, and increased thermal stability are obtained by their attachment through the carbohydrate parts to hydrazide-modified magnetic bead cellulose and P(HEMA-EDMA) microspheres (Bílková et al. 2002).

RNase A can be coupled to the magnetic bead cellulose or PHEMA microspheres by the cyanuric chloride method to degrade high-molecular-weight RNA contaminating plasmid DNA in bacterial lysates, which enables high-performance size exclusion chromatography of nucleic acids. Optionally, DNase I immobilized to the same microspheres degrades chromosomal and plasmid DNAs in the presence of divalent cations to avoid false results during PCR amplification (Horák et al. 2005).

Silica

Another suitable material for particle coating is silica due to its biocompatibility, hydrophilicity, chemical and thermal stability, optical transparency, and low non-specific protein adsorption (Bergna and Roberts 2005). Moreover, surface silanol groups offer the possibility of additional functionalization. Silica can also possess

(a)

(b)

(c)

(d)
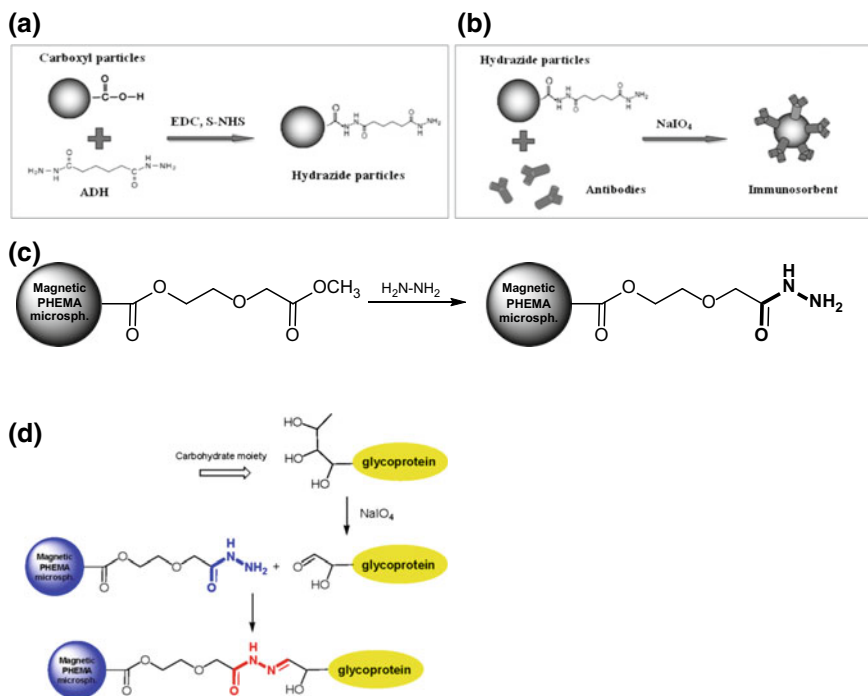
Fig. 5.18 Scheme of covalent coupling of **a** carboxyl-containing magnetic particles with adipic acid dihydrazide (ADH) and **b** subsequent site-specific immobilization of IgGs. Reproduced with permission from (Svobodová et al. 2018). Copyright 2018, with permission from Hindawi. **c** Hydrazidation of P(HEMA-MCMEMA-EDMA) microspheres and **d** isolation of glycoproteins; HEMA—2-hydroxyethyl methacrylate, MCMEMA—2-[(methoxycarbonyl)methoxy]ethyl methacrylate, EDMA—ethylene dimethacrylate. Reproduced with permission from (Horák et al. 2012). Copyright 2012, with permission from The Royal Society of Chemistry

porosity allowing imbibition of drug solutions. A variety of methods exist for the coating of the hydrophilic particles with silica, such as Stöber technique, sol–gel process, and microemulsion (Wu et al. 2008). Hydrophobic particles can be conveniently coated with silica by water-in-oil reverse microemulsion method, which can easily control the silica thickness (1.8–30 nm) and introduce functional groups on the particle surface (Yi et al. 2006). The process is based on alkali-catalyzed hydrolysis and condensation of tetramethyl orthosilicate (TMOS) inside micelles containing iron oxide particles; as a result, core–shell magnetic nanoparticles are obtained. Moreover, amino-containing silica precursors [e.g., (3-aminopropyl)triethoxysilane—APTES] enable surface decoration with amino groups, which can be used for introduction of specific bioactive or targeting moieties and/or PEG via reaction with its succinimidyl ester. Porosity of the silica shell is typically induced by cetyltrimethylammonium bromide (CTAB) as a porogen present in the silanization mixture; after completion of the reaction, CTAB is removed from the silica by washing with ethanol and water (Zasońska et al. 2016).
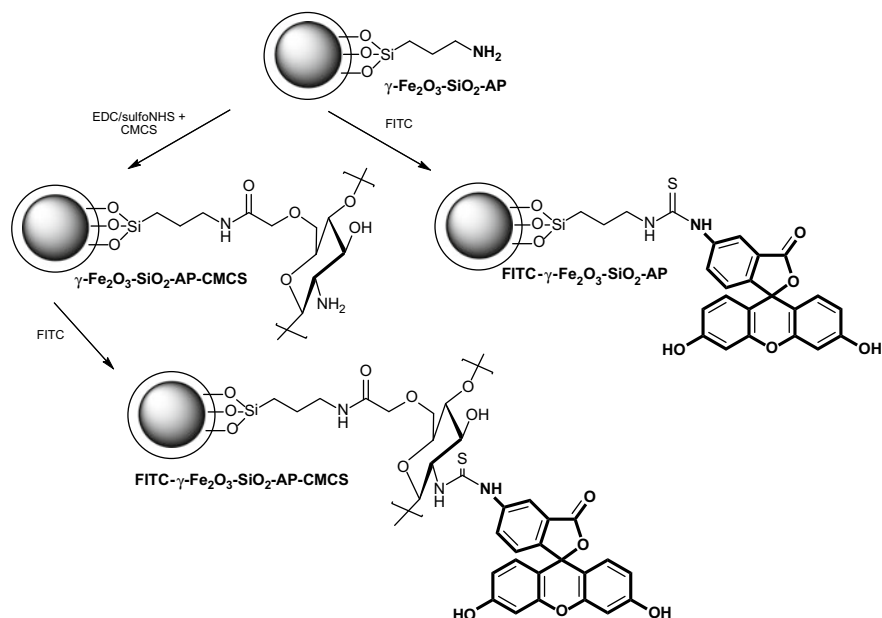
Fig. 5.19 Labeling of γ-Fe₂O₃@SiO₂-AP and γ-Fe₂O₃@SiO₂-AP-CMCS nanoparticles with FITC; AP—aminopropyl, CMCS—carboxymethyl chitosan, and FITC—fluorescein isocyanate. Reproduced with permission from (Chekina et al. 2011). Copyright 2011, with permission from The Royal Society of Chemistry

Fluorescent Magnetic Nanoparticles

The simultaneous combination of optical (fluorescent) and magnetic resonance imaging (MRI) with high spatial resolution and high depth of imaging, respectively, greatly benefits in vivo disease diagnosis as well as in situ monitoring of living cells (Chekina et al. 2011). The γ-Fe₂O₃ nanoparticles obtained by coprecipitation and oxidation were coated with silica (SiO₂) or carboxymethyl chitosan (CMCS) and labeled with fluorescein isocyanate (FITC; Fig. 5.19) covalently bound to the nanoparticles; quenching by the iron oxide core was prevented by the isolating silica and/or chitosan shell.

Streptavidin

Oxirane groups of the magnetic poly(2-hydroxyethyl methacrylate-*co*-glycidyl methacrylate) [P(HEMA-GMA)] microspheres were ammonolyzed and then functionalized with streptavidin using 2,4,6-trichloro-1,3,5-triazine for immobilization of biotinylated DNA and subsequent selective isolation of target DNA from complex samples using DNA/DNA hybridization (Fig. 5.20) (Horák et al. 2011). Optionally,
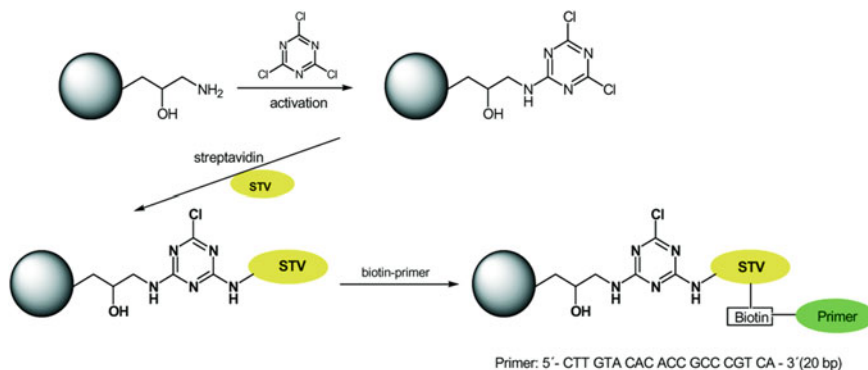
Fig. 5.20 Functionalization of P(HEMA-GMA)-NH$_2$ microspheres with streptavidin and DNA probe (biotinylated primer). Reproduced with permission from (Horák et al. 2011). Copyright 2011, with permission from Elsevier (Mosby, Saunders, Churchill Livingstone, Academic Press)

microspheres containing COOH can immobilize streptavidin with EDC and NHS (Salih et al. 2016). Based on the highly selective recognition of streptavidin with a biotin-labeled DNA probe, DNA sensor was constructed for magnetic separation of DNA from real samples.

Tosyl

PHEMA and/or poly[HEMA-2-(methacryloyl)oxyethyl acetate-GMA] [P(HEMA-Ac-GMA)] contain hydroxyl groups available for subsequent modification with p-toluenesulfonyl (tosyl) chloride (TsCl) (Fig. 5.21), which can be then used for nucleophilic substitution in various organic syntheses.

Miscellaneous Coatings

Optionally, dopamine-hyaluronate is used as a coating (Babič et al. 2012). Colloidal γ-Fe$_2$O$_3$@polyaniline (γ-Fe$_2$O$_3$@PANI) hybrid particles with an average size of about 350 nm obtained by PVP-stabilized oxidation of aniline with ammonium persulfate in the ferrofluid respond to electric field (Bober et al. 2016). Combination of magnetic (γ-Fe$_2$O$_3$) and conducting properties (PANI) can be beneficial for heavy metals removal from wastewater, where PANI can adsorb them and thanks to the magnetic properties they can be easily separated; optionally, such particles can be in vivo manipulated and imaged and at the same time electrochemically stimulate tissues and cell growth and/or differentiation. Optionally, chelating iminodiacetic groups were attached and Ni(II) or Fe(III) ions immobilized to bind protein (Přikryl et al. 2006).
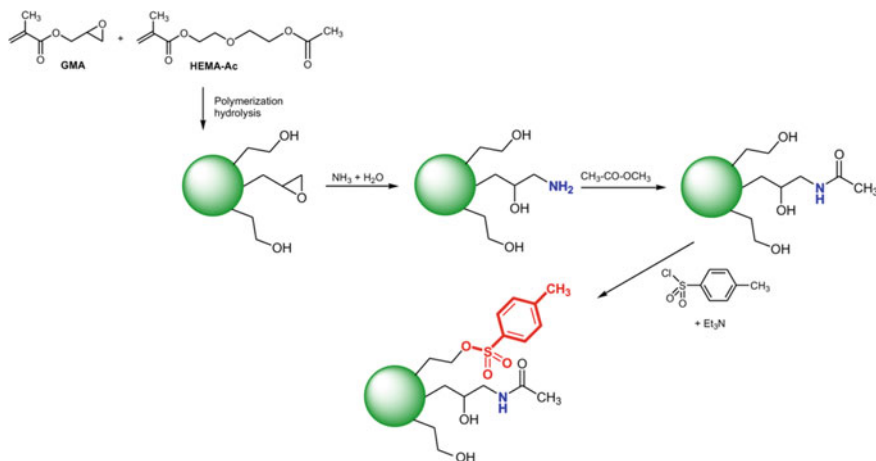
Fig. 5.21 Modification of P(HEMA-Ac-GMA) microspheres with ammonia, acetic anhydride, and tosyl chloride. Reproduced with permission from (Reymond et al. 2013). Copyright 2013, with permission from John Wiley & Sons (Wiley-Interscience, Wiley-VCH, Wiley-Blackwell)

Physicochemical Characterization of the Magnetic Particles

During all the synthetic and/or modification steps, the particles have to be thoroughly characterized by a plethora of physicochemical methods, such as electron microscopy (to determine morphology, particle size and distribution in dry state), dynamic light scattering (hydrodynamic size), X-ray diffraction (crystallinity), energy dispersive X-ray diffraction (structure), chemical analysis, atomic absorption spectroscopy (Fe content), and magnetic measurements, such as magnetometry (saturation magnetization) and Mössbauer spectroscopy (iron oxide phase). Thermogravimetric analysis, differential scanning calorimetry, X-ray photoelectron spectroscopy, Fourier-transform infrared spectroscopy (FTIR), secondary ion mass spectra, conductometry, potentiometry, and solid-state NMR have been used to investigate the surface properties.

Transmission Electron Microscopy

Transmission electron microscopy (TEM) determines the particle morphology, size and its distribution. The number average diameter is calculated by the measurement of at least 500 particles for each batch from micrographs using the image analysis software. The number average (D_n) particle diameter is $D_n = \Sigma N_i D_i / \Sigma N_i$, where N_i is the number of particles with the diameter D_i. Dispersity $Đ = D_w/D_n$ characterizes the width of the particle size distribution, where D_w is the weight average particle diameter and $D_w = \Sigma N_i D_i^4 / \Sigma N_i D_i^3$. Monodisperse particles have $Đ < 1.05$. TEM can

also confirm nanoparticle internalization in cell cytoplasm. Atomic force microscopy (AFM) is also useful to reveal topography of the particles.

Dynamic Light Scattering (DLS)

The size measured by DLS is that of water-swollen particles (hydrodynamic radius), whereas the number average diameter size deduced from TEM measurement corresponds to particles in a dried state. Therefore, DLS gives always higher values compared to TEM. This can also be ascribed to the effect of large particles on hydrodynamic radius, because the DLS provides z-average of the radius that is proportional to its sixth power and sensitive to the presence of large particles. Any other reason can consist in that modified iron oxide particles are slightly aggregated in water. Also, hydrophilic polymer coating of the particles increases significantly the hydrodynamic radius.

Atomic Absorption Spectroscopy and Thermogravimetric Analysis

Atomic absorption spectroscopy is used to analyze iron oxide content in the cells or in an extract from the particles obtained with dilute HCl at elevated temperature. Similarly, elemental analysis helps to estimate the amount of organic coating on the particles. The amount of polymer coating on the surface of magnetic cores is also determined by thermogravimetric analysis due to weight loss (decomposition) of organic compounds at 200–400 °C.

Inductively Coupled Plasma Mass Spectroscopy

Inductively coupled plasma mass spectroscopy (ICP-MS) provides chemical analysis of iron content in cells incubated with iron oxide magnetic nanoparticles.

Determination of Fe^{2+} Release from the Nanoparticles

The concentration of Fe^{2+} released from the iron oxide nanoparticles is determined using a colorimetric method with a Fe^{2+}-1,10-phenanthroline complex by measuring the absorbance at 510 nm (Zuo and Hoigné 1992).

Fourier-Transform Infrared Spectroscopy

Fourier-transform infrared (FTIR) spectroscopy with attenuated total reflection (ATR) system analyzes coating on the surface of the magnetic nanoparticles.

X-Ray Photoelectron Spectroscopy

X-ray photoelectron spectroscopy (XPS) can, for example, confirm the presence of Fe and/or Si and N in the magnetic and/or (amino)silica-coated magnetic particles, respectively.

Crystallographic Analysis

Crystallographic analysis uses X-ray powder diffraction to determine the magnetite or maghemite phase composition.

Magnetic Properties

Magnetic properties are primarily measured by a magnetometer. Mössbauer spectroscopy determines whether the particles are in superparamagnetic state, i.e., without hysteresis loops. Superparamagnetic character enables separation of the particles using a magnet, while the particles can be re-dispersed in aqueous media in the absence of magnetic field. The saturation magnetization >15 A m^2 kg^{-1} is sufficient for good attraction by a magnet. Moreover, by comparing saturation magnetization of the polymer-coated particles with that of uncoated particles it is possible to estimate the amount of coating and compare it with data from other analytical techniques (elemental analysis, TGA, etc.).

Magnetic Resonance Relaxometry and MR Imaging (MRI)

Magnetic resonance (MR) relaxometry and MR imaging of cells labeled by surface-modified nanoparticles show T_1 and T_2 relaxation times responsible for contrast enhancement in T_1- and T_2-weighted MR images. Relaxation time values are converted to relaxivities and related to the actual iron concentration. For example, relaxivity r_2 is calculated as the inverse relaxation time T_2 after deducting the contribution of gel and unlabeled cells. Relaxation measurements reflect the amount of iron oxide

taken up into the cells. The relaxivity rates decrease during cell differentiation, which might correspond to the cell proliferation and contrast dilution is also reported in several labeling studies (Jiráková et al. 2016). A minimum concentration required for detection with MR imaging in the case of magnetic nanoparticles is 1.4–3 pg Fe/cell (Heyn et al. 2005).

Flow Cytometry

Flow cytometry can screen the cell population to evaluate the labeling efficiency and to analyze the differentiation potential of labeled and unlabeled stem cells and quantify the presence of pluripotent neural and neuronal markers.

Toxicity of the Particles

Superparamagnetic iron oxide nanoparticles (Fe_3O_4 or $\gamma\text{-}Fe_2O_3$) are the most commonly used for magnetic cell labeling because their main component (iron) may be recycled by cells via natural metabolic pathways (Weissleder et al. 1989). In order to achieve efficient cell labeling, response of intracellular iron oxide content on the metabolism of the cells should be taken into account because the intracellular overload may cause cytotoxicity due to the formation of free radicals. The specific properties of nanoparticles, namely an enhanced reactive surface area and the ability to cross cell and tissue barriers, amplify their cytotoxic potential in comparison with bulk materials of the same composition (Nel et al. 2006; Shubayev et al. 2009). The toxicity of a nanomaterial may depend upon its chemical composition, size, shape, porosity, surface charge, colloidal stability, surface functionalization, and route of exposure (Harper et al. 2008). Moreover, the particle/cellular interactions and responses differ, depending on the cell type (Mahmoudi et al. 2011).

Cell Viability

Cell viability is often investigated parameter in cytotoxicity testing. The most common in vitro assays that determine two different cytotoxic pathways are based on metabolic activity and oxidative stress (Vrček et al. 2015), namely cell viability assays (MTT, MTS, and WST-8) and assays employing fluorescent dyes as markers for the production of reactive oxygen species (DCFH-DA and DHE) or glutathione level (MBCl). Interference with optical readouts and interactions between the particles and cellular systems, which were concentration type-, particle type- and assay type-dependent, were difficult to predict. Particle interaction with fluorescent dyes may compromise the measurement. MTT, MTS, and WST-8 use tetrazolium salts that are

reduced by dehydrogenases in metabolically active cells to a soluble formazan product, quantity of which is indicative of the number of viable cells in culture and can be determined spectrophotometrically. The MTT cell proliferation assay determines cellular metabolic activity by the reduction of the yellow tetrazolium salt MTT [3-(4,5-dimethylthiazol-2-yl)-2,5-diphenyltetrazolium bromide] to a purple MTT–formazan crystal, which is dissolved in DMSO and determined spectrophotometrically at 590 nm. The resulting optical density of the formazan product is dependent upon both the concentration of MTT and the incubation time. The MTS cell viability assay uses MTS [3-(4,5-dimethylthiazol-2-yl)-5-(3-carboxymethoxyphenyl)-2-(4-sulfophenyl)-2*H*-tetrazolium] that can be reduced to a soluble MTS–formazan product determined at 490 nm. The WST-8 assay utilizes 2-(2-methoxy-4-nitrophenyl)-3-(4-nitrophenyl)-5-(2,4-disulfophenyl)-2*H*-tetrazolium, which produces a water-soluble formazan dye determined spectrophotometrically at 450 nm. WST-1 colorimetric assay is based on the cleavage of the tetrazolium salt (4-[3-(4-iodophenyl)-2-(4-nitrophenyl)-2H-5-tetrazolio]-1,3-benzene disulfonate) to a highly water-soluble formazan dye by mitochondrial dehydrogenases in viable cells (Vrček et al. 2015).

The viability of labeled cells is assessed also using the trypan blue exclusion test of cell vitality (Horák et al. 2009). Due to the impaired plasma membrane, dead cells are blue, while the intact cells having undamaged plasma membrane are not stained (Horák et al. 2017). Optionally, the calcein acetoxymethyl (AM) ester/propidium iodide (PI) assay is used to assess the percentage of living cells (labeled with calcein AM) and dead cells (labeled with PI) (Pongrac et al. 2016). Labeling efficiency is also assessed by counting Prussian blue-positive cells. To monitor cytotoxicity of the nanoparticles, blood tests can be used to determine liver enzyme activities, such as bilirubin, alanineaminotransferase (ALT), and aspartate aminotransferase (AST) activities. Cell viability can be also determined using a real-time cytotoxicity-monitoring assay using the xCELLigence system (Zasonska et al. 2016), which has an advantage that it measures the growth and proliferation of the cells for a longer time (up to 10 days). In the system, the electrode impedance, which is displayed as a cell index value, is used to monitor cell viability, growth and morphology, and adhesion degree.

Oxidative Stress

The elicitation of reactive oxygen species (ROS) generation and cellular oxidative stress, subsequently resulting in oxidative damage to biological macromolecules, cellular dysfunction and cell death, are generally considered to be the underlying mechanisms involved in nanomaterial toxicity (Nel et al. 2006; Shubayev et al. 2009). Moreover, oxidative stress is involved in the pathogenesis of many diseases, such as cancer, diabetes, and respiratory problems, as well as in aging processes. The genotoxicity of the particles (DNA damage) is studied using an alkaline version of single cell gel electrophoresis (comet assay) with an analog of mammalian OGG1–formamidopyrimidine DNA glycosylase (FPG) and endonuclease III (ENDO III)

(Collins 2004). This approach enables the detection of single- and double-strand breaks in DNA, transient gaps arising as intermediates during base excision repair, alkali-labile sites, apoptotic DNA fragmentation and a broad spectrum of oxidized purines and pyrimidines (Singh et al. 1988; Møller 2005). Particle toxicity for the treated cells is often manifested by time-dependent evolution of vacuoles in the cell cytosol (Zasońska et al. 2013). Obviously, negatively charged particles can be responsible for such irritation of the living cells, in contrast to positively charged particles that do not invoke cytotoxicity effects.

To determine cytotoxicity of magnetic nanoparticles on immune response, in particular, lymphocyte proliferative and phagocytic activity, and leukocyte respiratory burst and in vitro production of interleukin-6 (IL-6) and 8 (IL-8), interferon-gamma (IFN-γ), tumor necrosis factor-alpha (TNF-α), and granulocyte macrophage colony-stimulating factor (GM-CSF) are analyzed (Zasońska et al. 2016) on human peripheral blood cells (T-lymphocytes and T-dependent B cells) after 24–72 h exposure (Zasońska et al. 2016). However, in vivo experiments are always needed to confirm non-toxicity of the material.

Oxidative stress assays utilize fluorescent molecular probes, such as 2′,7′-dichlorodihydrofluorescein-diacetate (DCFH-DA), dihydroethidium (DHE), and monochlorobimane (MBCl). The DCFH-DA assay is based on the oxidation of 2′,7′-dichlorodihydrofluorescein (DCFH) dye by reactive oxygen species (ROS) to highly fluorescent 2′,7′-dichlorofluorescein, which emits green fluorescence at 520 nm after excitation at 485 nm. DHE is oxidized in the presence of a superoxide to 2-hydroethidium (excitation and emission at 480 and 567 nm, respectively) and intermediate products, which can react with hydroxyl radical or hydrogen peroxide to form ethidium measured at excitation of 500–530 nm and emission of 590–620 nm. MBCl is a cell permeable dye which reacts with glutathione (GSH) to generate highly fluorescent adducts measured using excitation and emission at 380 and 460 nm, respectively. GSH is an important marker of oxidative stress.

To reveal toxicity of particles, levels of reactive oxygen species, intracellular glutathione, mitochondrial membrane potential, cell membrane potential, and activities of superoxide dismutase (SOD) and glutathione peroxidase (GPx) are examined (Pongrac et al. 2016). Mitochondrial homeostasis is the particle major cellular target. GPx activity is measured by reaction with glutathione reductase, while SOD activity is determined by xanthine oxidase and hypoxanthine. Changes in mitochondrial membrane potential are estimated using the fluorescent carbocyanine dye 3,3′-dihexyloxacarbocyanine iodide.

Real-Time Polymerase Chain Reaction (qPCR)

Real-time polymerase chain reaction can be also used to determine quality of particle coating with polymers, e.g., PEG (Horák et al. 2015; Trachtová et al. 2016). DNA amplification by qPCR is used for the evaluation of the efficiency of polymer coating of hydrophilic magnetic P(HEMA-GMA) and PGMA microspheres. Incomplete

encapsulation of magnetite cores (nanoparticles) influences the PCR course and PCR sensitivity (Španová et al. 2003).

Biomedical Applications of Magnetic Nano- and Microspheres

Magnetic nano- and microparticles are currently utilized in a wide variety of medical diagnostic and therapeutic applications, such as hyperthermia, cell sorting, cell tracking by MR imaging and tissue engineering, and for the manipulation and spatial organization of cells. Manipulation of D-mannose-coated γ-Fe_2O_3 nanoparticle-labeled brain nerve terminals by an external magnetic field has a potential for diagnostic or drug application and regeneration of injured neurons (Borisova et al. 2014); surface-modified magnetic nanoparticles are then promising for in vivo colon cancer theranostics. Moreover, methods based on antigen–antibody interaction have been used for protein purification, nucleic acid isolation, environment monitoring, and food safety. Many studies are then dealing with magnetic drug delivery systems.

Diagnostics

Magnetic Resonance Imaging (MRI)

In assessing the therapeutic possibilities of stem cells, accurate tracking methods for determining the function, dynamics of cell migration, and differentiation after implantation into the host organ are needed. Cell labeling with surface-modified magnetic nanoparticles is an increasingly common method for long-term in vivo cell separation and monitoring the fate of cells transplanted into a host organism, including their in vivo migration, localization and differentiation, in human and veterinary medicine, as the labeled cells can be detected by noninvasive MRI after implantation. These cell-based therapies are due to the iron oxide high relaxivities, which are responsible for contrast in MR imaging, and their easy internalization by cells. On the other hand, it is essential to preserve and not to violate any biological functions of the labeled cells or cause toxicity or affect unique stem cell characteristics, such as stemness and differentiation potential.

The ability to detect labeled cells by MRI depends on the quantity of iron oxide nanoparticles in the cells. The efficiency with which cells can be loaded with nanoparticles is thus a major determinant of MR sensitivity at the single-cell level. The efficacy of iron oxide nanoparticles depends mainly on their physicochemical properties, particularly on their size and surface chemistry, including surface charge and surface hydrophilicity (Sun et al. 2005). Conjugation with biologically active molecules, such as antibodies, receptor ligands, polysaccharides, or proteins, then governs their

MRI application. The cellular uptake of particles also depends on the number of passages of the cells, which is a characteristic physiological cell property. The lower the passage, the more efficient is the cell labeling. Labeling efficiency can be determined by relaxometry, spectrophotometrical iron content analysis, and by manual evaluation of Prussian blue-stained nanoparticle-labeled cells (Fig. 5.22). For example, poly(L-lysine) (PLL)-coated nanoparticles enter the cells via electrostatic interaction
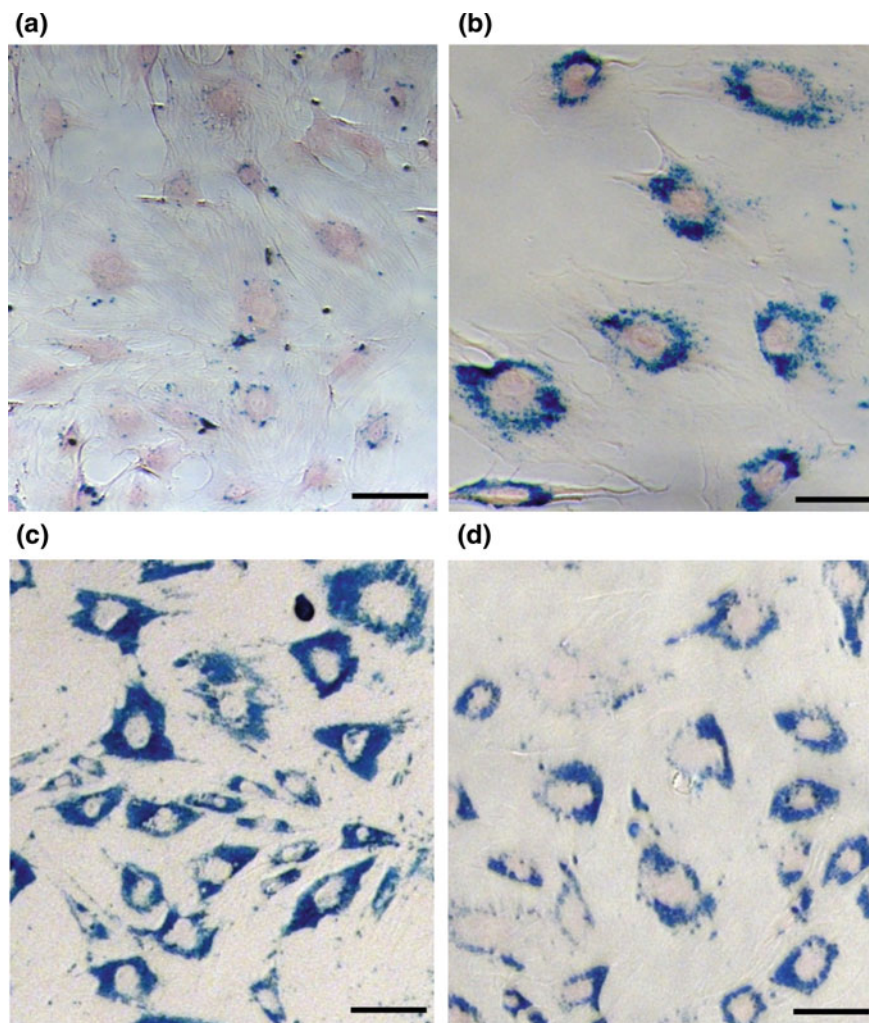
Fig. 5.22 Photomicrographs of Prussian blue-stained rat mesenchymal stem cells labeled with **a** Endorem$^{®}$, **b** γ-Fe$_2$O$_3$@D-mannose, **c** γ-Fe$_2$O$_3$@PLL, and **d** γ-Fe$_2$O$_3$@PDMA nanoparticles; scale bar 100 μm; PLL—poly(L-lysine), PDMA—poly(*N,N*-dimethylacrylamide). Reproduced with permission from (Horák et al. 2009). Copyright 2009, with permission from Elsevier (Mosby, Saunders, Churchill Livingstone, Academic Press)
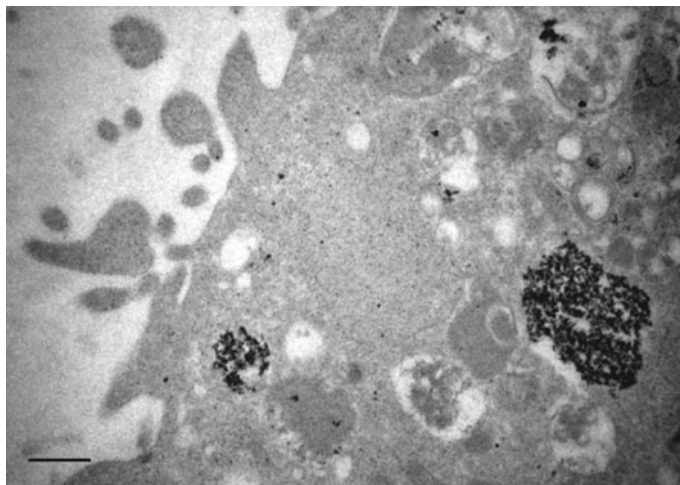
Fig. 5.23 TEM micrographs of rat mesenchymal stem cells labeled with γ-Fe$_2$O$_3$@PLL nanoparticles; scale bar 1 µm; PLL—poly(L-lysine). Reproduced with permission from (Babič et al. 2008). Copyright 2008, American Chemical Society

between positive charges of PLL and the negatively charged glycoconjugate moieties on the cell surface (Moskvin et al. 2018). The internalization of PLL-coated nanoparticles by the cells rather than simply their bonding to the cell surface was confirmed by TEM (Fig. 5.23). The majority of the internalized nanoparticles were located in the lysosomes of the cells, which supports their intracellular trafficking. Nanoparticles are transported in endosomes and finally fused with lysosomes, a process during which the vesicle membranes disappear. The very good ability of the cells to internalize the colloid can be explained by the extremely small size of the particles. The mechanism of nanoparticle uptake into the cells is different, depending on the type of the coating. The mechanism responsible for the cellular internalization of *ca*. 10 nm nanoparticles is thought to be receptor-mediated endocytosis involving macropinocytosis and/or diffusion through the cell membrane (Dormer et al. 2005). In contrast, D-mannose-coated iron oxide nanoparticles are supposed to be transported into the cells via the mannose transporter on the surface of the majority of mammalian cells. Improved cellular uptake significantly contributes to the high r_2 relaxation rate of cells labeled by modified iron oxide nanoparticles. The amount of iron inside the cells in the case of labeling with PLL- or D-mannose-modified iron oxide nanoparticles is up to ten times higher than in the case of cells labeled with Endorem®. PLL-modified iron oxide-labeled mesenchymal stem cells are also well visible on MR images as a hypointense area at the injection site and in the lesion after intracerebral grafting into the contralateral hemisphere of adult rat brain (Fig. 5.24) (Babič et al. 2008). In applications, cells are labeled in vitro with the nanoparticles prior to transplantation and in vivo imaging monitors their migration throughout the
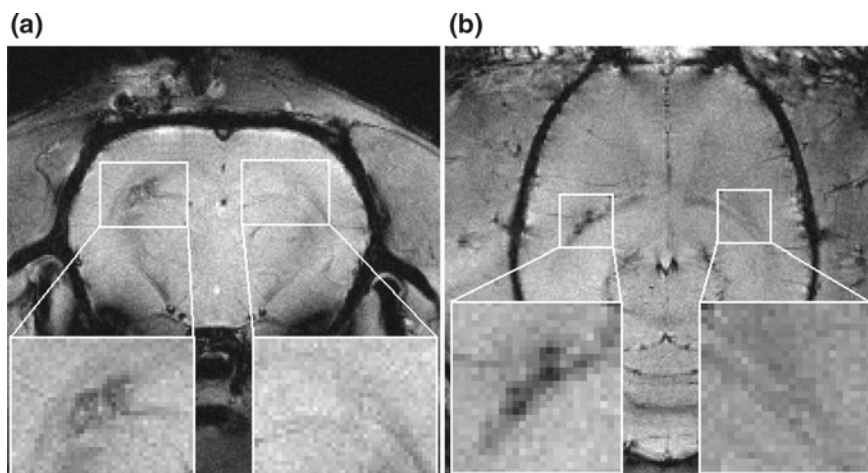
Fig. 5.24 a Axial and **b** coronal MR images of a rat brain with 1000 cells labeled with γ-Fe_2O_3@PLL nanoparticles implanted into the left hemisphere and 1000 Endorem®-labeled cells implanted into the right hemisphere. MR images were taken 3 days after implantation. Enlarged insets clearly show a hypointense signal in the left hemisphere; such a signal is not visible in the right one; PLL—poly(L-lysine). Reproduced with permission from (Babič et al. 2008). Copyright 2008, American Chemical Society

body after transplantation. Cellular monitoring is particularly important for evaluating cell-based therapies. γ-Fe_2O_3@PLL also excelled in labeling efficiency, viability, and proliferation of neural stem cells without influencing their identity and differentiation potential. Interaction of PLL-heparan sulfate proteoglycan on the cell surface may be the first step mediating γ-Fe_2O_3@PLL internalization by tumor cells (Fig. 5.25) (Siow et al. 2018). Epigallocatechin-3-gallate (EGCG; a component in tea) and magnetic force exert a synergistic effect on magnetic particle internalization by the cells. γ-Fe_2O_3@PLL nanoparticles can be thus considered as appropriate candidates not only for the future neural stem cell in vivo tracking studies, but also as drug carriers in targeting tumors (Pongrac et al. 2016; Siow et al. 2018).

As macrophages participate in many pathological processes, including heart disorders (atherosclerosis, myocardial infarction), Alzheimer's disease, diabetes, infectious diseases, obesity, and rejection of donor organs after transplantation, MRI detection of magnetically labeled macrophages is useful for imaging of pathological loci, e.g., inflammation site or atherosclerotic plaques, and prediction of risks and assessment of prospective therapies. A possibility to track the macrophages in vivo allows monitoring the immune response (Fleige et al. 2002), inflammations, and cell migration, as well as getting an insight into the development of different pathological states in the organism in cell therapy (Flogel et al. 2008). As an example, the transport of macrophages labeled with γ-Fe_2O_3@PLL nanoparticles in rats is confirmed by MRI (Babič et al. 2015). Reverse transport of cholesterol is able to slow down
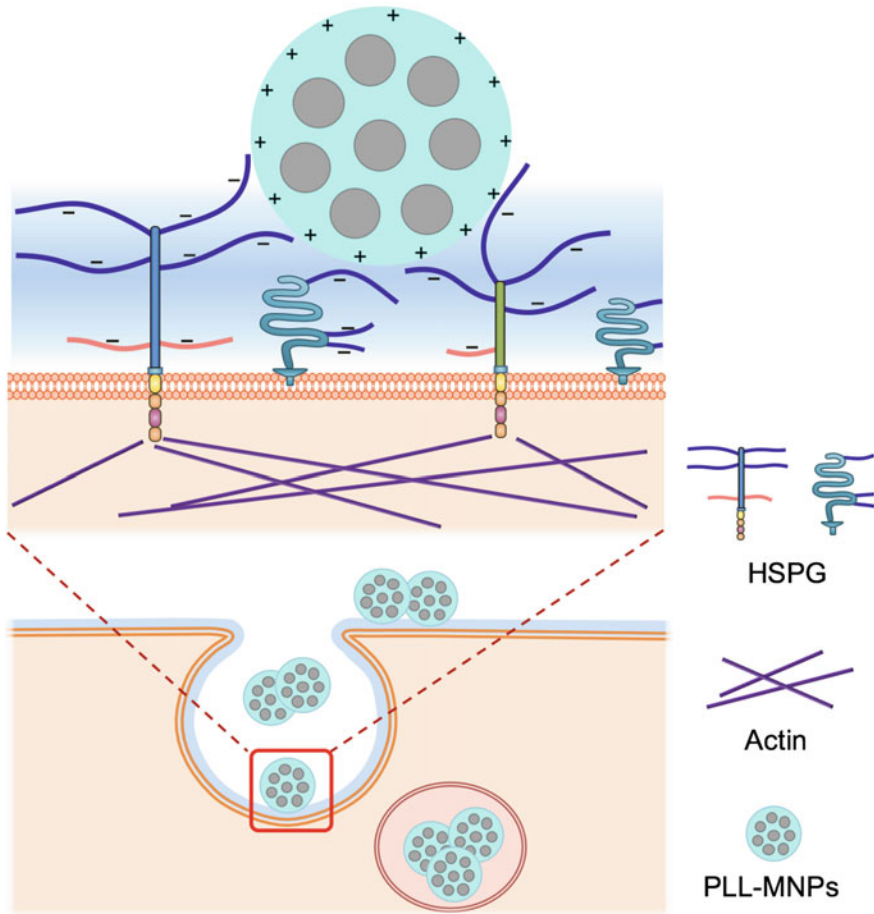
Fig. 5.25 Schematic diagram of the interaction of PLL-MNPs and HSPG on the cell surface. The amino groups of PLL coating endow positively charged residue (+) on the NP surface and interact with negatively charged residues (−) of heparan sulfate on cell surface. The upper diagram is an amplification of the red square in the lower diagram. Abbreviations: PLL—poly(L-lysine), MNPs—magnetic nanoparticles, HSPG—heparan sulfate proteoglycan. Reproduced with permission from (Siow et al. 2018). Copyright 2018, with permission from Dove Medical Press

gradual changes of macrophages to residual macrophages and to positively influence deceleration of the atherosclerosis process.

Diagnosis of Cancer

Cancer represents a major health concern because it causes approximately 13% of all deaths' worldwide (Ferlay et al. 2008), and approximately, 90% of cancer deaths
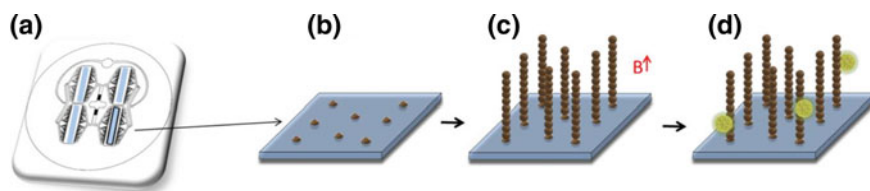
Fig. 5.26 Ephesia system principle. **a** Design of the chip, **b** the bottom layer of the chip with anchoring points, **c** self-assembly of magnetic beads under the magnetic field. **d** immunomagnetic-based capture of cancer cells. Reproduced with permission from (Guneri et al. 2014). Copyright 2014, with permission from The Royal Society of Chemistry

are caused by metastases originating from cancer stem cells (CSCs). Molecular characterization and development of specific therapies targeted to CSCs have scope for improvement of survival and quality of life of patients with cancer, in particular, for those with metastatic disease. To capture CSCs from blood, new technologies with enhanced sensitivities and specificities are required. For example, CD133-positive cells (CD133 is a marker of brain, colorectal, lung, and liver cancer stem cells) were effectively captured from human cancer cell lines (HepG2, HCT116, MCF7, and IMR-32) by using magnetic PGMA microspheres conjugated to an antihuman CD133 antibody; later they were detached from the microspheres (Kuan et al. 2014). Such microspheres are very promising for cancer diagnosis because the CD133-expressing cells in cancer cell lines have been suggested to be cancer stem cells. Monodisperse macroporous PGMA microspheres (~5 μm in size) containing carboxyl groups to immobilize DO-1 antibody can be used for the specific isolation of the tumor suppressor protein p53 (Koubková et al. 2014). Analysis of p53 expression level in cell lysates is important for the detection of human cancer biomarkers.

Microchips

There is increasing demand for the development of cost-effective and user-friendly lab-on-a-chip medical devices for in vitro molecular diagnostics of cancer and infectious, as well as neurodegenerative diseases. Analysis of clinically relevant nucleic acid targets is thus becoming an integral part of such novel point-of-care testing. Microfabrication (microchip) technology and integration of flow systems is preferable alternative to the conventional batch processes, offering a great potential for mass production of low-cost devices for protein identification (Bílková et al. 2006). Chip is typically the consumable part of the microfluidic platform consisting of array of independent micro-channels with inlets and outlets (Fig. 5.26). Implementation of enzymatic reactions in micro-channels allows a decrease in the amount of consumables and sample by several orders of magnitude. Detection sensitivity can also be improved for a sample with small total volume since no dilution is necessary, and the smaller scale increases the speed of diffusion-limited reactions allowing faster assays (Sakai-Kato et al. 2003). Finally, microfluidic integration may allow long-term higher
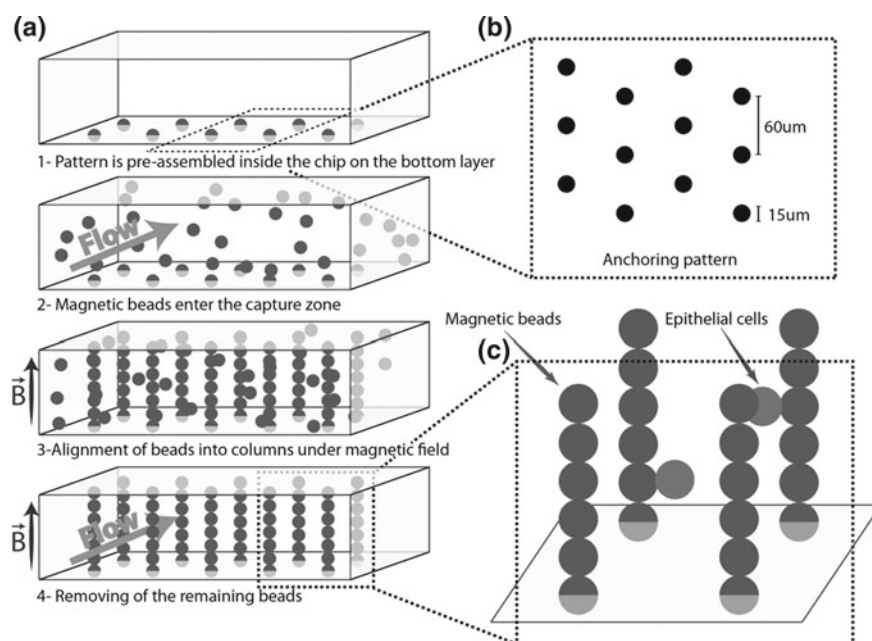
Fig. 5.27 Microchip system. **a** Column formation; 30 mT magnetic field is used to construct the columns; the remaining beads are washed out with the PBS flow. **b** The anchoring column system composed of 48 rows and 1000 columns; the hole depth is 5 µm. **c** Capture principle; epithelial cells pass through the column system and are caught by antibody/antigen interactions, PBS—phosphate buffer solution. Reproduced with permission from (Horák et al. 2013). Copyright 2013, with permission from John Wiley & Sons (Wiley-Interscience, Wiley-VCH, Wiley-Blackwell)

automation and better reproducibility. Magnetic microspheres, which are organized by an inhomogeneous external magnetic field perpendicularly to the direction of the channel, open the route to automated, high-throughput proteomic microchip devices. For example, antibodies of epithelial cell adhesion molecule (anti-EpCAM) immobilized on the albumin-coated monodisperse magnetic PGMA microspheres using the carbodiimide method can be used in microfluidic immunomagnetic cell sorting, with a specific application to the capture of circulating tumor cells (CTCs) (Horák et al. 2013). In the microfluidic technology, such microspheres bearing antibodies directed against the cancer cells are in magnetic field self-assembled in a microfluidic channel, onto a predefined array of "magnetic anchors" (Fig. 5.27). Thanks to appropriate positioning of the magnetic columns, the probability of collisions of cells and microspheres is very high, allowing thus the capture of all the EpCAM-expressing cells in the blood sample.

Proximity Ligation Assay (PLA) and Rolling Circle Amplification (RCA)

Also innovative, ligation-based assays, using highly specific padlock probes, are attractive for the detection of mutations or diagnostics of pathogens (Salih et al. 2016). In the solid-phase PLA, the target protein is captured via an antibody immobilized on a solid support such as magnetic microparticles. The protein is then recognized by a pair of PLA probes, each consisting of an antibody conjugated to a DNA oligonucleotide. Once in proximity, the DNA oligonucleotides are joined by enzymatic ligation in the presence of a connector oligonucleotide to form a template for amplification and quantification using quantitative real-time PCR. Functionality of the tosyl-activated magnetic bead cellulose as a solid support in PLA was tested on the detection of VEGF peptide in crude chicken serum (Yan et al. 2013).

Probed targets can be amplified also by rolling circle amplification (RCA) forming large DNA bundles which can be fluorescently labeled and digitally counted (Baner et al. 1998). Detection sensitivity is greatly improved by applying two rounds of RCA, so-called circle-to-circle amplification (C2CA) (Dahl et al. 2004). RCA of padlock probes guarantees high specificity to identify nucleic acid targets down to single nucleotide resolution in a multiplex fashion. This makes the assay suitable for molecular analysis of various diseases, and interesting to integrate into automated devices for point-of-care analysis. A critical prerequisite for many molecular assays is (i) target-specific isolation from complex clinical samples and (ii) removal of reagents, inhibitors, and contaminants between reaction steps. Efficient solid supports are therefore essential to enable multi-step, multi-analyte protocols. Superparamagnetic micro- and nanoparticles, with large surface area and rapid liquid-phase kinetics, are attractive for these multi-step protocols. Recently, streptavidin-modified magnetic monodispersed poly(2-hydroxyethyl methacrylate) microspheres were used as solid support in C2CA (Fig. 5.28) to detect DNA sequences from *Escherichia coli* (Salih et al. 2016).

Diagnosis of Neurodegenerative Disorders

Magnetic microspheres have been extensively used in ELISA applications due to increased active surface area and enhanced assay sensitivity. Combination of magnetic and non-magnetic microspheres functionalized with capture (anti-ferritin) and detection (biotinylated anti-ferritin) antibodies has been evaluated in view of amplifying the number of enzymatic labels in the immuno-complex for microfluidic immunoassay (Fig. 5.29), which is much more rapid and requires less volume than the conventional enzyme-linked immunosorbent assay (ELISA) and is amendable to automation. Applicability of such microspheres was demonstrated in microfluidic ELISA tests with electrochemical detection for the dosage of ferritin, which is recognized as a promising biomarker for early diagnosis of neurodegenerative disorders that are typically associated with L-ferritin mutation (Reymond et al. 2013).
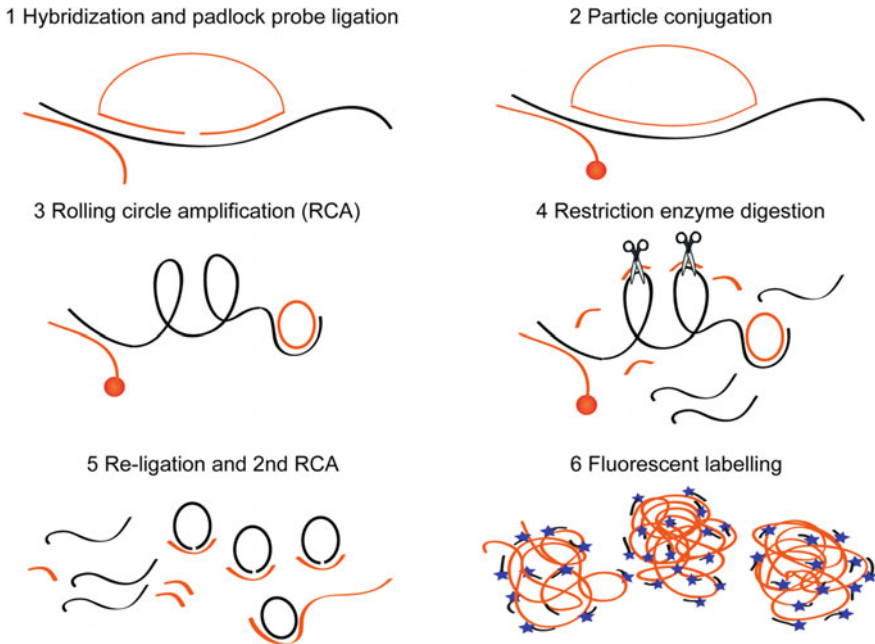
Fig. 5.28 Schematic C2CA protocol. (1) Hybridization of linear synthetic DNA capture probes and padlock probes (both in orange) to their bacterial target DNA strand (black). The padlock probes are specifically circularized by enzymatic ligation of their target complementary sequence motifs. They additionally contain a backbone sequence that enables further downstream processing and labeling as described below. (2) Probed targets are captured to the orange magnetic microspheres through biotin–streptavidin interaction. After conjugation, excess and unreacted probes are removed by washing. (3) Circularized padlock probes are amplified by rolling circle amplification (RCA) by a polymerase, utilizing the target as a primer to initiate the reaction and to form long single-stranded, concatenated rolling circle products, RCPs (black). (4) The RCPs are digested to monomers by introducing a probe (orange) to form double-stranded sites along the molecules that are recognized by a restriction enzyme (illustrated by scissors). (5) The monomers are re-circularized and ligated, and a second round of RCA is performed, followed by (6) fluorescent labeling of the amplification products (orange) through hybridization of short labeled probes (labels illustrated by blue stars). Finally, the RCPs are digitally counted by a fluorescent scanner. Reproduced with permission from (Salih et al. 2016). Copyright 2016, with permission from Elsevier (Mosby, Saunders, Churchill Livingstone, Academic Press)

Alzheimer's Disease Biomarkers Detection

Both ß-amyloid and ApoE4 biomarkers are considered as valid neurochemical indicators to estimate the risk or the presence of the disease. Their detection in some physiological fluids such as cerebrospinal fluid (CSF), serum, and plasma can be used to diagnose Alzheimer's disease in a very early stage and also to provide objective and reliable measures of disease progress. Of special interest are
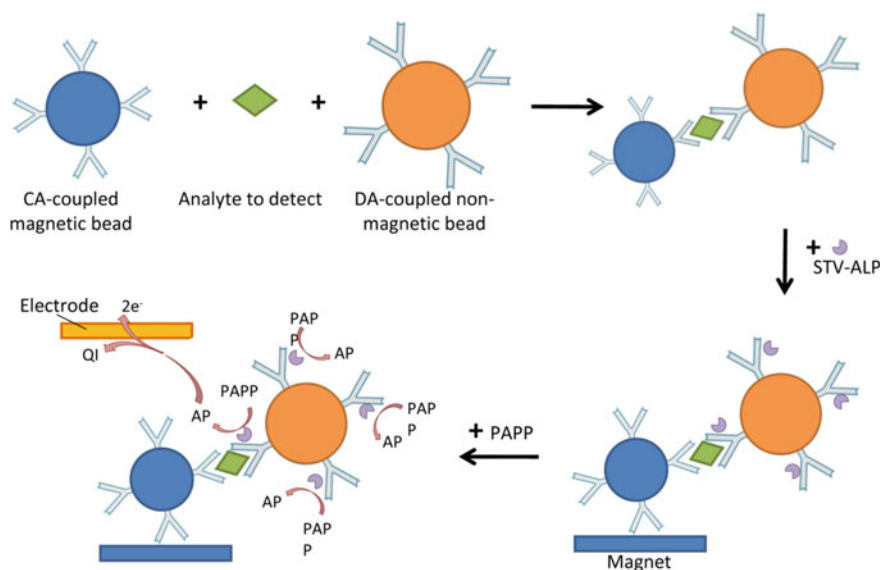
Fig. 5.29 Principle of electrochemical ELISA test with magnetic microspheres coated with capture antibody (CA) and non-magnetic microspheres coated with a biotinylated detection antibody (DA); PAPP stands for p-aminophenyl phosphate, AP for aminophenol, and QI for quinonimide. Reproduced with permission from (Reymond et al. 2013). Copyright 2013, with permission from John Wiley & Sons (Wiley-Interscience, Wiley-VCH, Wiley-Blackwell)

the recent approaches based on the use of magnetic particles for the analyte pre-concentration/purification before detection by gold nanoparticle tags, which catalyze hydrogen evolution (de la Escosura-Muñiz et al. 2015). Highly porous magnetic PHEMA-COOH microspheres with immobilized capture antibody were used in a sandwich immunoassay using Au particles with detection antibody to find ß-amyloid and ApoE4 biomarkers in human CSF and plasma of patients suffering from Alzheimer's disease. Another approach took advantage of magnetic PGMA-PEG-COOH microspheres with anti-Aß 6E10 antibody immobilized via EDC/NHS chemistry to enable pre-concentration of labeled Aß 1-40 amyloid peptides, which was determined by capillary electrophoresis with laser-induced fluorescence detection (Horák et al. 2014).

Diagnosis of Multiple Sclerosis Patients

Magnetic PHEMA microspheres coupled with a potential disease biomarker, p46/Myo1C protein purified from blood serum of multiple sclerosis (MS) patients, enabled easy isolation of monospecific anti-p46/Myo1C immunoglobulin G antibodies from crude antibody preparations of mouse blood serum (Fig. 5.30) (Horák et al. 2017). These microspheres are a promising tool for affinity purification of antibodies,
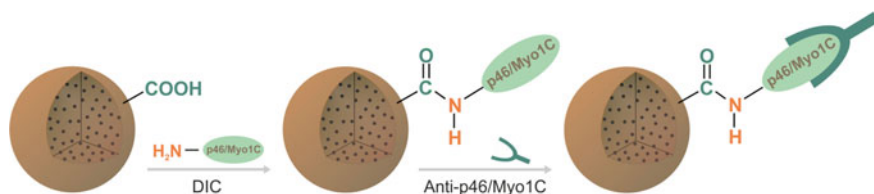
Fig. 5.30 Binding of p46/Myo1C antigen on magnetic PHEMA particle and capture of monospecific anti-p46/Myo1C antibody. Reproduced with permission from (Horák et al. 2017). Copyright 2017, with permission from Portland Press

which can improve diagnosis and effectiveness of treatment of MS patients, which is the most common chronic inflammatory disease of the central nervous system with supposed autoimmune etiology. If conjugated with any specific antigen present in cells of patients suffering from neurological disorders, they can be exploited for highly sensitive affinity isolation of any biomarkers.

Diagnosis of Autoimmune Diseases

Anti-histone antibodies were found in a variety of autoimmune disorders, including inflammatory, hepatic, malignant, infectious, and rheumatic diseases (Dunorier and Muller 2007). Detecting these antibodies in blood serum is thus useful for diagnosing specific diseases and for the prognostication and evaluation of treatment efficacy. Rapid purification of the anti-histone immunoglobulins from blood serum of systemic *lupus erythematosus* patients on calf thymus histone-conjugated magnetic poly(2-oxoethyl methacrylate) (POEMA-His) microspheres enabled the diagnosis and prognosis of this disease (Fig. 5.31) (Horák et al. 2015). The procedure might be
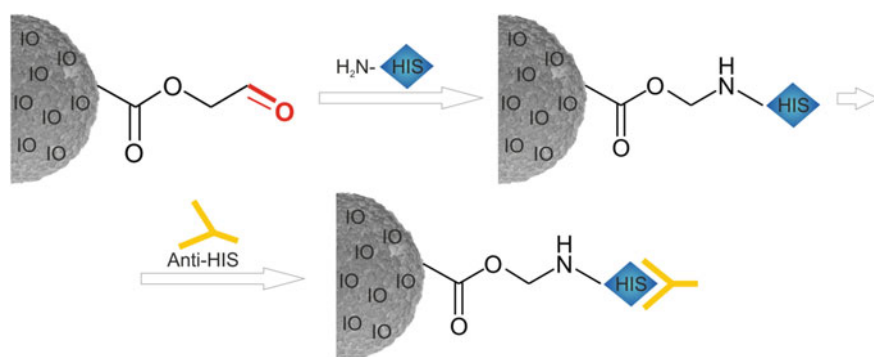
Fig. 5.31 Affinity isolation of anti-histone immunoglobulins from blood serum of systemic *lupus erythematosus* patients using histone-conjugated magnetic poly(2-oxoethyl methacrylate) microspheres; IO—iron oxide, HIS—histone. Reproduced with permission from (Horák et al. 2015). Copyright 2015, with permission from the Royal Society of Chemistry

suitable not only for patients with systemic *lupus erythematosus* but also for persons suffering from other autoimmune diseases.

Treatment

Controlled Drug Targeting

The aim of targeted drug delivery and therapy is to transport a drug directly to the disease loci with no or minimal side effects on the human body and to reduce the needed dosage. The potential of drug delivery systems based on the use of magnetic nanoparticles offers three major significant advantages: (i) the ability to target-specific locations in the body; local retention of nanocomposites may prolong the half-life of the drug and enhance therapeutic efficacy, (ii) the reduction of the drug quantity needed to attain a particular concentration in the vicinity of the target, and (iii) the reduction of the drug concentration at nontarget sites which minimizes severe side effects (Arruebo et al. 2007). Magnetic field can steer and concentrate magnetically labeled cells inside the body.

Antitumor Activity of Magnetic Nanoparticles

Example of antitumor activity of magnetic nanoparticles will be now shown on an animal model. Poly(*N,N*-dimethylacrylamide-*co*-acrylic acid)-modified γ-Fe_2O_3 (γ-Fe_2O_3@PDMA) nanoparticles showed higher antitumor (decreasing the tumor volume by 60%) and antimetastatic activities than commercial $CuFe_2O_4$ particles and the conventional antitumor agent cisplatin or doxorubicin, when administered *per os* to mice with Lewis lung carcinoma or Wistar rats with Walker-256 carcinosarcoma (a model of mammary gland carcinosarcoma) due to enhanced oxidative stress in tumor cells (Fig. 5.32) (Macková et al. 2015; Horák et al. 2017). The tumor size was measured with a caliper and tumor volume [V; cm^3] was calculated using Eq. 6: (Faustino-Rocha et al. 2013)

$$V = (4/3) \times \pi \times (L/2) \times (W/2) \times (D/2)/1000 \qquad (5.6)$$

where *L*, *W*, and *D* represent the tumor length, width, and depth (mm), respectively. The presence of tocopherol (Toc) enhanced spontaneous Fe^{2+} release from γ-Fe_2O_3@PDMA nanoparticles, increasing their antitumor activity (Horák et al. 2017). Iron is known to play an important role in tumor development and cancer treatment, and iron oxide nanoparticles induce dose-dependent cytotoxicity and generate oxidative stress by increasing the production of intracellular reactive oxygen species (superoxide anions and nitric oxide) in human umbilical endothelial cells via the Fenton reaction (Torti and Torti 2013; Voinov et al. 2011).
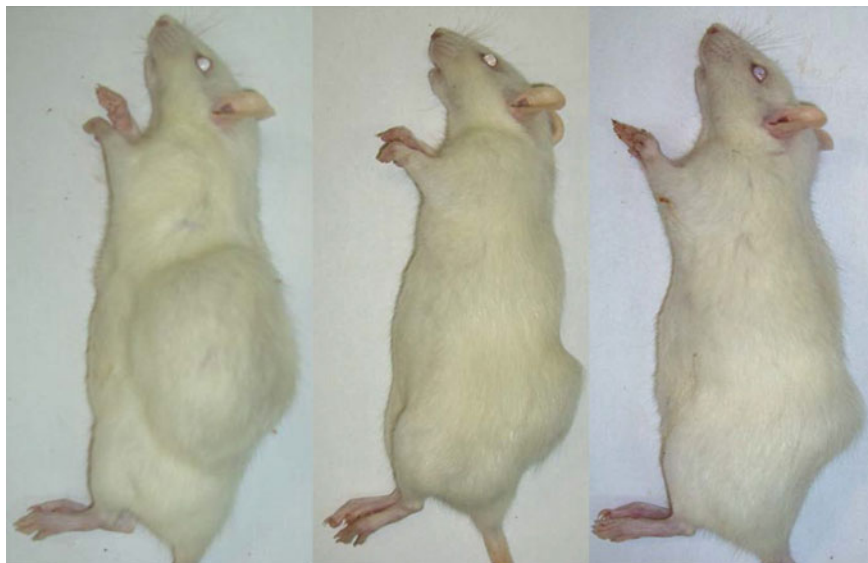
Fig. 5.32 Antitumor effect of γ-Fe$_2$O$_3$@PDMA nanoparticles on Walker-256 mammary gland carcinosarcoma in Wistar rats. From left to right: untreated rat with a tumor (control), rat with a tumor treated with intraperitoneally administered doxorubicin, and rat with a tumor treated with γ-Fe$_2$O$_3$@PDMA nanoparticles administered *per os*. Reproduced with permission from (Horák et al. 2017). Copyright 2017, with permission from Dove Medical Press

When considering the mechanism of the antitumor effect of γ-Fe$_2$O$_3$@PDMA nanoparticles, the particle dispersion has to first pass through the stomach and then enters the gastrointestinal tract and blood circulation system, reaching organs, such as the liver, kidney, and mesentery (Hughes et al. 2013). To be resorbed into the bloodstream, it is speculated that the particles penetrate the mucus barrier of the small intestine due to the small particle size, which allows secretion by the epithelium. Particles circulating in the bloodstream are preferentially accumulated by tumor cells due to their increased proliferative activity and passive transfer, which is known as the enhanced permeability and retention (EPR) effect (Duncan and Sat 1998). Differences in cellular uptake between cancer cells and normal cells have been observed by many authors, though the reasons for these differences are still under investigation (Zhang et al. 2016). This difference may be related to the difference in the endocytosis pathways between normal cells and cancer cells. Within tumor cells, cytotoxic Fe^{2+} is released under the formation of a singlet oxygen, leading to cell membrane and mitochondrial damage (Xu et al. 2009).

Hyperthermia

Hyperthermia is a minimally invasive procedure which destroys cancer cells by heat generated in alternating magnetic field (AMF) due to magnetization reversal losses of magnetic nanoparticles applied to a tumor. Different thermotolerance between tumor and healthy tissue cells enhances the sensitivity of the cancer cells to a simultaneous chemotherapy or radiotherapy (Pankhurst et al. 2003). The first application of magnetic iron oxide nanoparticles (20–100 nm) in hyperthermia was described already five decades ago (Gilchrist et al. 1957). Since that time many metal (Cherukuri et al. 2010) and metal oxide particles were suggested for hyperthermia using different magnetic field strengths and frequencies (Amiri and Shokrollahi 2013). However, iron oxide particles (maghemite γ-Fe_2O_3 and magnetite Fe_3O_4) are still considered as the best candidates for the biomedical applications since they exhibit minimum general toxic effects. Nevertheless, the mechanism of heat generation by the superparamagnetic nanoparticles is still not fully understood since the induced heat can be affected by viscosity, susceptibility, and hysteresis losses. Susceptibility losses have two relaxation times, i.e., Néel relaxation (τ_N) and Brownian rotation (τ_B), which differ in their dependence on the nanoparticle size. The susceptibility loss of particles of the identical size induced by the Brownian rotation is higher at low frequencies of alternating magnetic field than that due to Néel relaxation. A second mechanism addresses magnetic hysteresis losses, which occur for larger ferrimagnetic particles with a magnetic anisotropy. Coercivity and relative remanence and the heating efficiency are function not only of particle size and/or shape, but also the strength and frequency of the applied magnetic field. With increasing particle diameter, coercivity and relative remanence increase, which correspond to transition from superparamagnetic to ferrimagnetic behavior. This is reflected in enhanced specific absorption rate (SAR) of particles exposed to alternating magnetic field. Particles with sizes >10 nm and <50 nm are generally considered as best for tissue penetration and AMF-driven heat generation. Also, size distribution has an important influence on resulting SAR; particles with a broader size distribution result in increased SAR than narrow size distributed particles of comparable mean size (Patsula et al. 2016). The SAR value (W g^{-1}) was calculated according to Eq. (5.7):

$$\text{SAR} = \frac{C_p \rho}{m}\left(\frac{dT}{dt}\right) \tag{5.7}$$

where C_p (4.18 J K^{-1} g^{-1}) and ρ (1016.5 kg m^{-3}) are the specific heat and density of the colloid, respectively, and m is the mass of iron oxide per unit volume of the colloid.

As an example, Fig. 5.33 shows the SAR of γ-Fe_2O_3, poly(*N,N*-dimethylacrylamide-*co*-acrylic acid) (DMA)- and D-mannose (MAN)-coated (γ-Fe_2O_3@PDMA and γ-Fe_2O_3@MAN) nanoparticles extrapolated to 10 kA m^{-1} reaching about 15 W g^{-1}, which is promising for their application in magnetic hyperthermia (Babič et al. 2017).
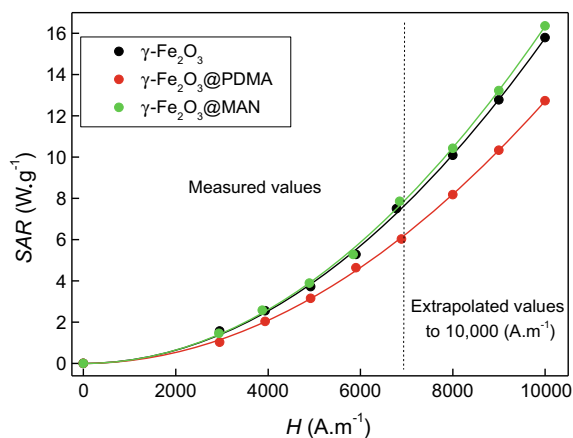
Fig. 5.33 *SAR* dependence of γ-Fe₂O₃, γ-Fe₂O₃@PDMA, and γ-Fe₂O₃@D-mannose nanoparticles on the applied magnetic field H at the frequency $f = 190$ kHz. Measured experimental data were fitted according to $\Delta T/\Delta t = (H/a)^n$ up to 10 kA m^{-1}; *SAR*—specific absorption rate, PDMA—poly(*N,N*-dimethylacrylamide). Reproduced with permission from (Babič et al. 2017). Copyright 2017, with permission from IOP Publishing

Separation of Biomolecules

The efficient isolation and concentration of protein antigens from complex biological samples are a critical step in several analytical methods, such as mass spectrometry, flow cytometry, and immunochemistry. These techniques take advantage of magnetic microspheres as immunosorbents. Magnetic separation advantageously replaces classical separation techniques, such as centrifugation, filtration, or column separation, including size exclusion or exchange chromatography, as the isolated cells or enzymes are subjected to very low mechanical stress, and the method is favorable for automation. The magnetic cell separation is beneficial for direct isolation from crude biological samples, such as blood, bone marrow, stool, water, and soil. The amino-, carboxyl-, hydroxyl-, tosyl- or hydrazide-containing particles can be functionalized with antibody or streptavidin to capture biotinylated antibody. Immobilized protein A or protein G then binds the antibody of conjugate. Application of immobilized enzymes, such as glucoamylase, cytochrome c oxidase, β-lactamase, chymotrypsin, alcohol dehydrogenase, glucose oxidase, galactose oxidase, urease, neuraminidase, papain, laccase, DNase, or RNase (Korecká et al. 2005; Chen and Liao 2002; Koneracká et al. 2002), in biotechnological practice offers a distinct advantage over soluble enzymes, because they can be rapidly and simply removed from the reaction mixture, can be used repeatedly and are more resistant to the unfolding of their native structure that may be caused by heat and pH changes. Immobilized enzyme avoids contamination of the digestion products by free enzymes or peptides, which can be very detrimental to analysis (Davis et al. 1995). This is especially important because increasingly larger amounts of various enzymes are consumed in

industrial applications. Important application involves large-scale chromatographic purification of chromosomal or plasmid DNA, peptides, polysaccharides, and lipids in biotechnological processes like gene therapy (Horák et al. 2001).

Control of Food Quality

Food quality has gained increased importance for consumers and food industry, and DNA-based methods, such as polymerase chain reaction (PCR), represent a useful tool for the identification of plants in foods, confirmation of foods authenticity, and genetically modified organism detection. In this context, magnetic hydrophilic P(HEMA-GMA) microspheres are used in the presence of PEG 6000/NaCl for low-cost and time-consuming extraction of DNA in a wide range of concentrations (0.1 pg μl^{-1} to 10 ng μl^{-1}) from raw vegetables and highly processed foods of plant origin (corn flakes, chocolate, and pickled red beetroot) (Trojánek et al. 2018). Magnetic PHEMA microspheres functionalized by polyclonal *Salmonella* antibodies or proteinase K via the trichlorotriazine method immunomagnetically separate *Salmonella* cells from intra- or extracellular inhibitors; *Salmonella* is then successfully identified using cultural and PCR methods in the presence of dominant background microflora in medical and food microbiology, foodstuffs, eggs, etc. (Španová et al. 2003). Other examples include determination of *E. coli*, *Staphylococcus aureus* and *Listeria monocytogenes*. A sandwich enzyme-labeled immunoassay (ELISA) for the detection of *Campylobacter jejuni* in food is based on magnetic PGMA-NH_2 microspheres with immobilized antibody against *Campylobacter jejuni* via the 2,4,6-trichloro-1,3,5-triazine method as a solid phase (Figs. 5.9 and 5.34) (Horák and Hochel 2005).

Another sandwich-type electrochemical immunosensor containing magnetic PGMA-COOH microspheres with immobilized anti-OVA antibodies was designed for rapid detection of ovalbumin (OVA) as an example of food allergen using secondary anti-ovalbumin antibodies conjugated with horseradish peroxidase as label tag (Čadková et al. 2015). This offers a very promising approach in comparison with methods based on a standard ELISA arrangement, especially due to the potential for miniaturization, low sample volumes, rapid analysis, and possible automation of analysis and the possibility of measurement outside the laboratory, while maintaining the sensitivity and specificity. The immunosensor could be reused after simple regeneration and washing steps; therefore, the overall costs of the analysis could be reduced substantially.

Magnetic P(HEMA-GMA)-NH_2-STV microspheres with immobilized DNA probe isolated *Lactobacillus paracasei* DNA from probiotic food supplements (Horák et al. 2011). Probiotic lactic bacteria present in dairy products confer health benefits controlling host gastrointestinal microflora. The identification of bacteria in real samples requires the preparation of PCR-ready DNA without inhibitors, which can be advantageously removed using magnetic separation on the magnetic microspheres.
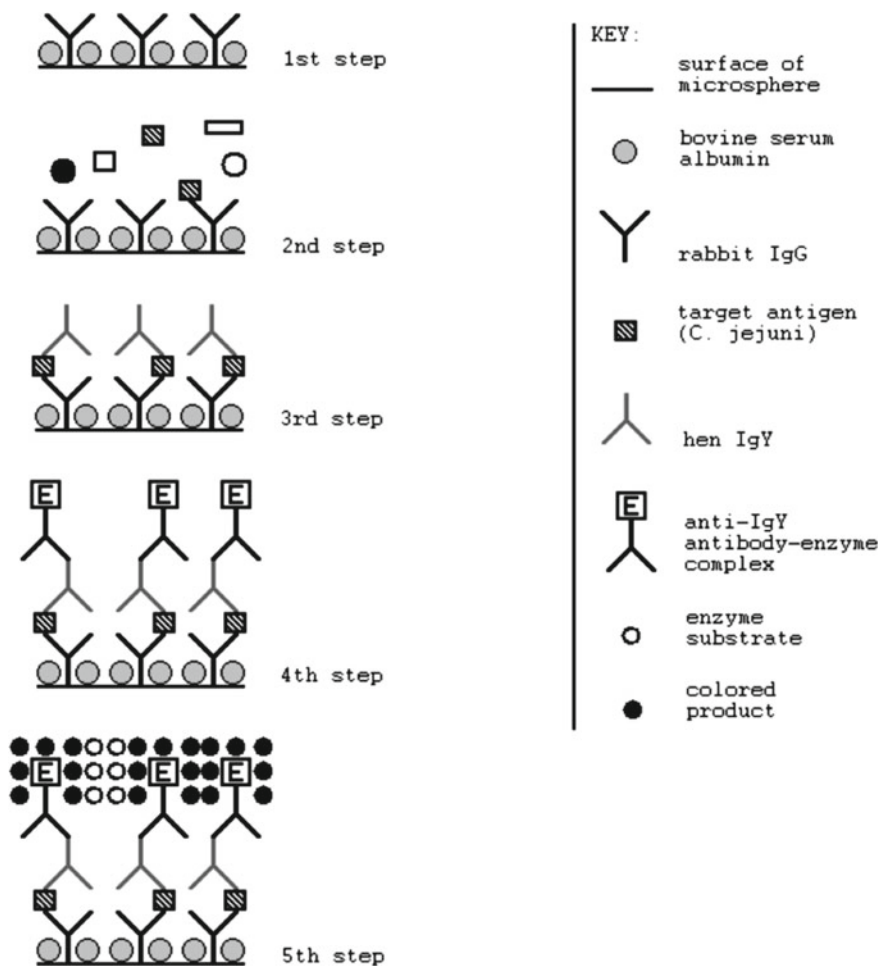
Fig. 5.34 Sandwich enzyme immunoassay. 1st step: covalent attachment of the antibody (IgG) to magnetic microspheres, saturation of the solid-phase surface with bovine serum albumin; 2nd step: incubation with the sample; 3rd step: addition of the second antibody (IgY); 4th step: addition of the anti-IgY antibody–enzyme complex; 5th step: addition of enzyme substrate, removal of microspheres and absorbance measurement. Reproduced with permission from (Horák and Hochel 2005). Copyright 2005, with permission from De Gruyter

Carboxyl group-containing magnetic P(HEMA-EDMA), PGMA, and P(HEMA-GMA) microspheres were used in solid-phase reversible adsorption of genomic DNA isolated from lactic acid bacteria (*Bifidobacterium longum* and *Lactobacillus*) in the presence of NaCl and PEG. Bacteria were separated from dairy products, such as cheese, butter, milk, kefir, and yoghurt, which was followed by PCR identification of DNA (Křížová et al. 2005). The proposed procedure is suitable also for the isolation of DNA from lake sediments, fungi, or for testing of genetically modified organisms.
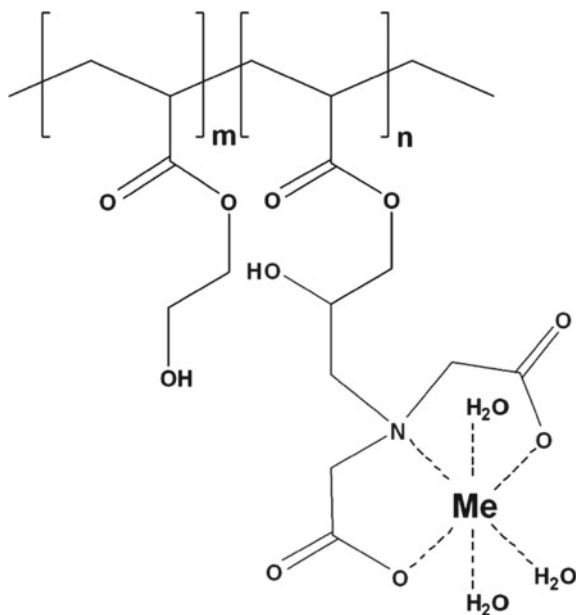
As an example of immobilized metal affinity chromatography purification, magnetic P(HEMA-GMA) particles coupled with iminodiacetic acid (IDA) to bind Ni(II) or Fe(III) ions were shown to separate or detect proteins (Fig. 5.35) (Přikryl et al. 2006). P(HEMA-GMA) microspheres modified with iminodiacetic acid (IDA) were employed for the immobilized metal (Fe^{3+}, Ga^{3+}) affinity chromatography (IMAC) separation of phosphopeptides from the proteolytic digests (dried milk) (Novotna et al. 2010).

Other Separations

Ion exchange-based separations on a magnetic support with weakly acid (COOH), weakly (NH_2), and strongly basic groups [$N^+(CH_3)_3$] found applications in water treatment, providing drinking water supplies from low-quality resources, sewage treatment, and economic purification of industrial wastewaters from toxic azo dyes, heavy metal ions or As(III) and As(V) traces (Bolto 1996; Bolto and Spurling 1991). Both batch and continuous procedures were developed for desalting brackish water, treatment of industrial, and household wastewater, e.g., for removal of nickel from electroplating rinse water, or to decolorize pulp mill eluent. Magnetic (diethylaminoethyl)agarose (DEAE-Magarose®) effectively bound DNA from crude cell lysates (Levison et al. 1998).

Outlook

Surface-modified magnetic iron oxide nanoparticles have been already used in many biomedical applications, such as in vitro cell labeling followed by in vivo MRI tracking, which is being investigated for stem cell therapy, or contrast agents to detect various diseases. Minimizing particle size is important for the ease of cellular internalization. Although gadolinium compounds represent here competition, they might be forbidden in the future due to their toxic effects, especially in nephropathic patients, which plays into the hands of biocompatible iron oxides. The uptake of iron oxide nanoparticles into the cells can be also well monitored by Prussian blue staining. Moreover, the iron oxide particles found applications not only as enzyme mimetics and sensors in clinical diagnostics, like early detection of cancer and/or neurodegenerative diseases, but also in combination with therapeutics, such as hyperthermia, photothermal treatment, or nanocarriers of chemo- and phototherapy agents. In addition, with continuing progress in new particle design, combinations of multiple functions will be achieved in the future. This will enable to achieve for example simultaneous MRI, positron emission tomography, single-photon emission computed tomography/computed tomography, NIR fluorescence and photoacoustic imaging in a single particle.

It is not only the core, which will have to be redesigned, but bright future is waiting also for the new shells. The coating material should possess some specific characteristics, such as biodegradability, biocompatibility, hydrophilicity, the presence of functional groups, and strong repulsion forces to allow long circulation time in blood. There is still no ideal stable hydrophilic coating available to avoid particle aggregation under physiological conditions of living organism. Probably the best compounds to prevent aggregation rely on the strong affinity of bisphosphonates toward iron oxides. However, new and more efficient stabilizing agents are definitely waiting to be discovered in the future.

In terms of magnetic microspheres as a solid support, they provide easy handling, e.g., with immobilized biomolecules and enzymes, which have much higher storage stability than the free enzyme and can be repeatedly removed from the complex reaction mixtures by a magnet. Immunomagnetic separation of DNA, which is important for the early detection of many inherited and malignant diseases, can be then effectively combined with PCR. Also, direct immunocapturing of circulating tumor or cancer stem cells on the microspheres from biological fluids is a very promising approach for improved diagnosis of cancer, aiding prognosis and follow-up. The magnetic microspheres are also vital to enable advanced processing in sophisticated protocols for multiplex molecular diagnostics. The possibility to implement them in automated systems favors their use in a broad range of bioassays, including clinical tests. Miniaturization is increasingly explored because of the numerous advantages it is promising. Combination of microfluidic devices with magnetic microspheres is creating new possibilities in innovative bioapplications, especially in point-of-care diagnostics and personalized medicine.

References

Amiri S, Shokrollahi H (2013) The role of cobalt ferrite magnetic nanoparticles in medical science. Mater Sci Eng C 33:1–8

Arruebo M, Fernández-Pacheco R, Velasco B, Marquina C, Arbiol J, Irusta S, Ibarra MR, Santamaría J (2007) Antibody-functionalized hybrid superparamagnetic nanoparticles. Adv Funct Mater 17:1473–1479

Babič M, Horák D, Trchová M, Jendelová P, Glogarová K, Lesný P, Herynek V, Hájek M, Syková E (2008) Poly(L-lysine)-modified iron oxide nanoparticles for stem cell labeling. Bioconjug Chem 19:740–750

Babič M, Horák D, Jendelová P, Glogarová K, Herynek V, Trchová M, Likavčanová K, Hájek M, Syková E (2009) Poly(*N,N*-dimethylacrylamide)-coated maghemite nanoparticles for stem cell labeling. Bioconjug Chem 20:283–294

Babič M, Horák D, Jendelová P, Herynek V, Proks V, Vaněček V, Syková E (2012) The use of dopamine-hyaluronate associate-coated maghemite nanoparticles to label cells. Int J Nanomed 7:1461–1474

Babič M, Schmiedtová M, Poledne R, Herynek V, Horák D (2015) *In vivo* monitoring of rat macrophages labeled with poly(*L*-lysine)-iron oxide nanoparticles. J Biomed Mater Res B 103:1141–1148

Babič M, Horák D, Molčan M, Timko M (2017) Heat generation of surface-modified magnetic γ-Fe_2O_3 nanoparticles in applied alternating magnetic field. J Phys D 50:345002

Bailey FEJ, Koleske JV (1976) Poly(Ethylene Oxide). Academic Press, New York

Baner J, Nilsson M, Mendel-Hartvig M, Landegren U (1998) Signal amplification of padlock probes by rolling circle replication. Nucleic Acids Res 26:5073–5078

Barry SE (2008) Challenges in the development of magnetic particles for therapeutic applications. Int J Hyperth 24:451–466

Bergna HE, Roberts WO (2005) Colloidal silica: fundamentals and applications. CRC Press, Santa Barbara

Bílková Z, Slováková M, Lyčka A, Horák D, Lenfeld J, Turková J, Churáček J (2002a) Oriented immobilization of galactose oxidase to bead and magnetic bead cellulose and poly(HEMA-*co*-EDMA) and magnetic poly(HEMA-*co*-EDMA) microspheres. J Chromatogr B 770:25–34

Bílková Z, Slováková M, Horák D, Lenfeld J, Churáček J (2002b) Enzymes immobilized on magnetic carriers: efficient and selective system for protein modification. J Chromatogr B 770:177–181

Bílková Z, Slováková M, Minc N, Futterer C, Cecal R, Horák D, Beneš M, le Potier I, Przybylski M, Viovy J-L (2006) Functionalized magnetic micro- and nanoparticles: optimization and application to μ-chip tryptic digestion. Electrophoresis 27:1811–1824

Bober P, Zasonska BA, Humpolíček P, Kuceková Z, Varga M, Horák D, Babayan B, Kazantseva N, Prokeš J, Stejskal J (2016) Polyaniline-maghemite based dispersion: electrical, magnetic properties and their cytotoxicity. Synth Metals 214:23–29

Bolto BA (1996) Magnetic particle technology: desalination and water reuse applications. Desalination 106:137–143

Bolto BA, Spurling TH (1991) Water purification with magnetic particles. Environ Monit Assess 19:139–143

Borisova T, Krisanova N, Borysov A, Sivko R, Ostapchenko L, Babič M, Horák D (2014) Manipulation of isolated brain nerve terminals by an external magnetic field using D-mannose-coated γ-Fe$_2$O$_3$ nano-sized particles and assessment of their effects on glutamate transport. Beilstein J Nanotechnol 5:778–788

Čadková M, Metelka R, Holubová L, Horák D, Dvořáková V, Bílková Z, Korecká L (2015) Magnetic beads-based electrochemical immunosensor for monitoring of allergenic food proteins. Anal Biochem Anal Biochem 484:4–8

Callister WD, Rethwisch DG (2006) Material science and engineering: an Introduction, 7th edn. Wiley, New York

Cao X, Horák D, An Z, Plichta Z (2016) RAFT polymerization of *N,N*-dimethylacrylamide from magnetic poly(2-hydroxyethyl methacrylate) microspheres to suppress nonspecific protein adsorption. J Polym Sci Part A Polym Chem 54:1036–1043

Chandrasekharan P, Maity D, Yong CX, Chuang KH, Ding J, Feng SS (2011) Vitamin E (d-α-tocopheryl-*co*-poly(ethylene glycol) 1000 succinate) micelles-superparamagnetic iron oxide nanoparticles for enhanced thermotherapy and MRI. Biomaterials 32:5663–5672

Chekina N, Horák D, Jendelová P, Trchová M, Beneš MJ, Hrubý M, Herynek V, Turnovcová K, Syková E (2011) Fluorescent magnetic nanoparticles for biomedical applications. J Mater Chem 21:7630–7639

Chen DH, Liao MH (2002) Preparation and characterization of YADH-bound magnetic nanoparticles. J Mol Catal B Enzym 16:283–291

Cherukuri P, Glazer ES, Curley SA (2010) Targeted hyperthermia using metal nanoparticles. Adv Drug Deliv Rev 62:339–345

Coey JMD (2010) Magnetism and magnetic materials. Cambridge University Press, Cambridge

Collins AR (2004) The comet assay for DNA damage and repair: principles, applications, and limitations. Mol Biotechnol 26:249–261

Covaliu CI, Berger D, Matei C, Diamandescu L, Vasile E, Cristea C, Ionita V, Iovu H (2011) Magnetic nanoparticles coated with polysaccharide polymers for potential biomedical applications. J Nanopart Res 13:6169–6180

Dahl F, Baner J, Gullberg M, Mendel-Hartvig M, Landegren U, Nilsson M (2004) Circle-to-circle amplification for precise and sensitive DNA analysis. Proc Natl Acad Sci USA 101:4548–4553

Dave PN, Chopda LV (2014) Application of iron oxide nanomaterials for the removal of heavy metals. J Nanotechnol 398569

Davis MT, Lee TD, Ronk M, Hefta SA (1995) Microscale immobilized protease reactor columns for peptide mapping by liquid chromatography/mass spectral analysis. Anal Biochem 224:235–244

de la Escosura-Muñiz A, Plichta Z, Horák D, Merkoçi A (2015) Alzheimer's disease biomarkers detection in human samples by efficient capturing through porous magnetic microspheres and labelling with electrocatalytic gold nanoparticles. Biosens Bioelectron 67:162–169

Dormer K, Seeney C, Lewelling K, Lian G, Gibson D, Johnson M (2005) Epithelial internalization of superparamagnetic nanoparticles and response to external magnetic field. Biomaterials 24:2061–2072

Duan S, Wang R (2013) Bimetallic nanostructures with magnetic and noble metals and their physicochemical applications. Prog Nat Sci 23:113–126

Duncan R, Sat YN (1998) Tumour targeting by enhanced permeability and retention (EPR) effect. Ann Oncol 9(Suppl 2):39

Dunorier H, Muller S (2007) Histone autoantibodies. In: Shoenfeld Y, Meroni P-L, Gershwin ME (eds) Autoantibodies, 2nd ed. Elsevier, Amsterdam, pp 169–177

Elaissari A, Fessi H (2010) Reactive and highly submicron magnetic latexes for bionanotechnology applications. Macromol Symp 288:115–120

Fairbanks BD, Thissen H, Maurdev G, Pasic P, White JF, Meagher L (2014) Inhibition of protein and cell attachment on materials generated from *N*-(2-hydroxypropyl)acrylamide. Biomacromol 15:3259–3266

Faustino-Rocha A, Oliveira PA, Pinho-Oliveira J, Teixeira-Guedes C, Soares-Maia R, da Costa RG, Colaço B, Pires MJ, Colaço J, Ferreira R, Ginja M (2013) Estimation of rat mammary tumor volume using caliper and ultrasonography measurements. Lab Anim (NY) 42:217–224

Ferlay J, Shin HR, Bray F, Forman D, Mathers C, Parkin DM (2008) GLOBOCAN Cancer incidence and mortality worldwide. http://globocan.iarc.fr/factsheet.asp

Fleige G, Seeberger F, Laux D, Kresse M, Taupitz M, Pilgrim H, Zimmer C (2002) *In vitro* characterization of two different ultrasmall iron oxide particles for magnetic resonance cell tracking. Invest Radiol 37:482–488

Flogel U, Ding Z, Hardung H, Jander S, Reichmann G, Jacoby C, Schubert R, Schrader J (2008) *In vivo* monitoring of inflammation after cardiac and cerebral ischemia by fluorine magnetic resonance imaging. Circulation 118:140–148

Gallo J, Long NJ, Aboagye EO (2013) Magnetic nanoparticles as contrast agents in the diagnosis and treatment of cancer. Chem Soc Rev 42:7816–7833

Ghazanfari MR, Kashefi M, Shams SF, Jaafari MR (2016) Perspective of Fe_3O_4 nanoparticles role in biomedical applications. Biochem Res Int 7840161

Gilchrist RK, Medal R, Shorey WD, Hanselman RC, Parrott JC, Taylor BC (1957) Selective inductive heating of lymph nodes. Ann Surg 146:596–606

Goddard ED, Gruber JV (eds) (1999) Principles of science and technology in cosmetics and personal care. Marcel Dekker, New York

Goss CJ (1988) Saturation magnetisation, coercivity and lattice parameter changes in the system Fe_3O_4-γ-Fe_2O_3, and their relationship to structure. Phys Chem Miner 16:164–171

Greenwood R (2003) Review of the measurement of zeta potentials in concentrated aqueous suspensions using electroacoustics. Adv Colloid Interface Sci 106:55–81

Guneri ET, Bureau C, Champ J, Mottet G, Perez-Toralla K, Bidard F-C, Pierga JY, Malaquin L, Viovy JL, Descroix S (2014) Ephesia: combining microfluidics and proximity ligation assay to analyze protein-protein interactions in single circulating tumour cells: a new tool for pharmaceutical research and personalized medicine. In: 18th International Conference on Miniaturized Systems for Chemistry and Life Sciences, San Antonio 2014, pp 588–590

Gupta AK, Gupta M (2005) Synthesis and surface engineering of iron oxide nanoparticles for biomedical applications. Biomaterials 26:3995–4021

Hafeli UO, Rifle JS, Harris-Shekhawat L, Carmichael-Baranauskas A, Mark F, Dailey JP, Bardenstein D (2009) Cell uptake and in vitro toxicity of magnetic nanoparticles suitable for drug delivery. Mol Pharm 6:1417–1428

Hao R, Xing R, Xu Z, Hou Y, Gao S, Sun S (2010) Synthesis, functionalization, and biomedical applications of multifunctional magnetic nanoparticles. Adv Mater 22:2729–2742

Harper S, Usenko C, Hutchison JE, Maddux BLS, Tanguay RL (2008) In vivo biodistribution and toxicity depends on nanomaterial composition, size, surface functionalisation and route of exposure. J Exp Nanosci 3:195–206

Harris MJ, Zalipsky S (eds) (1997) Poly(ethylene glycol), chemistry and biological applications. American Chemical Society, Washington

Hasany SF, Ahmed I, Rajan J, Rehman A (2012) Systematic review of the preparation techniques of iron oxide magnetic nanoparticles. J Nanosci Nanotechnol 2:148–158

Heyn C, Bowen CV, Rutt BK, Foster PJ (2005) Detection threshold of single SPIO-labeled cells with FIESTA. Magn Reson Med 53:312–320

Hlídková H, Kotelnikov I, Pop-Georgievski O, Proks V, Horák D (2017) Antifouling peptide dendrimer surface of monodisperse magnetic poly(glycidyl methacrylate) microspheres. Macromolecules 50:1302–1311

Ho D, Sun X, Sun S (2011) Monodisperse magnetic nanoparticles for theranostic applications. Acc Chem Res 44:875–882

Horák D (2001) Magnetic polyglycidylmethacrylate microspheres by dispersion polymerization. J Polym Sci A Polym Chem 39:3707–3715

Horák D, Hochel I (2005) Magnetic poly(glycidyl methacrylate) microspheres for ELISA *Campylobacter jejuni* detection in food. e-Polymers 5(060):2197–4586

Horák D, Boháček J, Šubrt M (2000) Magnetic poly(2-hydroxyethyl methacrylate-*co*-ethylene dimethacrylate) microspheres by dispersion polymerization. J Polym Sci A Polym Chem 38:1161–1171

Horák D, Rittich B, Šafář J, Španová A, Lenfeld J, Beneš MJ (2001) Properties of RNase immobilized on magnetic poly(HEMA) microspheres. Biotechnol Prog 17:447–452

Horák D, Rittich B, Španová A, Beneš MJ (2005) Magnetic microparticulate carriers with immobilized selective ligands in DNA diagnostics. Polymer 46:1245–1255

Horák D, Babič M, Macková H, Beneš MJ (2007a) Preparation and properties of magnetic nano- and microsized particles for biological and environmental separations. J Sep Sci 30:1751–1772

Horák D, Rittich B, Španová A (2007b) Carboxyl-functionalized magnetic microparticle carrier for isolation and identification of DNA in dairy products. J Magn Magn Mater 311:249–254

Horák D, Babič M, Jendelová P, Herynek V, Trchová M, Pientka Z, Pollert E, Hájek M, Syková E (2007c) D-mannose-modified iron oxide nanoparticles for stem cell labeling. Bioconjug Chem 18:635–644

Horák D, Pollert E, Trchová M, Kovářová J (2009) Magnetic poly(glycidyl methacrylate)-based microspheres prepared by suspension polymerization in the presence of modified $La_{0.75}Sr_{0.25}MnO_3$ nanoparticles. Eur Polym J 45:1009–1016

Horák D, Babič M, Jendelová P, Herynek V, Trchová M, Likavčanová K, Kapcalová M, Hájek M, Syková E (2009b) The effect of different magnetic nanoparticle coatings on the efficiency of stem cell labeling. J Magn Magn Mater 321:1539–1547

Horák D, Španová A, Tvrdíková J, Rittich B (2011) Streptavidin-modified magnetic poly(2-hydroxyethyl methacrylate-*co*-glycidyl methacrylate) microspheres for selective isolation of DNA. Eur Polym J 47:1090–1096

Horák D, Kučerová J, Korecká L, Jankovičová B, Palarčík J, Mikulášek P, Bílková Z (2012a) New monodisperse magnetic polymer microspheres biofunctionalized for enzyme catalysis and bioaffinity separations. Macromol Biosci 12:647–655

Horák D, Balonová L, Mann BF, Plichta Z, Hernychová L, Novotny MV, Stulík J (2012b) Use of magnetic hydrazide-modified polymer microspheres for enrichment of *Francisella tularensis* glycoproteins. Soft Matter 8:2775–2786

Horák D, Svobodová Z, Autebert J, Coudert B, Královec K, Plichta Z, Bílková Z, Viovy J-L (2013) Albumin-coated monodisperse magnetic poly(glycidyl methacrylate) microspheres with immobilized antibodies: application to the capture of epithelial cancer cells. J Biomed Mater Res 101A:23–32

Horák D, Hlídková H, Hiraoui M, Taverna M, Proks V, Mázl Chánová E, Smadja C, Kučerová Z (2014) Monodisperse carboxyl-functionalized poly(ethylene glycol)-coated magnetic poly(glycidyl methacrylate) microspheres: application to the immunocapture of ß-amyloid peptides. Macromol Biosci 14:1590–1599

Horák D, Hlídková H, Trachtová Š, Šlouf M, Rittich B, Španová A (2015a) Evaluation of poly(ethylene glycol)-coated monodisperse magnetic poly(2-hydroxyethyl methacrylate) and poly(glycidyl methacrylate) microspheres by PCR. Eur Polym J 68:687–696

Horák D, Plichta Z, Starykovych M, Myronovskij S, Kit Y, Chopyak V, Stoika R (2015b) Calf thymus histone-conjugated magnetic poly(2-oxoethyl methacrylate) microspheres for affinity isolation of anti-histone IgGs from blood serum of patients with systemic lupus erythematosus. RSC Adv 5:63050–63055

Horák D, Hlídková H, Klyuchivska O, Grytsyna I, Stoika R (2017) PEGylation controls attachment and engulfment of monodisperse magnetic poly(2-hydroxyethyl methacrylate) microspheres by murine J774.2 macrophages. Appl Surf Sci 426:315–324

Horák D, Hlídková H, Kit Y, Antonyuk V, Myronovsky S, Stoika R (2017) Magnetic poly(2-hydroxyethyl methacrylate) microspheres for affinity purification of monospecific anti-p 46 kDa/Myo1C antibodies for early diagnosis of multiple sclerosis patients. Biosci Rep 37

Horák D, Pustovyy VI, Babinskiy AV, Palyvoda OM, Chekhun VF, Todor IN, Kuzmenko OI (2017c) Enhanced antitumor activity of surface-modified iron oxide nanoparticles and α-tocopherol derivative in a rat model of mammary gland carcinosarcoma. Int J Nanomed 12:4257–4268

Hufschmid R, Arami H, Ferguson RM, Gonzales M, Teeman E, Brush LN, Browning ND, Krishnan KM (2015) Synthesis of phase-pure and monodisperse iron oxide nanoparticles by thermal decomposition. Nanoscale 7:11142–11154

Hughes MF, Long TC, Boyes WK, Ramabhadran R (2013) Whole-body retention and distribution of orally administered radiolabeled zerovalent iron nanoparticles in mice. Nanotoxicology 7:1064–1069

Jeong U, Teng X, Wang Y, Yang H, Xia Y (2006) Superparamagnetic colloids: controlled synthesis and niche applications. Adv Mater 19:33–60

Jiráková K, Šeneklová M, Jirák D, Turnovcová K, Vosmanská M, Babič M, Horák D, Veverka P, Jendelová P (2016) The effect of magnetic nanoparticles on neuronal differentiation of induced pluripotent stem cell-derived neural precursors. Int J Nanomed 11:6267–6281

Jun Y, Seo J, Cheon J (2008) Nanoscaling laws of magnetic nanoparticles and their applicabilities in biomedical sciences. Acc Chem Res 41:179–189

Justin C, Philip SA, Samrot AV (2017) Synthesis and characterization of superparamagnetic iron-oxide nanoparticles (SPIONs) and utilization of SPIONs in X-ray imaging. Appl Nanosci 7:463–475

Kammler HK, Mädler L, Pratsinis SE (2001) Flame synthesis of nanoparticles. Chem Eng Technol 24:583–596

Knobel M, Nunes WC, Socolovsky LM, De Biasi E, Vargas JM, Denardin JC (2008) Superparamagnetism and other magnetic features in granular materials: a review on ideal and real systems. J Nanosci Nanotechnol 8:2836–2857

Koneracká M, Kopčanský P, Timko M, Ramchand CN, de Sequeira A, Trevan M (2002) Direct binding procedure of proteins and enzymes to fine magnetic particles. J Mol Catal B Enzym 18:13–18

Kontogeorgis GM, Kiil S (2016) Colloid stability—Part I. In: Introduction to applied colloid and surface chemistry. Wiley, Chichester

Korecká L, Ježová J, Bílková Z, Beneš M, Horák D, Hradcová O, Slováková M, Viovy J-L (2005) Magnetic enzyme reactors for isolation and study of heterogeneous glycoproteins. J Magn Magn Mater 293:349–357

Kostiv U, Patsula V, Šlouf M, Pongrac I, Škokić S, Radmilović M, Pavičić I, Vinković Vrček I, Gajović S, Horák D (2017) Physico-chemical characteristics, biocompatibility, and MRI applicability of novel monodisperse PEG-modified magnetic Fe_3O_4 & SiO_2 core-shell nanoparticles. RSC Adv 7:8786–8797

Koubková J, Müller P, Hlídková H, Plichta Z, Proks V, Vojtěšek B, Horák D (2014) Magnetic poly(glycidyl methacrylate) microspheres for capture of proteins. New Biotechnol 31:482–491

Křížová J, Španová A, Rittich B, Horák D (2005) Magnetic hydrophilic methacrylate-based polymer microspheres for genomic DNA isolation. J Chromatogr A 1064:247–253

Kuan W-C, Horák D, Plichta Z, Lee W-C (2014) Immunocapture of CD133-positive cells from human cancer cell lines by using monodisperse magnetic poly(glycidyl methacrylate) microspheres containing amino groups. Mater Sci Eng C 34:193–200

Kwon SG, Piao Y, Park J, Angappane S, Jo Y, Hwang NM, Park JG, Hyeon T (2007) Kinetics of monodisperse iron oxide nanocrystal formation by "heating-up" process. J Am Chem Soc 129:12571–12584

Lanone S, Rogerieux F, Geys J, Dupont A, Maillot-Marechal E, Boczkowski J, Lacroix G, Hoet P (2009) Comparative toxicity of 24 manufactured nanoparticles in human alveolar epithelial and macrophage cell lines. Part Fibre Toxicol 6:14

Laurent S, Forge D, Port M, Roch A, Robic C, Elst LV, Muller RN (2008) Magnetic iron oxide nanoparticles: synthesis, stabilization, vectorization, physicochemical characterizations, and biological applications. Chem Rev 108:2064–2110

Levison PR, Badger SE, Hathi P, Davies MJ, Bruce IJ, Grimm V (1998) New approaches to the isolation of DNA by ion-exchange chromatography. J Chromatogr A 1(827):337–344

Lewis AL (2000) Phosphorylcholine-based polymers and their use in the prevention of biofouling. Colloids Surf B 18:261–275

Macková H, Proks V, Horák D, Kučka J, Trchová M (2011) Magnetic poly(*N*-propargylacrylamide) microspheres: preparation by precipitation polymerization and use in model click reactions. J Polym Sci A Polym Chem 49:4820–4829

Macková H, Horák D, Petrovský E, Kovářová J (2013) Magnetic hollow poly(N-isopropylacrylamide-*co*-N,N′-methylenebisacrylamide-*co*-glycidyl acrylate) particles prepared by inverse emulsion polymerization. Colloid Polym Sci 291:205–213

Macková H, Horák D, Donchenko GV, Andrijaka VI, Palyvoda OM, Chernishov VI, Chekhun VF, Todor IN, Kuzmenko OI (2015) Colloidally stable surface-modified iron oxide nanoparticles: preparation, characterization and anti-tumor activity. J Magn Magn Mater 380:125–131

Mahmoudi M, Sahraian MA, Shokrgozar MA, Laurent S (2011a) Superparamagnetic iron oxide nanoparticles: promises for diagnosis and treatment of multiple sclerosis. ACS Chem Neurosci 2:118–140

Mahmoudi M, Laurent S, Shokrgozar MA, Hosseinkhani M (2011) Toxicity evaluations of super-paramagnetic iron oxide nanoparticles: cell "vision" versus physicochemical properties of nanoparticles. ACS Nano 5:7263–7276

Majewski P, Thierry B (2007) Functionalized magnetite nanoparticles—synthesis, properties, and bio-applications. Crit Rev Solid State Mater Sci 32:203–215

May CA (ed) (1988) Epoxy resins chemistry and technology, 2nd edn. Marcel Dekker, New York

Møller P (2005) Genotoxicity of environmental agents assessed by the alkaline comet assay. Basic Clin Pharmacol Toxicol 96(Suppl 1):1–42

Moskvin M, Babič M, Reis S, Cruz MM, Ferreira LP, Deus Carvalho M, Costa Lima SA, Horák D (2018) Biological evaluation of surface-modified magnetic nanoparticles as a platform for colon cancer cell theranostics. Colloids Surf B 161:35–41

Narain R (ed) (2011) Engineered carbohydrate-based materials for biomedical applications: polymers, surfaces, dendrimers, nanoparticles and hydrogels. Wiley, Hoboken

Narayan R (ed) (2009) Biomedical materials. Springer, New York

Nel A, Xia T, Mädler L, Li N (2006) Toxic potential of materials at the nanolevel. Science 311:622–627

Novotna L, Emmerova T, Horak D, Kucerova Z, Ticha M (2010) Iminodiacetic acid-modified magnetic poly(2-hydroxyethyl methacrylate)-based polymer microspheres for phosphopeptide enrichment. J Chromatogr A 1217:8032–8040

Panagiotopoulos N, Duschka RL, Ahlborg M, Bringout G, Debbeler C, Graeser M, Kaethner C, Lüdtke-Buzug K, Medimagh H, Stelzner J, Buzug TM, Barkhausen J, Vogt FM, Haegele J (2015) Magnetic particle imaging: current developments and future directions. Int J Nanomed 10:3097–3114

Pankhurst QA, Connolly J, Jones SK, Dobson J (2003) Applications of magnetic nanoparticles in biomedicine. J Phys D—Appl Phys 36:167–181

Papell SS (1965) Low viscosity magnetic fluid obtained by the colloidal suspension of magnetic particles, US Pat. 3,215,572

Park J, An K, Hwang Y, Park JG, Noh HJ, Kim JY, Park JH, Hwang NM, Hyeon T (2004) Ultra-large-scale syntheses of monodisperse nanocrystals. Nat Mater 3:891–895

Park K, Lee S, Kang E, Kim K, Choi K, Kwon IC (2009) New generation of multifunctional nanoparticles for cancer imaging and therapy. Adv Funct Mater 19:1553–1566

Parton E, Palma RD, Borghs G (2007) Biomedical applications using magnetic nanoparticles. Solid State Technol 50:47–50

Patsula V, Petrovský E, Kovářová J, Konefal R, Horák D (2014) Monodisperse superparamagnetic nanoparticles by thermolysis of Fe(III) oleate and mandelate complexes. Colloid Polym Sci 292:2097–2110

Patsula V, Moskvin M, Dutz S, Horák D (2016) Size-dependent magnetic properties of iron oxide nanoparticles. J Phys Chem Solids 88:24–30

Pillai V, Kumar P, Hou MJ, Ayyub P, Shah DO (1995) Preparation of nanoparticles of silver halides, superconductors and magnetic materials using water-in-oil microemulsions as nano-reactors. Adv Colloid Interface Sci 55:241–269

Pongrac I, Dobrivojevic M, Brkic Ahmed L, Babič M, Šlouf M, Horák D, Gajovic S (2016a) Improved biocompatibility and efficient labeling of neural stem cells with poly(L-lysine)-coated maghemite nanoparticles. Beilstein J Nanotechnol 7:926–936

Pongrac I, Pavičić I, Milić M, Brkić Ahmed L, Babič M, Horák D, Vrček IV, Gajović S (2016b) Oxidative stress response in neural stem cells exposed to different superparamagnetic iron oxide nanoparticles. Int J Nanomed 11:1701–1715

Přikryl P, Horák D, Tichá M, Kučerová Z (2006) Magnetic IDA-modified hydrophilic methacrylate-based polymer microspheres for IMAC protein separation. J Sep Sci 29:2541–2549

Qiao R, Yang C, Gao M (2009) Superparamagnetic iron oxide nanoparticles: from preparations to *in vivo* MRI applications. J Mater Chem 19:6274–6293

Qiu Y, Wang F, Liu Y-M, Wang W, Chu L-Y, Wang H-L (2015) Microfluidic-based fabrication, characterization and magnetic functionalization of microparticles with novel internal anisotropic structure. Sci Rep 5:13060

Ramimoghadam D, Bagheri S, Hamid SBA (2014) Progress in electrochemical synthesis of magnetic iron oxide nanoparticles. J Magn Magn Mater 368:207–229

Rao SV, Anderson KW, Bachas LG (1998) Oriented immobilization of proteins. Microchim Acta 128:127–143

Reymond F, Vollet C, Plichta Z, Horák D (2013) Fabrication and characterization of tosyl-activated magnetic and non-magnetic monodisperse microspheres for use in microfluic-based ferritin immunoassay. Biotechnol Progr 29:532–542

Rittich B, Španová A, Ohlashenyy Yu, Lenfeld J, Rudolf I, Horák D, Beneš MJ (2002) Characterization of deoxyribonuclease I immobilized on magnetic hydrophilic polymer particles. J Chromatogr B 774:25–31

Roca AG, Morales MP, O'Grady K, Serna CJ (2006) Structural and magnetic properties of uniform magnetite nanoparticles prepared by high temperature decomposition of organic precursors. Nanotechnology 17:2783–2788

Rotková J, Šuláková R, Korecká L, Zdražilová P, Jandová M, Lenfeld J, Horák D, Bílková Z (2009) Laccase immobilized on magnetic carriers for biotechnology applications. J Magn Mater 321:1335–1340

Sakai-Kato K, Kato M, Toyooka T (2003) Creation of an on-chip enzyme reactor by encapsulating trypsin in sol-gel on a plastic microchip. Anal Chem 75:388–393

Salih T, Ahlford A, Nilsson M, Plichta Z, Horák D (2016) Streptavidin-modified monodisperse magnetic poly(2-hydroxyethyl methacrylate) microspheres as solid support in DNA-based molecular protocols. Mater Sci Eng C 61:362–367

Saravanan P, Alam S, Mathur GN (2003) Comparative study on the synthesis of γ-Fe$_2$O$_3$ and Fe$_3$O$_4$ nanocrystals using high-temperature solution-phase technique. J Mater Sci Lett 22:1283–1285

Shang H, Chang WS, Kan S, Majetich SA, Lee GU (2006) Synthesis and characterization of paramagnetic microparticles through emulsion-templated free radical polymerization. Langmuir 22:2516–2522

Sharma SK, Mudhoo A (eds) (2011) A handbook of applied biopolymer technology: synthesis, degradation and applications. Royal Society Chemistry, Cambridge

Shubayev VI, Pisanic TR, Jin S (2009) Magnetic nanoparticles for theragnostics. Adv Drug Deliv Rev 61:467–477

Shubhra QTH, Kardos AF, Feczkó T, Mackova H, Horák D, Tóth J, Gyenis J (2014) Co-encapsulation of human serum albumin and superparamagnetic iron oxide in PLGA nanoparticles: Part I. Effect of process variables on the mean size of magnetic PLGA nanoparticles. J Microencapsul 31:147–155

Singh NP, McCoy MT, Tice RR, Schneider EI (1988) A simple technique for quantitation of low levels of DNA damage in individual cells. Exp Cell Res 175:184–191

Siow WX, Chang Y-T, Babič M, Lu Y-C, Horák D, Ma Y-H (2018) Interaction of poly(L-lysine) coating and heparan sulfate proteoglycan modulate magnetic nanoparticle uptake in tumor cells. Int J Nanomed 13:1693–1706

Slavin S, Burns J, Haddleton DM, Becer CR (2011) Synthesis of glycopolymers via click reactions. Eur Polym J 47:435–446

Španová A, Rittich B, Horák D, Lenfeld J, Prodělalová J, Sučiková J, Štrumcová S (2003) Immuno-magnetic separation and detection of *Salmonella* cells using newly designed magnetic carriers. J Chromatogr A 1009:215–221

Strehl C, Maurizi L, Gaber T, Hoff P, Broschard T, Poole AR, Hofmann H, Buttgereit F (2016) Modification of the surface of superparamagnetic iron oxide nanoparticles to enable their safe application in humans. Int J Nanomed 11:5883–5896

Sun R, Dittrich J, Le-Huu M, Mueller MM, Bedke J, Kartenbeck J, Lehman JK, Krueger R, Bock M, Huss R, Seliger C, Grone HJ, Misselwitz B, Semmler W, Kiessling F (2005) Physical and biological characterization of superparamagnetic iron oxide- and ultrasmall superparamagnetic iron oxide-labeled cells: a comparison. Invest Radiol 40:504–513

Svobodová Z, Jankovičová B, Plichta Z, Horák D, Bílková Z (2018) Evaluation of colorimetric BCA-based quantification of hydrazide groups on magnetic particles. J Spectrosc 5492893

Tadros T, Tadros TF (eds) (2006) General Principles of colloid stability and the role of surface forces, in colloid stability: the role of surface forces, Part I, vol 1. Wiley-VCH, Weinheim

Tanyolac D, Ozdural AR (2000) A new low cost magnetic material: magnetic polyvinylbutyral microbeads. React Funct Polym 43:279–286

Teja AS, Koh PY (2009) Synthesis, properties, and applications of magnetic iron oxide nanoparticles. Prog Cryst Growth Ch 55:22–45

Teoh WY, Amal R, Mädler L (2010) Flame spray pyrolysis: an enabling technology for nanoparticles design and fabrication. Nanoscale 2:1324–1347

Thanh NTK (ed) (2018) Clinical applications of magnetic nanoparticles. CRC Press

Thurman JM, Serkova NJ (2013) Nano-sized contrast agents to non-invasively detect renal inflammation by magnetic resonance imaging. Adv Chronic Kidney Dis 20:488–499

Torti SV, Torti FM (2013) Iron and cancer: more ore to be mined. Nat Rev Cancer 13:342–355

Trachtová Š, Španová A, Horák D, Kozáková H, Rittich B (2016) Real-time polymerase chain reaction as a tool for evaluation of magnetic poly(glycidyl methacrylate)-based microspheres in molecular diagnostics. Curr Pharm Des 22:639–646

Trojánek Z, Kovařík A, Španová A, Marošiová K, Horák D, Rittich B (2018) Application of magnetic polymethacrylate-based microspheres for the isolation of DNA from raw vegetables and processed foods of plant origin. J Food Process Preserv 42:e13384

Ugelstad J (1984) Monodisperse polymer particles and dispersions thereof, US Patent 4,459,378

Umut E (2013) Surface modification of nanoparticles used in biomedical applications. In: Aliofkhazraei M (ed) Modern surface engineering treatments. InTech

Uthaman S, Lee SJ, Cherukula K, Cho CS, Park IK (2015) Polysaccharide-coated magnetic nanoparticles for imaging and gene therapy. Biomed Res Int 959175

Vohlídal J (1995) Makromolekulární chemie. Karolinum, Prague, Czech Republic

Voinov MA, Sosa Pagán JO, Morrison E, Smirnova TI, Smirnov AI (2011) Surface-mediated production of hydroxyl radicals as a mechanism of iron oxide nanoparticle biotoxicity. J Am Chem Soc 133:35–41

Vrček IV, Pavičić I, Crnković T, Jurašin D, Babič M, Horák D, Lovrić M, Ferhatović L, Ćurlin M, Gajović S (2015) Does surface coating of metallic nanoparticles modulate their interferences with *in vitro* assays? RSC Adv 5:70787–70807

Wang W, Dong H, Pacheco V, Willbold D, Zhang Y, Offenhaeusser A, Hartmann R, Weirich TE, Ma P, Krause H, Gu Z (2011) Relaxation behavior study of ultrasmall superparamagnetic iron oxide nanoparticles at ultralow and ultrahigh magnetic fields. J Phys Chem B 115:14789–14793

Weissleder R, Stark DD, Engelstad BL, Bacon BR, Compton CC, White DL, Jacobs P, Lewis J (1989) Superparamagnetic iron-oxide—pharmacokinetics and toxicity. Am J Roentgenol 152:167–173

Wichterle O, Lim D (1960) Hydrophilic gels for biological use. Nature 185:117–118

Wu W, He Q, Jiang C (2008) Magnetic iron oxide nanoparticles: synthesis and surface functionalization strategies. Nanoscale Res Lett 3:397–415

Xu C, Yuan Z, Kohler N, Kim J, Chung MA, Sun S (2009) FePt nanoparticles as an Fe reservoir for controlled Fe release and tumor inhibition. J Am Chem Soc 131:15346–15351

Yan J, Horák D, Lenfeld J, Hammond M, Kamali-Moghaddam M (2013) A tosyl-activated magnetic bead cellulose as solid support for sensitive protein detection. J Biotechnol 167:235–240

Yang J, Kopeček J (2015) Backbone degradable and coiled-coil based macromolecular therapeutics. In: Gu Z (ed) Bioinspired and biomimetic polymer systems for drug and gene delivery. Wiley-WCH, Weinheim

Yi DK, Lee SS, Papaefthymiou GC, Ying JY (2006) Nanoparticle architectures templated by SiO_2/Fe_2O_3 nanocomposites. Chem Mater 18:614–619

Zasonska BA, Boiko N, Horák D, Klyuchivska O, Macková H, Beneš M, Babič M, Trchová M, Hromádková J, Stoika R (2012) The use of hydrophilic poly(*N,N*-dimethylacrylamide) grafted from magnetic γ-Fe_2O_3 nanoparticles to promote engulfment by mammalian cells. J Biomed Nanotechnol 9:479–491

Zasonska BA, Bober P, Jošt P, Petrovský E, Boštík P, Horák D (2016) Magnetoconductive maghemite core/polyaniline shell nanoparticles as promising tools for biomedical applications. Colloids Surf B Biointerfaces 141:382–389

Zasońska BA, Boiko N, Klyuchivska O, Trchová M, Petrovský E, Stoika R, Horák D (2013a) Silica-coated γ-Fe_2O_3 nanoparticles: preparation and engulfment by mammalian macrophages. J Nanopharm Drug Deliv 1:182–192

Zasońska BA, Boiko N, Horák D, Klyuchivska O, Macková H, Beneš MJ, Babič M, Trchová M, Hromádková J, Stoika R (2013b) The use of hydrophilic poly(*N,N*-dimethylacrylamide) for promoting engulfment of magnetic γ-Fe_2O_3 nanoparticles by mammalian cells. J Biomed Nanotechnol 9:479–491

Zasońska BA, Líšková A, Kuricová M, Tulinská J, Pop-Georgievski O, Čiampor F, Vávra I, Dušinská M, Ilavská S, Horváthová M, Horák D (2016) Functionalized porous silica and maghemite core-shell nanoparticles for applications in medicine: design, synthesis, and immunotoxicity. Croat Med J 57:165–179

Zhang Q, Rajan SS, Tyner KM, Casey BJ, Dugard CK, Jones Y, Paredes AM, Clingman CS, Howard PC, Goering PL (2016) Effects of iron oxide nanoparticles on biological responses and MR imaging properties in human mammary healthy and breast cancer epithelial cells. J Biomed Mater Res B 104:1032–1042

Zhao B, Brittain WJ (2000) Polymer brushes: surface-immobilized macromolecules. Prog Polym Sci l25:677–710

Zuo Y, Hoigné J (1992) Formation of hydrogen peroxide and depletion of oxalic acid in atmospheric water by photolysis of iron(III)-oxalato complexes. Environ Sci Technol 26:1014–1022

Chapter 6
Superparamagnetic Iron Oxide Nanoparticles (SPIONs) as Multifunctional Cancer Theranostics

Ibrahim M. El-Sherbiny, Mousa El-Sayed and Asmaa Reda

Abstract Nanobiotechnology stemmed from the recruitment of tools developed by nanotechnology to be applied in many other sectors, including nanomedicine. Particularly, magnetic nanoparticles (MNPs) are of great interest, having successfully offered controlled sizes, capability to be manipulated externally, localized magnetic hyperthermia treatment (MHT), and enhanced magnetic resonance imaging (MRI). As a result, these MNPs are used as therapeutic and diagnostic tools in a variety of biomedical applications such as cancer, Alzheimer, and bacterial infections. In this regard, novel insights provide rationale for designing and development of superparamagnetic iron oxide nanoparticles (SPIONs) to be utilized in various biomedical applications, especially given that SPIONs are already used in clinical trials in late phases. These magic nanoparticles opened avenues to drug delivery, cellular-specific targeting, multi-modal imaging, and a new era of personalized medicine for management of cancer. Herein, we will unravel the extra-unique properties of SPIONs endowing the multifunctional characteristics and abilities for diagnosis, therapy, and online therapeutic monitoring that are referred to theranostics. Moreover, huge efforts have been exerted recently on designing and developing of SPIONs with enhanced biocompatibility, safety, drug-loading capacity, stability, and imaging ability. In addition, the minimization of cellular uptake by macrophages, preferential targeting of cancerous cells sparing normal cells, monitoring cancer cells prior to and after treatment, as well as triggering therapeutic drug release in a controlled fashion envisioned SPION as a golden therapeutic era tool. Overall, this book chapter will highlight the state-of-the-art designed SPIONs, their fabrication, characterization, and the mechanism of their action in targeting cancer cells.

Keywords SPIONs · Cancer · Theranostics · Drug delivery · Diagnosis · Magnetic · Nanoparticles

I. M. El-Sherbiny (✉) · M. El-Sayed · A. Reda
Center for Materials Science, Zewail City of Science and Technology, 12578 Giza, Egypt
e-mail: ielsherbiny@zewailcity.edu.eg

A. Reda
Molecular and Cellular Biology Division,
Zoology Department, Faculty of Science, Benha University, Benha, Egypt

Introduction

Cancer is described as the worst monster nightmare for all humanity. It is characterized by uncontrolled cell proliferation, evasion all tumor suppressors, invasion, metastasize, immortality, angiogenesis, and evasion of host defense mechanisms of immune system (Hanahan and Weinberg 2000; Hanahan and Weinberg 2011). Meanwhile, cancer deaths increases exponentially, and according to the WHO, the expected deaths number by 2030 is 13.1 million (Stewart and World Cancer Report 2014). Herein, the real prerogative is to use multifunctional nanotheranostics for effective diagnosis, imaging, and treatment of cancer. This challenge is achieved by using superparamagnetic iron oxide nanoparticles (SPIONs) (Yigit et al. 2012; Rosen et al. 2012; Tong et al. 2011). SPIONs are considered as the most promising tool in cancer theranostics as they are characterized by a superparamagnetic behavior, stability at physiological pH, non-toxicity, biocompatibility, and biodegradability. Also, they are metabolized easily and transported by trans-ferritin, ferritin, and hemosiderin to endogenous iron reservoir to be used later for hemoglobin synthesis. Besides, SPIONs are very small in size (1–20 nm) and having large surface to volume ratio. Moreover, they are characterized by reactive surface that can be easily modified with biocompatible capping agents. Their surface could also be potentiated via covalently attaching to ligands, antibodies or peptides for targeted drug delivery (Zou et al. 2010). What is really exciting here is the multifunctional ability of SPIONs for improving cancer therapy. There is a great potential lies within the in vivo imaging by (MRI), hyperthermia, magnetic separation, biosensing application, tissue repair, and targeted drug delivery (Dilnawaz et al. 2010; Veiseh et al. 2010; Perez et al. 2002; Frullano and Meade 2007; Corot et al. 2006; Solanki et al. 2008).

SPIONs Design for Cancer Theranostics

Precise design of SPIONs can lead to the formation of a smart multifunctional nanocarrier specific for personalized medicine via combining the therapeutic, diagnostic, and targeted drug delivery ability in a single biodegradable and biocompatible particle. Basically, SPIONs are formed of three main layers (Fig. 6.1): the first layer (core), which is formed of iron oxide and acts as MRI contrast agent, the second layer (capping layer), which is usually biocompatible and biodegradable material preventing aggregation, and the third layer which is the therapeutic coating with targeted moiety.
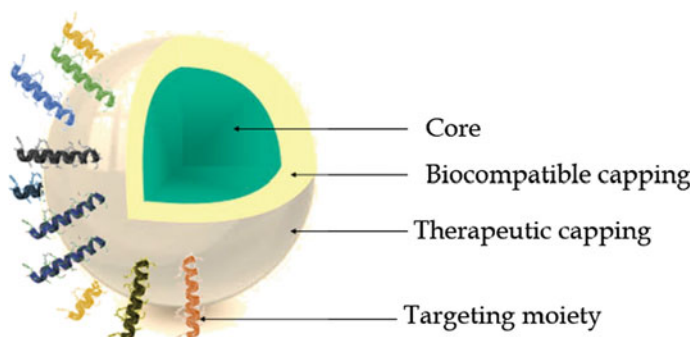
Fig. 6.1 Schematic illustration of SPIONs design for cancer theranostics

SPIONs Structure and Types

SPIONs are considered as a pivotal therapeutic and diagnostic tool in cancer treatment in addition to their ability to overcome the multi-drug resistance and many of the drawbacks of conventional chemotherapy approach of cancer treatment, such as biocompatibility, poor solubility, and hydrophobicity of the anticancer drugs. Basically, SPIONs consist of core made from iron oxide and a coating material. Herein, there are three types of SPIONs core—maghemite (γ-Fe_2O_3), hematite (α-Fe_2O_3), and magnetite (Fe_3O_4)—with the magnetite being the prevailing one among others. Substantially, magnetite contains Fe^{2+} and Fe^{3+} ions with molar ratio 1:2. Ostensibly, magnetite is of great importance as it triggers Fenton reaction that leads to the formation of reactive oxygen species (ROS) in cancer cells (Huang et al. 2013) (Fig. 6.2).

Fenton reaction:

$$Fe^{2+} + H_2O_2 \rightarrow Fe^{3+} + OH^. + OH^-$$

$$Fe^{3+} + H_2O_2 \rightarrow Fe^{2+} + OOH^. + H^+$$

Strikingly, SPIONs exhibit superparamagnetic characteristics below 30 nm size at room temperature. In this regard, superparamagnetism can be defined as the ability of magnetic nanoparticles to show paramagnetic nature with intensive saturation and susceptibility magnetization under the effect of magnetic field and the tendency of losing this nature totally once the magnetic field is removed leading to zero coercivity and zero magnetic remanence.

Concomitantly, SPIONs surface at the very small size is so reactive due to the increased surface area-to-volume ratio. As a result, SPIONs surface is dominantly coated with capping agent or surfactant or even polymers to prevent their aggregation in colloidal solutions and to preserve fixed shape and size. Otherwise, SPIONs will aggregate and settle down forming bulk structures in colloidal solutions. However,
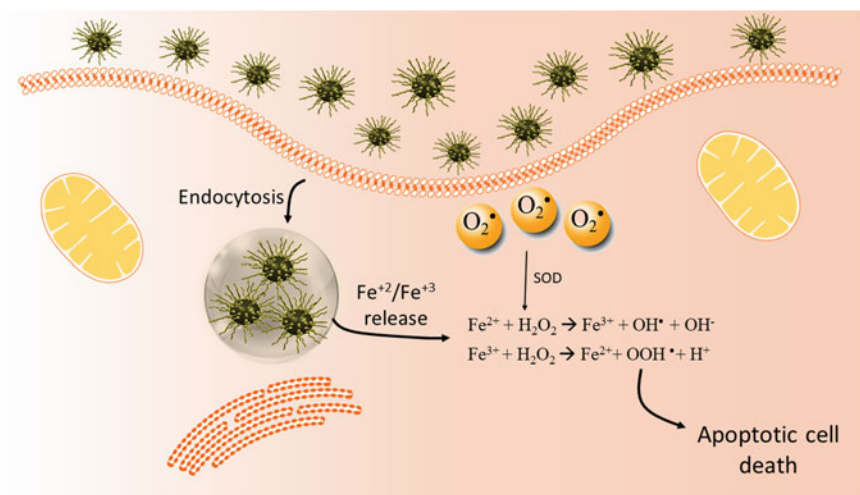
Fig. 6.2 Schematic illustration of SPIONs initiated fenton reaction and ROS formation

these coating materials affect the superparamagnetic properties of SPIONs depending on their amount, nature, composition, and thickness.

SPIONs Synthesis Methods

SPIONs have been fabricated using different techniques including physical, chemical, and microbial methods. The chemical methods are mainly utilized and they are favored over other fabrication approaches. In this section, we report the commonly used wet chemical methods for SPIONs fabrications, preceded by a summary for each method's advantages and disadvantages as illustrated in Table 6.1.

Co-precipitation Method

Co-precipitation method is a facile and convenient approach for the fabrication of SPIONs from aqueous solutions of Fe^{+2}/Fe^{+3} salts (in a 2:1 stoichiometric ratio) by the addition of a base under inert atmosphere at room or an elevated temperature (70–90 °C). It has been quite established that in order to obtain monodispersed particles, a burst nucleation followed by a slow controlled growth should be achieved. The size, geometry, and composition of SPIONs are highly depending on the type of salt used (chlorides, sulfates, nitrates), reaction temperature, ferric and ferrous stoichiometric ration, ionic strength, and pH of the solution. Vikram et al. demonstrated that the Fe^{2+}/Fe^{3+} ratio and the rate of base addition also affect the magnetic properties of the resulting SPIONs (Vikram et al. 2015) that may lead to particles with

Table 6.1 Common synthesis methods of SPIONs

Method	Synthesis conditions	Reaction temperature (°C)	Reaction period	Solvent	Size distribution	Shape	Yield
Co-precipitation	Very simple and ambient condition	Room temperature up to 90	Minutes	Aqueous	Quite narrow	Not so good	High
Thermal decomposition	Hard, inert atmosphere	100–320	Hours-days	Organic	Very narrow	Good	High
Hydrothermal	Hard, ambient condition	220	Hours-days	Aqueous-ethanol	Very narrow	Very good	Medium
Microemulsion	Simple, ambient condition	20–50	Hours	Organic/aqueous	Relatively narrow	Good	Low
Sonochemical	Simple and ambient condition	Room temperature	Minutes	Aqueous	Quite narrow	Not good	Medium
Microwave	Simple and ambient condition	Microwave irradiation	Very fast	Aqueous	Quite narrow	Not so good	Medium

ferromagnetic properties instead of superparamagnetism. In order to obtain small and monodispersed particles, organic additives such as surfactants or capping agents are used during the synthesis (Bee et al. 1995; Ishikawa et al. 1993). For instance, SPIONs with narrow sizes of 4–10 nm can be stabilized in aqueous media of 1 wt% polyvinyl alcohol (PVA) (Lee et al. 1996). The main disadvantage of this synthesis method is the formation of polydispersed and improper crystalline SPIONs which highly affects the saturation magnetization value to be in the rage of 30–50 emu/g and lower than the bulk magnetization value of 90 emu/g. Nevertheless, SPIONs with monodispersed size of 9 nm were obtained via co-precipitation method using a tetramethylammonium hydroxide (Cheng et al. 2005).

Thermal Decomposition

Inspired by a well-established approach of thermal decomposition for the synthesis of well-defined semiconductor nanocrystals and oxides in organic media (Murray et al. 1993; O'Brien et al. 2001), modified methods for the synthesis of highly crystalline and monodispersed SPIONs with a control over sizes and shapes have been developed. The method involves the thermal decomposition of an organometallic precursor in the presence of a surfactant (such as oleic acid) and organic solvent with elevated boiling points (Maity et al. 2009). The resulting SPIONs tend to disperse only in non-aqueous solvent by the hydrophobic–hydrophobic interaction between the surfactant and the solvent. The concentration of the precursor and surfactant, reaction temperature, stoichiometric ratio of precursor to surfactants, and the reaction time are highly affecting the magnetic and physicochemical properties of SPIONs. Given that different applications, especially biomedical applications, require SPIONs to be rendered water soluble, this can be achieved by ligand exchange method (Lam 2016; Korpany et al. 2016; Xu et al. 2011) or bilayer surfactant stabilization method (Xu et al. 2011; Maity et al. 2008).

Hydrothermal Method

In hydrothermal approach, SPIONs of uniformed sizes and shapes can be synthesized by dissolving the precursors in an aqueous media alongside with surfactants under maintained high pressure and temperature in a pressure autoclave vessel. Adjusting heating temperatures, reaction timing and precursor to surfactants ratio influence the sizes, shapes, and magnetic characteristics of the resulting SPIONs. Mitchell et al. successfully prepared ultrafine SPIONs using hydrothermal route to be used for high-performance energy materials. Their electrochemical analysis also encouraged their potential application as ultra-capacitors (Mitchell et al. 2014). However, this fabrication route often yields in moderately crystalline particles in a prolonged time frame compared to other synthesis methods such as thermal decomposition method.

Microemulsion Method

Another reported method for SPIONs synthesis is the microemulsion approach where two immiscible micro-domains are thermodynamically stabilized by an interface layer of surfactant. The microemulsion systems used for synthesis of different nanoparticles are either water-in-oil (w/o) or oil-in-water (o/w) system. In w/o microemulsions (frequently used for synthesis of SPIONs), the aqueous phase microdroplets of iron oxide reactants are stabilized and protected by a monolayer of surfactant migrated from the continuous oil phase. Wang et al. have synthesized magnetite nanoparticles using a modified single microemulsion method. The magnetite nanoparticles have an average size of 10 nm and showed perfect supermagnetism with high Curie temperature, T_c value of 860 K (Liu et al. 2004). Nonetheless, this method produces a wide range of magnetic nanoparticles without full control over the sizes and shapes. Furthermore, the working window is quite limited when compared with other previously reported methods. Also, this synthesis approach requires large amount of solvents, which narrows its large-scale practice.

Sonochemical Method

SPIONs can be synthesized by sonolysis of organometallic precursors in the presence of organic additives (surfactants/capping agents) to control the growth of particles (Durdureanu-Angheluta et al. 2010). Sound energy creates cavitation of microbubbles in aqueous media where unusual reactions occur leading to the desired products (Ashokkumar et al. 2007). The physicochemical characteristics of the produced nanoparticles can be controlled by varying the irradiation power and time. Dolores et al. demonstrated a linear increase in the production of SPIONs with refluxing time at a constant sonication frequency (Dolores et al. 2015). Sodibo et al. studied the required amount of time (from 1 to 20 min) for sonochemical capping of SPIONs with 3-amino propyl triethoxylsilane (APTES). The results showed that the surface functionalization was achieved only after one minute of refluxing under ultrasonic irradiation (Sodipo and Aziz 2018). Nevertheless, thermolysis methods usually yield in crystalline nanoparticles while sonolysis usually produce amorphous nanoparticles (Pinkas et al. 2008).

Microwave-Assisted Synthesis

Microwave-assisted synthesis gained a great attention in recent years as a green synthesis technique (Kijima et al. 2011). In a fractional time and low energy consumption, microwave irradiation results in successful fabrication of SPIONs from iron salts. Bano et al. reported the microwave-assisted synthesis of stable SPIONs functionalized with PEG-6000 with a size range of 17–25 nm (Bano et al. 2016). The

main drawback of this fabrication tool is the shorter crystallinity time and homogeneous nucleation period which can be attributed to the uniformed heat distribution of microwave that leads to reduced surface reactivity (Pascu et al. 2012).

SPIONs Capping

It is noteworthy that naked SPIONs are highly unstable in water and at physiological pH, and tend to aggregate and rapidly precipitate. Furthermore, uncapped SPIONs could be easily engulfed by phagocytes as foreign bodies. Thus, significant attentions have been paid to SPIONs capping, as it acts as a protected shield from the immune system giving it stability, increase the circulation time, and enable their conjugation with targeting moieties. Substantial summary of the most common capping agents for SPIONs is described in Table 6.2.

Table 6.2 Most common SPIONs capping agents

Capping agent	Characteristics	Application	References
Chitosan	Hydrophilic, biodegradable, and biocompatible	Contrast agent for MRI	(Hong 2010)
Silica	Transparent, biocompatible, and reduced toxicity	Contrast agent for MRI	(Alwi et al. 2012; Ren et al. 2008)
Polyacrylic acid	Increases cellular uptake	Cell labeling for MRI	(Vetter et al. 2011)
Dextran	Increases cellular uptake, enhances stability, and biodegradable	In vivo cell tracking, contrast agent for MRI	(Yu et al. 2012; Tassa et al. 2011)
Polyethylene glycol (PEG)	Increases stability, reduces nanoparticles aggregation, biocompatible, biodegradable, and water soluble.	MRI, gene and drug delivery, and bio-labeling	(Yu et al. 2012; Allard-Vannier 2012)
Polyethyleneimine	Offers high positive charge and high cellular uptake	MRI, gene and drug delivery, and sensing	(Cen 2019; Hoang MD 2015; Kim et al. 2017)
Polyvinyl alcohol	Biocompatible, biodegradable, hydrophilic, and increases stability	MRI, gene and drug delivery	(Nadeem M 2016; Bannerman et al. 2017)

SPIONs and Therapeutic Payload

The ultimate goal of cancer therapy is to eradicate cancer cells leaving normal cells healthy and unaffected. Thus, the chemotherapy is developed everyday as a marathon runner. However, most of the known chemotherapy can elaborate unsolicited side effects to healthy cells. At this glance, targeted drug delivery and integration between SPIONs and chemotherapy could limit the side effects to normal cells. Furthermore, it could prolong the circulation time, achieve maximum targeting efficacy and sustain the release of the therapeutic molecules.

Successful integration between therapeutic payload and SPIONs includes several design strategies:

a. Conjugation of the therapeutic payload to SPIONs surface.
b. Physical interaction through co-encapsulation of therapeutic payload into coating material of SPIONs.

The first approach is conjugation, where cleavable bond between therapeutic molecule and SPIONs is created like amide ($CO-NH_2$), hydrazone (CN-NH), and disulfide bond (S-S) (Nigam and Bahadur 2017; Shang et al. 2017). The advantages of this approach include enhancing the loading efficiency and protection of therapeutic drugs to maximize its effect. Furthermore, it is suitable for conjugation of peptides and proteins to protect them from oxidative degradation. Basically, several chemotherapies have been conjugated with SPIONs like doxorubicin, paclitaxel, and methotrexate (MTX) (Shaghaghi et al. 2019; Kang et al. 2018; Moura et al. 2014).

The second approach is the physical interaction through co-encapsulation of therapeutic payload into coating material of SPIONs. It occurs via electrostatic interactions or hydrophilic–hydrophobic interactions. As an example, the SPIONs coated with positively charged polyethyleneimine (PEI) interact electrostatically with negatively charged DNA (Tutuianu R 2017). In addition, SPIONs coated with hydrophobic polymers can strongly interact with hydrophilic drugs where the drug molecules are released when the coating material degrade. The main advantage of this approach is the ability to overcome the low entrapment efficiency and limited stability.

Role of SPIONs in Cancer Theranostics

SPIONs act as theranostics particles that can perform multiple functions at the same time such as diagnosis, targeting, and treatment. The pivotal role of SPIONs is not only improving diagnosis but also increasing the efficacy of cancer treatment as illustrated below:

SPIONs in Diagnosis by MRI

Unraveling the complexity of magnetic resonance imaging (MRI) is of great importance. Substantially, it is a spectroscopic technique based on the principles of nuclear magnetic resonance (NMR) and used for imaging of deeper tissue in human body. Thus, it is considered as a vital non-invasive tool for cancer diagnosis (imaging and tracking) (Turkbey et al. 2010; Morrow et al. 2011). However, the obtained MRI images of abnormal and normal tissues are very difficult to differentiate between them. Therefore, exogenous contrast agents are in urgent need to increase sensitivity, image contrast, and acquiring higher resolution (Fig. 6.3). For this purpose, SPIONs are designed and used as contrast agents that should have the following criteria to be used as MRI imaging probes (Qin et al. 2007; Wei et al. 2017).

a. Magnetism: SPIONs should exhibit higher magnetization when exposed to external source of magnetic field. Furthermore, the magnetization should return to zero when the external magnetic field is removed.
b. Well-designed surface coating: This includes the integration of targeting moieties to SPIONs surface such as peptides, proteins, antibodies, targeting ligands, carbohydrates, polymers, aptamers, RNA, and DNA. These targeting moieties will enhance the specific targeting to the tumors.
c. SPIONs water solubility is very important factor to avoid any aggregation.
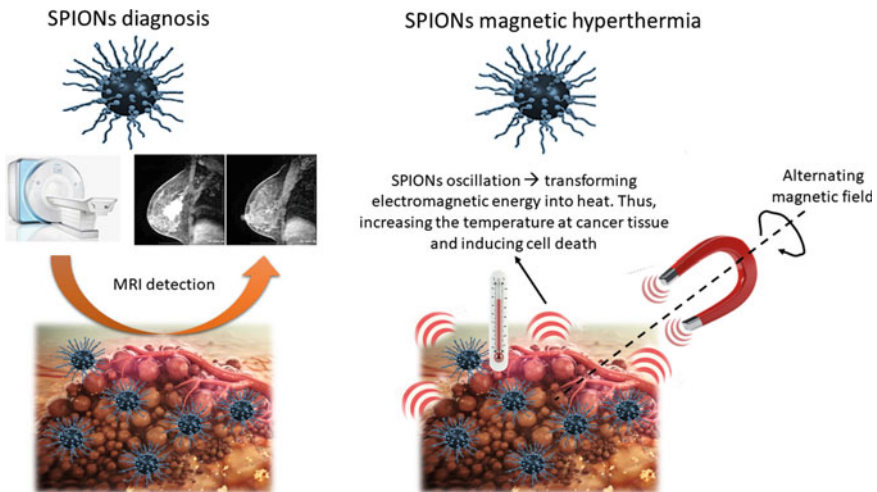
Fig. 6.3 Schematic illustration of SPIONs role in cancer theranostics: diagnosis and magnetic hyperthermia

SPIONs in Cancer Treatment

Efficient cancer therapy remains the hardest challenge facing scientific community. Thus, hyperthermia emerged on scene as an effective method for cancer treatment. In this regard, when body tissue is exposed to elevated temperature ranging from 42 to 48 °C, the tumor cells are more sensitive and susceptible to damage than normal cells. Thus, tumor cells will undergo apoptotic death. Preponderance of literature indicated that apoptosis can take place when temperature range of 42–46 °C is applied, while necrosis can happen when temperature exceeds the 46–48 °C range. Such therapeutic strategy is limited only to tumor cells thus minimizing the harm to normal cells (Ding et al. 2017).

It is noteworthy to mention that SPIONs act as heat generators. In this context, the magnetic targeting is used to localize SPIONs at the tumor site. After that upon exposure to alternating magnetic field for certain time, SPIONs generate heat of about 42–45 °C inducing apoptotic cell death that is called magnetic hyperthermia (Fig. 6.3). However, heat generation varies and depends on the shape, size, SPIONs crystallinity, magnetic properties, and the applied magnetic field. Herein, the efficiency of SPIONs magnetic hyperthermia is measured by specific absorption rate (SAR) that converts the magnetic field into heat (Chen et al. 2011).

SPIONs Coinciding with Other Therapeutic Agents

Grouped with Photodynamic Therapeutic Agents

A widely used method for cancer tackling is photodynamic therapy (PDT) where a light source and a photosensitizer agent are utilized to initiate photonecrotic effect for tumor cells by selectively producing reactive oxygen species in those tissues. Generally, SPIONs are used as supporting cargos to deliver photosensitizing agents for combined imaging with MRI, magnetic navigation, and PDT. Recently, Ostrokonkove et al. (Ostroverkhov et al. 2019) successfully loaded different bacteriochlorin-based photosensitizers on human serum albumin (HSA) coated iron oxide magnetic nanoparticles (IONPs). In vitro and in vivo studies demonstrated the stability of the fabricated nanoparticles and their capabilities to deliver photosensitizer to malignancies guided by MRI. Similarly, Yan et al. (Yan L 2018) directly immobilized a photosensitizer protoporphyrin IX (PpIX) for PDT within SPIONs for diagnosis by MRI without the use of any additional carriers, thereby high loading capacity of the therapeutic agent was achieved. Their practice at the in vivo level showed a significant reduction of the tumor growth rate. Du et al. (Du et al. 2018) co-delivered a natural photosensitizer phycocyanin alongside with a synthetic photosensitizer hematoporphyrin monomethyl ether (HMME) on the surface of IONPs. The in vivo and in vitro results demonstrated a significant inhibition of MCF-7 breast cancer cells proliferation upon exposure of near infrared (NIR) irradiation. In another

study, pheophorbide (a photosensitizer agent) conjugated acetylated hyaluronic acid (PAH) was used as a surface coating for magnetic NPs to target integrin CD44 over-expressed in breast cancer cells. The self-assembled NPs showed higher biocompatibility and water solubility. In vitro studies showed that PAH@MNPs enhanced heat generation (up to 43 °C) and singlet oxygen production when exposed to external magnetic and laser irradiation (Kim et al. 2016). In addition, SPIONs was combined with carbon fullerene (C60) and HMME as a nanocomposite system. In vitro studies showed a 23-fold enhancement in its therapeutic efficacy (Shi et al. 2013).

Grouped with Photothermal Therapeutic Agents

Photothermal therapy (PTT) recently gained greater interests as a non-invasive, selective, and controlled therapeutic approach in tumor treatment. Compared with photodynamic therapy, PTT do not generate reactive oxygen to cause damage to cancer cells. Rather, PTT cause thermal ablation of cancer cells by converting the light irradiation (in the wavelength of infrared and longer ranges) into heat. The therapeutic efficacy of the photothermal agents (PTAs) highly depends on their ability to transform light into sufficient heat enough for the thermal ablation of cancer cells. Therefore, SPIONs were extensively reported in combination with other PTAs such as gold and graphene oxide. Recently, Salaheldin et al. (Salaheldin et al. 2019) examined the photothermal efficacy of graphene/IONPs (G/Fe_3O_4) nanocomposite when exposed to 808 nm infrared laser excitation. Interestingly, a significant reduction of HepG2 cell viability was observed at the in vitro level. Ghaznavi et al. (Ghaznavi et al. 2018) reported the fabrication of core-shell Au@IONPs coated with PEG. When tested at the in vitro level, a significant lethality was observed for KB nasopharyngeal cancer cells (around 62%) and MCF-7 breast cancer cells (around 33%) following exposure to 808 nm laser irradiation. Wang et al (Wang Y 2018) fabricated a multistage photothermal-based nanosystem by coating IONPs with polydopamine as a PTT agent. Eyvazzadeh et al (Eyvazzadeh et al. 2017) studied the effect of using core-shell Au@IONPs for enhanced PTT. The MTT essay on KB cell showed substantial cell lethality (up to 70% cell death) following the photothermal treatment. Fu et al. (Fu et al. 2014) used Prussian blue dye (as a PTT agent) coated SPIONs for the photothermal treatment of HeLa cells. The blue-colored dye showed significant mortality by killing up to 80% of tumor cells and substantial tumor inhibition rate around 87.2% upon exposure to NIR irradiation.

Grouped with Sonodynamic Therapeutic Agents

Sonodynamic therapy (SDT) found its comprehensive biomedical applications. Cancer treatment performed using mechanical waves of ultrasound in the presence of sonosensitizer. SDT agents such as TiO_2 and HMME get activated upon exposure to ultrasound waves to produce reactive oxygen species triggering the cancer cells death.

Compared to PDT, using SDT for cancer treatment is preferred due to the higher tissue penetration of ultrasound irradiation, especially in solid tumor tissues, than the NIR irradiation. An increasing interest is developed in using magnetic nanoparticles in combination with sonosensitizers to enhance the cancer treatment efficacy. Zhang et al. (Zhang et al. 2018) compared the ability of a sonosensitizer chlorin e6 (E6) alone and in combination with PEG-IONPs (PIONPs) as a coating for the production of intracellular ROS sufficient enough for cancer cells ablation. They found out that IONPs@E6 substantially increased the generation of ROS compared to the use of free E6. Moreover, the E6 coating onto the surface of PIONPs significantly enhanced its solubility and bioavailability. Shen et al. (Shen et al. 2015) reported the use of multifunctional nanosystem of Fe_3O_4@TiO_2 and DOX for a combined therapy of SDT by TiO_2 NPs and chemotherapy by DOX in presence of Fe_2O_3 as a guiding tool by MRI. This combination showed a superior anticancer effect when compared by their solo utilization. Interestingly, Niu et al. (Niu et al. 2013) prepared SPIONs@PLGA microbubbles in combination with DOX for dual delivery of therapeutic agents (SDT and chemotherapy) and dual imagining by ultrasound/MR for the treatment of metastatic lymph nodes at in vivo level.

Other Usages of SPIONs in Biomedical Applications

SPIONs for Alzheimer's Disease Diagnosis and Therapy

Alzheimer's disease is considered as the most devastating neurodegenerative disorder that prevalent among people over 65 years of age. It is generally marked by the amyloid plaques. Attributed to the unique characteristics of SPIONs such as high ability to pass through biological barriers, high surface, and ease of surface decoration with ligands of choice, they are progressively utilized as potential candidates for Alzheimer's disease diagnosis and treatment (Krol et al. 2013). Cheng et al. (Cheng et al. 2015) reported the use of SPIONs surface modified with curcumin (SPIONs-Cur) as a detection tool of amyloid plaques. A further coating with PEG was applied so as to enhance particles' circulation. Interestingly, SPIONs-Cur were capable of localizing the amyloid plaques. Bellova et al. (Bellova et al. 2010) found out magnetite nanoparticles significantly reduced the amyloid aggregations of lysozyme in vitro which makes them good as therapeutic agents for the prevention of amyloid fibrillogenesis. Luckily, the encouraging research highlights of the nanoparticle usage in this field paved the way for new diagnostic/therapeutic agents to overcome the reported limitation of the current approaches in clinical practice.

SPIONs Against Bacterial Diseases

Antimicrobial resistance against antibiotics is widely considered as a serious global health issue (Kruijshaar et al. 2008; Snell 2003). Frightening figures are described of estimating that by 2050 about 300 million death incidence will be caused by antimicrobial resistance strains as well as heavy economical loss approximated to be around $ 100 trillion (Munita and Arias 2016). In this regard, different nanotherapeutics entailing antimicrobial activities have been studied. Magnetic nanoparticles physicochemical properties such as their relatively simple synthesis methods, innate antimicrobial activity, and most importantly their biocompatibility favored their usage as antimicrobial agents (Torres-Sangiao et al. 2016; Malekkhaiat Haffner and Malmsten 2017). Moreover, the magnetic nanoparticles' surface could be functionalized to actively target the microbes (Jallouk et al. 2015; Zazo et al. 2016; Mohammed et al. 2016). For example, SPIONs functionalized with cationic moieties succeeded in capturing over 97% of bacteria (Huang et al. 2010). Although the antimicrobial activities of nanomaterials are not fully understood, they are mostly working according to the following mechanisms: damage the cell membrane due to mechanical stress caused by the particles themselves, intriguer loss of microbial protein functions by releasing toxic metals, and incite reactive oxygen generation damaging the microbial DNA, RNS, and protein (Reddy et al. 2012; Huang et al. 2014).

Conclusion

The reported advantages of SPIONs paved the way for their greater practice in the medical and clinical fields. A wide range of different formulations was developed for imaging, diagnosis, and treatments of different biomedical diseases. SPIONs characteristics and so their functions are mostly determined by their fabrication method. Therefore, selecting the synthesis method is one of the most important aspects of their usage so as to control the SPIONs size and shape. Furthermore, the surface coating highly affects SPIONs' biocompatibility, stability, and targeting capabilities, providing a mean to control their physical characteristics and surface chemical activity. In addition, surface modification help escape the phagocytes, which substantially increase their circulation time, and works as an anchor for further surface decoration with targeting ligands and peptides to enhance their affinity to target sites and cells. Overall, the success of using SPIONs in drug delivery and MRI applications increased the interest of their utilization in advanced theranostic clinical applications. Nevertheless, further studies are needed to improve their targeting, reduce their toxicity, and enhance their stability in vivo.

References

Allard-Vannier E et al (2012) Pegylated magnetic nanocarriers for doxorubicin delivery: a quantitative determination of stealthiness in vitro and in vivo. Eur J Pharm Biopharm: official journal of Arbeitsgemeinschaft fur Pharmazeutische Verfahrenstechnik e.**81**: 498–505. https://doi.org/10.1016/j.ejpb.2012.04.002

Alwi R et al (2012) Silica-coated super paramagnetic iron oxide nanoparticles (SPION) as biocompatible contrast agent in biomedical photoacoustics. Biomed Opt Express 3:2500–2509. https://doi.org/10.1364/boe.3.002500

Ashokkumar M, Lee J, Kentish S, Grieser F (2007) Bubbles in an acoustic field: an overview. Ultrason Sonochemistry 14:470–475. https://doi.org/10.1016/j.ultsonch.2006.09.016

Bannerman AD, Li X, Wan W (2017) A 'degradable' poly (vinyl alcohol) iron oxide nanoparticle hydrogel. Acta Biomater 58:376–385. https://doi.org/10.1016/j.actbio.2017.05.018

Bano S et al (2016) Microwave-assisted green synthesis of superparamagnetic nanoparticles using fruit peel extracts: surface engineering, T 2 relaxometry, and photodynamic treatment potential. Int J Nanomedicine 11:3833–3848. https://doi.org/10.2147/ijn.s106553

Bee A, Massart R, Neveu S (1995) Synthesis of very fine maghemite particles. J Magn Magn Mater, pp 6–9. https://doi.org/10.1016/0304-8853(95)00317-7

Bellova A et al (2010) Effect of Fe_3O_4 magnetic nanoparticles on lysozyme amyloid aggregation. Nanotechnology 21:065103. https://doi.org/10.1088/0957-4484/21/6/065103

Cen C et al (2019) Improving magnetofection of magnetic polyethylenimine nanoparticles into MG-63 osteoblasts using a novel uniform magnetic field. Nanoscale research letters 14(90). https://doi.org/10.1186/s11671-019-2882-5

Chen B, Wu W, Wang X (2011) Magnetic iron oxide nanoparticles for tumor-targeted therapy. Curr Cancer Drug Targets 11:184–189

Cheng FY et al (2005) Characterization of aqueous dispersions of Fe_3O_4 nanoparticles and their biomedical applications. Biomaterials 26:729–738. https://doi.org/10.1016/j.biomaterials.2004.03.016

Cheng KK et al (2015) Curcumin-conjugated magnetic nanoparticles for detecting amyloid plaques in Alzheimer's disease mice using magnetic resonance imaging (MRI). Biomaterials 44:155–172. https://doi.org/10.1016/j.biomaterials.2014.12.005

Corot C, Robert P, Idee JM, Port M (2006) Recent advances in iron oxide nanocrystal technology for medical imaging. Adv Drug Deliv Rev 58:1471–1504. https://doi.org/10.1016/j.addr.2006.09.013

Dilnawaz F, Singh A, Mohanty C, Sahoo SK (2010) Dual drug loaded superparamagnetic iron oxide nanoparticles for targeted cancer therapy. Biomaterials 31:3694–3706. https://doi.org/10.1016/j.biomaterials.2010.01.057

Ding Z et al (2017) Redox-responsive dextran based theranostic nanoparticles for near-infrared/magnetic resonance imaging and magnetically targeted photodynamic therapy. Biomater Sci 5:762–771. https://doi.org/10.1039/c6bm00846a

Dolores R, Raquel S, Adianez GL (2015) Sonochemical synthesis of iron oxide nanoparticles loaded with folate and cisplatin: effect of ultrasonic frequency. Ultrason Sonochemistry 23:391–398. https://doi.org/10.1016/j.ultsonch.2014.08.005

Du SW et al (2018) Combined phycocyanin and hematoporphyrin monomethyl ether for breast cancer treatment via photosensitizers modified Fe_3O_4 nanoparticles inhibiting the proliferation and migration of MCF-7 cells. Biomacromol 19:31–41. https://doi.org/10.1021/acs.biomac.7b01197

Durdureanu-Angheluta A et al (2010) Synthesis and characterization of magnetite particles covered with a-trietoxysilil-polydimethylsiloxane. J Magn Magn Mater 322:2956–2968. https://doi.org/10.1016/j.partic.2010.05.013

Eyvazzadeh N et al (2017) Gold-coated magnetic nanoparticle as a nanotheranostic agent for magnetic resonance imaging and photothermal therapy of cancer. Lasers Med Sci 32:1469–1477. https://doi.org/10.1007/s10103-017-2267-x

Frullano L, Meade TJ (2007) Multimodal MRI contrast agents. J Biol Inorg Chem JBIC Publ Soc Biol Inorg Chem 12:939–949. https://doi.org/10.1007/s00775-007-0265-3

Fu G et al (2014) Magnetic prussian blue nanoparticles for targeted photothermal therapy under magnetic resonance imaging guidance. Bioconjugate chemistry 25:1655–1663. https://doi.org/10.1021/bc500279w

Ghaznavi H et al (2018) Folic acid conjugated PEG coated gold-iron oxide core-shell nanocomplex as a potential agent for targeted photothermal therapy of cancer. Artif Cells Nanomedicine, Biotechnol 46:1594–1604. https://doi.org/10.1080/21691401.2017.1384384

Hanahan D, Weinberg RA (2000) The hallmarks of cancer. Cell 100:57–70

Hanahan D, Weinberg RA (2011) Hallmarks of cancer: the next generation. Cell 144:646–674. https://doi.org/10.1016/j.cell.2011.02.013

Hoang MD et al. (2015) Branched polyethylenimine-superparamagnetic iron oxide nanoparticles (bPEI-SPIONs) improve the immunogenicity of tumor antigens and enhance Th1 polarization of dendritic cells. Journal of immunology research **2015**, 706379. https://doi.org/10.1155/2015/706379

Hong S (2010) Chitosan-coated ferrite (Fe3O4) nanoparticles as a T2 contrast agent for magnetic resonance imaging. J Korean Phys Soc 56:868–873

Huang YF, Wang YF, Yan XP (2010) Amine-functionalized magnetic nanoparticles for rapid capture and removal of bacterial pathogens. Environmental science & technology 44:7908–7913. https://doi.org/10.1021/es102285n

Huang G et al (2013) Superparamagnetic iron oxide nanoparticles: amplifying ROS stress to improve anticancer drug efficacy. Theranostics 3:116–126. https://doi.org/10.7150/thno.5411

Huang KS, Shieh DB, Yeh CS, Wu PC, Cheng FY (2014) Antimicrobial applications of water-dispersible magnetic nanoparticles in biomedicine. Current medicinal chemistry 21:3312–3322

Ishikawa T, Kataoka S, Kandori K (1993) The influence of carboxylate ions on the growth of p-FeOOH particles. J Mater Sci 28:2693–2698. https://doi.org/10.1007/bf00356205

Jallouk AP, Palekar RU, Pan H, Schlesinger PH, Wickline SA (2015) Modifications of natural peptides for nanoparticle and drug design. Adv Protein Chem Struct Biol 98:57–91. https://doi.org/10.1016/bs.apcsb.2014.12.001

Kang SH, Hong SP, Kang BS (2018) Targeting chemo-proton therapy on C6 cell line using superparamagnetic iron oxide nanoparticles conjugated with folate and paclitaxel. Int J Radiat Biol 94:1006–1016. https://doi.org/10.1080/09553002.2018.1495854

Kijima N, Yoshinag M, Awaka J, Akimoto J (2011) Microwave synthesis, characterization, and electrochemical properties of α-Fe2O3 nanoparticles. Solid State Ions **192**: 293–297. https://doi.org/10.1016/j.ssi.2010.07.012

Kim KS et al (2016) Correction: stimuli-responsive magnetic nanoparticles for tumor-targeted bimodal imaging and photodynamic/hyperthermia combination therapy. Nanoscale 8:12843. https://doi.org/10.1039/c6nr90122k

Kim MC et al (2017) Polyethyleneimine-associated polycaprolactone-Superparamagnetic iron oxide nanoparticles as a gene delivery vector. J Biomed Mater Res Part B Appl Biomater 105:145–154. https://doi.org/10.1002/jbm.b.33519

Korpany KV et al (2016) One-step ligand exchange and switching from hydrophobic to water-stable hydrophilic superparamagnetic iron oxide nanoparticles by mechanochemical milling. Chem Commun 52:3054–3057. https://doi.org/10.1039/c5cc07107k

Krol S et al (2013) Therapeutic benefits from nanoparticles: the potential significance of nanoscience in diseases with compromise to the blood brain barrier. Chem Rev 113:1877–1903. https://doi.org/10.1021/cr200472g

Kruijshaar ME et al (2008) Increasing antituberculosis drug resistance in the United Kingdom: analysis of national surveillance data. BMJ 336:1231–1234. https://doi.org/10.1136/bmj.39546.573067.25

Lam T et al (2016) Fabricating water dispersible superparamagnetic iron oxide nanoparticles for biomedical applications through ligand exchange and direct conjugation. Nanomaterials 6. https://doi.org/10.3390/nano6060100

Lee J, Isobe T, Senna M (1996) Magnetic properties of ultrafine magnetite particles and their slurries prepared via in-situ precipitation. Colloids SurfS A PhysChemical Eng Asp 109:121–127. https://doi.org/10.1016/0927-7757(95)03479-X

Liu B, Liu ZL, Li XW (2004) Synthesis of magnetite nanoparticles in W/O microemulsion. J Mater Sci 39:2633–2636. https://doi.org/10.1023/b:jmsc.0000020046.68106.22

Maity D, Ding J, Xue JM (2008) Synthesis of magnetite nanoparticles by thermal decomposition: time, temperature, surfactant and solvent effects. Funct Mater Lett 1:189–193. https://doi.org/10.1142/s1793604708000381

Maity D, Choo SG, Yi J, Ding J, Xue JM (2009) Synthesis of magnetite nanoparticles via a solvent-free thermal decomposition route. J Magn Magn Mater 321:1256–1259. https://doi.org/10.1016/j.jmmm.2008.11.013

Malekkhaiat Haffner S, Malmsten M (2017) Membrane interactions and antimicrobial effects of inorganic nanoparticles. Adv Colloid Interface Sci 248:105–128. https://doi.org/10.1016/j.cis.2017.07.029

Mitchell E et al (2014) Probing on the hydrothermally synthesized iron oxide nanoparticles for ultra-capacitor applications. Powder Technol. https://doi.org/10.1016/j.powtec.2014.12.02

Mohammed L, Gomaa HG, Ragab D, Zhu J (2016) Magnetic nanoparticles for environmental and biomedical applications: a review. Particuology https://doi.org/10.1016/j.partic.2016.06.001

Morrow M, Waters J, Morris E (2011) MRI for breast cancer screening, diagnosis, and treatment. Lancet 378:1804–1811. https://doi.org/10.1016/S0140-6736(11)61350-0

Moura CC, Segundo MA, Neves J, Reis S, Sarmento B (2014) Co-association of methotrexate and SPIONs into anti-CD64 antibody-conjugated PLGA nanoparticles for theranostic application. Int J Nanomedicine 9:4911–4922. https://doi.org/10.2147/ijn.s68440

Munita JM, Arias CA (2016) Mechanisms of antibiotic resistance. Microbiol Spectr 4. https://doi.org/10.1128/microbiolspec.vmbf-0016-2015

Murray CB, Noms DJ, Bawend MG (1993) Synthesis and characterization of nearly monodisperse CdE (E = S, Se, Te) semiconductor nanocrystallites. J Am Chem Soc 115:8706–8715. https://doi.org/10.1021/ja00072a025

Nadeem M et al. (2016) Magnetic properties of polyvinyl alcohol and doxorubicin loaded iron oxide nanoparticles for anticancer drug delivery applications. PloS one 11: e0158084. https://doi.org/10.1371/journal.pone.0158084

Nigam S, Bahadur D (2017) Dendrimer-conjugated iron oxide nanoparticles as stimuli-responsive drug carriers for thermally-activated chemotherapy of cancer. Colloids Surf B Biointerfaces 155:182–192. https://doi.org/10.1016/j.colsurfb.2017.04.025

Niu C et al (2013) Doxorubicin loaded superparamagnetic PLGA-iron oxide multifunctional microbubbles for dual-mode US/MR imaging and therapy of metastasis in lymph nodes. Biomaterials 34:2307–2317. https://doi.org/10.1016/j.biomaterials.2012.12.003

O'Brien S, Brus L, Murray CB (2001) Synthesis of monodisperse nanoparticles of barium titanate: toward a generalized strategy of oxide nanoparticle synthesis. J Am Chem Soc 123:12085–12086. https://doi.org/10.1021/ja011414a

Ostroverkhov PV et al (2019) Synthesis and characterization of bacteriochlorin loaded magnetic nanoparticles (MNP) for personalized MRI guided photosensitizers delivery to tumor. J Colloid Interface Sci 537:132–141. https://doi.org/10.1016/j.jcis.2018.10.087

Pascu Oana et al (2012) Surface reactivity of iron oxide nanoparticles by microwave assisted synthesis; comparison with the thermal decomposition route. J Phys Chem. https://doi.org/10.1021/jp303204d

Perez JM, Josephson L, O'Loughlin T, Hogemann D, Weissleder R (2002) Magnetic relaxation switches capable of sensing molecular interactions. Nat Biotechnol 20:816–820. https://doi.org/10.1038/nbt720

Pinkas J et al (2008) Sonochemical synthesis of amorphous nanoscopic iron(III) oxide from Fe(acac)3. Ultrason Sonochemistry 15:257–264. https://doi.org/10.1016/j.ultsonch.2007.03.009

Qin J et al (2007) A high-performance magnetic resonance imaging T2 Contrast Agent. Adv Mater 19:1874–1878. https://doi.org/10.1002/adma.200602326

Reddy LH, Arias JL, Nicolas J, Couvreur P (2012) Magnetic nanoparticles: design and character-ization, toxicity and biocompatibility, pharmaceutical and biomedical applications. Chem Rev 112:5818–5878. https://doi.org/10.1021/cr300068p

Ren C et al (2008) Synthesis of organic dye-impregnated silica shell-coated iron oxide nanoparticles by a new method. Nanoscale Res Lett 3:496–501. https://doi.org/10.1007/s11671-008-9186-5

Rosen JE, Chan L, Shieh DB, Gu FX (2012) Iron oxide nanoparticles for targeted cancer imaging and diagnostics. Nanomedicine 8:275–290. https://doi.org/10.1016/j.nano.2011.08.017

Salaheldin TA, Loutfy SA, Ramadan MA, Youssef T, Mousa SA (2019) IR-enhanced photothermal therapeutic effect of graphene magnetite nanocomposite on human liver cancer HepG2 cell model. Int J Nanomedicine 14:4397–4412. https://doi.org/10.2147/ijn.s196256

Shaghaghi B, Khoee S, Bonakdar S (2019) Preparation of multifunctional Janus nanoparticles on the basis of SPIONs as targeted drug delivery system. Int J Pharm 559:1–12. https://doi.org/10.1016/j.ijpharm.2019.01.020

Shang L, Wang QY, Chen KL, Qu J, Zhou QH, Luo JB, Lin J (2017) SPIONs/DOX loaded polymer nanoparticles for MRI detection and efficient cell targeting drug delivery. RSC Advances **7**. https://doi.org/10.1039/c7ra08348c

Shen S et al (2015) Core-shell structured Fe3O4@TiO2-doxorubicin nanoparticles for targeted chemo-sonodynamic therapy of cancer. Int J Pharm 486:380–388. https://doi.org/10.1016/j.ijpharm.2015.03.070

Shi J et al (2013) PEGylated fullerene/iron oxide nanocomposites for photodynamic therapy, tar-geted drug delivery and MR imaging. Biomaterials 34:9666–9677. https://doi.org/10.1016/j.biomaterials.2013.08.049

Snell NJ (2003) Examining unmet needs in infectious disease. Drug Discov Today 8, 22–30

Sodipo BK, Aziz AA (2018) One minute synthesis of amino-silane functionalized superparamag-netic iron oxide nanoparticles by sonochemical method. Ultrason Sonochemistry 40:837–840. https://doi.org/10.1016/j.ultsonch.2017.08.040

Solanki A, Kim JD, Lee KB (2008) Nanotechnology for regenerative medicine: nanomaterials for stem cell imaging. Nanomedicine 3:567–578. https://doi.org/10.2217/17435889.3.4.567

Stewart BW, W. C. World Cancer Report (2014)

Tassa C, Shaw SY, Weissleder R (2011) Dextran-coated iron oxide nanoparticles: a versatile platform for targeted molecular imaging, molecular diagnostics, and therapy. Acc Chem Res 44:842–852. https://doi.org/10.1021/ar200084x

Tong L, Zhao M, Zhu S, Chen J (2011) Synthesis and application of superparamagnetic iron oxide nanoparticles in targeted therapy and imaging of cancer. Front Med 5:379–387. https://doi.org/10.1007/s11684-011-0162-6

Torres-Sangiao E, Holban AM, Gestal MC (2016) Advanced nanobiomaterials: vaccines, diagnosis and treatment of infectious diseases. Molecules 21. https://doi.org/10.3390/molecules21070867

Turkbey B, Thomasson D, Pang Y, Bernardo M, Choyke PL (2010) The role of dynamic contrast-enhanced MRI in cancer diagnosis and treatment. Diagn Interv Radiol 16:186–192. https://doi.org/10.4261/1305-3825.dir.2537-08.1

Tutuianu R et al. (2017) Evaluation of the ability of nanostructured PEI-coated iron oxide nanoparticles to incorporate cisplatin during synthesis. Nanomaterials 7. https://doi.org/10.3390/nano7100314

Veiseh O, Gunn JW, Zhang M (2010) Design and fabrication of magnetic nanoparticles for targeted drug delivery and imaging. Adv Drug Deliv Rev 62:284–304. https://doi.org/10.1016/j.addr.2009.11.002

Vetter A et al (2011) Thiolated polyacrylic acid-modified iron oxide nanoparticles for in vitro labeling and MRI of stem cells. J Drug Target 19:562–572. https://doi.org/10.3109/1061186x.2010.542243

Vikram S et al (2015) Tuning the magnetic properties of iron oxide nanoparticles by a room-temperature air-atmosphere (RTAA) co-precipitation method. J Nanosci Nanotechnol 15:3870–3878. https://doi.org/10.1166/jnn.2015.9544

Wang Y et al. (2018) Multistage targeting strategy using magnetic composite nanoparticles for synergism of photothermal therapy and chemotherapy. Small **14**: e1702994. https://doi.org/10.1002/smll.201702994

Wei H et al (2017) Exceedingly small iron oxide nanoparticles as positive MRI contrast agents. Proc Natl Acad Sci USA 114:2325–2330. https://doi.org/10.1073/pnas.1620145114

Xu Y, Qin Y, Palchoudhury S, Bao Y (2011) Water-soluble iron oxide nanoparticles with high stability and selective surface functionality. Langmuir ACS J Surf Colloids 27:8990–8997. https://doi.org/10.1021/la201652h

Yan L et al. (2018) Protoporphyrin IX (PpIX)-coated superparamagnetic iron oxide nanoparticle (SPION) nanoclusters for magnetic resonance imaging and photodynamic therapy. Adv Funct Mater 28. https://doi.org/10.1002/adfm.201707030

Yigit MV, Moore A, Medarova Z (2012) Magnetic nanoparticles for cancer diagnosis and therapy. Pharm Res 29:1180–1188. https://doi.org/10.1007/s11095-012-0679-7

Yu M, Huang S, Yu KJ, Clyne AM (2012) Dextran and polymer polyethylene glycol (PEG) coating reduce both 5 and 30 nm iron oxide nanoparticle cytotoxicity in 2D and 3D cell culture. Int J Mol Sci 13:5554–5570. https://doi.org/10.3390/ijms13055554

Zazo H, Colino CI, Lanao JM (2016) Current applications of nanoparticles in infectious diseases. J Control Release Off J Control Release Soc 224:86–102. https://doi.org/10.1016/j.jconrel.2016.01.008

Zhang P et al (2018) Iron oxide nanoparticles as nanocarriers to improve chlorin e6-based sonosensitivity in sonodynamic therapy. Drug Des Dev Ther 12:4207–4216. https://doi.org/10.2147/dddt.s184679

Zou P et al (2010) Superparamagnetic iron oxide nanotheranostics for targeted cancer cell imaging and pH-dependent intracellular drug release. Mol Pharm 7:1974–1984. https://doi.org/10.1021/mp100273t

Chapter 7
Ferrite Nanoparticles for Biomedical Applications

M. Irfan Hussain, Min Xia, Xiao-NaRen, Kanwal Akhtar, Ahmed Nawaz, S. K. Sharma and Yasir Javed

Abstract Iron oxide nanoparticles specially ferrites have gained a lot of attention in recent years due to their applications in diverse field and particularly in biomedical field where their enhanced magnetic properties offer diversity in imaging, diagnosis, and treatment. There are numerous types of ferrites that have been synthesized and presented for different applications but ferrite based on Co, Ni, and Zn has shown potential for biomedical applications due to high magnetic anisotropy and biocompatability. Ferrites nanoparticles can be prepared by different protocols such as co-precipitation, and sol-gel, hydrothermal. These methods are very efficient and produce high yield of ferrite powder. In this chapter, we have summarized the basic introduction of ferrites, types of ferrites, their crystal structures, and applications in the biomedical field.

Keywords Nanoferrites · Synthesis · Superparamagnetism · Diagnosis and therapy

Introduction

Generally, the word *ferrite* is used to explain a group of magnetic oxides that contain iron oxide as a main constituent. Ferrites are black or dark gray in appearance, brittle and hard in physical character (Gubin 2009). The first well-known natural ferrite to ancient people was magnetite (Fe_3O_4), or loadstone. The ferrites contain elements such as manganese, iron, transition metals, and lanthanides with iron oxide (Maaz et al. 2007). Ferrite materials exhibit high permeability and high value of saturation

M. Irfan Hussain (✉) · M. Xia · Xiao-NaRen
Institute of Powder Metallurgy and Advanced Ceramics, University of Science and Technology Beijing, Beijing 100083, China
e-mail: h.irfan.uaf@outlook.com

K. Akhtar · A. Nawaz · Y. Javed
Department of Physics, University of Agriculture, Faisalabad, Pakistan

S. K. Sharma
Department of Physics, Faculty of Science and Technology, The University of the West Indies, Saint Augustine, Trinidad and Tobago

magnetization, low eddy current, moderate permittivity, and high electric resistance (Ichiyanagi et al. 2007).

Ferrites are sensitive to sintering conditions, preparation methods, the basic amount of metal oxides and different additives. Ferrite components are commonly used in innovative and conventional applications due to their economical cost, and variety of morphologies (Liu et al. 2000; Zi et al. 2009). Ferrites are used in microwave, memory chips, transformer cores, transducers, activators, magnetic recording and as a permanent magnet Kefeni et al. (2017). Several chemical techniques are being employed for the preparation of nanoscale powder ferrites such as hydrothermal method (Köseoğlu et al. 2012), sol-gel technique (Chen and He 2001; Srivastava et al. 2009), chemical co-precipitation method, and pulse lased deposition (Rao et al. 2006). In addition, from the last few decades, nanoscale ferrites also become an interesting material for new applications including gas sensors, drug delivery, humidity sensor, and catalyst (Lu et al. 2007; Sanpo et al. 2013; Sharifi et al. 2012). Ferrites due to the presence of iron usually show ferromagnetic behavior but with reduction in size, a unique nature called superparamagnetism is appeared (Srivastava and Yadav 2012). Where due to low number of spins in a single particle, spins become free from the influence of each other as is the case of ferrimagnetic and consequently presented paramagnetic like behavior (Liu and Zhang 2001; Yang et al. 2010). In the commercial point of view, ferrites are successfully divided into the following three important groups (Wang et al. 2010); each group possess a specific crystalline structure, i.e.,

- Soft ferrite with garnet structure (yttrium iron garnet) having 560 K curie temperature.
- Soft ferrites (e.g., nickel or manganese zinc ferrite) with spinel cubic structure.
- Hard ferrites (e.g., strontium hexaferrite) with hexagonal structure.

Ferrites are further classified into four groups based on their structure, i.e., garnet cubic structure, hexagonal structure, spinel cubic structure, and ortho-ferrite structure (Sugimoto 1999). All these ferrites are having different chemical formulae.

Garnet Ferrite: The unique ceramic ferrimagnetic garnet ferrite is represented by $Me_3Fe_5O_{12}$ chemical formula (Uchida et al. 2013). The Me represents a trivalent ion, e.g., yttrium (Y) or rare earth ions. The cubic unit cell contains 160 atoms or eight molecules of $Me_3Fe_5O_{12}$. The Me ions exist on regular dodecahedral sites also called (c sites) with eight surrounding oxygen ions, while Fe^{3+} ions with (3:2) ratio occupy octahedral and tetrahedral positions (Valenzuela 2012).

Hexagonal Ferrite: In 1952, ferrites with novel characteristics were discovered, namely as hexagonal ferrites. Hexagonal ferrite is represented by general $(MeFe_{12}O_{19})$ chemical formula. Me represents large ionic radius divalent ions, e.g., Barium ion (Ba^{2+}), and Lead ion (Pb^{2+}). In hexagonal ferrite, direction of magnetization spins cannot be transformed into another axis (Li et al. 2006; Meshram et al. 2004).

Spinel Ferrite: The magnetically soft spinel ferrite is generally represented by MFe_2O_4 chemical formula. The Me represents a divalent metal ion, e.g., zinc (Zn), nickel (Ni), magnesium (Mg), etc. (Mathew and Juang 2007). Spinel ferrites have

unique properties, e.g., less magnetic losses and high electric resistance. The structure of spinel ferrite exhibits two interstitial positions, i.e., tetrahedral site and octahedral site (Andersen et al. 2018). Ni-Zn ferrite and Mn-Zn ferrite are the two major ceramic ferrites of this family. The properties of spinel cubic ferrites depend upon the behavior of divalent cations. These properties can be changed by varying the cations position at octahedral and tetrahedral sites. In spinel cubic structure, cation radii exist between 40 and 90 pm. All cations on the octahedral lattice point have magnetic moment directed in same direction. Whereas all cations at the tetrahedral sites have magnetic moments aligned in identical direction, but opposite as compared to cations of octahedral site (da Silva et al. 2019).

The spinel ferrite can be further classified on the basis of cations distribution over tetrahedral and octahedral positions, namely

- Normal/regular spinel
- Inverse spinel
- Random spinel

Normal/regular spinel structure is cubic close-packed. Eight M^{2+} divalent ions exist over tetrahedral while 16 Fe^{3+} trivalent ions exist over octahedral site. Generally, at octahedral sites are occupied by nonmagnetic cations such as cadmium or zinc (Ng 2018).

Inverse spinel structure has different cations arrangement, e.g., eight M^{2+} ions exist over octahedral site while Fe^{3+} ions occupy tetrahedral sites. Nickel ferrite and cobalt ferrite are the typical examples of inverse spinel ferrites (Adeela et al. 2018).

In random spinel ferrite, the proportion of cations is not fixed between tetrahedral and octahedral sites, both divalent and trivalent metal ions can exist randomly over these sites. Magnesium ferrite is general example of random ferrite (Hernández-Gómez et al. 2018).

Ortho-Ferrite: The disorder perovskite with orthorhombic structure based ortho-ferrites have generally represented by $MeFeO_3$, while, Me represents a trivalent ion, e.g., yttrium (Y) or rare earth ions. Ortho-ferrite exhibits weak ferromagnetism. These ferrites are widely used in magnetic and electric current sensors, communication routes, and for optical Internet due to the high velocity (Kumar et al. 2018; Pinho et al. 2018).

Ferrite-Based Materials

Ferrite has been extensively studied in recent years and regarded the milestone technological material which possesses both magnetic and electrical properties since its versatile application in various fields. It is known that naturally occurring magnetic materials are soft and hard ferrites (Anderson 1956). Soft ferrites possess low coercive field less than 12.5 Oe and easily demagnetized, whereas hard ferrites exhibit permanent magnetization and high coercive field. Ferrites having formula MFe_2O_4,
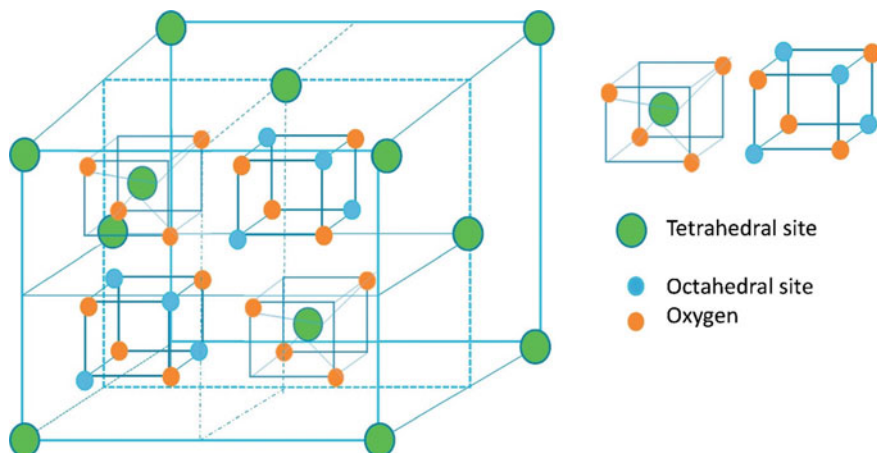
Fig. 7.1 Structural arrangement of spinel ferrite. Reprinted with permission from (Kefeni et al. 2017)

where M is the divalent metal such as Fe, Cu, Zn, Mn, Co, Mg, and Ni (Pardavi-Horvath 2000). The prime concerns of soft ferrites properties are variation in saturation magnetization with shape, initial permeability, remanence, magnetic loss factor, and Curie temperature. In order to tune the properties of new types of ferrites with specific magnetic properties, researchers have adopted various strategies along with precursor type, surfactants, heating temperature, etc. Spinel ferrites are considered as important class from different types of ferrites widely employed in the magnetic applications (Fig. 7.1). Potential biomedical applications of magnetic nanoferrites are drug delivery agents, specific cell labeling, detoxification, sono-imaging, and MRI (Sugimoto 1999; Harris 2012; Pullar 2012).

Cobalt Ferrite

Cobalt ferrite ($CoFe_2O_4$) is one of the most promising ferrite nanomaterial owing to its special physio-chemical and magnetic properties such as high anisotropy and high coercivity which make them suitable in the nanomedicine field. The high magnetic anisotropy in cobalt ferrite appears thanks to the presence of cobalt ions at the octahedral sites in the crystal structure (Tourinho et al. 1990; Gul and Maqsood 2008; Caltun et al. 2008). Cobalt ferrite also exhibited superparamagnetic behavior when size of the particles reduces to critical limit of 10 nm. Addition of other metal ions and their distribution in the crystal lattice can influence their technologically relevant properties, i.e., heat generation efficiency, contrast agent properties, etc. (Figure 7.2). Physicochemical properties and better mechanical properties make
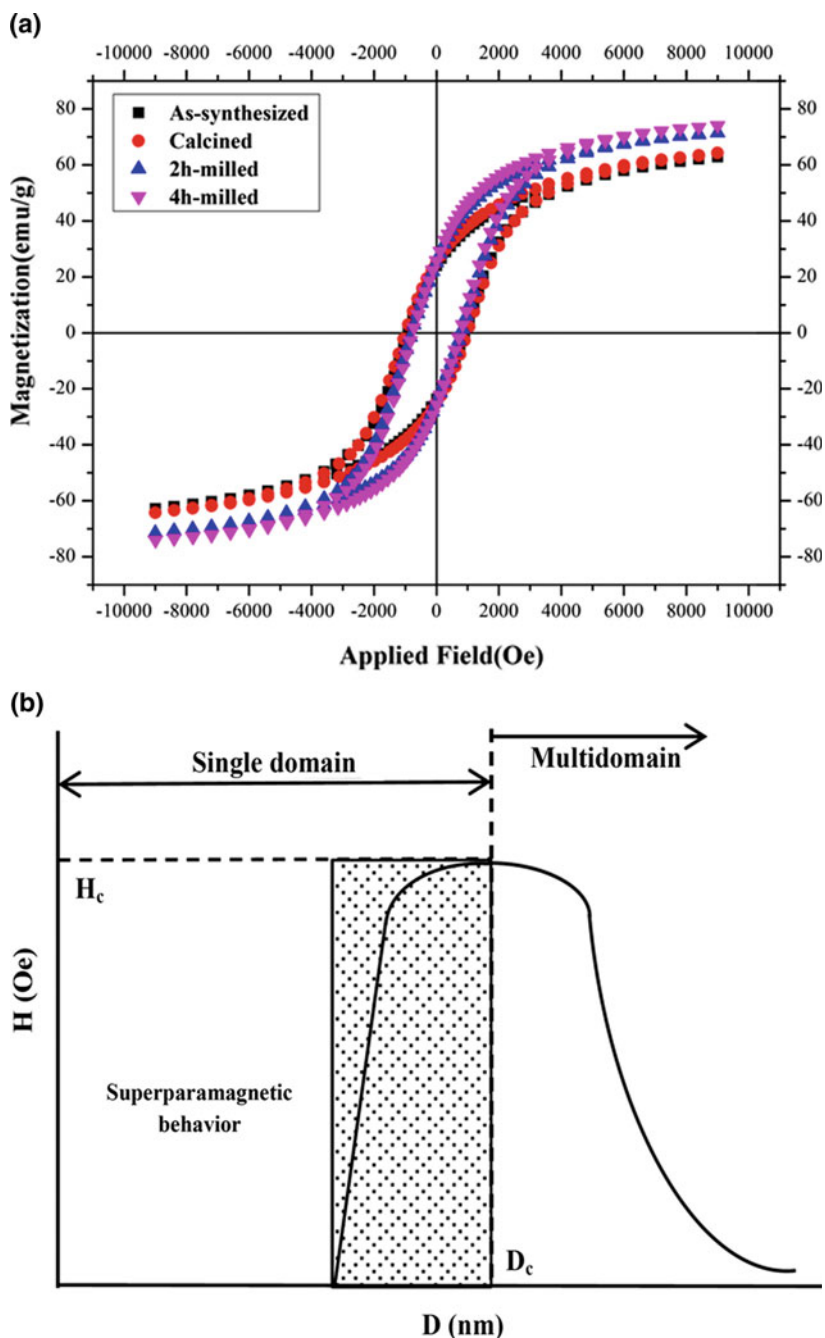
Fig. 7.2 **a** Magnetic properties of cobalt ferrite NPs under different conditions: black; as synthesized, red; calcined, blue; 2 h ball milling, pink; 4 h ball milling. **b** Comparison of coercivity values against particle size; decrease in coercivity was observed with the increase in particles size. Reprinted with permission from (Maleki et al. 2018)

cobalt ferrite NPs stable and dispersible in physiological conditions. Adjustable magnetic and other properties make cobalt ferrite NPs much better option than iron oxide in biomedical applications, especially for sensitive magneto systems such as magnetic resonance imaging (MRI), drug delivery, medical diagnostics, and hyperthermia radio-frequency treatment (Tamura and Matijevic 1982; Franco and e Silva 2010).

Nickel Ferrite

Nickel ferrite is ferrimagnetic in nature and possesses inverse spinel structure in which Ni^{2+} present at octahedral sites, whereas Fe^{3+} occupies both octahedral and tetrahedral sites. When particle size is small, mixed spinel structure is prominent as compared to bulk form where inverse spinel structure is existed (Joshi et al. 2016; Samoila et al. 2017). The magnetic disorder in the nickel ferrite NPs causes high-field irreversibility, hysteresis loop shift and unexpected relaxation dynamics. In addition, nickel ferrite shows p-type semiconductor properties due to cation vacancies and can attract oxygen during heating. Ferrimagnetic behavior arises due to the antiparallel spins of Fe^{3+}ions and Ni^{2+} ions. Nickel ferrite also shows superparamagnetic nature; therefore, it has applications in gas sensing, magnetic ferrofluids, catalysis, targeted drug delivery and magnetic resonance imaging (Singhal and Chandra 2007; Liu et al. 2001; Ishaque et al. 2010).

Zinc Ferrite

Zinc ferrite is another example of spinel ferrite and possesses high electromagnetic performance, low coercivity, and moderate magnetization. These properties make zinc ferrite suitable as soft magnets and low loss material for biomedical applications. These properties can be controlled by tuning chemical composition and structural parameters which finally affected by the size and shape of the nanomaterial. Both superparamagnetic and ferrimagnetic nature have been reported for zinc ferrite NPs (Leclerc et al. 2003; Petitt and Forester 1971). Zinc ferrite has potential applications in photocatalysis, gas sensor, magnetic hyperthermia, magnetic resonance imaging, and Li-ion batteries. Spinel ferrites (Fe, Zn) Fe_2O_4 seem to be a solid tan-color that is insoluble in diluted alkali, water, or acids. Due to their high opacity, it can be used as pigments, galvanizing iron, especially in requiring heat stability purpose. It is also interesting when ZnO-doped-Gd with size less than 6 nm being used for both magnetic and optical response in magnetic resonance imaging. Zinc ferrite is offered versatile nanoplatforms for drug delivery application because of their large surface chemistry and phototoxic effect (Verma et al. 2000; Mohan et al. 1999; Verma et al. 2005) (Fig. 7.3).
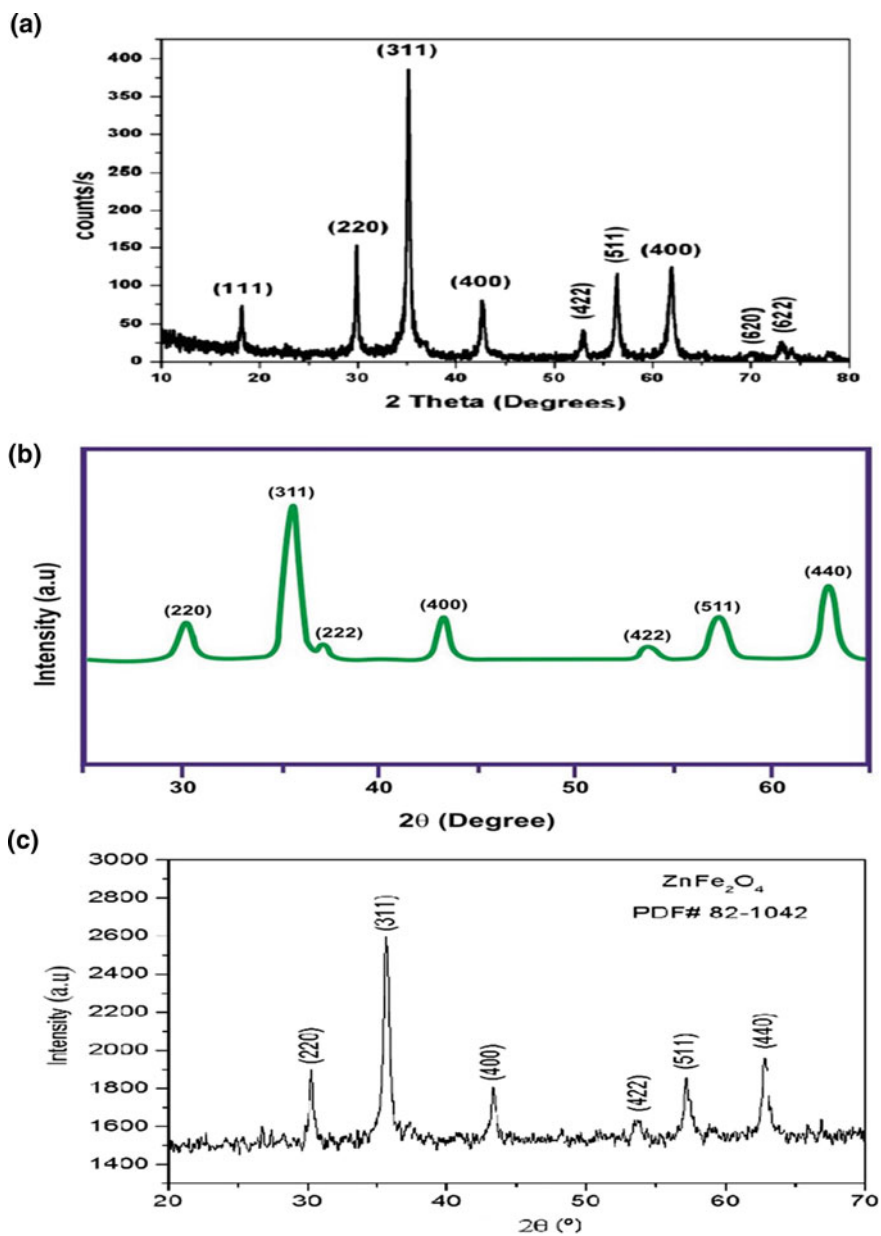
Fig. 7.3 Experimental X-ray diffraction patterns of **a** Cobalt ferrite (Elbeshir 2018), **b** nickel ferrite (Sagadevan et al. 2018) and **c** zinc ferrite (Kanagesan et al. 2016) with peak indexing

Mixed Ferrites

In addition to simple ferrites as discussed above, there are different ferrites where the addition of the number of elements in the iron is more than one. In the following section, we will discuss properties, synthesis, and applications of these ferrites. George and co-workers (George et al. 2017) used sol-gel technique to synthesize Ni-Zn ferrites doped with Ce^{3+} ions. It was observed that by increasing doping of cerium ions, lattice parameters were decreased. Doping also changed the average crystallite size, i.e., size of cerium doped ferrite was smaller as compared to undoped ferrites. Ce addition to ferrites showed low value of saturation magnetization. Samavati and co-workers (Samavati et al. 2016) employed chemical co-precipitation route to prepare Cu-doped Co-ferrites NPs. These mixed ferrites showed high value of coercivity and saturation magnetization. The crystallite average size was decreased by co-doping of metal ions. Different parameters such as coercivity, saturation, and remanent magnetization increased gradually by increasing temperature. Sertkol et al. (2009) synthesized zinc-doped Ni-ferrite NPs. One of the advantages of this method is high yield powder ferrite production. NPs have crystal size of 20 nm and spinel structure. By increasing the doping level of zinc, magnetic properties of these mixed ferrites changed dramatically.

Sanpo and colleagues (Sanpo and Wang 2013) explained Cu-substituted Co-ferrite ($CoCuFe_2O_4$) NPs. $CoCuFe_2O_4$ showed irregular morphology, average crystallite size of 35 to 45 nm and spinel cubic structure. The improvement of antibacterial properties and diameter of particle was highly influenced by copper ion substitution in Co-ferrite NPs. De-León-Prado et al. (2017)employed thermal decomposition and sol-gel techniques to synthesize mixed Mg–Mn ferrite NPs. These NPs have shown superparamagnetic behavior and single-crystal inverse spinel structure. The particles showed spherical morphology with size between 11 and 15 nm. Considering these aspects, mixed ferrites can be a favorable candidate for cancer treatment. In another study (Vaidyanathan et al. 2007), Co-substituted Zn-ferrite NPs were prepared via co-precipitation route. Zn ion substitution highly influenced average particle size, magnetic and structural properties. It was observed that by increasing Zn ion substitution, coercivity, saturation, and remanent magnetization decreased, whereas value of lattice constant increased. On the other hand, when Zn substituted in cobalt-ferrite nanoparticles, coercivity and magnetization decreased and observed in the range 140-40 Oe, and 134–100 emu/g, respectively (Hankare et al. 2010). In addition, increase in copper ion content in nickel-copper ferrite also decreased magnetization (Kurian and Nair 2016). These ferrites were widely used in medical diagnosis and as microwave absorber due to its magnetic permeability and saturation magnetization. Lin et al. (2019) used sol-gel auto-combustion technique to synthesize spinel single-phase Co-Mg ferrite NPs. Calcination temperature played a key role in the properties of these mixed ferrites, i.e., by increasing calcination temperature, increase in average crystalline size, change in hyperfine field and distribution of iron ion at different lattice sites were observed. These mixed ferrites showed ferrimagnetic behavior at room temperature (Fig. 7.4).
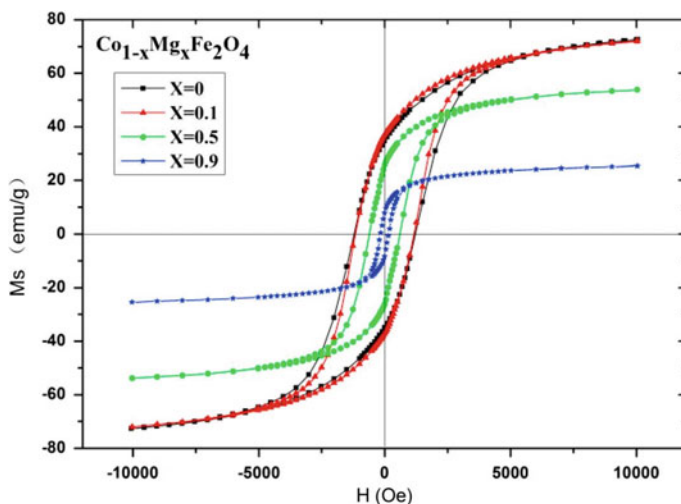
Fig. 7.4 Magnetic properties of Mg substituted cobalt-ferrite nanoparticles annealed at 800 °C. Reprinted with permission from (Lin et al. 2019)

Conventional Synthesis Protocols

Wet Chemical-Based Seed-Mediated Growth Toward Functional Hybrids

The wet chemical route has emerged the most convenient and promising to produce high-quality multifunctional hybrid NPs. The growth strategy of hybrid nanomaterials can be achieved either by bottom-up or top-down ways (Ali Umar and Oyama 2005). The base of wet chemical synthesis process is bottom-up approach, e.g., species of atomic-molecular integrated to develop nanostructures, which largely used and offers relatively simple, scalable, and modular functional hybrids. Unique properties of multifunctional hybrids NPs such as shape control, highly stable, phase and selective surface structure are possible through wet chemical synthesis method (Zeng et al. 2010). The wet chemical process allows significantly fine modification of reaction conditions, i.e., concentration of substrate, temperature additives, pH, etc., that helps to change in thermodynamics and kinetics of the nanohybrids (Jana et al. 2001). Controlled synthesis and reaction parameters such as type of precursor, heating/cooling rates, heating method, concentration, temperature, mixing, ligands of all types, solvent properties, and addition sequence decide the morphology and hybrid formation of NPs (Maaz et al. 2007). For control over better morphology, it is important to understand mechanism of the conversion precursor, reagents in the system, surface stabilizing agent, and its correlation with growth mediation toward nucleation rate (Baig et al. 2019). Growth kinetics and nucleation of a particle are

also controlling factor toward size and shape of nanohybrids in the solution. Therefore, it is necessary to collect data by reviewing the literature and compiled to control the wet chemical synthesis for the functional hybrid NPs Mefford et al. (2018).

Co-precipitation method is simple and convenient for the preparation of ferrites from salt aqueous solution (Nasrin et al. 2018). This method has noteworthy benefits such as environment friendly, requires low temperature to complete reaction, narrow size distribution and obtained high yield product. Owing to these promising advantages, co-precipitation route has been widely employed for the synthesis of various ferrites including FeO nanomaterials, e.g., hematite (γ-Fe_2O_3), magnetite (Fe_3O_4) (Lassoued et al. 2018; Nosrati et al. 2018). However, fabricated NPs through the aqueous solution are not reliable because it is arduous to control shape and ultrafine particles. Thus, it requires more efforts to control the morphology of ferrites-based NPs (Gjorup et al. 2018).

Sol-Gel Process

Sol-gel method has received enormous attention for the preparation of ferrites NPs due to its several advantages such as short processing time, good control of stoichiometry, and production of narrow size distribution at lower temperature. In aqueous sol-gel process, the formation of the self-linking network of a metallo-inorganic colloidal suspension by the gelation of sol to form a continuous gel of liquid phase. Thus, the obtained gel from concentrated aqueous solution can be employed for the fabrication of different kinds of nanostructure and nanomaterials such as xerogels, aerogels, and powder (Chen and He 2001; Yue et al. 2004) (Fig. 7.5). Recently, through sol-gel route, pure spinel Ni-ferrite NPs were synthesized using a chelating agent of polyacrylic acid (PAA) (Chen and He 2001). Chen et al. (2001) controlled the crystallinity and morphology of $NiFe_2O_4$ NPs by changing the molar ratio of polyacrylic acid with metal ions at calcination temperature. Barium ferrite ($BaFe_{12}O_{19}$) NPs were prepared by sol-gel combustion way with a particle size range between 55 and 110 nm using the solution of glycine and metal nitrates precursor (Meng et al. 2014). Diverse type of precursors that can be concentrated to form as sol, including metal organic compound, organic salts, metal alkoxide and salts of inorganic acids. Among these precursors, metal alkoxides are mostly employed for metal to bond with multiple alkyl groups in the presence of oxygen atoms. Moreover, this typical process allows the precursor solution to dissolve in an organic solvent or a mixture of solvents. During the formation of the sol in aqueous sol-gel process, base catalyst or acid can be added which increase the reaction growth. The metal-organic metal bonds formation occurs during polycondensation and hydrolysis process due to the precursors. In the polycondensation process, the hydrolyzed species accumulate within an inorganic polymer made by the removal of water molecule. Sol properties can be modified based on the chemical constitutes and process condition in the sol-gel bath process. Typically, this process is most favorable to design and achieve colloidal particles with long or short polymeric chains. Advantageously, these sol properties can
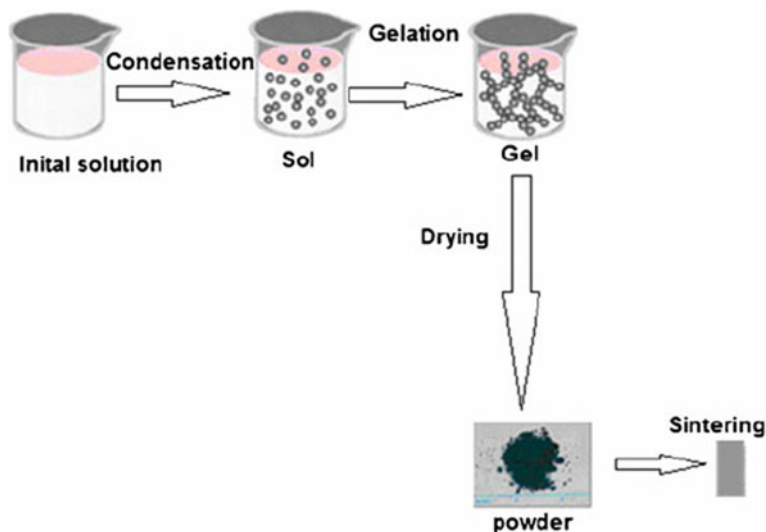
Fig. 7.5   Schematic diagram of different steps involved in sol-gel process

be used for specific applications including, thin coating, spray pyrolysis, and powder preparation. The obtained sol can proceed to a gel state through solvent evaporation and continuous polycondensation. The resulting gel and leftover solvent can be further refined by removing solvent residue and processing with different chemical ways.

Hydrothermal Approach

The hydrothermal technique is a convenient and useful for the fabrication of hybrids NPs which performed in aqueous media in small reactors. During the preparation of hybrids NPs, the temperature inside the autoclave can be higher than 200 °C and pressure also higher than 2000 psi. Recently, this method has been extensively used for the preparation of a broad range of ferrites nanostructure materials (Fig. 7.6). Wang et al., successfully synthesized Fe_3O_4NPs adopting hydrothermal approach at temperature of 140 °C for 6 h, showing saturation magnetization 85.8 emu/g. Results revealed that their saturation magnetization is not higher than corresponding bulk Fe_3O_4 (92 emu/g) (Wang et al. 2004). Chitosan-modified route magnetic manganese ferrite NPs have been achieved using hydrothermal approach. The obtained NPs have a cubic shape structure with mean diameter of ∼100 nm. As described by Song et al., small addition of gadolinium oleate (Gd oleate) complex can improve the shape and size of iron oxide NPs. Interestingly, in FeO NPs the shape change was obtained from sphere to cube due to the addition of gadolinium oleate (Song et al. 2017). Shape change was also studied theoretically by density functional theory
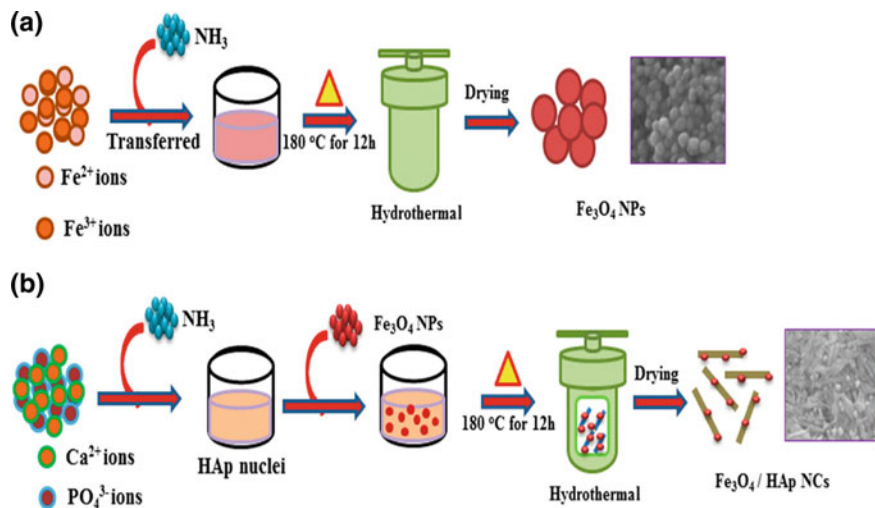
Fig. 7.6 Graphical representation of hydrothermal method of the synthesis of iron oxide **a** and iron oxide-hydroxyapatite **b** nanomaterials (Govindan et al. 2017)

which confirmed that Gd oleate complexes fully chain with (100) plane, as compared to (111) plane that shows lower energy passivation at the surface, and significant slow growth was observed along (100) planes. Park et al. (2013) prepared monodisperse metal oxide nanohybrids at large scale including Fe_2O_3, MnO, CoO, $MnFe_2O_4$, and FeO@Fe with high-boiling solvent as the precursor of metal oleate. Sun et al., reported monodisperse MFe_2O_4 NPs(M = Fe, Co, Mn) using benzyl ether ($C_{14}H_{14}O$) and phenyl ether which yield 6 nm and 4 nm NPs, respectively. It was observed that particle size was directly proportional to reaction temperature and obtained results exhibit higher growth rates. Comparatively, it was quite hard and complex to control the crystallinity, composition, and synthesis of mixed metal oxides than the monometallic oxide.

Microwave-Assisted Synthesis

Microwave organic synthesis is an attractive and flexible platform in the form of chemical reaction, widely employed for chemical reaction with microwave radiations due to its significant benefits such as rapid volumetric heating and high carrier reaction rate and precise product yield than other wet chemical synthesis methods. Gyedye and Majetih first reported the use of microwave in wet chemical synthesis from a domestic oven in 1986 (Jain and Singla 2011). In microwave approach, the electromagnetic waves having vacuum wavelength range are taken near to 0.1–100 cm and a frequency range between 0.3 and 300 GHz (Fariñas et al. 2018; Perdomo et al. 2019). Recently, the efficiency of microwave heating has proven toward

different fields of organic synthesis and reduction in reaction time. In traditional organic synthesis, time saving regarded as key factor for the preparation of diverse types of ferrites nanohybrids. The kinetics of crystallization can be modified in the localized solution under the influence of microwave radiations (Grindi et al. 2018; Shukla et al. 2018). Wang et al. (2006) proposed the structure of spinal MFe_2O_4 (M = Co, Mn) NPs by employing polyol solvent in microwave method. They observed that by adjusting the volume ratio of distilled water to ethylene glycol, crystal quality, and reaction temperature can be controlled. For fabrication of pharmaceutical ingredients, microscale-type approaches such as integrated 'lab-on-chip', biological screening, and meso-scale flow would be dynamically pursued. Therefore, to evaluate the combinational system for parallel fabrication required great efforts. However, recent investigations show that microwave synthesis is the most productive and most promising route than that of the conventional methods and also regarded as the future chemical synthesis protocol.

Biomedical Applications of Ferrite-Based Nanohybrids

In the recent years, the study of magnetic NPs provides the most promising opportunity for biomedical applications to investigate the cancer treatment and infectious diseases through enhancing magnetic resonance imaging, magnetic hyperthermia, tissue engineering, and fast development in delivery drugs systems (Sanpo et al. 2013; Sharifi et al. 2012). In medical research, cancer is regarded as one of the worst-case challenges faced by the researcher (Srinivasan et al. 2018). The goals are to use magnetic NPs not only to improve the therapeutic performance but also to observe progress in advanced metastatic cancer. In addition, nanotechnology and use of magnetic NPs consisting of active elements such as iron, nickel, and cobalt can make an important contribution for boosting trend in biomedical and industrial purpose (Latorre-Esteves et al. 2009). Magnetic NPs holding magnetic behavior obey the coulomb's law (electrostatic force of interaction) and these properties make them favorable for magnetic field gradient. With the response of alternating current, magnetic NPs produce hysteresis loop with localized thermo-abrasive effect (hyperthermia) leading to cellular death in bacterial and cancerous cells. In drug delivery procedure, potential of magnetic NPs for functional binding with different species such as chemotherapeutic agents, nucleic acid, antibodies, and radionuclides is utilized (Rana et al. 2007). Magnetic NPs can accumulate and also induce hyperthermia due to an alternating magnetic field which gives another therapeutic option. Magnetic NPs may also be practically effective for overcoming cancer drug resistance. In addition, their contribution is perceived as combination of investigation and therapy in theranostic field. The promising and multifaceted results have provided the potential platform to investigate and diagnose of advanced cancer therapy. Bean and Livingston (Bean and Livingston 1959) reported that when magnetic material having a diameter lower than a critical value (D_c) and their range lies between 3 and 50 nm, they exhibited ferrimagnetic and ferromagnetic single domain superparamagnetic

behavior. The metallic core of magnetic NPs becomes more functionalized and stable when functional groups are introduced with magnetic NPs. Typically, magnetic NPs whose size below than 100 nm can be prepared with some degree of magnetism (Maity et al. 2009; Gupta and Curtis 2004). Interestingly, in iron oxide case, it was observed that NPs exhibited decrease in magnetism along with smaller size (Respaud et al. 1998).

Different polymers such as dextran and PEG are widely used where chances of opsonization increase (Ritchie et al. 2015). Very recently, using chemical stable metallic core-shell NPs enhance the bio-compatibility and stability of NPs through combining different magnetic moieties which improve the magnetic behavior by exchange-bias effect (Brubaker et al. 2014). Superparamagnetic NPs exhibit many promising and desirable features, such as low coercivity and remanence, coupled with strong magnetic susceptibility (Kneller and Luborsky 1963; Konczykowski et al. 1992). When two magnetic phases are paired mechanically, e.g., interface between two magnetic moieties can create the exchange-bias effect (Stamps 2001). The observed exchange coupling with Fe_3O_4-CoO has been explained in different systems which can further provide anisotropy in addition to stabilize unreliable nanocomposites materials Zeng (1998). In addition, these protection strategies ensure the longer circulation time of magnetic NPs for biomedical applications.

Therapeutic Uses of MNPs

As mentioned above, magnetic NPs have a wide range of application including as strengthening the signal obtained from MRI, enhancing deposition and accumulation of bio-therapeutic compounds, for example, peptides and genes for facilitating the destruction of bio-film and cancer cells through the creation of a local thermo-ablative, named as magnetic hyperthermia (Shete et al. 2014; Bhattacharyya et al. 2011).

Magnetic Resonance Imaging

MRI is one of the versatile techniques employed in the diagnosis and investigation of cancer treatment and other pathologies (Schoots et al. 2015; Feldman et al. 2013). In contrast with other imaging conditions, MRI does not directly utilize the ionizing radiation for tissue imaging, but rather magnetically attributed protons used for image creation. It was found that when proton orientated randomly under the normal condition, no magnetic moment obtained. Once the magnetic field has established, protons align themselves to the induced primary magnetic field and results net magnetic vector in the direction of the magnetic field. In 1997, Schick et al. (1997) reported that the strength of the magnetic field was directly proportional to the strength of protons

motion along the long axis in the form of in-phase or out-phase primary magnetic field.

Contrast agents: Contrast agents are extensively used to enhance contrast in the MRI images, categorized on the basis of relaxation times T1 or T2/T2* (Kato et al. 2003; Xing et al. 2008). T1 contrast agents customize the effect of water proton in longitudinal (T1) relaxation times that show positive bright signal intensity inside the images and improve the brightness of cells. Similarly, T2/T2* agents change the transverse relaxation times spatially, generating negative signal intensity in the images. However, superparamagnetic NPs-based contrast agents mainly alter T2* relaxation enable the regions to be detected as hypo-intense signals (Qin et al. 2007). Superparamagnetic NPs can impact T2 and T2* relaxation time and such contrast agents having relaxivity and higher magnetic susceptibility are acquired and presented in the literature. In addition, these NPs have extensively used for imaging cell clusters and tissues and for labeling and tracking of individual cells (Nitin et al. 2004). For general purpose targeted imaging, various non-specific superparamagnetic-based contrast agents are suitable (Tan et al. 2010). These can also be used for targeted drug delivery by applying specific tumor targeting moieties as covering shell and make easier for their agglomeration in cancer sites enhancing MRI resolution, for example, anti-glypican antibodies and anti-α-fetoprotein as outer shell can be employed for selectively targeting on hepatocellular carcinoma (primary malignancy part of liver with chronic disease) (Li et al. 2015). Despite lack of specific biomarkers, a small amount of superparamagnetic NPs contrast agents can produce better contrast unambiguously (Bakhtiary et al. 2016). Non-specific superparamagnetic contrast agents have played significant role for diagnostics and tissue imaging (Fig. 7.7) (Ghasemian et al. 2015).The future research study with targeted contrast agents will increase the opportunity for MRI as a robust and non-invasive system for imaging and early cancer detection (Wang 2011).

Magnetic Hyperthermia in Cancer Therapy

Although the growth of tumor can be ceased by warming cells up to 45 °C for 30 min (Fig. 7.8), it is challenging to raise the temperature of whole-body without causing hostile biochemical side effects (Yadavalli et al. 2016). At present, most of the studies have focused on the influence and level of efficiency of magnetic hyperthermia as a potential therapy for cancer treatment (Balivada et al. 2010; Jordan et al. 2006; Katafuchi et al. 1998). Yanase et al. (1998) in his initial work used magnetite with liposomes for the treatment of brain gliomas in mics and observed tumor size reduction from 30,376 to 2683 mm^3 with three cycles of treatment. Interestingly, this specific case reveals utilization of magnetic hyperthermia in multi-site treatment, but metastatic tumor demands more systematic treatment. In 2006, Jordan et al. employed dextran-coated magnetic NPs for in vivo treatment of harmful glioblastomas with Fisher rats (Jordan et al. 2006). The researchers concluded like Yanase et al. (1998) also observed that there was substantial difference ($p < 0.01$) for the mean survival
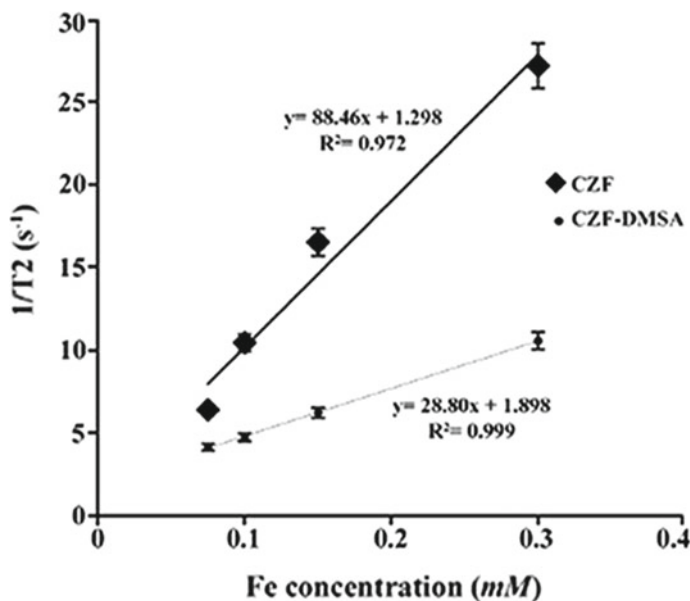
Fig. 7.7 Graph between transverse relaxation and iron concentration (mM) for cobalt zinc ferrite and dimercaptosuccinic acid coated cobalt zinc ferrite NPs (Ghasemian et al. 2015)

within monitoring and therapy groups statistically. When intra-tumoral temperature increased from 43 to 47 °C, the formation of precipitates also increased, indicating survival rate of the animal from 15.4 ($\pm$6.3) to 39.7 ($\pm$3.5) days, 4.5-fold further increase their survivability. In 2010, Balivada et al. (2010) separately utilized iron oxide and iron-based magnetic NPs for in vivo therapeutics of melanoma. It was revealed that statistically ($p < 0.1$) tumor weight decreased from 1.6 to 0.75 (control) mg as a result of magnetic NPs therapy. These studies confirmed that magnetic hyperthermia can decrease the viability of cancer cell lines and make it ineffective for whole tumor eradication.

Magnetic NPs in Targeted Drug Delivery

The usage of nucleic acids, proteins, and therapeutic agents for the cure of the different diseases is a rapidly expanding in recent years (Liang et al. 2015). Regrettably, ineffective distribution in the body often restrains the utilization of these biotherapeutics. The importance of magnetic-based delivery systems is to facilitate the efficient, fast response, and targeted delivery of bio-therapeutic agents (Fig. 7.9) (Ravichandran et al. 2018).

Therapeutic viruses: The coupling of adenoviral with magnetic NPs employs electrostatic interactions which can preserve the virus from deactivation through
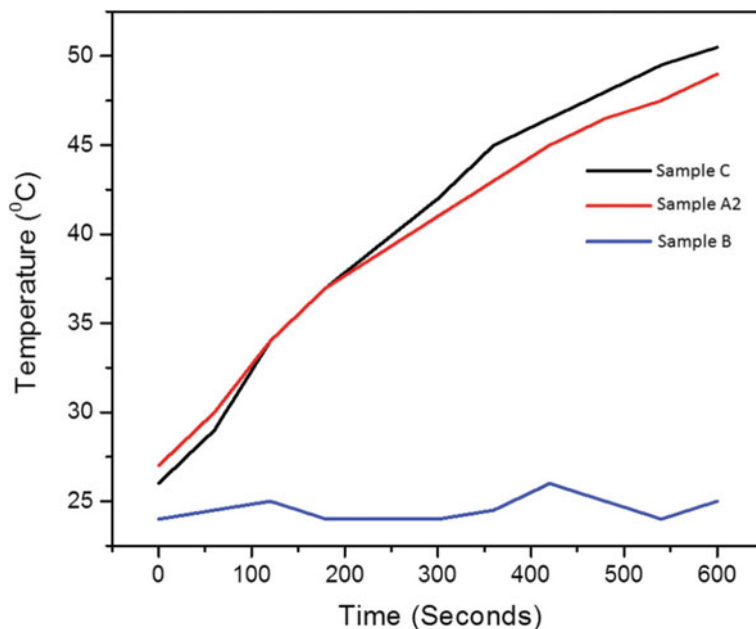
Fig. 7.8 Graph between rise in hyperthermia temperature with time at alternating field of 35mT at frequency of 250 kHz for cobalt ferrite powder synthesized by low temperature method (**a**), co-precipitation method (**b**) and hydrothermal method (**c**) (Yadavalli et al. 2016)

cells. However, using the external magnetic field, conjugated magnetic NPs virus can be directed to specific sites developing gene transfection productivity; mechanism called magnetofection (Dai et al. 2015). Superparamagnetic NPs in a complex form with adenovirus-based particles have shown 3–4-fold more transfection rate invivo (NIG-3T3 cells) in comparison with adenovirus particles (Sapet et al. 2012).

Nucleic acid and protein delivery: Nucleic acid biopolymer and protein-based therapeutics are largely based on favorable cellular absorptions. Given the attention to costly production routes, surrounding viral safety, and non-viral vectors, the use of magnetic NPs in the form of vectors is highly required. In addition, external magnetic fields are manipulated for superparamagnetic NPs and facilitated the accumulation and precipitation of nucleic-based therapies, many researchers have proved significantly decrease gene manifestation rates in vitro (Kim et al. 2011).

Conclusion and Future Prospects

In this chapter, it is pointed out that ferrite-based NPs are categories as medical devices used for regulatory purposes. For faster translation of progressive research
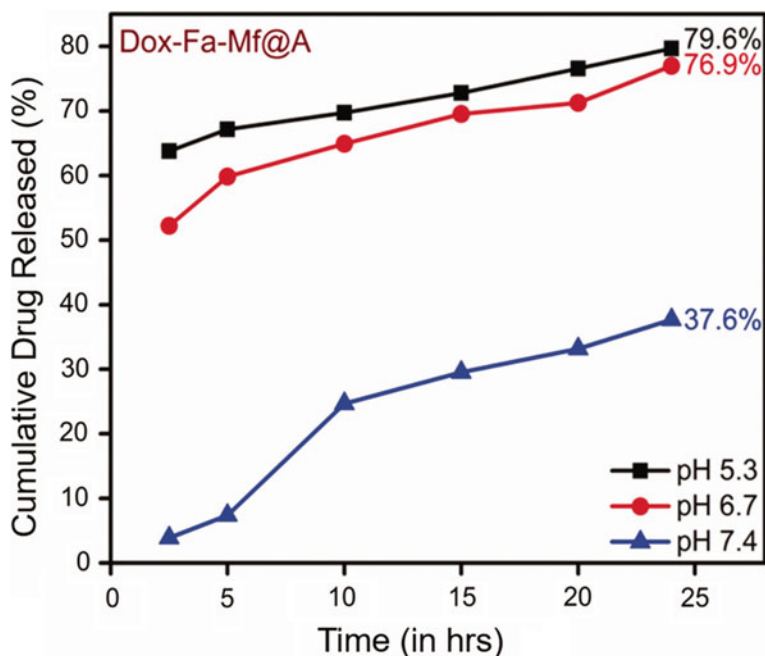
Fig. 7.9 Cumulative release of doxorubicin loaded with manganese ferrite NPs at different pH values. Reprinted with permission from (Ravichandran et al. 2018)

through ferrite-based nanomaterials in MRI, cancer diagnosis and therapy is important topic these days. We have summarized different ferrite-based nanomaterials currently used for MRI cancer detection and therapy. Possibilities to create nanoshells and core-shell ferrite-based nanomaterials, particularly the opportunities to employ the self-assembly layer-by-layer approaches will result in innovative protocols for diagnosis of different types of cancer. Such type of combinations will proffer multi-therapeutic modalities in single treatment. With the progression of this field, new epitome including magneto-mechanical stimuli based on induced magnetic disks for cancer detection through magnetic resonance imaging can be added also under this umbrella. Finally, we picturized a future in which ferrite-based nanomaterials will be synthesized with multifunctional and optimized pharmacodynamics and pharmacokinetics offering most intelligent and effective therapies. These combinations will provide attractive candidates for cancer diagnosis through appropriate imaging methods such as fluorescence imaging and MRI can create intelligent theranostic. In future, biomedical nanotechnology and cancer diagnosis through MRI based on ferrite-based nanomaterials will lead pharmaceutical industry from a model based on blockbuster drug to personalized medicine.

References

Adeela N et al (2018) Role of Ni concentration on structural and magnetic properties of inverse spinel Ferrite. Mater Res Bull 107:60–65

Ali Umar A, Oyama M (2005) Growth of high-density gold nanoparticles on an indium tin oxide surface prepared using a "touch" seed-mediated growth technique. Cryst Growth Des 5(2):599–607

Andersen HL et al (2018) Crystalline and magnetic structure–property relationship in spinel ferrite nanoparticles. Nanoscale 10(31):14902–14914

Anderson PW (1956) Ordering and antiferromagnetism in ferrites. Phys Rev 102(4):1008

Baig MM.et al. (2019) Optimization of different wet chemical routes and phase evolution studies of MnFe2O4 nanoparticles. Ceram Int

Bakhtiary Z et al. (2016) Targeted superparamagnetic iron oxide nanoparticles for early detection of cancer: Possibilities and challenges. Nanomedicine: Nanotechnol, Biol Med 12(2): 287–307

Balivada S et al (2010) A/C magnetic hyperthermia of melanoma mediated by iron (0)/iron oxide core/shell magnetic nanoparticles: a mouse study. BMC Cancer 10(1):119

Bean C, Livingston UD (1959) Superparamagnetism. J Appl Phys 30(4):S120–S129

Bhattacharyya S et al (2011) Inorganic nanoparticles in cancer therapy. Pharm Res 28(2):237–259

Brubaker C et al (2014) Using frankencerts for automated adversarial testing of certificate validation in SSL/TLS implementations. In: 2014 IEEE symposium on security and privacy, IEEE

Caltun O et al (2008) Substituted cobalt ferrites for sensors applications. J Magn Magn Mater 320(20):e869–e873

Chen D-H, He X-R (2001) Synthesis of nickel ferrite nanoparticles by sol-gel method. Mater Res Bull 36(7–8):1369–1377

da Silva F et al (2019) Structural and Magnetic Properties of Spinel Ferrite Nanoparticles. J Nanosci Nanotechnol 19(8):4888–4902

Dai L et al (2015) Metal-free catalysts for oxygen reduction reaction. Chem Rev 115(11):4823–4892

De-León-Prado LE et al (2017) Synthesis and characterization of nanosized $Mg_xMn_{1-x}Fe_2O_4$ ferrites by both sol-gel and thermal decomposition methods. J Magn Magn Mater 427:230–234

Elbeshir EIA (2018) Magnetic and thermal properties of CoFe2O4 nanoparticles for magnetic hyperthermia treatment. Int J Adv Appl Sci 5(8):34–36

Fariñas J et al (2018) Microwave-assisted solution synthesis, microwave sintering and magnetic properties of cobalt ferrite. J Eur Ceram Soc 38(5):2360–2368

Feldman D et al (2013) The 2013 international society for heart and lung transplantation guidelines for mechanical circulatory support: executive summary. J Hear Lung Transplant 32(2):157–187

Franco A Jr, e Silva F (2010) High temperature magnetic properties of cobalt ferrite nanoparticles. Appl Phys Lett 96(17):172505

George L et al (2017) Structural, dielectric, magnetic and optical properties of cerium substituted Ni-Zn mixed ferrite. Mater Sci Res India 14(2):133–139

Ghasemian Z, Shahbazi-Gahrouei D, Manouchehri S (2015) Cobalt zinc ferrite nanoparticles as a potential magnetic resonance imaging agent: an in vitro study. Avicenna J Med Biotechnol 7(2):64–68

Gjorup FH et al (2018) Coercivity enhancement of strontium hexaferrite nano-crystallites through morphology controlled annealing. Materialia 4:203–210

Govindan B et al (2017) Designed synthesis of nanostructured magnetic hydroxyapatite based drug nanocarrier for anti-cancer drug delivery toward the treatment of human epidermoid carcinoma. Nanomaterials 7(6):138

Grindi B et al (2018) Microwave-assisted synthesis and magnetic properties of M-SrFe12O19 nanoparticles. J Magn Magn Mater 449:119–126

Gubin SP (2009) Magnetic nanoparticles. Wiley

Gul I, Maqsood A (2008) Structural, magnetic and electrical properties of cobalt ferrites prepared by the sol–gel route. J Alloy Compd 465(1–2):227–231

Gupta AK, Curtis AS (2004) Surface modified superparamagnetic nanoparticles for drug delivery: interaction studies with human fibroblasts in culture. J Mater Sci Mater Med 15(4):493–496

Hankare P et al (2010) Effect of zinc substitution on structural and magnetic properties of copper ferrite. J Alloy Compd 501(1):37–41

Harris VG (2012) Modern microwave ferrites. IEEE Trans Magn 48(3):1075–1104

Hernández-Gómez P et al (2018) Synthesis, structural characterization and broadband ferromagnetic resonance in Li ferrite nanoparticles. J Alloy Compd 765:186–192

Ichiyanagi Y et al (2007) Magnetic properties of Mg-ferrite nanoparticles. J Magn Magn Mater 310(2):2378–2380

Ishaque M et al (2010) Structural, electrical and dielectric properties of yttrium substituted nickel ferrites. Physica B 405(6):1532–1540

Jain AK, Singla RK (2011) An overview of microwave assisted technique: green synthesis. Webmed Centra, pp 1–15

Jana NR, Gearheart L, Murphy CJ (2001) Wet chemical synthesis of high aspect ratio cylindrical gold nanorods. J Phys Chem B 105(19):4065–4067

Jordan TB, Seen AJ, Jacobsen GE (2006) Levoglucosan as an atmospheric tracer for woodsmoke. Atmos Environ 40(27):5316–5321

Joshi S et al (2016) Nickel substitution induced effects on gas sensing properties of cobalt ferrite nanoparticles. J Alloy Compd 654:460–466

Kanagesan S et al (2016) Evaluation of antioxidant and cytotoxicity activities of copper ferrite ($CuFe_2O_4$) and zinc ferrite ($ZnFe_2O_4$) nanoparticles synthesized by sol-gel self-combustion method. Appl Sci 6(9):184

Katafuchi R et al (1998) Glomerular score as a prognosticator in IgA nephropathy: its usefulness and limitation. Clin Nephrol 49(1):1–8

Kato H et al (2003) Lanthanoid endohedral metallofullerenols for MRI contrast agents. J Am Chem Soc 125(14):4391–4397

Kefeni KK, Msagati TA, Mamba BB (2017a) Ferrite nanoparticles: synthesis, characterisation and applications in electronic device. Mater Sci Eng B 215:37–55

Kefeni KK, Mamba BB, Msagati TA (2017b) Application of spinel ferrite nanoparticles in water and wastewater treatment: a review. Sep Purif Technol 188:399–422

Kim D et al (2011) Amphiphilic polymer-coated hybrid nanoparticles as CT/MRI dual contrast agents. Nanotechnology 22(15):155101

Kneller E, Luborsky F (1963) Particle size dependence of coercivity and remanence of single-domain particles. J Appl Phys 34(3):656–658

Konczykowski M et al (1992) Bean-livingston barriers a new source for magnetic irreversibility in $YBa_2Cu_3O_7$ crystals. Physica C 194(1–2):155–156

Köseoğlu Y et al (2012) Low temperature hydrothermal synthesis and characterization of Mn doped cobalt ferrite nanoparticles. Ceram Int 38(5):3625–3634

Kumar Y et al (2018) Efficient electrochemical detection of guanine, uric acid and their mixture by composite of nano-particles of lanthanides ortho-ferrite $XFeO_3$ (X = La, Gd, Pr, Dy, Sm, Ce and Tb). J Electroanal Chem 830:95–105

Kurian M, Nair DS (2016) Effect of preparation conditions on nickel zinc ferrite nanoparticles: a comparison between sol–gel auto combustion and co-precipitation methods. J Saudi Chem Soc 20:S517–S522

Lassoued A et al (2018) Synthesis, structural, morphological, optical and magnetic characterization of iron oxide (α-Fe_2O_3) nanoparticles by precipitation method: effect of varying the nature of precursor. Physica E 97:328–334

Latorre-Esteves M et al (2009) Synthesis and characterization of carboxymethyl dextran-coated Mn/Zn ferrite for biomedical applications. J Magn Magn Mater 321(19):3061–3066

Leclerc N, Meux E, Lecuire J-M (2003) Hydrometallurgical extraction of zinc from zinc ferrites. Hydrometallurgy 70(1–3):175–183

Li B-W et al (2006) Enhanced microwave absorption in nickel/hexagonal-ferrite/polymer composites. Appl Phys Lett 89(13):132504

Li Y-W et al (2015) Preparation of magnetic resonance probes using one-pot method for detection of hepatocellular carcinoma. World J Gastroenterol 21(14):4275–4283

Liang W et al (2015) Development and validation of a nomogram for predicting survival in patients with resected non–small-cell lung cancer. J Clin Oncol 33(8):861–869

Lin Q et al (2019) Structural and magnetic studies of Mg substituted cobalt composite oxide catalyst $Co_{1-x}Mg_xFe_2O_4$. J Magn Magn Mater 469:89–94

Liu C, Zhang ZJ (2001) Size-dependent superparamagnetic properties of Mn spinel ferrite nanoparticles synthesized from reverse micelles. Chem Mater 13(6):2092–2096

Liu C et al (2000) Chemical control of superparamagnetic properties of magnesium and cobalt spinel ferrite nanoparticles through atomic level magnetic couplings. J Am Chem Soc 122(26):6263–6267

Liu J et al (2001) Synthesis of nanosized nickel ferrites by shock waves and their magnetic properties. Mater Res Bull 36(13–14):2357–2363

Lu AH, Salabas EE, Schüth F (2007) Magnetic nanoparticles: synthesis, protection, functionalization, and application. Angew Chem Int Ed 46(8):1222–1244

Maaz K et al (2007) Synthesis and magnetic properties of cobalt ferrite (CoFe2O4) nanoparticles prepared by wet chemical route. J Magn Magn Mater 308(2):289–295

Maity JP et al (2009) Effects of gamma irradiation on long-storage seeds of Oryza sativa (cv. 2233) and their surface infecting fungal diversity. Radiat Phys Chem 78(11): 1006–1010

Maleki A, Hosseini N, Taherizadeh A (2018) Synthesis and characterization of cobalt ferrite nanoparticles prepared by the glycine-nitrate process. Ceram Int 44(7):8576–8581

Mathew DS, Juang R-S (2007) An overview of the structure and magnetism of spinel ferrite nanoparticles and their synthesis in microemulsions. Chem Eng J 129(1–3):51–65

Mefford OT, Rinaldi C, Andrew JS (2018) Synthesis and surface functionalization of ferrite nanoparticles, in nanomagnetic actuation in biomedicine. CRC Press, pp 9–40

Meng Y et al (2014) Synthesis of barium ferrite ultrafine powders by a sol–gel combustion method using glycine gels. J Alloy Compd 583:220–225

Meshram M et al (2004) Characterization of M-type barium hexagonal ferrite-based wide band microwave absorber. J Magn Magn Mater 271(2–3):207–214

Mohan GR et al (1999) Dielectric properties of polycrystalline mixed nickel–zinc ferrites. Mater Lett 40(1):39–45

Nasrin S et al (2018) Effect of zinc substitution on structural, morphological and magnetic properties of cobalt nanocrystalline ferrites prepared by co-precipitation method. J Mater Sci Mater Electron 29(21):18878–18889

Ng SE (2018) Sol-gel synthesis and characterization of spinel ferrite nanoparticles. Tunku Abdul Rahman University College

Nitin N et al (2004) Functionalization and peptide-based delivery of magnetic nanoparticles as an intracellular MRI contrast agent. J Biol Inorg Chem 9(6):706–712

Nosrati H et al (2018) Preparation of magnetic albumin nanoparticles via a simple and one-pot desolvation and co-precipitation method for medical and pharmaceutical applications. Int J Biol Macromol 108:909–915

Pardavi-Horvath M (2000) Microwave applications of soft ferrites. J Magn Magn Mater 215:171–183

Park D-H et al (2013) Polymer–inorganic supramolecular nanohybrids for red, white, green, and blue applications. Prog Polym Sci 38(10–11):1442–1486

Perdomo CPF, Kiminami RHA, Garcia D (2019) Microwave assisted sintering of nanocristalline PMN-PT/CoFe2O4 prepared by rapid one pot pechini synthesis: Dielectric and magnetoelectric characteristics. Ceram Int 45(6):7906–7915

Petitt G, Forester D (1971) Mössbauer study of cobalt-zinc ferrites. Phys Rev B 4(11):3912

Pinho SL et al (2018) Synthesis and characterization of rare-earth orthoferrite LnFeO3 nanoparticles for bioimaging. Eur J Inorg Chem 2018(31):3570–3578

Pullar RC (2012) Hexagonal ferrites: a review of the synthesis, properties and applications of hexaferrite ceramics. Prog Mater Sci 57(7):1191–1334

Qin J et al (2007) A high-performance magnetic resonance imaging T2 contrast agent. Adv Mater 19(14):1874–1878

Rana S et al (2007) On the suitability of nanocrystalline ferrites as a magnetic carrier for drug delivery: functionalization, conjugation and drug release kinetics. Acta Biomater 3(2):233–242

Rao BP et al (2006) Synthesis and magnetic studies of Ni-Zn ferrite nanoparticles. J Optoelectron Adv Mater 8(5):1703–1705

Ravichandran M et al (2018) Biofunctionalized MnFe2O4@Au core–shell nanoparticles for pH-responsive drug delivery and hyperthermal agent for cancer therapy. Artif Cells Nanomedicine Biotechnol 46(sup3):S993–S1003

Respaud M et al (1998) Surface effects on the magnetic properties of ultrafine cobalt particles. Phys Rev B 57(5):2925

Ritchie ME et al (2015) limma powers differential expression analyses for RNA-sequencing and microarray studies. Nucleic Acids Res 43(7):e47–e47

Sagadevan S, Chowdhury ZZ, Rafique RF (2018) Preparation and characterization of nickel ferrite nanoparticles via co-precipitation method. Mater Res 21(2)

Samavati A et al (2016) Copper-substituted cobalt ferrite nanoparticles: structural, optical and antibacterial properties. Mater Express 6(6):473–482

Samoila P et al (2017) Remarkable catalytic properties of rare-earth doped nickel ferrites synthesized by sol-gel auto-combustion with maleic acid as fuel for CWPO of dyes. Appl Catal B 202:21–32

Sanpo N et al (2013a) Transition metal-substituted cobalt ferrite nanoparticles for biomedical applications. Acta Biomater 9(3):5830–5837

Sanpo N, Wang J, Berndt CC (2013) Sol-gel synthesized copper-substituted cobalt ferrite nanoparticles for biomedical applications. In Journal of nano research. Trans Tech Publication

Sapet C et al (2012) Magnetic nanoparticles enhance adenovirus transduction in vitro and in vivo. Pharm Res 29(5):1203–1218

Schick F et al (1997) Highly selective water and fat imaging applying multislice sequences without sensitivity to B1 field inhomogeneities. Magn Reson Med 38(2):269–274

Schoots IG et al (2015) Magnetic resonance imaging–targeted biopsy may enhance the diagnostic accuracy of significant prostate cancer detection compared to standard transrectal ultrasound-guided biopsy: a systematic review and meta-analysis. Eur Urol 68(3):438–450

Sertkol M et al (2009) Microwave synthesis and characterization of Zn-doped nickel ferrite nanoparticles. J Alloy Compd 486(1–2):325–329

Sharifi I, Shokrollahi H, Amiri S (2012) Ferrite-based magnetic nanofluids used in hyperthermia applications. J Magn Magn Mater 324(6):903–915

Shete P et al (2014) Magnetic chitosan nanocomposite for hyperthermia therapy application: preparation, characterization and in vitro experiments. Appl Surf Sci 288:149–157

Shukla A et al (2018) Microwave assisted scalable synthesis of titanium ferrite nanomaterials. J Appl Phys 123(16):161411

Singhal S, Chandra K (2007) Cation distribution and magnetic properties in chromium-substituted nickel ferrites prepared using aerosol route. J Solid State Chem 180(1):296–300

Song H-W et al (2017) Shape-controlled syntheses of metal oxide nanoparticles by the introduction of rare-earth metals. Nanoscale 9(8):2732–2738

Srinivasan SY et al (2018) Applications of cobalt ferrite nanoparticles in biomedical nanotechnology. Nanomedicine 13(10):1221–1238

Srivastava R, Yadav B (2012) Ferrite materials: introduction, synthesis techniques, and applications as sensors. Int J Green Nanotechnol 4(2):141–154

Srivastava M, Chaubey S, Ojha AK (2009) Investigation on size dependent structural and magnetic behavior of nickel ferrite nanoparticles prepared by sol–gel and hydrothermal methods. Mater Chem Phys 118(1):174–180

Stamps J (2001) 16. Habitat selection by dispersers: integrating proximate and ultimate approaches

Sugimoto M (1999) The past, present, and future of ferrites. J Am Ceram Soc 82(2):269–280

Tamura H, Matijevic E (1982) Precipitation of cobalt ferrites. J Colloid Interface Sci 90(1):100–109

Tan BK, Adya R, Randeva HS (2010) Omentin: a novel link between inflammation, diabesity, and cardiovascular disease. Trends Cardiovasc Med 20(5):143–148

Tourinho FA, Franck R, Massart R (1990) Aqueous ferrofluids based on manganese and cobalt ferrites. J Mater Sci 25(7):3249–3254

Uchida K et al (2013) Longitudinal spin Seebeck effect in various garnet ferrites. Phys Rev B 87(10):104412

Vaidyanathan G, Sendhilnathan S, Arulmurugan R (2007) Structural and magnetic properties of $Co_{1-x}Zn_xFe_2O_4$ nanoparticles by co-precipitation method. J Magn Magn Mater 313(2):293–299

Valenzuela R (2012) Novel applications of ferrites. Phys Res Int

Verma A et al (2000) Magnetic properties of nickel–zinc ferrites prepared by the citrate precursor method. J Magn Magn Mater 208(1–2):13–19

Verma A et al (2005) *Temperature dependence of electrical properties of nickel–zinc ferrites processed by the citrate precursor technique*. Mater Sci Eng, B 116(1):1–6

Wang Y-XJ (2011) Superparamagnetic iron oxide based MRI contrast agents: current status of clinical application. Quant Imaging Med Surg 1(1):35

Wang Z et al (2004) Image quality assessment: from error visibility to structural similarity. IEEE Trans Image Process 13(4):600–612

Wang L et al (2006) A biocompatible method of decorporation: bisphosphonate-modified magnetite nanoparticles to remove uranyl ions from blood. J Am Chem Soc 128(41):13358–13359

Wang L et al (2010) Controlled synthesis of magnetic spinel-type nickel ferrite nanoparticles by the interface reaction and hydrothermal crystallization. J Alloy Compd 490(1–2):656–660

Xing G et al (2008) The Strong MRI Relaxivity of Paramagnetic Nanoparticles. J Phys Chem B 112(20):6288–6291

Yadavalli T et al (2016) Magnetic hyperthermia heating of cobalt ferrite nanoparticles prepared by low temperature ferrous sulfate based method. AIP Adv 6(5):055904

Yanase M et al (1998a) Antitumor immunity induction by intracellular hyperthermia using magnetite cationic liposomes. Jpn J Cancer Res 89(7):775–782

Yanase M et al (1998b) Intracellular hyperthermia for cancer using magnetite cationic liposomes: an in vivo study. Jpn J Cancer Res 89(4):463–470

Yang H et al (2010) Water-soluble superparamagnetic manganese ferrite nanoparticles for magnetic resonance imaging. Biomaterials 31(13):3667–3673

Yue Z et al (2004) Synthesis of nanocrystilline ferrites by sol–gel combustion process: the influence of pH value of solution. J Magn Magn Mater 270(1–2):216–223

Zeng N et al (2005) Impact of 1998–2002 midlatitude drought and warming on terrestrial ecosystem and the global carbon cycle. Geophys Res Lett 32(22)

Zeng J et al (2010) Gold-based hybrid nanocrystals through heterogeneous nucleation and growth. Adv Mater 22(17):1936–1940

Zi Z et al (2009) Synthesis and magnetic properties of CoFe2O4 ferrite nanoparticles. J Magn Magn Mater 321(9):1251–1255

Chapter 8
Target Delivery of Iron Oxide Magnetic Nanoparticles for Imaging and Treatment

Hamed Nosrati, Marziyeh Salehiabar, Naser Sefidi, Siamak Javani, Soodabeh Davaran and Hossein Danafar

Abstract At this time, passive targeting with the aid of enhanced permeability and retention (EPR effect), active targeting with the aid of molecular or other targeting agents, and employing external magnetic field are used to successfully deliver IONPs to aim tumor site. Latest progresses in treatment of disease are toward targeted delivery. With fast progresses in this field, researchers employed the IONPs as a hopeful theranostic vehicle. In this chapter, we focused on passive and active target delivery of IONPs for diagnosis, imaging, and therapy purpose.

Keywords Iron oxide · Magnetic nanoparticle · Magnetic targeting · Target delivery · Theranostic

Introduction

The ability to target specific cell types and achieve the ideal of treatment and imaging in the patient's tissues, while limiting the untargeted side effects, has long been the target of the research teams. Passive or active targeting prolonged drug nanoparticle and/or theranostic tools circulation time, enhanced solubility of drugs, protected payload therapeutic agents from inactivation or biodegradation, and reduced systemic toxicity of highly potent but toxic drugs (Huang et al. 2016). Multifunctional and

H. Nosrati · N. Sefidi · H. Danafar (✉)
Department of Pharmaceutical Biomaterials, School of Pharmacy, Zanjan University of Medical Sciences, Zanjan, Iran
e-mail: danafar@zums.ac.ir

M. Salehiabar · S. Davaran
Drug Applied Research Center, Tabriz University of Medical Sciences, P.O. Box: 51656-65811, Tabriz, Iran

S. Javani
Medical Cellular and Molecular Research Center, Golestan University of Medical Sciences, Gorgan, Iran

H. Danafar
Zanjan Pharmaceutical Nanotechnology Research Center, Zanjan University of Medical Sciences, Zanjan, Iran

multimodal treatments and imaging through simultaneous delivery are some unique advantages of nanomedicine. Nanodrug delivery systems may provide a more proficient, less harmful solution to overcome common treatment problems (Huang et al. 2016). Latest progresses in nanomedicine have shown a talent for targeted delivery. Theranostic target delivery systems enhanced the efficacy of therapeutic compound by direction to aim site and reducing the side effect of toxic drugs (Manish and Vimukta 2011).

Among the nanoscale systems, iron oxide nanoparticles (IONPs) have attracted considerable attention, in catalytic systems (Shojaei et al. 2017), biological (Sakulkhu et al. 2015; Wang et al. 2013) treatment, and imaging in medicine (Hu et al. 2015; Manjili et al. 2016) fields. With fast progresses in nanomedicine, IONPs have developed as a hopeful theranostic tool in biomedical and pharmaceutical applications, including diagnostic imaging, drug delivery, and innovative novel therapeutics. IONPs have been widely investigated as magnetic resonance imaging (Lee et al. 2015) (MRI), hyperthermia (Guardia et al. 2012), and targeted drug delivery in tumor therapy (Li et al. 2015; Garanger et al. 2007). The IONP theranostic systems should have imaging capability, and at the same time should be able to load drugs, protect the biological activity of drugs, and enhance biocompatibility to reach the targeted sites for achieving effective treatment and treatment (Huang et al. 2016).

Surface properties and size of IONPs affect the stability and fate of these particles in vivo.

Since spleen phagocytic cells and blood macrophages rapidly eliminated the large IONPs (>200 nm), the best size range to achieve suitable blood circulation in vivo is 10–100 nm (Lu and Low 2012). In addition, the IONPs with the size of less than 10 nm are rapidly eliminated by the renal clearance process (Choi et al. 2007). Also, many reports show that the overall size and size of coating ligands play an important role in long circulation and effective purpose (Xie et al. 2007; Liu et al. 2011; Lamanna et al. 2011). Protein adsorption can affect the colloidal stability of IONPs in vitro and in vivo. Proteins with isoelectric points higher than 5.5 can be adsorbed and bonded with negatively charged IONPs. Also, proteins with isoelectric points less than 5.5 can be adsorbed and bonded with positively charged IONPs (Aggarwal et al. 2009).

Many different types of materials are used to cover IONP surface for different applications, which effectively tailor the surface of IONPs. Surface coating of IONPs can prevent IONPs from aggregation and caused colloidal stability of IONPs, make IONPs biocompatible and low or non-toxic, and provide functional groups to linkage biologically active substances for nano-bioapplications and non-immunogenicity, non-antigenicity, and protection from opsonization by plasma proteins (McCarthy and Weissleder 2008; Bohara et al. 2016). Modification or covering IONPs with specific proteins can inhibit protein adsorption in physiologic solutions and can further be used to propose applications. Apolipoprotein modified nanoparticles can be passed biological barriers, e.g., the blood–brain barrier (Göppert and Müller 2005). Vinca alkaloids, metal-based drugs, taxanes, anthracyclines, antimetabolites, and so on are some examples of chemotherapeutic drugs that loaded on targeted IONPs for effective cancer therapy. For effective treatment, IONPs are usually conjugated with aptamers (Kim et al. 2010), peptides, antibodies (Gao et al. 2004), proteins, peptides

(Von Maltzahn et al. 2011), and small molecules (Low et al. 2007). These targeted IONPs can direct nanoparticles for multimodal imaging and therapy with target specificity. Also, these targeted IONPs can be used for delivery of photodynamic, radiosensitizer, photothermal, and sonodynamic agents to form combinatorial hybrid nanomaterials for effective cancer therapy (Kandasamy and Maity 2015). In this chapter, we focused on the target drug delivery of IONPs for imaging and treatment.

Passive Targeting (EPR Effect)

First driven force that delivers the IONPs to the diseased tissues is enhanced permeability and retention (EPR) effect. The EPR effect, first reported by Maeda and his colleagues in 1986 (Maeda et al. 2013; Matsumura and Maeda 1986), describes the enhanced permeability of the tumor vasculature that allows macromolecules, lipids, and nanoparticles circulating in the blood to extravasate through the leaky tumor blood vessel, then enter the tumor interstitial space (Iyer et al. 2006; Fang et al. 2011). Gaps and fenestrations between the endothelial cells of the tumor vasculature walls have a size range of 200–2000 nm, allowing IONPs to cross through the leaky vessel walls (Hashizume et al. 2000; Hobbs et al. 1998). Once extravasated, the penetration of the IONPs into the tumor tissues is a diffusion-mediated process, which is oppositely correlated with the particle size.

In that case, only nanoparticles smaller than 50 nm can pierce into these poorly permeable tumors. The results of Perrault et al. studies show that particle accumulation (40–100 nm) depends only on the blood residence half-life and is independent of nanoparticle size; in contrast, for smaller particles (around 20 nm), the accumulation depends on both blood residence half-life and nanoparticle size (Peer et al. 2007). While, small nanoparticles arrive rapidly at the tumor site, but also have a short residence time, whereas larger nanoparticles (>40 nm) take longer to arrive the tumor sites, but reside for longer in the blood.

In the meantime, by inhibiting the return of nanoparticles to the circulation due to loss of lymphatic drainage in the tumor, IONPs maintain within the tumor (Konno et al. 1984). Compared to the tissues and organs, most solid tumors have a rapid tumor vasculature with free tight junction of endothelial cells and abnormal basement membrane of blood vessels, which increases the permeability of the tumor vessels (Maeda et al. 2013; Hashizume et al. 2000; Folkman 1971). IONP is suitable for EPR drugs at 10–500 nm in size for tumor accumulation (Peer et al. 2007). Since the luminal surface of the vascular endothelial layer is negative, cationic charge nanoparticles can quickly join with endothelial cells. It causes a non-specific connection that reduces the half-life of the plasma and then reduces the effect of EPR (Gusev et al. 1988; Campbell et al. 2002). For the accumulation in tumor tissue with the aid of EPR effect, nanoparticles should have a long circulating time. Furthermore, IONPs hydrophilicity/hydrophobicity, biocompatibility, and also surface charge are

a number of IONPs properties that affect EPR effect (Maeda 2010). Low vascularization, reducing vascular permeability, and dense fibrosis are some properties of stubborn tumors (Cabral et al. 2011).

Also, to abnormal vascular structures, altered metabolic profile of tumor tissue can be used to target tumors (Lee et al. 2015). Rapidly developing tumor cells generally increase glucose uptake and show very high glycolytic rates compared to normal tissues (Cairns et al. 2011). Basu and co-authors were applied for the uptake of 2-18F-deoxyglucose in positron emission tomography, PET, and imaging (Basu and Alavi 2009).

Recently, scientists used different approaches such as magnetic resonance spectroscopy and paramagnetic chemical exchange saturation transfer to diagnosis the tumors by measuring the low PH level (Wu et al. 2010). The passive targeting process for drug delivery systems based on IONPs is outlined in Fig. 8.1. Clauson and co-workers synthesized IONPs coated with lipid-like molecules. This structure increased loading capacity tenfold and 200-fold higher than common IONPs. Since in vivo, these IONPs keep their size less than 100 nm, their target lymph node 9–40-folds higher than common systems.

Figure 8.2 shows gradient echo (GE), MRI images, and IVIS fluorescence images before and 1 h after the administration of theranostic nanoplatforms. In this work, the control of size in vivo was used as a targeting factor to lymph node (Clauson et al. 2018).
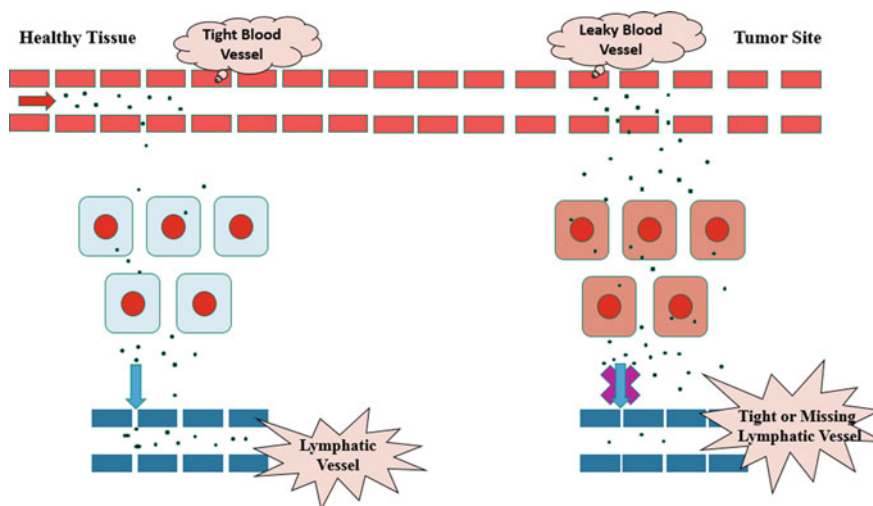
Fig. 8.1 Schematic illustration of accumulation of nanoparticles in solid tumors with EPR effect
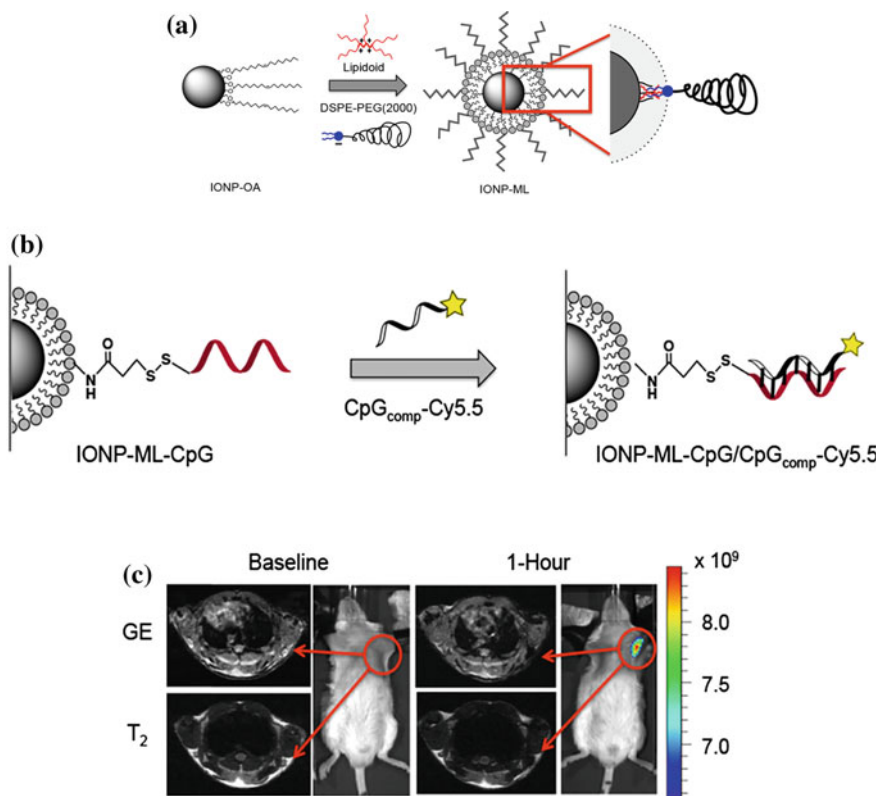
Fig. 8.2 **a** Schematic illustration of multilipid coated IONPs (IONP-ML), **b** labeling of IONP-ML CpG oligonucleotides and also with a fluorescently tagged CpGcomp-Cy5.5 (IONP-ML-CpG/CpGcomp-Cy5.5), **c** gradient echo (GE), MRI images, and IVIS fluorescence images before and 1 h after the administration of theranostic nanoplatforms. The arrows identify brachial lymph node on GE and MRI images. Reproduced with permission from Clauson et al. (2018). Copyright 2018, with permission from American Chemical Society

Active Targeting

Ligand Facilitated Active Targeting

However, passive targeting through the EPR effect provides the public mechanism for sending carriers, and targeting ligand aided active targeting of molecular or cellular biomarkers further enhances the targeted delivery of the therapeutic agents (Huang et al. 2016). A wide variety of ligands can be used to bind with cell membrane receptors and increase the internalization of the carriers into the cell. In this case to increase the efficiency of active targeting, the choice of appropriate ligands and biomarkers is crucial. For example, galactose, fucose and mannose, and folic acid

Table 8.1 Some demonstrative receptors and the corresponding ligands

Cell membrane receptor	Cell or receptor-specific ligand	References
Asialoglycoprotein receptor	Glucose	D'souza and Devarajan (2015)
Kupfer cells	Mannose, Fucose	Dahms et al. (1989)
Biotin receptor (MCF7 cells)	Biotin (Vitamin B7)	Le Droumaguet et al. (2012), YoungáKim and SeungáKim (2015)
Folate receptor	Folic acid (Vitamin B9)	Assaraf et al. (2014)
Integrins (αvβ5, αvβ3)	RGD, c(RGDfK)	Garanger et al. (2007)
EGF-R	EGF, Erbitux, GE11 peptide	Mendelsohn and Baselga (2000)
CD20 (B cells)	Rituximab	Suresh et al. (2014)
CD52 (lymphocytes)	Alemtuzumab	Lundin et al. (2002)
VEGF-A	Bevacizumab	Jain et al. (2006)
CD30	Brentuximab	Subbiah et al. (2014)
HER2/Neu	Trastuzumab	Tai et al. (2010)
Transferrin receptor	Transferrin	Daniels et al. (2006)

have been used to encourage the binding to parenchymal liver cells, Kupfer cells, and folate receptors expressing cancer cells, respectively (Seymour et al. 1991; Seymour et al. 2002; Hillery et al. 2002; Assaraf et al. 2014; Lu and Low 2012). In addition, antibodies are one of the specific ligands because of their high specificity and wide availability. In Table 8.1, some demonstrative tumor cell membrane receptors and their corresponding ligands are listed.

Functionalization of IONPs with the specific active targeting ligand promotes binding with surface receptors of cells and as a result can increase intracellular transport via receptor-mediated endocytosis (Fig. 8.3).

In other example, since IONPs have MRI contrast effect, conjugation with epidermal growth factor is applied to MR imaging of glioblastoma and delivery of doxorubicin (Hadjipanayis et al. 2010; Liao et al. 2011). Transferrin (Tf, 80 kDa), an iron-chelating protein, targets a transmembrane glycoprotein receptor, transferrin receptor (TfR, 180 kDa, also known as CD71) (Daniels et al. 2006; Islam and Josephson 2009). Since proliferating cancer cells need high amount of iron, the TfR overexpressed in its surface. Typically targeting ligands can be classified into proteins, peptides, aptamers, and small molecules. Furthermore, Herceptin, a monoclonal antibody (commercially marketed as Trastuzumab) targets HER2/neu receptor. HER2/neu is a human epidermal growth factor receptor and is critical for cell proliferation that overexpressed in some breast cancer cells. Now, Herceptin used to cure early stage breast cancer. The studies confirm that Trastuzumab usage can increase survival time of HER2-positive breast cancer patients (Ross et al. 2004).

Conjugation of Herceptin to IONPs was achieved by theranostic system that used for cancer therapy and imaging (Ross et al. 2004; Chen et al. 2013). These types of
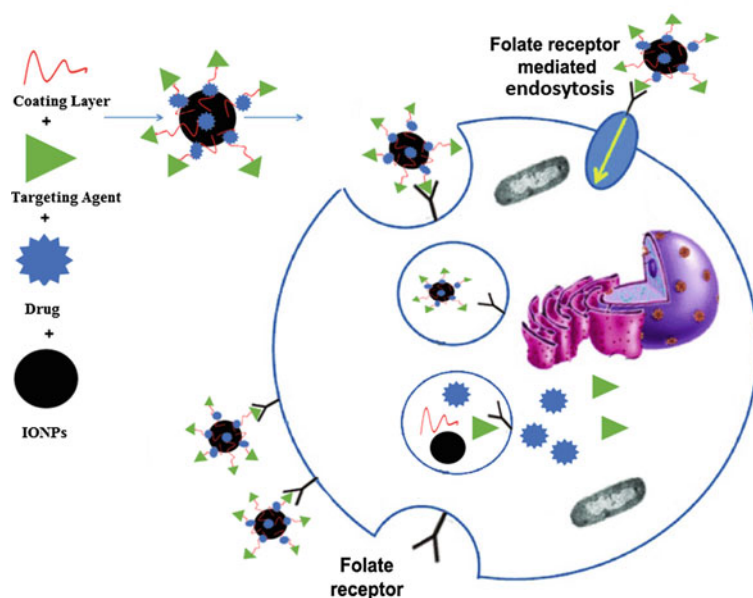
Fig. 8.3 Presentation of the mechanism of active targeting to tumor cells

theranostic systems can be used for MRI detection of tumors at the dose of less than 50 mg (Jae-Hyun et al. 2007). Monoclonal antibodies have some disadvantage such as immunogenic side effect, low stability, and the high cost for clinical claims. Recently, antibody fragment can be formed and used as targeting ligands with preserved binding domain to the target. For example, single-chain anti-EGFR antibody, ScFvEGFR, has size ranging from 25 to 28 kDa, less than 20% of the whole antibody, can be targets EGFR, specificity (Huang et al. 2016). IONPs conjugated with ScFvEGFR is a theranostic system that used for targeted cancer therapy and imaging at the same time (Yang et al. 2009, Liang et al. 2015).

Urokinase-type plasminogen activator (uPA) receptor is one of the multidomain glycoproteins that elevated expression level in many human cancers (Smith and Marshall 2010). uPA receptor becomes an attractive biomarker in cancer due to its essential roles in cell migration, proliferation, and survival by coordinating extracellular matrix proteolysis and cell signaling (Smith and Marshall 2010). Urokinase plasminogen activator (uPA), the natural ligand has a high affinity for uPA receptor. The amino-terminal fragment of uPA has been effectively applied to conjugate IONPs for uPA receptor targeting in breast cancer (Yang et al. 2008, 2009), pancreatic cancer (Yang et al. 2009; Lee et al. 2013), and prostate cancer (Abdalla et al. 2011).

Moreover, Lee et al. prepared IONPs-based theranostic nanoparticles for target delivery of gemcitabine (Gem) (Lee et al. 2013). To achieve more therapeutic efficacy, Lee's research group prepared uPA receptor targeted IONPs and evaluated
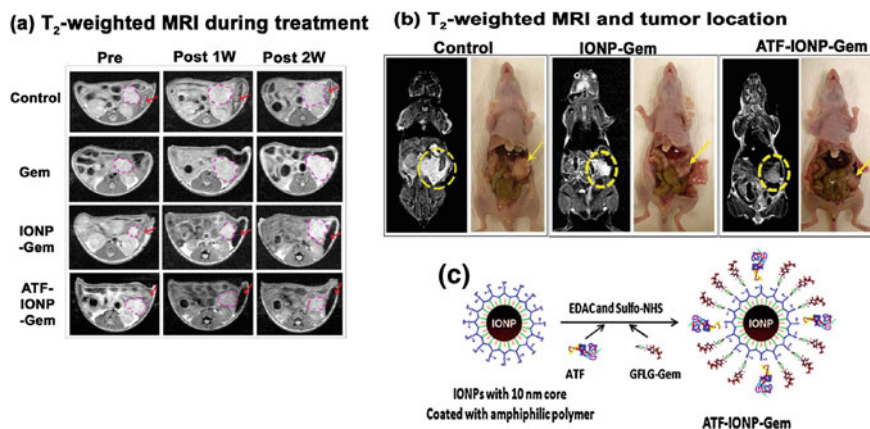
Fig. 8.4 **a** MRI of targeted ATF-IONP-Gem; Axial T_2-weighted MR images before, one and two weeks after administrating nanoparticles. Post-treatment images were obtained 48 h following the second (1 week) and fourth (2 weeks) injection, **b** coronal T_2-weighted MR images and corresponding bright field images after systemic delivery of nanoparticles, **c** synthetic scheme of GFLG-Gem conjugates, **d** schematic illustration of the conjugation of ATF peptides and GFLG-Gem to IONPs. Reproduced with permission from Lee et al. (2013). Copyright 2013, with permission from American Chemical Society

targeted delivery efficacy into uPA receptor expressing tumor and stromal cells. For this aim, amino-terminal fragment (ATF) peptide of the receptor-binding domain of uPA, a natural ligand of uPA receptor, was conjugated on the surface of IONPs (Fig. 8.4c). These nanoparticles not only enable the release of Gem within cell following receptor-mediated endocytosis of ATF-IONP-Gem into tumor cells but also can create contrast enhancement in MRI of tumors (Fig. 8.4a, b).

As mentioned, small molecules and/or synthetic peptides that show appropriate affinity to specific site or receptor also can be used as targeting ligands. Small targeting agents compared with antibodies have some advantages, including non-immunogenicity, low cost, high stability, and convenience of use (Zhang et al. 2012; Jalalian et al. 2013). Folic acid has been used for target drug delivery and tumor imaging because of extra affinity to folate receptor. The folate receptor is a glycosyl-phosphatidylinositol-linked membrane protein (Islam and Josephson 2009; Zhao et al. 2008). Since folate receptors overexpressed in a wide series of cancer cells of various origins such as HeLa cells (a human cervical carcinoma), B16F0 cells (mouse melanoma), and KB cells (human epidermoid carcinoma), it can be useful target for cancer imaging and therapy. Targeting power of folic acid-conjugated IONPs has been established with above-mentioned various cell lines (Bhattacharya et al. 2011; Fan et al. 2011). Uptake of folic acid-conjugated IONPs are 12-fold more than non-targeted IONPs in HeLa cells (Sun et al. 2006). Another in vitro and in vivo MRI study specified folic acid-conjugated IONPs can target KB cells (Chen et al. 2007). In other study, it has been informed that FA-conjugated IONPs compared to non-conjugated IONPs demonstrated three to 16-fold higher uptake in FR expressing

cancer cells (Sonvico et al. 2005). FA has some advantage, for instance, relatively higher binding affinity for its receptor ($\kappa d = 10$–10 M), low cost, easy conjugation with both therapeutic and imaging agents, compatibility in both organic and aqueous solvents, and lack of immunogenicity used as a targeting ligand for tumor imaging and therapy (Low et al. 2007).

Recently, a research group from Nagoya University combined diagnosis and treatment in one theranostic system. This group applied heat generation and MRI contrast power of IONPs for MRI-monitored thermo-chemotherapy. Also, folic acid was conjugated to the designed multifunctional IONPs as a targeting agent (Hayashi et al. 2016).

Methotrexate (MTX), a small molecule analog of FA which can exhibit both a targeting role and a therapeutic effect on the cancer cells overexpresses folate receptor on their surface (Peng et al. 2008). MTX-conjugated IONPs have been investigated for targeted MR imaging and drug delivery of glioma (Kohler et al. 2006). Because of that MTX is also a therapeutic agent, the MTX functions not only as a ligand for tumor targeting, but also as a drug when released after breaking the MTX-IONPs linkage under lysosomal conditions. Results of MTX-conjugated IONPs showed that cells expressing the human folate receptor internalized a higher level of MTX-conjugated IONPs than negative control cells (Kohler et al. 2005). Also, their results of MTX-conjugated IONPs showed that MTX released only from the IONPs within lysosomes inside the targeted cells at low pH by cleavage of the amide, furthermore drug delivery to the tumor sites may be monitored in vivo by MRI in real time (Kohler et al. 2005).

MTX can be easily conjugated to the IONPs surface by covalent bonding which is usually favored. Covalent bonding makes the highly stable nanoparticle in the bond strength so to be disrupted only under harsh environments inside lysosomes. Danafar et al. synthesized glycine-coated IONPs (F-Gly NPs) and conjugated with methotrexate (MTX) (F-Gly-MTX NPs). The synthesized process is simple and green. In detail, the F-Gly NPs synthesized through a coprecipitation method which followed by amidation reaction between the carboxylic acid end groups on MTX and the amine groups on the F-Gly NPs surface (Nosrati et al. 2018). The synthesis process and amidation reaction were shown in Fig. 8.5a. MTX release on this conjugated
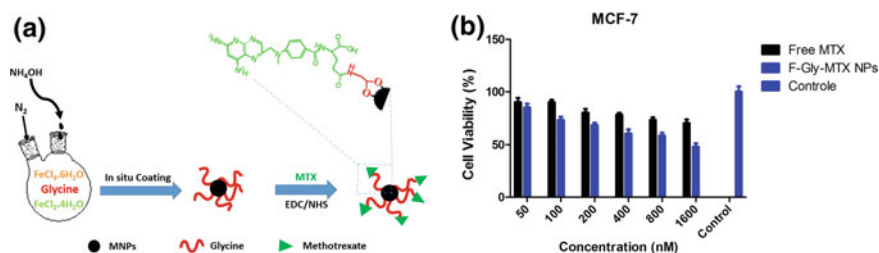
Fig. 8.5 **a** Schematic illustration synthesis process of MTX-conjugated IONPs, **b** cytotoxicity analysis against MCF7 cell line. Reproduced with permission from Nosrati et al. (2018). Copyright 2018, with permission from Wiley

target drug delivery system showed enzymatic stimuli-responsive trait. Following the uptake of MTX-conjugated IONPs via receptor-mediated endocytosis, lysosome proteases can be cleaving the covalent peptide bond and the release of MTX within the target cell (Kohler et al. 2005; Nosrati et al. 2018). For this reason, the release of the MTX is higher in the presence of proteinase K enzyme compared to the absence of enzyme in release medium. This feature causes higher toxicity of MTX-conjugated IONPs on MCF-7 cells (Fig. 8.5b).

Among the 24 known integrins, since αvβ3 has crucial role in tumor angiogenesis has received significant attention as cancer biomarker and target. αvβ3 overexpressed in a wide series of cancer cells (Schottelius et al. 2009). One of the targeting ligands that have high affinity to integrin αvβ3 is RGD peptide. RGD peptide is a tripeptide composed of L-arginine, glycine, and L-aspartic acid. RGD peptide has received wide attention as nanoparticle director and targeting agent to tumor site for facilitating treatment and imaging (Luo et al. 2015; Yang et al. 2011).

Glutathione (GSH) is one of the other types of small targeting agents that have gotten the most progressive steps in clinical claim as blood–brain barrier shuttle peptides. Nosrati et al. (2019) reported the possibility of GSH-conjugated IONPs as theranostic novel system (Nosrati et al. 2019). This IONPs conjugated with GSH in detail is an MRI-monitored paclitaxel delivery vehicle across the blood–brain barrier. In this work, Nosrati et al. discovered one of the other ways to confirm the passing of IONPs from blood–brain barrier by MRI and as well as by naked eye observation. In naked eye observation brain delivery, the authors were used to high magnetic susceptibility of IONPs navigate (Nosrati et al. 2019). Figure 8.6 shows the passed IONPs through blood–brain barrier with the aid of GSH by eye naked observation experiment.

Aptamers are identified through the systemic evolution of ligands by an exponential enrichment (SELEX) process for target molecules. Aptamers have similar binding affinity in comparison with antibodies. The nanoparticles can be functionalized simply with aptamers because of their simple structure. IONPs conjugated with aptamers recently have been used to colon and prostate cancer therapy as well as for imaging of these organs (Jalalian et al. 2013; Wang et al. 2008; Gu et al. 2008).

Magnetic Targeting

External magnetic field can affect the properties of IONPs. Because of this, IONPs can be applied in local delivery of drugs and probe agents. Drug loaded IONPs due to magnetic navigate can be directed to target site by the magnetic force of external magnet or gradient magnetic field in aim site (Fig. 8.7).

In this item, nanoparticles with great magnetic properties have greater local delivery efficacy. Comparing this case with other targeting ligand mediated delivery shows that magnetic targeting is extremely operational in vitro (Huang et al. 2016; Wang et al. 2015; Li et al. 2014).
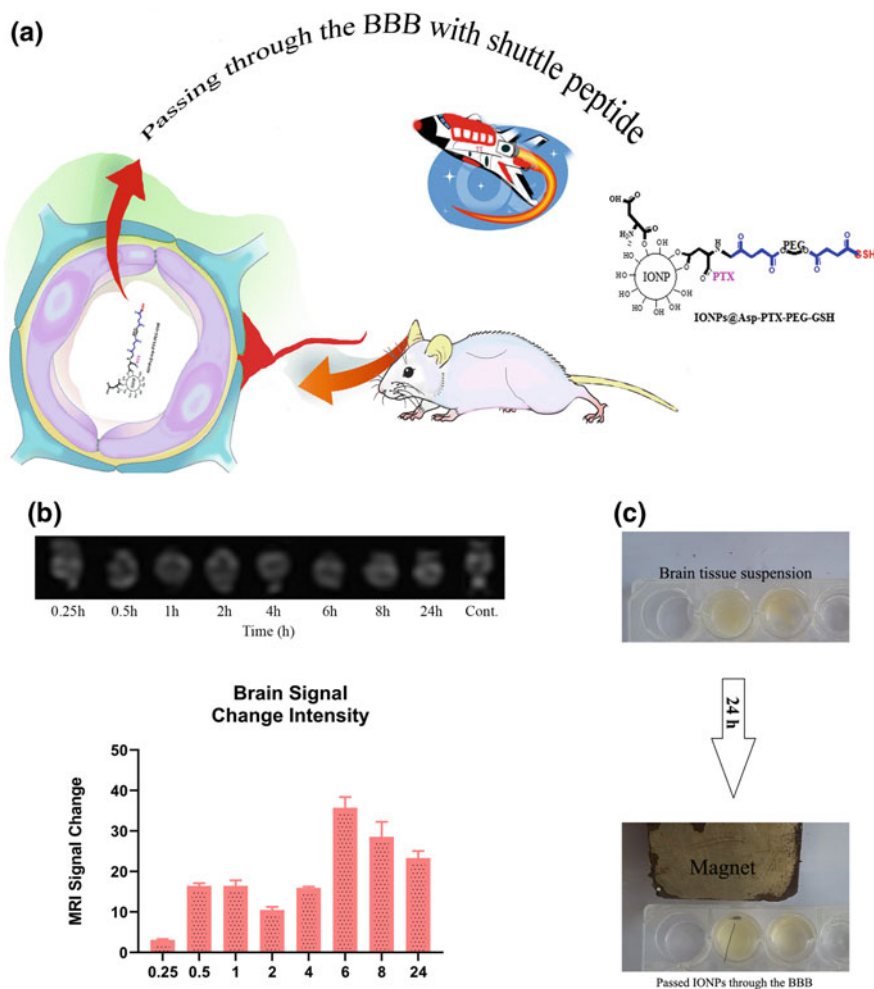
Fig. 8.6 a Enhanced brain delivery of IONPs with the aid of GSH shuttle peptide, **b** tracking brain delivery of GSH modified IONPs with MRI, **c** naked eye observation brain delivery of GSH modified IONPs. Reproduced with permission from Nosrati et al. (2019). Copyright 2019, with permission from American Chemical Society

The circulation time of IONPs is fundamental and important for effective magnetic targeting. Furthermore, to overcome the drag forces associated with blood flow, the external magnetic force must be strong (Cole et al. 2011). The external magnetic field targeted drug delivery using IONPs was initiated in the late 1970s for the transfer of drugs for cancer therapy (Widder et al. 1978, 1979). Next, it was used with chemodrugs, such as Adriamycin and dexamethasone 21-acetate continued for successful cancer treatments. Boncel et al. reported Fe-encapsulated multi-wall
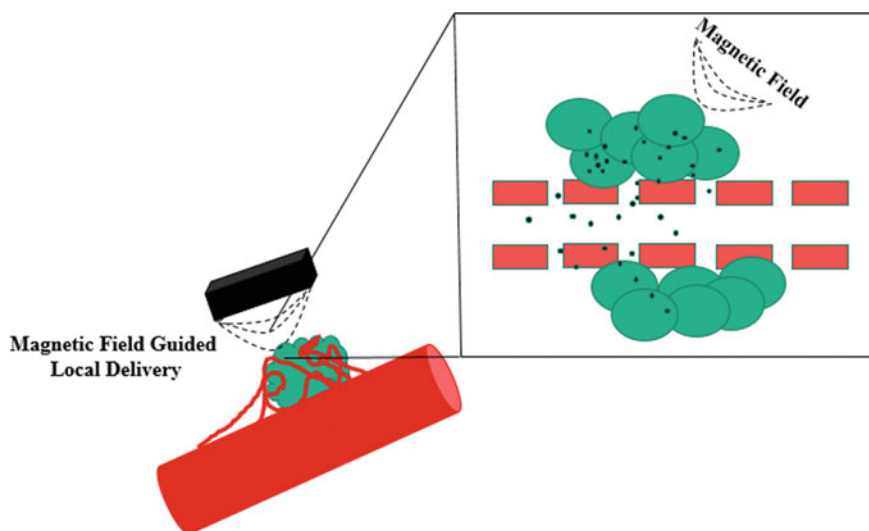
Fig. 8.7 Magnetic accumulated IONPs in tumors using external magnetic field

carbon nanotubes as magnetically directed 5-FU delivery vehicle. Use of a magnetic field enhanced uptake and toxicity in T47D cells (Boncel et al. 2016). Furthermore, the magnetic directing has been used to deliver drugs across blood–brain barrier to brain. One example for this case studied with Cole and colleagues showed that delivery of polyethylene glycol functionalized IONPs to brain can be increased with the aid of magnetic direction (Cole et al. 2011). As a result, brain delivery of PEG-IONPs was increased 15-fold in 9L-glioma tumor.

Also, delivery of the anticancer drug 4′-epidoxorubicin to advanced solid tumors that was conducted in 1996 is the first clinical trial of magnetically targeted nanoparticles (Lübbe et al. 1996). In case of cancer therapy, Bae et al. developed an effective heat nanomediator based on chitosan oligosaccharide-stabilized ferrimagnetic iron oxide nanocubes (Chito-FIONs) as for cancer hyperthermia by magnetic targeting method (Fig. 8.8) (Bae et al. 2012). The synthesized Chito-FIONs displayed higher saturation magnetization. This property responds rapidly to magnetic field which is suitable for magnetic guiding applications. The improved saturation magnetization and heat generation ability were related to the magnetic dipolar coupling. Because of almost four FIONs, particles encapsulated with chitosan oligosaccharide and formed one Chito-FION particle. Applying magnetic field gradients in the tumor site enabled this group to attract Chito-FIONs only in the tumor area. They destroyed the tumors selectively without any damage to healthy tissues by restriction of thermal energy only in the tumor area. Positive charge of chitosan oligosaccharides under acidic tumor microenvironments caused that a large amount of Chito-FIONs remained within the tumor tissue. This high tumor affinity of Chito-FIONs is valuable for cancer therapy.
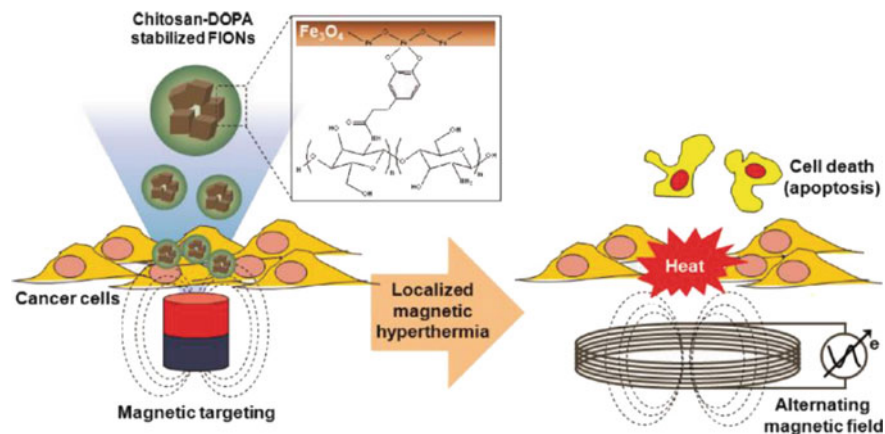
Fig. 8.8   Schematic presentation of Chito-FIONs and their applications with the aid of magnetic targeting. Reproduced with permission from Bae et al. (2012). Copyright 2018, with permission from American Chemical Society

In 2018, Ni and co-workers applied magnetic targeting strategy to high tumor accumulation of their designed nanoparticles. The Ni research group results confirm that IONPs with [89]Zr and porphyrin ([89]Zr-MNP/TCPP) have effective therapeutic effect and multimodal imaging power with the aid of magnetic targeting (Fig. 8.9) (Ni et al. 2018).

Conclusion and Perspectives

The targeted and image-guided drug and detection probe delivery have received extensive attention in cancers and other diseases therapy. IONPs with the aid of EPR effect, ligand facilities targeting, and magnetic targeting can be used for local delivery of drugs and probe agents. Since IONPs have simple synthesis ways and many advantages such as proper size, convenience of administration, biocompatibility, biodegradability, magnetic properties, easy functionalization, and so on, there is a high potential for clinical applications in the future.
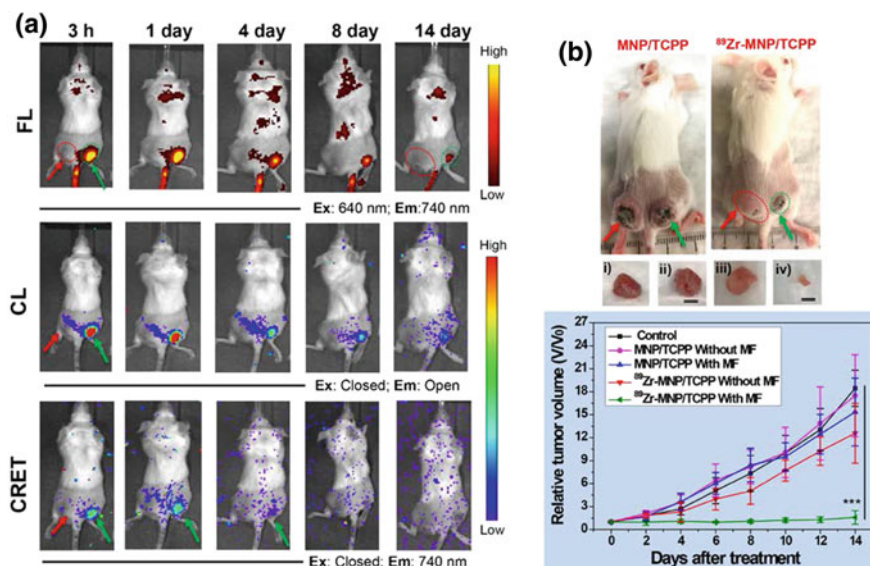
Fig. 8.9 a Magnetic-targeted fluorescence (FL), Cerenkov luminescence (CL), and Cerenkov resonance energy transfer (CRET) imaging of bilateral 4T1 tumor-bearing mice, **b** illustrative photos of mice and tumor growth profiles of 4T1 tumor-bearing mice. Non-magnetic targeting was indicated with red arrows, and magnetic targeting was indicated with green arrows. Reproduced with permission from Ni et al. (2018). Copyright 2019, with permission from American Chemical Society

References

Abdalla MO, Karna P, Sajja HK, Mao H, Yates C, Turner T, Aneja R (2011) Enhanced noscapine delivery using uPAR-targeted optical-MR imaging trackable nanoparticles for prostate cancer therapy. J Controlled Release 149(3):314–322

Aggarwal P, Hall JB, McLeland CB, Dobrovolskaia MA, McNeil SE (2009) Nanoparticle interaction with plasma proteins as it relates to particle biodistribution, biocompatibility and therapeutic efficacy. Adv Drug Deliv Rev 61(6):428–437

Assaraf YG, Leamon CP, Reddy JA (2014) The folate receptor as a rational therapeutic target for personalized cancer treatment. Drug Resist Updates 17(4):89–95

Bae KH, Park M, Do MJ, Lee N, Ryu JH, Kim GW, Kim C, Park TG, Hyeon T (2012) Chitosan oligosaccharide-stabilized ferrimagnetic iron oxide nanocubes for magnetically modulated cancer hyperthermia. ACS Nano 6(6):5266–5273

Basu S, Alavi A (2009) Revolutionary impact of PET and PET-CT on the day-to-day practice of medicine and its great potential for improving future health care. Nucl Med Rev Cent East Eur 12(1):1–13

Bhattacharya D, Das M, Mishra D, Banerjee I, Sahu SK, Maiti TK, Pramanik P (2011) Folate receptor targeted, carboxymethyl chitosan functionalized iron oxide nanoparticles: a novel ultra dispersed nanoconjugates for bimodal imaging. Nanoscale 3(4):1653–1662

Bohara RA, Thorat ND, Pawar SH (2016) Role of functionalization: strategies to explore potential nano-bio applications of magnetic nanoparticles. RSC Adv 6(50):43989–44012

Boncel S, Herman AP, Budniok S, Jędrysiak RG, Jakóbik-Kolon A, Skepper JN, Müller KH (2016) In vitro targeting and selective killing of T47D breast cancer cells by purpurin and 5-Fluorouracil

anchored to magnetic CNTs: nitrene-based functionalization versus uptake, cytotoxicity, and intracellular fate. ACS Biomater Sci Eng 2(8):1273–1285

Cabral H, Matsumoto Y, Mizuno K, Chen Q, Murakami M, Kimura M, Terada Y, Kano M, Miyazono K, Uesaka M (2011) Accumulation of sub-100 nm polymeric micelles in poorly permeable tumours depends on size. Nat Nanotechnol 6(12):815–823

Cairns RA, Harris IS, Mak TW (2011) Regulation of cancer cell metabolism. Nat Rev Cancer 11(2):85–95

Campbell RB, Fukumura D, Brown EB, Mazzola LM, Izumi Y, Jain RK, Torchilin VP, Munn LL (2002) Cationic charge determines the distribution of liposomes between the vascular and extravascular compartments of tumors. Can Res 62(23):6831–6836

Chen H, Gu Y, Hu Y, Qian Z (2007) Characterization of pH-and temperature-sensitive hydrogel nanoparticles for controlled drug release. PDA J Pharm Sci Technol 61(4):303–313

Chen H, Wang L, Yu Q, Qian W, Tiwari D, Yi H, Wang AY, Huang J, Yang L, Mao H (2013) Anti-HER2 antibody and ScFvEGFR-conjugated antifouling magnetic iron oxide nanoparticles for targeting and magnetic resonance imaging of breast cancer. Int J Nanomed 8:3781

Choi HS, Liu W, Misra P, Tanaka E, Zimmer JP, Ipe BI, Bawendi MG, Frangioni JV (2007) Renal clearance of quantum dots. Nat Biotechnol 25(10):1165–1170

Clauson RM, Chen M, Scheetz LM, Berg B, Chertok B (2018) Size-controlled iron oxide nanoplatforms with lipidoid-stabilized shells for efficient magnetic resonance imaging-trackable lymph node targeting and high-capacity biomolecule display. ACS Appl Mater Interfaces 10(24):20281–20295

Cole AJ, David AE, Wang J, Galbán CJ, Hill HL, Yang VC (2011a) Polyethylene glycol modified, cross-linked starch-coated iron oxide nanoparticles for enhanced magnetic tumor targeting. Biomaterials 32(8):2183–2193

Cole AJ, David AE, Wang J, Galbán CJ, Yang VC (2011b) Magnetic brain tumor targeting and biodistribution of long-circulating PEG-modified, cross-linked starch-coated iron oxide nanoparticles. Biomaterials 32(26):6291–6301

Dahms N, Lobel P, Kornfeld S (1989) Mannose 6-phosphate receptors and lysosomal enzyme targeting. J Biol Chem 264(21):12115–12118

Daniels TR, Delgado T, Rodriguez JA, Helguera G, Penichet ML (2006) The transferrin receptor part I: biology and targeting with cytotoxic antibodies for the treatment of cancer. Clin Immunol 121(2):144–158

D'souza AA, Devarajan PV (2015) Asialoglycoprotein receptor mediated hepatocyte targeting—strategies and applications. J Controlled Release 203:126–139

Fan C, Gao W, Chen Z, Fan H, Li M, Deng F, Chen Z (2011) Tumor selectivity of stealth multifunctionalized superparamagnetic iron oxide nanoparticles. Int J Pharm 404(1):180–190

Fang J, Nakamura H, Maeda H (2011) The EPR effect: unique features of tumor blood vessels for drug delivery, factors involved, and limitations and augmentation of the effect. Adv Drug Deliv Rev 63(3):136–151

Folkman J (1971) Tumor angiogenesis: therapeutic implications. N Engl J Med 285(21):1182–1186

Gao X, Cui Y, Levenson RM, Chung LW, Nie S (2004) In vivo cancer targeting and imaging with semiconductor quantum dots. Nat Biotechnol 22(8):969–976

Garanger E, Boturyn D, Dumy P (2007) Tumor targeting with RGD peptide ligands-design of new molecular conjugates for imaging and therapy of cancers. Anti-Cancer Agents Med Chem (Formerly Curr Med Chem-Anti-Cancer Agents) 7(5):552–558

Göppert TM, Müller RH (2005) Polysorbate-stabilized solid lipid nanoparticles as colloidal carriers for intravenous targeting of drugs to the brain: comparison of plasma protein adsorption patterns. J Drug Target 13(3):179–187

Gu F, Zhang L, Teply BA, Mann N, Wang A, Radovic-Moreno AF, Langer R, Farokhzad OC (2008) Precise engineering of targeted nanoparticles by using self-assembled biointegrated block copolymers. Proc Natl Acad Sci 105(7):2586–2591

Guardia P, Di Corato R, Lartigue L, Wilhelm C, Espinosa A, Garcia-Hernandez M, Gazeau F, Manna L, Pellegrino T (2012) Water-soluble iron oxide nanocubes with high values of specific absorption rate for cancer cell hyperthermia treatment. ACS Nano 6(4):3080–3091

Gusev S, Povaliǐ T, Volobueva T, Zakharchenko V (1988) The distribution of negative charges on the luminal surface of Descemet's endothelium. Tsitologiia 30(8):1022–1026

Hadjipanayis CG, Machaidze R, Kaluzova M, Wang L, Schuette AJ, Chen H, Wu X, Mao H (2010) EGFRvIII antibody–conjugated iron oxide nanoparticles for magnetic resonance imaging–guided convection-enhanced delivery and targeted therapy of glioblastoma. Can Res 70(15):6303–6312

Hashizume H, Baluk P, Morikawa S, McLean JW, Thurston G, Roberge S, Jain RK, McDonald DM (2000) Openings between defective endothelial cells explain tumor vessel leakiness. Am J Pathol 156(4):1363–1380

Hayashi K, Sato Y, Sakamoto W, Yogo T (2016) Theranostic nanoparticles for MRI-guided thermochemotherapy: "tight" clustering of magnetic nanoparticles boosts relativity and heat-generation power. ACS Biomater Sci Eng 3(1):95–105

Hillery AM, Lloyd AW, Swarbrick J (2002) Drug delivery and targeting: for pharmacists and pharmaceutical scientists. CRC Press

Hobbs SK, Monsky WL, Yuan F, Roberts WG, Griffith L, Torchilin VP, Jain RK (1998) Regulation of transport pathways in tumor vessels: role of tumor type and microenvironment. Proc Natl Acad Sci 95(8):4607–4612

Hu Y, Li J, Yang J, Wei P, Luo Y, Ding L, Sun W, Zhang G, Shi X, Shen M (2015) Facile synthesis of RGD peptide-modified iron oxide nanoparticles with ultrahigh relaxivity for targeted MR imaging of tumors. Biomater Sci 3(5):721–732

Huang J, Li Y, Orza A, Lu Q, Guo P, Wang L, Yang L, Mao H (2016) Magnetic nanoparticle facilitated drug delivery for cancer therapy with targeted and image-guided approaches. Adv Funct Mater

Islam T, Josephson L (2009) Current state and future applications of active targeting in malignancies using superparamagnetic iron oxide nanoparticles. Cancer Biomark 5(2):99–107

Iyer AK, Khaled G, Fang J, Maeda H (2006) Exploiting the enhanced permeability and retention effect for tumor targeting. Drug Discov Today 11(17):812–818

Jae-Hyun L, Yong-Min H, Young-wook J, Seo J-W, Jang J-T, Ho-Taek S, Sungjun K, Eun-Jin C, Yoon H-G, Suh J-S (2007) Artificially engineered magnetic nanoparticles for ultra-sensitive molecular imaging. Nat Med 13(1):95

Jain RK, Duda DG, Clark JW, Loeffler JS (2006) Lessons from phase III clinical trials on anti-VEGF therapy for cancer. Nat Clin Pract Oncol 3(1):24–40

Jalalian SH, Taghdisi SM, Hamedani NS, Kalat SAM, Lavaee P, ZandKarimi M, Ghows N, Jaafari MR, Naghibi S, Danesh NM (2013) Epirubicin loaded super paramagnetic iron oxide nanoparticle-aptamer bioconjugate for combined colon cancer therapy and imaging in vivo. Eur J Pharm Sci 50(2):191–197

Kandasamy G, Maity D (2015) Recent advances in superparamagnetic iron oxide nanoparticles (SPIONs) for in vitro and in vivo cancer nanotheranostics. Int J Pharm 496(2):191–218

Kim D, Jeong YY, Jon S (2010) A drug-loaded aptamer-gold nanoparticle bioconjugate for combined CT imaging and therapy of prostate cancer. ACS Nano 4(7):3689–3696

Kohler N, Sun C, Wang J, Zhang M (2005) Methotrexate-modified superparamagnetic nanoparticles and their intracellular uptake into human cancer cells. Langmuir 21(19):8858–8864

Kohler N, Sun C, Fichtenholtz A, Gunn J, Fang C, Zhang M (2006) Methotrexate-immobilized poly (ethylene glycol) magnetic nanoparticles for MR imaging and drug delivery. Small 2(6):785–792

Konno T, Maeda H, Iwai K, Maki S, Tashiro S, Uchida M, Miyauchi Y (1984) Selective targeting of anti-cancer drug and simultaneous image enhancement in solid tumors by arterially administered lipid contrast medium. Cancer 54(11):2367–2374

Lamanna G, Kueny-Stotz M, Mamlouk-Chaouachi H, Ghobril C, Basly B, Bertin A, Miladi I, Billotey C, Pourroy G, Begin-Colin S (2011) Dendronized iron oxide nanoparticles for multimodal imaging. Biomaterials 32(33):8562–8573

Le Droumaguet B, Nicolas J, Brambilla D, Mura S, Maksimenko A, De Kimpe L, Salvati E, Zona C, Airoldi C, Canovi M (2012) Versatile and efficient targeting using a single nanoparticulate platform: application to cancer and Alzheimer's disease. ACS Nano 6(7):5866–5879

Lee GY, Qian WP, Wang L, Wang YA, Staley CA, Satpathy M, Nie S, Mao H, Yang L (2013) Theranostic nanoparticles with controlled release of gemcitabine for targeted therapy and MRI of pancreatic cancer. ACS Nano 7(3):2078–2089

Lee N, Yoo D, Ling D, Cho MH, Hyeon T, Cheon J (2015) Iron oxide based nanoparticles for multimodal imaging and magnetoresponsive therapy. Chem Rev 115(19):10637–10689

Li Z, Yin S, Cheng L, Yang K, Li Y, Liu Z (2014) Magnetic targeting enhanced theranostic strategy based on multimodal imaging for selective ablation of cancer. Adv Func Mater 24(16):2312–2321

Li Z, Xu F, Li Q, Liu S, Wang H, Möhwald H, Cui X (2015) Synthesis of multifunctional bovine serum albumin microcapsules by the sonochemical method for targeted drug delivery and controlled drug release. Colloids Surf, B 136:470–478

Liang H, Li X, Chen B, Wang B, Zhao Y, Zhuang Y, Shen H, Zhang Z, Dai J (2015) A collagen-binding EGFR single-chain Fv antibody fragment for the targeted cancer therapy. J Controlled Release 209:101–109

Liao C, Sun Q, Liang B, Shen J, Shuai X (2011) Targeting EGFR-overexpressing tumor cells using Cetuximab-immunomicelles loaded with doxorubicin and superparamagnetic iron oxide. Eur J Radiol 80(3):699–705

Liu D, Wu W, Ling J, Wen S, Gu N, Zhang X (2011) Effective PEGylation of iron oxide nanoparticles for high performance in vivo cancer imaging. Adv Func Mater 21(8):1498–1504

Low PS, Henne WA, Doorneweerd DD (2007) Discovery and development of folic-acid-based receptor targeting for imaging and therapy of cancer and inflammatory diseases. Acc Chem Res 41(1):120–129

Lu Y, Low PS (2012) Folate-mediated delivery of macromolecular anticancer therapeutic agents. Adv Drug Deliv Rev 64:342–352

Lübbe AS, Bergemann C, Huhnt W, Fricke T, Riess H, Brock JW, Huhn D (1996) Preclinical experiences with magnetic drug targeting: tolerance and efficacy. Can Res 56(20):4694–4701

Lundin J, Kimby E, Björkholm M, Broliden P-A, Celsing F, Hjalmar V, Möllgård L, Rebello P, Hale G, Waldmann H (2002) Phase II trial of subcutaneous anti-CD52 monoclonal antibody alemtuzumab (Campath-1H) as first-line treatment for patients with B-cell chronic lymphocytic leukemia (B-CLL). Blood 100(3):768–773

Luo Y, Yang J, Yan Y, Li J, Shen M, Zhang G, Mignani S, Shi X (2015) RGD-functionalized ultrasmall iron oxide nanoparticles for targeted T 1-weighted MR imaging of gliomas. Nanoscale 7(34):14538–14546

Maeda H (2010) Tumor-selective delivery of macromolecular drugs via the EPR effect: background and future prospects. Bioconjug Chem 21(5):797–802

Maeda H, Nakamura H, Fang J (2013) The EPR effect for macromolecular drug delivery to solid tumors: improvement of tumor uptake, lowering of systemic toxicity, and distinct tumor imaging in vivo. Adv Drug Deliv Rev 65(1):71–79

Manish G, Vimukta S (2011) Targeted drug delivery system: a review. Res J Chem Sci 1(2):135–138

Manjili HK, Ma'mani L, Tavaddod S, Mashhadikhan M, Shafiee A, Naderi-Manesh H (2016) D, L-Sulforaphane loaded Fe 3 O 4@ gold core shell nanoparticles: a potential sulforaphane delivery system. PloS one 11(3):e0151344

Matsumura Y, Maeda H (1986) A new concept for macromolecular therapeutics in cancer chemotherapy: mechanism of tumoritropic accumulation of proteins and the antitumor agent smancs. Cancer Res 46(12 Part 1):6387–6392

McCarthy JR, Weissleder R (2008) Multifunctional magnetic nanoparticles for targeted imaging and therapy. Adv Drug Deliv Rev 60(11):1241–1251

Mendelsohn J, Baselga J (2000) The EGF receptor family as targets for cancer therapy. Oncogene 19(56):6550

Ni D, Ferreira CA, Barnhart TE, Quach V, Yu B, Jiang D, Wei W, Liu H, Engle JW, Hu P (2018) Magnetic targeting of nanotheranostics enhances cerenkov radiation-induced photodynamic therapy. J Am Chem Soc 140(44):14971–14979

Nosrati H, Mojtahedi A, Danafar H, Kheiri Manjili H (2018) Enzymatic stimuli-responsive methotrexate-conjugated magnetic nanoparticles for target delivery to breast cancer cells and release study in lysosomal condition. J Biomed Mater Res Part A 106(6):1646–1654

Nosrati H, Tarantash M, Bochani S, Charmi J, Bagheri Z, Fridoni M, Abdollahifar M-A, Davaran S, Danafar H, Kheiri Manjili H (2019) Glutathione (GSH) peptide conjugated magnetic nanoparticles as blood–brain barrier shuttle for mri-monitored brain delivery of paclitaxel. ACS Biomater Sci Eng

Peer D, Karp JM, Hong S, Farokhzad OC, Margalit R, Langer R (2007) Nanocarriers as an emerging platform for cancer therapy. Nat Nanotechnol 2(12):751–760

Peng X-H, Qian X, Mao H, Wang AY, Chen Z, Nie S, Shin DM (2008) Targeted magnetic iron oxide nanoparticles for tumor imaging and therapy. Int J Nanomed 3(3):311–321

Ross JS, Fletcher JA, Bloom KJ, Linette GP, Stec J, Symmans WF, Pusztai L, Hortobagyi GN (2004) Targeted therapy in breast cancer the HER-2/neu gene and protein. Mol Cell Proteomics 3(4):379–398

Sakulkhu U, Mahmoudi M, Maurizi L, Coullerez G, Hofmann-Amtenbrink M, Vries M, Motazacker M, Rezaee F, Hofmann H (2015) Significance of surface charge and shell material of superparamagnetic iron oxide nanoparticle (SPION) based core/shell nanoparticles on the composition of the protein corona. Biomater Sci 3(2):265–278

Schottelius M, Laufer B, Kessler H, Wester H-Jr (2009) Ligands for mapping αvβ3-integrin expression in vivo. Acc Chem Res 42(7):969–980

Seymour L, Ulbrich K, Wedge S, Hume I, Strohalm J, Duncan R (1991) N-(2-hydroxypropyl) methacrylamide copolymers targeted to the hepatocyte galactose-receptor: pharmacokinetics in DBA2 mice. Br J Cancer 63(6):859

Seymour LW, Ferry DR, Anderson D, Hesslewood S, Julyan PJ, Poyner R, Doran J, Young AM, Burtles S, Kerr DJ (2002) Hepatic drug targeting: phase I evaluation of polymer-bound doxorubicin. J Clin Oncol 20(6):1668–1676

Shojaei S, Ghasemi Z, Shahrisa A (2017) Cu (I)@ Fe3O4 nanoparticles supported on imidazolium-based ionic liquid-grafted cellulose: green and efficient nanocatalyst for multicomponent synthesis of N-sulfonylamidines and N-sulfonylacrylamidines. Appl Organomet Chem

Smith HW, Marshall CJ (2010) Regulation of cell signalling by uPAR. Nat Rev Mol Cell Biol 11(1):23–36

Sonvico F, Mornet S, Vasseur S, Dubernet C, Jaillard D, Degrouard J, Hoebeke J, Duguet E, Colombo P, Couvreur P (2005) Folate-conjugated iron oxide nanoparticles for solid tumor targeting as potential specific magnetic hyperthermia mediators: synthesis, physicochemical characterization, and in vitro experiments. Bioconjug Chem 16(5):1181–1188

Subbiah V, Brown RE, McGuire MF, Buryanek J, Janku F, Younes A, Hong D (2014) A novel immunomodulatory and molecularly targeted strategy for refractory Hodgkin's lymphoma. Oncotarget 5(1):95

Sun C, Sze R, Zhang M (2006) Folic acid-PEG conjugated superparamagnetic nanoparticles for targeted cellular uptake and detection by MRI. J Biomed Mater Res, Part A 78(3):550–557

Suresh T, Lee LX, Joshi J, Barta SK (2014) New antibody approaches to lymphoma therapy. J Hematol Oncol 7(1):58

Tai W, Mahato R, Cheng K (2010) The role of HER2 in cancer therapy and targeted drug delivery. J Controlled Release 146(3):264–275

Von Maltzahn G, Park J-H, Lin KY, Singh N, Schwöppe C, Mesters R, Berdel WE, Ruoslahti E, Sailor MJ, Bhatia SN (2011) Nanoparticles that communicate in vivo to amplify tumour targeting. Nat Mater 10(7):545–552

Wang AZ, Bagalkot V, Vasilliou CC, Gu F, Alexis F, Zhang L, Shaikh M, Yuet K, Cima MJ, Langer R (2008) Superparamagnetic iron oxide nanoparticle–aptamer bioconjugates for combined prostate cancer imaging and therapy. ChemMedChem 3(9):1311–1315

Wang Y, Su P, Wang S, Wu J, Huang J, Yang Y (2013) Dendrimer modified magnetic nanoparticles for immobilized BSA: a novel chiral magnetic nano-selector for direct separation of racemates. J Mater Chem B 1(38):5028–5035

Wang L, An Y, Yuan C, Zhang H, Liang C, Ding F, Gao Q, Zhang D (2015) GEM-loaded magnetic albumin nanospheres modified with cetuximab for simultaneous targeting, magnetic resonance imaging, and double-targeted thermochemotherapy of pancreatic cancer cells. Int J Nanomed 10:2507

Widder KJ, Senyei AE, Scarpelli DG (1978) Magnetic microspheres: a model system for site specific drug delivery in vivo. Exp Biol Med 158(2):141–146

Widder KJ, Senyei AE, Ranney DF (1979) Magnetically responsive microspheres and other carriers for the biophysical targeting of antitumor agents. Adv Pharmacol 16:213–271

Wu Y, Soesbe TC, Kiefer GE, Zhao P, Sherry AD (2010) A responsive europium (III) chelate that provides a direct readout of pH by MRI. J Am Chem Soc 132(40):14002–14003

Xie J, Xu C, Kohler N, Hou Y, Sun S (2007) Controlled PEGylation of monodisperse Fe3O4 nanoparticles for reduced non-specific uptake by macrophage cells. Adv Mater 19(20):3163–3166

Yang L, Cao Z, Sajja HK, Mao H, Wang L, Geng H, Xu H, Jiang T, Wood WC, Nie S (2008) Development of receptor targeted magnetic iron oxide nanoparticles for efficient drug delivery and tumor imaging. J Biomed Nanotechnol 4(4):439–449

Yang L, Mao H, Wang YA, Cao Z, Peng X, Wang X, Duan H, Ni C, Yuan Q, Adams G (2009a) Single chain epidermal growth factor receptor antibody conjugated nanoparticles for in vivo tumor targeting and imaging. Small 5(2):235–243

Yang L, Mao H, Cao Z, Wang YA, Peng X, Wang X, Sajja HK, Wang L, Duan H, Ni C (2009) Molecular imaging of pancreatic cancer in an animal model using targeted multifunctional nanoparticles. Gastroenterology 136(5):1514–1525

Yang X, Hong H, Grailer JJ, Rowland IJ, Javadi A, Hurley SA, Xiao Y, Yang Y, Zhang Y, Nickles RJ (2011) cRGD-functionalized, DOX-conjugated, and 64 Cu-labeled superparamagnetic iron oxide nanoparticles for targeted anticancer drug delivery and PET/MR imaging. Biomaterials 32(17):4151–4160

YoungáKim W, SeungáKim J (2015) Biotin-guided anticancer drug delivery with acidity-triggered drug release. Chem Commun 51(45):9343–9345

Zhang F, Huang X, Zhu L, Guo N, Niu G, Swierczewska M, Lee S, Xu H, Wang AY, Mohamedali KA (2012) Noninvasive monitoring of orthotopic glioblastoma therapy response using RGD-conjugated iron oxide nanoparticles. Biomaterials 33(21):5414–5422

Zhao X, Li H, Lee RJ (2008) Targeted drug delivery via folate receptors. Expert Opin Drug Deliv 5(3):309–319

Chapter 9
Design of Magnetic-Luminescent Nanoplatforms: Applications in Theranostics and Drug Delivery

Navadeep Shrivastava, Sarveena, Naveed A. Shad, Muhammad Munir Sajid, Adam Duong and S. K. Sharma

Abstract Recent time has witnessed a progressive growth in the fabrication multifunctional upconversion-magnetic hybrid nanostructured materials due to their important applications. The magnetic-luminescent hybrid nanostructures, which combine luminescent nanoparticles with magnetic nanoentities, exhibit potentials for enhanced bioimaging, controlled drug delivery, and enhanced thermal therapy. Such nanoparticles have potential to have simultaneous systematic use of theranostics and drug delivery and could lead to new opportunities in nanobiomedicines. In the present chapter, we have discussed an important class of magnetic-luminescent nanomaterials for their application in theranostic and drug delivery.

Keywords Nanoscale functional materials · Magnetic up/down conversion · Diagnosis and sensing · Therapy · Drug delivery

Introduction

Nanoscale Functional Materials

Nanoscale materials are a topic of considerable interest across a number of science, engineering, and biomedical disciplines (Rao et al. 2012). The basic rationale is that nanoscale materials, typically 1–100 nm, exhibit exceptional structural and functional

N. Shrivastava · A. Duong
Département de chimie, biochimie et physique, Université du Québec à Trois-Rivières, Trois-Rivières, QC, Canada

Sarveena
Alakh Prakash Goyal Shimla University, Shimla, Himachal Pradesh, India

N. A. Shad · M. M. Sajid
Department of Physics, Government College University Faisalabad, Faisalabad, Pakistan

S. K. Sharma (✉)
Department of Physics, Faculty of Science & Technology, The University of the West Indies, Saint Augustine, Trinidad and Tobago
e-mail: surender76@gmail.com

properties that are not available in bulk materials or discrete molecules and have a significant commercial impact, due to their unique properties such as finite size and surface effects (Liz-Marzán and Kamat 2003). Finite size effects are related to manifestation of so-called quantum size effects, which arises when the size of the system is commensurable with the de-Broglie wavelengths of the electrons, phonons or excitons propagating in them. Surface effects can be related, in simplest case, to the symmetry breaking of the crystal structure at the boundary of each particle, but can also be due to different chemical and magnetic structures of internal "core" and surface "shell" parts of nanoparticles (Sharma 2017; Sarveena et al. 2017).

Few major classes of functional nanoplatforms have been extensively studied such as: (i) magnetic nanoparticles; (ii) nanophotonic materials; and (iii) plasmonic nanoparticles and widely used in a variety of fields.

Magnetic nanoparticles, commonly consisting of magnetic elements such as iron (Fe), cobalt (Co), and nickel (Ni), and their chemical compounds, show alignment of their magnetic moment in the presence of an external magnetic field and concentrate on the external magnetic flux density (Wu et al. 2008; Mikhaylova et al. 2004). This makes the magnetic nanoparticles useful for many important applications around. **Nanophotonics** is an emerging frontier that deals with the interaction of light with matter on a nanometer scale exhibiting unique tunable optical features (Prasad 2004). The design and control of the excitation dynamics in nanomaterials constitute a major area of nanophotonics; they can be utilized to produce new frequency-converting (light converting) capabilities for instant using lanthanide-doped nanophosphors (Joseph et al. 2008; Chen et al. 2015). Optical nanoparticles are typically composed of quantum dots (CdSe, ZnS, ZnTe, etc.), dyes, or rare earth-based materials. **Plasmonic nanoparticles** including gold, silver, and platinum are highly efficient at absorbing and scattering light. By changing nanoparticle size, shape, and composition, the optical response can be tuned from the ultraviolet (UV) to the visible to the near-infrared (NIR) regions of the electromagnetic spectrum (Bao et al. 2007). They exhibit unique localized surface plasmon resonance (LSPR), the collective oscillation of the conduction electrons of the nanoparticles in resonance with the electric field of the incident light.

Bifunctionality at Nanoscale

The design and synthesis of materials that simultaneously consist of more than one functional part called multifunctional or bifunctional material (Prasad 2004). Bifunctional nanoparticles have exhibited potentially promising physicochemical properties, which can revolutionize and transform the landscape from bio-clinical industry to next-generation advanced devices. In particular, colloidal nanoparticles have been extensively investigated as probes in biomedical/devices industries due to their unique size-dependent electronic, optical, and magnetic properties among all possible building blocks (Murray et al. 2000; Howes et al. 2014).

Individually, magnetic nanoparticles are one most frequent example of bifunctionality because of its several biomedical and other industrial applications (Liz-Marzán and Kamat 2003; Sharma 2017; Wu et al. 2008). Magnetic nanoparticles can be ignited by an applied magnetic field gradient. This non-invasive approach provides several applications including transportation and confinement of nanoparticles and delivery of a package at a preferential biological component, such as cancer cure medicine to a designated part of the body. Additionally, they can respond to time altering magnetic field and as a result, transfer energy from applied field to the nanoparticles, and they can heat up (Espinosa et al. 2016). The most common magnetic nanoparticles are iron oxide nanoparticles including magnetite (Fe_3O_4) or maghemite (γ-Fe_2O_3). These magnetic nanoparticles have advantages of ease-of-preparation, bio-degradability, excellent stability, and the tunability of magnetic properties through alteration in size and shape, making them the most attractive platforms. When the sizes of these magnetic nanoparticles are below a critical size (generally $\leq$ 20 nm), they are superparamagnetic; otherwise, they are ferromagnetic. Superparamagnetic nanoparticles avoid the induced aggregation associated with the residual magnetization of ferromagnetic nanoparticles (Sharma 2017). Magnetic nanoparticles can be spherical or anisotropic such as rods, cubes, and stars and hence provide versatile structural platforms for generations of different nanostructures (Sarveena et al. 2017). However, due to the high surface-to-volume ratio, the magnetization of bare iron oxide nanoparticles is usually prone to aggregation. This makes them inadequate candidates for biological applications (Laurent et al. 2008; Ling et al. 2015). Therefore, they are generally functionalized with SiO_2, carbon, carboxylates, amines, diols, phosphates, phosphonates and sulfonates, in order to ensure the colloidal stability of these in an organic or aqueous medium (Ling et al. 2015). These magnetic nanoparticles are being exploited for applications such as data storage, spintronics, molecular cellular isolation, biosensors; hyperthermia, magnetic resonance imaging (MRI), and cell manipulation and contributed to an extraordinary advance in nanoengineering due to their multifunctional characteristics (Sarveena et al. 2017; Laurent et al. 2008).

On the other hand, lanthanide optical materials have captured attention worldwide in the last two decades due to their versatile up or down frequency-converting capabilities utilizing a low-energy continuous-wave excitation provided by inexpensive diode lasers or using other means of source such as xenon lamps (Prasad 2004; Dong et al. 2015). Rare earth chemical elements are rich in optical and magnetic properties owing to the unique properties of 4f electrons and have widely been used in catalysis, magnets, phosphors, etc. The recent accomplishments in rare earth nanoparticles synthesis with tunable shape and size have aroused great interest of researchers to further explore their biological and biomedical applications (Dong et al. 2015; Wang et al. 2011). For example, Gd-chelates are widely used as contrast agents for MRI in clinics, promoting in vivo applications of rare earth nanomaterials (Wang et al. 2011; Yang and Chuang 2012). Hence, rare earth-based materials have great potential to be used as bifunctional materials.

However, besides possessing interesting physicochemical properties, magnetic nanoparticles and lanthanide optical materials have several limitations, e.g., in imaging application as shown in Fig. 9.1. For instance, optical imaging techniques offer improved high spatial resolution allowing the visualization of cell structures, but have limited depth of imaging and poor absolute quantitative accuracy due to the absorption of light in tissues (Sun et al. 2013; Sudheendra et al. 2014). On the other hand, magnetic imaging has no practical limitation in terms of the depth of imaging; however, spatial resolution is worse and imaging with more than one probe is problematic (Camarero et al. 2016; Haun et al. 2010). Hence, the concept of combining (hybridizing) the two entities such as magnetic nanoparticles and luminescent nanoparticles complements each other and provides best sensitive tool for sensitive label for imaging in cells and tissue engineering (Zhang et al. 2013). Hence, this combination of multiple imaging techniques (Wang et al. 2011; Yang and Chuang 2012) provides complementary and complete information about the imaged object (Fig. 9.1). Thus, hybrid nanoparticles with combined magnetic and optical properties are much more powerful and can be used in a broad range of applications (Kell et al. 2011; Singh et al. 2014; Su 2017; Nguyen and Tran 2014; Kaewsaneha et al. 2015; Chem et al. 2011). Moreover, they offer new modalities that neither luminescence nor magnetic nanoparticles exhibit. For example, the demonstration of real field-dependent luminescence phenomenon called magneto-luminescence (Comby et al. 2014) and magnetomotive-photoacoustic phenomenon (Blandford et al. 2017; Gao and O'Donnell 2017; Li et al. 2015). These novel phenomenons show remarkable potential in several other important applications such as high accuracy and secure communication, (Kuo et al. 2017) aircraft guidance and radiation field detection and
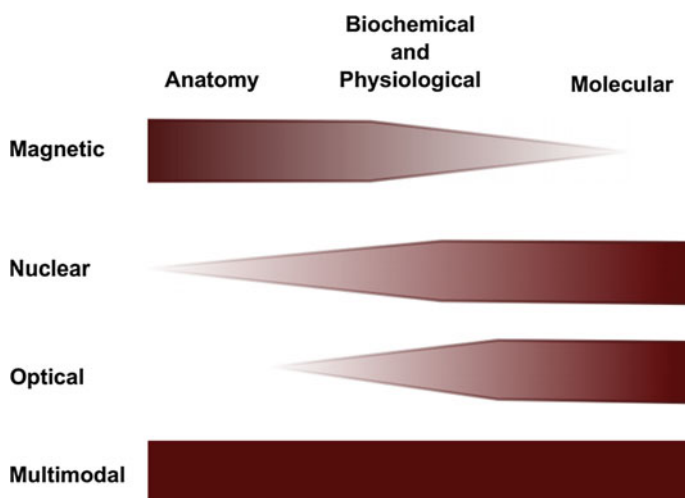
Fig. 9.1 Schematic of overall information retrieved from different imaging modalities from anatomy imaging to molecular imaging and how multimodality can be used to cover limitations of each to provide more complete information

modulation of magnetic and optical field. Furthermore, these nanocomposites can be used as nanoblocks to build various nanoelectronic and photonic devices by applying an external magnetic field to manipulate or arrange the magnetic nanoparticles and optical signals (Yu et al. 2007; Sun et al. 2014).

Major Challenges for Magnetic-Luminescent Bifunctional Nanoparticles

Since magnetic-luminescent bifunctional nanoparticles may provide a new and promising two-in-one characteristics, there are some challenges also to overcome in their fabrication: (i) the complexity in the preparation, which frequently involves multi-step synthesis and many purification stages leading their production, is quite technical and time demanding; (Kas et al. 2010) (ii) the risk of quenching of the luminophore on the surface of the particle by the magnetic core; and (iii) quenching each other by number of fluorescent molecules attached to the surface of the particle. However, to resolve these challenges, several techniques have been proposed to integrate the luminescence and magnetic nanomaterials (Khan and Khan 2017). The fabrications of these are commonly achieved as hybrid conjugates of magnetic and luminescent entities or core–shell or composite structures using coating, layer-by-layer deposition, and optical materials (quantum dots) on magnetic nanoparticles or vice versa. Another way is the functionalization of magnetic iron oxide with fluorescent dyes and luminescent complexes, called cross-linking attachment of molecule. Moreover, the use of SiO_2, ZnS, or C as spacer between iron oxide and luminescent materials is of great importance on the performance of nanohybrids. Table 1 reviews some important works related to the engineering of magnetic-luminescent nanomaterials.

Core–shell structure is the most common type of bifunctional nanosystems. In this type of nanoarchitecture, generally a magnetic core is combined with fluorescent molecules, metal nanoparticles or semiconductor nanocrystals, etc. (Ling et al. 2015) and therefore exhibits unique optical, magnetic, and electrical properties. However, different components in these kinds of bifunctional nanoparticles interact with each other, which generally weaken or reduce the functionality of each unit. Recent advances in the synthesis of various functional superparamagnetic iron oxide nanoparticles with heterostructures offer a promising solution to this problem by creating anisotropic nanoparticles. They consist of functional units with different chemistry, polarity, or other physicochemical properties on asymmetric sides without sacrificing their own properties (Choi et al. 2006; Srinivasan et al. 2015). The superior properties of these heterostructures rely on synergistically enhanced magnetism and synthesis strategies on the precise control of particle size, morphology, chemical composition along with functionalization of fluorescent material and engineering like dumbbell nanoparticles. The desire to design more sophisticated nanoarchitecture with unusual properties is definitely needed. This kind of integration offers

Table 1 Examples of few magnetic-luminescent nanomaterials

Luminescent material	Magnetic material	Type	Synthesis
$NaGdF_4$: Yb^{3+}, Er^{3+}	Fe_3O_4	Core–shell	Thermolysis process (Zhong et al. 2012)
LaF_3:Ce^{3+}, Tb^{3+}	Fe_3O_4	Core–shell	Coprecipitation (He et al. 2009)
YVO_4:Eu^{3+}	Fe_3O_4	Core–shell	Coprecipitation (Peng et al. 2011)
CdSe	Fe_3O_4	Core–shell	Thermal decomposition (Jie and Yuan 2012)
ZnS	Fe_3O_4	Core–shell	Thermal decomposition (Du et al. 2006)
Gd_2O_3:Eu^{3+}	Fe_3O_4	Core–shell	Heating/calcination (Wu et al. 2016)
α-$NaYF_4$:Yb^{3+}, Er^{3+}	Fe_3O_4	Core–shell	Hydrothermal/calcination (Zhang et al. 2012)
$LaPO_4$:Ce^{3+}:Tb^{3+}	Fe_3O_4	Cross-linking, Calix	Coprecipitation (Fang et al. 2010)
Eu^{3+} and Tb^{3+} complexes	Fe_3O_4	Cross-linking, Calix	Coprecipitation (Khan et al. 2014)
CdSe/ZnS	γ-Fe_2O_3	Polymer having $-SH$ and $-COOH$	Organic/water two-phase mixture (Wang et al. 2004)
	Fe_3O_4	PEG-diacid/polyethylene glycol-bis-carboxymethyl ether	Covalently conjugation via amide bond formation (Barick et al. 2015)
$NaYF_4$:Yb^{3+}, Er^{3+}	Fe_3O_4	1,10-decanedicarb-oxylic acid or 11-mercaptoundecanoic acid	Crosslinker anchoring strategy (Shen et al. 2010)
Tb^{3+} *N*-(4-benzoic acid-yl),*N*'-(propyltriethoxysilyl) urea)	Fe_3O_4	SiO_2	Coprecipitation and Stöber method (Yu et al. 2007)

exciting opportunities for discovering new materials, processes, and phenomenon. At nanoscale, these kind of bifunctional materials have their own advantage (Gao et al. 2009; Li et al. 2013): (i) tuned and controlled size depending on application, (ii) nanoparticles be manipulated by external magnetic field "action at a distance," and (iii) dual-mode applications, e.g., MRI contrast agents and multimodal imaging.

In spite of the growing attention paid on the bifunctional nanoparticles comprising of magnetic and luminescence materials responding to magnetic and optical excitation simultaneously, (Zhang et al. 2015; Liu et al. 2013) the coupling between magnetism and luminescence of lanthanide ions in these systems remains largely ignored. From some recent reports, it has been found that the external magnetic field has direct influence on the spectral positions and luminescence intensity of

lanthanide ions doped in various inorganic hosts. In Er^{3+}/Yb^{3+} doped Gd_2O_3 phosphor, for instance, optical bistability in the magnetic field-dependent luminescence intensity was observed and ascribed to the residual magnetization in the material. In several other systems, with the increase in the magnetic field, the suppression of the luminescence intensity was usually observed, accompanied by the steady shift of the spectral positions for lanthanide ions like Er^{3+} and Eu^{3+}. This is generally understood based on the interplay of field-induced Zeeman splitting. However, the exact mechanism with the application of magnetic field remains obscure. For example, Eu^{3+} doped $NaGdF_4$ nanoparticles, where the obvious shift and splitting of the luminescence bands have been detected in the presence of magnetic field. These results can be interpreted in terms of Zeeman effects and the magnetic field-induced change of local site symmetry around Eu^{3+}. Besides optical hysteresis behavior of integrated luminescence intensity for different transitions of Eu^{3+} is found when the magnetic field is scanned (from 0 to 40 T), which relates to the magnetic ordering in the lanthanide sub-lattice.

Lanthanides and Luminescence Mechanism Involved in Bifunctional Materials

Lanthanide-doped nanophosphors are dilute guest-host systems, where trivalent lanthanide ion emitters are dispersed as guests in an appropriate dielectric host lattice (Peng et al. 2015). The luminescence (or magnetic) generally arises from 4f-4f orbital electronic transitions, with associated wave functions localized within a single lanthanide ion (Bunzli and Piguet 2005). The shielding of 4f electrons by the outer complete 5s and 5p shells gives non-blinking and line-like sharp emissions, which exhibit high resistance to photobleaching and photochemical degradation. Strictly speaking, the main intra-4f electronic dipole transitions of lanthanide ions are forbidden by quantum mechanical selection rules; however, they are still manifested due to local crystal field-induced intermixing of the f states with higher electronic configurations. Besides, the dipole-forbidden nature of the 4f-4f transitions yields very long lifetimes for these energy levels of lanthanide ions. These long lifetimes play an important role in increasing the probability of sequential excitations in the excited states of a single lanthanide ion, as well as in permitting favorable ion–ion interactions in the excited states to allow energy transfers between two or more lanthanide ions. Through a judicious selection of one or more lanthanide dopants, nanophosphors can display either frequency upconversion (UC) such as infrared (IR) to shorter wavelength near-infrared (NIR), visible, or ultraviolet (UV) or downconversion (DC), such as IR being further red-shifted. Further, it may also happen that UV excitation can be converted into visible color lines through quantum cutting or downconversion. Unlike the quantum-confined systems, the electronic energy gap of lanthanide-doped nanophosphors does not change with a change in the size or shape.

However, their emission properties (color, efficiency, and lifetime) are indeed dependent on nanoscale structures of nanophosphors, which influence the electron–phonon coupling, local crystal field, and nanoscopic ion–ion interactions. Manipulation of a nanoscale dielectric environment (host) to control the excitation dynamics is, therefore, of great importance in order to control their frequency-converting capabilities. Two typical energy transfer modes have been established in rare earth ion-activated materials to understand the emission behavior, namely downshifting or quantum cutting, and upconversion (UC).

Upconversion Process

Upconversion refers to a process generating higher energy emission under low-energy excitation (Muhr et al. 2014; Auzel 2004). Upconversion processes are mainly divided into four classes (Fig. 9.2): excited-state absorption (ESA), energy transfer upconversion (ETU), photon avalanche (PA) and energy migration-mediated upconversion (EMU). All the first three mechanisms involve the sequential absorption of two or more photons by metastable, long-lived energy states. This sequential absorption promotes the ion to high-lying excited-state results in upconversion emission. A sensitizer ion (type I) first transfers its excitation energy to an acceptor ion (type II). The energy transfer from the high-lying excited state of the acceptor to a migrator ion (type III) then occurs, followed by the migration of excitation energy via the migrator ion sub-lattice through the core–shell interface. Subsequently, the migrating energy is trapped by the activator ion (type IV), resulting in upconversion emission. The "nx" represents the occurrence of random hopping through many type-III ions (Auzel 2004; Ren et al. 2016).
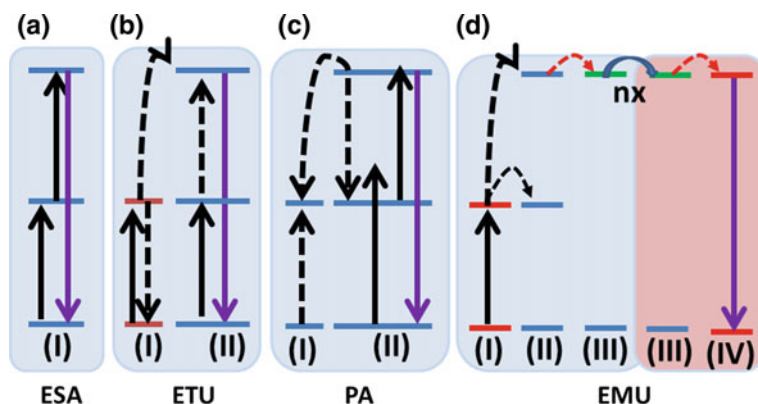
Fig. 9.2 Upconversion processes. **a** Excited-state absorption (ESA). **b** Energy transfer upconversion (ETU). **c** Photon avalanche (PA). **d** Energy migration-mediated upconversion (EMU) involving four types of lanthanide ions doped in different region of core–shell nanocrystals. Note that core and shell regions are highlighted with different background colors in (**d**)

Downconversion/Quantum Cutting Process

The energy of a UV or vacuum UV (VUV) photon is more than twice of a visible photon. Theoretically, it is possible to generate two visible photons for a single UV/VUV photon absorbed; this two-photon luminescence phenomenon is called as quantum cutting (QC) as shown in Fig. 9.3a (Chen et al. 2014). The efficiency gain in QC materials is based on the principle that a QC phosphor can result in two visible/infrared photons for each absorbed VUV/vis photon. QC has been demonstrated based on different mechanisms. Downconversion (DC) is a special case of quantum cutting. DC is a new route to realize visible/IR quantum cutting effect. Figure 9.3b–d illustrates the generalized energy-level diagrams for three DC mechanisms involving energy transfer (ET) between two different rare earth ions (I and II) (Chen et al. 2014). It is not only the cross-relaxation processes but also cooperative process involved in energy transfer mechanism between rare earth ions (Yi and Chow 2007; Yadav et al. 2014; van Wijngaarden et al. 2010).

Figure 9.3 illustrates the energy-level diagrams for two (hypothetical) types of RE ions (I and II) showing the concept of downshifting. Efficient visible QC via two-photon emission from a high energy level for a single RE ion is theoretically possible as shown in Fig. 9.3a. However, competing emissions in the IR and UV
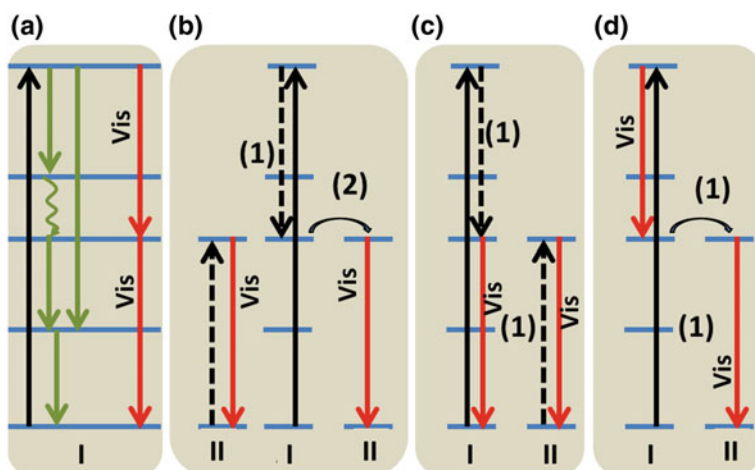
Fig. 9.3 a QC on a single ion I by the sequential emission of two visible photons. Type I is an ion for which emission from a high energy level can occur. Type II is an ion to which ET takes place. **b** The possibility of QC by a two-step ET. In the first step [indicated by (1)], a part of the excitation energy is transferred from ion I to ion II by mainly cross-relaxation. Ion II returns to the ground state by emitting one photon of visible light. Ion I is still in an excited state and can transfer the remaining energy to a second ion of type II [indicated by (2)], which also emits a photon in the visible spectral region, giving a QE ≤ 200%. **c, d** The remaining two possibilities involve only one ET step from ion I to ion II, enough to obtain visible QC if one of two visible photons can be emitted by ion I

(the green lines of Fig. 9.3a) can also occur and prevent efficient visible QC on a single RE ion. Figure 9.3b–d presents generalized energy-level diagrams for three DC mechanisms involving ET between two different RE ions I and II. Type I is an ion for which emission from a high-lying level occurs. Type II is an activator ion in which ET takes place. Figure 9.3b indicates two-photon emission from ion pairs from ions I to II [denoted by (1)], and ET from ions I to II [denoted by (2)] with emission from ion II. Figures 9.3c and d show a cross-relaxation mechanism followed by the emission of photons from both ions I and II. In all three cases, if the two-step ET process is efficient, theoretical visible quantum efficiency (QE) of 200% can be achieved because the previous IR and UV losses existing in a single ion can be avoided.

In addition to the energy migration processes, as mentioned earlier, the size, shape, and surface of lanthanide-doped nanophosphors are important in relation to a specific application, while their composition and the local dielectric environment are essential for their excitation dynamics (Chander 2005). Owing to the high surface-to-volume ratio of nanophosphors, most of the lanthanide dopants are exposed to surface deactivations caused by surface lattice defects and dangling bonds, as well as by surrounding ligands and solvents that possess high phonon energy. The deactivation can occur directly or through an indirect pathway involving energy migrations from the interior lattice points to the surface sites. Hence, the excitation dynamics is also coupled to the surface properties of nanophosphors due to these nanosize-induced surface effects, which are not so pronounced in bulk crystals. These factors create interests to synthesize nanophosphors of stoichiometric composition in a precisely controlled way and to tailor their interface to generate highly efficient nanophosphors for a specific frequency conversion. Furthermore, tailoring the interface is also important for the colloidal solubility of nanophosphors.

The broad applications of lanthanide-doped up/downconversion nanomaterials in various fields have prompted the development of a new class of novel nanoparticles with desirable optical window via up/downconverting mechanism for technological applications. At the same time, the development of the subject nanomagnetism especially by considering iron oxide improved the several perspectives in the field of biomedicine/device industries. Although considerable strategies have been developed for fine-tuning of up/downconversion luminescence with magnetic entity at nanoscale, this field is still immature in terms of fabrication of the material because of compromised magnetic response and tuned photoluminescence characteristics and challenging structural templates. Therefore, we have attempted to design bifunctional nanomaterials with better structural, optical, and magnetic characteristics in search of their potential applications particularly in the field of scintillation.

Design of Magnetic up/Downconversion Luminescent Nanomaterials

Before discussing the synthesis procedures and protocols to prepare different bifunctional nanomaterials, it is important to understand the general synthesis procedure for hydro (solvo) thermal, microemulsion, coprecipitation method, polyol and microwave-assisted approach to provide a better idea about the synthesis protocol. Several chapters in this present book have covered main synthesis techniques for the preparations of nanomaterials of different sizes, shapes, and functionalities. Some of the famous methods can be mentioned such as:

(i) hydro(solvo) thermal synthesis, (ii) coprecipitation method, (iii) polyol synthesis, (iv) microwave-assisted method, (v) coatings over magnetic nanoparticles. As mentioned earlier in the Sect. 2, preparations of the magnetic-luminescent NPs are a big challenge. Usually, preparations involve complex multi-step processes.

Synthesis of Single Component Magnetic-Luminescent Nanoparticles

Shrivastava et al. (2017) used polyol synthesis procedure (Nguyen and Tran 2014; Kharissova et al. 2013) based on mild temperature with the protocol for y mol% doped europium precursor. They prepared LaF_3:xCe^{3+}, xGd^{3+}, yEu^{3+} nanomaterials using diethyleneglycol (DEG) in a three-neck round-bottom flask under magnetic stirring with addition of oleic acid (OA) and under continuous flow of N_2, and a solution of 7.29 mmol (0.28 g) of NH_4F in DEG (25 mL) was injected at 70 °C. The temperature of the reaction mixture was further increased to 215 °C and vigorously stirred under the same temperature for 2 h under refluxing conditions. Then, the obtained suspension was cooled to room temperature, diluted with methanol, and stored overnight, and the supernatant was decanted. The solid particles were further separated by centrifugation. To remove the residual DEG, the solid powders were dispersed in methanol three times, centrifuged, and dried in oven at 115 °C to get powder product (Fig. 9.4).

Wang and co-workers (Wang et al. 2014) provided a detailed synthesis protocol for the preparation of core–shell $NaGdF_4$ nanoparticles to be used as upconversion-based probes utilizing lanthanide ions into different layers for efficiently converting a single-wavelength, near-IR excitation into a tunable visible emission. The precipitation of uniform nanoparticles from a mother solution is governed by a temporally discrete nucleation step followed by controlled growth of the nanoparticles. Owing to the relatively low-energy barrier between the nucleation and growth stages of $NaGdF_4$, the conventional synthesis of monodisperse $NaGdF_4$ nanoparticles typically requires strict attention to several experimental variables, such as solvent identity, reaction time, temperature, and so on. They resolved a facile and robust synthesis
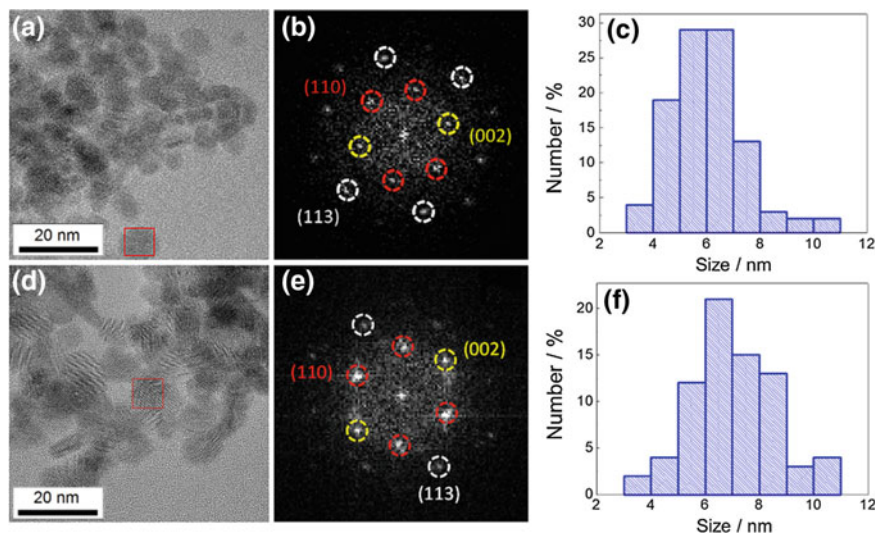
Fig. 9.4 **a**, **d** HRTEM images for LaF$_3$:xCe^{3+}, xGd^{3+}, yEu^{3+} ($x = 5$ mol% $y = 5$, 15 mol%) sample and corresponding. **b**, **e** Regions of the images analyzed by applying fast Fourier transforms (FFT) are highlighted; and **c**, **f** particle size distribution and (**d**). Reprinted with permission from (Shrivastava et al. 2017). Copyright Royal Society of Chemistry 2017

of lanthanide-doped NaGdF$_4$ nanoparticles through coprecipitation of lanthanide-oleate complex prompted by ammonium fluoride. In this reaction, the nucleation and growth of the NaGdF$_4$ nanoparticles are separated by carrying out the two stages at low (50 °C) and elevated (280 °C) temperatures, respectively. The nucleation and growth rates can be further controlled by adjusting the concentration of the precipitator, leading to largely tunable particle sizes. Importantly, by changing the composition of the lanthanide-oleate precursor, different combinations of lanthanide ions can be easily incorporated into the nanoparticles. The core–shell NaGdF4 structure can be prepared by following the same procedure as the NaGdF$_4$ core, except for the inclusion of the pre-synthesized NaGdF4 nanoparticles to the precursor solution as seed crystals before the addition of the precipitator. In addition, the shell thickness can be tuned by adjusting the amount of shell precursors with respect to the core particles. By using the pre-synthesized core–shell NaGdF$_4$ nanoparticle as the seed crystal, the same epitaxial growth process can be repeated to fabricate a multilayered core–shell structure resembling that of an onion. By tuning experimental variables such as the concentration ratios of oleic acid to 1-octadecene and fluoride to metal ions, the protocol for the synthesis of NaGdF$_4$ and its core–shell nanoparticles can be adapted to a wide variety of fluoride nanocrystals comprising rare earth, alkaline earth, and alkali metal ions. Apart from the optical tunability offered by the dopant–host interactions, the use of different fluoride nanocrystals could enable the predetermination and control of the shape of the growing nanocrystals.

Further, the above-described protocol was used by several groups to perform several applications. Liu et al. (2013) prepared single-phase magnetic-luminescent $NaGdF_4$:18%Yb,2%Er NPs-based dual-modal molecular probes for imaging tiny tumors in vivo. In a typical synthesis, they used rare earth chloride hexa-hydrates (80%Gd,Yb,Er). OA (14 mL) and ODE (16 mL) were used as solvent/capping agent. A homogeneous solution was formed when the mixture heated around 150 °C, under nitrogen protection. NaOH (2.5 mmol) and NH_4F (4 mmol) in methanol solution were used for Na and F source. Overall reaction was performed at 300 °C for 1 h in reflux condition. After cooling, NPs were precipitated by using ethanol and further centrifuged and cleaned using ethanol. These NPs were stored in THF or cyclohexane for other experiments. To show the impact of the reactant ratio on the size, size distribution, and phase structure of the resultant $NaGdF_4$:Yb,Er nanoparticles, in the following preparations, the feeding molar ratios of $F:Ln^{3+}$ and $Na:Ln^{3+}$ were tuned independently between 8:1 and 2.4:1 and between 3:1 and 0.75:1, respectively, while the feeding molar ratio among the lanthanide ions, i.e., $Gd^{3+}:Yb^{3+}:Er^{3+}$, was fixed at ratio 80:18:2.

Boyer and co-workers (Boyer et al. 2007) used lanthanide trifluoroacetate precursors to prepare $NaGdF_4$ NPs. The non-coordinating, high-boiling solvent octadecene was selected as the growth medium for the NPs. Oleic acid and oleylamine were employed as the coordinating organic ligands, which attach to the particle surface during the crystal growth and keep the NPs well separated from each other. The overall reaction was obtained at 270 °C at a rate of 10 °C/min under argon for 45 min. The whole solution was then allowed to cool to room temperature; and NPs were precipitated using ethanol and isolated via centrifugation. Dong et al. (2011) used similar procedure with slight modification in reflux temperature and solvent ratios to investigate dopant distributions in $NaGdF_4$ matrix. Mi et al. (2012) prepared bifunctional $NaGdF_4$:Ce, Tb nanoparticles utilizing a two-phase mechanism, with rare earth stearate as the precursor, oleic acid, ethanol, and water as the solvent. After surface-aminated modification through typical Stöber method, the as-prepared nanoparticles were applied for the LRET with Au nanoparticles, and an effective LRET system was established through the covalent interaction of amino and carboxyl groups. There are sufficient amount literature published of the single-phase magnetic-luminescent (specially Gd based) NPs using several synthesis processes (Natarajan Prakash et al. 2016; Schneider et al. 2016; Chen et al. 2012).

Synthesis of Multi-component Magnetic-Luminescent Nanoparticles

Shrivastava et.al used a three-step synthesis procedure to prepare green-emitting magnetic optical nanocomposites named Fe_3O_4/ZnS@LaF_3:xCe^{3+}, xGd^{3+}, yTb^{3+} which is given in several steps (Fig. 9.5): Firstly, the hydrothermal method was used to prepare oleic acid-coated monodisperse magnetic core nanoparticles, according to
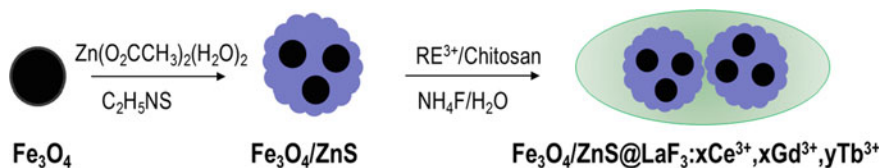
Fig. 9.5 General synthesis scheme of $Fe_3O_4/ZnS@LaF_3:xCe^{3+}$, xGd^{3+}, yTb^{3+} ($x = 5$; $y = 5, 10$ and 15 mol%) bifunctional green-emitting magnetic nanocomposite. Reprinted with Permission (Shrivastava et al. 2017). Copyright Royal Society of Chemistry 2017

the previous report published elsewhere (Zhang et al. 2012; Ge et al. 2009). In the second step, Fe_3O_4/ZnS nanoparticles were prepared using microemulsion procedure, (Yu et al. 2009) by dispersing Fe_3O_4 nanoparticles were in n-propanol by adding the solution of $Zn(O_2CCH_3)_2(H_2O)_2$ in n-propanol. This reaction mixture was stirred at room temperature for 24 h. Thereafter, 60 mL solution of 0.2 g (2.66 mmol) thioacetamide in milli-Q water was added dropwise in above solution. Simultaneously, the resulting solution was heated at 65 °C under vigorous stirring for 5 h. Then, the reaction mixture was cooled to room temperature and gently stirred for overnight. The solid product was collected by magnetic separation method and washed with water and ethanol for five times to remove the excess ZnS nanoparticles. Finally, it was dried under reduced pressure for 12 h and stored in a vacuum desiccator.

Further, $Fe_3O_4/ZnS@LaF_3:xCe^{3+}$, xGd^{3+}, yTb^{3+} nanocomposites were prepared by chitosan-assisted coprecipitation method through general procedure (Liu et al. 2013) using specific amount of Fe_3O_4/ZnS nanoparticles as seeds and stoichiometric amounts of $LaCl_3 \cdot 6H_2O$, $Ce(NO_3)_3 \cdot 6H_2O$, $GdCl_3 \cdot 6H_2O$, and $TbCl_3 \cdot 6H_2O$ precursors (Sankar et al. 2009). In this procedure, Fe_3O_4/ZnS seeds were dispersed in milli-Q water and further coated with CTAB. Appropriate amounts of rare earth precursors were dissolved together in a solution of chitosan in acetic acid/milli-Q water in a three-neck flask under magnetic stirring. The pH of the solution was adjusted to 7. The aqueous dispersion of $Fe_3O_4/ZnS@CTAB$ was added in and stirred under continuous N_2 atmosphere. The 15 mL aqueous NH_4F solution (0.1802 g; 4.86 mmol) was injected slowly to the reaction mixture. Finally, it was heated at refluxing condition for 3 h under continuous N_2 flow. The brown color suspension was cooled to room temperature, and the solid sample was separated from the aqueous suspension using magnetic separation. The collected solid material was washed with milli-Q water and methanol to obtain brown $Fe_3O_4/ZnS@LaF_3:xCe^{3+}$, xGd^{3+}, yTb^{3+} ($x = y = 5$ mol%). The products were found to be water dispersible (Fig. 9.6).

Synthesis of Iron Oxide/NaGdF$_4$:Ln^{3+}

The iron oxide nanoparticles were prepared using method described in reference (Shrivastava et al. 2018a, b) (Fig. 9.7). A facile microwave-assisted solvothermal reaction has been proposed for the synthesis of $NaGdF_4:Ln^{3+}$ and iron
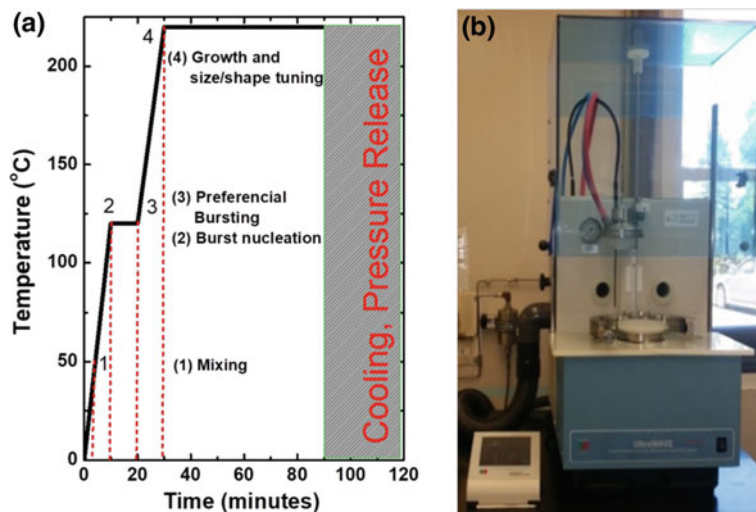
Fig. 9.6 a Shows temperature and time scheme adopted during synthesis. **b** Displays the commercial microwave instrument used for the synthesis available at Federal University of Maranhão, Brazil
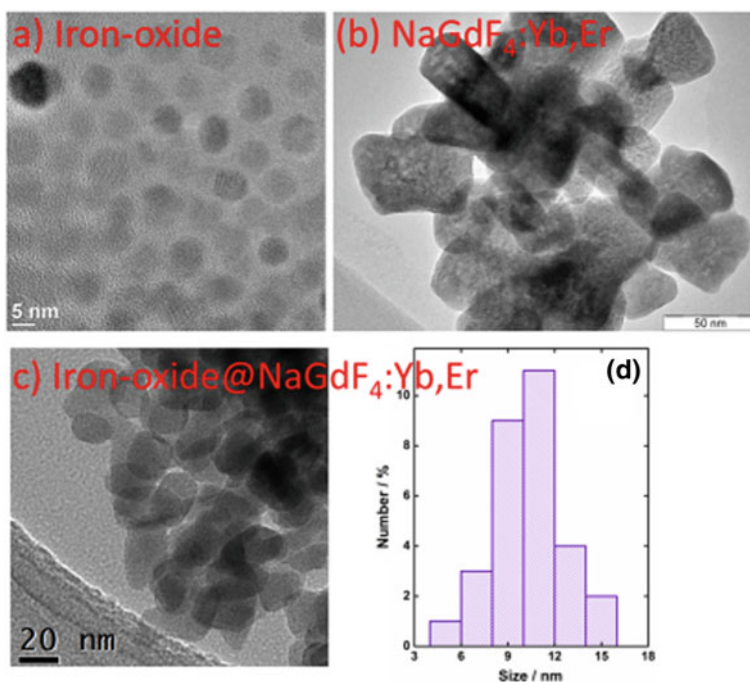
Fig. 9.7 TEM images of synthesized nanomaterials and sized distribution of overall NP. Reused with permission (Shrivastava et al. 2018b). Copyright AIP publishing 2017

oxide/$NaGdF_4$:Ln^{3+} (Ln^{3+} = 20%Yb, 2% Er) NPs. The shell $NaGdF_4$:Ln^{3+} was prepared in the following way. Firstly, 0.78 mmol $GdCl_3 \cdot 6H_2O$, 0.20 mmol $YbCl_3 \cdot 6H_2O$, and 0.02 mmol $ErCl_3 \cdot 6H_2O$ were added into solution containing 16 mL oleic acid to form rare earth oleate and 8 mL of 1-octadecene under continuous stirring at ambient temperature for 20 min. Meanwhile, 2.5 mmol NaOH was dissolved in 10 mL methanol, and then, 8 mL oleic acid was added by stirring to prepare Na-oleate translucent solution. The above two solutions were mixed quickly and stirred for additional 5 min. A separate solution of iron oxide seed prepared in 1-octadecene was poured in above solution slowly and stirred for 10 min at room temperature. A separate solution of 4 mmol fluoride source (NH_4F) in 15 mL methanol was mixed properly in above solution. The mixture was transferred into the reaction vessel of a commercial microwave reactor with an output power of 1000 W. The working cycle of the microwave reactor was set as (i) 20 °C/min rapid heating until 150 °C and (iii) 40 min at 150 °C. The system was allowed to cool quickly to room temperature, and the obtained samples were washed sequentially with methanol and ethanol, and then dried in an air oven at 50 °C for 6 h. Similarly, Shrivastava and co-workers added another library by using Yb^{3+} and Er^{3+} as dopant and observed upconversion phenomenon (Shrivastava et al. 2018a, b).

Zhang et al. (Zhang et al. 2012) used two-step synthesis protocols to prepare multicomponent and (Yb, Er) activated Fe_3O_4@SiO_2@Y_2O_3:Yb, Er magnetic upconversion oxide nanospheres (MUC-O-NS) NPs for targeted chemotherapy. They used reverse microemulsion method to prepare Fe_3O_4@SiO_2 core–shell NPs (Fig. 9.8) (Zhang et al. 2012). By carefully controlling the hydrolysis conditions, uniform iron
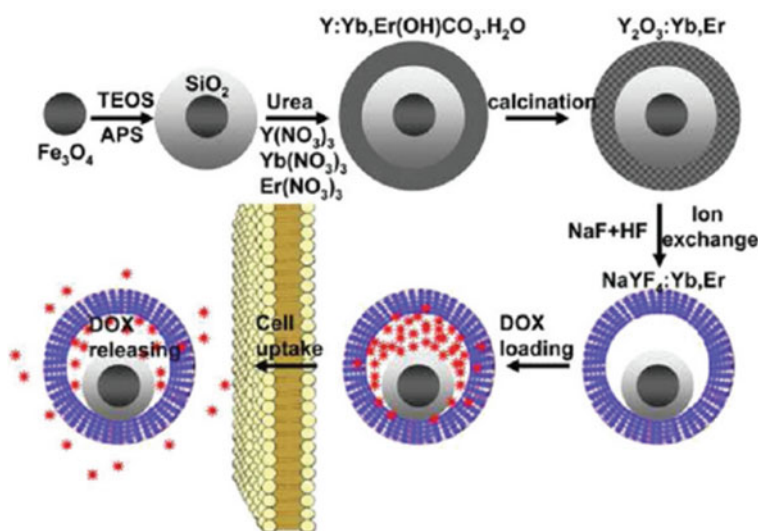
Fig. 9.8 Synthetic procedure for the drug-loaded Fe_3O_4@SiO_2@α-$NaYF_4$/Yb, Er nanorattles (DOX-MUC-F-NR). Reprinted with permission from Zhang et al. (2012). Copyright American Chemical Society 2012

oxide@SiO_2 nanoparticles were prepared with diameters of $\sim$90 nm. Further, they coated these core–shell spheres with a layer of Y/Yb, Er(OH)CO_3*$3H_2O$ via a homogeneous precipitation method from an aqueous solution of yttrium nitrate and urea and heated at 90 °C for 2 h. This by-product was treated by heat at 550 °C for 2 more hours and the layer converted into cubic Y_2O_3. To prepare fluoride nanorattles, they utilized ion-exchange process in the presence of HF and NaF solutions under continuous stirring for 2 h while heating. Size of nanospheres remained similar but surface was roughened, forming hollow nanorattles structure in broken particles (Zhang et al. 2012).

Li et al. (2007) proposed a strategy to encapsulate therapeutic drugs, magnetic Fe_3O_4 nanoparticles, and fluorescent CdTe QDs into chitosan nanoparticles. Superparamagnetic Fe_3O_4 nanoparticles allow for external manipulation of the systems by magnetic field, and CdTe QDs can be used for real-time fluorescent monitoring of drug delivery. They showed pH-sensitive drug release over a long period of time. Such NPs were prepared in water-in-oil (W/O) microemulsion. The Triton X-100 surfactant system contained 20 ml cyclohexane, ml Triton X-100, and n-hexanol. Fe_3O_4 nanoparticles, CdTe QDs, and cefradine (drug) were dispersed in 0.1% chitosan (in 1 vol% acetic acid) solution and permitted enough electrostatic adsorption. The mixed solution was added to the microemulsion system to form a transparent brown reverse microemulsion. After 30 min, 200 µl 1% glutaraldehyde was added and gently stirred. The reaction could continue for a desired time to produce magnetic and fluorescent chitosan composite nanoparticles. The composite particles were isolated by magnetic separation or by centrifugation and washed with ethanol and water repeatedly to completely remove surfactant molecules.

Zhong et al. (2012) performed first time the synthesis of monodisperse, magnetic, and upconversion luminescent Fe_3O_4@NaGdF_4:Yb/Er@NaGdF_4:Yb/Er core–shell-structured nanoparticles (NPs) by a seed-growth process (high-temperature thermolysis) to enhance the upconversion emission intensity. Oleic acid-capped Fe_3O_4 core NPs were obtained from the thermal decomposition of the iron-oleate precursors. A luminescence shell was grown using the Fe_3O_4@NaGdF_4:Yb/Er as seeds.

Xia and co-workers (2011) reported the synthesis of bifunctional magnetic upconversion NIR-to-NIR nanophosphors that are composed of NaYF_4 nanocrystals as cores and magnetic Fe_xO_y shells. Such NaYF_4:Yb^{3+}, Tm^{3+}@Fe_xO_y nanocrystals modified with dopamine showing excellent solubility in water, UCL emission, superparamagnetic properties, and low cytotoxicity. Gai et al. (2010) prepared monodisperse magnetic Fe_3O_4 nanocrystals that were coated by Stöber procedure to have a non-porous silica layer (Fe_3O_4@nSiO_2). Subsequently, cetyltrimethylammonium bromide (CTAB) was selected as the organic template for the formation of the outer mesoporous silica layer on Fe_3O_4@nSiO_2. The CTAB-removed sample was designated as Fe_3O_4@nSiO_2@mSiO_2. Finally, NaYF_4:Yb^{3+}, Er^{3+}/Tm^{3+} phosphor layer was deposited on the outer mesoporous silica layer by a modified reported process, to realize the formation of the final multifunctional (magnetic, mesoporous, and upconversion luminescent) materials.

Biomedical Applications

Bioimaging

Multimodal imaging in biomedicine is attracting increasing attention because it can integrate the advantages of different imaging modes and improve the efficiency of diagnosis and research. Photoluminescence imaging and magnetic resonance (MR) imaging are important strategies in bioscience and medicine. Photoluminescence imaging has high sensitivity, while MR imaging has good dimensional resolution. Integration of photoluminescence imaging and MR imaging in one system will combine their sensitivity and resolution and enhance the quality of bioimaging. Due to their great potential in photoluminescence and MR multimodal imaging in biomedicine, differently structured fluorescent and magnetic nanomaterials, such as embedded, dumbbell-like, linker-coupled, and core–shell structures, have recently been reported as bioimaging probes. Most of them show downconversion luminescence, which limits their applicability in deep penetration observation, particularly in small-animal in vivo imaging.

It is novel approach to use multi-component magnetic-luminescent nanohybrids for bioimaging and sensing applications. Rare earth ions in matrixes and attached with magnetic nanomaterials give hope to use a complete information at anatomy and molecular level. This facilitates to utilize the high energy radiations (X-ray or gammas) or low-energy radiations (near-infrared radiations). Magnetic entity enables the MR imaging (dark field, T2). When X-rays irradiate radioluminescence nanoparticles, they generate visible and near-infrared light that can penetrate through centimeters of tissue called X-ray luminescence tomography (XLT) maps and the location of these radioluminescent contrast agents at high resolution by scanning a narrow X-ray beam through the tissue sample. Similarly, nowadays, upconverting nanoparticles (UCNPs) can be utilized for imaging by exciting tissue samples/in vivo using 808 nm or 980 nm. Typical rare earth ions that convert low-energy radiations to visible light are Er and Tm. Coupled with low background autofluorescence offered by NIR excitation, UCNPs render particularly useful for sensing applications. To date, UCNPs have been widely exploited for sensing a variety of biological variables (temperature and pH) and species (specific ions and molecules). Temperature is crucial in biological processes including enzyme reaction and metabolism in cells. UCL is sensitive to temperature owing to some closely spaced energy levels in the emitting ions that are thermally coupled. Adding magnetic functionality to these luminescent particles would enable them to be guided, oriented, and heated using external magnetic fields, while their location and spectrum could be imaged with XLT/UCL and complementary magnetic resonance imaging. If rare earth ions have been used for light converting purposes, they are characterized by multiple and sharp emission peaks along with their defined lifetimes of the emission peaks. For example, the population in the $^4S_{3/2}$ and $^2H_{11/2}$ states of Er^{3+} approximately follows the Boltzmann distribution under steady-state excitations. The relative emission intensities of

Er3+ at 520 nm and 550 nm, which are respectively due to the $^2H_{11/2}{\rightarrow}^4I_{15/2}$ and $^4S_{3/2}{\rightarrow}^4I_{15/2}$ transitions, are thus a direct indicator of the surrounding temperature.

Xia and co-workers (2011) have reported bifunctional magnetic upconversion NIR-to-NIR nanophosphors named as $NaYF_4$:Yb^{3+}, Tm^{3+}@Fe_xO_y nanocrystals modified with dopamine, and these NPs show excellent solubility in water, UCL emission, superparamagnetic properties, and low cytotoxicity. Furthermore, these nanocrystals have been applied in multimodal T2-enhanced magnetic resonance (MR) and in vivo UCL imaging of the lymphatic system.

Chen et al. (2012) prepared a multifunctional monodispersed magnetic radioluminescent (γ-Fe_2O_3@SiO_2@Gd_2O_3:Eu) nanoparticles for potential drug delivery carriers and radioluminescence imaging agents. Particles with intermediate core sizes displayed both strong magnetophoresis and luminescence properties. They also served as MRI contrast agents with relaxivities of up to 58 mM^{-1} s^{-1} (r_2) and 120 mM^{-1} s^{-1} (r_2*). These T2 relaxivities were several times higher than typical gadolinium chelates (Gd-DTPA, 4.9 mM^{-1} s^{-1}) and Gd_2O_3 nanoparticles (14.1–16.9 mM^{-1} s^{-1}) (Bridot et al. 2007). Additionally, cell viability is not significantly affected by the Gd_2O_3:Eu nanoparticles up to concentration of at least 250 mg ml^{-1} (24 h exposure). These particles offer promising multimodal MRI/fluorescence/X-ray luminescence contrast agents.

Ge et al. (2009) prepared magnetic nanoparticles (MNPs) coated by FITC-labeled chitosan (FITC-CS) and a covalently attached fluorescent dye and applied them at in vitro experiments. The FITC-CS@MNPs could be efficiently internalized into SMMC-7721 because of their electrostatic interactions with the cell membrane. These labeled cells can be visualized in a clinical 1.5-T MRI imager with detectable cell numbers of about 104 in vitro. Magnetic fluorescent nanoparticles serve as both magnetic resonance contrast agents for MRI and optical probes for intravital fluorescence microscopy.

A very interesting approach used by Xia and co-workers (2011) integrates NIR-to-NIR UCL and magnetic dual functions in a single nanocrystal. Core–shell nanocrystals were further developed to image the lymphatic system of small animals in vivo. For in vivo UCL imaging of the lymphatic system, a nude mouse was placed in the prostrate position under pentobarbital anesthesia, and then 60 mL (1 mg/mL) of a suspension of $NaYF_4$:Yb^{3+}, Tm^{3+}@Fe_xO_y nanocrystals was injected into its right forepaw (Fig. 9.9). The special NIR-to-NIR UCL optical property of the $NaYF_4$:Yb^{3+}, Tm^{3+} core avoids the absorption of the magnetic Fe_xO_y shell and promises high signal-to-noise ratio and deep penetration for in vivo imaging, while the Fe_xO_y nanoshell makes the core–shell-structured nanocrystals suitable for T2-enhanced MR imaging. MTT assays and histological analyses of lymph have indicated low toxicity and good biocompatibility of the nanocrystals. We have also shown that $NaYF_4$:Yb^{3+}, Tm^{3+}@Fe_xO_y nanocrystals can be applied in living cell imaging by virtue of their MR and UCL bimodal imaging and long-term lymph tagging in vivo. Thereby, $NaYF_4$:Yb^{3+}, Tm^{3+}@Fe_xO_y nanocrystals may be proposed to help guide clinical lymph nodal study and diagnosis without skin surgery.
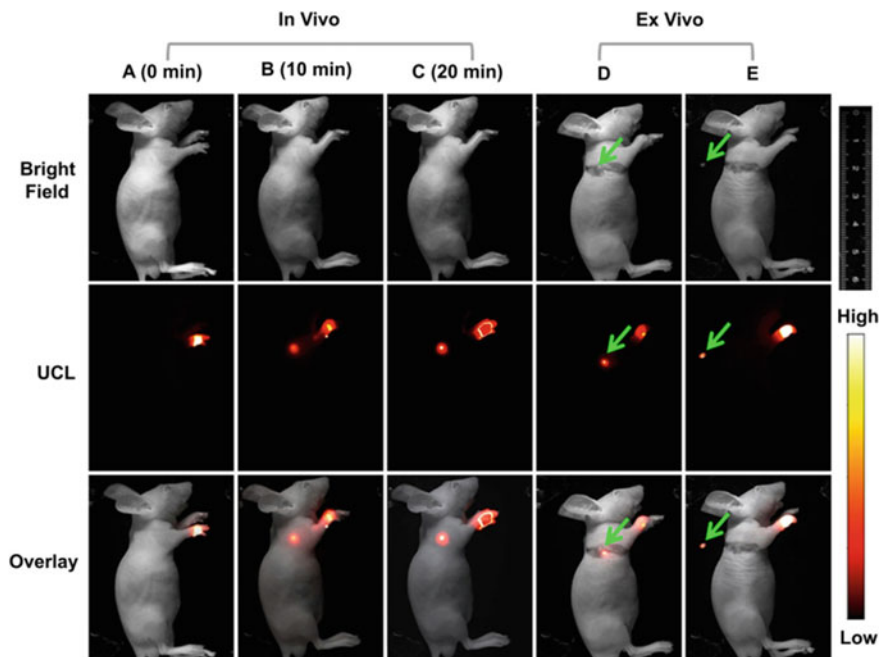
Fig. 9.9 In vivo UCL imaging of lymphatic system after injection with NaYF$_4$: Yb^{3+}, Tm^{3+}@Fe$_x$O$_y$ nanocrystals into a nude mouse at various time. **a** 0 min, **b** 10 min, and **c** 20 min. All images were acquired under the same instrumental conditions (power density w 150 mW/cm^2 on the surface of nude mouse). **d, e** UCL ex vivo images of the lymphatic system of a nude mouse killed after injection with NaYF$_4$:Yb^{3+}, Tm^{3+}@Fe$_x$O$_y$ nanocrystals for 40 min. Green arrow marked the lymphatic nodes. All images were acquired under the same instrumental conditions (power density w 100 mW/cm^2). Reprinted with permission from (Xia et al. 2011). Elsevier Publishing 2011

Drug Delivery

A need exists to be able to focus medicine to disease locations. During chemotherapy, for example, typically less than 0.1 to 1% of the drug is taken up by tumor cells, with the remaining 99% going into healthy tissue causing harms. The ability to actively position medicine, to physically direct and focus it to specific locations in the body, would allow better treatment of not only cancer but other diseases. Research into biocompatible drug delivery and targeting systems based on nanomaterials is at the forefront of nanomedicine. An ideal drug delivery system should intelligently find the diseased tissue, accumulate in this location, and controllably release therapeutic molecules to the state, just like a "magic bullet." Among the efficient drug delivery systems, biodegradable polymeric nanoparticles have been extensively developed due to their excellent biocompatibility, long-term circulation in the bloodstream, and controllable size and surface properties. To solve these problems, surface-functionalized nanoparticles that contain drug molecules have been

investigated as a promising candidate for enhancing the therapeutic effect with minimal side effects. The nanoparticles can hold drugs during the circulation without leakage. An interesting approach to increase the accumulation of nanoparticles in a target tissue is to take advantage of the magnetic responsiveness of superparamagnetic nanoparticles to an external magnetic field, which is referred to as magnetic targeting. Magnetic drug targeting refers to the attachment of therapeutics to magnetic particles, and then applying magnetic fields to concentrate them to disease locations such as to solid tumors, regions of interest. Even though in some special cases, the magnetic particles can be introduced into the body outside the blood flow. Once the nanoparticles reach the target site, they should release the therapeutic molecules. There are several distinctive characteristics (e.g., acidic pH, hypoxia, and matrix metalloproteinase-2 concentration), which can be utilized not only for targeting but also for triggering gene or drug release. The process of drug delivery is quite complex and beyond the coverage of the chapter. Light filed can also be exploited to excite the drug releases. If such mechanisms are combined together, they could be a potential candidate for drug delivery at the specified locations.

As mentioned in Sect. 4, Gai et al. (2010) reported that controlled drug release is reported for monodisperse core–shell-structured Fe_3O_4@$nSiO_2$@$mSiO_2$@$NaYF_4$:Yb^{3+}, Er^{3+}/Tm^{3+} nanocomposites with mesoporous, upconversion luminescent, and magnetic properties, capable enough for the drug targeting. Upconversion phenomenon, when excitation wavelength is 980 nm, help to release the attached drug IBU in above example. Drug release was monitored using upconversion emission intensity of the IBU–Fe_3O_4@$nSiO_2$@$mSiO_2$@$NaYF_4$:Yb^{3+}, Er^{3+}/Tm^{3+} system. The upconversion emission intensity increases with the cumulative release of IBU, reaching a maximum when the IBU is completely released from the drug storage system. Li et al. (2007) used water-soluble superparamagnetic Fe_3O_4 nanoparticles, CdTe quantum dots, and pharmaceutical drugs into chitosan nanoparticles, cross-linking the composite particles with glutaraldehyde. The system showed superparamagnetic and strong fluorescent properties and was used as a controlled drug release vehicle, which showed pH-sensitive drug release over a long time. The composite magnetic and fluorescent chitosan nanoparticles are potential candidates as a smart drug delivery system.

Other illustrations can be explained by considering the work by Zhang and co-workers (2012). They prepared nanorattles containing rare earth-doped $NaYF_4$ shells each containing a loose magnetic nanoparticle (Fig. 9.8). The innermagnetic Fe_3O_4 nanoparticles are coated with a SiO_2 layer to avoid iron leaching in acidic biological environments. This multifunctional mesoporous nanostructure with both upconversion luminescent and magnetic properties has excellent water dispersibility and a high drug-loading capacity. The material emits visible luminescence upon NIR excitation and can be directed by an external magnetic field to a specific target, making it an attractive system for a variety of biological applications. Measurements on cells incubated with the nanorattles show them to have low cytotoxicity and excellent cell imaging properties. In vivo experiments yield highly encouraging tumor shrinkage with the antitumor drug doxorubicin (DOX) and significantly enhanced

tumor targeting in the presence of an applied magnetic field. These multifunctional nanorattles show advantages for in vivo enhancement of therapy efficacy by reducing the systemic toxicity of antitumor drugs both through protection of the drug during circulation and by using magnetic fields to target the material to the lesion.

Therapy

There are mainly three categories of therapeutic applications of the magnetic-luminescent nanoparticles, which initially and largely depend on the synthesis methodologies and further on surface modifications, have in good biocompatibility, and be chemically stable to be used as nanoheaters in biomedical applications: magnetic hyperthermia and photothermal therapy; magnetic hyperthermia with light-activated enhanced photodynamic therapy; and photothermal therapy, magnetic hyperthermia, and photodynamic therapy. It must be noted that in real practices, even at laboratory scale from nanomaterials points of view, these have been a challenge. It could take a time to have convincing results that might push for clinical testings. There is not much convincing literature available based on multi-component magnetic-luminescent nanoparticles. Great efforts are ongoing to synthesize novel multifunctional nanoplatform to combine nano-magnetic hyperthermia and nano-photothermal therapy increasing the effect. Iron oxide and gold-based magneto-plasmonic nanostructures exhibit remarkable optical and magnetic properties originating from their two different components. Depending on morphology, spherical and non-spherical or core–satellite and core–shell may be used for different applications (Espinosa et al. 2016, 2018; Kolosnjaj-tabi et al. 2015; Mazuel et al. 2017; Di Corato et al. 2014). Espinosa et al. recently reported promising results of magneto-photo thermal approach, choosing iron oxide nanotubes to improve their efficiency using only magnetic hyperthermia (Espinosa et al. 2016, 2018). They compared to both an alternating magnetic field and near-infrared laser irradiation (808 nm), either individually or jointly. The obtained results in solid tumors in vivo show that single-mode treatments (magnetic or laser hyperthermia) reduced the tumor growth, while combined-mode resulted in complete tumor regression. This is not the case of our chapter. Recently, Ortigies et al. (2018) prepared optomagnetic hybrid nanostructures (OMHSs) that simultaneously satisfy magnetic-luminescent characteristics together and above-mentioned two conditions. Polymeric encapsulation of magnetic nanoparticles with neodymium-doped nanoparticles (LaF_3:Nd) results in a hybrid structure capable of sub-tissue thermal feedback while making the heating efficiency of magnetic nanoparticles independent of the medium. The potential application of the OMHSs developed for fully controlled thermal therapies is demonstrated by an ex vivo endoscope-assisted controlled intracoronary heating experiment. Still the research for combined thermal therapy is far more away from reality, where the construction and architecture of such hybrid formulation to combined therapies require the optimization of physicochemical properties to maximize their potential as nanoheaters.

Conclusions and Prospectus

We have described the developments in the synthesis and important biomedical applications of magnetic-luminescent nanoparticles. This research continues to be a vibrant and growing interdisciplinary field. The developments of new theranostics plus diagnostics (a new term "theranostic") nanoplatforms are continuously in progress with their own promises and advantages, but suffer from some weaknesses. So an effort to introduce this subject to the general audiences to understand the challenges and limitation and how can one open the doors of new possibilities. The major issue is the synthesis of the multi-component magnetic-luminescent nanoparticles that include a multi-step process. Usually, core–shell nanoparticles are prepared, but such nanoparticles compromise the magnetic-luminescent characteristics. To utilize them for theranostics, more intelligent nanosystems (encapsulations/dimers) guaranteeing of high photoluminescence efficiency optical property and strong magnetic property are required by a more simple protocol (e.g., one-pot method) to obtain the hybrid materials. There are some countable successful results, but the development of multifunctional nanoprobes for multimodal imaging is still in its early stage. It is still a major challenge to design a multifunctional nanoprobe for simultaneous bioimaging covering optical imaging, MRI, CT, and other kinds of monitoring. In near future, active targeted multimodal imaging and drug delivery system could be reality to realize the disease detection and therapy simultaneously.

References

Auzel F (2004) Upconversion and Anti-Stokes processes with f and d ions in solids. Chem Rev 104:139–174. https://doi.org/10.1021/cr020357g

Bao J, Chen W, Liu T, Zhu Y, Jin P, Wang L, Liu J, Wei Y, Li Y (2007) Bifunctional Au–Fe$_3$O$_4$ nanoparticles for protein separation. ACS Nano 1:293–298. https://doi.org/10.1021/nn700189h

Barick KC, Sharma A, Shetake NG, Ningthoujam RS, Vatsa RK, Babu PD, Pandey BN, Hassan PA (2015) Covalent bridging of surface functionalized Fe$_3$O$_4$ and YPO$_4$: Eu nanostructures for simultaneous imaging and therapy. Dalt Trans 44:14686–14696. https://doi.org/10.1039/C5DT01522G

Blandford R, Yuan Y, Hoshino M, Sironi L (2017) Magnetoluminescence. Space Sci Rev 207:291–317. https://doi.org/10.1007/s11214-017-0376-2

Boyer J, Gagnon J, Cuccia LA, Capobianco JA (2007) Synthesis, characterization, and spectroscopy of nanoparticles. Chem Mater 19:3358–3360

Bridot JL, Faure AC, Laurent S, Rivière C, Billotey C, Hiba B, Janier M, Josserand V, Coll JL, Vander Elst L, Muller R, Roux S, Perriat P, Tillement O (2007) Hybrid gadolinium oxide nanoparticles: multimodal contrast agents for in vivo imaging. J Am Chem Soc 129:5076–5084. https://doi.org/10.1021/ja068356j

Bunzli J-CG, Piguet C (2005) Taking advantage of luminescent lanthanide ions. Chem Soc Rev 34:1048–1077. https://doi.org/10.1039/b406082m

Camarero J, Perna P, Bollero A, Teran FJ, Miranda R (2016) Role of magnetic anisotropy in magnetic nanostructures: from spintronic to biomedical applications 104:202407

Chander H (2005) Development of nanophosphors—a review. Mater Sci Eng R Rep 49:113–155. https://doi.org/10.1016/j.mser.2005.06.001

Chem JM, Chekina N, Hor D, Jendelov P, Horák D, Jendelová P, Trchová M, Beneš MJ, Hrubý M, Herynek V, Turnovcová K, Syková E (2011) Fluorescent magnetic nanoparticles for biomedical applications. J Mater Chem 21:7630. https://doi.org/10.1039/c1jm10621j

Chen G, Ohulchanskyy TY, Liu S, Law WC, Wu F, Swihart MT, Ågren H, Prasad PN (2012a) Core/shell $NaGdF_4:Nd_{3+}/NaGdF_4$ nanocrystals with efficient near-infrared to near-infrared downconversion photoluminescence for bioimaging applications. ACS Nano 6:2969–2977. https://doi.org/10.1021/nn2042362

Chen H, Colvin DC, Qi B, Moore T, He J, Mefford OT, Alexis F, Gore JC, Anker JN (2012b) Magnetic and optical properties of multifunctional core-shell radioluminescence nanoparticles. J Mater Chem 22:12802–12809. https://doi.org/10.1039/C2JM15444G

Chen X, Liu Y, Tu D (2014) Lanthanide-doped luminescent nanomaterials. doi: 10.1007/978-3-642-40364-4

Chen G, Agren H, Ohulchanskyy TY, Prasad PN, Ågren H, Ohulchanskyy Y, Prasad PN, Agren H, Ohulchanskyy TY, Prasad PN (2015) Light upconverting core-shell nanostructures: nanophotonic control for emerging applications. Chem Soc Rev 44:1680–1713. https://doi.org/10.1039/C4CS00170B

Choi J, Jun Y, Yeon S-I, Kim HC, Shin J-S, Cheon J (2006) Biocompatible heterostructured nanoparticles for multimodal biological detection. J Am Chem Soc 128:15982–15983. https://doi.org/10.1021/ja066547g

Comby S, Surender EM, Kotova O, Truman LK, Molloy JK, Gunnlaugsson T (2014) Lanthanide-functionalized nanoparticles as MRI and luminescent probes for sensing and/or imaging applications. Inorg Chem 53:1867–1879. https://doi.org/10.1021/ic4023568

Di Corato R, Espinosa A, Lartigue L, Tharaud M, Chat S, Pellegrino T, Ménager C, Gazeau F, Wilhelm C (2014) Magnetic hyperthermia efficiency in the cellular environment for different nanoparticle designs. Biomaterials 35:6400–6411. https://doi.org/10.1016/j.biomaterials.2014.04.036

Dong C, Pichaandi J, Regier T, Van Veggel FCJM (2011) Nonstatistical dopant distribution of Ln 3 + -doped NaGdF 4 nanoparticles. J Phys Chem C 115:15950–15958

Dong H, Du S-RR, Zheng XY, Lyu G-MM, Sun L-DD, Li L-DD, Zhang P-ZZ, Zhang C, Yan C-HH (2015) Lanthanide nanoparticles: from design toward bioimaging and therapy. Chem Rev 115:10725–10815. https://doi.org/10.1021/acs.chemrev.5b00091

Du GH, Liu ZL, Lu QH, Xia X, Jia LH, Yao KL, Chu Q, Zhang SM (2006) Fe_3O_4/CdSe/ZnS magnetic fluorescent bifunctional nanocomposites. Nanotechnology 17:2850–2854. https://doi.org/10.1088/0957-4484/17/12/004

Espinosa A, Di Corato R, Kolosnjaj-Tabi J, Flaud P, Pellegrino T, Wilhelm C (2016) Duality of iron oxide nanoparticles in cancer therapy: amplification of heating efficiency by magnetic hyperthermia and photothermal bimodal treatment. ACS Nano 10:2436–2446. https://doi.org/10.1021/acsnano.5b07249

Espinosa A, Kolosnjaj-Tabi J, Abou-Hassan A, Plan Sangnier A, Curcio A, Silva AKA, Di Corato R, Neveu S, Pellegrino T, Liz-Marzán LM, Wilhelm C (2018) Magnetic (Hyper)Thermia or photothermia? Progressive comparison of iron oxide and gold nanoparticles heating in water, in cells, and in vivo, Adv Funct Mater 28:1803660. https://doi.org/10.1002/adfm.201803660

Fang J, Saunders M, Guo Y, Lu G, Raston CL, Iyer KS (2010) Green light-emitting LaPO4:Ce3+:Tb3+ koosh nanoballs assembled by p-sulfonato-calix[6]arene coated superparamagnetic Fe3O4. Chem Commun 46:3074. https://doi.org/10.1039/c001098g

Gai S, Yang P, Li C, Wang W, Dai Y, Niu N, Lin J (2010) Synthesis of magnetic, up-conversion luminescent, and mesoporous core-shell-structured nanocomposites as drug carriers. Adv Funct Mater 20:1166–1172. https://doi.org/10.1002/adfm.200902274

Gao X, O'Donnell M (2017) Method and system for background suppression in magneto-motive photoacoustic imaging of magnetic contrast agents. http://www.google.ch/patents/US8701471. Accessed 5 Nov 2017

Gao J, Gu H, Xu B (2009) Multifunctional magnetic nanoparticles: design, synthesis, and biomedical applications. Acc Chem Res 42:1097–1107. https://doi.org/10.1021/ar9000026

Ge S, Shi X, Sun K, Li C, Uher C, Baker JR, Banaszak Holl MM, Orr BG (2009) Facile hydrothermal synthesis of iron oxide nanoparticles with tunable magnetic properties. J Phys Chem C 113:13593–13599. https://doi.org/10.1021/jp902953t

Ge Y, Zhang Y, He S, Nie F, Teng G, Gu N (2009b) Fluorescence modified chitosan-coated magnetic nanoparticles for high-efficient cellular imaging. Nanoscale Res Lett 4:287–295. https://doi.org/10.1007/s11671-008-9239-9

Haun TJ, Yoon H, Lee R, Weissleder JB (2010) Magnetic nanoparticle biosensors. Magnetic nanoparticle biosensors. Wiley Interdiscip Rev Nanomed Nanobiotechnol 2:291–304. https://doi.org/10.1002/wnan.84

He H, Xie MY, Ding Y, Yu XF (2009) Synthesis of Fe3O4@LaF3:Ce, Tb nanocomposites with bright fluorescence and strong magnetism. Appl Surf Sci 255:4623–4626. https://doi.org/10.1016/j.apsusc.2008.11.086

Howes PD, Chandrawati R, Stevens MM (2014) Colloidal nanoparticles as advanced biological sensors. Science 346:1247390. https://doi.org/10.1126/science.1247390

Jie G, Yuan J (2012) Novel magnetic Fe3O4@CdSe composite quantum dot-based electrochemiluminescence detection of thrombin by a multiple DNA cycle amplification strategy. Anal Chem 84:2811–2817. https://doi.org/10.1021/ac203261x

Joseph LK, Dayas KR, Damodar S, Krishnan B, Krishnankutty K, Nampoori VPN, Radhakrishnan P (2008) Photoluminescence studies on rare earth titanates prepared by self-propagating high temperature synthesis method. Spectrochim Acta—Part A Mol Biomol Spectrosc 71:1281–1285. https://doi.org/10.1016/j.saa.2008.03.030

Kaewsaneha C, Tangboriboonrat P, Polpanich D, Elaissari A (2015) Multifunctional fluorescent-magnetic polymeric colloidal particles: preparations and bioanalytical applications. ACS Appl Mater Interfaces 7:23373–23386. https://doi.org/10.1021/acsami.5b07515

Kas R, Sevinc E, Topal U, Acar HY (2010) A universal method for the preparation of magnetic and luminescent hybrid nanoparticles. J Phys Chem C 114:7758–7766. https://doi.org/10.1021/jp100312e

Kell AJ, Barnes ML, Jakubek ZJ, Simard B (2011) Toward brighter hybrid magnetic-luminescent nanoparticles: luminosity dependence on the excited state properties of embedded dyes. J Phys Chem C 115:18412–18421. https://doi.org/10.1021/jp203239z

Khan LU, Khan ZU (2017) Bifunctional nanomaterials: magnetism, luminescence and multimodal biomedical applications. In: Complex magnetic nanostructures. Springer International Publishing, Cham, pp 121–171. https://doi.org/10.1007/978-3-319-52087-2_4

Khan LU, Brito HF, Holsa J, Pirota KR, Muraca D, Felinto MCFC, Teotonio EES, Malta OL (2014) Red-green emitting and superparamagnetic nanomarkers containing Fe₃O₄ functionalized with calixarene and rare earth complexes. Inorg Chem 53:12902–12910. https://doi.org/10.1021/ic5018856

Kharissova OV, Kharisov BI, Jiménez-Pérez VM, Muñoz Flores B, Ortiz Méndez U (2013) Ultra-small particles and nanocomposites: state of the art. RSC Adv 3:22648. https://doi.org/10.1039/c3ra43418d

Kolosnjaj-tabi j, Espinosa A, Cle O, Di Corato R, Wilhelm C, Silva AKA, Me C, Corato DI, Al ET (2015) Combining magnetic hyperthermia and photodynamic therapy for tumor ablation with photoresponsive magnetic liposomes 2904–2916. https://doi.org/10.1021/nn506949t

Kuo CT, Peng HS, Rong Y, Yu J, Sun W, Fujimoto B, Chiu DT (2017) Optically encoded semiconducting polymer dots with single-wavelength excitation for barcoding and tracking of single cells. Anal Chem 89:6232–6238. https://doi.org/10.1021/acs.analchem.7b01214

Laurent S, Forge D, Port M, Roch A, Robic C, Vander Elst L, Muller RN, Vander Elst L, Muller RN (2008) Magnetic iron oxide nanoparticles: synthesis, stabilization, vectorization, physicochemical

characterizations, and biological applications (vol 108, pg 2064), Chem Rev 108:2064–2110. doi: 10.1021/Cr900197g

Li L, Chen D, Zhang Y, Deng Z, Ren X, Meng X, Tang F, Ren J, Zhang L (2007) Magnetic and fluorescent multifunctional chitosan nanoparticles as a smart drug delivery system. Nanotechnology 18. https://doi.org/10.1088/0957-4484/18/40/405102

Li X, Zhao D, Zhang F (2013) Multifunctional upconversion-magnetic hybrid nanostructured materials: synthesis and bioapplications. Theranostics 3:292–305. https://doi.org/10.7150/thno.5289

Li J, Arnal B, Wei C-W, Shang J, Nguyen T-M, O'Donnell M, Gao X (2015) Magneto-optical nanoparticles for cyclic magnetomotive photoacoustic imaging. ACS Nano 9:1964–1976. https://doi.org/10.1021/nn5069258

Ling D, Lee N, Hyeon T (2015) Chemical synthesis and assembly of uniformly sized iron oxide nanoparticles for medical applications. Acc Chem Res 48:1276–1285. https://doi.org/10.1021/acs.accounts.5b00038

Liu Y, Wang D, Shi J, Peng Q, Li Y (2013a) Magnetic tuning of upconversion luminescence in lanthanide-doped bifunctional nanocrystals. Angew Chemie—Int Ed 52:4366–4369. https://doi.org/10.1002/anie.201209884

Liu C, Gao Z, Zeng J, Hou Y, Fang F, Li Y, Qiao R, Shen L, Lei H, Yang W, Gao M (2013b) Magnetic/upconversion fluorescent dual-modal molecular probes for imaging tiny tumors in vivo. ACS Nano 7:7227–7240. https://doi.org/10.1021/nn4030898

Liz-Marzán LM, Kamat PV (2003) Nanoscale materials. In: Nanoscale materials. Kluwer Academic Publishers, Boston, pp 1–3. https://doi.org/10.1007/0-306-48108-1_1

Mazuel F, Espinosa A, Radtke G, Bugnet M, Neveu S, Lalatonne Y, Botton GA, Abou-hassan A, Wilhelm C (2017) Magneto-thermal metrics can mirror the long-term intracellular fate of magneto-plasmonic nanohybrids and reveal the remarkable shielding effect of gold, 201605997 (2017). https://doi.org/10.1002/adfm.201605997

Mi C, Gao H, Li F, Xu S (2012) Colloids and surfaces a : physicochemical and engineering aspects synthesis of surface amino-functionalized NaGdF4: Ce, Tb nanoparticles and their luminescence resonance energy transfer (LRET) with Au nanoparticles. Colloids Surf A Physicochem Eng Asp 395:152–156. https://doi.org/10.1016/j.colsurfa.2011.12.022

Mikhaylova M, Kim DKDK, Bobrysheva N, Osmolowsky M, Semenov V, Tsakalakos T, Muhammed M, Tetal T, Tsakalakos T, Muhammed M (2004) Superparamagnetism of magnetite nanoparticles: dependence on surface modification. Langmuir 20:2472–2477. http://www.ncbi.nlm.nih.gov/pubmed/15835712. Accessed 3 Dec 2017

Muhr V, Wilhelm S, Hirsch T, Wolfbeis OS (2014) Upconversion nanoparticles: from hydrophobic to hydrophilic surfaces. Acc Chem Res 47:3481–3493. https://doi.org/10.1021/ar500253g

Murray CB, Kagan CR, Bawendi MG (2000) Synthesis and characterization of monodisperse nanocrystals and close-packed nanocrystal assemblies. Annu Rev Mater Sci 30:545–610. https://doi.org/10.1146/annurev.matsci.30.1.545

Natarajan Prakash RK , Dheivasigamani Thangaraju YS, Mukannan Arivanandhan YH (2016) UV-visible and near-infrared active $NaGdF_4$:Yb:Er/Ag/TiO_2 nanocomposite for enhanced photocatalytic applications. RSC Adv 6:26770–26775. https://doi.org/10.1039/c7ra03380j

Nguyen T-D, Tran T-H (2014) Multicomponent nanoarchitectures for the design of optical sensing and diagnostic tools. RSC Adv 4:916–942. https://doi.org/10.1039/c3ra44056g

Ortgies DH, Teran FJ, Rocha U, de la Cueva L, Salas G, Cabrera D, Vanetsev AS, Rähn M, Sammelselg V, Orlovskii YV, Jaque D, De Cueva L, Salas G, Cabrera D, Vanetsev AS, Rähn M, Sammelselg V, Orlovskii YV, Jaque D (2018) Optomagnetic nanoplatforms for in situ controlled hyperthermia. Adv Funct Mater 1704434:1704434. https://doi.org/10.1002/adfm.201704434

Peng H, Liu G, Dong X, Wang J, Xu J, Yu W (2011) Preparation and characteristics of Fe3O4@YVO4:Eu3+ bifunctional magnetic–luminescent nanocomposites. J. Alloys Compd 509:6930–6934. https://doi.org/10.1016/j.jallcom.2011.04.004

Peng D, Ju Q, Chen X, Ma R, Chen B, Bai G, Hao J, Qiao X, Fan X, Wang F (2015) Lanthanide-doped energy cascade nanoparticles: full spectrum emission by single wavelength excitation. Chem Mater 27:3115–3120. https://doi.org/10.1021/acs.chemmater.5b00775

Prasad PN (2004) Nanophotonics. Wiley, New York

Rao CNR, Ramakrishna Matte HSS, Voggu R, Govindaraj A (2012) Recent progress in the synthesis of inorganic nanoparticles. Dalt Trans 41:5089–5120. https://doi.org/10.1039/c2dt12266a

Ren J, Jia G, Guo Y, Wang A, Xu S (2016) Unraveling morphology and phase control of NaLnF$_4$ upconverting nanocrystals. J Phys Chem C 120:1342–1351. https://doi.org/10.1021/acs.jpcc.5b11048

Sankar K, Plumley JB, Akins Ba, Memon Ta, Withers NJ, Smolyakov Ga, Osinski M, Osi M (2009) Synthesis and characterization of scintillating cerium-doped lanthanum fluoride nanocrystals 7189:718909. https://doi.org/10.1117/12.816894

Sarveena, Shrivastava N, Singh M, Sharma SK (2017) Multifunctional magnetic nanostructures: exchange bias model and applications. In: Complex magnetic nanostructures. Springer International Publishing, Cham, pp 225–280. https://doi.org/10.1007/978-3-319-52087-2_7

Schneider L, Rinkel T, Voß B, Chrobak A, Klare JP, Neethling J, Olivier J, Schaniel D, Bendeif E, Bondino F, Magnano E, Balinski K (2016) Characterization of multifunctional β-NaEuF$_4$/NaGdF$_4$ core–shell nanoparticles with narrow size distribution. Nanoscale 8:2832–2843. https://doi.org/10.1039/c5nr06915g

Sharma SK (2017) Complex magnetic nanostructures: synthesis, assembly and applications. Springer International Publishing, Cham

Shen J, Sun L-D, Zhang Y-W, Yan C-H (2010) Superparamagnetic and upconversion emitting Fe$_3$O$_4$/NaYF$_4$:Yb, Er hetero-nanoparticles via a crosslinker anchoring strategy. Chem Commun 46:5731. https://doi.org/10.1039/c0cc00814a

Shrivastava N, Khan LU, Vargas JM, Ospina C, Coaquira JAQ, Zoppellaro G, Brito HF, Javed Y, Shukla DK, Felinto MCFC, Sharma SK (2017a) Efficient multicolor tunability of ultrasmall ternary-doped LaF$_3$ nanoparticles: energy conversion and magnetic behavior. Phys Chem Chem Phys 19:18660–18670. https://doi.org/10.1039/C7CP02235B

Shrivastava N, Khan LU, Khan ZU, Vargas JM, Moscoso-Londoño O, Ospina C, Brito HF, Javed Y, Felinto MCFC, Menezes AS, Knobel M, Sharma SK, de Menezes AS, Knobel M, Sharma SK (2017b) Building block magneto-luminescent nanomaterials of iron-oxide/ZnS@LaF3:Ce3+, Gd3+, Tb3+ with green emission. J Mater Chem C 5:2282–2290. https://doi.org/10.1039/C6TC05053K

Shrivastava N, Rocha U, Muraca D, Silva W, Jacinto C, Kumar R, Sharma SK (2018a) Insight into dual-modality of triply doped magnetic-luminescent iron-oxide/NaGdF4:RE3+(RE = Ce, Tb, Dy) nanoparticles. Mater Lett 213:358–361. https://doi.org/10.1016/j.matlet.2017.11.037

Shrivastava N, Rocha U, Muraca D, Jacinto C, Moreno S, Vargas JM, Sharma SK (2018b) Magnetic upconverting fluorescent NaGdF4:Ln3+ and iron-oxide@NaGdF4:Ln3+ nanoparticles. AIP Adv 8:056710. https://doi.org/10.1063/1.5007748

Singh RK, Patel KD, Kim J-J, Kim T-H, Kim J-H, Shin US, Lee E-J, Knowles JC, Kim H-W (2014) Multifunctional hybrid nanocarrier: magnetic CNTs ensheathed with mesoporous silica for drug delivery and imaging system. ACS Appl Mater Interfaces 6:2201–2208. https://doi.org/10.1021/am4056936

Srinivasan M, Rajabi M, Mousa SA (2015) Multifunctional nanomaterials and their applications in drug delivery and cancer therapy. Nanomaterials (Basel, Switzerland) 5:1690–1703. https://doi.org/10.3390/nano5041690

Su C (2017) Environmental implications and applications of engineered nanoscale magnetite and its hybrid nanocomposites: a review of recent literature. J Hazard Mater 322. https://doi.org/10.1016/j.jhazmat.2016.06.060

Sudheendra L, Das GK, Li C, Stark D, Cena J, Cherry S, Kennedy IM (2014) NaGdF 4 :Eu 3+ nanoparticles for enhanced X-ray excited optical imaging

Sun L, Qiu Y, Liu T, Peng H, Deng W, Wang Z, Shi L (2013) Visible-light sensitized sol-gel-based lanthanide complexes (Sm, Yb, Nd, Er, Pr, Ho, Tm): microstructure, photoluminescence study, and thermostability. RSC Adv 3:26367–26375. https://doi.org/10.1039/c3ra45202f

Sun L, Wang Z, Zhang JZ, Feng J, Liu J, Zhao Y, Shi L (2014) Visible and near-infrared luminescent mesoporous titania microspheres functionalized with lanthanide complexes: microstructure and luminescence with visible excitation. RSC Adv 4:28481–28489. https://doi.org/10.1039/c4ra03781b

van Wijngaarden A, Scheidelaar JT, Vlugt S, Reid TJH, Meijerink MF, Vlugt TJH, Reid MF, Meijerink A (2010) Energy transfer mechanism for downconversion in the (Pr^{3+}, Yb^{3+}) couple. Published for the American Physical Society by the American Institute of Physics. https://dspace.library.uu.nl/handle/1874/202777. Accessed 4 Dec 2017

Wang D, He J, Rosenzweig N, Rosenzweig Z (2004) Superparamagnetic Fe_2O_3 beads−CdSe/ZnS quantum dots core−shell nanocomposite particles for cell separation. Nano Lett 4:409–413. https://doi.org/10.1021/nl035010n

Wang G, Peng Q, Li Y (2011) Lanthanide-doped nanocrystals: synthesis, optical-magnetic properties, and applications. Acc Chem Res 44:322–332. https://doi.org/10.1021/ar100129p

Wang F, Deng R, Liu X (2014) Preparation of core-shell NaGdF4 nanoparticles doped with luminescent lanthanide ions to be used as upconversion-based probes. Nat Protoc 9:1634–1644. https://doi.org/10.1038/nprot.2014.111

Wu W, He Q, Jiang C (2008) Magnetic iron oxide nanoparticles: synthesis and surface functionalization strategies. Nanoscale Res Lett 3:397–415. https://doi.org/10.1007/s11671-008-9174-9

Wu T, Pan H, Chen R, Luo D, Zhang H, Shen Y, Li Y, Wang L (2016) Effect of solution pH value changes on fluorescence intensity of magnetic-luminescent $Fe_3O_4@Gd_2O_3:Eu^{3+}$ nanoparticles. J Rare Earths 34:71–76. https://doi.org/10.1016/S1002-0721(14)60581-0

Xia A, Gao Y, Zhou J, Li C, Yang T, Wu D, Wu L, Li F (2011) Core-shell NaYF4:Yb^{3+}, $Tm^{3+}@Fe_xO_y$ nanocrystals for dual-modality T2-enhanced magnetic resonance and NIR-to-NIR upconversion luminescent imaging of small-animal lymphatic node. Biomaterials 32:7200–7208. https://doi.org/10.1016/j.biomaterials.2011.05.094

Yadav R, Singh SK, Verma RK, Rai SB (2014) Observation of multi-mode: Upconversion, down-shifting and quantum-cutting emission in Tm^{3+}/Yb^{3+} co-doped Y_2O_3 phosphor. Chem Phys Lett 599:122–126. https://doi.org/10.1016/J.CPLETT.2014.03.025

Yang C-T, Chuang K-H (2012) Gd(iii) chelates for MRI contrast agents: from high relaxivity to "smart", from blood pool to blood–brain barrier permeable, Medchemcomm 3. https://doi.org/10.1039/c2md00279e

Yi G, Chow G-M (2007) Water-soluble NaYF4:Yb, Er(Tm)/NaYF4/polymer core/shell/shell nanoparticles with significant enhancement of upconversion fluorescence. Chem Mater 19:341–343. https://doi.org/10.1021/cm062447y

Yu S-Y, Zhang H-J, Yu J-B, Wang C, Sun L-N, Shi W-D (2007) Bifunctional magnetic−optical nanocomposites: grafting lanthanide complex onto core−shell magnetic silica nanoarchitecture. Langmuir 23:7836–7840. https://doi.org/10.1021/la700735m

Yu X, Wan J, Shan Y, Chen K, Han X (2009) A facile approach to fabrication of bifunctional magnetic-optical $Fe_3O_4@ZnS$ microspheres. Chem Mater 21:4892–4898. https://doi.org/10.1021/cm902667b

Zhang F, Braun GB, Pallaoro A, Zhang Y, Shi Y, Cui D, Moskovits M, Zhao D, Stucky GD (2012) Mesoporous multifunctional upconversion luminescent and magnetic "nanorattle" materials for targeted chemotherapy. Nano Lett 12:61–67. https://doi.org/10.1021/nl202949y

Zhang L, Dong W-F, Sun H-B (2013) Multifunctional superparamagnetic iron oxide nanoparticles: design, synthesis and biomedical photonic applications. Nanoscale 5:7664–7684. https://doi.org/10.1039/c3nr01616a

Zhang Y, Xiao Q, He H, Zhang J, Dong G, Han J, Qiu J (2015) Simultaneous luminescence modulation and magnetic field detection via magneto-optical response of Eu3+-doped NaGdF$_4$ nanocrystals. J Mater Chem C 3:10140–10145. https://doi.org/10.1039/C5TC02364E

Zhong C, Yang P, Li X, Li C, Wang D, Gai S, Lin J (2012) Monodisperse bifunctional Fe3O4@NaGdF4:Yb/Er@NaGdF4:Yb/Er core–shell nanoparticles. RSC Adv 2:3194. https://doi.org/10.1039/c2ra20070h

Chapter 10
Evaluation of Hyperthermic Properties of Magnetic Nano-Heterostructures Based on Gold-Iron Oxide and Noble Metal-Ferrite Systems

Sarveena, Navadeep Shrivastava, Naveed A. Shad, Muhammad Munir Sajid, M. Singh, Yasir Javed and S. K. Sharma

Abstract Magnetic particle hyperthermia is potentially the most significant and promising methods for cancer treatment. The high efficiency of this magnetic hyperthermia therapy is derived from a capability of nano-heterostructures to generate site-specific heating of tumors tissues due to their unique physicochemical properties with an ability to be functionalized at molecular and cellular level for biochemical interactions. Au-Fe_3O_4 nano-heterostructures are gaining ample significance in industry and research because of their superior properties coming from both individual and combinational features of gold and iron oxide nanoparticles. In this chapter, we have discussed the heat dissipation mechanisms and various parameters crucial for assessing the hyperthermia efficacy of gold-iron oxide and noble metal-ferrite systems.

Keywords Magnetic particle hyperthermia · Nano-heterostructures · Specific absorption rate · Cytotoxicity

Sarveena (✉)
Alakh Prakash Goyal Shimla University, Shimla, Himachal Pradesh 171009, India
e-mail: sarveenahp@gmail.com

N. Shrivastava
Département de Chimie Biochimie et Physique, Université du Québec á Trois-Rivières, Trois-Rivières, QC, Canada

N. A. Shad · M. M. Sajid
Department of Physics, Government College University Faisalabad, Faisalabad, Pakistan

M. Singh
Department of Physics, Himachal Pradesh University, Shimla, Himachal Pradesh 171005, India

Y. Javed
Magnetic Materials Laboratory, Department of Physics, University of Agriculture Faisalabad, University Main Rd, Faisalabad 38000, Pakistan

S. K. Sharma (✉)
Department of Physics, Faculty of Science and Technology, The University of the West Indies, St. Augustine, Trinidad and Tobago
e-mail: surender.sharma@uwi.sta.edu

Introduction

Magnetic hyperthermia is an antitumoral therapy using magnetic nanoparticles (MNPs) to heat tumor cells above normal physiological conditions under the influence of an alternating magnetic field (AMF). It is based on the biological principle that normal cells usually possess higher heat resistance and resilience to temperature than tumor cells, and the cancerous cells can be selectively destroyed by increasing the temperature to a desired temperature range (41–46 °C), without damaging the surrounding healthy tissue (Yu et al. 2020). The use of magnetic hyperthermia to achieve spatially localized tumor heating as an adjunct to cancer immunotherapy both in vitro and in vivo is supported by an increasing number of research data.

In recent years, advances in the use of magnetic hyperthermia have led to overcome the multitude of side effects like discomfort to the development of secondary tumors and severe toxicity to multiple systems including immune system associated with the standard cancer treatments like chemotherapy, radiotherapy, or their combination (Lettieri-Barbato and Aquilano 2018). The additional feature of controlled drug delivery opens up possibilities for the development of multifunctional and multi-therapeutic approaches for treating a number of diseases.

The heating efficiency of MNPs relies on external characteristics (e.g., frequency and amplitude of the applied field) as well as intrinsic particle characteristics (e.g., core size, surface chemistry, crystallinity, colloidal) (Lemal et al. 2019). The special properties of MNPs arise from their structure, size, and composition. The amount of heat generated strongly depends on the spatial distribution of the nanoparticles, size, coating, magnetic field strength and frequency, etc., and the most commonly used materials (LeBrun and Zhu 2018). Therefore, the use of nanoparticles in this treatment is also a concern. For cancer therapy, NPs must have a low toxicity, biocompatibility, non-immunogenic, ease of functionalization, cell acceptance and, essentially, able to make effective heating profiles when exposed to an applied magnetic field. The fundamentals of MNPs for cancer therapy lies in the four unique characteristics: magnetic manipulation, nanoscale heat generator, localized magnetic field, and enzyme-mimics with abundant active sites (Zhang et al. 2018; Negut and Grumezescu 2019). The successful applications of cancer therapy lie in smart design of the nanoparticle with tailoring properties for safer and more effective cancer treatment. Among all materials, noble and magnetic metals are two groups of the most promising materials which can be coupled together to yield diversified nanostructures, including noble metal decorated-metal oxide NPs, nanoarrays, noble metal/metal oxide core/shell, noble metal/metal oxide yolk/shell, and Janus noble metal–metal oxide nanostructures (Sanchez and Alvarez 2019). In this context, iron oxide-based nanocomposites are typically used for hyperthermia treatment (Gutiérrez and Alvarez 2018; Kozissnik et al. 2013).

Heat Generation Mechanism

When magnetic materials are placed in a tuned AMF, the heat is dissipated in the form of thermal energy. Magnetic particles heat inductively due to magnetic losses associated with their magnetization reversal processes. The three main mechanisms responsible for these losses are: eddy current, hysteresis, and relaxation. The more relevant mechanism of heat dissipation to nanoparticles is relaxation mechanisms, i.e., Néel and Brownian relaxation mechanisms. Relative portion of each mechanism is mainly determined by size, magnetic anisotropy, and fluid viscosity (Shaterabadi et al. 2018). Magnetic losses are the main physical phenomena involved in magnetic hyperthermia treatments to target and kill cancerous cells.

Eddy Current Losses

The generation of eddy currents is a consequence of the law of induction. Heating occurs due to the induced currents which are the flows of electrons against the electrical resistance of the material (Suriyanto et al. 2017). This opposing tendency of the eddy current causes energy loss. The power density for eddy current heating is given by Gilchrist et al. (1957);

$$P_{\mathrm{E}} = E f^2 B_{\mathrm{max}}^2 d^2 \tag{10.1}$$

where E = eddy current coefficient, f = frequency in cycles, B_{max} = maximum flux density, and d = particle diameter.

This equation shows that current losses will rise as we increase the frequency or applied field and particle diameter. Eddy currents are induced mostly by bigger particles (a few millimeters in size), and their contribution to heat generation is negligible in nano-sized materials. Magnetic nanoparticles have a rather poor electrical conductivity to produce a noticeable induction heating and the nano-sized dimension of particles cannot generate a substantial electrical voltage (Suriyanto et al. 2017; Javed et al. 2017).

Eddy currents are not only restricted to magnetic materials it also occurs in tissues owing to their low specific electrical conductivity, but their heating effect is far below the required therapeutic dose. Eddy current losses can cause unwanted temperature rise in healthy tissues in high frequencies, depending on the electrical conductivity of the tissue. These eddy currents have been shown to limit treatment efficacy in clinical trials (Stigliano et al. 2016). The reported side effects of eddy currents in the body are limited to disturb the patient comfort and cause pain and damage (blistering) in skin (Dabbagh et al. 2015).

Hysteresis Loss

In multi-domain NPs (ferrimagnetic or ferromagnetic material), the production of heat is due to hysteresis losses. When they are exposed to an applied magnetic field, some magnetic domains containing moments parallel to the magnetic field will grow, whereas the others shrink, so long as all of moments align themselves in the same direction as the applied magnetic field. The saturation magnetization is reached as soon as each moment of each domain is aligned toward this direction. When the applied field is removed, the magnetization does not revert back to zero, and this is the remanent magnetization. In order to demagnetize, the coercive field is applied. This sequence of magnetization and demagnetization is usually represented in the form of a nonlinear curve called a hysteresis loop. Hysteresis losses may be determined by integrating the area of hysteresis loops, a measure of energy dissipated per cycle of magnetization (Javed et al. 2017; Sangaa et al. 2018) as shown in Fig. 10.1.
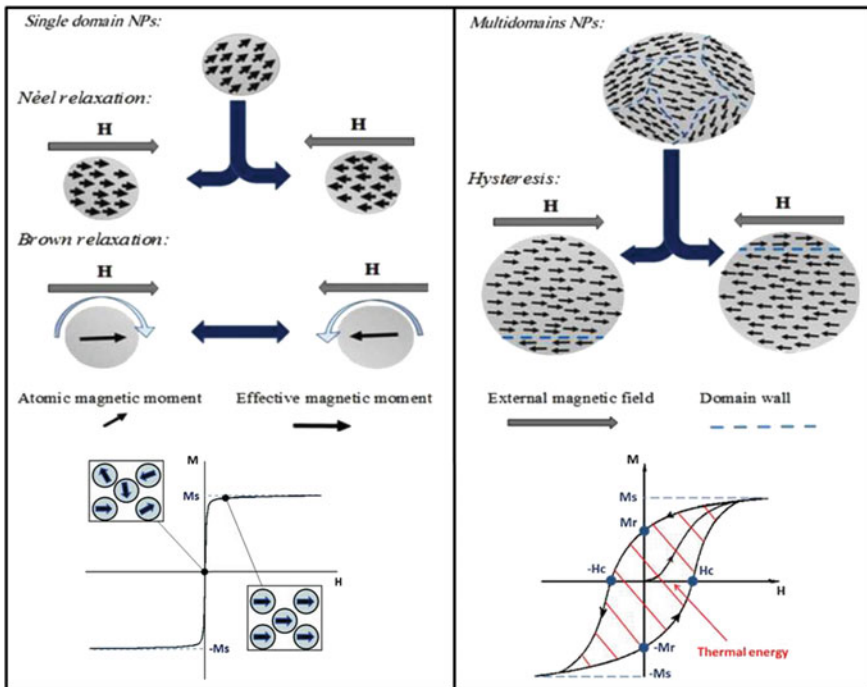
Fig. 10.1 Different heat dissipation mechanism. Reprinted with the permission from Beik et al. (2016) and Hervault and Thanh (2014)

Néel and Brownian Relaxation Mechanisms

In single-domain MNPs, where no domain wall exists at all, the reorientation of the magnetic moments can occur due to (i) the rotation of the moment within the MNP, overcoming their anisotropy energy barrier (Néel relaxation) or (ii) the mechanical rotation of the MNPs that will create frictional losses with the environment (Brownian relaxation) (Colombo et al. 2012). In such particles, heating is accomplished by rotating the magnetic moment of each particle against an energy barrier. It is primarily observed in superparamagnetic, single-domain nanoparticles.

Neel relaxation mechanism: When superparamagnetic nanoparticles are subjected to an alternating magnetic field, the individual magnetic moment rotates away from the crystal axis toward the field to minimize its potential energy but it does not necessarily involve a physical rotation of every particle (Fig. 10.1). The anisotropy energy barrier is overcome and the remaining energy is released as heat (LeBrun and Zhu 2018). These fluctuations in the magnetization occur at a specific time, called the relaxation time τ_N and its temperature dependence was proposed by Louis Néel. These fluctuations develop above a certain critical temperature T_B. Below T_B, spin blocks are assumed to be fixed. Consequently, T_B is called the blocking temperature and suggests the superparamagnetic limit for steady magnetization. The time period of fluctuations can alter by changing the temperature and volume of a particle. The Néel (τ_N) relaxation times of a particle are given by LeBrun and Zhu (2018) and Javed et al. (2017)

$$\tau_N = \frac{\sqrt{\pi}}{2} \tau_0 \frac{e^\Gamma}{\sqrt{\Gamma}} \qquad (10.2)$$

where

$$\Gamma = \frac{K_\mu V_M}{k_B T} \qquad (10.3)$$

Here, τ_0 is the attempt time (typically between 10^{-9} and 10^{-10} s), Γ is the ratio of anisotropy to thermal energies, K_μ is the anisotropy energy density, k_B is Boltzmann's constant, and V_M is the volume of the suspension given by

$$V_M = \frac{4\pi r^3}{3} \qquad (10.4)$$

where r is the radius of the magnetic core. From Eqs. (10.2)–(10.4), it is apparent that Néelian relaxation depends on the magnetic anisotropy energy of the material, thermal energy, and the size of the inner magnetic core.

Brownian relaxation: Brownian relaxations pertain to the physical rotation of the MNP by itself and align with the external field (Fig. 10.1). Thermal energy is produced by friction arising from shear stress in the fluid and the characteristic Brownian relaxation (τ_B) time determined by the rotational mobility of the colloidal

magnetic particles is given by Shaterabadi et al. (2018)

$$\tau_B = \frac{3\eta V_H}{K_B T} \tag{10.5}$$

where η is viscosity of the surrounding medium, V_H is the particle hydrodynamic volume (including magnetic core, coating, and hydration layers), K_B is the Boltzmann constant, and T is the temperature. Brownian relaxation relies on viscosity of the fluid, hydrodynamic volume of the nanoparticle.

Néel relaxation dominates for smaller particle sizes as the fastest process, whereas above a certain critical size range, the Brownian relaxation mechanism takes over. For close to the critical size limit, both mechanisms can be observed and the relative contributions are determined by the effective relaxation time, τ, expressed as:

$$\frac{1}{\tau} = \frac{1}{\tau_N} + \frac{1}{\tau_B} \tag{10.6}$$

However, the effective relaxation time is predominated by the term that has shorter relaxation time. It is very challenging to distinguish the contribution of the two mechanisms and experimental studies are being carried out to meet this challenge.

Specific Absorption Rate (SAR)

The most common parameter for quantifying the efficiency of MNPs colloids to transform magnetic energy into heat is known as specific absorption rate (SAR), or specific power absorption (SPA) or specific loss power (SLP). In biomedical applications, SAR is one of the most crucial parameters in the design of MNPs for magnetic hyperthermia because the higher the specific absorption rate, the lower the injected dose to the patient. SAR expresses the rate of absorption of an electromagnetic field impinging on human body tissue. It is defined as the absorbed power, normalized by the mass of MNPs, under an applied AMF of certain frequency and intensity (Perigo et al. 2015).

$$SAR = \frac{\text{Absorbed power}}{\text{Mass of MNPs}}$$

SAR units are watts per gram because it is the parameter related to MNPs mass, which can be directly calculated from the molar concentration.

It is important to note that SAR is a system-dependent parameter and depends on a large number of parameters namely: size, size distribution, shape, and chemical composition of particles, magnetic properties of nanoparticles, the frequency and amplitude of the applied external alternating magnetic field, and on the characteristics of coating material and surface functionalization. SAR also depends on which mode

of heat loss is dominant. SAR for the same nanoparticle batch can be different in a colloidal dispersion, powder sample or inserted into a biological tissue; therefore, more reliable protocols for measuring SAR in MNPs need to be established. There are currently two main groups under which SAR measurements methods can be classified: calorimetric and magnetometric methods (Perigo et al. 2015; Abenojar et al. 2016; Garaio et al. 2015).

Calorimetric Method

The calorimetric approach is the most commonly adapted method and heat quantification is usually performed through the measurement of the temperature evolution of the sample under study. In this method, the temperature increase in the sample is recorded over a period of time as the magnetic NPs are exposed to an AC field of a particular amplitude and frequency (Fig. 10.2a). A fiber optic temperature probe
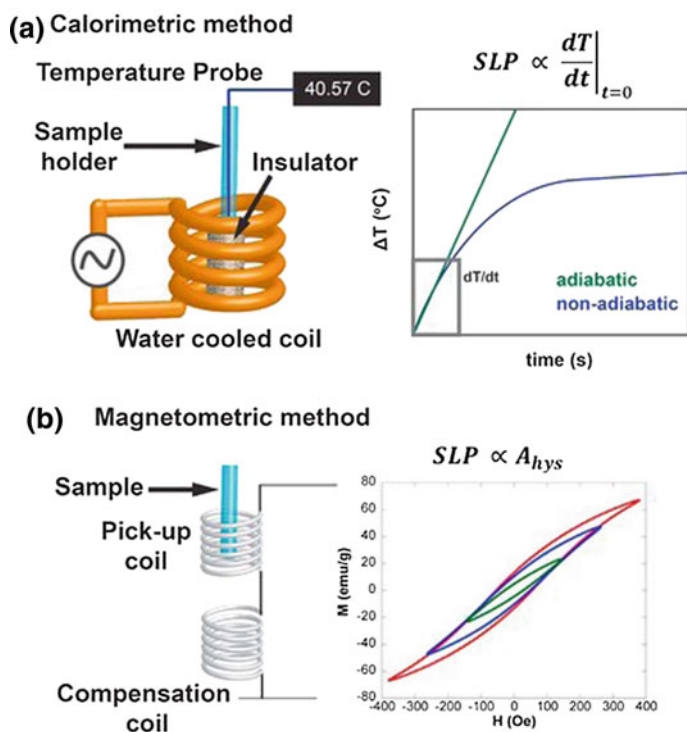
Fig. 10.2   a Calorimetric method and **b** magnetometric method for measuring specific absorption rate. Reprinted with the permission from Abenojar et al. (2016)

is typically used in conjunction with a magnetic induction heating system consisting of a water-cooled coil that is connected to a high power radio frequency (rf) generator. Samples are placed in a thermally insulated container to avoid heat loss to the environment during measurement (Abenojar et al. 2016). Experimentally, for a suspension of NPs in a fluid carrier, the SAR is obtained from the slope of the temperature curve by the formula (Garaio et al. 2015)

$$\text{SAR} = \frac{m_\text{d} C_\text{p,d}}{m_\text{NP}} \left. \left| \frac{\text{d}T}{\text{d}t} \right| \right|_{t=0}$$

where m_d and $C_\text{p,d}$ are the mass and heat capacity of the dispersion medium, respectively, while m_NP is the mass of NPs (including all the elements of the magnetic material, such as oxygen for oxides). $\text{d}T/\text{d}t$ indicates the initial rate of field-induced temperature rise (T) in the magnetic fluid sample as a function of time (t).

Evaluation of the heating efficiency by calorimetric method yields more reliable values when measurements are performed under adiabatic conditions. The thermal dependence can be measured only when the setup is perfectly adiabatic. SAR measurements by calorimetry are based, indeed, on the measurement of the initial temperature slope. However, the extension of the linear regime is always limited (except for ideal adiabatic conditions) by a plateau value ΔT_max as indicated in Fig. 10.2a, which occurs after an elapsed time that increases with the sample volume. The effects of thermal losses in non-adiabatic conditions cause the decrease of the time derivative of temperature until the steady state is reached as shown in Fig. 10.2a. To eliminate conduction, convection, and thermal radiation heat losses, high vacuum conditions, and adiabatic shields are used during measurements. However, adiabatic systems are rarely used because they are costly and difficult to setup. Hence, non-adiabatic systems are commonly adopted because of the quick measurement time and ease of operation.

SAR measurement in non-adiabatic setup can be reliable approach to measure the heating efficiency of magnetic NPs by taking into account all the thermal losses. Wildeboer et al. (2014) proposed an alternative method using the corrected slope method to better evaluate the SAR by adding a thermal loss parameter, L, which can be estimated by determining the slope for multiple temperatures along the heating curve. When thermal loss L of the system is known SAR is calculated using

$$\text{SAR}_\text{Corrected-slope} = \frac{\left(C \frac{\text{d}T}{\text{d}t} + L\Delta T \right)}{m_\text{mnp}}$$

In this equation, ΔT is the (mean) temperature difference between the sample and baseline and must be within the bounds of the linear-loss regime. Even when the loss L is not known, it is possible to calculate its most probable value by determining the slope for multiple temperatures along the heating curves.

Magnetometric Method

Magnetometric method is based on measuring the dynamic magnetization $M(t)$ of the sample. SAR values are subsequently obtained by integrating the dynamic magnetization with respect to the magnetic field (Abenojar et al. 2016);

$$\text{SAR} = \frac{f}{c} \oint M(t) \mathrm{d}H$$

where f is the frequency and c is the weight concentration of the NP. The integration is performed over one period $(2\pi/f)$. In this approach, the SLP is proportional to the area of the AC hysteresis loop as shown in Fig. 10.2b.

Assessing the Hyperthermic Properties of Magnetic Nano-Heterostructures

To achieve improved efficacy in cancer therapy, the crucial factor is the designing biocompatible nanoplatforms and selection of appropriate magnetic nanomaterial to increase the specific absorption rate. A variety of magnetic nanoparticles have been used as diagnostic tools for cancer cells but nano-heterostructures have elicited much interest because of their distinct characteristics that influence physical, electrical, chemical, biological, and optoelectrical properties. The heterostructured systems provide new degrees of freedom to control nanoparticle functionality. In this context, $Au\text{-}Fe_3O_4$ heterostructures have received considerable attentions not only because of their superior properties but also from their complementary function and synergistic effect. The study of the $Au\text{-}Fe_3O_4$ interphase and the interaction between the magnetic and plasmonic domains as a function of the morphology make these systems very interesting also from a fundamental point of view (Fantechi et al. 2017).

The direct interaction due to spin polarization transfer between the magnetic moment and the non-magnetic–plasmonic counterpart induce finite magnetization in Au. Simultaneously, it has been reported that the magnetic properties of Fe_3O_4 are influenced due to the presence of Au in direct contact, which is evidenced as exchange bias (EB) effect, modified magnetization response to alternating fields, enhanced blocking temperature, etc. (Chandra et al. 2014). Recent breakthroughs in heterostructures have revealed that the EB effect can overcome the superparamagnetic limit at room temperature, which is believed to provide the capability of satisfying the growing miniaturization demands of spintronic devices (Zhu et al. 2018).

The structural features of heterostructured nanomaterials can mainly be classified as core-shell, shell-core-shell, core-satellite, dimmers, Janus, flower-like nanostructures, etc. To enhance the properties of these nano-heterostructures, crucial issues are the design and synthesis of heterostructures with controlled and well-defined

morphology. The coating of metallic NPs with a thin shell of a magnetic material is synthetically challenging. The higher degree of synthetic control as compared to single-component nanoparticles can provide an avenue for synthesizing next-generation and complex composite materials. To promote the heterogeneous growth of Fe_3O_4 on Au seeds suppression of the homogenous nucleation is important. Most promising approach for the synthesis of nano-heterostructures is based on a thermal decomposition approach following a seeded-mediated growth approach (Fantechi et al. 2017; Mezni et al. 2013; López-Ortega et al. 2015; Liu et al. 2018; Shevchenko et al. 2008; Nguyen et al. 2011; Xu et al. 2007). Seed-mediated growth is the most commonly used for preparing homogeneous core-shell heterostructures with controlled magnetic and plasmonic properties.

Few studies have demonstrated the heating effect of gold-iron oxide nano-heterostructures. Guardia et al. (2017) synthesized Au-iron oxide dimers by two synthesis routes, a two-pot, and a one-pot method. The key factor for the synthesis of dimers at low temperature was the addition of chloride ions and the absence of 1,2-hexadecandiol (HDDOL). Chloride ions helped in lowering the reaction temperature at 200 °C and tuned the size of the iron oxide domain. The one-pot synthesis is more cost-effective due to fewer steps and by varying the reaction time size of iron oxide domain can be tuned. SAR was analyzed as a function of iron oxide domain and gold presence. As shown in Fig. 10.3a, high SAR value (1330 ± 20 W/g) was observed for gold-iron oxide dimers with an iron oxide domain of 23 nm at 300 kHz. It was found that the SAR values for the full dimers were slightly higher than those of the empty dimers, especially at 110 and 220 kHz (Fig. 10.3a).

This suggests that the gold NP might boost the dissipation of the heat by the iron oxide NP with higher efficiency than that of iron oxide NPs alone. SAR values of both full and empty dimers recorded under patient-safe conditions ($H \cdot f < 5 \cdot 10^9$ $Am^{-1}s^{-1}$) were in the 600–690 W/g Fe range. These dimers are promising candidates for in vivo applications offering advanced features than bare iron oxide NPs.

The most challenging aspect of applying Au–Fe_3O_4 NPs involves the colloidal stability and self life, surface functionalization, cellular internalization, and biocompatibility. Therefore, designing a properly grafted surface is of paramount importance (Abedin et al. 2018). Daboin et al. (2019) present a reproducible synthesis of multicore magnetic nanocomposites for hyperthermia therapy. Magnetic mixed manganese-cobalt ferrite nanoparticles $Mn_{1-x}Co_xFe_2O_4$ ($0 \leq x \leq 1$) were synthesized using the thermal decomposition method, then coated with silica (SiO_2) following the Stöber method and decorated with Au@Fe_3O_4 nanoparticles as magnetic fluid hyperthermia heat mediators, employing a hydrogel as a tissue-equivalent. Figure 10.4c shows the relation of SAR with the coercive field, and both exhibit the same trend with increasing Mn^{+2} content.

This might be attributed to the magnetic anisotropy as a central parameter controlling both coercivity (H_C) and SAR. This dependence is justified by the contribution of the superparamagnetic Au@Fe_3O_4 nanoparticles to the SiO_2-$Mn_{1-x}Co_xFe_2O_4$ nanocomposite. The higher hyperthermic effect has been achieved in the nanocomposite of Au@Fe_3O_4-SiO_2-$CoFe_2O_4$ using the hydrogel. Therefore, the decrease in the SAR values observed in Fig. 10.4d, larger particle size could be attributed to

$d_{Fe_xO_y}$ (nm)	d_{Au} (nm)	d_H (nm)
17 ± 2	12 ± 1	30 ± 10
21 ± 4	11 ± 1	30 ± 10
23 ± 6	12 ± 2	34 ± 10
26 ± 5	15 ± 4	40 ± 10
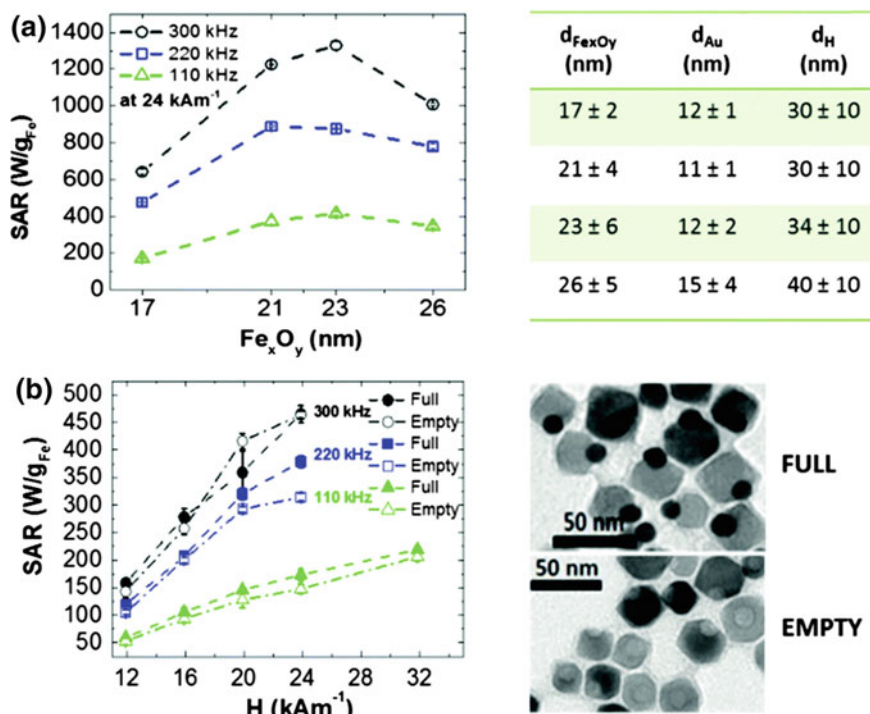
Fig. 10.3 **a** SAR values at three frequencies and 24 kA m^{-1} for Au-Fe$_2$O$_3$ dimers with different sizes of the iron oxide domain (from 17 to 26) obtained by one-pot 200 method and different annealing times; in the table, the size of the gold and iron oxide domains together with the hydrodynamic size by number, of the measured dimers are reported. **b** Comparative SAR values at three different frequencies for full and empty dimers, the latter obtained by etching out the Au NP: 300 kHz (black full and empty circles ●, ○), 220 kHz (blue full and empty squares ■, □), and 110 kHz (green full and empty triangles ▲, △). Each SAR value is the mean of at least 4 data points. Reprinted with the permission from Guardia et al. (2017)

the difficulty of motion of the nanocomposite in the viscous medium. These results strongly show that the magnetic properties and SAR of the nanocomposites are simultaneously improved by decorating with Au@Fe$_3$O$_4$ nanoparticles.

Mohammad et al. (2010) demonstrated experimentally that the hyperthermic effect of superparamagnetic iron oxide nanoparticles (SPIONs) enhances dramatically on coating with Au. The excellent hyperthermia property exhibited by SPIONs@Au nanoparticles coupled with their lack of cytotoxicity makes them suitable candidates for thermolysis of cancer cells. The cytotoxicity of SPIONs@Au was compared with SPIONs. The feasibility of using SPIONs@Au nanoparticles for targeted cancer therapy was analyzed quantitatively by estimating the cell viability of SPIONs and SPIONs@Au with different concentrations. For the studies, they used H9c2 cardiomyoblasts (Fig. 10.5a), a non-cancerous stable cell line derived from
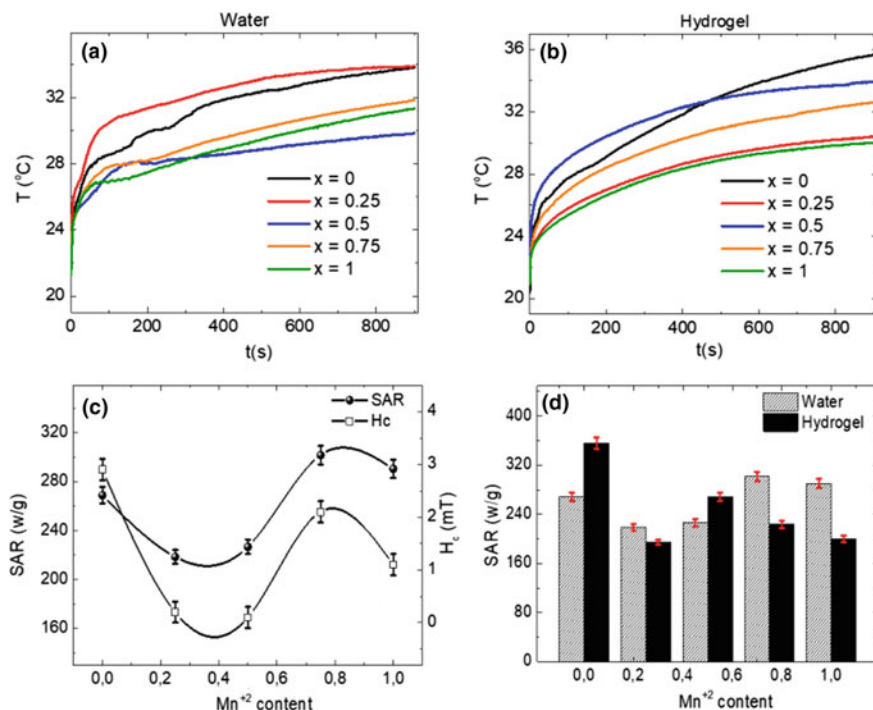
Fig. 10.4 Time evolution of the temperature for $SiO_2.Mn_{1-x}Co_xFe_2O_4$ decorated with $Au@Fe_3O_4$ NPs in **a** water, **b** hydrogel, **c** SAR and H_c as a function of the Mn^{+2} content, **d** comparison of the SAR in water and in a hydrogel as a function of the Mn^{+2} content. Reprinted with the permission from Daboin et al. (2019)

embryonic rat heart and known to express specific cardiac markers (considered a close proxy for adult cardiac cells).

Their results indicate that both SPIONs and SPIONs@Au are inherently least cytotoxic up to 250 µg/mL concentration, and for 500 µg/mL, a 20% reduction in cell viability was observed when studied in the absence of oscillating magnetic field. Similar results were obtained when MCF-7 breast carcinoma cells were exposed to either SPIONs or SPIONs@Au in the concentration range of 25–250 µg/mL and with a 500 µg/mL concentration, a 20–30% reduction in viability for 24 h, that is, in the absence of oscillatory magnetic field (Fig. 10.5b). The maximum decrease in viability of cells occurred at the highest concentration of 500 µg/mL. Oleic acid and oleylamine used as co-dispersants for SPIONs and SPIONs@Au can preventing the agglomeration and can impart significant protection against Fe-mediated toxicity, if any.

Poly (ethylenimine) (PEI)PEI-coated Fe_3O_4 nanoparticles (PEI-Fe_3O_4 NPs) (León Félix et al. 2019) were analyzed for heating efficiency and cellular toxicity. In the specific absorption power with applied magnetic field is governed only by the properties of the magnetic cores, being experimentally identical for blocked NPs
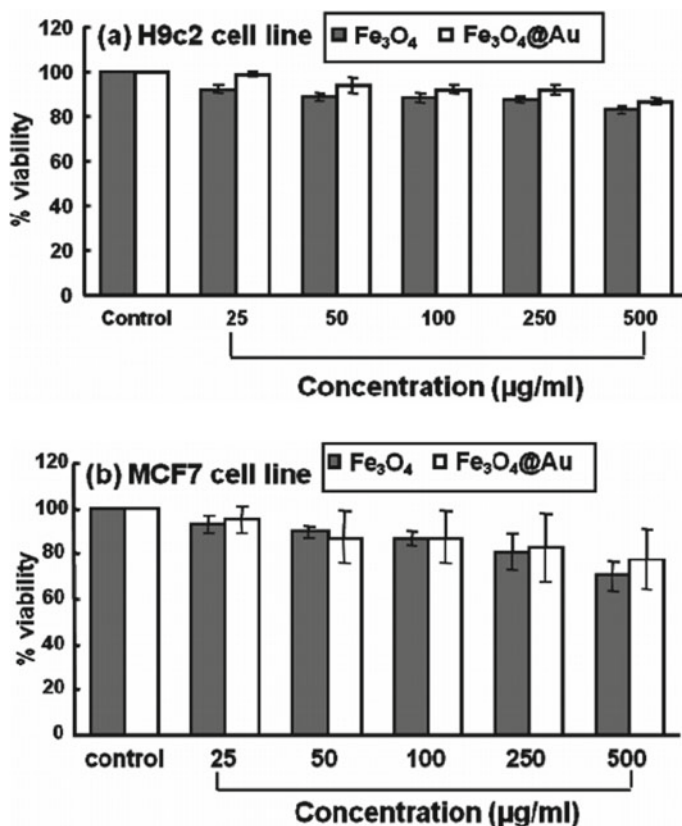
Fig. 10.5 In vitro toxicity comparison of SPIONs and SPIONs@Au at different concentrations with **a** the H9c2 cardiomyoblast cell line and **b** MCF-7 breast carcinoma cells. Reprinted with the permission from Mohammad et al. (2010)

within solid matrix and/or within the intracellular space. The toxicity of Au@PEI-Fe_3O_4 NPs was evaluated on the microglial cell line (BV2) at different concentrations of NPs from 10 to 100 μg/mL. All experiments were performed after 24 h of NPs co-incubation. High values of cell viability (>97%) were observed for all concentrations of Au@PEI-Fe_3O_4 NPs tested. They were found to have very low in vitro cytotoxicity, which can provide an interesting multifunctional nanoplatform for bimodal application of light and magnetic hyperthermia.

Wu et al. (2011) reported that the Fe@Au NPs before oxidation cause cancer-cell specific cytotoxicity. Since the oxidation status of Fe@Au NPs determines their therapeutic effectiveness because once it is oxidized the cytotoxicity of NPs depleted and could limit its clinical use. NPs were applied to the cytotoxicity assay immediately after synthesis or stored under argon. Gold-coated iron nanoparticles selectively suppressed squamous cell carcinoma (SCC) and colorectal cancer (CRC) cell growth,

Fig. 10.6 After a single treatment of Fe@Au NPs, cancer-cell proliferation was significantly inhibited in a hamster de novo oral-cancer model. (P b 0.0001, $n = 9$) The images were taken after 2 weeks of Fe@Au treatment. The ruler scale is 1 mm. Reprinted with the permission from Wu et al. (2011)
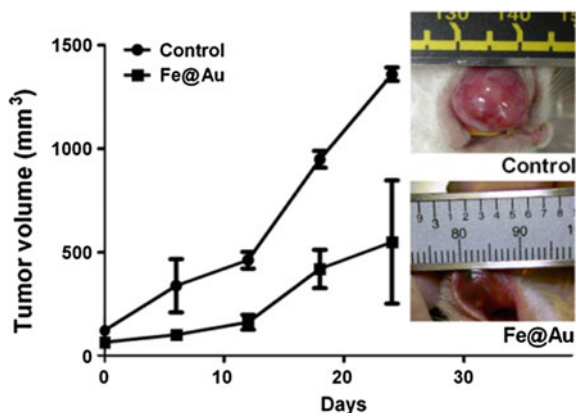
but left healthy control cells unaffected both in vitro and in vivo. The cytotoxicity properties of Fe@Au were estimated in vivo in a hamster de novo oral-cancer model. The Fe@Au and vehicle control was injected into the tumor region once the tumor volume reached 100 mm^3. Fe@Au NPs showed a significant inhibition ($P < 0.001$) of tumor growth with single-dose injection compared with the control group (Fig. 10.6). Fe@Au NPs thus show great promise as a highly specific therapy for squamous carcinoma.

Specific absorption rate and intrinsic loss power were calculated for $CoFe_2O_4@Au$ core-shell (CS) synthesized by a thermal decomposition method (Sabale et al. 2019) within the human tolerable range of frequency and amplitude, suggesting their potential in magnetic fluid hyperthermia therapy for possible cancer treatment. ILP values decreased with an increase in MNPs concentration and amplitude of the magnetic field. The maximal value of SAR obtained was 68.85 Wg^{-1} for $CoFe_2O_4$ NPs and 54.97 Wg^{-1} for $CoFe_2O_4@Au$ CSs at a concentration of 5 mg mL^{-1} and 13.3 kA m^{-1} and 276 kHz of amplitude and frequency, respectively. The presence of Au affects the anisotropy of particles, which plays a vital role in obtaining higher values of SAR. It was found that the increasing particle concentration is not only criteria to obtain high SAR, SAR dependent upon many factors like magnetic field, frequency, anisotropy, and other physical parameters such as particle size and morphology.

$MnFe_2O_4@Au$ (Mf@A) nanoparticles surface functionalized with folic acid (Fa) and doxorubicin (Dox) (Ravichandran et al. 2018) were tested as hyperthermia agents under the microwave (Mw) irradiation. The stability of Mf@A NPs was analyzed by measuring the zeta potential measurements. It was observed that the temperature increment was very rapid and reached 45 ± 1 °C around 70 s and temperature raised up to 51 ± 1.5 °C within 120 s for Mf@A. The superparamagnetic behavior of $MnFe_2O_4@Au$ nanoparticles retained which leads to the increment of energy by magnetic anisotropy within the Au nanoshell.

Conclusion

Systemic administration of Au-iron oxide and noble metal-ferrite nano-heterostructures induced magnetic hyperthermia could revolutionize clinical practice in the treatment of cancer via modulation of various cellular processes. Therefore, one important factor that determines their heating efficiency is the ability of magnetic nanoparticles to be driven and accumulated in the desired area inside the body. Hence, the various parameters on which specific absorption rate depends such as on the magnetization, relaxation time, size, morphology, composition, saturation magnetization, and magnetic anisotropy of the magnetic NPs must be administered carefully. Magnetic nanoparticles must be strategically designed and surface functionalized to selectively target the injured cells and tissues with low or minimum cytotoxicity. Computable molecular modeling could be very beneficial for the design of those complex hybrid systems.

References

Abedin MR, Umapathi S, Mahendrakar H, Laemthong T, Coleman H, Muchangi D, Santra S, Nath M, Barua S (2018) J Nanobiotechnol 16:1

Abenojar EC, Wickramasinghe S, Bas-Concepcion J, Samia ACS (2016) Prog Nat Sci Mater Int 26:440

Beik J, Abed Z, Ghoreishi FS, Hosseini-Nami S, Mehrzadi S, Shakeri-Zadeh A, Kamrava SK (2016) J Control Release 235:205

Chandra S, Frey Huls NA, Phan MH, Srinath S, Garcia MA, Lee Y, Wang C, Sun S, Iglesias Ò, Srikanth H (2014) Nanotechnology 25:055702

Colombo M, Carregal-Romero S, Casula MF, Gutiérrez L, Morales MP, Böhm IB, Heverhagen JT, Prosperi D, Parak WJ (2012) Chem Soc Rev 41:4306

Dabbagh A, Abdullah BJJ, Abdullah H, Hamdi M, Kasim NHA (2015) J Pharm Sci 104:2414

Daboin V, Briceño S, Suárez J, Carrizales-silva L, Silva P, Gonzalez G, Daboin V, Brice S (2019) J Magn Magn Mater 479:91

Fantechi E, Roca AG, Sepúlveda B, Torruella P, Estradé S, Peiró F, Coy E, Jurga S, Bastús NG, Nogués J, Puntes V (2017) Chem Mater 29:4022–4035

Garaio E, Sandre O, Collantes JM, Garcia JA, Mornet S, Plazaola F (2015) Nanotechnology 26:15704

Gilchrist RK, Medal R, Shorey WD, Hanselman RC, Parrott JC, Taylor CB (1957) Ann Surg 146:596

Guardia P, Nitti S, Materia ME, Pugliese G, Yaacoub N, Greneche JM, Lefevre C, Manna L, Pellegrino T (2017) J Mater Chem B 5:4587

Gutiérrez TJ, Alvarez VA (2018) In: Hussain CM (ed) Handbook of nanomaterials for industrial applications. Elsevier, pp 563–576

Hervault A, Thanh NTK (2014) Nanoscale 6:11553

Javed Y, Ali K, Jamil Y (2017) In: Sharma SK (ed) Complex magnetic nanostructures. Springer International, pp 393–424

Kozissnik B, Bohorquez AC, Dobson J, Rinaldi C (2013) Int J Hyperth 29:706

LeBrun A, Zhu L (2018) In: Shrivastava D (ed) Theory and applications of heat transfer in humans, pp 631–667

Lemal P, Balog S, Geers C, Taladriz-Blanco P, Palumbo A, Hirt AM, Rothen-Rutishauser B, Petri-Fink A (2019) J Magn Magn Mater 474:637

León Félix L, Sanz B, Sebastián V, Torres TE, Sousa MH, Coaquira JAH, Ibarra MR, Goya GF (2019) Sci Rep 9:1

Lettieri-Barbato D, Aquilano K (2018) Front Oncol 8:148

Liu B, Zhang H, Ding Y (2018) Chin Chem Lett 29:1725

López-Ortega A, Estrader M, Salazar-Alvarez G, Roca AG, Nogués J (2015) Phys Rep 553:1

Mezni A, Balti I, Mlayah A, Jouini N, Smiri LS (2013) J Phys Chem C 117:16166

Mohammad F, Balaji G, Weber A, Uppu RM, Kumar CSSR (2010) J Phys Chem C 114:19194

Negut I, Grumezescu V (2019) In: Grumezescu AM (ed) Biomedical applications of nanoparticles. William Andrew, pp 63–90

Nguyen DT, Park DW, Kim KS (2011) J Nanosci Nanotechnol 11:7214

Perigo EA, Hemery G, Sandre O, Ortega D, Garaio E, Plazaola F (2015) Appl Phys Rev 2:041302

Ravichandran M, Velumani S, Ramirez JT, Vera A, Leija L (2018) Artif Cells Nanomed Biotechnol 46:S993

Sabale S, Jadhav V, Mane-Gavade S, Yu XY (2019) Acta Metall Sin (Engl Lett) 32:719

Sanchez LM, Alvarez VA (2019) Bioengineering 6:75

Sangaa D, Khongorzul B, Uyanga E, Jargalan N, Tsogbadrakh N, Hirazawa H (2018) Solid State Phenom 271:51

Shaterabadi Z, Nabiyouni G, Soleymani M (2018) Prog Biophys Mol Biol 133:9

Shevchenko EV, Bodnarchuk MI, Kovalenko MV, Talapin DV, Smith RK, Aloni S, Heiss W, Alivisatos AP (2008) Adv Mater 20:4323

Stigliano RV, Shubitidze F, Petryk JD, Shoshiashvili L, Petryk AA, Hoopes PJ (2016) Int J Hyperth 32:735

Suriyanto, Ng EYK, Kumar SD (2017) Biomed Eng Online 16(1)

Wildeboer RR, Southern P, Pankhurst QA (2014) J Phys D Appl Phys 47

Wu YN, Chen DH, Shi XY, Lian CC, Wang TY, Yeh CS, Ratinac KR, Thordarson P, Braet F, Bin Shieh D (2011) Nanomed Nanotechnol Biol Med 7:420

Xu Z, Hou Y, Sun S (2007) J Am Chem Soc 129:8698

Yu X, Yang R, Wu C, Zhang W, Deng D, Zhang X, Li Y (2020) In: Wahab MA (ed) Proceedings of the 13th international conference on damage assessment of structures. Lecture notes in mechanical engineering. Springer, Singapore, pp 937–943

Zhang H, Zhang YF, Gao F, Li GL, He Y, Peng ML, Fan HM, Liu XL (2018) Sci China Life Sci 61:400

Zhu L, Deng X, Hu Y, Liu J, Ma H, Zhang J, Fu J, He S, Wang J, Wang B, Xue D, Peng Y (2018) Nanoscale 10:21499

Chapter 11
Thermal Response of Iron Oxide and Metal-Based Iron Oxide Nanoparticles for Magnetic Hyperthermia

M. Zubair Sultan, Yasir Jamil, Yasir Javed, S. K. Sharma and M. Shoaib Tahir

Abstract Magnetic nanoparticles have been extensively in the biomedical field as drug delivery agent, diagnosis of different diseases and more recently in the treatment of different types of cancer. Majority of these studies reported the use of iron oxide nanoparticles or formulation contains at least iron in most of magnetic-based nanosystems. Focus on iron oxide nanoparticles is mainly due to their superparamagnetic nature at nanoscale and other features such as higher surface to volume ratio, biocompatibility and low toxicity. For further improvement in their properties, doping with different transition metal elements is also under investigations. This chapter covers most commonly used types of iron oxide NPs, behavior with few doping metals in iron oxide nanoparticles and their synthesis protocols through different physical and chemical methods. Finally, heat generation mechanisms responsible for localized heat in tissues have been discussed.

Keywords Metal-based iron oxide · Wet chemical synthesis · Ferrofluid · Heat generation · Localized heating

Introduction

During the final decade of twentieth century, the research in the field of materials science has been focused toward nanomaterials. The cause of interest in nanomaterials was due to the advancement in preparation methods, structural control and

M. Zubair Sultan · Y. Jamil (✉) · M. Shoaib Tahir
Laser Spectroscopy Lab, Department of Physics, University of Agriculture Faisalabad, Faisalabad, Pakistan
e-mail: yasirjamil@yahoo.com

Y. Javed
Magnetic Materials Lab, Department of Physics, University of Agriculture Faisalabad, Faisalabad, Pakistan

S. K. Sharma
Department of Physics, Faculty of Science and Technology, The University of the West Indies, Saint Augustine, Trinidad and Tobago

tunable properties of new materials. During the last two decades, a large amount of knowledge has been developed about the techniques and properties of several types of nanomaterials. During studies, iron oxide NPs have emerged as an important candidate for biomedical applications (Riviere et al. 2006; Niemirowicz et al. 2012). Iron oxide nanoparticles (NPs) have great importance due to their superparamagnetic properties. Iron oxide NPs having size less than 20 nm show superparamagnetic nature, property important for biomedical applications (Ali et al. 2016). There are sixteen forms of iron, including oxides, hydroxide and oxyhydroxides. From these different forms, Fe_3O_4 (magnetite) is the most studied one due to high saturation, low hysterics losses and biocompatibility (Cornell and Schwertmann 2003).

Iron oxide NPs are being used for protein immobilization, thermal therapy, drug delivery and as contrast agents in magnetic resonance imaging (MRI). Nanomaterials based on iron oxide can produce heat locally around tumor site and kill cancer cells under alternating magnetic field (Yang et al. 2008; Lee and Hyeon 2012; Laurent et al. 2011; Cao et al. 2012). Several factors such as shape, size, synthesis method, crystal structure and surface coating of iron oxide NPs have effect on their technologically important properties. The morphology of NPs can control the crystal facets and arrangement of atoms where facet shows its effects on the properties of NPs (Raghunath and Perumal 2017). The efforts for developing the protocols to synthesize NPs of desired shape and size are still required. Figure 11.1 shows different shapes of iron oxide NPs. Doping is also another important factor which affects the properties of iron oxide NPs (Cai et al. 2014). For example, cobalt (Co) is highly magnetically anisotropic, and doping of Co in iron oxide can certainly enhance its magnetic character. This creates an important class of materials called ferrites. There are many groups studying the effect of doping elements on iron oxide in the form of
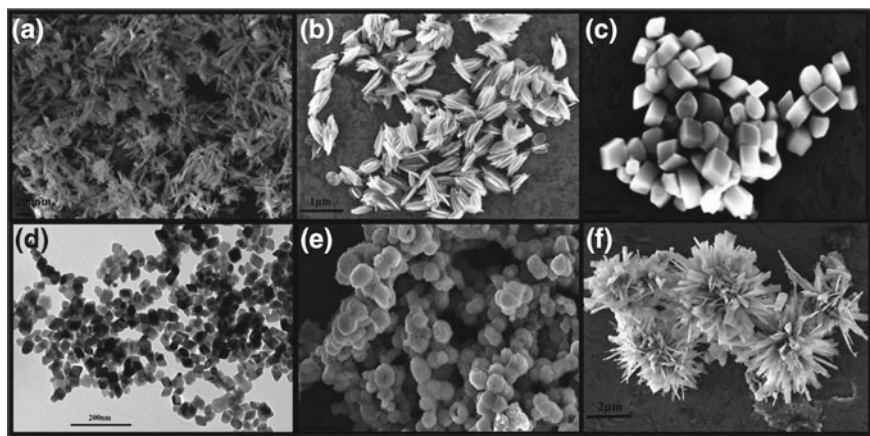
Fig. 11.1 Different morphologies of iron oxide nanoparticles: **a** nanorod, **b** nanohusk, **c** distorted cubes, **d** nanocubes, **e** porous spheres and **f** highly anisotropic flowers. Reprinted from Sayed and Polshettiwar (2015)

ferrites (Chakrabarti et al. 2005; Anjum et al. 2017; Feng et al. 2018; Casula et al. 2016; O'Hara et al. 2016).

Chemical or/and mechanochemical protocols have been used for the synthesis of iron oxide NPs. Sol–gel (Ba-Abbad et al. 2017), co-precipitation (Daoush 2017), hydrothermal (Ge et al. 2009) and template-assisted synthesis (Confalonieri et al. 2011) are examples of chemical method, whereas laser ablation (Iwamoto and Ishigaki 2013), pyrolysis (Cao et al. 2007), electrodeposition (Sequeira 2018) and combustion (Punitha and Nehru 2018) are mechanochemical methods. Different morphologies such as rods, cubes, flowers, spheres, triangles and distorted cubes can be produced using same chemical method just by modifying different parameters such as precursor amount, stirring time, stabilizing agent and heating temperature (Chen and Carroll 2002; Sibokoza 2017). The newly explored protocols can be easy to implement and economical as well.

Surface functionalization is a key step in synthesis procedure by which stable and more biocompatible iron oxide NPs can be made. Surface modification can be done during and after the synthesis reaction (Gupta and Gupta 2005; Gupta 2007). Proper and homogeneous polymer coating on iron oxide NPs decides its different parameters in vivo such as circulation time, biodegradation, internalization and distribution in different organs (Wu et al. 2015). To increase the biochemical activities and reactivity, NPs with high surface to volume ratio are produced, but still, the interaction mechanisms of NPs with biological system are quite unknown. In this chapter, we will discuss different types of iron oxides, doping characteristics with other metals, synthesis protocols and thermal response of these NPs.

Types of Iron Oxide NPs

Iron oxide is found in eight different oxidation states (Cornell and Schwertmann 2003). Among these eight forms, three are the most promising, i.e., (i) hematite (α-Fe_2O_3) (ii) maghemite (γ-Fe_2O_3) (iii) magnetite (Fe_3O_4). Each of this form is used in different biomedical applications due to their structural and magnetic properties.

Hematite (α-Fe_2O_3)

Hematite (α-Fe_2O_3) is a common and most stable form of iron oxide. It has rhombohedral lattice system as shown in Fig. 11.2. Hematite is found in colors like brown, reddish brown (Anthony 1990). Under ambient conditions, α-Fe_2O_3 behaves as n-type semiconductor, and its band gap is 2.3 eV. Its valance band (VB) had mixture of occupied 3d orbitals of Fe^{3+} and 2p nonbonding orbitals of O, whereas there are only empty d-orbitals of Fe^{3+} in the conduction band (CB) of α-Fe_2O_3 (Wu et al. 2010; Zhang et al. 1993). α-Fe_2O_3 is also widely used in biomedical applications,
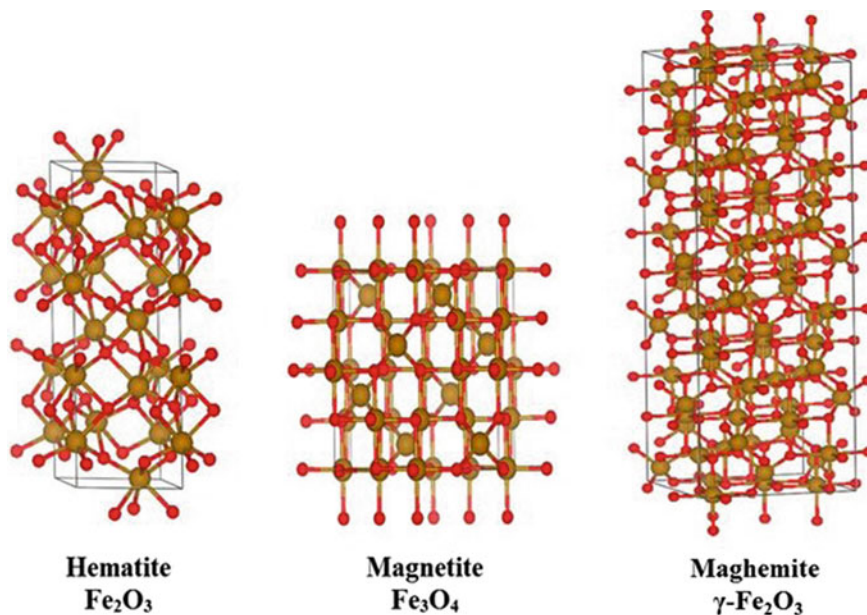
Fig. 11.2 Atomic structures of different forms of iron oxide NPs. Reprinted from Kuchma et al. (2018)

gas sensors, pigments and catalysts due to their unique properties. It has high resistance to corrosion. Hematite is also used as an important material for the synthesis of maghemite (γ-Fe$_2$O$_3$) and magnetite (Fe$_3$O$_4$) which are widely using in scientific research and technological applications.

Maghemite (γ-Fe$_2$O$_3$)

Maghemite (γ-Fe$_2$O$_3$) is another important member of iron oxide family. It has cubic structure as shown in Fig. 11.2. Maghemite can be supposed as Fe^{II} deficient form of magnetite, according to the formula

$$\left(\text{Fe}_8^{III}\right)_A \left[\text{Fe}_{\frac{40}{3}}^{III} \square_{\frac{8}{3}}\right]_B \text{O}_{32} \tag{11.1}$$

where A and B are representing tetrahedral and octahedral positioning, respectively, and $\square$ is representing a vacancy (Cornell and Schwertmann 2003). Each unit of (γ-Fe$_2$O$_3$) contains 32 ions of O^{2-}, $21\frac{1}{3}$ ions of Fe^{3+} and $2\frac{1}{3}$ vacancies for 32 cations of iron with $+3$ valiancy. Oxygen ions form cubic closed pack array whereas Fe^{3+} are distributed over octahedral and tetrahedral sites. This form of iron oxide acts as

n-type semiconductor. The band gap of maghemite is 2.0 eV. It is found in brown and bluish black shades (Wu et al. 2015).

Magnetite (Fe₃O₄)

Magnetite (Fe_3O_4) is also an important form of iron oxide. It is found in black or brownish black color (Anthony 2017). The structure of magnetite is face-centered cubic, and the atomic arrangement is shown in Fig. 11.2. It is based upon 32 ions of O^{2-} which are closely packed along (Zhang et al. 2010) directions. One of the unique properties of magnetite which makes it different from other forms of iron oxide is that it has both divalent (Fe^{2+}) and trivalent (Fe^{3+}) forms of iron. In the crystal structure of Fe_3O_4, all the divalent ions of iron (Fe^{2+}) occupy half of the octahedral sites, whereas trivalent irons of iron (Fe^{3+}) are split evenly across the rest of the octahedral and tetrahedral sites. Magnetite can be acted both as an n-type and p-type semiconductor; because of stoichiometric alloy in magnetite $Fe^{II}/Fe^{III} = \frac{1}{2}$, the divalent iron ions can be replaced with other divalent ions such as Zn, Co and Ni. The band gap of Fe_3O_4 is only 0.1 eV. Due to this small band gap, magnetite has lowest resistivity than other forms of iron oxide (Boxall et al. 1996).

Doped Iron Oxide NPs

Doping of NPs can greatly change their properties such as structural, physical, optical and magnetic properties. Various types of interactions between dopant and host materials are the main cause of variation in properties of doped NPs (Cai et al. 2014; Adeleye et al. 2018).

Cobalt-Doped Iron Oxide NPs

Cobalt is one of the most useful materials and has become center of interest for researchers over a long time due to its applicability in many fields. Typically, cobalt possesses very good catalytic, magnetic and electrical properties, which are of great interest in technological and scientific fields such as magnetic sensors, magnetic composites, magnetic fluids and magnetic memories (Feldheim and Foss 2002; Wang et al. 2010; Lim and Majetich 2013; Puntes et al. 2001). Intrinsically, cobalt has high value of saturation magnetization and large anisotropy field which makes it advantageous in biomedical-related fields, e.g., hyperthermia, MRI and drug delivery (Feldheim and Foss 2002; Pankhurst et al. 2009). Therefore, cobalt is usually used as dopant in iron oxide NPs to get better magnetic and thermal response. Venkatesan et al. (2015) synthesized cobalt-doped iron oxide NPs with average crystalline size

of 16 ± 5 nm. These NPs showed good magnetic properties. Anjum et al. (2017) studied the effects of cobalt doping on iron oxide NPs. Structural studies showed that with increase of doping ratio of cobalt, lattice parameters of inverse spinal cubic structure of Fe_3O_4 decreased. FTIR analysis gives major band at 887 cm^{-1} and confirms single-phase structure of Co-doped Fe_3O_4 NPs. Doping of cobalt significantly increases the magnetic anisotropy and coercivity of $Co_xFe_{3-x}O_4$ NPs. The DSC analysis exhibited that with increase in doping, the maghemite phase transferred to hematite. Skoropata et al. (2014) in another study used 3–12% Co as dopant in iron oxide. Doped samples showed improved magnetic results as compared to undoped iron oxide NPs. Chakrabarti et al. (2005) used wet chemical technique to synthesize the Co-doped γ-Fe_2O_3 NPs. Significant change in properties such as blocking temperature, saturation magnetization and magnetic anisotropy was observed with the increase in cobalt contents. Increase in blocking temperature might be due to the substitution of cobalt ions with iron ions. The saturation magnetization increases up to 5% doping and diminished significantly beyond this limit.

Copper-Doped Iron Oxide NPs

Copper is an important metal and has good electrical and thermal conductivity. In bulk form, copper is weakly diamagnetic, but on nanoscale, it shows superparamagnetic behavior (Garcia et al. 2007; Litrán et al. 2006; Karna et al. 2011; de la Venta et al. 2007; Batsaikhan et al. 2015). Therefore, at nanoscale, copper has attained considerable attention in industrial and biological sectors. Due to its changing magnetic behavior on nanoscale, copper is used as doping element in iron oxide NPs to obtain nanocomposites which have improved magnetic behavior (Batsaikhan et al. 2015; Vitulli et al. 2002; Huang et al. 1997; Garitaonandia et al. 2008; Liu et al. 2006). Mohanraj and Sivakumar (2017) used the sono-chemical method for the synthesis of Cu-doped Fe_3O_4 NPs with three different doping concentrations (0.5M, 0.1M and 1.5M). XRD analysis showed higher order of crystallinity for doped materials as compared to undoped samples. The average crystallite size is increased by increasing Cu concentration. The presence of magnetite and hematite was confirmed by FTIR analysis with the increase in particle size. Fernández-Barahona et al. (2019) synthesized the Cu-doped iron oxide NPs to check the effect of Cu doping on the magnetic, relaxometric and physiochemical properties of iron oxide NPs. It is observed that the Cu doping enhanced the positive contrast in MRI. Wong et al. (2012) reported the synthesis of dextran-coated Cu-doped iron oxide NPs. The average size of NPs was 50 nm. These NPs have shown excellent potential as dual-modality probes for use in positron emission tomography. Feng et al. (2018) used Cu-doped core-shell iron oxide NPs for the removal of arsenic from waste water. These NPs have ability to remove arsenic within 30 min from wastewater at neutral pH. The doping of Cu enhances the O_2 activation and also improves the electron transfer ability. The presence of Cu increased the removal rate of arsenic up to 10 times in aerobic system. Aghazadeh et al. (2018) synthesize the Cu-doped iron oxide NPs by using facile

electrodeposition procedure. The average size of NPs was about 20 nm. The values of saturation magnetization (M_s), coercivity (H_c) and remanent magnetization (M_r) were 54.47 emug^{-1}, 10.53G and 0.41 emug^{-1}, respectively. The electrochemical study showed that specific capacitance was 189.6 Fg^{-1} at 2 Ag^{-1} discharging current.

Mn-Doped Iron Oxide NPs

Manganese (Mn) is a transition metal. It is paramagnetic in bulk, but its oxides show both paramagnetic and diamagnetic behavior. In comparison with other transition metals, manganese is advantageous because it has high magnetic moment (Shatnawi et al. 2016). From the literature, it is found that by adding a small quantity, manganese changes the magnetic behavior of host lattice (Wolf et al. 2001). Therefore, manganese is widely used as dopant material to change the magnetic properties of NPs. Warner et al. (2012) reported the synthesis of Mn-doped iron oxide NPs and found the doped NPs have very high affinity as compared to the precursor material. Sorbent affinity was tuned by adjusting the dopant quantity. The doping of Mn also increases the absorption capacity for heavy metals such as Cd, Hg, Ti, Co, Ni, As, Ag and Zn. Capacity measurements were performed on river water to remove cadmium from it. Casula et al. (2016) used one-pot method for the synthesis of Mn-doped iron oxide NPs and observed flower-like morphology; with the increase in Mn contents, NPs retained their shape and structure; however, the increase in magnetic properties was observed. These NPs have shown good results for MRI as contrast agents and for magnetic hyperthermia. Haribabu et al. (2016) used the folic acid functionalized Mn-doped ferrite NPs and polyamidoamide dendrimers. To get optical performance, Mn:Fe ratio was set carefully. These NPs were used in cancer therapy to produce T_1 and T_2 contrast. This helps in better diagnosis of cancer. NPs were characterized by dynamic light scattering, UV–Vis spectroscopy, absorption spectroscopy, XRD and FTIR spectroscopy. The relaxivity ratio, r_2/r_1, was 4.6 at 1.5 T at molar ratio of 0.5. Wahab (2019) also reported the synthesis of Mn-doped Fe_3O_4 NPs via co-precipitation method. Mn-doped iron oxide NPs showed cubic shape having size 8–12 nm. Doping of Mn showed red shift in absorption wavelength as analyzed by UV–Vis spectroscopy. O'Hara et al. (2016) used Mn-doped Fe_3O_4 NPs to study the uptake performance of the α-emitting radionuclide in groundwater having pH range from 2 to 8. Further, the radioactive element uptake experiment was performed on seawater, human urine and Columbia River water. Mn-doped magnetite showed good extraction performance as compared to magnetite, and uptake was observed up to a broader range of pH. Overall discussion and above-mentioned examples show that Mn-doped iron oxide NPs have much potential to use in many applications.
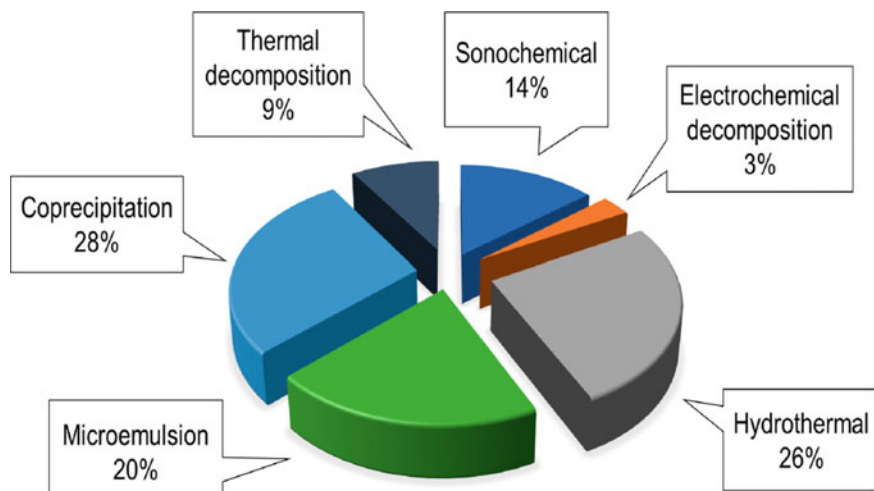
Fig. 11.3 Pie chart distribution among the prevalence of the main methods currently being used for the synthesis of IONPs. Modified from Ali et al. (2016)

Synthesis of Iron Oxide NPs

It is not easy to synthesize nanomaterials based collides precisely, even a small variation during synthesis can change the results dramatically. In the literature, different methods have been discussed for the synthesis of iron oxide NPs. Co-precipitation, sol–gel synthesis, laser-assisted photochemical synthesis, thermal decomposition and sono-chemical synthesis are most commonly methods used for the synthesis of iron oxide NPs (Wu et al. 2008; Pascal 1999). Prevalence of different methods for preparation of iron oxides NPs is shown in Fig. 11.3. The detail of few approaches is given below.

Chemical Co-precipitation Method

It is the most common method used for the synthesis of iron oxide NPs. In this method, typically, the salts of ferric and ferrous are mixed with 1:2 molar ratio, respectively, in highly basic solution. The reaction occurs at room temperature or at mild temperature conditions. The size and shape of the NPs can be affected by many factors such as type of salt, pH, stirring rate, reaction temperature, ionic strength of media and molar ratio of basic solutions. Figure 11.4 shows the different steps involved in co-precipitation method. Kang et al. (1996) synthesized the Fe_3O_4 NPs via co-precipitation method. Massart (1981) did pioneering work in co-precipitation method. After this work, a lot of studies were done to synthesize iron oxide NPs via co-precipitation. Wu et al. (2011a) reported the synthesis of Fe_3O_4 nanopowders
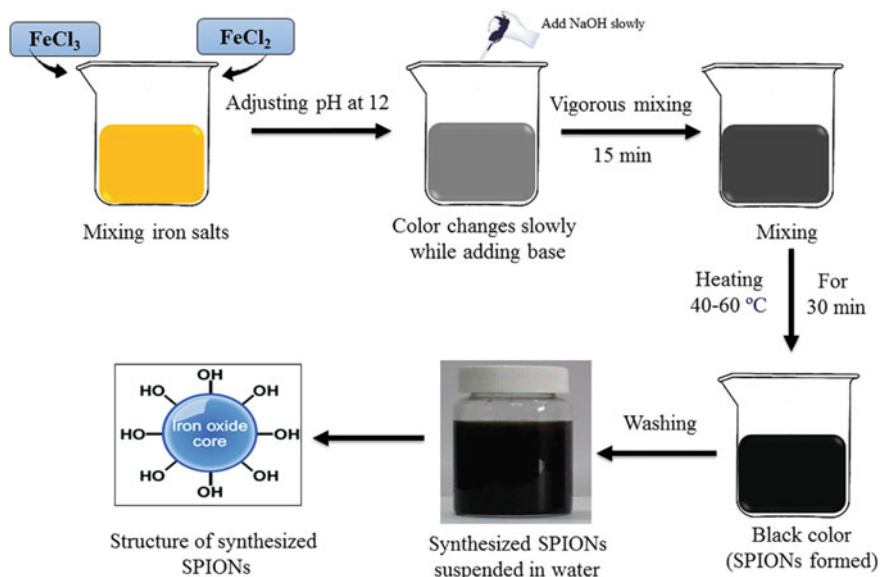
Fig. 11.4 Different steps involved in chemical co-precipitation method. Reproduced with permission from Singh et al. (2018)

having 15 nm as average diameter via ultrasonic-assisted co-precipitation method. This is a very useful and successful method to synthesize good-quality iron oxide NPs but has some limitations such as strong base is required for this method, large size distribution and limited control on the morphology of nanospecies.

Thermal Decomposition Method

Thermal decomposition method can be divided into two strategies. The first is the injection of precursors into a hot mixture of reaction called hot injection approach, and secondly, a reaction mixture is heated and prepared at room temperature, called conventional reaction strategies. The decomposition of ferric salts, such as $[Fe_4(CON_2H_4)_6]$ $(NO_3)_3$(Iron-Ultra Complex), $[Fe_4(CN)_6 . 14H_2O]$ (Prussian Blue) (Hu et al. 2010, 2012), $Fe_3(CO)_{12}$ (Ferric Carbonate) (Maity et al. 2009), $Fe(C_5H_5)_2$(Ferrocene), $Fe(CO)_5$, Fe (acec)$_3$(Acec-acetylacenate) (Wang et al. 2012), Fe(Cup)3 (Cup-*N*-nitro–suphenylhydroylamine) (Rockenberger et al. 1999; Liang et al. 2006), followed by oxidation, results high-quality iron oxide NPs. Park et al. (2004) synthesize the monodisphere iron oxide NPs via thermal decomposition of iron chloride salt. Almost 40 g of iron oxide NPs were synthesized in single reaction. Amara et al. (2012) reported the synthesis of nanospheres and

nanocubes of Fe_3O_4 (maghemite) via solvent-less thermal decomposition. Different mixtures of poly-vinyl pyrrolidone (PVP) and ferrocene were used as precursors. Ibrahim et al. (2018) synthesized the γ-Fe_2O_3NPs via facile thermal decomposition of $[Fe(C_{32}H_{22}N_4O_4)] \cdot 2H_2O$ complexes. The average diameter of γ-Fe_2O_3 was 9 nm and with superparamagnetic behavior at room temperature.

Microwave-Assisted Method

It is also a very common method used for the synthesis of iron oxide NPs with various shapes and sizes. From few years, chemists are using microwave-assisted synthesis as reaction methodology. Molecules align their dipoles with externally applied field when excited by microwave radiations. Due to becoming the electrical field excitation in phase with strong agitation, a lot of internal heating is produced (Hu et al. 2007; Wu et al. 2011b; Ai et al. 2010; Qiu et al. 2011). Sreeja and Joy (2007) synthesized the superparamagnetic iron oxide NPs of γ-Fe_2O_3 using microwave-assisted method. The reaction was preceded at 150 °C for 25 min. The average diameter of γ-Fe_2O_3 NPs was 10 nm. Jiang et al. (2010) used microwave-assisted approach and observed that by changing the experimental conditions, the shape and magnetic properties were changed. Henam et al. (2019) reported the synthesis of Fe_3O_4 NPs from extract of Euphorbia helioscopis leaves and iron (III) nitrate nona-hydrate. They claimed the size of iron oxide NPs was 7–10 nm.

Sonolysis Method

The sonolysis, also called sono-chemical method, is based on chemical effects of ultrasound waves which occur due to the acoustic cavitation. Novel structures were produced by using high-intensity ultrasound waves. Sonolysis does not require long reaction time, bulk high temperature or high pressure (Rajabi et al. 2019). Ultrasound waves create and oscillate the bubbles, produced due to alternating expansion and compressive of acoustic waves. After growing to a specific size (~ in the order of tens of mm), oscillating bubbles start to accumulate the ultrasound energy in an effective way. Under suitable conditions, a bubble can grow and collapse in very short time releasing all the stored energy. This implosion of cavity bubbles is very fast and highly localized with temperature (5000 K) and pressure (1000 bar) (Wu et al. 2008; Bang and Suslick 2010). Sonolysis method is also used to synthesize iron oxide NPs. The salt solutions of ferric and ferrous can be sonicated under specific conditions (Mukh-Qasem and Gedanken 2005; Abu-Much and Gedanken 2008; Morel et al. 2008; Wu et al. 2007; Zhang et al. 2012). Zhu et al. (2013) reported the synthesis of Fe_3O_4NPs, dispersed on a sheet of graphene oxide, (Fe_3O_4/RGO), by sonolysis method. The range of these NPs was 30–40 nm. Theerdhala et al. (2010) used sonolysis for binding

L-arginine onto Fe_3O_4 NPs surface. These surface modified iron oxide NPs can be more useful in drug delivery.

Laser-Assisted Synthesis

Laser-assisted synthesis of NPs is an emerging method which is showing extraordinary potential for synthesis NPs in well-controlled environment. In this method, a metal target is dipped in liquid phase such as water, acetone or other organic solvents. The laser beam is focused on the target surface and ablates the target surface which is converted into NPs. Different parameters can control the shape and size of nanoparticle, such as laser energy, focusing, nature of solvent and ablation time. Figure 11.5 shows the general schematic setup for synthesis of iron oxide NPs by using Nd:YAG pulsed laser (Huang et al. 2019). Lasemi et al. (2018) synthesized the polycrystalline iron oxide NPs via laser ablation technique. During ablation of iron target in water, Fe_xO_y was produced, whereas in ethanol, core shell, Fe/Fe_xO_yNPs was obtained. The size of Fe_xO_y and Fe/Fe_xO_yNPs was around 15 nm and 20 nm, respectively. Zhang et al. (2018) reported the synthesis of α-Fe_2O_3 NPs via laser ablation. They ablate the iron target in acetone using femto-second pulsed laser. The size of NPs was 4–5 nm. Iwamoto and Ishigaki (2013) used laser ablation on bulk targets of Fe_2O_3, FeO and Fe_3O_4 for their ablation in water and observed the size of NPs from 1 to 5 nm. The small particles were dispersed, and larger were agglomerated in the solution.
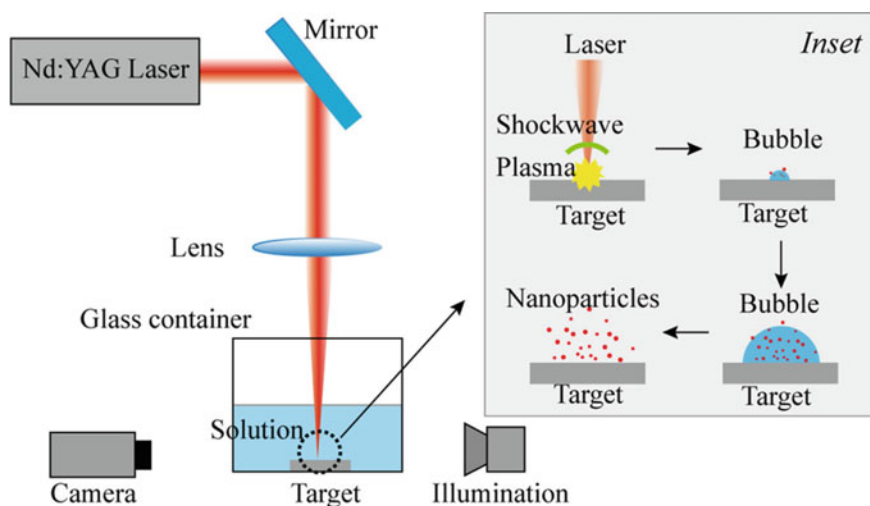
Fig. 11.5 Schematic diagrams of experimental setup and laser-assisted synthesis process. Reproduced with permission from Huang et al. (2019)

Thermal Response Mechanisms of Magnetic NPs

When magnetic NPs are subjected to AC magnetic field, they produce heat. To understand the physical basis of this heat generation, a most important point is the tuning of magnetic NPs. The heating effect is due to the energy losses during magnetization and demagnetization of magnetic NPs (Deatsch and Evans 2014; Dutz and Hergt 2013; Fortin et al. 2007). A magnetic field can be produced by a number of ways, but the most efficient source is the inductive coils. A uniform magnetic field can be established inside of these coils. The following is the formula to find the intensity of the field produced by the coils

$$H_\alpha = \frac{NI}{L} \tag{11.2}$$

where N, I and L are the number of turns, current and length of coil, respectively.

Three mechanisms are responsible for the energy losses in magnetic materials under the action of changing magnetic field.

i.   Eddy currents (Shreshtha et al. 2015)
ii. Hysteresis losses
iii. Neel and Brownian Relaxation.

Eddy Current

Eddy current is one of the two less effective mechanisms for heat generation at nanoscale; other is hysteresis losses. When a conducting material is kept in an alternating magnetic field, then a current is produced, called eddy current. According to Lenz's law, "the induce current always opposes the cause producing it." To do so, electrons are moved in a plane which is normal to the applied field in the conductor. This results in energy loss due to opposing tendency of eddy currents. In all this process, some of the K.E of electrons is converted into heat. This phenomenon is responsible for heat generating in bulk materials.

It is thought that losses in eddy current case can be induced higher in those sections which have larger area of cross section. This is due to the radially escalation of eddy currents. The power generation in a cylinder of uniform area of cross section, placed in a uniform magnetic field, can be calculated by

$$P = \sigma(\pi\mu_o f H_\alpha)^2 r^2 \tag{11.3}$$

where σ express (conductivity of tissues in bulk)
μ_o is the permeability of free space
f is the frequency
H_α is the strength of field

and *r* is the effective radius.

It can be seen from the above equation that power losses in the form of current depend upon the square of frequency, effective radius and field strength. Therefore, due to increase in any of the above three factors, the losses will rise. Tissues have also the ability to produce eddy currents because of their small specific electrical conductivity. Their magnetic field is much weaker than the required for therapeutic dose (Ramprasad et al. 2004; Andrä and Nowak 2007). As eddy currents are induced in bulk material (around 1 cm in size) (Shreshtha et al. 2015), consequently for nanoscale particles, their contribution is nearly zero in heat generation. Figure 11.6a shows the schematic of eddy current generation.

Hysteresis Losses

The ferromagnetic materials have regions in which magnetic spins of all the atoms aligned in same direction or have uniform magnetization. Such regions are said to be magnetic domains. Domains are separated from each other by a domain wall as shown in Fig. 11.6b. When such type of magnetic materials is placed in AC magnetic field, they magnetize during positive half cycle due to alignment of magnetic domains and demagnetize during negative half cycle. The graphical representation of this magnetization and demagnetization process is a nonlinear curve which is called hysteresis loop as shown in Fig. 11.6b. The area of the loop gives information about the strength of material, i.e., either it is soft or hard magnetic material, secondly about the heat loss during AC cycle (Gubin et al. 2005). In fact, the magnetic moments align themselves in the direction of externally applied alternating magnetic field and lower their potential energy. In case of multi-domain nanomaterial, the domains align and expand at the cost of other domains in their surroundings. Once the domain walls moved, they will never adopt their previous positions even the externally applied field reduces to zero. Such behavior is responsible for hysteresis loop (Burrows et al. 2010). In case of nanomedicine applications, the commonly used strength of applied magnetic field (H) is 0–40 KA/m, and frequency range is kept b/w KHz to MHz. The reversal processes, like buckling, fanning and curling, also contributed in relaxation of spins but much complicated to explain with the help of classical models, like Stoner–Wohlfarth model. On the other hand, Hergt and his coworkers (2006) derived an expression which gives the losses on the basis of particle size distribution and parameters of applied field (Hergt et al. 2008). Their theoretical estimations and experimental values give specific loss power for superparamagnetic NPs. Figure 11.6c shows reversal mechanisms for a single domain (Gubin et al. 2005).
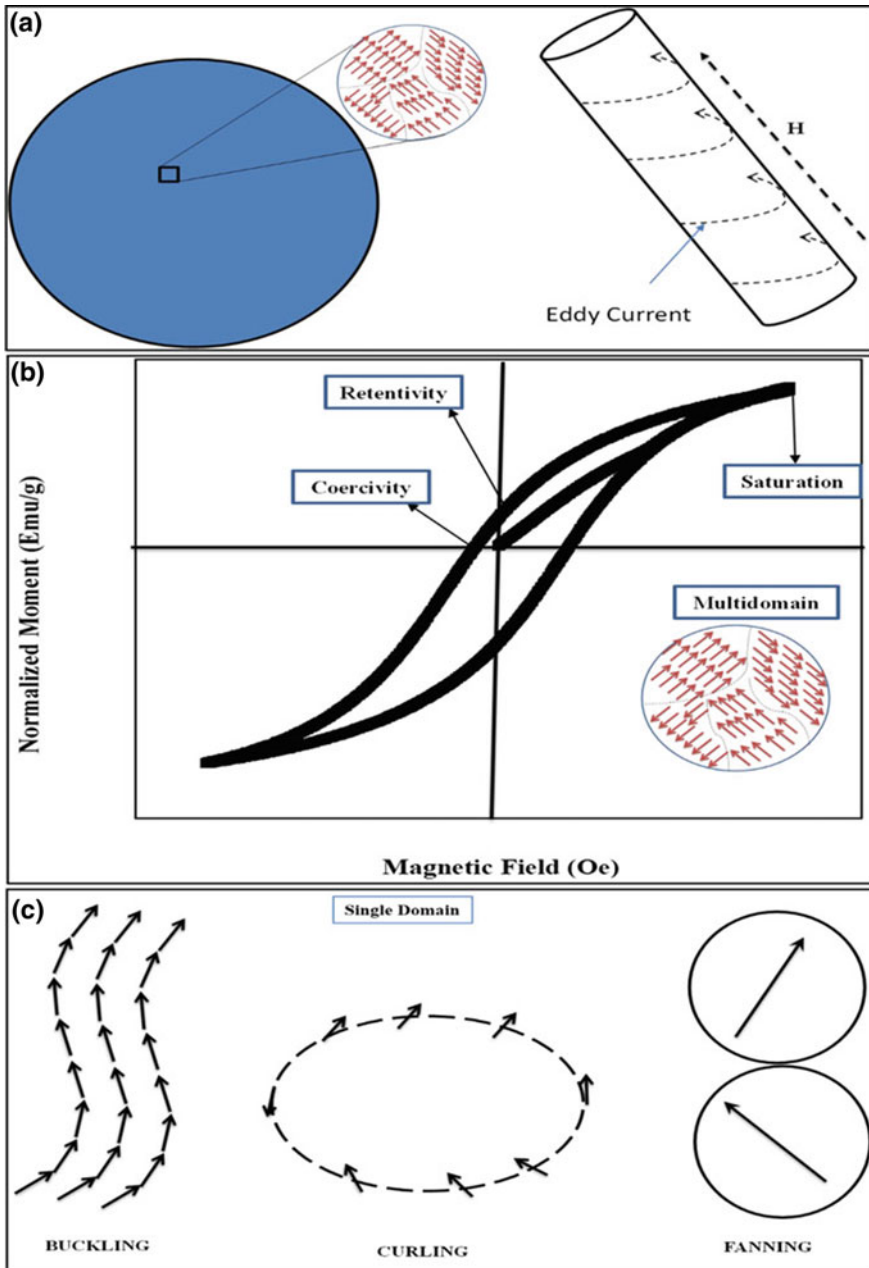
Fig. 11.6 **a** Schematic representation of eddy current formation and direction, **b** representative B–H curve of magnetic nanoparticles, **c** possible reversal processes of single-domain ferromagnetic NPs, buckling, curling, fanning. Reproduced with permission from Ramprasad et al. (2004), Rosensweig (2002)
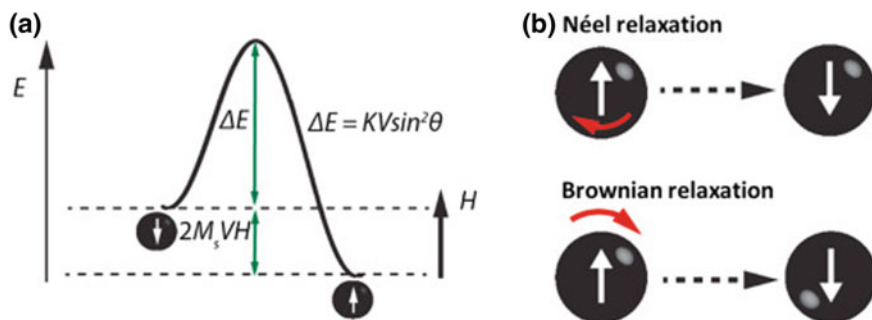
Fig. 11.7 **a** Representative curve of energy barrier controlling single-domain particle, **b** schematic representation of Neel and Brownian relaxation

Neel and Brownian Relaxations

At nanometer scale, the total magnetization of a particle is taken as single spin, which is the resultant of all the magnetic moments in the magnetic particle. Relaxation in superparamagnetic NPs occurs under two mechanisms; Neel relaxation and Brownian relaxation (Fig. 11.7). In Neel relaxation, the movement of all types of spins in the particles is involved, but it does not essentially involve the particle's physical movement. Such oscillations in magnetization occur in specific time, T_B called the blocking temperature. This blocking temperature suggests the limit of superparamagnetic to get a steady magnetization. A certain value of temperature is required to develop the oscillations discussed above. The temperature for these oscillations should be greater than critical temperature T_B, where spins are blocked and considered to be fixed. By changing the volume and temperature of the particle, the time period of oscillation can be controlled.

The following equation shows this temperature dependency

$$\tau_N = \frac{\sqrt{\pi}}{2} \tau_o \frac{e^{\Gamma}}{\sqrt{\Gamma}} \tag{11.4}$$

This equation was given by Lawis Neel (Néel and Kurti 1988; Néel 1950), where τ is attempt time (10^{-9} s) and Γ is ration of anisotropy to thermal energies.

Value of Γ is given by

$$\Gamma = \frac{K_\mu V_M}{k_B T} \tag{11.5}$$

In Eq. 11.5,

K_μ is anisotropy energy density
V_M is volume of suspension
k_B is Boltzmann constant

T is temperature.

A strong relationship can be seen among the values of thermal energy kT and anisotropic energy K in Neel relaxation equation. This provides the inner magnetic core relaxation.

In Brownian relaxation, itself particle's rotation is involved. The particle can be aligned with externally applied field by rotation. Hydrodynamic volume and fluid's viscosity are two factors which control the Brownian relaxation (Brown 1963). The characteristic relaxation time depends upon the rotational mobility of magnetic NPs, suspended in liquid media. The mathematical expression for Brownian relaxation,

$$\tau_B = \frac{3\eta V_H}{k_B T} \tag{11.6}$$

where η is viscosity of liquid solvent
V_H is hydrodynamic volume
K_B is Boltzmann constant
T is temperature.

At small particle level, Neel relaxation is dominated whereas Brownian relaxation becomes more prominent above a specific size of particles. Both mechanisms can be observed close to a critical size limit where total effect is calculated by taking geometric mean of their values (Deissler et al. 2014).

The equation for this is

$$\tau = \frac{\tau_B \tau_N}{\tau_B + \tau_N} \tag{11.7}$$

However, it is difficult to find the contribution of each of the mechanisms separately. Scientists have performed experimental studies to solve this difficulty and observed that NPs of maghemite and cobalt ferrite show higher specific absorption rate (SAR) values in water than in intracellular endosomes. Neel relaxation was prominent for maghemite NPs whereas Brownian relaxation was notable for cobalt ferrite. In similar way, Zhang et al. (2010) studied the magnetite NPs in water and polydimethylsiloxome (PMDS) to differentiate between two mechanisms of relaxation. They found that magnetite NPs have high SAR value in water for both relaxation mechanisms. Despite that, by increasing the strength of applied field and frequency, Neel relaxation gives some additional contribution.

Ferrofluids for Hyperthermia

Due to a valuable heat loss under applied field, several mediators (magnetic NPs which produce high heat power) of heat have been made. Therefore, many types of magnetic NPs of different shapes and sizes have been studied to use as heat generating

source in biological systems. These include metals like Co, Fe, Gd, Mg, Mn, Zn, Ni and their oxide. Particularly, iron oxide-based NPs have been studied widely, due to their potential applications (Gubin et al. 2005; Javed et al. 2017; Obaidat et al. 2015; Thanh 2012).

Iron oxide NPs are superparamagnetic and have shown great properties for heat generation. Other ferrites such as $CoFe_2O_4$, $CuFe_2O_4$, $Li_{-0.5}Fe_{2.5}O_4$, $MgFe_2O_4$, $NiFe_2O_4$, $ZnFe_2O_4$, etc., are also being used for hyperthermia (Basti 2014; Raveendran and Kannan 2019; Céspedes et al. 2014; Hanini et al. 2016; Lin et al. 2014; Veverka et al. 2014). Zinc ferrite NPs having size 11 nm have ability to self-regulate the magnetic heating in local glioma therapy. Nanocomposite of ferromagnetic material such as Zn, Mn and Gd with iron oxide (Hanini 2016; Hilger and Kaiser 2012) and Fe with gold (Wijaya et al. 2007) are also been studied.

However, due to their unique features like biocompatibility, less toxicity and easy recycling in the body, iron oxide NPs have main focus by researchers in recent years (Neuberger et al. 2005). The value of SAR depends upon the type of liquid media, used as solvent to suspend NPs. Hiergeistand coworkers (Hiergeist et al. 1999) studied the heat generation ability of ferrofluids in solidified and molten gel. They observed that liquid phase gel has valuable power loss than in solid phase. Fortin et al. (2007) performed a detailed study to differentiate between two relaxation mechanisms (Brownian and Neel relaxation mechanisms). They found that with the increase in viscosity of medium, the main contribution is from Neel relaxation, whereas, Brownian relaxation contribution faints out. In case of water, Brownian relaxation was dominated, and Neel relaxation depends upon frequency of AC field. Kandasamy et al. (2018a) used the superparamagnetic iron oxide NPs for in vitro hyperthermia studies. The average size of NPs was about 20 nm after coating with terephthalic and aminoterephthalic acid. They reported that about 90% of breast cancer cells dead due to thermal response of these coated superparamagnetic iron oxide NPs. In the same year, Kandasamy et al. (2018b) reported the use of superparamagnetic iron oxide NPs, having size 6–10 nm, in thermotherapy for the treatment of liver cancer cells. Gupta et al. (2018) studied the HeLa cells by hyperthermia-assisted treatment. They used the DOX-loaded Fe_3O_4—reduced graphene oxide NPs having average size 10 nm. Arachchige et al. (2017) used dextran-coated iron oxide NPs. Arachchige et al. used dextran coatediron NPs with average size of 8 nm for multimode imaging and treatment of cancer via hyperthermia treatment and for curing pancreaticcancer. Mazario et al. (2017) used iron oxide NPs to produce localized heat when placed under the influence of externally applied magnetic field. The value of saturation magnetization was 63 emug^{-1} at 37 °C. Espinosa et al. (2016) used iron oxide nanocubes having size about 20 nm for hyperthermia studies. After dual-mode exposure, complete cell death was observed in both in vivo and in vitro systems. Shen et al. (2015) synthesize Fe_3O_4 NPs with average size 15 nm and observed that the thermal response of clustered NPs was much better than dispersed NPs, but clustered NPs were more cytotoxic. Chen et al. (2016) used crystallized iron oxide NPs for thermal therapy of SUM-159 tumor bearing mice. The size of NPs was 15 nm. Zhou et al. (2014) synthesize PEGylated Fe@Fe_3O_4 multifunctional NPs of 13.4 ± 0.8 nm average diameter. These iron-coated Fe_3O_4 NPs have shown good
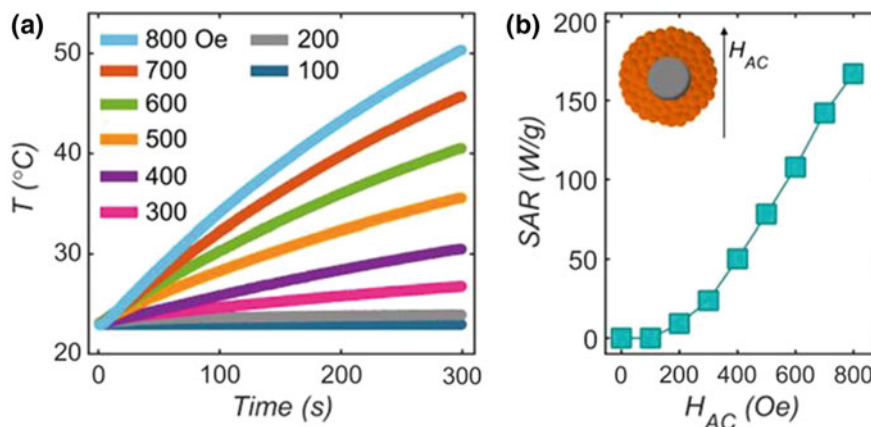
Fig. 11.8 **a** Temperature increases for iron oxide-based nanoflowers with different AC magnetic field strengths at frequency 310 Hz, **b** curve between heat generation and applied magnetic field

heating efficiency. Figure 11.8 shows the trend of temperature and heat generation in the presence of externally applied AC magnetic field strengths of different values at frequency 310 Hz.

Conclusion

In this chapter, we focused on thermal response and synthesis of simple and metal-based iron oxide NPs. The synthesis of iron oxide, having different range of composition, sizes and shapes, has made great progress over the last decade. Iron oxide NPs have very promising response for imaging purposes, but commercial scale use of these nanoparticles is not very common as there gadolinium nanoparticles are still used. May be T1 contrast utilization of iron oxide can be more useful as mostly studies are focused on negative contrast generated by the nanoparticles. Magnetic properties of the iron oxide nanoparticles for the localized heat production are good but to produce enough therapeutic response, morphology and composition of the iron-based nanoparticles should be set to get reasonably high specific absorption rate. Doped iron oxide nanoparticles have shown better response for heat generation, but still, the final translation into a medicine is still far because there are many other parameters that are still needed investigations such as optimum concentration of nanoparticles, metabolization, uptake, circulation time and toxicity.

References

Abu-Much R, Gedanken A (2008) Sonochemical synthesis under a magnetic field: structuring magnetite nanoparticles and the destabilization of a colloidal magnetic aqueous solution under a magnetic field. J Phys Chem C 112(1):35–42

Adeleye AS et al (2018) Influence of nanoparticle doping on the colloidal stability and toxicity of copper oxide nanoparticles in synthetic and natural waters. Water Res 132:12–22

Aghazadeh M, Maragheh MG, Norouzi P (2018) Enhancing the supercapacitive properties of iron oxide electrode through Cu^{2+}-doping: cathodic electrosynthesis and characterization. Int J Electrochem Sci 13(2):1355–1366

Ai Z et al (2010) Facile microwave-assisted synthesis and magnetic and gas sensing properties of Fe_3O_4 nanoroses. J Phys Chem C 114(14):6237–6242

Ali A et al (2016) Synthesis, characterization, applications, and challenges of iron oxide nanoparticles. Nanotechnol Sci Appl 9:49

Amara D, Grinblat J, Margel S (2012) Solventless thermal decomposition of ferrocene as a new approach for one-step synthesis of magnetite nanocubes and nanospheres. J Mater Chem 22(5):2188–2195

Andrä W, Nowak H (2007) Magnetism in medicine: a handbook. Wiley

Anjum S et al (2017) Effect of cobalt doping on crystallinity, stability, magnetic and optical properties of magnetic iron oxide nano-particles. J Magn Magn Mater 432:198–207

Anthony JW et al (1990) Handbook of mineralogy, vol 1. Mineral Data Publ. Tucson

Anthony J et al (2017) Handbook of mineralogy. Chantilly (VA), mineralogical society of America

Arachchige MP et al (2017) Functionalized nanoparticles enable tracking the rapid entry and release of doxorubicin in human pancreatic cancer cells. Micron 92:25–31

Ba-Abbad MM et al (2017) Size and shape controlled of α-Fe_2O_3 nanoparticles prepared via sol–gel technique and their photocatalytic activity. J Sol-Gel Sci Technol 81(3):880–893

Bang JH, Suslick KS (2010) Applications of ultrasound to the synthesis of nanostructured materials. Adv Mater 22(10):1039–1059

Basti H et al (2014) Size tuned polyol-made Zn0. 9M0. 1Fe₂O₄ (M = Mn, Co, Ni) ferrite nanoparticles as potential heating agents for magnetic hyperthermia: from synthesis control to toxicity survey. Mater Res Exp 1(4):045047

Batsaikhan E et al (2015) Development of ferromagnetic superspins in bare Cu nanoparticles by electronic charge redistribution. Int J Mol Sci 16(10):23165–23176

Boxall C, Kelsall G, Zhang Z (1996) Photoelectrophoresis of colloidal iron oxides. Part 2.—magnetite (Fe_3O_4). J Chem Soc Faraday Trans 92(5):791–802

Brown WF (1963) Thermal fluctuations of a single-domain particle. Phys Rev 130(5):1677–1686

Burrows F et al (2010) Energy losses in interacting fine-particle magnetic composites. J Phys D Appl Phys 43(47):474010

Cai L et al (2014) The effect of doping transition metal oxides on copper manganese oxides for the catalytic oxidation of CO. Chin J Catal 35(2):159–167

Cao F et al (2007) Synthesis of carbon–Fe_3O_4 coaxial nanofibres by pyrolysis of ferrocene in supercritical carbon dioxide. Carbon 45(4):727–731

Cao M et al (2012) Food related applications of magnetic iron oxide nanoparticles: enzyme immobilization, protein purification, and food analysis. Trends Food Sci Technol 27(1):47–56

Casula MF et al (2016) Manganese doped-iron oxide nanoparticle clusters and their potential as agents for magnetic resonance imaging and hyperthermia. Phys Chem Chem Phys 18(25):16848–16855

Céspedes E et al (2014) Bacterially synthesized ferrite nanoparticles for magnetic hyperthermia applications. Nanoscale 6(21):12958–12970

Chakrabarti S, Mandal S, Chaudhuri S (2005) Cobalt doped γ-Fe_2O_3 nanoparticles: synthesis and magnetic properties. Nanotechnology 16(4):506

Chen S, Carroll DL (2002) Synthesis and characterization of truncated triangular silver nanoplates. Nano Lett 2(9):1003–1007

Chen M et al (2016) Inhibitory effect of magnetic Fe_3O_4 nanoparticles coloaded with homohar-ringtonine on human leukemia cells in vivo and in vitro. Int J Nanomed 11:4413

Confalonieri GB et al (2011) Template-assisted self-assembly of individual and clusters of magnetic nanoparticles. Nanotechnology 22(28):285608

Cornell RM, Schwertmann U (2003) The iron oxides: structure, properties, reactions, occurrences and uses

Daoush W (2017) Co-precipitation and magnetic properties of magnetite nanoparticles for potential biomedical applications. J Nanomed Res 5(1):e6

de la Venta J et al (2007) Magnetism in polymers with embedded gold nanoparticles. Adv Mater 19(6):875–877

Deatsch AE, Evans BA (2014) Heating efficiency in magnetic nanoparticle hyperthermia. J Magn Magn Mater 354:163–172

Deissler RJ, Wu Y, Martens MA (2014) Dependence of Brownian and Néel relaxation times on magnetic field strength. Med Phys 41(1):012301

Dutz S, Hergt R (2013) Magnetic nanoparticle heating and heat transfer on a microscale: basic principles, realities and physical limitations of hyperthermia for tumour therapy. Int J Hyperth 29(8):790–800

Espinosa A et al (2016) Duality of iron oxide nanoparticles in cancer therapy: amplification of heating efficiency by magnetic hyperthermia and photothermal bimodal treatment. ACS Nano 10(2):2436–2446

Feldheim D, Foss C (2002) Metal nanoparticles: synthesis, characterization, and applications. Dekker, New York

Feng H et al (2018) Cu-Doped Fe@ Fe_2O_3 core–shell nanoparticle shifted oxygen reduc-tion pathway for high-efficiency arsenic removal in smelting wastewater. Environ Sci Nano 5(7):1595–1607

Fernández-Barahona I et al (2019) Cu-doped extremely small iron oxide nanoparticles with large longitudinal relaxivity: one-pot synthesis and in vivo targeted molecular imaging. ACS Omega 4(2):2719–2727

Fortin J-P et al (2007) Size-sorted anionic iron oxide nanomagnets as colloidal mediators for magnetic hyperthermia. J Am Chem Soc 129(9):2628–2635

Garcia M et al (2007) Magnetic properties of ZnO nanoparticles. Nano Lett 7(6):1489–1494

Garitaonandia JS et al (2008) Chemically induced permanent magnetism in Au, Ag, and Cu nanoparticles: localization of the magnetism by element selective techniques. Nano Lett 8(2):661–667

Ge S et al (2009) Facile hydrothermal synthesis of iron oxide nanoparticles with tunable magnetic properties. J Phys Chem C 113(31):13593–13599

Gubin SP et al (2005) Magnetic nanoparticles: preparation, structure and properties. Russ Chem Rev 74(6):489

Gupta AK et al (2007) Recent advances on surface engineering of magnetic iron oxide nanoparticles and their biomedical applications

Gupta AK, Gupta M (2005) Synthesis and surface engineering of iron oxide nanoparticles for biomedical applications. Biomaterials 26(18):3995–4021

Gupta J et al (2018) Superparamagnetic iron oxide-reduced graphene oxide nanohybrid-a vehicle for targeted drug delivery and hyperthermia treatment of cancer. J Magn Magn Mater 448:332–338

Hanini A et al (2016) Zinc substituted ferrite nanoparticles with $Zn0. 9Fe_2. 1O4$ formula used as heating agents for in vitro hyperthermia assay on glioma cell*s*. J Magn Magn Mater 416:315–320

Hanini A et al (2016) Thermosensitivity profile of malignant glioma U87-MG cells and human endothelial cells following γ-Fe_2O_3 NPs internalization and magnetic field application. RSC Adv 6(19):15415–15423

Haribabu V et al (2016) Optimized Mn-doped iron oxide nanoparticles entrapped in dendrimer for dual contrasting role in MRI. J Biomed Mater Res B Appl Biomater 104(4):817–824

Henam SD et al (2019) Microwave synthesis of nanoparticles and their antifungal activities. Spectrochim Acta Part A Mol Biomol Spectrosc 213:337–341

Hergt R et al (2006) Magnetic particle hyperthermia: nanoparticle magnetism and materials development for cancer therapy. J Phys: Condens Matter 18(38):S2919

Hergt R, Dutz S, Röder M (2008) Effects of size distribution on hysteresis losses of magnetic nanoparticles for hyperthermia. J Phys: Condens Matter 20(38):385214

Hiergeist R et al (1999) Application of magnetite ferrofluids for hyperthermia. J Magn Magn Mater 201(1–3):420–422

Hilger I, Kaiser WA (2012) Iron oxide-based nanostructures for MRI and magnetic hyperthermia. Nanomedicine 7(9):1443–1459

Hu X et al (2007) α-Fe$_2$O$_3$ nanorings prepared by a microwave-assisted hydrothermal process and their sensing properties. Adv Mater 19(17):2324–2329

Hu M, Jiang J-S, Zeng Y (2010) Prussian blue microcrystals prepared by selective etching and their conversion to mesoporous magnetic iron (III) oxides. Chem Commun 46(7):1133–1135

Hu M et al (2012) Hierarchical magnetic iron (III) oxides prepared by solid-state thermal decomposition of coordination polymers. RSC Adv 2(11):4782–4786

Huang H et al (1997) Synthesis, characterization, and nonlinear optical properties of copper nanoparticles. Langmuir 13(2):172–175

Huang H (2019) Pulsed laser ablation of bulk target and particle products in liquid for nanomaterial fabrication. AIP Adv 9(1):015307

Ibrahim E et al (2018) Electric, thermoelectric and magnetic characterization of γ-Fe$_2$O$_3$ and Co$_3$O$_4$ nanoparticles synthesized by facile thermal decomposition of metal-Schiff base complexes. Mater Res Bull 99:103–108

Iwamoto T, Ishigaki T (2013) Fabrication of iron oxide nanoparticles using laser ablation in liquids. J Phys Conf Ser

Javed Y, Ali K, Jamil Y (2017) Magnetic nanoparticle-based hyperthermia for cancer treatment: factors affecting heat generation efficiency. In: Complex magnetic nanostructures. Springer, Berlin, pp 393–424

Jiang F et al (2010) Synthesis of iron oxide nanocubes via microwave-assisted solvolthermal method. J Alloy Compd 503(2):L31–L33

Kandasamy G et al (2018a) Systematic investigations on heating effects of carboxyl-amine functionalized superparamagnetic iron oxide nanoparticles (SPIONs) based ferrofluids for in vitro cancer hyperthermia therapy. J Mol Liq 256:224–237

Kandasamy G et al (2018b) Functionalized hydrophilic superparamagnetic iron oxide nanoparticles for magnetic fluid hyperthermia application in liver cancer treatment. ACS Omega 3(4):3991–4005

Kang YS et al (1996) Synthesis and characterization of nanometer-size Fe$_3$O$_4$ and γ-Fe$_2$O$_3$ particles. Chem Mater 8(9):2209–2211

Karna SK et al (2011) Observations of large magnetic moments in icosahedral Pb nanoparticles. J Phys Chem C 115(18):8906–8910

Kuchma E, Kubrin S, Soldatov A (2018) The local atomic structure of colloidal superparamagnetic iron oxide nanoparticles for theranostics in oncology. Biomedicines 6(3):78

Lasemi N et al (2018) Laser-assisted synthesis of colloidal FeWxOy and Fe/FexOy nanoparticles in water and ethanol. ChemPhysChem 19(11):1414–1419

Laurent S et al (2011) Magnetic fluid hyperthermia: focus on superparamagnetic iron oxide nanoparticles. Adv Coll Interface Sci 166(1–2):8–23

Lee N, Hyeon T (2012) Designed synthesis of uniformly sized iron oxide nanoparticles for efficient magnetic resonance imaging contrast agents. Chem Soc Rev 41(7):2575–2589

Liang X et al (2006) Synthesis of nearly monodisperse iron oxide and oxyhydroxide nanocrystals. Adv Func Mater 16(14):1805–1813

Lim J, Majetich SA (2013) Composite magnetic–plasmonic nanoparticles for biomedicine: manipulation and imaging. Nano Today 8(1):98–113

Lin M, Huang J, Sha M (2014) Recent advances in nanosized Mn–Zn ferrite magnetic fluid hyperthermia for cancer treatment. J Nanosci Nanotechnol 14(1):792–802

Litrán R et al (2006) Magnetic and microstructural analysis of palladium nanoparticles with different capping systems. Phys Rev B 73(5):054404

Liu M-S et al (2006) Enhancement of thermal conductivity with Cu for nanofluids using chemical reduction method. Int J Heat Mass Transf 49(17–18):3028–3033

Maity D et al (2009) Synthesis of magnetite nanoparticles via a solvent-free thermal decomposition route. J Magn Magn Mater 321(9):1256–1259

Massart R (1981) Preparation of aqueous magnetic liquids in alkaline and acidic media. IEEE Trans Magn 17(2):1247–1248

Mazario E et al (2017) Functionalization of iron oxide nanoparticles with HSA protein for thermal therapy. IEEE Trans Magn 53(11):1–5

Mohanraj K, Sivakumar G (2017) Synthesis of γ-Fe$_2$O$_3$, Fe$_3$O$_4$ and copper doped Fe$_3$O$_4$ nanoparticles by sonochemical method. Sains Malaysiana 46(10):1935–1942

Morel A-L et al (2008) Sonochemical approach to the synthesis of Fe$_3$O$_4$@ SiO$_2$ core-shell nanoparticles with tunable properties. ACS Nano 2(5):847–856

Mukh-Qasem RA, Gedanken A (2005) Sonochemical synthesis of stable hydrosol of Fe$_3$O$_4$ nanoparticles. J Colloid Interface Sci 284(2):489–494

Néel L (1950) Théorie du traînage magnétique des substances massives dans le domaine de Rayleigh. J Phys Radium 11(2):49–61

Néel L, Kurti N (1988) Selected works of Louis Néel. Gordon and Breach Science Publ, New York

Neuberger T et al (2005) Superparamagnetic nanoparticles for biomedical applications: possibilities and limitations of a new drug delivery system. J Magn Magn Mater 293(1):483–496

Niemirowicz K et al (2012) Magnetic nanoparticles as new diagnostic tools in medicine. Adv Med Sci 57(2):196–207

Obaidat I, Issa B, Haik Y (2015) Magnetic properties of magnetic nanoparticles for efficient hyperthermia. Nanomaterials 5(1):63–89

O'Hara MJ et al (2016) Magnetic iron oxide and manganese-doped iron oxide nanoparticles for the collection of alpha-emitting radionuclides from aqueous solutions. RSC Adv 6(107):105239–105251

Pankhurst Q et al (2009) Progress in applications of magnetic nanoparticles in biomedicine. J Phys D Appl Phys 42(22):224001

Park J et al (2004) Ultra-large-scale syntheses of monodisperse nanocrystals. Nat Mater 3(12):891

Pascal C et al (1999) Electrochemical synthesis for the control of γ-Fe$_2$O$_3$ nanoparticle size. Morphology, microstructure, and magnetic behavior. Chem Mater 11(1):141–147

Punitha S, Nehru L (2018) Direct synthesis of iron oxide (α-Fe$_2$O$_3$) nanoparticles by the combustion approach. Adv Sci Lett 24(8):5608–5610

Puntes VF, Krishnan KM, Alivisatos AP (2001) Colloidal nanocrystal shape and size control: the case of cobalt. Science 291(5511):2115–2117

Qiu G et al (2011) Microwave-assisted hydrothermal synthesis of nanosized α-Fe$_2$O$_3$ for catalysts and adsorbents. J Phys Chem C 115(40):19626–19631

Raghunath A, Perumal E (2017) Metal oxide nanoparticles as antimicrobial agents: a promise for the future. Int J Antimicrob Agents 49(2):137–152

Rajabi A et al (2019) Synthesis, characterization, and antibacterial activity of Ag$_2$O-loaded polyethylene terephthalate fabric via ultrasonic method. Nanomaterials 9(3):450

Ramprasad R et al (2004) Magnetic properties of metallic ferromagnetic nanoparticle composites. J Appl Phys 96(1):519–529

Raveendran S, Kannan S (2019) Polymorphism and phase transitions in t-ZrO$_2$/CoFe$_2$O$_4$ composite structures: impact of composition and heat treatments. Cryst Growth Des 19(8):4710–4720

Riviere C et al (2006) Nano-systems for medical applications: biological detection, drug delivery, diagnosis and therapy. Annales de Chimie 31(3):351–367

Rockenberger J, Scher EC, Alivisatos AP (1999) A new nonhydrolytic single-precursor approach to surfactant-capped nanocrystals of transition metal oxides. J Am Chem Soc 121(49):11595–11596

Rosensweig RE (2002) Heating magnetic fluid with alternating magnetic field. J Magn Magn Mater 252:370–374

Sayed FN, Polshettiwar V (2015) Facile and sustainable synthesis of shaped iron oxide nanoparticles: effect of iron precursor salts on the shapes of iron oxides. Sci Rep 5:9733

Sequeira CA (2018) Electrochemical synthesis of iron oxide nanoparticles for biomedical application. Org Med Chem Int J 5(2):1–12

Shatnawi M et al (2016) Influence of Mn doping on the magnetic and optical properties of ZnO nanocrystalline particles. Res Phys 6:1064–1071

Shen S et al (2015) Magnetic nanoparticle clusters for photothermal therapy with near-infrared irradiation. Biomaterials 39:67–74

Shreshtha P, Mohite S, Jadhav M (2015) Review on thermal seeds in magnetic hyperthermia therapy. IJITR 3(4):2283–2287

Sibokoza S et al (2017) The effect of temperature and precursor concentration on the synthesis of cobalt sulphide nanoparticles using cobalt diethyldithiocarbamate complex. Chalcogenide Lett 14(2)

Singh H et al (2018) Development of superparamagnetic iron oxide nanoparticles via direct conjugation with ginsenosides and its in-vitro study. J Photochem Photobiol, B 185:100–110

Skoropata E et al (2014) Intra-and interparticle magnetism of cobalt-doped iron-oxide nanoparticles encapsulated in a synthetic ferritin cage. Phys Rev B 90(17):174424

Sreeja V, Joy P (2007) Microwave–hydrothermal synthesis of γ-Fe_2O_3 nanoparticles and their magnetic properties. Mater Res Bull 42(8):1570–1576

Thanh NT (2012) Magnetic nanoparticles: from fabrication to clinical applications. CRC press

Theerdhala S et al (2010) Sonochemical stabilization of ultrafine colloidal biocompatible magnetite nanoparticles using amino acid, L-arginine, for possible bio applications. Ultrason Sonochem 17(4):730–737

Venkatesan K et al (2015) Structural and magnetic properties of cobalt-doped iron oxide nanoparticles prepared by solution combustion method for biomedical applications. Int J Nanomed 10(Suppl 1):189

Veverka M et al (2014) Magnetic heating by silica-coated Co–Zn ferrite particles. J Phys D Appl Phys 47(6):065503

Vitulli G et al (2002) Nanoscale copper particles derived from solvated Cu atoms in the activation of molecular oxygen. Chem Mater 14(3):1183–1186

Wahab A et al (2019) Dye degradation property of cobalt and manganese doped iron oxide nanoparticles. Appl Nanosci 1–10

Wang M-H et al (2010) Fabrication of large-scale one-dimensional Au nanochain and nanowire networks by interfacial self-assembly. Mater Chem Phys 119(1–2):153–157

Wang Y et al (2012) One-pot reaction to synthesize superparamagnetic iron oxide nanoparticles by adding phenol as reducing agent and stabilizer. J Nanopart Res 14(4):755

Warner CL et al (2012) Manganese doping of magnetic iron oxide nanoparticles: tailoring surface reactivity for a regenerable heavy metal sorbent. Langmuir 28(8):3931–3937

Wijaya A (2007) Magnetic field heating study of Fe-doped Au nanoparticles. J Magn Magn Mater 309(1):15–19

Wolf S et al (2001) Spintronics: a spin-based electronics vision for the future. Science 294(5546):1488–1495

Wong RM et al (2012) Rapid size-controlled synthesis of dextran-coated, 64Cu-doped iron oxide nanoparticles. ACS Nano 6(4):3461–3467

Wu W et al (2007) Sonochemical synthesis, structure and magnetic properties of air-stable Fe_3O_4/Au nanoparticles. Nanotechnology 18(14):145609

Wu W, He Q, Jiang C (2008) Magnetic iron oxide nanoparticles: synthesis and surface functionalization strategies. Nanoscale Res Lett 3(11):397

Wu W et al (2010) Large-scale and controlled synthesis of iron oxide magnetic short nanotubes: shape evolution, growth mechanism, and magnetic properties. J Phys Chem C 114(39):16092–16103

Wu S et al (2011a) Fe_3O_4 magnetic nanoparticles synthesis from tailings by ultrasonic chemical co-precipitation. Mater Lett 65(12):1882–1884

Wu L et al (2011b) Unique lamellar sodium/potassium iron oxide nanosheets: facile microwave-assisted synthesis and magnetic and electrochemical properties. Chem Mater 23(17):3946–3952

Wu W et al (2015) Recent progress on magnetic iron oxide nanoparticles: synthesis, surface functional strategies and biomedical applications. Sci Technol Adv Mater 16(2):023501

Yang L et al (2008) Development of receptor targeted magnetic iron oxide nanoparticles for efficient drug delivery and tumor imaging. J Biomed Nanotechnol 4(4):439–449

Zhang Z, Boxall C, Kelsall G (1993) Photoelectrophoresis of colloidal iron oxides 1. Hematite (α-Fe$_2$O$_3$). In: Colloids in the aquatic environment. Elsevier, pp 145–163

Zhang X et al (2010) Role of Néel and Brownian relaxation mechanisms for water-based Fe$_3$O$_4$ nanoparticle ferrofluids in hyperthermia. Biomed Eng Appl Basis Commun 22(05):393–399

Zhang S et al (2012) Sonochemical formation of iron oxide nanoparticles in ionic liquids for magnetic liquid marble. Phys Chem Chem Phys 14(15):5132–5138

Zhang D et al (2018) Magnetic Fe@ FeO$_x$, Fe@ C and α-Fe$_2$O$_3$ single-crystal nanoblends synthesized by femtosecond laser ablation of fe in acetone. Nanomaterials 8(8):631

Zhou Z et al (2014) Iron/iron oxide core/shell nanoparticles for magnetic targeting MRI and near-infrared photothermal therapy. Biomaterials 35(26):7470–7478

Zhu S et al (2013) Sonochemical fabrication of Fe$_3$O$_4$ nanoparticles on reduced graphene oxide for biosensors. Ultrason Sonochem 20(3):872–880

Chapter 12
Manganite Pervoskite Nanoparticles: Synthesis, Heating Mechanism, Toxicity, and Self-regulated Hyperthermia

Check for updates

Navadeep Shrivastava, Yasir Javed, Khuram Ali, Muhammad Raza Ahmad, Kanwal Akhtar and S. K. Sharma

Abstract In the present chapter, we have reviewed the possibility of LaMnO$_3$ and Sr-doped perovskite manganites LaMnO$_3$ (LMO) nanomaterials in therapeutics and diagnostics with a special attention for hyperthermia applications. In addition, we have also emphasized on the importance of synthesis, heating mechanism, concept of self-regulated hyperthermia, and toxicity issue of this important class of nanomaterials for their safer use in biological applications.

Keywords LSMO nanoparticles · Synthesis and surface modifications · Heating mechanism · Hyperthermia applications · Toxicity study

Introduction

Magnetic nanostructured materials have a great amount of benefit in several important biomedical applications (Gupta and Gupta 2005; Mornet et al. 2004) for instance

N. Shrivastava
Institute of Physics, Federal University of Goias, Goiania-Go 74690-900, Brazil

Department of Chemistry, Biochemistry and Physics, University of Quebec at Trois-Rivieres, Trois-Rivières, QC, Canada

Y. Javed · K. Akhtar
Magnetic Materials Laboratory, Department of Physics, University of Agriculture, University Main Rd, Faisalabad 38000, Pakistan

K. Ali
Nano-Optoelectronics Research Laboratory, Department of Physics, University of Agriculture Faisalabad, Faisalabad 38040, Pakistan

M. R. Ahmad
Centre for Advanced Studies in Physics (CASP), GC University Lahore, Lahore, Pakistan

S. K. Sharma (✉)
Department of Physics, Faculty of Science and Technology, The University of the West Indies, Saint Augustine, Trinidad and Tobago
e-mail: surender.sharma@sta.uwi.edu; surender76@gmail.com

imaging, thermal therapy for cancer, drug delivery, sensing, and magnetic fluid hyperthermia (MFH) for cancer therapy. In the recent time, MFH has been gaining a tremendous interest amongst scientific community as a method for curing cancer especially as an accessory to other modalities such as chemotherapy and radiotherapy (Mornet et al. 2006; Hilger et al. 2004, 2005; Bubnovskaya et al. 2014; Lee et al. 2014; Epherre et al. 2011a). The knowledge of hyperthermia is based on the higher heat sensitivity of cancerous cells as compared to normal/healthy ones. Therefore, treating cancerous cells at elevated temperatures between 42 and 47 °C would allow to destroy tumour cells and to spare the healthy ones. MFH is a promising hyperthermia modality taking benefit from the dimension of magnetic nanoparticles (MNPs) to transform into heat the energy absorbed from a high-frequency AC magnetic field generally via magnetic energy losses. The clinical modus operandi would involve in the administration of stable and non-toxic colloidal suspensions of the MNP fluids followed by a short time (generally a few minutes) exposure to the AC magnetic field. Temperature rising above 42 °C may cause necrosis and can be controlled by using MNPs with a Curie temperature, T_C of 42 °C. The most widely used materials for MFH applications are inorganic magnetic spherical cores which are (a) essentially stabilized by electrostatic repulsive forces in the case of a direct injection into the tumour (Jordan et al. 2001) or (ii) preferentially embedded in a hydrophilic macromolecular corona for improving their blood half-time in the case of intravenous administration (Mornet et al. 2006).

Neglecting frictional or viscosity losses, two foremost loss mechanisms and subsequently two kinds of magnetic cores are generally prominent. In single-domain superparamagnetic nanoparticles, loss mechanism results from the rotation of magnetic moments in overcoming the energy barrier $E = KV$, where K is the magnetic anisotropy constant and V is the volume of the magnetic core. Energy is dissipated when the particle moment relaxes to its equilibrium orientation and this phenomenon is known as Neel relaxation. In multidomain ferromagnetic/ferrimagnetic nanoparticles, heating is mainly due to hysteresis losses (Andra and Nowak 2007; Pandalai 2002) and the better use of the latter type requires the protection of the magnitude of magnetization for small particles as high as possible. Further, the coercive force should be adjusted to a genuine value assuring enough heating efficiency, but not too high with respect to technical restrictions on the field amplitude for practical medical heating application. At the same time, consideration should be paid to the applied frequency. Generally, it has to be higher than 50 kHz to avoid neuromuscular electrostimulation and lower than 1 MHz, in order to achieve a sensible penetration depth of the radio frequency field. Thus, it is apparent that an improvement cannot be achieved only by modulation of the parameters of the applied AC magnetic field, but also by finely controlling a number of parameters of the nanoparticles such as particle size, size distribution, shape, chemical phase composition, and tunes them in such a way to enhance the overall magnetic properties of the materials.

The most widely used compounds for MFH applications are magnetic iron oxides (Fe_3O_4, γ-Fe_2O_3) and substituted iron oxides. This is due to their good biocompatibility, their easy synthesis to form of stable aqueous magnetic fluids and their equivalent development as contrast agents in magnetic resonance imaging (MRI)

(Corot et al. 2006). As a result, the majority of in vitro and in vivo experiments on animals models (and very lately on humans) are done with heat mediators based on Fe_3O_4 or γ-Fe_2O_3 cores (Jordan et al. 2001). However, they associated with some inconveniencies concerned with a partial possibility to control magnetic properties in the desired way. Most importantly, they consist of reasonable heating capability, characterized by specific absorption rate (SAR), expressed in Watt/g, which is vital for clinical purposes. This is due to the fact that the higher value of SAR significant to reduce the required dose to be injected to the patient. Another important factor concerns the control of in vivo temperature growth during hyperthermia because the heat conduction and energy adsorption in vivo are widely unknown, and therefore, the local overheating may damage healthy or normal tissue. Therefore, scientist and researcher are trying the way to design the nanoparticles and manipulate the Curie temperature of materials and tune it in the range of 42–50 °C, so that the heating would spontaneously stop as soon as the environment temperature reaches close to T_c. Subsequently, the nanoparticles would act not only as heat mediators but also as in vivo temperature controller (Jordan et al. 2001). It is obvious that these settings can be barely fulfilled by simple magnetic iron oxides nanoparticles. A possible solution to handle this issue is to design complex magnetic oxides, whose magnetism can be properly tailored by different ways, for example, (i) the modification of essential properties depending on the phase composition and crystal structure or (ii) the modification of physical properties like particle size, shape depending on the synthesis protocols and otherwise employing multiphase materials.

Indeed, these approaches are combined, and in the present chapter, a simple attempt is made to review the possibility $LaMnO_3$ and Sr-doped perovskite manganites $LaMnO_3$ (LMO) nanomaterials in therapeutics and diagnostics with a special attention for hyperthermia application. This is due to its decent capability for controlling the heating temperature up to 47 °C in the presence of a high magnetic field, high AC frequency, and the long duration of induction heating because of low Curie temperature (T_C ~ 50 to 70 °C) (Corot et al. 2006; Hedayatnasab et al. 2017; Sharma and Chen 2009; Goya et al. 2008).

There are many reports which show that $LaMnO_3$ and $La_{1-x}Sr_xMnO_3$ nanoparticles are applied successfully to MFH. Generally, LMO has an antiferromagnetic (AFM) phase transition temperature with Neel temperature, T_N ~ 140 K which increases with decreasing particle diameter to T_N ~ 260 K (d = 40 nm) (Ghosh et al. 2014) and to 246 K (d = 18 nm) (Markovich et al. 2010). On the other hand, in $La_{1-x}Sr_xMnO_3$, however, the magnetic interactions as well as the particle diameter change with the concentration (x) of Sr ions, which makes it a much more complex system for which to improve the hyperthermia response. $La_{1-x}Sr_xMnO_3$ in the form of nanoparticles is ferromagnetic with high magnetization M and T_C but below 70 °C and hence enables its use for MFH treatment of cancerous cells with a possibility of in vivo temperature control (ur Rashid and Manzoor 2016; Kulkarni et al. 2015; AOTrauma 2001; McBride et al. 2016; Bahadur et al. 2007; Uskokovic et al. 2006). The T_C value depends strongly on the Sr-concentration x (Kulkarni et al. 2016; Soleymani et al. 2017). As reported by in Uskokovic et al. (2006) and Prasad et al. (2007), for x = 0.24 and x = 0.27, T_C is about 40 and 45 °C,

respectively, whereas for $x = 0.30$, it is 49 °C (AOTrauma 2001). Literature shows (Das et al. 2006) that in LMO nanoparticles with reduction or decreasing particle size, M increases, while in Sr-doped LMO nanoparticles, it decreases. The lattice parameters decrease with decreasing particle size for LMO, LSMO, and (La, Ca) MnO_3 nanoparticles. Kulkarni et al. (2016) showed that radio frequency response LSMO nanoparticles, combined with drugs for simultaneous MFH and drug delivery, are potential anti-cancer agents. Similarly, Silver (Ag) (Melnikov et al. 2009) and Sodium (Na) (Shlyakhtin et al. 2007) doped manganite nanoparticles are also recommended for temperature-controlled MFH. Ebrahimi et al. (2016) have studied temperature change pattern in tumour and neighbouring tissue. The proposed model system could be useful to gain insight on the self-controlled MFH (SCMFH) and for treatment strategy determination.

Properties of LSMO Nanoparticles

LSMO are mixed metal oxide having perovskite structure ABO_3 where La^{3+} or Sr^{2+} are cations at the A-site and Mn^{3+} or Mn^{4+} are cations at the B-site. They are generally ferromagnetic in bulk form. However, super paramagnetic and ferromagnetic nanoparticles of LSMO have been reported widely in literature. Perovskites have a face-cantered cubic lattice with A-sites found on the corners, and B-sites in the centre of the unit cell. When a larger Sr^{2+} ion (0.144 nm) substitutes the La^{3+} ion (0.136 nm), a distortion of the local crystal lattice from the ideal cubic geometry is observed. Orthorhombic and rhombohedral structures (Fig. 12.1) are observed depending on the concentration x of the Sr^{2+} ions (Epherre et al. 2011b; Urushibara et al. 1995).

The doping of Sr^{2+} changes the strain within the lattice and the bond length Mn–O and the Mn–O–Mn band angles are reformed. The Mn atoms are ionized to Mn^{3+} or
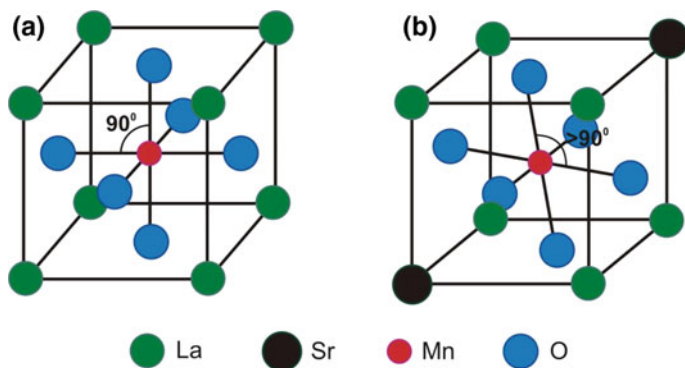
Fig. 12.1 Structure of perovskites of type ABO_3: **a** undoped $LaMnO_3$; **b** lattice distortion caused by the dopant in $La_{1-x}Sr_xMnO_3$ compounds

Mn^{4+} in dependence on the Sr dopant concentration x. When x increases, the three phases are observed: spin-canted antiferromagnetic insulator in low doped region (for $x < 0.1$), a ferromagnetic insulator for $0.1 < x < 0.15$, and a ferromagnetic metal phase when $x > 0.15$ (Rao and Raveau 1998; Zener 1951; Rao et al. 1998; Mahendiran et al. 1996). The ferromagnetic order and the behaviour of itinerant electrons are both explained by the Zener's double-exchange mechanism (Zener 1951). This mechanism is a type of a magnetic exchange whereby a d-hole (electron) is transferred from Mn^{3+} (d^4, t_{2g}^3 e^1, $S = 2$) to Mn^{4+} (d^3, t_{2g}^3, $S = 3/2$) via the oxygen ion O^{2-}. It is well known that in these compounds, the ferromagnetism depends not only on the double-exchange but also on the super-exchange interaction, i.e. their physical properties and rich phase diagrams arise from these competing interactions (Rao and Raveau 1998). On the one hand, the charge and orbital order lead to insulating and antiferromagnetically ordered ground state and on the other hand, the double-exchange interactions lead to metallic and ferromagnetically ordered ground state. This competition depends on external fields as well as on carrier concentration, lattice structure, and ionic sizes. The double-exchange interaction Mn^{3+}–O–Mn^{4+} is ferromagnetic while the super-exchange interactions Mn^{4+}–O–Mn^{4+} and Mn^{3+}–O–Mn^{3+} are antiferromagnetic.

As depicted before, the thermal heating of the cancer tissues should not exceed 42–50 °C, since, at higher temperatures, the denaturation of the proteins in the normal healthy cells results in the formation of necrosis with a subsequent lethal outcome. Therefore, the nanoparticles examined, here, must have a magnetic phase transition temperature between 315 and 323 K. Beyond this temperature, the nanoparticles pass into a paramagnetic state and the heating is terminated. Therefore, this allows one to choose in advance LSMO compounds with such x values, most appropriate for such study. Further, conditions necessary for the properties of nanoparticles to be suitable for MFH are: (i) a large saturation moment for a large response by applying an external AC magnetic field; (ii) a large value of coercive force which gives larger specific absorption rate for the best heating results; (iii) the size of nanoparticles is smaller or close to single-domain size range.

Synthesis of LSMO Nanoparticles

Combustion Methods

Preparing materials of using combustion methods (also called as self-propagating high-temperature synthesis) is an effective and low-cost method for production of various industrially and laboratory useful materials. Recently, a number of important breakthroughs in this field have been made, notably for development of new catalysts and nanocarriers with properties better than those for similar traditional materials. There are two ways for combustion synthesis:(i) solid-state combustion (SSC) and (ii) solution combustion synthesis (SCS) (Shinde et al. 2010; Mukasyan et al. 2007)

(Fig. 12.2). The second method (SCS) is relatively new and equally important for nanoscaled materials synthesis. In this method, initial reaction medium is aqueous solution and the process involves a self-sustained reaction in homogeneous solution of different oxidizers (e.g. metal nitrates) and fuels such as urea, glycine, hydrazides. Depending on the type of the precursors and conditions used for the synthesis protocols, the SCS process can be obtained as either volume or layer-by-layer propagating combustion modes. This process provides nanosize oxide materials and uniform doping of trace amounts of rare-earth impurity ions in a single-step preparation of materials. For perovskite magnetic nanomaterials synthesis, this is favourite methods of researchers which are discussed below (Shinde et al. 2010; Mukasyan et al. 2007).

Makni and colleagues studied the molybdenum and titanium substitution on manganese site of $La_{0.7}Sr_{0.3}MnO_3$ (LSMO), $La_{0.7}Sr_{0.3}Mn_{0.95}TiO_3$ (LSM–TiO), $La_{0.7}Sr_{0.3}Mn_{0.95}Mo_{0.05}O_3$ (LSM–Mo–O) nanoparticles (~18 nm) and synthesised such NPs using an aqueous combustion process (glycine nitrate process, GNP), for hyperthermia applications by choosing the two "oxidizing and fuelling" reagents (Makni et al. 2018). They used nitrate precursors (nitrates "N" work as oxidizing agents) and varying amount of Glycine "G" as fuel. They kept G/N molar ratio equal to 0.56 to improve the chelation and maintained the flame temperature inducing the crystallization of compounds. For the materials cooking, nitrate precursor preparation, i.e. titanium nitrate and molybdenum nitrate, was added to the mixture of glycine. Further, the nitrate solution was thoroughly mixed by stirring and dehydrated by heating on a hot plate at $T = 100$ °C for 2 h. The mixture becomes transparent viscous gel. In the next stage, this gel was heated to $T = 350$ °C, to initiate auto-combustion. Due to this, very bulky black ash was obtained as product. During characterization, a decrease in Curie temperature (T_C) was observed for both compounds, whereas the magnetization increases for LSM–Mo–O and is reduced for LSM–Ti–O. Additionally, SAR values were found to be 10.363 W/g for the LSMO; however, it is about 8.927 and 9.135 W/g for LSM–Ti–O and LSM–Mo–O, respectively (Makni et al. 2018).
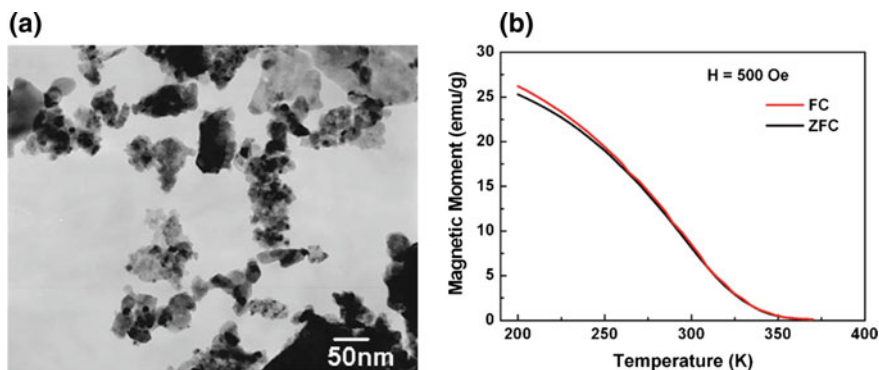
Fig. 12.2 a TEM images LSMO nanoparticles, **b** FC and ZFC graphs of the nanoparticles. Reprinted with permission from Shinde et al. (2010)

Similarly, Epherre and co-workers (2011a) prepared the un-aggregated (following fast calcination) $La_{0.82}Sr_{0.18}MnO_{3+\delta}$ perovskite NPs (with crystallite size of 22 nm) using n-glycine nitrate process (GNP). This GNP process utilizes the benefits of exothermic, fast and self-sustaining chemical reactions between metal nitrates and glycine as a suitable reducing agent. In the case of the GNP synthesis of LSMO, the redox combustion reaction has been provided as follows (Note that it is a debatable reaction) (Epherre et al. 2011a):

$$0.82La(NO_3)_3 + 0.18Sr(NO_3)_2 + Mn(NO_3)_2 +_n H_2N(CH_2)CO_2H$$
$$+ (2.25n - 5.73)O_2 \rightarrow La_{0.82}Sr_{0.18}MnO_3 + 2nCO_2$$
$$+ 2.5nH_2O + (2.41 + 0.5n)N_2$$
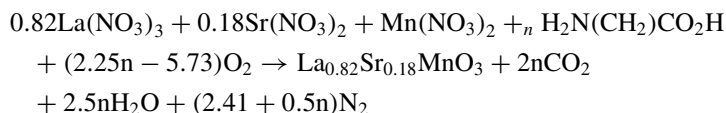
They studied effect of *G/N* ratios to understand phase purity, crystallite size, and manganese valency. Additionally, to improvise the chelation of the cations in acidic pH, fuel abundant conditions were selected for accurate control of the cationic composition.

Sol–Gel Method

The sol–gel process is a wet-chemical technique that uses either a chemical solution or colloidal particles to produce an integrated gel network (Rao et al. 2017; Feldhoff et al. 2008) with subsequent post-treatment and transition into solid oxide (novel metal oxide NPs and mixed oxide composites) material. This method provides potential control over the textural and surface properties of the materials. Sol–gel method mainly undergoes in few steps such as hydrolysis, condensation, and drying process to deliver the final metal oxide. Sol–gel method is divided into two categories: aqueous (water is solvent) and as non-aqueous (organic solvent as reaction medium). It is possible to get high purity and uniform nanostructure at low temperatures using this process. The reaction pathway using the sol–gel method has been shown in Fig. 12.3. Nature of metal precursor and types of solvents are important factors to prepare metal oxides NPs (Rao et al. 2017; Feldhoff et al. 2008). Several perovskite NPs have been prepared in context of magnetic hyperthermia applications.

A nanocrystalline manganese perovskite phase of mean crystallite size ~30 nm was synthesized by Kaman et al. (2009) utilizing above-mentioned technique employing citric acid and ethylene glycol as solvent and subsequent evaporation of water, drying, calcination, and annealing (750 °C, 3 h). The resulting single-phase product was subjected to rolling and ball milling in ethanol that provided to individual 20-nm NPs without signal of sintering. This mechanical treatment was carried out to break "connecting bridges" which might initiate in a rising tendency to sinter at high annealing temperature. Bubnovskaya and group studied a wide range of experiments of magnetic fluid hyperthermia of rodent tumours using manganese perovskite NPs

Fig. 12.3 The reaction pathway for the production of metal oxide nanostructures in the sol–gel method
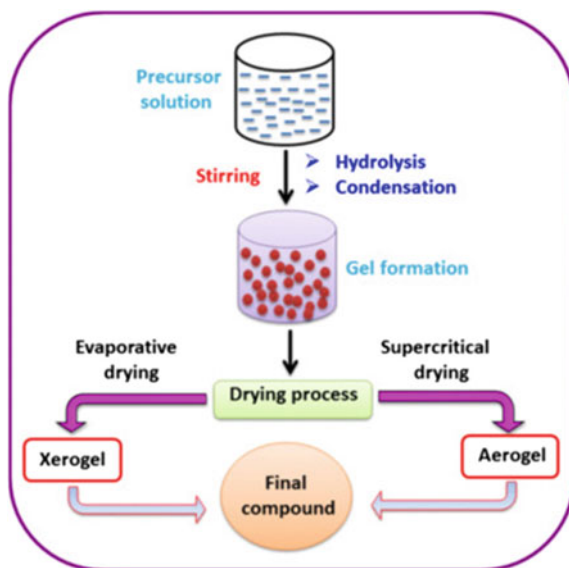
prepared using sol–gel methods using similar synthetic approaches (Bubnovskaya et al. 2014).

Citrate Gel Method

One of the most common small organic molecules used in sol–gel chemistry is citric acid which is cheap, effective chelating agent. It is a weak triprotic acid with three carboxylic acid moieties that are able to dissociate as in equations:

$$H_3Cit \rightleftharpoons H_2Cit^- + H^+ \quad K_{a1} = 7.10 \times 10^{-4};$$

$$H_2Cit \rightleftharpoons HCit^{2-} + H^+ \quad K_{a2} = 1.68 \times 10^{-5};$$

$$HCit^{2-} \rightleftharpoons Cit^{3-} + H^+ \quad K_{a1} = 6.40 \times 10^{-6}.$$
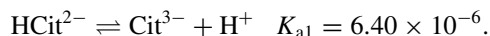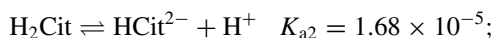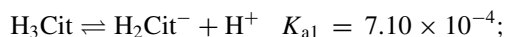
In a typical synthesis procedure, aqueous metal salts (e.g. nitrates) are mixed with citric acid which is further treated by heat to form a viscous solution or gel. It is also possible to change the pH and enhance cation binding to the citrate by using bases such as ammonia or ethylenediamine (Lassa et al. 2015). Conversion of the "viscous solution/gel" to a metal oxide is performed pyrolysis process in air, with the maximum temperature that is specific for individual system. The method is very useful to prepare binary, ternary, and quaternary metal oxides and also to prepare

crystalline and amorphous forms. The major benefits of citrate sol–gel method over traditional sol–gel synthesis are the uniformity of the starting material. When the metal–citrate viscous solvents are heated at ∼300 to 400 °C, the organic components in the mixture start combustion process that strongly depends on the metal counterion and presence of additives, and pH. In the first step of the synthesis, i.e. sol–gel preparation, the presence of the organic matrix promotes a small crystallite size after the nucleation starts, where the crystal sites are evenly dispersed and numerous (Rao et al. 2017; Lassa et al. 2015; Balamurugan and Melba 2015).

Vasseur and others prepared manganese perovskite ($La_{0.75}Sr_{0.25}MnO_3$) NPs of the crystallite size 20–180 nm, starting from citrate gel precursor by annealing in the range of 570–900 °C (Vasseur et al. 2006). Oxide source of La, carbonate precursors of Sr and Mn were dissolved in the required amount in nitric acid and further mixed with citric acid and ethylene glycol in a ratio 2:3 and NH_4OH was used for basic pH (~9). Further, a three-step process was included: (i) water evaporation (80–90 °C); (ii) drying the obtained gel-like material (~160 °C), and (iii) calcination (~400 °C, 4 h) in air. To prepare the final NPs of different sizes, annealing (570–900 °C) is required (Vasseur et al. 2006). The parent compound $LaMnO_3$ is a single-valent (Mn^{3+}) antiferromagnetic insulator and replacement of lanthanum by strontium ions in the perovskite A-sites causes a gradual decrease of the steric distortions and the structure changes from the orthorhombic (Pbnm) to rhombohedral $R\bar{3}c$ symmetry. It leads to a decrease of the resistivity, insulator–metal transition for the compositions of $x > 0.17$ and due to double-exchange interactions to ferromagnetic ordering with Curie temperature in the range of 320–370 K for $0{:}2 < x < 0{:}3$ (Epherre et al. 2011a). The materials thus offer a unique possibility of the self-controlled heating power for magnetic hyperthermia application (Brusentsov et al. 2007; Falk and Issels n.d.).

Thermal Decomposition Methods

In general, the thermal decomposition of various organometallic complexes (e.g. iron pentacarbonyl, acetylacetonate, oleate, or stearate in polar organic solvents) in the presence of ligands (oleic acid and/or oleylamine) was reported as a synthesis path leading to the best geometrically defined nanocrystals. These syntheses are performed at reflux of high boiling point solvents, commonly 1 octadecene ($T_b = 318$ °C), octyl ether ($T_b = 288$ °C), ordiphenyl ether ($T_b = 268$ °C). There are two types of the thermal decompositions of the reactants: (i) "hot injection" protocol at the high reaction temperature, leading to a rapid formation of nuclei called "burst", caused by the sudden supersaturation of the solution with precursors and (ii) reactants can be introduced following a "heating-up" protocol: the solvent, the precursors, and the ligands are mixed at a lower temperature before being heated at a controlled rate up to the reaction temperature, leading to the formation of nanocrystals. In principle, several factors such as the ratio of organometallic reagents, surfactant(s), solvents, the reaction time in absence of stirring affect sizes/morphologies. In some cases, further oxidation improves the crystallinity of the materials, as it is also the case

by applying a magnetic hyperthermia treatment that acts as an annealing process. MNPs obtained this way are dispersible in polar solvents which are a limitation for biological applications and hence require a ligand-exchange strategy.

In comparison with other methods (combustion/sol-gel), thermal decomposition has not been favourite methods for magnetic perovskite materials for hyperthermia applications due to expensive and time-consuming. For an illustration, Daengsakul et al. (2009) prepared magnetic $La_{0.7}Sr_{0.3}MnO_3$ nanoparticles by thermal decomposition method using acetate salts of La, Sr, and Mn as starting materials. For this, thermal decomposition of the precursor is carried out at the temperatures of 600, 700, 800, 900, and 1000 °C for 6 h. Further, they characterized them for cytotoxicity. Further, by the same group (Daengsakul et al. 2009), magnetic nanoparticles of $La_{1-x}Sr_xMnO_3$ (LSMO) with $x = 0$, 0.1, 0.2, 0.3, 0.4, 0.5 were prepared via the thermal hydro-decomposition method. In this process, high purity acetates of La, Mn, and Sr were used as starting materials (in ratio La: Sr: Mn of $1 - x$: x: 1) were dissolved and stirred in deionized water (DI water) at a ratio of volume/weight of DI water to total acetate salts and were thermally decomposed in an oven under normal atmosphere at different temperatures of 600, 700, 800, and 900 °C for 6 h and left to cool down to room temperature before being ground to obtain LSMO nanoparticles (Daengsakul et al. 2009).

Coatings

The nanoparticles of pure LSMO have a very low colloidal stability in the aqueous environment and encapsulation without previous stabilization of the nanoparticles would lead to the growth of silica on their aggregates. The employed stabilization procedure involves adsorption of citric acid and its ionization by increasing the pH which leads to the separation of individual grains due to the repulsive forces of negatively charged surfaces (peptization).Silica coating has been a preference for the coating over LSMO. First, LSMO can be treated by diluted ice-cold nitric acid (0.1M) in an ultrasound bath (Epherre et al. 2011a). After the removal of the nitric acid, the nanoparticles were re-dispersed in ice-cold citric acid (1M) using ultrasound (Fig. 12.4) (Lassa et al. 2015). The particles separated by centrifugation were washed with water and re-dispersed in water alkalized by a few drops of ammonia. Then the suspension was exposed to ultrasound irradiation, and the solution of citrated particles was poured into a volume of ethanol/water/ammonia solution. The encapsulation was carried out at a temperature of 40 °C under the simultaneous action of mechanical stirring and ultrasound irradiation by adding tetra-ethoxysilane (618 µL). The product of the required size can be separated using centrifugation involving removal of heavy fractions present in the raw mixture and separation of nanoparticles from the corresponding supernatant. It was washed two times with ethanol and three times with water using centrifugation and re-dispersion in an ultrasound bath and the final product LMSO@SiO_2 is obtained (Kaman et al. 2009).
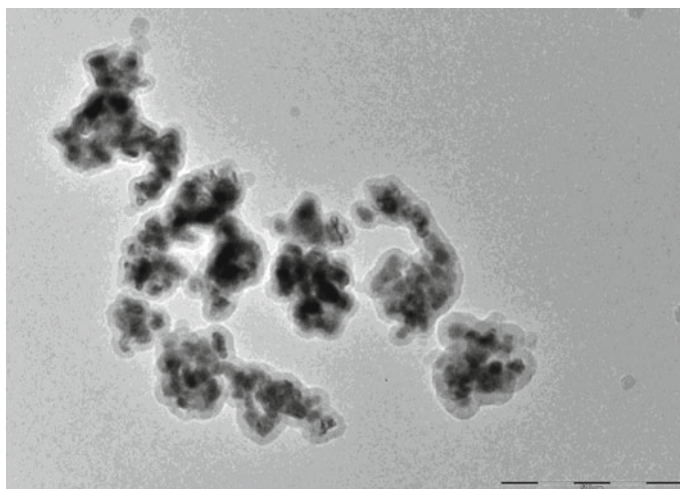
Fig. 12.4 TEM image of SiO$_2$ coated LSMO nanoparticles. Scale bar 500 nm (Kaman et al. 2009)

Heating Mechanism

LSMO Nanoparticles for Magnetic Fluid Hyperthermia

Rare-earth metals-based ferromagnetic materials, for example, LSMO compounds, have gained much attention in biomedical field especially in hyperthermia applications. La$_{1-x}$ Sr$_x$MnO$_3$ showed wide transition temperature range of 283–370 K with large magnetic moment values. These physical properties make LSMO compounds as promising candidate towards hyperthermia therapy. Amongst LSMO compounds, La$_{0.7}$Sr$_{0.3}$MnO$_3$ possessed zero coercivity ($H_c = 0$ Oe), magnetic moment value (40 emu g^{-1}) under magnetic field of 300–400 Oe at room temperature, which is usually applied during hyperthermia therapy (Epherre et al. 2011a; Zhang et al. 2010).

To enhance the biocompatibility and stability of LSMO NPs, different type of coating materials including dextran, bovine serum albumin, citrate ligands, fatty amines (Rajagopal et al. 2006), SiO$_2$ (Bhayani et al. 2007), and dextran (Hong et al. 2009) was reported. However, few reports regarding amphiphilic polymer (PVP)-coated LSMO NPs are presented recently. PVP is amorphous, hygroscopic, and available in powder form. It is neutral, non-toxic, and possessed many pharmaceutical, industrial, cosmetic, and medical applications. Jadhav et al. reported LSMO nanoparticles prepared by combustion method with size 23 nm and functionalized through polyvinylpyrrolidone (PVP) for their use in magnetic fluid hyperthermia. In double-distilled water and phosphate buffer saline, stable suspension of the resulted PVP-coated particles were suspended which revealed narrow hydrodynamical size distributions. At different alternating values of magnetic fields, i.e. 167.6, 251.4 and

335.2 Oe, heat induction studies were performed in the two-suspension media. In phosphate buffer saline, PVP-coated LSMO NPs exhibited higher specific absorption rate as compared to double-distilled water (Jadhav et al. 2013). Jadhav et al. also investigated the water-dispersible LSMO magnetic NPs for their use in hyperthermal treatment of cancer as effective heating source. Oleic acid–betaine coated LSMO NPs possessed narrow hydrodynamical size distribution as they formed stable suspension in physiological and aqueous media. MFH studies revealed high heating efficacy of oleic acid-coated LSMO NPs as compared to the bare LSMO. Functionalized LSMO NPs with oleic acid showed no toxicity for in vivo use because of their biocompatibility with L929 and HeLa cell lines (Jadhav et al. 2015). Jadhav et al. also synthesized LSMO NPs through solution combustion method and functionalized further with polyethylene glycol and polyvinyl alcohol. NPs have induction heating at very low concentration (5 mg/mL) and possess higher specific absorption rate at constant frequency and varying magnetic field (Jadhav et al. 2015).

Self-controlled Hyperthermia

Nanoparticles with high specific absorption rate (SAR) are the best candidate in magnetic hyperthermia. Specific absorption rate is the amount of heat generated by the per unit mass of magnetic material under radio frequency magnetic field. To minimize the dosage of hyperthermia agent, high SAR is required. One of the most sophisticated forms of magnetic hyperthermia is self-controlled hyperthermia in which range of Curie temperature lies between 315 and 320 K (Prasad et al. 2007; Natividad et al. 2012). Cancerous cells can be destroyed effectively at this Curie temperature range with nominal damage to the healthy cells. By maintaining the Curie temperature range of the magnetic materials, they can be used as self-controlled heating agent in the anticipated range of temperature to avoid any type of heating process. Such type of magnetic materials provides less heating in paramagnetic state while more heating in the ferromagnetic state. Hence, Curie temperature maintains constant current in the tumour targeted area. LSMO NPs are considered as promising candidates for self-controlled hyperthermia therapy. Magnetization of LSMO based NPs is higher and the range for the Curie temperature is 315–320 K (Kaman et al. 2009; Prasad et al. 2008; ur Rashid et al. 2013). Rashid et al. investigated the heating behaviour of LSMO nanoparticles prepared through citrate gel route by correlating structural and magnetic properties with linear response theory. Perovskite structure of the NPs was confirmed with the crystallite size varies from 33 to 44 nm range. Under radio frequency magnetic field of 214 kHz and 800 A/m, adiabatic magnetothermal measurements were noted. SAR was calculated by using linear response theory, whereas Curie temperature was determined through thermal demagnetization measurements. These Curie temperature values were compatible with the required values of self-controlled hyperthermia (Gogoi et al. 2014).

Gogoi et al. prepared magnetic vesicles consisting of paclitaxel, iron oxide, and dextran-coated biphasic LSMO NPs for their use in self-controlled hyperthermia

and chemotherapy. Encapsulation efficiencies of those paclitaxel and prepared NPs were 83 ± 3% and 67 ± 5%, respectively. At 37 °C, sequential release performed for 60 min followed by 55 °C for same duration. Intra-tumoral injection revealed cumulative release of 109.6 µg (6.6%) which was more as compared to the inhibitor concentration (IC50 ~ 112 nM). Combined effect of chemotherapy and hyperthermia was observed to be more effective in nature while temperature was maintained at 44 °C (Gogoi et al. 2014). Bhayani et al. used LSMO NPs stabilized with dextran (Dex-LSMO) as alternative agent for the hyperthermia treatment. They carried out experiment by inducing heat and extraneous heat of Dex-LSMO by applying radio frequency (~264 kHz). Induction of heat changed the proliferation pattern, morphology, and heat shock protein induced in human melanoma A375 cell line. A clear cellular effect with extraneous heating at 43 °C for 60 min was observed (Bhayani et al. 2012).

Drug Loading and Combinational Therapy Using LSMO Nanoparticles

For apoptosis in cancer cells, many post-treatments like radiation, chemotherapy, and hyperthermia have already been extensively studied. Along with hyperthermia treatment, many clinical tests have exhibited improved therapeutic response when applied with radio and chemotherapy. Many studies reported the transient improvement of tumour removal by hyperthermia, which deliver many chemotherapeutic drugs successfully. Hyperthermia enhances anti-cancer drugs efficacy for the treatment of different cancer types such as breast cancer, brain cancer, etc. (Sen et al. 2011; Song et al. 1984; Mulier et al. 2012). To increase the lifespan of ovarian and gastric cancer patients, combinational therapies (chemotherapy and hyperthermia) are usually preferred. In patients of phase III study (patients bearing cervical carcinoma), hyperthermia therapy in combination with radiotherapy and chemotherapy revealed 15% improvement in survival when compared to conventional therapies. Hyperthermia in combination with radiotherapy showed better results as compared to radiotherapy in glioblastoma, cervical, and prostate cancer patients (Westermann et al. 2005; Heijkoop et al. 2012; Fodale et al. 2011; Kulkarni et al. 2016) (Fig. 12.5). The quiescent and hypoxic cells within tumours are resistive to radiotherapies. These cells are more sensitive towards heat; therefore, combinational therapies are preferred because hyperthermia treatment may damage quiescent and hypoxic cells. Major concern along with the use of chemotherapeutics such as doxorubicin is dose-dependent nephrotoxicity, hepatotoxicity (Carvalho et al. 2014), and cardiotoxicity (Babincová et al. 2008) resistance of tumour-bearing cells till the extent of high doses of drugs (Kerr et al. 1994; Koning et al. 2010; Singh et al. 2014; Sun et al. 2012; Louguet et al. 2012).
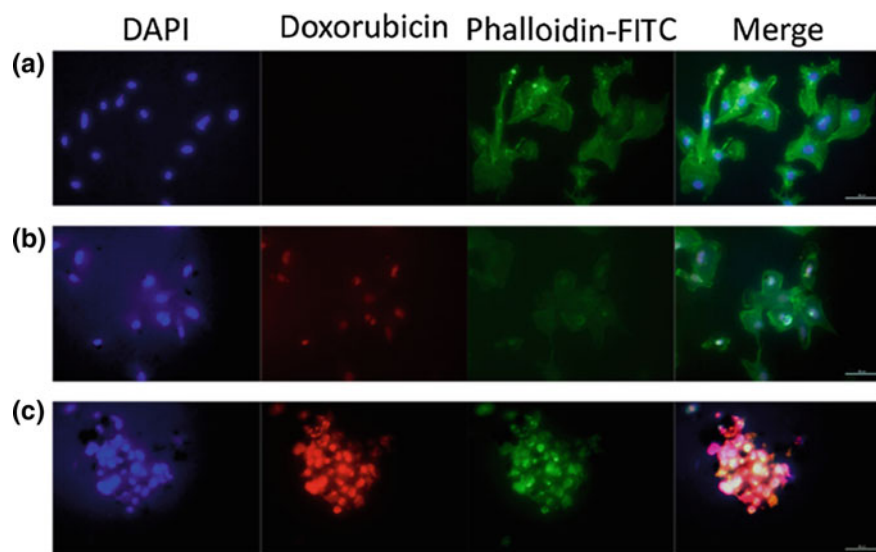
Fig. 12.5 Uptake studies of doxorubicin-loaded LSMO nanoparticles in MDA-MB-231 cells where **a** Control (absence of radiofrequency), **b** 3 h and **c** 3 h. Red fluorescence indicates doxorubicin; green indicates phalloidin—FITC stain for actin and blue shows DAPI for nuclear staining. Reprinted with permission from Kulkarni et al. (2016b)

To localize and restrict the activity of drugs to the specified site of interest through magnetic drug targeting is one of the most attractive options. Many chemotherapeutic drugs used for the treatment of cancer significantly reduce the drug-associated toxicity inside healthy tissues. It also increases the concentration at target of pharmacologically active agents. Many approaches can be adapted for drug loading using LSMO nanoparticles. Drug attached electrostatically or covalently at the surface, or drugs and nanoparticles can be encapsulated together.

To ensure the retention of maximum number of nanoparticles at the site of tumours, external magnetic field is applied. To trigger the drug release mechanism, heating of nanoparticles usually preferred. LSMO nanoparticles coated with silica and modified further with copolymer structures including (polyether and poly 1-lysine segments) have been used for encapsulation of hydrophobic drug to trigger drug release thermally through doxorubicin (Kulkarni et al. 2015). Doxorubicin-loaded chitosan-based LSMO NPS have been used for hyperthermia and drug delivery treatment of breast cancer in vitro. Primary coatings of positively charged polymer chitosan on LSMO nanoparticles enhance the colloidal stability. Radio frequency radiations stimuli the drug release from the nanoparticles system (Gogoi et al. 2017).

In another recent report, hybrid magnetic nanovesicle consisting of iron oxide and LSMO NPs coated with dextran was combined with chemotherapy and hyperthermia therapy. These "biphasic" nanovesicles were encapsulated with 83% of drug and studied by using their combined effect with chemotherapy and hyperthermia on human breast cancer cells MCF-7 (Kačenka et al. 2011).

Fluorescence Imaging and MRI Contrast Agents

In cell imaging and contrast agents in magnetic resonance imaging, core structure of LSMO with double-layer fluorescent tetra-ethoxysilane and tetra-ethoxy/alkoxidesilane can act as fluorescent probes. These modified nanoparticles bear overall diameter of 89 nm and a manganite core of 57 nm. These nanoparticles showed maximum excitation at 514 nm and correspond the maximum emission to fluorescein. These nanoparticles showed high spin–spin relaxivity values ($r_2 = 580$, 540 and 520 s^{-1} mmol (Mn)$^{-1}$L) when magnetic field of (0.5, 1.5, and 3 T) was applied along with the fluorescence properties (Berkova et al. 2013). Relaxivity values of those LSMO NPs much higher as compared to relaxivity values reported for iron oxide NPs. Recent study revealed the similar results of SiF@Si modified LSMO and used successfully for contrast agents and cell labelling along with fluorescent probe. In magnetic resonance imaging, magnetic pulse corresponds to magnetic field provided to the sample which causes the magnetization change of protons present in water molecules. Protons will be relaxed depending on tissue types which produce contrast for differential visualization (Javed et al. 2017). Relaxation process consists of longitudinal relaxation time ($T1$) and transverse relaxation time ($T2$) (Haghniaz et al. 2016). MRI shows the anatomical detail through magnetic contrast agents. Magnetic single domains comprise magnetic moments, which are surrounded by magnetic field generated from the magnetic moments. In water molecules, hydrogen nucleus interacts with magnetic field in body. Hence, it affects different resonance properties. MRI enhances the cancer detection abilities and their metastases. Conventionally used T_1 and T_2 contrast agents are gadolinium and superparamagnetic iron oxide nanoparticles, respectively. Dextran stabilized LSMO NPs have been used nowadays because they are compatible and safe for in vivo use (Gogoi et al. 2017). Haghniaz et al. performed in vivo experiment by using Dex-LSMO NPs as contrast agents in magnetic resonance imaging (MRI). Dex-LSMO NPs with the average diameter ≤ 50 nm showed both positive and negative contrasts with r_1 and r_2 relaxivity values approaches to 6. 741 s^{-1} mg^{-1} mL and 778 s^{-1} mg^{-1} mL, respectively. Dex-LSMO NPs exhibited strong magnetomotive signals when injected at tumour site clearly revealed their use in therapeutic and diagnostic purposes (Haghniaz et al. 2016) (Fig. 12.6). Veverka et al. synthesized LSMO NPs with perovskite phase ($x = 0.2 - 0.45$) through sol–gel method followed by mechanical and thermal treatments. LSMO NPs were coated with silica to gain higher colloidal stability. Higher transverse relaxivity values up to 290–430 s^{-1} mg^{-1} mL under external magnetic field of 0.5 T were reported (Veverka et al. 2015). Kačenka et al. synthesized LSMO core coated with double layer of silica and used as novel dual fluorescence/MRI probe. High spin–spin relaxivity values ($r_2 = 520$, 540, 580 s^{-1}mmol(Mn)$^{-1}$ L) at magnetic field of 0.5, 1.5, and 3 T were reported respectively (Kačenka et al. 2011).
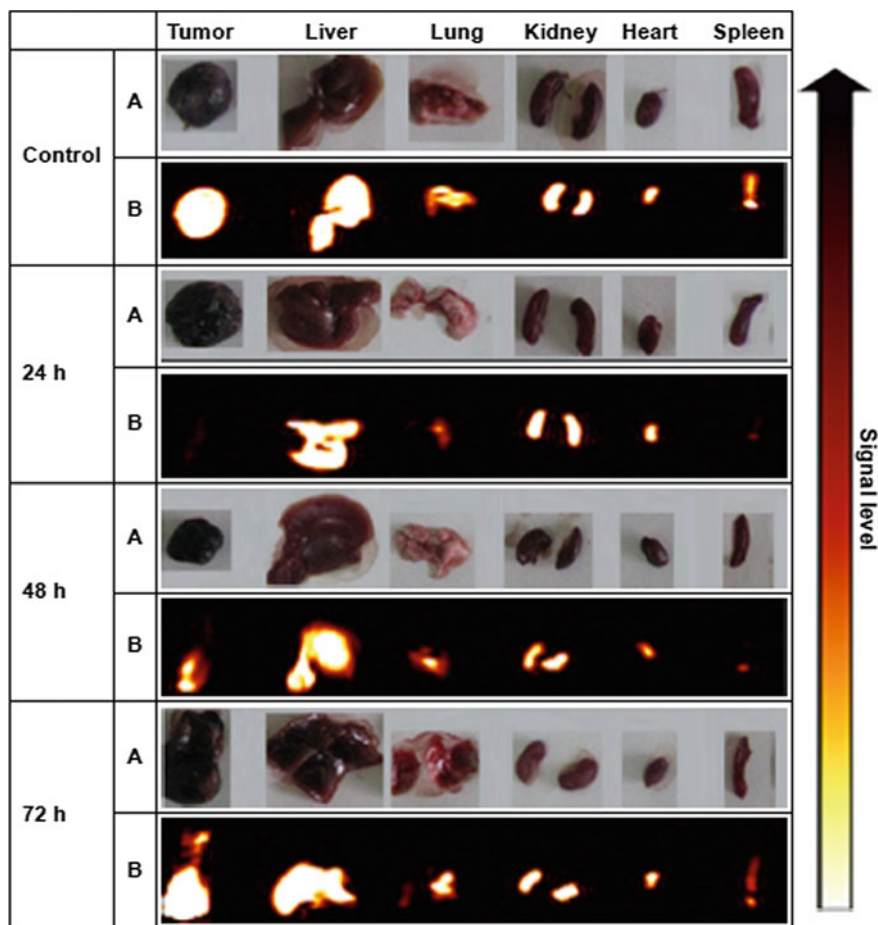
Fig. 12.6 Distribution studies of dextran-coated LSMO nanoparticles using magnetic resonance imaging, **a** photographs and **b** Ex vivo magnetic resonance images. Lighter colour indicates lower concentration levels and darker colour represents higher concentrations levels of nanoparticles (Haghniaz et al. 2016)

Förster Resonance Energy Transfer (FRET) Using LSMO Nanoparticles

FRET is an energy transfer mechanism involving two molecules usually named as acceptor and donor molecules. FRET is considered as most sensitive technique which can be used for determination and measurements of distances between two molecules. Interaction of different type of biomolecules with LSMO can be conducted through FRET; LSMO NPs stabilized with citrate were studied through interaction of covalently bounded chromophore 4-nitrophenylanthralinate and adsorption at the NPs

surface of fluorescent adenine analogue. Giri et al. reported the solubility of LSMO NPs in the aqueous media. FRET studies of covalently attached capped NPs with the probe 4-nitrophenylanthranilate (NPA) confirmed its ligand attachment at the functional group (–OH) surface of citrate ligand (Giri et al. 2010).

Toxicity Study

Studies on nanoparticle toxicity involved interdisciplinary science including biology, chemistry, and physics which has developed over recent years due to their increasing prevalence in common everyday materials. Most of MNPs used in biomedical applications are showing toxicity, which is not favourable for in vivo administration. So, the functionalization of MNPs with biocompatible organic/inorganic molecules is necessary. It is natural that the synthesizing of particles with chemical composition can make them toxic. Therefore, toxicity and its relating issues have serious concerns in the perspective of regenerative medicine which includes the production and tissue engineering (Barakat 2009; Ferreira 2009; Ito and Kamihira 2011; Jin et al. 2010; Lin et al. 2008; Mahmoudi et al. 2010). Besides of extensive work has been published on LSMO nanoparticles, their toxic effects have been discussed very little. Several NPs enhance the process of mucus secretion which can damage the airway and can create different complication in respiration mechanism. But the results of lanthanum strontium manganite (LSM) NPs show less toxic effects as compared to other NPs because of their biocompatibility in various contexts and ability to perform with an appropriate host response in a specific situation. The surface functionalization of NPs plays the main character for the biocompatibility which causes less toxicity. The biocompatibility of the bare LSMO MNPs is improved after functionalization with dextran and betaine HCl. The most common method, which is used to evaluate the cytotoxicity of nanoparticles, is MTT assay. The dextran and betaine HCl functionalized LSMO MNPs are about 90% cell viability for up to 48 h. The real meaning of biocompatibility of MNPs is to study their exact cytotoxicity mechanism by using multiple assays on multiple cell lines. The results show that there is not any apoptosis or necrosis by LSMO MNPs and the observed cell death is only because of presence of MNPs on cell surface. For improving the surface functionalization of $La_{0.7}Sr_{0.3}MnO_3$ (LSMO) nanoparticles, polymer (dextran) on their colloidal stability in physiological media is studied and correlated with their hyperthermia properties but their long-term stability when such complexes are exposed to physiological media is still not well understood (Kulkarni et al. 2015; Daengsakul et al. 2009; Shinoda et al. 2014).

The engaging of NPs for the long duration of time may cause the reduction of efficient needful therapeutic results for the therapy of cell (Huang et al. 2008). The toxicity causes to reduce the efficiency of the cell due to the un-favoured and dangerous outcomes of chemicals, physical, and biological agents in persons and environment (Liu et al. 2013). The cell toxicity and its effects are responsible for weakening the mitochondria and its activity due to which cell cannot retain its original

working position and cannot fulfil and maintain its energetic needs and can stop the practicality of the cell. The rapid reproduction and self-sustaining activities start to alarm and damage the rapid pace of therapeutic efficiency (Bhayani et al. 2012). The other concerns about the magnetic nanoparticles are their incorporation effects on the therapy while these NPs have been transplanted within the body and there is a risk of migration of MNPs through the organism which produces serious concerning issues and body starts to perform undesirable responses such as inflammation (Bhayani et al. 2007; Mahmoudi et al. 2010; Liu et al. 2013).

Extensive work has been published on the $La_{1-x}Sr_xMnO_3$ (LSMO) nanoparticles for their unique applications in field of cancer hyperthermia and has been now considered as potential candidates for the treatment of cancer. The LSMO are considered a new kind of ferromagnetic $La_{1-x}Sr_xMnO_3$ (LSMO) compounds and are found more suitable for hyperthermia treatment because of their capability of tuning the Curie temperature (T_c).

Before ferromagnetic lanthanum strontium manganese oxide (LSMO) nanoparticles, iron oxide NPs such as magnetite (Fe_3O_4) and maghemite (Fe_2O_3) are extensively in use and they are applied for hyperthermia, but the heating is not self-controlled in the therapeutic range owing to their high Curie temperature. This problem has been solved by the dextran-coated $La_{0.7}Sr_{0.3}MnO_3$ (Dex-LSMO) nanoparticles (30–50 nm) with Curie temperature of ~360 K (~86 °C). They exhibit self-controlled heating property and have potential to use for localized hyperthermia (Bhayani et al. 2007; Kale et al. 2006) and magnetic resonance imaging (MRI) (Haghniaz et al. 2013). In vitro cancer-killing effect, Dex-LSMO nanoparticles showed less toxicity in mice (Bhayani et al. 2007). These NPs have also possible application in vivo hyperthermia.

When NPs interact and absorb with the cells for performing the biological function, they produce cytotoxicity but it does not happen when these are attached to the cell membrane (Kulkarni et al. 2015; Solanki et al. 2008). Different other physical characteristics like size, shape, and thin layered surface of nanoparticles can also play a toxic evoking character which may aggregate and coagulate in accord to their sizes and shapes. The other main considering parameter about toxic is the location of nanoparticles (Huang et al. 2008; Liu et al. 2013). The probable destined location of magnetic NPs during in vivo case are considered on their fate when these NPs are released by the cells. The applied NPs start to degrade and their outcomes or by-products produce toxicity. These by-products can reside in tissues and organs (Mahmoudi et al. 2011a; Bulte 2009). At micro-level, oxidative stress is the major reason for repairing the damages of the cell. So, when NPs are used for the treatment of hyperthermia, there is a chance of production of toxicity due to imbalance between free radicals and antioxidants in the body (Kim et al. 2011). Oxidative stress is also mentioned with name of reactive oxygen species (ROS). These species are consisting of hydrogen peroxide group, hydroxyl radicals' group, and shield protecting antioxidants and production of these products are mainly due to the partial formation of the ROS (Khaing et al. 2012). Generally, lanthanum strontium manganite (LSM) is used in solar oxidized fuel cells (SOFCs). Its effect on airway cells was investigated after treating trachea cells with increasing concentrations of LSM ranging

up to 500 µg/mL. It has been observed a moderate effect on cell viability, reactive oxygen species (ROS) production, cytochrome C, and caspase 3 expression. Despite its minimal impact on stated apoptosis-inducing characteristics, LSM illustrated an inhibiting effect on mucus secretion and reported a decreasing trend in mucus secretion with an increased concentration of the LSM treatment. Overall, LSM does not show a significant toxicity to trachea cells; LSM reduces mucus secretion and can potentially interfere with airway clearance (Getzlaff 2007).

The presence of toxicity in LSMO is studied via a set of in vitro along with in vivo experimentations series. The in vitro toxic investigatory tests on the initially gathering data present rapid and straight ways initial information about toxicity. This is a low cost and least moral concerned issue (Mahmoudi et al. 2010). During in vitro experimental studies, the important factor is to recognize and to be able to reproduce in vivo environments in terms of such growing and developing conditional situations along with the preparation of sample in vitro (Mahmoudi et al. 2011a). The data of in vitro tests reveal the minimal presence of toxicity, and in some cases, no toxicity is seen. It can then be moved onto in vivo studies (Weissleder et al. 1989). Such experimental set ups are brought under similar conditions of trial on small animals. The outcomes of these experiments are noted under continuous monitoring over time. The injected sites and metabolic sites are studied through histology. The microscopic studies provide the small scale search and accumulating behaviour of such nanoparticles on these sites. The metabolic sites are liver kidneys, brain, and pancreas where the metabolism reactions take place. The sections are stained for iron by Prussian blue stain and caspase 3 as an indicator for apoptosis within these areas (Schlachter et al. 2011). It is not unlikely to have contradicting in vitro and in vivo results. This may be recognized to in vivo bodily functions/processes such as homoeostasis, working to eject extraneous substances which are not presented in vitro, such as, kidneys are performing to purify the blood (Mahmoudi et al. 2010). The safety concerns for the clinical usage of such NPs are very important and are approved by regulatory bodies (Food and Drug Agency, FDA) after their complete evaluation. This approval depends upon the direct use of these NPs on human behaviours after their usage and research findings of clinical trials. For this noble cause, people have to present themselves voluntarily for testing the interventions, new treatments, or tests as means/resources to detect and manage the new kind of diseases. This practice would bring different respond and side effects of volunteers and would be helpful for the approval or rejection of the clinical use. For this purpose, the use of nanoparticles (NPs) must be used when both regulators and the patients are satisfied. The use of contrast agents has some compulsions. They are to be quick in excretion process and their presence in the body should not be prolonged in the body. However, for some special cases, particularly within the situ of remitted domain of regenerative medicine, long-term facilitated behaviour of fine magnetic particle may be needed in body. The approval of FDA contrast agents (CA) would make it an easier assignment (Shinoda et al. 2014).

Toxicity results in situations of in vitro and in vivo differ from each other which are due to the attribution of protein adsorption which performs a key role at the surfaces of nanoparticles in several natural processes. It has brought a vast interest

in various domains of research which has been for biological and tissue engineering. These resolves may have advantage to bio-organic fluids produced by organism prior to the process of implantation. It would let an appropriate condition to establish a layer of pre-adsorbed proteins which have the ability of adherence with the surface of the material and propose numerous benefits in regards of cellular mediated immune responses (Li et al. 2008). There has been no such report about LSM concerning the apoptosis progression evaluated by cytochrome c, localized between inner and outer mitochondrial membranes. The mitochondrial reliable integrity is measured by monomer JC-1 fluorescence. There are no traces of expressions concerning to caspase 3 which produce survival of the cell and production of mitochondrial reactive oxygen species. Different amount of concentrations of NPs have been tested. Each amount of treatment resulted as suppression of mucus secretion. The increase in concentration of NPs decreases the production of mucus secretion. This proves their non-toxic attitude towards airway epithelial cells and no report was seen about major changes in apoptosis stages. In addition to that, such NPs lower the mucus secretion that can jeopardize cell viability (Wang et al. 2012; Huang et al. 2012; Tsai et al. 2019).

Conclusion

Rare earth-based half-metallic ferromagnetic materials have demonstrated wide transition temperature range and large magnetic moment at ambient temperature. Blocking temperature can be modified of LSMO by different divalent dopants. These materials due to their metallic nature and higher conductivity can be applied for different biomedical field. These nanomaterials can be used as biomarkers, for imaging in MRI and in magnetic hyperthermia. Although LSMO nanomaterials have shown potential for different biomedical applications, said nanomaterials have not been studied extensively on preclinic and clinical level and there is plenty of room on the investigation to make these nanomaterials more suitable for biological systems.

References

Andra W, Nowak H (eds) (2007) Magnetism in medicine. Eiley-VCH Verlag GmbH
AOTrauma (2001) Swiss society for biomaterials, tissue and cell engineering society. Eur Cells Mater
Babincová M, Altanerova V, Altaner C, Bergemann C, Babinec P (2008) In vitro analysis of cisplatin functionalized magnetic nanoparticles in combined cancer chemotherapy and electromagnetic hyperthermia. IEEE Trans Nanobiosci 7:15–19
Bahadur D, Prasad NK, Rathinasamy K, Panda D (2007) TC-Tuned biocompatible suspension of La0.73Sr0.27MnO3 for magnetic hyperthermia. Wiley-Interscience
Balamurugan S, Melba K (2015) Zn(1-x)CuxO (0.02 ≤ x ≤ 0.1) nanomaterials prepared by ball milling, citrate sol gel, and molten salt flux methods. J Nanosci Nanotechnol 15:4632–4640
Barakat NS (2009) Magnetically modulated nanosystems: a unique drug-delivery platform. Nanomedicine 4:799–812

Berkova Z, Jirak D, Zacharovova K, Lukes I, Kotkova Z, Kotek J, Kacenka M, Kaman O, Rehor I, Hajek M (2013) Gadolinium-and manganite-based contrast agents with fluorescent probes for both magnetic resonance and fluorescence imaging of pancreatic islets: a comparative study. ChemMedChem 8:614–621

Bhayani K, Kale S, Arora S, Rajagopal R, Mamgain H, Kaul-Ghanekar R, Kundaliya DC, Kulkarni S, Pasricha R, Dhole S (2007) Protein and polymer immobilized La0. 7Sr0. 3MnO3 nanoparticles for possible biomedical applications. Nanotechnology 18:345101

Bhayani K, Rajwade J, Paknikar K (2012) Radio frequency induced hyperthermia mediated by dextran stabilized LSMO nanoparticles: in vitro evaluation of heat shock protein response. Nanotechnology 24:015102

Brusentsov NA, Brusentsova TN, Filinova EY (2007) Principles of magnetohydrodynamic thermochemotherapy of malignant tumors (a review). Pharm Chem J 41:455–460

Bubnovskaya L, Belous A, Solopan S, Kovelskaya A, Bovkun L, Podoltsev A, Kondtratenko I, Osinsky S (2014) Magnetic fluid hyperthermia of rodent tumors using manganese perovskite nanoparticles. J Nanopart 2014:1–9

Bulte JW (2009) In vivo MRI cell tracking: clinical studies. Am J Roentgenol 193:314–325

Carvalho FS, Burgeiro A, Garcia R, Moreno AJ, Carvalho RA, Oliveira PJ (2014) Doxorubicin-induced cardiotoxicity: from bioenergetic failure and cell death to cardiomyopathy. Med Res Rev 34:106–135

Corot C, Robert P, Idée J-M, Port M (2006) Recent advances in iron oxide nanocrystal technology for medical imaging. Adv Drug Deliv Rev 58:1471–1504

Daengsakul S, Mongkolkachit C, Thomas C, Siri S, Thomas I, Amornkitbamrung V, Maensiri S (2009a) A simple thermal decomposition synthesis, magnetic properties, and cytotoxicity of La0.7Sr0.3MnO3 nanoparticles. Appl Phys A 96:691–699

Daengsakul S, Thomas C, Thomas I, Mongkolkachit C, Siri S, Amornkitbamrung V, Maensiri S (2009b) Magnetic and cytotoxity properties of La(1-x)Sr(x)MnO(3) (0. Nanoscale Res Lett 4:839–845

Daengsakul S, Thomas C, Thomas I, Mongkolkachit C, Siri S, Amornkitbamrung V, Maensiri S (2009b) Magnetic and cytotoxity properties of $La_{(1-x)}Sr_{(x)}MnO_{(3)}$ ($0 </= x </= 0.5$) nanoparticles prepared by a simple thermal hydro-decomposition. Nanoscale Res Lett 4(8):839–845

Das N, Mondal P, Bhattacharya D (2006) Particle-size dependence of orbital order-disorder transition in La Mn O 3. Phys Rev B 74:014410

Ebrahimi M (2016) On the temperature control in self-controlling hyperthermia therapy. J Magn Magn Mater 416:134–140

Epherre R, Duguet E, Mornet S, Pollert E, Louguet S, Lecommandoux S, Schatz C, Goglio G (2011a) Manganite perovskite nanoparticles for self-controlled magnetic fluid hyperthermia: about the suitability of an aqueous combustion synthesis route. J Mater Chem 21:4393–4401

Epherre R, Pepin C, Penin N, Duguet E, Mornet S, Pollert E, Goglio G (2011b) Evidence of non-stoichiometry effects in nanometric manganite perovskites: influence on the magnetic ordering temperature. J Mater Chem 21:14990

Falk MH, Issels RD (n.d.) Hyperthermia in oncology. Int J Hyperthermia 17:1–18

Feldhoff A, Arnold M, Martynczuk J, Gesing TM, Wang H (2008) The sol–gel synthesis of perovskites by an EDTA/citrate complexing method involves nanoscale solid state reactions. Solid State Sci 10:689–701

Ferreira L (2009) Nanoparticles as tools to study and control stem cells. J Cell Biochem 108:746–752

Fodale V, Pierobon M, Liotta L, Petricoin E (2011) Mechanism of cell adaptation: when and how do cancer cells develop chemoresistance? Cancer J (Sudbury, Mass) 17:89

Getzlaff M (2007) Fundamentals of magnetism. Springer Science & Business Media

Ghosh B, Siruguri V, Raychaudhuri AK, Chatterji T (2014) Effect of size reduction on the structural and magnetic order in LaMnO$_{3+\delta}$ ($\delta \approx 0.03$) nanocrystals: a neutron diffraction study. J Phys Condens Matter 26:025603

Giri A, Makhal A, Ghosh B, Raychaudhuri A, Pal SK (2010) Functionalization of manganite nanoparticles and their interaction with biologically relevant small ligands: picosecond time-resolved FRET studies. Nanoscale 2:2704–2709

Gogoi M, Sarma HD, Bahadur D, Banerjee R (2014) Biphasic magnetic nanoparticles–nanovesicle hybrids for chemotherapy and self-controlled hyperthermia. Nanomedicine 9:955–970

Gogoi M, Jaiswal MK, Sarma HD, Bahadur D, Banerjee R (2017) Biocompatibility and therapeutic evaluation of magnetic liposomes designed for self-controlled cancer hyperthermia and chemotherapy. Integr Biol 9:555–565

Goya G, Grazu V, Ibarra M (2008) Magnetic nanoparticles for cancer therapy. Curr Nanosci 4:1–16

Gupta AK, Gupta M (2005) Synthesis and surface engineering of iron oxide nanoparticles for biomedical applications. Biomaterials 26:3995–4021

Haghniaz R, Bhayani KR, Umrani RD, Paknikar KM (2013) Dextran stabilized lanthanum strontium manganese oxide nanoparticles for magnetic resonance imaging. RSC Adv 3:18489–18497

Haghniaz R, Umrani RD, Paknikar KM (2016) Hyperthermia mediated by dextran-coated $La_{0.7}Sr_{0.3}MnO_3$ nanoparticles: in vivo studies. Int J Nanomed 11:1779

Hedayatnasab Z, Abnisa F, Daud WMAW (2017) Review on magnetic nanoparticles for magnetic nanofluid hyperthermia application. Mater Des 123:174–196

Heijkoop ST, Franckena M, Thomeer MG, Boere IA, Van Montfort C, Van Doorn HC (2012) Neoadjuvant chemotherapy followed by radiotherapy and concurrent hyperthermia in patients with advanced-stage cervical cancer: a retrospective study. Int J Hyperth 28:554–561

Hilger I, Kießling A, Romanus E, Hiergeist R, Hergt R, Andrä W, Roskos M, Linss W, Weber P, Weitschies W, Kaiser WA (2004) Magnetic nanoparticles for selective heating of magnetically labelled cells in culture: preliminary investigation. Nanotechnology. 15:1027–1032

Hilger I, Hergt R, Kaiser WA (2005) Towards breast cancer treatment by magnetic heating. J Magn Magn Mater 293:314–319

Hong R, Li J, Qu J, Chen L, Li H (2009) Preparation and characterization of magnetite/dextran nanocomposite used as a precursor of magnetic fluid. Chem Eng J 150:572–580

Huang D-M, Chung T-H, Hung Y, Lu F, Wu S-H, Mou C-Y, Yao M, Chen Y-C (2008) Internalization of mesoporous silica nanoparticles induces transient but not sufficient osteogenic signals in human mesenchymal stem cells. Toxicol Appl Pharmacol 231:208–215

Huang J, Wang J, Su X, Hao W, Wang T, Xia Y, Da G, Fan Y (2012) Biocompatibility of nanoporous TiO_2 coating on NiTi alloy prepared via dealloying method. J Nanomater 2012:8

Ito A, Kamihira M (2011) Tissue engineering using magnetite nanoparticles. In: Progress in molecular biology and translational science. Elsevier, pp 355–395

Jadhav S, Nikam D, Khot V, Thorat N, Phadatare M, Ningthoujam R, Salunkhe A, Pawar S (2013) Studies on colloidal stability of PVP-coated LSMO nanoparticles for magnetic fluid hyperthermia. New J Chem 37:3121–3130

Jadhav S, Nikam D, Khot V, Mali S, Hong C, Pawar S (2015) PVA and PEG functionalised LSMO nanoparticles for magnetic fluid hyperthermia application. Mater Charact 102:209–220

Javed Y, Akhtar K, Anwar H, Jamil Y (2017) MRI based on iron oxide nanoparticles contrast agents: effect of oxidation state and architecture. J Nanopart Res 19:366

Jin Y, Jia C, Huang S-W, O'donnell M, Gao X (2010) Multifunctional nanoparticles as coupled contrast agents. Nat Commun 1:41

Jordan A, Scholz R, Maier-Hauff K, Johannsen M, Wust P, Nadobny J, Schirra H, Schmidt H, Deger S, Loening S, Lanksch W, Felix R (2001) Presentation of a new magnetic field therapy system for the treatment of human solid tumors with magnetic fluid hyperthermia. J Magn Magn Mater 225:118–126

Kačenka M, Kaman O, Kotek J, Falteisek L, Černý J, Jirák D, Herynek V, Zacharovová K, Berková Z, Jendelová P (2011) Dual imaging probes for magnetic resonance imaging and fluorescence microscopy based on perovskite manganite nanoparticles. J Mater Chem 21:157–164

Kale SN, Arora S, Bhayani KR, Paknikar KM, Jani M, Wagh UV, Kulkarni SD, Ogale SB (2006) Cerium doping and stoichiometry control for biomedical use of La0. 7Sr0. 3MnO3 nanoparticles: microwave absorption and cytotoxicity study. Nanomed Nanotechnol Biol Med 2:217–221

Kaman O, Pollert E, Veverka P, Veverka M, Hadová E, Knížek K, Maryško M, Kašpar P, Klementová M, Grünwaldová V, Vasseur S, Epherre R, Mornet S, Goglio G, Duguet E (2009) Silica encapsulated manganese perovskite nanoparticles for magnetically induced hyperthermia without the risk of overheating. Nanotechnology 20:275610

Kerr JF, Winterford CM, Harmon BV (1994) Apoptosis. Its significance in cancer and cancer therapy. Cancer 73:2013–2026

Khaing Oo MK, Yang Y, Hu Y, Gomez M, Du H, Wang H (2012) Gold nanoparticle-enhanced and size-dependent generation of reactive oxygen species from protoporphyrin IX. ACS nano 6:1939–1947

Kim T, Momin E, Choi J, Yuan K, Zaidi H, Kim J, Park M, Lee N, McMahon MT, Quinones-Hinojosa A (2011) Mesoporous silica-coated hollow manganese oxide nanoparticles as positive T_1 contrast agents for labeling and MRI tracking of adipose-derived mesenchymal stem cells. J Am Chem Soc 133:2955–2961

Koning GA, Eggermont AM, Lindner LH, ten Hagen TL (2010) Hyperthermia and thermosensitive liposomes for improved delivery of chemotherapeutic drugs to solid tumors. Pharm Res 27:1750–1754

Kulkarni VM, Bodas D, Paknikar KM (2015) Lanthanum strontium manganese oxide (LSMO) nanoparticles: a versatile platform for anticancer therapy. RSC Adv 5:60254–60263

Kulkarni VM, Bodas D, Dhoble D, Ghormade V, Paknikar K (2016) Radio-frequency triggered heating and drug release using doxorubicin-loaded LSMO nanoparticles for bimodal treatment of breast cancer. Colloids Surf B Biointerfaces 145:878–890

Lassa MS, Luques CG, Albornoz C, Leyva AG, Roig LV, Vazquez PG (2015) Magnetic nanoparticles of $La_{0.78}Sr_{0.22}MnO_3$, coated with SiO_2: preparation and cytotoxicity in human cell cultures. Procedia Mater Sci 8:358–365

Lee M-Y, Song M-K, Kim J-S, Seo J-H (2014) Synthesis of single-phase gd-doped ceria nanopowders by radio frequency thermal plasma treatment. J Am Ceram Soc 97:1379–1382

Li X, van Blitterswijk CA, Feng Q, Cui F, Watari F (2008) The effect of calcium phosphate microstructure on bone-related cells in vitro. Biomaterials 29:3306–3316

Lin MM, Kim DK, El Haj AJ, Dobson J (2008) Development of superparamagnetic iron oxide nanoparticles (SPIONS) for translation to clinical applications. IEEE Trans Nanobiosci 7:298–305

Liu Y, Du J, Yan M, Lau MY, Hu J, Han H, Yang OO, Liang S, Wei W, Wang H (2013) Biomimetic enzyme nanocomplexes and their use as antidotes and preventive measures for alcohol intoxication. Nat Nanotechnol 8:187

Louguet S, Rousseau B, Epherre R, Guidolin N, Goglio G, Mornet S, Duguet E, Lecommandoux S, Schatz C (2012) Thermoresponsive polymer brush-functionalized magnetic manganite nanoparticles for remotely triggered drug release. Polym Chem 3:1408–1417

Mahendiran R, Tiwary SK, Raychaudhuri AK, Ramakrishnan TV, Mahesh R, Rangavittal N, Rao CNR (1996) Structure, electron-transport properties, and giant magnetoresistance of hole-doped $LaMnO_3$ systems. Phys Rev B 53:3348–3358

Mahmoudi M, Simchi A, Imani M, Shokrgozar MA, Milani AS, Häfeli UO, Stroeve P (2010) A new approach for the in vitro identification of the cytotoxicity of superparamagnetic iron oxide nanoparticles. Colloids Surf, B 75:300–309

Mahmoudi M, Hofmann H, Rothen-Rutishauser B, Petri-Fink A (2011a) Assessing the in vitro and in vivo toxicity of superparamagnetic iron oxide nanoparticles. Chem Rev 112:2323–2338

Mahmoudi M, Sant S, Wang B, Laurent S, Sen T (2011b) Superparamagnetic iron oxide nanoparticles (SPIONs): development, surface modification and applications in chemotherapy. Adv Drug Deliv Rev 63:24–46

Makni J, Riahi K, Ayadi F, Nachbaur V, Cheikhrouhou-Koubaa W, Koubaa M, Hamayun MA, Hlil EK, Cheikhrouhou A (2018) Evaluation of La0.7Sr0.3Mn1-xBxO3 (B = Mo, Ti) nanoparticles synthesized via GNP method for self-controlled hyperthermia. J Alloys Compd 746:626–637

Markovich V, Jung G, Fita I, Mogilyansky D, Wu X, Wisniewski A, Puzniak R, Titelman L, Vradman L, Herskowitz M, Gorodetsky G (2010) Magnetotransport properties of ferromagnetic LaMnO3 + δ nano-sized crystals. J Magn Magn Mater 322:1311–1314

McBride K, Cook J, Gray S, Felton S, Stella L, Poulidi D (2016) Evaluation of La $_{1-x}$ Sr $_x$ MnO $_3$ ($0 \leq x < 0.4$) synthesised *via* a modified sol–gel method as mediators for magnetic fluid hyperthermia. CrystEngComm 18:407–416

Melnikov OV, Gorbenko OY, Markelova MN, Kaul AR, Atsarkin VA, Demidov VV, Soto C, Roy EJ, Odintsov BM (2009) Ag-doped manganite nanoparticles: new materials for temperature-controlled medical hyperthermia. J Biomed Mater Res Part A 91A:1048–1055

Mornet S, Vasseur S, Grasset F, Duguet E (2004) Magnetic nanoparticle design for medical diagnosis and therapy. J Mater Chem 14:2161

Mornet S, Vasseur S, Grasset F, Veverka P, Goglio G, Demourgues A, Portier J, Pollert E, Duguet E (2006) Magnetic nanoparticle design for medical applications. Prog Solid State Chem 34:237–247

Mukasyan AS, Epstein P, Dinka P (2007) Solution combustion synthesis of nanomaterials. Proc Combust Inst 31:1789–1795

Mulier S, Claes J-P, Dierieck V, Amiel J-O, Pahaut J-P, Marcelis L, Bastin F, Vanderbeeken D, Finet C, Cran S (2012) Survival benefit of adding hyperthermic intraperitoneal chemotherapy (HIPEC) at the different time-points of treatment of ovarian cancer: review of evidence. Curr Pharm Des 18:3793–3803

Natividad E, Castro M, Goglio G, Andreu I, Epherre R, Duguet E, Mediano A (2012) New insights into the heating mechanisms and self-regulating abilities of manganite perovskite nanoparticles suitable for magnetic fluid hyperthermia. Nanoscale 4:3954–3962

Pandalai SG (2002) Recent research developments in materials science and engineering, vol 1, pt 1. Transworld Res Netw

Prasad N, Rathinasamy K, Panda D, Bahadur D (2007) Mechanism of cell death induced by magnetic hyperthermia with nanoparticles of γ-Mn x Fe 2–x O 3 synthesized by a single step process. J Mater Chem 17:5042–5051

Prasad N, Rathinasamy K, Panda D, Bahadur D (2008) TC-tuned biocompatible suspension of La0. 73Sr0. 27MnO3 for magnetic hyperthermia. J Biomed Mater Res Part B: Appl Biomater Off J Soc Biomater, Jpn Soc Biomater, Aust Soc Biomater Korean Soc Biomater 85:409–416

Rajagopal R, Mona J, Kale S, Bala T, Pasricha R, Poddar P, Sastry M, Prasad B, Kundaliya DC, Ogale S (2006) La 0.7 Sr 0.3 Mn O 3 nanoparticles coated with fatty amine. Appl Phys Lett 89:023107

Rao CNR, Raveau B (1998) Colossal magnetoresistance, charge ordering and related properties of manganese oxides. World Scientific, Singapore

Rao CNR, Mahesh R, Raychaudhuri AK, Mahendiran R (1998) Giant magnetoresistance, charge ordering and other novel properties of perovskite manganates. J Phys Chem Solids 59:487–501

Rao BG, Mukherjee D, Reddy BM (2017) Novel approaches for preparation of nanoparticles. Nanostruct Nov Ther 1–36

Schlachter EK, Widmer HR, Bregy A, Lönnfors-Weitzel T, Vajtai I, Corazza N, Bernau VJ, Weitzel T, Mordasini P, Slotboom J (2011) Metabolic pathway and distribution of superparamagnetic iron oxide nanoparticles: in vivo study. Int J Nanomed 6:1793

Sen A, Capitano ML, Spernyak JA, Schueckler JT, Thomas S, Singh AK, Evans SS, Hylander BL, Repasky EA (2011) Mild elevation of body temperature reduces tumor interstitial fluid pressure and hypoxia and enhances efficacy of radiotherapy in murine tumor models. Can Res 71:3872–3880

Sharma R, Chen CJ (2009) Newer nanoparticles in hyperthermia treatment and thermometry. J Nanopart Res 11:671–689

Shinde KP, Deshpande NG, Eom T, Lee YP, Pawar SH (2010) Solution-combustion synthesis of La$_{0.65}$Sr$_{0.35}$MnO$_3$ and the magnetocaloric properties. Mater Sci Eng B 167:202–205

Shinoda K, Nakajima T, Tsuchiya T (2014) Fabrication of La$_{1-x}$Sr$_x$MnO$_3$ thin films by chemical solution deposition for high-temperature resistive materials. J Ceram Soc Jpn 122(6):415–420

Shlyakhtin OA, Leontiev VG, Oh Y-J, Kuznetsov AA (2007) New manganite-based mediators for self-controlled magnetic heating. Smart Mater Struct 16:N35–N39

Singh S, Armstrong A, Robke J, Waggoner S, Debernardo R (2014) Hyperthermic intra-thoracic chemotherapy (HITeC) for the management of recurrent ovarian cancer involving the pleural cavity. Gynecol Oncol Case Rep 9:24

Solanki A, Kim JD, Lee K-B (2008) Nanotechnology for regenerative medicine: nanomaterials for stem cell imaging

Soleymani M, Edrissi M, Alizadeh AM (2017) Tailoring La $_{1-x}$ Sr $_x$ MnO $_3$ ($0.25 \leq x \leq 0.35$) nanoparticles for self-regulating magnetic hyperthermia therapy: an in vivo study. J Mater Chem B 5:4705–4712

Song CW, Lokshina A, Rhee JG, Patten M, Levitt SH (1984) Implication of blood flow in hyperthermic treatment of tumors. IEEE Trans Biomed Eng 9–16

Sun J, Song Y, Wang Z, Gao P, Chen X, Xu Y, Liang J, Xu H (2012) Benefits of hyperthermic intraperitoneal chemotherapy for patients with serosal invasion in gastric cancer: a meta-analysis of the randomized controlled trials. BMC Cancer 12:526

Tsai S-M, Mesina M, Goshia T, Chiu M-H, Young J, Sibal A, Chin W-C (2019) Perovskite nanoparticles toxicity study on airway epithelial cells. Nanoscale Res Lett 14:14

ur Rashid A, Manzoor S (2016) Optimizing magnetic anisotropy of La1 − xSrxMnO3 nanoparticles for hyperthermia applications. J Magn Magn Mater 420:232–240

ur Rashid A, Ahmed A, Ahmad S, Shaheen S, Manzoor S (2013) Study of specific absorption rate of strontium doped lanthanum manganite nanoparticles for self-controlled hyperthermia applications. J Magn Magn Mater 347:39–44

Urushibara A, Moritomo Y, Arima T, Asamitsu A, Kido G, Tokura Y (1995) Insulator-metal transition and giant magnetoresistance in La$_{1-x}$Sr$_x$MnO$_3$. Phys Rev B 51:14103–14109

Uskokovic V, Kosak A, Drofenik M, Drofenik M (2006) Preparation of silica-coated lanthanum-strontium manganite particles with designable curie point, for application in hyperthermia treatments. Int J Appl Ceram Technol 3:134–143

Vasseur S, Duguet E, Portier J, Goglio G, Mornet S, Hadová E, Knížek K, Maryško M, Veverka P, Pollert E (2006) Lanthanum manganese perovskite nanoparticles as possible in vivo mediators for magnetic hyperthermia. J Magn Magn Mater 302:315–320

Veverka P, Kaman O, Kačenka M, Herynek V, Veverka M, Šantavá E, Lukeš I, Jirák Z (2015) Magnetic La 1–x Sr x MnO 3 nanoparticles as contrast agents for MRI: the parameters affecting 1 H transverse relaxation. J Nanopart Res 17:33

Wang J, Gao Y, Hou Y, Zhao F, Pu F, Liu X, Wu Z, Fan Y (2012) Evaluation on cartilage morphology after intra-articular injection of titanium dioxide nanoparticles in rats. J Nanomater 2012:1

Weissleder RA, Stark DD, Engelstad BL, Bacon BR, Compton CC, White DL, Jacobs P, Lewis J (1989) Superparamagnetic iron oxide: pharmacokinetics and toxicity. Am J Roentgenol 152:167–173

Westermann AM, Jones EL, Schem BC, van der Steen-Banasik EM, Koper P, Mella O, Uitterhoeve AL, de Wit R, van der Velden J, Burger C (2005) First results of triple-modality treatment combining radiotherapy, chemotherapy, and hyperthermia for the treatment of patients with Stage IIB, III, and IVA cervical carcinoma. Cancer 104:763–770

Zener C (1951) Interaction between the d-Shells in the transition metals. II. Ferromagnetic compounds of manganese with perovskite structure. Phys Rev 82:403–405

Zhang K, Holloway T, Pradhan J, Bahoura M, Bah R, Rakhimov R, Pradhan A, Prabakaran R, Ramesh G (2010) Synthesis and magnetic characterizations of La1 − x Sr x MnO3 nanoparticles for biomedical applications. J Nanosci Nanotechnol 10:5520–5526

Chapter 13
Toxicity Assessment of Nanomaterials

**Mariana Tasso, Maria Amparo Lago Huvelle, Ines Diaz Bessone
and Agustin S. Picco**

Abstract In the last decades, nanoscience had a spectacular evolution providing new, versatile engineered nanomaterials and nanotools with a plethora of applications in very diverse fields ranging from energy storage to medicine. Among the palette of nanomaterials, magnetic nanoparticles (in particular iron oxide-based) present unique physicochemical properties that are actively being exploited in the biomedical field. Currently, they are used for induced magnetic hyperthermia cancer treatments, as contrast agents for magnetic resonance imaging, as cell tracking elements, and for drug delivery modalities. In parallel to the growth of nanoscience and the ever-increasing applications of nanomaterials, concerns regarding the safety and toxicity of nanoparticles have arisen, both during and post-administration. In this chapter, we review key concepts related to nanotoxicology and to the fate of nanomaterials in the human body. A detailed description about the most accepted and practiced in vitro and in vivo methods used to evaluate the toxicity of nanomaterials is provided, with emphasis in magnetic nanomaterials for nanomedicine applications.

Keywords Nanotoxicity · Cell-nanomaterial interactions · In vitro and in vivo evaluation · 3D culture system · Animal model

Introduction

To begin, a foreword defines and delimits the scope of this chapter: Here, we deal with the toxicity of nanomaterials that are employed in biomedical applications and among those about nanomaterials used in nanomedicine. Therefore, toxicological effects related to biomaterials used in implants or for regenerative therapies, to nanoparticles

M. Tasso · A. S. Picco (✉)
Departamento de Química, Facultad de Ciencias Exactas, Instituto de Investigaciones Fisicoquímicas Teóricas y Aplicadas (INIFTA), Universidad Nacional de La Plata—CONICET, Diagonal 113 y 64, 1900 La Plata, Argentina
e-mail: apicco@inifta.unlp.edu.ar

M. A. Lago Huvelle · I. Diaz Bessone
Instituto de Nanosistemas, Universidad Nacional de San Martín, 25 de mayo 1021, 1650 Villa Lynch, Argentina

naturally or anthropogenically present in the environment (ecotoxicity, occupational health, and safety), and to nanoparticles employed in the food, cosmetics, or clothing industry are out of the scope of this chapter. Furthermore, we will focus on the toxicity evaluation of magnetic nanomaterials, which are an extended and significant subgroup of the nanomaterials used in nanomedicine.

The chapter opens with an introduction that begins with a general description of nanomaterials for nanomedicines and their potential routes of uptake and administration in animals and humans. The nanomaterials' fate in the body and the associated physiological response to them are thereafter discussed depending on the exposure pathway. Fundamental mechanisms of cell response to the stress associated with cell interactions with the nanomaterial as well as prominent nanoparticle features responsible for nanotoxicological effects are subsequently described. Finally, examples of magnetic nanomaterials used in nanomedical applications are provided, with emphasis on iron oxide nanoparticles. Noteworthy, the introduction section does not intend to provide a comprehensive, thorough overview of the referred topics but rather a pertinent and concise description that will serve as a foundation to better comprehend the subjects dealt with in the subsequent sections.

In the following sections, a detailed description of the most accepted and reported methods to evaluate toxicity of magnetic nanomaterials is presented. In vitro cyto- and genotoxicity, 3D cultures, and in vivo methods are discussed and illustrative examples provided. In vitro methods with organoids are included due to their potential to provide more translatable, and possibly also more relevant, information from in vitro to in vivo assays.

Nanomaterial Definition and the "Nano" Hazard

The International Organization for Standardization (ISO) defines "nanomaterial" as a "material with any external dimension in the nanoscale or having internal structure or surface structure in the nanoscale" and "nano object" as a "discrete piece of material with one, two or three external dimensions in the nanoscale", with nanoscale being in the 1–100 nm range (ISO/TS 80004-1 2015). Though it is generally accepted in the scientific community that nanomaterials are those whose main dimensions are below 100 nm, numerous initiatives exist within the framework of regulatory norms for better definitions to be adopted with the unequivocal aim to protect human health and the environment (Boverhof et al. 2015; Miernicki et al. 2019; Auffan et al. 2009). For some materials, nanoscale dimensions can drastically change material properties unveiling characteristics that could not be predicted from the large-scale features of those same materials, e.g., the size-dependent optical and electronic properties of quantum dots (Alivisatos 1996) or the size-dependent temperature transitions in ferromagnetic materials (Gangopadhyay et al. 1992). These unusual and novel attributes have propelled the design, production, and use of nanomaterials for a myriad of applications, ranging from food additives, cosmetics, pharmaceuticals, and flat-panel displays to sensitive biosensors, contrast agents in magnetic resonance imaging (MRI),

and nanomedicines. Noteworthy, for a vast range of materials, nanoscale dimensions do not impose a drastic alteration in material properties but a rather smooth, predictable, and continuous transition from the bulk materials (Donaldson and Poland 2013). The nanoscale feature, however, irremediably changes the proportion of atoms present at the surface compared to those in the core (or the surface-to-volume ratio), thereby leading to innate nanoscale attributes that will effectively differentiate these entities from their large-scale counterparts. Indeed, nanoparticles below 20–30 nm in size are characterized by their thermodynamic instability and enhanced surface reactivity; properties that may increase dissolution processes, redox reactions, or the generation of reactive oxygen species (ROS) (Auffan et al. 2009). These properties, together with other innate nanoparticle attributes, such as size, shape, or the presence of surface ligands, could constitute leading driving forces for undesirable cellular responses that may result in cellular and organ toxicity (Nel et al. 2006a; Sahu and Hayes 2017; Oberdörster et al. 2005; Xia et al. 2009). Compared to larger particles, nanoparticles of certain dimensions can enter the cells and have access to the intracellular milieu and its organelles, something that is precluded for larger particles and that could be potentially toxic (Pietroiusti et al. 2013; Oh and Park 2014; Shvedova et al. 2010). Though there appears to be a general consensus regarding the health and safety concerns associated with the biomedical use of nanoparticles, some argue that the mechanisms behind nanoparticle health hazard are already evident for larger particles, meaning that there is no evidence of novel "nanospecific hazard" (Donaldson and Poland 2013; Fubini et al. 2010). What appears then critical is the understanding of the mechanisms that are set up by the body during its interaction with nanoparticles, either naturally entering the body via inhalation, ingestion, or penetration through the skin or intentionally administered via intravenous or retro-orbital, intrapulmonary, intraperitoneal, oral delivery or subcutaneous routes, and the possible consequences of those interactions onto cell and organ viability and function.

Nanomedicine

Differing from the commonly accepted understanding of nano-objects in nanotechnology areas having an upper size limit of 100 nm, in the drug delivery field the definition is extended to cover medicines in the size range from a few nanometers to <1000 nm in diameter. In practice, the useful range of nanomedicines normally falls within the range of 5–250 nm (Garnett and Kallinteri 2006). The sort of materials that could be called nanomedicines can include proteins, polymers, dendrimers, micelles, liposomes, emulsions, nanoparticles, and nanocapsules. Besides nanomaterials employed as drug delivery units, other nanomaterial types and applications exist that currently belong to the nanomedicine field. Magnetic nanomaterials are since long being used as contrast agents in magnetic resonance imaging, as therapeutic tools in hyperthermia for ablation of malignant cancer tissue, or as carriers for (image-guided) drug/gene delivery (Pankhurst et al. 2003; Banerjee et al. 2010; Wu et al.

2018; Kang et al. 2018). Recent developments in nanomaterials have produced small (SPIOs) and ultra-small superparamagnetic iron oxide particles (USPIOs) (Wu et al. 2018; Barry 2008; Bourrinet et al. 2006), as well as multimodal variants that combine magnetic nanomaterials with, for instance, near-infrared fluorescent quantum dots (Sitbon et al. 2014) or fluorochromes (Kircher et al. 2003) for double-imaging capacities. Further applications of magnetic nanomaterials in nanomedicine are described at the end of this section.

Exposure Pathways to Nanomaterials and Possible End Locations in the Body

Given their very small size, comparable to those of viruses and pathogens, engineered nanoparticles can naturally enter the human body: Some nanoparticles can penetrate lung, intestinal, or dermal skin barriers and translocate to the circulatory, lymphatic, and nervous systems, reaching most bodily tissues and organs including the brain, and potentially disrupting cellular processes and causing disease (Buzea et al. 2007; Ali and Rytting 2014; Kreyling et al. 2009; Elder et al. 2006; Oberdörster et al. 2004; Pietroiusti et al. 2013). Once in the body, they will come into contact with the immune system in charge of clearing them if potentially dangerous. Immune cells (and secreted biomolecules) present in the airway and digestive mucosae, as well as in the skin, are the first to intercept nanomaterials upon natural or accidental exposure. When nanomaterials are intentionally administered to the body, as with nanodrugs or nanomaterials for diagnostics and therapy, the immune cells present in blood, muscle tissue, liver, spleen, and kidney are those who will mainly interact with the nano-objects (Buzea et al. 2007; De Matteis 2017; Arami et al. 2015). Upon inhalation, specific sizes of nanoparticles are deposited by diffusional mechanisms in all regions of the respiratory tract, where they are uptaken by immune cells and translocating across epithelial and endothelial cells into the blood and lymph circulation to reach potentially sensitive organs, such as the bone marrow, lymph nodes, spleen, and heart (Oberdörster et al. 2005; Kreyling et al. 2009). Access to the central nervous system has also been reported (Elder et al. 2006; Oberdörster et al. 2004). Nanoparticles adsorbed through the skin distribute via uptake into lymphatic channels (Buzea et al. 2007). Nanomaterials ingested are primarily degraded in the gut, though if they survive the acidic environment of the gastrointestinal tract, they may reach the intestine and the bloodstream (this, if not eliminated in the liver) (Arami et al. 2015). Figure 1 depicts various pathways of human body exposure to nanoparticles, as well as the potentially affected organs and associated diseases.

Though hard to implement and standardize, cellular assays should reflect portal-of-entry toxicity in lungs, skin, and mucous membranes, as well as deleterious effects on target and non-target tissue, such as endothelium, blood cell elements, spleen, liver, nervous system, heart, and kidney (Nel et al. 2006b). Without such a broad interpretation of the nanotoxicity evaluation issue, results shall be deemed as incomplete,
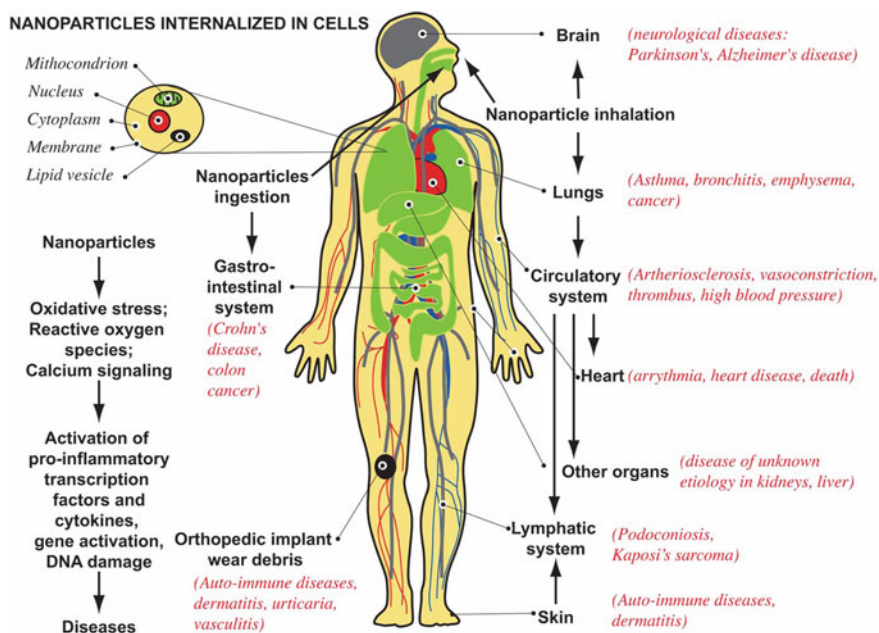
Fig. 1 Schematic representation of the various pathways of human body exposure to nanoparticles, with emphasis in various organs they could reach depending on the exposure pathway, as well as the potentially affected organs and associated diseases. Strategies to enable long-term nanoparticle circulation in the bloodstream together with immune system evasion have been reported. Such strategies are not depicted in this figure, though they constitute an alternative regarding the fate of these nanomaterials upon body exposure. Figure taken from Buzea et al. (2007). Reprinted with permission from AIP Publishing

partial representations of the short- and long-term toxicological hazard represented by nanomaterials.

The Immune Response and the Mononuclear Phagocytic System (MPS)

If the nanoparticles happen to elicit an immune response, a cascade of events is set in place to rapidly eliminate the nanoparticles via phagocytic, metabolic, and degradative processes in immune cells (e.g., white blood cells such as monocytes and residential tissue macrophages). An important part of the immune system, the mononuclear phagocytic system (MPS) also known classically as reticuloendothelial system (RES), has been defined as a family of cells comprising bone marrow progenitors, blood monocytes, and macrophages located in different organs, such as liver, spleen, lymph nodes, bone marrow, lung, and brain that play an active role in

defense reactions against certain microorganisms, interaction with lymphoid cells in immunity, disposal of cell debris, among others (Hume et al. 2019; Chow et al. 2011; Territo and Cline 1975). The major specialized tissue-resident macrophages are dermal macrophages and Langerhans cells in the skin, Kupffer cells in the liver, alveolar macrophages in the lungs, osteoclasts in bones, microglia in the brain, and histiocytes in interstitial connective tissues (Davies et al. 2013; Hirayama et al. 2017; Gordon and Martinez-Pomares 2017). Macrophages are a major cell population in most of the tissues in the body, and their numbers increase further in inflammation, wounding, and malignancy (Hume 2006). Tissue macrophages such as those found in the liver and spleen are the most critical cells in the clearance of NPs from blood circulation: They can eliminate nanoparticles from the bloodstream within seconds of intravenous administration, thereby imposing tremendous challenges to drug delivery nanomaterials or those designed to be site-specific (Arami et al. 2015; Gref et al. 1994). In particular for the liver, this is related to one of its physiologic functions that is to efficiently capture and eliminate particles in the ~10–20 nm size range for the clearance of viruses and other small particles (Choi et al. 2007; Longmire et al. 2008).

Opsonization and How to Evade It

Macrophages cannot directly identify the nanoparticles as such but rather recognize specific opsonin proteins bound to the surface of the nanoparticles following parental injection (Gustafson et al. 2015; Owens and Peppas 2006). Opsonins are blood serum components that adsorb to the surface of foreigner objects with the aim of making them visible to phagocytic cells. Once opsonization has occurred, phagocytes attach to the surface of the foreigner object and engulf it, typically by endocytosis. Endocytosed material will be eventually degraded by the phagocytes and if not, undigested material will either be removed by the renal system or sequestered and stored in one of the MPS organs (Gustafson et al. 2015; Owens and Peppas 2006; Aggarwal et al. 2009). Removal by the renal system occurs for molecules with a molecular weight of 5000 or less, but can be as high as 100,000 for more dense polymers such as dendrimers (Owens and Peppas 2006). For nanoparticles, the size threshold for renal clearance is <10 nm, meaning that nanoparticles of that size range are removed from blood and excreted through the urine (Arami et al. 2015). Noteworthy, if nanomaterials are intended to be used as nanomedicines, it is imperative to endow them with particular properties so that they could evade immune system recognition and elimination and persist in the organism sufficiently long time to reach their target and exert their beneficial effect. Surface modification of nanoparticles with antifouling molecules, such as PEG or zwitterionic polymers, has demonstrated utility at reducing opsonization and minimizing clearance by the MPS leading to improved pharmacokinetic properties (Li and Huang 2009; Guo and Huang 2011). Recent review articles provide a detailed and comprehensive overview of the various uptake pathways of nanoparticles and their fate for each uptake route, from their interactions

with biological barriers and elicited immune responses to biodistribution, pharmacokinetics, and clearance pathways (Sahu and Hayes 2017; Buzea et al. 2007; De Matteis 2017; Arami et al. 2015; Crisponi 2017).

From Extravasation of Nanoparticles to Uptake by Cells

As explained, parental injection of nanoparticles encounters tight immune defensive mechanisms arising from the MPS acting on opsonized nanoparticles, with the most likely result of vast nanoparticle clearance from circulation to the liver and spleen. If opsonization can be reduced and the MPS evaded, nanoparticles with increased blood circulation times still may need to trespass the vascular endothelium barrier, which has tight junctions of lower than 2 nm, to reach target organs. In the liver and spleen, the endothelium is fenestrated, thus allowing material up to 100 nm (liver) or higher than 150 nm (spleen) to pass from the endothelium to the underlying parenchymal cells, so exiting circulation (Garnett and Kallinteri 2006). Some NPs can pass through the endothelial cells by transcytosis mediated by caveolae. If the endothelium becomes leaky due to certain diseases or upon inflammation, nanomaterials can also exit circulation. In some cancers, the epithelium is not only leaky, but it also loses the lymphatics (Garnett and Kallinteri 2006; Greish 2010). For that reason, nanomaterials passing through the leaky epithelium can selectively accumulate in cancer tissue, a process named enhanced permeability and retention (EPR) effect.

Once out of the circulation, nanomaterials will be located in the extracellular matrix, composed of proteins, polysaccharides, and glycoproteins. Some macromolecules and nanoparticles can move through the extracellular matrix via its water channels. Nanomaterials in the extracellular matrix can be spontaneously internalized by cells. As partitioning across membranes is not possible for macromolecules or nanomaterials, entry into cells is largely governed by the mechanisms of endocytosis (Garnett and Kallinteri 2006; Foroozandeh and Aziz 2018). Large particles (0.25–10 µm) are uptaken by phagocytosis, performed by specialized cells such as macrophages and neutrophils, and a variety of other endocytic processes at a smaller scale (Garnett and Kallinteri 2006). Most of these endocytic routes end up in a degradative compartment of the cell, the lysosome, where materials are exposed to high concentrations of a wide variety of hydrolytic enzymes active on proteins, polysaccharides, and nucleic acids. Depending on the nature of the nanomaterial, the lysosomal compartment may be the final destination of the nanomaterial. Besides cell internalization of nanoparticles through endocytosis, positively charged nanomaterials can gain access to the cytoplasm. It is well known that positively charged polymers and polyelectrolyte DNA delivery systems can trigger cytotoxicity due to their interaction with cell membrane phospholipids that results in disruption of the cellular membrane structure (Foroozandeh and Aziz 2018; Gratton et al. 2008).

Consequences of Cell–Nanomaterial Interactions

Besides the description of general uptake pathways of nanoparticles, with their corresponding biodistribution, pharmacokinetics, and clearance routes from the body, it is of particular importance to describe the specific mechanisms set in place during cell–nanomaterial interactions and their dependence with the intrinsic properties of the designed nanomaterials as well as with the biologically modified forms of those nanomaterials when in contact with biological fluids. As noted, the increased surface area per mass compared with larger-size materials of the same chemistry renders nanoparticles thermodynamically unstable, more surface reactive, and more biologically active. This activity relates to a potential for inflammatory and pro-oxidant, but also antioxidant capacity (Oberdörster et al. 2005). Nanoparticle-mediated cytotoxicity mechanisms commonly proposed in the literature include oxidative stress (reactive oxygen and nitrogen species), inflammation, cell membrane damage, genotoxicity, immune system response, autophagy dysfunction, ultrastructural changes in cell or cell organelle morphology, lactate dehydrogenase release, inhibition of cell growth and cell death, among others. The first four mechanisms are described more extensively below.

1. *Reactive Oxygen Species*

    Reactive oxygen species (ROS) are a number of reactive molecules and free radicals derived from molecular oxygen, like superoxide anion, hydrogen peroxide, and nitric oxide. These molecules, produced as byproducts during the mitochondrial electron transport of aerobic respiration or by oxidoreductase enzymes and metal-catalyzed oxidation, can be responsible for a series of deleterious events. As stated, ROS are continually produced during cell metabolic processes, though their generation is normally counterbalanced by the action of antioxidant enzymes and other redox (reduction–oxidation) molecules. An imbalance toward the pro-oxidative state is often referred to as "oxidative stress." Glutathione may be the most important intracellular non-enzymatic small molecule that acts in the defense against the damaging effects of reactive oxygen species. Reduced glutathione (GSH) is regenerated from its oxidized form (GSSG) by the action of an NADPH-dependent reductase. The ratio of the oxidized form of glutathione (GSSG) and the reduced form (GSH) is a dynamic indicator of the oxidative stress of an organism (Jones 2002). The generation of ROS and the related oxidative stress responses are frequent causes of nanoparticle toxicity. The production of ROS has been found in a diverse range of nanomaterials, including semiconductor nanocrystals, fullerenes, carbon nanotubes, and metal oxides (Nel et al. 2006a; De Matteis 2017; Sharifi et al. 2012; Malvindi et al. 2014; Huang et al. 2010). Oxidative stress induced by engineered nanoparticles is due to acellular factors such as particle surface, size, composition, and presence of metals, while cellular responses such as mitochondrial respiration, nanoparticle-cell interaction, and immune cell activation are responsible for ROS-mediated damage (Manke et al. 2013). Nanoparticle-induced oxidative stress responses are behind genotoxicity,

carcinogenesis, inflammation, and fibrosis effects, as demonstrated by activation of associated cell signaling pathways (Xia et al. 2009; Manke et al. 2013). Most of the metal-based (Fe, Si, Cu, Cr, Va) nanoparticles elicit oxidative stress via the generation of free radicals following Fenton-type reactions (Huang et al. 2010). Intracellularly produced free radicals have adverse effects on cell components, like proteins (protein oxidation), lipids (lipid peroxidation), and DNA (DNA strand break) and also alter mitochondrial membrane potential (Manke et al. 2013; Huang et al. 2010). Extremely toxic levels of oxidative stress result in mitochondrial dysfunction and membrane damage, which finally lead to cell death. For transition metal oxide nanoparticles, the physicochemical properties that determine toxicity include surface catalytic activity (e.g., metallic, semiconducting properties), nanoparticle uptake, and nanoparticle dissolution (Huang et al. 2010). In particular for iron oxide nanoparticles, their physical interactions with cellular structures involved in the catalysis of biological redox processes, as well as their dissolution in biological media, catalyze ROS generation and formation of OOH· and OH$^-$ radicals from H_2O_2 via Fenton reaction (Ling and Hyeon 2013; Gaharwar et al. 2017). Indeed, zero-valent iron at the surface of iron oxide nanoparticles is oxidized by dissolved oxygen in aerobic organisms to give rise to Fe^{2+} and OH$^-$. Fe^{2+} can be further oxidized to Fe^{3+}. Redox-active iron may enhance the generation of more highly reactive and highly toxic hydroxyl radicals from less reactive hydrogen peroxide (a product of mitochondrial oxidative respiration) via Fenton chemistry: $Fe^{2+} + H_2O_2 \rightarrow Fe^{3+} + OH· + OH^-$ (Ling and Hyeon 2013). Therefore, by their involvement in catalytic redox reactions, zero-valent iron and iron oxide nanoparticles can be directly linked to the production of ROS, in particular of hydroxyl radicals. Protecting the surface of these nanoparticles from oxidation and dissolution in biological media, both intra- and extracellularly, is therefore a *sine qua non* condition for the translation of these nanomaterials to clinical trials.

1.1. *Mitochondrial iron homeostasis*: Mitochondrial iron homeostasis is indispensable for cellular iron management in particular by controlling the synthesis of heme and Fe–S clusters, functional groups that are essential to the functionality of numerous proteins, including those participating in energy production via the respiratory chain (Bresgen et al. 2015). About 0.2–5% of the total cellular iron is considered as transiently mobile, non-protein-bound low-molecular-weight redox-active iron which together with chelatable protein-bound iron defines the dynamic, intracellular "labile" iron pool (LIP) encompassing compartment-specific LIPs of the cytosol, the mitochondria, and the endo-/lysosomal compartment in total containing about 6–16 μM iron, mainly as Fe^{2+} (Bresgen et al. 2015). Iron is shuttled between these pools by distinct mechanisms and can also be directly delivered from endosomes to mitochondria via a "*kiss-and-run*" mechanism, characterized by the docking of iron-containing endosomes or vesicles to the outer mitochondrial membrane followed by the passing over of iron to mitoferrin (Bresgen et al. 2015). This mechanism enables a direct transfer of iron to

the mitochondria, which may be beneficial under physiologic conditions but can have deleterious effects under conditions of iron overload, as those observed upon administration of iron or iron oxide nanoparticles. Transfers involving free Fe^{2+} ions represent a constant hazard of Fenton reactions and their consequent generation of ROS and derived oxidative stress (Bresgen et al. 2015). The highly reactive hydroxyl radical can damage macromolecules within mitochondria, including lipids, proteins, and DNA, and generate genomic instability, organelle dysregulation, and cellular injury or apoptosis (Guo et al. 2013). Therefore, by disrupting the natural balance between generated ROS species, antioxidant defenses, and repair enzymes in mitochondria, zero-valent iron and iron oxide nanoparticles can lead to mitochondrial dysfunction and apoptosis through the transfer of free Fe^{2+} ions to the organelle.

1.2 *Sources of oxidative stress in SPIONs*. Superparamagnetic iron oxide nanoparticles (SPION), and the equivalent for iron oxide nanoparticles, have been associated with four primary sources of oxidative stress: (a) direct generation of ROS from the surface of the nanoparticle, (b) production of ROS via leaching of iron molecules from the surface due to enzymatic degradation, (c) altering mitochondrial and other organelle functions, and (d) induction of cell signaling pathways together with their consequent activation of inflammatory cells, which results in the generation of ROS and reactive nitrogen species (Buzea et al. 2007; Mahmoudi et al. 2012). Protein and lipid oxidation by SPIONs has also been reported (Stroh et al. 2004; Singh et al. 2010; Wei et al. 2016).

2. *Inflammation*

Inflammation is the major process through which the body repairs tissue damage and defends itself against foreign materials. Acute inflammation is typically caused by an external chemical, mechanical, or pathogenic influence, has a relatively short duration (hours to days), and is a necessary protection tool that removes foreign bodies and damaged tissue, preventing further damage (Stevenson et al. 2011). As explained previously, tissue-resident macrophages are involved in the primary immune response of tissues, producing various cytokines and immune regulators. Upon macrophage interaction with nanoparticles, macrophages can get polarized toward pro-inflammatory or anti-inflammatory phenotypes depending on the nanoparticle type (Miao et al. 2017; Reichel et al. 2019). The net effect of such a polarization may be the disruption of the stable equilibrium between macrophage-produced pro- and anti-inflammatory cytokines, a fact that has been linked to the pathogenesis of a number of inflammatory disorders, e.g., tumor necrosis factor-α (TNF-α) cytokine related to rheumatoid arthritis (RA) (Stevenson et al. 2011). Furthermore, oxidative stress also results in the release of cytokines. Indeed, several reports demonstrate that the exposure to nanomaterials is associated with inflammation, with various particle-related parameters, like size, playing a defining role (Kharazian et al. 2018; Manshian et al. 2018; Gojova et al. 2007; Deng et al. 2011).

3. *Cell membrane damage*

Nanoparticles have been involved in cell and organelle membrane damage through various mechanisms, typically depending on nanoparticle attributes, such as size, surface charge, or hydrophilicity (Leroueil et al. 2007; Fischer et al. 2003; Contini et al. 2018; Chen et al. 2009a; Zhu et al. 2013a; Beddoes et al. 2015). Nanoparticles can cause cell membrane disruptions and, eventually, cell death (Ali and Rytting 2014; Pietroiusti 2012). Hemolysis, or the damage of red blood cell membrane, is one insightful parameter to measure nanoparticle-induced toxicity when interactions with the bloodstream are envisaged. Noteworthy, cell transfection and in vivo gene delivery applications rely upon nanostructures that can non-selectively cross the cell membrane and access the cytosol without inducing major cytotoxic effects. A vast literature supports the idea that polycationic organic polymers, such as PLL (polylactic acid), PEI (polyethyleneimine), and PAMAM (polyamidoamine) dendrimers, permeabilize the cell plasma membrane and, if sufficiently concentrated, result in cell lysis (Leroueil et al. 2007; Fischer et al. 2003; Hong et al. 2004, 2006). Regarding inorganic nanomaterials, examples abound too; for instance, copper metal (Cu; 100–200 nm size) and Cu–Zn (3.8 nm size) alloy nanoparticles induced significant membrane damage upon exposure to lung epithelial cells (A549), while CuO (20–50 nm) nanoparticles showed no such effect (Karlsson et al. 2013). Iron oxide nanoparticles coated with a copolymer of chitosan and PEG could pass the blood-brain barrier (Veiseh et al. 2009a), though other formulations could achieve the same result after magnetic field application and radiofrequency radiation to modulate blood-brain barrier integrity, thereby increasing its permeability (Busquets et al. 2015a). Nakamura and Watano have compiled information about organic and inorganic nanomaterials passing through the cell membrane, either by endocytosis or by direct penetration (Nakamura and Watano 2018). Whether such nanomaterial passages through the cell membrane elicit irreversible damage and nanotoxicity or not, that certainly depends on administered concentration and nanoparticle properties. Cell membrane damage can be determined by measuring the degree to which lactate dehydrogenase (LDH), a cytosolic enzyme present in many different cell types, leaks from the cells (Decker and Lohmann-Matthes 1988). The amount of enzyme that leaks into the extracellular medium can be quantified by an enzymatic reaction that colorimetrically indicates the amount of LDH present.

4. *Genotoxicity*

Alterations in cell redox equilibrium between generated reactive oxygen species and antioxidant elements result in oxidation of critical cell biomolecules, like membrane lipids or nuclear DNA. DNA damage covers a wide range of DNA lesions, which include genome rearrangements, strand breaks, and the formation of modified DNA bases. These different types of DNA lesions can lead to chromosomal aberrations, gene mutations, apoptosis, carcinogenesis, or cellular senescence if left unrepaired (Singh 2017). Epidemiological, in vitro, and in vivo studies show that nanoparticles of various materials (diesel, carbon black, welding fumes, and transition metals) are genotoxic to humans and rats (Buzea et al. 2007). DNA damage was observed upon cell exposure to TiO_2 (Kansara et al.

2015), cobalt (Wan et al. 2017), silver (Ahamed et al. 2008), carbon nanotubes and graphite nanofibres (Lindberg et al. 2009), and iron oxide (Ahamed et al. 2013; Alarifi et al. 2014) nanoparticles. Furthermore, some nanomaterials, such as metal and metal oxide, quantum dots, fullerenes and fibrous nanomaterials, were found to induce chromosomal fragmentation, DNA strand breakages, point mutations, oxidative DNA adducts, and alterations in gene expression, sometimes even through cellular barriers (Singh et al. 2009; Bhabra et al. 2009).

5. *Others*

   Nanoparticles can cause negative physiological effects, such as inflammation, immune system response, autophagy dysfunction, ultrastructural changes in cell or cell organelle morphology, inhibition of cell growth and cell death, among others, that may partially or completely impair normal cell and organ functioning.

Autophagy and lysosomal dysfunction are proposed as emerging mechanisms of nanomaterial toxicity (Stern et al. 2012; Wang et al. 2018). Since most endocytosed nanoparticles accumulate within the lysosomal compartments without evident exit, the evaluation of the effects of nanoparticle accumulation in lysosomes, as well as in autophagy, a lysosomal degradative pathway, needs to be addressed. If the nanoparticles are taken up into the lysosomal compartment but are not biodegradable, they could potentially accumulate there and cause lysosomal dysfunction and hence cellular toxicity.

Nanoparticle Uptake by Cells

Cell–nanomaterial interactions also comprise cell internalization of nano-objects, unspecific adsorption of nanoparticles to the cell membrane, as well as induced cell responses when nanoparticles are functionalized with, e.g., targets of cell receptors or specific ligands that promote cell membrane permeabilization, as already discussed (Oh and Park 2014; Gratton et al. 2008; Beddoes et al. 2015; Salatin et al. 2015; Kurtz-Chalot et al. 2014; Pan et al. 2018). Nanoparticles adsorbed on cell membranes can block cellular ducts, cause structural changes to the membranes, or inhibit mobility and nutrient or ion intake and result in cell death (Kurtz-Chalot et al. 2014; Pan et al. 2018; Warren and Payne 2015). Nanoparticles have been functionalized with a variety of biomolecules that can bind to cell membrane receptors and promote nanoparticle internalization, e.g., endothelial growth factor (EGF)-functionalized nanoparticles to target EGF receptor (EGFR), folate-functionalized nanoparticles to target the folate receptor, RGD peptide, integrin receptor, among others (Xu et al. 2013).

When nanomaterials extravasate and leave circulation, they encounter the extracellular matrix (ECM), composed of proteins, polysaccharides, and glycoproteins. Through water channels present at the ECM, some biomolecules, but also nanoparticles, can pass through the ECM. As partitioning across membranes is not possible for macromolecules, entry into cells is largely governed by biological mechanisms

of endocytosis. These include the uptake of large particles (0.25–10 µm) by phago-cytosis, performed by specialized cells such as macrophages and neutrophils, and a variety of other endocytic processes at a smaller scale (Garnett and Kallinteri 2006). Most of these endocytic routes end up in a degradative compartment of the cell, the lysosome, where materials are exposed to acidic pH and high concentrations of a wide variety of hydrolytic enzymes active on proteins, polysaccharides, and nucleic acids (Garnett and Kallinteri 2006; Foroozandeh and Aziz 2018). The hostile lyso-somal can degrade all but the most biopersistent of the nanomaterials. In addition to the endolysosomal pathway, recent evidence suggests nanomaterials can also induce autophagy (Stern et al. 2012).

Technologies based on cell/organ imaging, targeted drug delivery, or localized therapy depend on nanoparticle uptake by cells. The safety of these techniques depends, however, on cellular uptake of nanoparticles without affecting normal cellular function, both at the target site and elsewhere in the body (Buzea et al. 2007).

A battery of cellular tests exists that can elucidate the actual mechanisms involved in cellular toxicity, such as the MTT or MTS assays that assess cell metabolic activ-ity relying on the presence of cellular oxidoreductases (NADPH) enzymes in the cytosol, or the LDH assay that analyzes the activity of the cytoplasmic enzyme lac-tate dehydrogenase when released to culture media upon cell membrane damage. These methods will be described, and examples are provided in Sect. 13.2.

Nanomaterial Properties Affecting Cells and Organs

Nanomaterials properties are critical at defining possible cellular responses when interaction takes place. It is generally believed that the interactions with biologi-cal components (e.g., proteins, opsonins), cellular uptake, in vivo fate, and toxicity of nanoparticles are strongly correlated with their physicochemical characteristics. Some relevant properties include size, size uniformity, shape, composition, surface area, surface charge, state of aggregation, degree of crystallinity, aspect ratio, surface functionalization, aging in biological media, and the potential to generate ROS (Oh and Park 2014; Buzea et al. 2007; Zhang et al. 2012a). Plentiful reviews provide a comprehensive description of these factors and their implication in toxicological responses (Shvedova et al. 2010; Buzea et al. 2007; Arami et al. 2015; Crisponi 2017; Zhang et al. 2012a). For that reason, we are going to refer to some of them and to focus on magnetic nanomaterials.

1. *Size*

Size is a significant property that can influence the toxicity of a material and its distribution within the body and the cell (Nabiev et al. 2007). Numerous studies have demonstrated size-dependent cell toxicity and organ biodistribution (Kim et al. 2012; Vedantam et al. 2013; Feng et al. 2018a; Xie et al. 2016). In a recent study, Xie et al. investigated the effect of iron oxide (Fe_3O_4) nanoparticle size

onto cytotoxicity in two human hepatoma cell lines, SK-Hep-1 and Hep3B. While 6-nm-size nanoparticles exhibited negligible cytotoxicity, 9-nm nanoparticles affected cytotoxicity through mitochondrial dysfunction and by inducing necrosis through mitochondria-dependent ROS generation. On the other hand, 14-nm nanoparticles were found cytotoxic by impairing the integrity of the plasma membrane and promoting massive lactate dehydrogenase leakage (Xie et al. 2016). In an in vivo trial with naked gold nanoparticles, those with sizes ranging from 8 to 37 nm induced severe sickness in mice, such as fatigue, loss of appetite, change of fur color, and weight loss. From day 14, mice in this group exhibited a camel-like back and crooked spine, and the majority of mice in these groups died within 21 days. However, researchers could not find sickness or lethality in mice injected with gold nanoparticles of 5 and 3 nm (Chen et al. 2009b). Iron oxide nanoparticles with a hydrodynamic diameter higher than 100 nm quickly accumulate in the liver and spleen through macrophage phagocytosis and entrapment in liver and spleen sinusoids, while nanoparticles below 10–15 nm (SPIOs) are likely to be eliminated through the kidneys (Arami et al. 2015; Amstad et al. 2011). Importantly, nanoparticle size is a relevant factor to promote the unspecific retention of nanoparticles in tumors through the enhanced permeation and retention mechanism (Barry 2008).

2. *Size uniformity, shape, composition, and surface charge*

Size uniformity of nanoparticles is a prerequisite for the proper evaluation of any type of nanomaterial to be employed in biological applications. Low polydispersity index nanomaterials are desirable for repeatable performance. Considering the shape, generally, one-dimensional nanostructures, such as polymer filaments, carbon nanotubes, and gold nanorods with a high length-to-width aspect ratio, have shown longer blood circulation times over the spherical counterparts (Arami et al. 2015). Short-rod mesoporous silica nanoparticles (MSNs) are easily trapped in the liver, while long-rod MSNs distribute in the spleen. MSNs are mainly excreted by urine and feces, and the clearance rate of MSNs is primarily dependent on the particle shape, where short-rod MSNs have a more rapid clearance rate than long-rod MSNs in both excretion routes (Huang et al. 2011a). Moreover, carbon nanotubes can interact directly with the cellular cytoskeleton, including the microtubule system during the formation of the mitotic spindle apparatus, leading to aberrant cell division (Sargent et al. 2009).

Composition is another factor that influences the toxicity of nanomaterials. Quantum dots (QD), for instance, may create a health hazard due to the presence of toxic heavy metal elements. It may, however, be possible to reduce the potential toxicity of nanomaterials such as QDs by adding a coating or nanoshell: Core–shell CdSe/CdS/ZnS QDs demonstrated acceptable cytotoxicity (as determined with the MTT test) after 48-h incubation with HeLa cells (Tasso et al. 2015). As stated in previous subsections, iron and iron oxide nanomaterials are, per se, biocompatible, so toxicity related to composition is not a concern, unless toxicity arises from the composition of surface functionalization.

Surface charge is another critical parameter that influences protein adsorption, the formation of the protein corona, and the subsequent biological behavior of the

nanoparticle. Positively charged SPIO nanoparticles interact with the negatively charged cell membrane more than their negatively charged or neutral counterparts (Thorek and Tsourkas 2008). Increased in vitro cytotoxicity and in vivo pulmonary toxicity have been observed for cationic polystyrene nanospheres when compared with anionic or neutral polystyrene (Xia et al. 2008).

3. *Surface functionalization and aging in biological media*

   Surface functionalization may contemplate both the addition of a shell around the nanoparticle core and the surface binding of (bio)macromolecules, polymers, short peptides or others, commonly referred to as ligands.

   3.1 *Shell*: Since pure metals, such as Fe, Co, and Ni and their metal alloys, are very sensitive to air, covering them with a shell could prevent oxidation and hence the release of metal ions to the biological environment. Coatings with inorganic components, like silica, carbon, precious metals (Au, Ag), or oxides, have been reported (Lu et al. 2007). Noteworthy, the shell can also serve the purpose of carrying a drug or a fluorescent label.

   3.2 *Ligand*: Without a ligand, nanoparticles would rapidly aggregate through interactions between themselves or with biological molecules and precipitate out of solution. Commercially available superparamagnetic iron oxide NPs are typically coated with sugars, such as dextran, or synthetic polymers such as silicone. These ligands have high molecular weights (>10 kDa) and poor affinity to the iron oxide core, which leads to the frequent binding of several particles. When shorter (molecular weight <10 kDa) ligands with a precise control over their structure are employed, higher reproducibility, nanoparticle stability, and narrower particle distributions are obtained. Rational design of ligands include the presence of (a) anchoring groups, (b) spacing groups, and (c) biofunctionalization groups (Amstad et al. 2011). Anchoring groups are especially relevant at ensuring a strong binding between the ligand and the nanoparticle surface, which in turns prevents ligand desorption from the surface or even its displacement by competitive species (e.g., proteins) present in biological media, as well as particle aggregation. This is particularly important in conditions of high dilution, as those employed in nanomedicine. Ligands that strongly bind to the nanoparticle surface and have a good surface coverage can overcome the attractive van der Waals and magnetic potentials imparting long-term colloidal stability under dilute conditions, high salt concentrations, and elevated temperatures (Amstad et al. 2011). Spacing groups are usually designed to contain protein-repelling units, such as PEG or zwitterions, to render the nanoparticle "stealth," i.e., able to prevent protein/biomolecule adsorption. Stealth nanoparticles are a *sine qua non* condition for in vivo applications and to increase circulation time by preventing the binding of opsonin proteins and therefore a prompt nanoparticle uptake by the RES system. Biofunctionalization groups are added to enable bioconjugation of targeting species, like folic acid to specifically direct nanoparticles to tumor tissue. Various types of iron oxide nanoparticles conjugated to folic acid were recently

employed for imaging and therapy of different cancer types. (Bonvin et al. 2017; Huang et al. 2017; Li 2015).

A novel approach to nanoparticle coating relies on the use of the membrane materials of the target cells, a strategy that could bypass immune system recognition and rapid clearance, as well as homologous targeting (Zhen et al. 2019). The red blood cell membrane-camouflaged nanoparticles are the first reported cell-membrane biomimetic system, and currently the most popular natural carriers in biomedical applications (Zhen et al. 2019).

3.3 *Aging in biological media*: Depending on the characteristics of the surface ligands, nanoparticles in contact with biological media may suffer from the unspecific adsorption of opsonins and other biomolecules that will form a so-called protein corona. The formation of this protein corona onto nanoparticles irremediably changes their innate physicochemical properties, such as size, surface charge, surface composition, biofunctionality if target-recognition species were added, hence giving nanoparticles a new biological identity (Corbo et al. 2016; Nguyen and Lee 2017; Lundqvist 2017; Yallapu et al. 2015). This nanoparticle–protein complex, not the bare nanoparticle, determines various biological responses such as fibrillation, cellular uptake, circulation time, bioavailability, and even toxicity (Nguyen and Lee 2017). The major proteins that form the protein corona are albumin, fibrinogen, apolipoprotein, and immunoglobulin G, though their relative composition in the protein corona varies with the physicochemical properties of the nanoparticles, as well as with the specific pool of proteins present at a given place (Aggarwal et al. 2009). In other words, the protein corona is dynamic. Nanoparticle hydrophobicity, size, and surface charge determine the number and types of adsorbed proteins (Aggarwal et al. 2009). As previously explained, the formation of a protein corona is a prelude for nanoparticle uptake by the RES system. Protein structural changes upon binding may also be a cause for macrophage uptake. Nanoparticles with bound albumin demonstrated increased circulation time and increased tumor permeating rates (Aggarwal et al. 2009; Nguyen and Lee 2017).

Besides the almost immediate formation of a protein corona upon nanoparticle interaction with biological fluids, long-term exposure can result in nanoparticle partial degradation and continuous modifications of its physicochemical properties, thereby altering the biological response. For instance, silver nanodots encapsulated in silica demonstrated a survival half-life of 2.6 ± 0.3 h in DMEM, a typical cell culture medium, prior degradation of the silica outer layer. Though silica nanoparticles showed extraordinary stability in PBS, a synergistic etching of silica by medium components, particularly the amino-rich compounds in cell culture medium, as well as blood, deteriorated the silica layers (Yang et al. 2018). Ligand destabilization, nanoparticle aggregation and dissolution, dynamic exchange of biomolecules onto the destabilized nanoparticle surface, catalytic processes, among others, are all consequences of long-term nanomaterials aging in biological conditions.

Magnetic Nanomaterials and Their Applications in Nanomedicine

1. *Magnetic nanomaterials*

    There exist a wide range of magnetic nanomaterials that include oxides (γ-Fe_2O_3, Fe_3O_4), pure metals (Fe, Co, Ni, etc.), ferromagnetic alloys ($CoPt_3$, FePt, FeNi, FeCo), or spinel-type ferromagnets ($MgFe_2O_4$, $MnFe_2O_4$, and $CoFe_2O_4$) (Pankhurst et al. 2003; Wu et al. 2018; Lu et al. 2007; Biehl 2018). Although pure metals are able to yield higher saturation magnetizations, they are not suitable for clinical use due to their high toxicity and oxidative properties that result in non-magnetic oxides (Wu et al. 2018; Biehl 2018). Similarly, since most of the ferromagnetic alloys contain toxic components, like Co or Ni, they have been excluded from biomedical applications.

    The shape, size, and composition of magnetic nanoparticles depend on parameters such as the type and concentration of salts used like chlorides, sulfates, and nitrates, ferrous and ferric ratio, pH and ionic strength of media, as well as on the specific synthesis method (Banerjee et al. 2010; Lu et al. 2007; Biehl 2018). For magnetic nanoparticles, nanoparticle stability and size have to be traded off against high saturation magnetization (Ms) values, a key property in MRI applications (Jun et al. 2008). Ms is one essential parameter that describes magnetic response: Higher MS enables easier magnetic separation and magnetic transport to other locations, as well as induce higher magnetic field gradients if dispersed in solutions and subjected to an external homogeneous magnetic field (Amstad et al. 2011). These magnetic field perturbations are responsible for changed relaxivities r2 of water molecules measured in MRI. Thus, the higher the Ms of magnetic nanoparticles with everything else being equal, the more effective they are as MR contrast agents. Ms of magnetic nanoparticles is always below that of the respective bulk materials and decreases with decreasing core size and with the presence of surface ligands (Amstad et al. 2011; Jun et al. 2008). Properties such as saturation magnetization, specific absorption rate (SAR), chemical stability, scalability of the synthetic route, non-toxic composition, and narrow size distribution are determinant of the potential for transfer of any of these materials to the biomedical field.

2. *Iron and iron oxide*

    Iron, one of the most abundant metallic elements in living organisms, is essential for various biological processes, such as oxygen transport by hemoglobin and cellular respiration by redox enzymes. Iron oxide nanoparticles are one of the few nanomaterials that can be injected into the body and incorporated into natural metabolic pathways of the humans (Ling and Hyeon 2013). Fe^{3+} ions resulting from iron oxide dissolution under acidic conditions can be fed into the natural iron storage pathway. Compared with many other nanoparticles, iron oxide nanoparticles are benign, non-toxic, and biologically tolerated. The most common biocompatible magnetic nanomaterials are pure iron oxides, such as maghemite (γ-Fe_2O_3) and magnetite (Fe_3O_4). For in vivo use, iron-based magnetic particles

have an attractive combination of high magnetization, well-described cellular metabolism, and relatively low toxicity (Barry 2008). Also, iron oxide particles under about 30 nm are superparamagnetic, with no magnetization in the absence of an externally applied magnetic field that can lead to aggregation. Iron oxide nanoparticles have been produced according to a variety of protocols resulting in nano-objects of various sizes, shell types, ligands, and diverse interactions with biological fluids, cells, and organs (Wu et al. 2018; Ling and Hyeon 2013; Amstad et al. 2011; Lu et al. 2007).

Although iron oxide nanoparticles are relatively biocompatible, naked iron oxide nanocrystals can contribute to in vitro cytotoxicity as a result of ROS generation. Similarly, iron oxide nanoparticles doped with magnetically susceptible elements (e.g., $MnFe_2O_4$ and $CoFe_2O_4$), and metal alloy nanoparticles (e.g., FeCo and FePt) are little employed in biomedical applications due to their potential toxicity and rapid oxidation, though their magnetism is stronger than for pure iron oxide nanoparticles. In spite of its biocompatibility, iron oxide nanoparticles are subjected to the release of iron from dissolved iron oxide nanoparticles: When in the bloodstream, the amount of dissolved iron is negligible if iron oxide nanoparticle concentrations in the $\mu g\, kg^{-1}$ body weight range are injected (Amstad et al. 2011); when accumulating locally, e.g., within the tumor tissue, the amount of dissolved iron can prove toxic, though.

3. *Applications of magnetic materials*

Magnetic nanomaterials have practical applications in the biomedical field, including magnetic cell labeling, separation, and tracking, for therapeutic purposes in hyperthermia and drug delivery, and for diagnostic purposes, e.g., as contrast agents for magnetic resonance imaging (MRI) or photodynamic therapy (PDT) (Banerjee et al. 2010; Amstad et al. 2011; Paul and Sharma 2010). Magnetic nanoparticles are also being tested for tissue engineering applications, for example, in the mechanical conditioning of cells growing in culture, and in magnetic biosensing, using, for instance, magnetic nanoparticles coupled to analyte-specific molecules to detect target molecules via nanoparticle aggregation upon target binding, and that monitored by changes in proton relaxation times on a bench-top nuclear magnetic resonance system (Pankhurst et al. 2003; Banerjee et al. 2010). For binding of nucleic acid molecules to nanomaterials and applying a magnetic field to preferentially locate those nano-objects at the target site with the posterior release of the genetic material, an application named gene therapy has also been proposed (Dobson 2006). Alternatively named magnetofection, this method has been used to site-specifically deliver SPIONs-PAA-PEI-pDNA complexes to murine B16F1 melanoma cells, while SPIO nanoparticles bound to siRNAs (targeting the HOTAIR sequence in human glioma) effectively mediated low expression of HOTAIR and inhibited the proliferation, invasion, and in vivo tumorigenicity of CD133^{+} human glioma stem cells (Fang et al. 2016; Prosen et al. 2013).

For imaging, iron oxide nanomaterials are advantageous since they are biocompatible, biodegradable, and have deeper imaging penetration in tissues than, for instance, fluorescent probes (quantum dots). Nevertheless, as previously

explained, they can be uptaken, opsonized, and rapidly cleared from the body by phagocytes. On the other hand, certain USPIO nanoparticles possess extended residence time in the bloodstream that make them well suited for vasculature imaging and also for imaging lesions where the particles can extravasate through leaky vasculature, as occured in cancer tissue. For the latter, USPIOs can provide valuable information on cancer stage and potential for metastasis, increased neovascularization, and vascular leakiness with tumor malignancy (Barry 2008). Furthermore, USPIOs, such as ferumoxytol and ferumoxtran-10, have shown excellent potential for brain tumor imaging because brain tumors often have an impaired blood-brain barrier (Neuwelt et al. 2009). Finally, multimodal variants of magnetic materials that include fluorescent nanoparticles for dual magnetic and fluorescence imaging (Mulder et al. 2007; Kwon et al. 2018), magnetic and photothermal (Nima et al. 2019), optoacoustic (Bell et al. 2019), or plasmonic (Stafford et al. 2018) modalities are flourishing these days and show great promise for enhanced diagnostics and therapy (Tomitaka et al. 2019). For further examples about magnetic nanoparticle applications, the reader is conveyed to a series of review articles (Pankhurst et al. 2003; Banerjee et al. 2010; Wu et al. 2018; Barry 2008; Lu et al. 2007; Huang et al. 2011b; Friedrich et al. 2007; Singamaneni et al. 2011).

Further Considerations

Though in vitro and in vivo assays are a fundamental part of the toxicological evaluation of nanomaterials, they shall remain a first approximation to the problem in as much as they do not consider aspects related to the long-term and whole-body impact of these nano-objects. Furthermore, in vitro assays should not only be restrained to the cell type that is the expected target of that nanomaterial (e.g., cancer cells for hyperthermia applications), but they should be widened to include all possible cell types that will have potential interactions with that nanomaterial, such as blood cells for systemic administration or the mucosa lining for inhalation of nanoparticles. Macrophages in the different organs that compose the mononuclear phagocytic system (MPS), as well as other cells representative of those organs, should also be considered. In vivo experiments would substantially increase our understanding of nanotoxicity if pharmacokinetic profiles and long-term toxicity of both, nanoparticles and their degradation products, could be clearly and systematically addressed. Systematic preclinical and clinical studies in relevant animal or human models should be performed in order to elucidate clearance mechanisms and residual biodistribution over several periods of time, e.g., from one day to months.

From the point of view of the nanomaterials, much is needed to foster material characterization in physiologically relevant biological conditions. Colloidal and chemical nanoparticle stability should be evaluated in blood serum and with suspensions mimicking the mucous lining. A better approximation than phosphate buffer

saline certainly consists in employing the serum-supplemented cell medium used for culturing cells. Colloidal stability and its relationship to nanoparticle aggregation and to potential toxicity or to an unintended nanoparticle removal from the body due to its higher-than-expected size should be carefully considered prior incurring in further in vivo tests. Similarly, chemical stability in different biologically relevant media, specially at high and low pH, e.g., in the presence of enzymes, should be systematically scrutinized to adopt strategies that limit nanoparticle degradation and to be able to separate nanoparticle degradation products from the nanoparticle characteristics themselves in toxicological examinations.

In Vitro Evaluation of Cytotoxicity

In vitro (toxicity) assays refer to experiments performed using subcellular systems (e.g., organelles), cellular systems (e.g., cell cultures, barrier systems), tissues, or whole organs. Within the context of nanomedicine, they are used to screen the adverse effects of potentially therapeutic nanomaterials before their in vivo evaluation. The toxicity of materials is frequently assessed first in vitro in order to ascertain suitability and dosage for further in vivo studies, thus reducing the use of research animals (Sutariya 2015; Mitjans et al. 2018).

Cytotoxicity is a broad and ill-defined term that refers to the potential of a compound (or treatment) to cause cell damage or death (Jain et al. 2018; Niles et al. 2008). Within this context, a material can be recognized as cytotoxic if alters cell growth rate, attachment, or morphology, or causes cell death (Horváth 1980). Usually, the cytotoxicity of a test nanomaterial is determined by evaluating the number of viable cells or some surrogate biomarker related to cell viability after a defined incubation time (Riss et al. 2011). Alternatively, the number of damaged/dead cells or parameters related to the degree of cell death, rather than cell viability, can be determined. The former and latter strategies constitute the basis for the so-called cell viability and cytotoxicity assays, respectively (Niles et al. 2008), though these terms are frequently used interchangeably.

There are several methods described in the literature to assess cell viability and cytotoxicity (Inglese 2010; Stoddart 2011; Gilbert and Friedrich 2017), ranging from assays that measure dye inclusion (e.g., neutral red assay) or exclusion (e.g., Trypan blue assay), metabolic activity (e.g., MTT assay), activity of released enzymes (e.g., LDH assay), apoptosis biomarkers (e.g., caspase 3/7 assay), the colony formation ability (i.e., clonogenic assay), among others. The instrumentation required for these assays is very diverse, implying the use of optical, fluorescence or confocal microscopy, flow cytometry, or microplate readers for absorbance, fluorescence, or luminescence measurements, depending on the case.

In this chapter section, we will focus on microplate-based cell viability/cytotoxicity assays. Compared to other methodologies, these cost-effective assays offer the possibility of assessing a large number of samples using simple equipment (frequently available in most laboratories) in short periods of time (Niles et al. 2008;
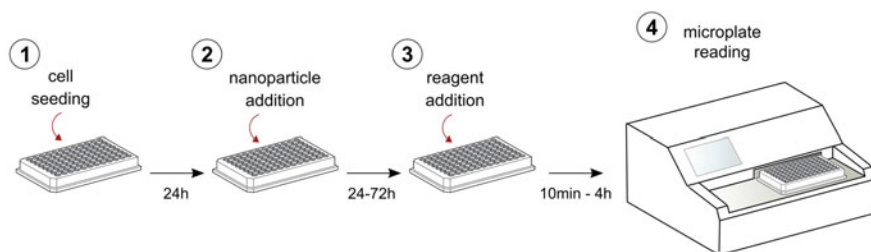
Fig. 2 Schematic representation of the general procedure followed in microplate-based cell viability/cytotoxicity assays

Riss et al. 2010). The general procedure for the evaluation of candidate nanomaterial toxicity using these methods is schematized in Fig. 2. Briefly, the cell line (or primary cell) of interest is seeded in a microplate and allowed to grow during a determined time (usually 24 h). After this, cells are exposed to varying concentrations of the nanomaterial under study for a given incubation time (usually 24–72 h). Then, the assay reagent, which measures a surrogate biomarker, is added to the microplates and allowed to react until the "response" is developed (usually in 10 min to 4 h). The response (absorbance, fluorescence, or luminescence) is measured in a microplate reader, and it is (ideally) proportional to the number of viable or damaged cells. When a clear dose–response curve is observed, quantitative parameters are derived, being the most important the inhibitory concentration 50 (IC_{50}) which, in cell viability assays, is the concentration that causes 50% of the measured response compared to control cells not exposed to the nanomaterial.

Table 1 summarizes the cell viability/cytotoxicity assays that will be explained in the following sections. They are based on the determination of cellular metabolic activity (tetrazolium-based, resazurin-based, and ATP–luciferase assays), dye-binding ability (neutral red and sulforhodamine B assays), or activity of released enzyme (LDH assay). In addition, Table 1 collects the main references that have applied these methods to study the cytotoxicity produced by (mostly iron oxide-based) magnetic nanomaterials.

Tetrazolium Salt-Based Assays

This group of colorimetric assays is based on the ability of metabolically viable cells to reduce tetrazolium salts into formazan products (Berridge et al. 2005). The first widely accepted assay to determine cell viability based on this kind of compounds was introduced by Mosmann in 1983 using MTT (3-(4,5-dimethylthiazol-2-yl)-2,5-diphenyltetrazolium bromide) (Mosmann 1983).

MTT is a yellow dye that upon (intracellular) reduction forms a purple formazan product (see Fig. 3a). The reduction is mainly catalyzed by dehydrogenases and oxidoreductases that use NADH and NADPH as cofactors (electron donors) and can

Table 1 Main cell viability/cytotoxicity assays used for the evaluation of magnetic nanomaterials

Assay	Principle	Response	References[a]
Tetrazolium salts	Metabolic activity (NADH dehydrogenase)	Absorbance	Arbab et al. (2003), Choi et al. (2009), Oliveira et al. (2013), Cai et al. (2013), Zhu et al. (2011), Xuan et al. (2011), Schleich et al. (2013), Halamoda Kenzaoui et al. (2012), Aranda et al. (2013), Kunzmann et al. (2011), Könczöl et al. (2011), Zou et al. (2010), Zhu et al. (2013b), Liu et al. (2011), Li et al. (2013), Hanot et al. (2015), Klein et al. (2012), Lee et al. (2009a), Hsiao et al. (2008), Mejías et al. (2013), Müller et al. (2007), Costa (2015), Sadeghi et al. (2015)
Resazurin	Metabolic activity (NADH dehydrogenase)	Fluorescence	Costa (2015), Kievit et al. (2011), Guarnieri et al. (2014), Narayanan et al. (2012), Boyer et al. (2010), Mok et al. (2010), Fernández-Bertólez et al. (2018a), Kiliç (2015), Kievit et al. (2009), Sun et al. (2008), Tse et al. (2015), Lartigue et al. (2012)
ATP–luciferase	Metabolic activity (ATP content)	Luminescence	Khandhar et al. (2012), Chu et al. (2013), Luo et al. (2015), Joris et al. (2016), Huth et al. (2004), Park (2014), Sharkey et al. (2017)

Table 1 (continued)

Assay	Principle	Response	References[a]
Neutral red	Dye binding (lysosomes)	Absorbance Fluorescence	Könczöl et al. (2011), Müller et al. (2007), Costa (2015), Fernández-Bertólez et al. (2018a), Kiliç (2015), Granot and Shapiro (2011)
Sulforhodamine B	Dye binding (proteins)	Absorbance Fluorescence	Hanot et al. (2015), Wang et al. (2014), Shi et al. (2013), Zheng et al. (2018), Barick et al. (2009), Thu (2009), Shanavas et al. (2017), Fu et al. (2017), Guo et al. (2015)
Lactate dehydrogenase	Enzyme leakage (LDH activity)	Absorbance	Malvindi et al. (2014), Gaharwar et al. (2017), Ahamed et al. (2013), Choi et al. (2009), Sadeghi et al. (2015), Park (2014), Sharkey et al. (2017), Soenen et al. (2010), Hirsch et al. (2013), Alarifi et al. (2014), Han et al. (2011)

[a]Selected references accounting for the use of these cell viability/cytotoxicity assays to determine cytotoxicity of magnetic (mostly iron oxide-based) nanoparticles

take place at mitochondria, cytoplasm, and the plasma membrane (Berridge et al. 2005; Präbst et al. 2017). Since the formazan crystals are insoluble and intracellularly formed, cell lysis (detergent solutions) and solubilization (organic solvents like DMSO or isopropanol) steps are required prior absorbance measurement.

MTT assay can be used to determine viability of adherent or suspended cells from animal, plant, or fungal origin, offering good sensitivity and wide linear dynamic range (from 200–1000 to 50,000–100,000 cells, depending on the cell) (Präbst et al. 2017; Kupcsik 2011). In contrast to other well-established methods such as Trypan blue counting, ^{3}H-thymidine incorporation, fluorometric DNA assays, or flow cytometry-based techniques, MTT assay does not produce toxic or radioactive damage and is faster, relatively cheap, and easy to perform requiring only simple instrumentation (Sylvester 2011). Owing to these features, the assay has become popular in the screening of new drugs (Kupcsik 2011; Sylvester 2011).

In addition to MTT, other tetrazolium salts that produce water-soluble formazan products have been developed. Among them, MTS (Barltrop et al. 1991; Cory et al. 1991), XTT (Scudiero et al. 1988; Paull et al. 1988), WST-1 (Ishiyama et al. 1993),
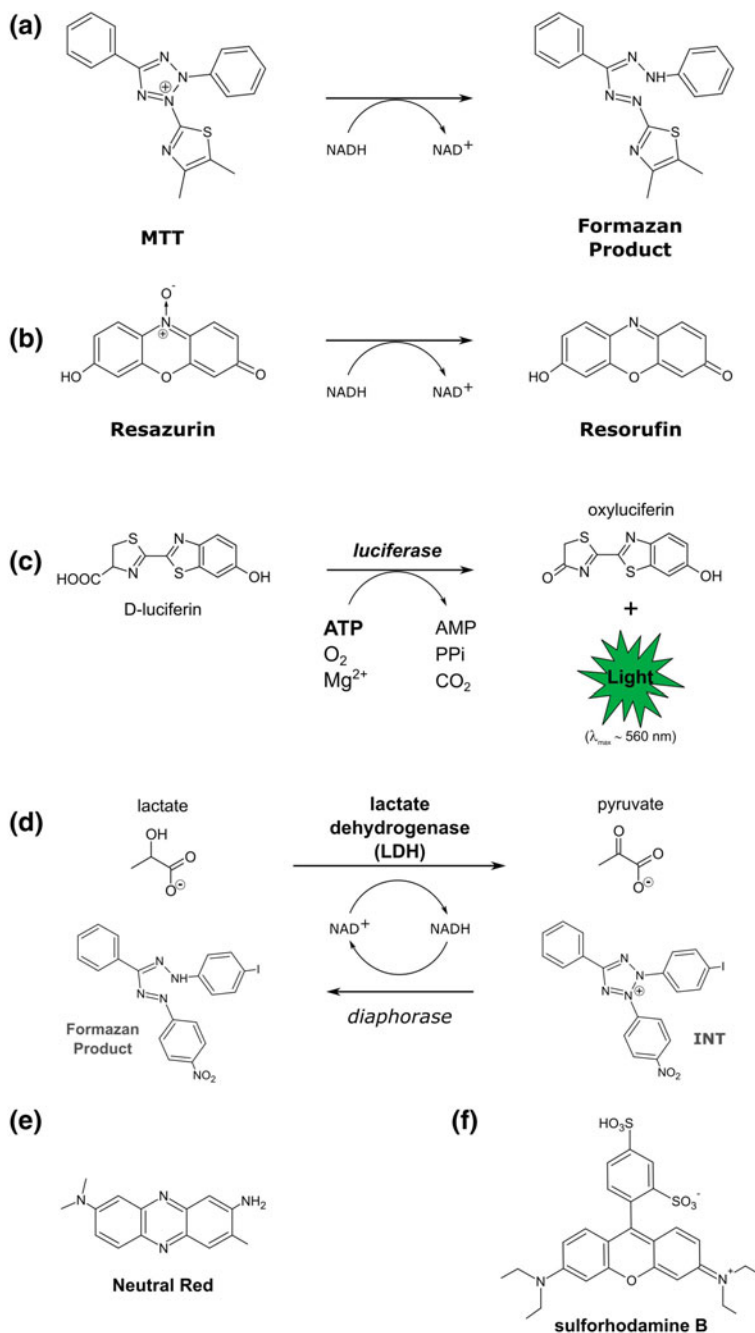
Fig. 3 Reagents and reactions involved in the cell viability/cytotoxicity assays explained in this section. **a–d** depict the reactions used in MTT, resazurin-based, ATP–luciferase, and LDH assays, respectively. **e** and **f** show the chemical structure of the dyes used in the neutral red and sulforhodamine B assays, respectively

and WST-8 (Tominaga et al. 1999) are the most widely used. In these compounds (and their derived formazans), the solubility is increased by decorating their phenyl moieties with sulfonates groups. Contrary to MTT, which is weakly cationic, these derivates are neutral or negatively charged and, as consequence, their passage through the cellular membrane is restricted. Therefore, the reduction of these molecules is mainly performed extracellularly, and intermediate electron acceptors, such as 5-methyl-phenazinium methyl sulfate (PMS) or 1-methoxy-5-methyl-phenazinium methyl sulfate (mPMS), are used to link the intracellular metabolism with the extracellular reduction (Berridge et al. 2005; Präbst et al. 2017; Cory et al. 1991).

The assays that use water-soluble formazans require fewer experimental steps (lysis and solubilization steps are no longer necessary) are more sensitive and present less cytotoxicity than MTT assay (Kupcsik 2011; Berridge et al. 1996; Bernas and Dobrucki 2002). Moreover, owing to the solubility of the reduced product and the absence of lysis and solubilization steps, they can be used in real-time assays (Berridge et al. 2005).

The practical procedure can be summarized as follows. For MTT assay, after incubation of cells with the test nanomaterial, the culture medium is removed and the cells washed with PBS. Then, the cells are incubated with MTT (dissolved in culture medium) for 1–4 h. The incubation time will depend on cell type, cell density, and incubation conditions among other variables. After this step, the medium is removed and the cells are incubated under shaking with the lysis solution (~10 min), followed by incubation with the solubilization solvent (~10 min). Depending on the commercial kit used, these steps may be combined into a unique one. Once solubilization is achieved, the absorbance is read at 570–590 nm.

In the cases of MTS, XTT, WST-1, and WST-8 assays, after incubation (1–4 h) with the tetrazolium compound, the absorbance is directly measured without performing any lysis or solubilization step. These soluble formazan products present maxima at around 450–500 nm, depending on the dye used (Berridge et al. 2005; Barltrop et al. 1991; Cory et al. 1991; Scudiero et al. 1988; Paull et al. 1988; Ishiyama et al. 1993; Tominaga et al. 1999).

Resazurin-Based Assay

Resazurin is a blue dye that upon reduction by metabolically active cells is converted to resorufin, a pink-colored dye which exhibits red fluorescence (see Fig. 3b). Discovered by Weselsky (Weselsky 1871) in the nineteenth century and used to assess metabolic activity since the late 1920s (for the evaluation of microbial contamination in milk) (Palmer et al. 1930), this redox indicator has been applied to study the growth/viability of different organisms, ranging from bacteria to mammalian cells (O'Brien et al. 2000).

The reduction of resazurin has been attributed to the enzymatic activity of dehydrogenases, oxidoreductases, and cytochromes that use NADH and NADPH as electron sources, located in the mitochondria, cytosol, and microsomes (O'Brien et al. 2000;

Gonzalez and Tarloff 2001; Candeias et al. 1998). Many of the enzymes that reduce resazurin have shown to reduce MTT as well (Niles et al. 2008; Gonzalez and Tarloff 2001). Both resazurin and its reduced form resorufin are water-soluble and able to diffuse through cell membrane. Resorufin can be further reduced to dihydroresorufin if cells are incubated for too long with the redox indicator or high cell density is used (Präbst et al. 2017; O'Brien et al. 2000; Twigg 1945; Nakayama et al. 1997). The latter is not fluorescent and toxic to cells, and its presence may lead to inaccurate results.

Considering that resazurin has an absorbance maximum at 605 nm (and is weakly fluorescent) and resorufin presents an absorption peak at 573 nm and fluoresces with excitation/emission maxima at 579/584 nm, the assay may be performed colorimetrically or fluorometrically, though the second option is preferred because it provides greater sensitivity (Präbst et al. 2017; Czekanska 2011).

The assay is simple, relatively rapid, cost-effective, and safe. If executed by measuring fluorescence, it is able to achieve remarkable sensitivity (better than tetrazolium assays) and linear dynamic range (200–50,000 cells, in 96-well plate, depending on cell type) (O'Brien et al. 2000; Czekanska 2011; Riss and Moravec 2006). Moreover, resazurin assays can be multiplexed with other methods (e.g., caspase assay, LDH assay, Hoechst stain) (Wu et al. 2009; Węsierska-Gądek et al. 2005) and, to a certain extent, used for high-throughput screening (Riss et al. 2010; Hamid et al. 2004).

The practical procedure can be summarized as follows. After incubation of cells with the test nanomaterial, the culture medium is removed and the cells washed. Then, the cells are incubated with resazurin reagent (dissolved in culture medium) for 1–4 h. As in the case of MTT, incubation time must be optimized for each cell type and incubation conditions. After incubation, the assay is read in a fluorescence plate reader using 560 and 590 nm as excitation and emission wavelength, respectively. Alternatively, absorbance can be measured (losing sensitive compared to fluorescence). In this case, both resazurin and resorufin contributions to the total absorbance should be considered.

ATP–Luciferase Assay

ATP (adenosine triphosphate) is the most important energy carrier molecule in cells, used to drive a variety of biochemical processes. In living animal cells, ATP is mainly produced by mitochondria, through the enzymes of the respiratory chain, and a lesser amount is generated by glycolysis in the cytosol (Alberts 2015). Dead cells lose the ability to synthesize new ATP, and the remaining ATP is rapidly depleted by endogenous ATPases. Owing to this, ATP is considered a well-founded marker of cell viability (Riss et al. 2006).

The assessment of cell viability using ATP quantification is performed by taking advantage of the firefly luciferase enzyme (Lundin et al. 1986). The luciferase is able to oxidize the pigment D-luciferin, in the presence of ATP (O_2 and Mg^{2+} are

also required), to oxyluciferin (see Fig. 3c). The reaction also produces ADP, PPi, CO_2, and the emission of light (luminescence). The emitted light is proportional to ATP concentration, and this latter is proportional to the number of viable cells. Since ATP is intracellularly located, a lysis step is performed before (or together with) the enzymatic reaction.

In its current versions, the ATP–luciferase assay presents outstanding features (Niles et al. 2008; Riss et al. 2011). The low background luminescence provides the assay with a high signal-to-noise ratio that makes it extremely sensitive, being able to detect even 4–5 cells in a well in 384-well plates. In addition, the assay possesses a wide linear dynamic range, typically from 50 to 50,000 cells (in 96-well plates) (Riss and Moravec 2006). On the other hand, it is really simple to perform, only having a few steps, and it is fast (results can be obtained in less than 30 min).

The practical procedure can be summarized as follows. After incubation of cells with the test nanomaterial, a reagent containing a detergent (to lyze cells), ATPase inhibitors (to stabilize the released ATP), the substrate luciferin and the luciferase, is added to cells and incubated for few minutes under shaking. Then the plates are left stand for 5–10 min (for luminescence stabilization). After this period, the luminescence is measured using a luminometer.

Neutral Red Uptake Assay (NRU Assay)

Neutral red (3-amino-7-dimethylamino-2-methylphenazine hydrochloride, see Fig. 3d) is a weakly cationic dye that at physiological pH presents almost no net charge, enabling it to penetrate the cell membrane by non-ionic diffusion. Inside the cell, it accumulates in lysosomes owing to a proton gradient that maintains the pH lower than that of the cytoplasm. In such condition, the dye becomes positively charged and remains retained in the lysosomes.

The ability of cells to uptake neutral red relies on their capacity to maintain pH gradients through the production of ATP. Dead cells, or those which cannot maintain the correct pH gradient, are not able to retain the dye. As a consequence, the amount of retained dye is proportional to the number of viable cells. Furthermore, the incorporation, binding, and cell retention of neutral red can be affected by alterations of lysosomal membrane or cell surface in viable cells.

The neutral red uptake assay presents many advantages. It is fast (3–4 h), cheap, relatively simple to perform, and very sensitive, and it can be used to test viability on most animal cells (primary cells and cell lines). Moreover, it is suitable for automation and high-throughput screening of test compounds (Bouhifd et al. 2012; Rodrigues et al. 2013). Compared to tetrazolium salt-based assays, the NRU assay is more sensitive, presents fewer interferences, uses more stable reagents, and is cheaper (Borenfreund et al. 1988), while it is simpler and cheaper than sulforhodamine B-based assay (Vichai and Kirtikara 2006). Perhaps one of its main drawbacks is that once started, it must be completed immediately without the possibility of pausing the sequence by adding a stop reagent or freezing the cells (Repetto et al. 2008).

The practical procedure can be summarized as follows. After incubation of cells with the test nanomaterial, the culture medium is removed and the cells washed with PBS. Then, the cells are incubated with neutral red containing culture medium for 1–3 h. After this step, the medium is removed and the cells are washed with PBS again. Thereafter, the incorporated neutral red is extracted from the cells using a destaining solution (usually containing ethanol and acetic acid) that is applied for 10–40 min under shaking until a homogeneous solution is formed. Finally, the absorbance of the neutral red extract is read at 540 nm. Alternatively, it is possible to use the fluorescence of neutral red to quantify the dye with higher sensitivity and fewer interferences. In this case, the measurement is performed using excitation and emission wavelengths of 530 nm and 645, respectively (Repetto et al. 2008).

Sulforhodamine B Assay (SRB Assay)

The SRB assay is based on the measurement of cellular protein content in order to determine cell density/viability. The assay was developed by Skehan et al. (1990), and since then it has become a popular method for cytotoxicity screening of test compounds (Vichai and Kirtikara 2006; Woolston and Martin 2011). Sulforhodamine B (SRB) is a bright pink aminoxanthene dye that possesses two sulfonic groups in its structure (see Fig. 3e). Owing to these groups, the dye binds to basic amino acid residues in proteins under mild acidic conditions and dissociates from them under basic condition. In the assay, after the binding of SRB to proteins of cells fixed with trichloroacetic acid (TCA), the dye is extracted and quantified spectrophotometrically. The amount of extracted dye is (ideally) proportional to cell mass/number.

As a result of the strong absorbance presented by SRB, the assay is very sensitive, showing higher sensitivity than other protein-staining colorimetric methods, such as Lowry and Bradford (Skehan et al. 1990), and comparable to fluorescent dye-staining methods like DAPI and Hoechst 33342 (McCaffrey et al. 1988). Moreover, it presents the advantage that TCA-fixed cells and SRB-stained cells can be stored indefinitely at room temperature. On the other hand, the multiple washing and drying steps may discourage some people from using the assay (Woolston and Martin 2011), which also makes the method hard to automate (Vichai and Kirtikara 2006).

It is important to mention that unlike cell viability assays based on metabolic activity (e.g., tetrazolium salt- or resazurin-based methods) that only detect viable cells, SRB assay does not distinguish between viable and live cells. In spite of this fact, the ability of SRB assay to evaluate cell viability and cytotoxic effects is not compromised. For instance, as demonstrated in the works by Rubinstein et al. (1990), Haselsberger et al. (1996), Perez et al. (1993), the results obtained with SRB assay correlate fairly well with those derived from MTT assay, being the main difference the slightly higher IC_{50} values estimated for the tested compound when SRB assay was used.

The practical procedure can be summarized as follows. After incubation of cells with the test nanomaterial, the cells are fixed by the addition of a TCA aqueous solution and incubated at 4 °C for 1 h. If the tested material does not interfere with SRB, the later step can be performed without changing the incubation media. Then, the plates are washed with water (several times) and dried. At this point, the SRB solution (usually SRB in 1% v/v acetic acid) is added, the plates incubated for 10–30 min at room temperature, and then rinsed with acetic acid solution, to remove unbound dye, and dried thereafter. After this step, the solubilization of SRB is performed by adding a base solution (usually Tris Base solution; pH ~10.5). Finally, the absorbance of the SRB extract is measured at 564 nm. In the case of high absorbance values (above the linear range of the instrument), readings at suboptimal wavelengths (490–530 nm) are recommended. In addition, SRB amounts can be determined fluorometrically using 488 nm and 585 nm as excitation and emission wavelengths, respectively.

Lactate Dehydrogenase Assay (LDH Assay)

Lactate dehydrogenase is a tetrameric enzyme present in the cytosol of almost all living cells that catalyzes the conversion of pyruvate to lactate and, depending on the conditions, is able to catalyze the reverse reaction. Owing to the intracellular location of the enzyme, LDH assay has been considered a gold standard for assessing membrane integrity and has a long tradition in the evaluation of cell or tissue damage (Kroll et al. 2012; Koh and Choi 1987).

In order to measure LDH activity, the medium containing the enzyme is incubated with lactate (substrate) and NAD+ (cofactor) which are converted to pyruvate and NADH, respectively. The produced NADH is used by a diaphorase to reduce a tetrazolium salt (2-(4-iodophenyl)-3-(4-nitrophenyl)-5-phenyl-2H-tetrazolium; abbreviated as INT) yielding a cherry red formazan product that can be quantified by its absorbance at 492 nm and which is proportional to LDH activity (see Fig. 3f) (Nachlas et al. 1960).

The LDH assay can be used to assess membrane damage/cell lysis (as a cytotoxicity assay) by measuring LDH activity on the culture supernatants after incubating the cells with the test compound for a determined time. In this case, the higher the LDH activity measured, the higher the number of damaged/dead cells. Alternatively, it can be used to estimate the total cell number (viable and non-viable) by incorporating a cell lysis step (to release LDH from non-damaged cells) prior determination of enzymatic activity (Riss and Moravec 2006). An aqueous solution of Triton X-100 is frequently used to perform the lysis step. In this case, the higher the detected LDH activity, the higher the cell number.

The practical procedure can be summarized as follows. For assessing membrane damage (cytotoxicity), after incubation of cells with the test nanomaterial, aliquots from culture supernatants are transferred to a new microplate and incubated with the reagent used for measuring LDH activity (containing lactate, NAD+, diaphorase, and INT) for around 30 min at room temperature. Then, absorbance is read at ~490 nm.

On the other hand, to estimate total cell number, after incubation with the test nano-material and prior LDH activity measurement, the samples are incubated with a lysis solution (usually containing Triton X-100) for 45–60 min at 37 °C. Then, aliquots are transferred to a new microplate, and the procedure retaken as explained before.

In Vitro Evaluation of Genotoxicity

The term genotoxicity refers to the ability of a compound (or treatment) to induce damage in the genetic material (Doak et al. 2017; Kumar and Dhawan 2013). The damage may involve small lesions at DNA level (e.g., strand breaks, adducts, abasic sites, and point mutations) or abnormalities in chromosomes (e.g., alterations in the number of chromosomes, termed aneuploidy, and chromosome fragmentation, termed clastogenicity). The damage caused by genotoxic agents may or may not be transmitted to the next generation of cells. On the other hand, when an agent causes an alteration in the genetic material that is fixed and transmitted to daughter cells, it is considered a mutagen (Benigni and Bossa 2011).

Among the different methodologies used for the evaluation of genotoxicity (Sierra and Gaivão 2014; Dhawan and Bajpayee 2013; Graziano and Jacobson-Kram 2015), the comet and the micronucleus assays are the most popular tools for the screening of genotoxic potential of nanomaterials (Kumar et al. 2018; Azqueta et al. 2015; Magdolenova 2014) and will be described in the following subsections. The former is devoted to the detection of primary DNA damage, while the latter is performed to ascertain chromosomal aberrations in proliferating cells. Lesions detected by comet assay are potentially reversible, while those detected by micronucleus assay are irreversible. Table 2 summarizes the main concepts behind these two assays and collects the main references that applied them to study genotoxicity produced by (iron oxide-based) magnetic nanomaterials.

Comet Assay

The comet assay, also known as single-cell gel electrophoresis assay, is a widespread technique used to detect primary DNA damage at early stages, by measuring DNA strand breaks in individual cells. It was first introduced by Ostling and Johanson (neutral version of the assay) for the study of DNA damage induced by radiation in single cells (Ostling and Johanson 1984). Later, Singh and coworkers developed the alkaline version of the assay (Singh et al. 1988), which is more sensitive toward smaller amounts of DNA damage, being able to detect single and double DNA breaks, alkali-labile sites, among other damages (Singh et al. 1988; McKelvey-Martin et al. 1993; Fairbairn et al. 1995). This version is the recommended and most widely spread to identify agents with genotoxic activity (Tice et al. 2000), and in this subsection, we will only refer to it.

Table 2 Main assays used for the assessment of genotoxic potential of magnetic nanomaterials

Assay	Damage detected	Required equipment	References[a]
Comet assay	*DNA primary damage* (potentially reversible)	Gel electrophoresis equipment Fluorescence microscope	Malvindi et al. (2014), Ahamed et al. (2013), Könczöl et al. (2011), Fernández-Bertólez et al. (2018a), Kiliç (2015), Han et al. (2011), Karlsson et al. (2009), Bhattacharya et al. (2012), Kain et al. (2012), de Lima et al. (2013), Shaw et al. (2014), Gaharwar et al. (2017), Fernández-Bertólez et al. (2018b), Mishra et al. (2018), Turiel-Fernández et al. (2018), Abakumov et al. (2018), Sadiq et al. (2015), Zhang et al. (2012b), Buliaková (2017), Seo et al. (2017), Fernández-Bertólez et al. (2018c), Auffan et al. (2006), Seabra et al. (2014), Cowie et al. (2015), Harris et al. (2015), Magdolenova et al. (2015), Shydlovska et al. (2017)
Micronucleus assay	*Chromosome fragments Lagging chromosomes* (irreversible)	Optical or fluorescent microscope	Könczöl et al. (2011), Fernández-Bertólez et al. (2018a), Kiliç (2015), Sadiq et al. (2015), Zhang et al. (2012b), Buliaková (2017), Seo et al. (2017), Fernández-Bertólez et al. (2018c), Magdolenova et al. (2015), Evans et al. (2019), Shah et al. (2013), Pöttler et al. (2015)

[a]Selected references accounting for the use of the comet or micronucleus assays to determine genotoxic potential of magnetic (mostly iron oxide-based) nanoparticles

In the assay, after exposure to the tested nanomaterial, cells are embedded in agarose, placed in a microscope slide and lyzed by means of detergents and high concentration of salts. Then, the slide is incubated in alkaline electrophoresis buffer (pH >13), promoting the unwinding of the liberated DNA, and submitted to electrophoresis. Under the applied electric field, the fragmented DNA migrates out of the nucleoid body, toward the anode. After neutralization, DNA is stained with a fluorescent dye (e.g., ethidium bromide) for visualization. Cells with higher DNA damage display increased migration of chromosomal DNA and form an electrophoretic pattern that, under observation with a fluorescent microscope, resembles the shape of a comet where the nucleoid is the head and the migrated DNA the tail. Usually, the damage is quantified by image analysis measuring the tail length or estimating other metrics such as percentage of tail DNA and tail moment.

The procedure exhibits many advantages. Among them, it can be performed in almost any eukaryotic cell (proliferating and non-proliferating) as long as a cell suspension can be obtained, is very sensitive, requires low number of cells (<10,000 cells per slide), and is relatively fast and cost-effective.

Micronucleus Assay

The micronucleus assay is a popular method to detect chromosomal aberrations in proliferating cells, used for the evaluation of compounds with clastogenic (potential to break chromosomes) and aneuplodogenic activity (potential for lagging entire chromosomes) (Countryman and Heddle 1976; Bolognesi and Fenech 2013; Wolff and Müller 2006; Fenech and Morley 1985). Micronuclei are chromosome fragments or whole chromosomes that have failed to attach onto the spindle during anaphase and are not included in the main nucleus. During subsequent interphase, they condense to form characteristic small nuclei, much smaller than the principal nucleus (Zelazna et al. 2011).

For micronuclei to be generated, the cells must be undergoing mitosis, and consequently, they appear only in dividing cells. In order to improve the assay, many methods have been proposed to identify cells that have completed cellular division (Fenech and Morley 1985; Pincu et al. 1984; Fenech 2000). At present, the most widespread in vitro method used for the evaluation of micronuclei is the cytokinesis-block micronucleus (CBMN) assay, usually performed using (human) lymphocytes (Bolognesi and Fenech 2013; Fenech 2000). In CBMN assay, the cytokinesis is blocked using cytochalasin B, and cells that have completed one cell cycle appear binucleated being easily distinguished from undivided cells. These micronuclei are identified by microscopic observation of Giemsa-stained samples.

CBMN assay is sensitive, and its performance and result analysis is easier than the classical chromosomal aberration analysis performed in metaphasic cells. Furthermore, combined with fluorescence in situ hybridization (FISH) technique (using centromeric probes), it is able to discriminate between clastogenic and aneuplodogenic activity (Marshall et al. 1996; Eastmond and Pinkel 1990).

It is important to mention that cytochalasin B also inhibits endocytosis and, as a consequence, might interfere with the proper evaluation of nanoparticle genotoxicity (Doak et al. 2009; Gonzalez et al. 2011). Owing to this, it is important to treat the cells with nanoparticles and without cytochalasin B before the CBMN assay is performed.

The Use of 3D Cultures

Nanoparticle toxicity is initially evaluated in 2D cell culture as described in the previous section. The usual next step is to contrast those results in an entire animal, but oftentimes results obtained in cell culture do not translate in the same in vivo outcome. The limitations of cell culture in a monolayer to recreate three-dimensional morphologies of cells in tissues, as well as the dynamics and complex interactions of cells with their supporting extracellular materials, could explain those differences.

As demonstrated in multiple in vivo delivery tests and also discussed in the introductory section, nanoparticles have to overcome numerous biological barriers in order to reach target organs. In their review, Blanco et al. (2015) summarize those obstacles and propose different strategies to succeed. Those impediments include opsonization of nanoparticles with posterior sequestration by macrophages, what in turn leads nanoparticles to organs with filtration capability where nanoparticles can exert toxic effects.

In 2D cell culture, nanoparticles administered in a bulk solution reach cell membranes without impediments. In contrast, nanoparticles delivered in vivo face a hindrance, such as the extracellular matrix (ECM), in which nanoparticles could be retained. Furthermore, depending on their surface properties, NP can interact with charged ECM components (Goodman et al. 2007; Ruponen et al. 1999).

Another factor that can explain differences in toxicity observed between 2D culture and animal studies is that cell culture assays do not take into account the hydrostatic and osmotic pressures in tissues. In particular for tumors, poor lymphatic drainage, extensive fibrosis, and a dense ECM result in particularly elevated interstitial fluid pressures (Heldin et al. 2004). This high intratumoral pressure prevents extravasation of nanoparticles to distal regions, resulting in lower toxicity compared to a monolayer, where studies are performed under static conditions. Furthermore, 2D cell monolayer cultures are generally exposed to a uniform environment, whereas cells in tissues such as solid tumors are exposed to pH and concentration gradients that can affect nanoparticle internalization.

For the reasons mentioned above, there is an increasing interest in utilizing 3D culture systems in order to mimic more accurately the in vivo situation and ultimately the human clinical setting (Kenny et al. 2007). Test toxicity of nanoparticles in vitro 3D systems will allow obtaining more predictable results, not replacing in vivo assays but making it in a more efficient way and shortening the gap in translation from cell culture to animal studies and clinical trials.

3D Culture Systems to Test Magnetic Nanoparticle Toxicity

There are different types of 3D culture formats that can be used in order to answer specific biological questions. In their reviews, Shamir et al. and Goodman et al. make a comprehensive analysis of the different culture systems (Goodman et al. 2008; Shamir and Ewald 2014). Here, we are going to focus on the most relevant toxicity studies for magnetic nanoparticle.

1. *Hydrogels and 2.5D cultures*

    The use of hydrogels with no cells is the simplest model for assessing nanoparticle interaction with ECM components. In the case of magnetic nanoparticles, the same biophysical characteristics that limit the application of traditional therapies can be exploited to improve biodistribution. Magnetic NPs can be specifically localized within a fluid-filled cavity to the site of a lesion or target tissue by an external magnetic field. Kuhn et al. calculated the average velocity of different size and surface coating superparamagnetic NP in hydrogels (Kuhn et al. 2006). Although the usefulness of this systems is limited as it does not provide any information of cell toxicity, it offers valuable information about the effect of size, shape, and surface chemistry on the mobility of vectors through the ECM.

    The addition of ECM proteins to the medium in 2D cultures is sufficient to induce tissue-specific differentiation of diverse epithelial cells, including mammary (Streuli et al. 1991), kidney (O'Brien et al. 2001), and lung (Yu et al. 2007). This a very important feature since the expression of cell membrane receptors can change in the presence of ECM proteins, thus affecting nanoparticle uptake. This system is known as 2.5D culture. Even though this system does not perfectly resemble the in vivo environment, as cells are still in contact with a large fluid reservoir, it induces cells to form a more physiological tissue architecture than 2D assays and the cells remain accessible for molecular analysis (Debnath et al. 2003).

2. *Multicellular spheroids*

    In this culture system, cells form spherical clusters. There are different ways to form spheroids: culturing cells in spinner flasks, in agar-coated culture plates, or the hanging drop method (Nederman and Twentyman 1984; Timmins and Nielsen 2007). Under these conditions, spheroids can survive for weeks and can reach sizes of up to several millimeters in diameter. Large spheroids are characterized by an external proliferating zone, an internal quiescent zone caused by the limited distribution of oxygen, nutrients, and metabolites, and a necrotic core (Vinci et al. 2012) resembling the cellular heterogeneity of solid in vivo tumors (Mueller-Klieser 1987, 2017). As spheroids are relatively easy to handle, they are amenable to confocal analysis, cryosectioning, and commonly used fixing methods. They can also be disaggregated by trypsin treatment and individual cells collected for cytotoxic assays like LHD and MTT, or flow cytometry analysis. These properties make spheroids a very useful and widely used model for investigating nanoparticle–tissue interactions. Although it is not the aim of this section to make a detailed description of cell culture types, it is important to

differentiate multicellular tumor spheroids from tumorospheres. Both are characterized by their well-rounded shape, the presence of cancer cells, and their capacity to be maintained as free-floating cultures, but tumorosphere is a type of culture that allows the selection of cancer stem cell subpopulation.

3. *Multilayer cell cultures*

Multilayer cultures are most commonly formed by growing a monolayer culture beyond confluence in transwell cell culture dishes, composed by a microporous filter membrane insert within a chamber. The transwell dishes produce isolation between the apical and basal layer of the multilayer, so that any compound delivered to one side must go through the cell layers to reach the opposing side. This allows for easy assessment of transcellular nanoparticle delivery by incubating drugs on one side of the growing culture and collecting media on the opposite side to assess the amount of nanoparticles that passed through the cell layer.

Transwell inserts are also commonly used to reproduce the blood-brain barrier (BBB). This barrier is built up by the brain capillary endothelial cells connected by tight junctions and supporting pericytes and astrocytic end-feet. Polar molecules and small ions are almost totally excluded by the tightly closed intercellular cleft. Although they are well suited for magnetic resonance imaging (MRI), magnetic nanoparticles employed as contrast agents are not suited to cross biological barriers like the BBB (Veiseh et al. 2009b). Thus, in vivo application of magnetic nanoparticles as MRI contrast agents for brain imaging is still limited. For these reasons, there are several research groups designing new strategies to overcome this barrier, utilizing the multilayer cell culture in transwell to perform in vitro assays (Qiao et al. 2012; Shi et al. 2016; Busquets et al. 2015b). For example, Qiao et al. tested a brain delivery probe based on the PEG-coated Fe_3O_4 nanoparticles in an in vitro BBB model based on primary porcine brain capillary endothelial cells (PBCECs) cultured over transwells (Qiao et al. 2012).

4. *Organ-on-a-chip*

This system consists of a device for culturing living cells in continuously perfused, micrometer-sized chambers in order to model physiological functions of tissues and organs. The goal is not to build a whole living organ but rather to synthesize minimal functional units that recapitulate tissue and organ-level functions. The simplest system is a single, perfused microfluidic chamber containing one kind of cultured cell that exhibits functions of one tissue type. In more complex designs, two or more microchannels are connected by porous membranes, lined on opposite sides by different cell types, to recreate interfaces between different tissues (e.g., lung alveolar-capillary interface or BBB) (Bhatia and Ingber 2014). Similar analyses can be conducted with chips lined by cells from different organs that are linked fluidically, to mimic physiological interactions between different organs or to study drug distribution in vitro (Bhatia and Ingber 2014).

Differing form 3D static cultures, in this system, many cell parameters can be controlled, such as tissue barrier integrity (Douville et al. 2010), cell migration (Nguyen et al. 2013), and fluid pressure (Liu et al. 2013).

Organ-on-a-chip platforms are of great relevance to evaluate the potential hazards of nanoparticles for human health, as they have the advantage of using human cell lines—a more similar context to an in vivo environment. For example, there are several works testing the toxicity of nanoparticles in lung-on-a-chip. Since inhalation is a potential route of administration, it is fundamental to have a device that recreates the alveolar–blood barrier (Zhang et al. 2018).

In the same way, models to accurately predict transvascular permeation of nanoparticles to the brain are highly valuable. Kim et al. have probed nanoparticle translocation across the endothelium in a model that mimics the BBB (Kim et al. 2014).

Magnetic Nanoparticle Toxicity in 3D Culture

As mentioned before, 3D culture is a useful tool for the study of nanoparticle toxicity since it gives different information from monolayer cell culture. It has been reported that nanoparticle uptake and cell viability are significantly lower when cells are cultured in 3D.

In this subsection, we are going to describe methods found in the literature for the study of cell toxicity in multicellular spheroids, the most widely used model to asses nanotoxicity in 3D culture. Some of those methods will be briefly mentioned as they were fully described in the previous subsection.

1. *Nanoparticle uptake*

   1.1 *Prussian blue*: To verify whether magnetic nanoparticles are endocytosed, the Prussian blue (PB) method (Perls' acid ferrocyanide) can be employed to detect iron within the cell cultures. The PB method reduces ferric iron to the ferrous state with the formation of a blue precipitate (Neri et al. 2007). This method can be utilized both in 2D and in 3D culture. Wang et al. (2012) used PB to detect PLL-modified γ-Fe2O3 nanoparticles within glioblastoma spheres, and observed that the staining is preserved even when the spheres grow and cells become differentiated.

   1.2 *Confocal microscopy*: Magnetic nanoparticles can also be labeled with a dye and be tracked inside the spheroid. To achieve it, different cell structures (e.g., endosomes, nucleus) can be stained in order to study the subcellular localization of the NPs. In their work, Theumer et al. (2015) measured NP uptake in spheroids covering the magnetic core of coated SPION with a green lipophilic dye. Taking images in confocal microscopy in several z-stacks allowed them to calculate spatial location within the middle cross section of the spheroid (see Fig. 4).

   1.3 *Transmission electron microscopy*: Spheroids can be cryo-sectioned or fixed, inserted in resin and cut into ultrathin sections to observe them with
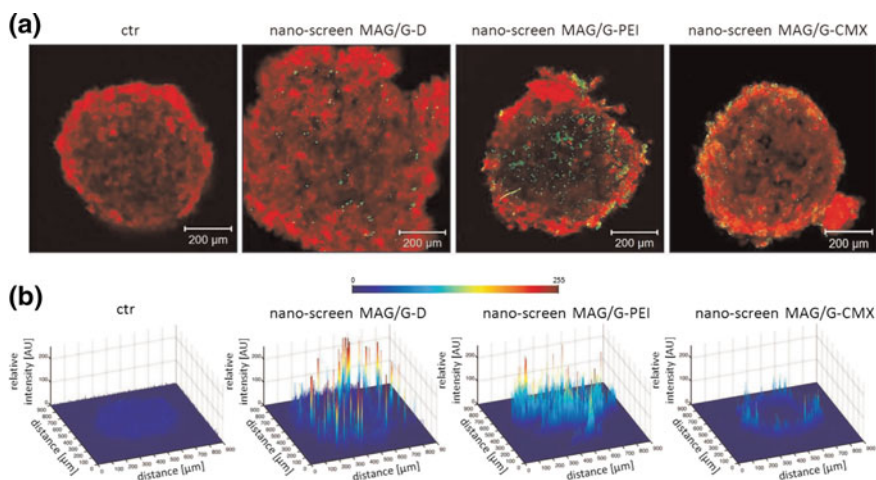
Fig. 4 Spatial nanoparticle distribution in human brain microvascular endothelial cell spheroids. Spheroids were treated with NPs with a core made of iron oxide and a shell of differently charged polymers (green) in a concentration of 25 mg/cm^2 for 3 h. F-actin of fixed and permeabilized cells was stained using Alexa Fluor 633 phalloidin (red). NP distribution was analyzed by confocal laser scanning microscopy. **a** 3D overlays of spheroids' z-stacks recorded at a magnification of 100. Scale bars indicate 200 μm. **b** Relative fluorescence intensity of labeled NP was plotted according to their spatial location within the middle cross section of the spheroid. Dark blue color indicates no fluorescence; red color indicates high fluorescence. Figure taken from Theumer et al. (2015). Reprinted with permission from Elsevier

TEM. Child et al. (2011) demonstrated by TEM that magnetic NPs penetrate spheroids following application of a magnetic field.

2. *Cytotoxicity assays*

Assessing NP toxicity on 3D-cultured cells is usually performed using common viability assays originally designed for drug studies in monolayers. Since most of them are fully described in the previous section, here we are going to make a brief account of the most utilized methods focusing on particularities of their application to 3D cultures.

2.1 *MTT and LDH*: The MTT assay measures the amount of enzymatically reduced MTT by viable cells. In the case of spheroids, due to their composition of proliferating, quiescent, and dead cells, a lower mitochondrial activity is measured compared to 2D culture when a similar number of cells are tested.

Lactate dehydrogenase (LDH) assay detects the amount of LDH that leaks out through the plasma membrane of damaged cells. This extracellular protein assay protocol is carried out identically in both 2D and spheroid cultures. In their work, Lee et al. (2009b) analyze nanoparticle cytotoxicity in spheroids utilizing this assay for gold nanoparticles toxicity testing.

2.2 *Acid phosphatase assay*: A modified acid phosphatase (APH) assay, which is based on quantification of cytosolic acid phosphatase activity, was validated for determining cell viability in spheroids. Intracellular acid phosphatases in viable cells hydrolyze *p*-nitrophenyl phosphate to *p*-nitrophenol. Its absorption at 405 nm is directly proportional to the cell number in the range of 10^3–10^5 monolayer cells. In the case of spheroids, they are centrifuged, supernatant is discarded, and the pellet is washed with PBS. Then, the assay performed similar to the one developed for monolayer cell culture. For a full description of the method adapted for spheroids, we refer the readers to Friedrich et al. (2009)

2.3 *Live/Dead staining*: This assay is based in staining cells with colored or fluorescent dyes that differentially label live and dead cells. For example, Wang et al. (2012) use PI and FDA double-staining protocol (Kristensen et al. 2003) to detect the cellular viability of the magnetically labeled glioblastoma spheres and their differentiated progenies, as well as to determine if cell death occurred after magnetic labeling. PI is a DNA-binding fluorescent dye that only enters dead or dying cells with damaged or leaky membranes. On the other hand, FDA, which stains cells with intact membranes, produces a bright green fluorescence. Cells then can be seen in a microscope or analyzed by flow cytometry.

Trypan blue stains dead cells since the colorant is not able to go through the membrane in viable cells. However, it is able to penetrate dead cells, in which the cell membrane is comprised. In their work, De Simone et al. (2018) utilize Trypan blue to asses cell toxicity in spheroids treated with iron oxide nanoparticles.

There are commercial kits used to test cell viability, as used by Theumer et al. (2015) They determined the ratio of living to dead cells with a kit based on two fluorescent dyes: calcein (excitation: 494 nm, emission: 517 nm) and ethidium homodimer-1 (excitation: 528 nm, emission: 617 nm) to establish the effects of iron oxide NP onto the viability of spheroids. Stocke et al. (2017) also used a commercial dye to evaluate the toxicity that magnetic hyperthermia induced by magnetic NPs exerted in breast cancer spheroids. This dye is a high-affinity nucleic acid stain that easily penetrates cells with compromised plasma membranes and can be excited with argon 406 lasers, making it a useful indicator of dead cells within a population.

Newer commercial kits specially designed for determining cell viability in 3D microtissue spheroids are also used. In their work, Zanoni et al. (2016) compare two of these commercial kits to common cell viability staining protocols. These kits allow the reagent to penetrate large spheroids and have increased lytic capacity for more accurate determination of viability.

2.4 *Spheroid morphology*: As spheroids can be cultured for long periods of time, morphological parameters are important factors linked to cell viability. For example, spheroid size is related to cell proliferation according to Gompertz law:

$$\ln\left(\ln\frac{V}{V0}\right) = \alpha t + \frac{V\max}{V0}$$

where V is a measure of spheroid size, V_0 the initial size, $V_{\max}$ the final size, and α is the cell proliferation rate (Helmlinger et al. 1997).

Variations in spheroid shape were also accompanied by changes in the dimension of the inner core and in the thickness of the surrounding shell that consists of proliferative, actively dividing cells. Zanoni et al. (2016) demonstrated by a luminescence metabolic assay that spherical spheroids showed a significantly reduced viability compared to irregular-shaped ones. This correlates with Mina Bissell's group work, in which an association between distinct morphologies and tumor cell invasiveness is demonstrated (Kenny et al. 2007).

To conclude, we consider of great importance taking into account the cell environment in magnetic nanoparticles toxicity testing. This will lead not only to produce more accurate results that can be more easily translated to the clinic, but also to diminish the number of animals in high-throughput screenings.

In Vivo Evaluation of Toxicity

Relevance of in Vivo Assays

In vitro assays for toxicity evaluation are limited due to incomplete consideration of the number of actors involved and the interactions between them. Among leading restrictions, we can highlight: (1) Only in limited cases, target cells are evaluated in the presence of cells from other origins, such as immune system cells. For example, nanoparticles (NP) uptake was found to be enhanced in cocultures of epithelial, macrophages and dendritic cells compared to monocultures (Rivera Gil et al. 2010); (2) the relevance of biological fluid hydrodynamics (e.g., blood, biliary, and lymphatic transport) is usually not contemplated. To overcome these limitations, cocultures that take into account spatial organization of tissues and heterogeneity of cell interactions (Costa et al. 2013; Müller et al. 2018), and microdevices that mimic vascular networks (Rosano et al. 2009; Prabhakarpandian et al. 2008) have been developed, but their degree of similarity to in vivo processes is controversial (Sayes et al. 2007). In the same line, some reactions that alter the toxic properties of NP can only occur inside a living organism. Metabolic processing of NP can alter their shape, coating, composition, size, and rugosity, which are properties relevant to their toxicity degree (Chouly et al. 1996). On the other hand, NP surfaces are subject to catalytic and oxidation reactions that can also modify their cytotoxicity (Nel et al. 2006b). Currently, toxicokinetic studies and unequivocal identification of NP target tissues can only be accomplished by using in vivo models (Sahu and Casciano 2009).

In this section, we do not intend to present an exhaustive list of the strategies used to perform toxicological short-term in vivo analysis but only to highlight contemporary procedures prevailing in the literature.

Animal Models to Test in Vivo Magnetic NP Toxicity

NP attempting to enter the biomedical field will have to go through animal preclinical trials almost exclusively, although a part of the scientific community is making big efforts to find novel human-specific approaches which could model human diseases with lower costs, higher predictive power, and absence of ethical concerns (Langley et al. 2015). Particularly in the magnetic NP (MNP) research area, rodent models such as mice and rats have been the most frequently selected to test in vivo toxicology, and therefore, methods to evaluate toxicity in them will be further detailed. Mice and rats are representative of the two types of mammalian spleens (mice have non-sinusoidal spleens, whereas rats, like humans, have sinusoidal spleens). Both have different microcirculatory pathways and distinct mechanisms of blood clearance (Adiseshaiah et al. 2010). Toxicity has been shown to be dependent on the species tested. Studies with the dextran-coated USPIO Ferumoxtran-10, proposed for MRI differentiation of metastatic lymph nodes and recently discontinued, demonstrated a clear difference in the kinetics of blood clearance among different animal species (Bourrinet et al. 2006). The plasma clearance was much faster in rats compared to monkeys, a difference that is probably accountable to alterations in RES organ distribution and activity across animal species.

In vivo toxicity of MNP has also been evaluated on zebrafish (*Danio rerio*), since the community working with this organism has proposed its use as an intermediate screening step between cell culture assays and studies in rodents (Caro et al. 2019). To evaluate toxicity, authors usually quantify the proportion of alive or dead larvae after a certain period of treatment, e.g., in a study where ferrite or manganese ferrite oxide MNP was used, and survival rate was evaluated (Caro et al. 2019). Moreover, the zebrafish's pattern of development is similar to higher vertebrates (Grunwald and Eisen 2002), making it a good model to study toxicity associated with alterations in embryogenesis. For instance, in one study, uncoated, flavin mononucleotide or guanosine monophosphate-coated USPIO was applied to fertilized eggs, and development of the zebrafish embryos was evaluated by optical microscopy up to 168 h post-fertilization (Rizzo et al. 2013).

With less frequency, other organisms like *Caenorhabditis elegans* (Gonzalez-Moragas 2017) and *Daphnia magna* (Kumar et al. 2017) have also been used.

Administration Routes and Fate of NP In Vivo

A comprehensive assessment of NP suitability for medical purposes should include the evaluation of its pharmacokinetics (PK). PK research includes the examination of absorption, distribution, metabolism, and excretion of a drug, which are characteristics that determine the appropriate duration and concentration for drug administration. Regarding absorption, NP can enter the organism through six principal routes: intravenous, dermal, subcutaneous, inhalation, intraperitoneal, and oral (Fischer and Chan 2007). Other ways of administration for specific purposes have been developed, like intratracheal instillation (NP administration via incision of trachea) and pharyngeal/laryngeal aspiration for research on pulmonary toxicity due to environmental hazards (Fadeel 2015). Depending on the administration route, different organs could suffer cytotoxicity. In one study in rats, intratracheally instilled ferric oxide NP produced acute lung injury due to accumulation in alveolar macrophages and epithelial cells (Zhu et al. 2008). Concerning MNP, intravenous injection is currently among the most studied routes, due to their interest in nanomedicine (Choi and Frangioni 2010); inhalation and intratracheal instillation have also been used (Sahu and Casciano 2009).

Once NP comes into biological fluids, they will interact with proteins, such as complement (Reddy et al. 2007) and immunoglobulins (Walkey and Chan 2012), during a process called opsonization (Moghimi et al. 2011). This novel structure, formed by the original nanoparticle covered by proteins termed corona, may influence subsequent interactions of the particles with biological systems and consequently affect their in vivo distribution and cytotoxicity (Liu et al. 2016; Lundqvist et al. 2008). It has been shown, for example, that bare or coated SPIONs can induce irreversible conformational changes in iron-saturated human transferrin, producing the release of iron (Mahmoudi et al. 2011). Although with limitations, among which enzymatically plasma inactivation and depletion of coagulation factors from serum outstand, different ex situ toxicity assays have been performed to emulate in vivo conditions considering NP opsonization (Walkey and Chan 2012). Most of them are based on isolated serum or plasma usage (Shi et al. 2012; Chonn et al. 1992).

In the distribution process, NPs can remain unaltered or suffer modifications (Borm et al. 2006). Researchers must carefully select the administration procedure to maximize targeting to selected organs since NP could encounter obstacles in the form of body barriers (skin, placenta, gastrointestinal epithelial barrier, blood-brain barrier), preventing them to freely distribute through all biological systems (Pietroiusti et al. 2013). To track MNP inside an alive or dead organism, the most frequent techniques are radiolabeling (Same et al. 2016), inductively coupled plasma mass spectrometry (ICP-MS) (Al Faraj et al. 2014), and magnetic resonance imaging (MRI) (Liu et al. 2010). Complementary, two other strategies have also been proposed: conjugation of NP with NIR fluorophores to be measured by near-infrared fluorescence (Lee 2010), though penetration depth is typically lower, and electron spin resonance spectroscopy (Chertok et al. 2010). Most of existing reports, heterogeneous in administration doses and selected time points for observation, focused

on describing the relationship between physicochemical properties of NP and their distribution. Although targeting and circulation half-life are highly dependent on the NP coating, size, and surface charge, the liver appears to be the major accumulation site via uptake by liver-resident macrophages termed Kupffer cells, followed by the spleen (Sahu and Casciano 2009). These two organs, together with lymph nodes and bone marrow, form the reticuloendothelial system (RES), outstanding for its large phagocytic monocytes and macrophages population. This is also the case for MNP, where studies conducted in rats showed that after SPIO-alginate intravenous injection, NP was eliminated rapidly from serum with a half-life of 0.27 h and accumulated dominantly in liver and spleen with a total percentage of more than 90% of dose (Ma et al. 2008). It has been suggested for iron oxide MNP (IONPs) that larger ones are more quickly taken up by the liver and spleen and have shorter circulation time in blood, whereas smaller have increased access to organs such as the lymph nodes and longer circulation time (Almeida et al. 2011). However, both are usually cleared from blood circulation relatively fast compared to other NP, normally within 36 h post-administration.

According to their properties and target tissues, NP could be metabolized in different ways, or not metabolized at all. In the case of superparamagnetic iron oxide nanostructures (SPIONs) for MRI contrast agents, they are shown to degrade (Briley-Saebo et al. 2004). Lysosomal degradation within Kupffer cells and transference to the spleen has been described as the metabolic pathway chosen by IONPs for their final breakdown (Levy et al. 2011).

Lastly, excretion routes also depend on the type and size of the NP. Among existing mechanism, elimination through exhalation, urination (via the kidneys), defecation (via the biliary duct), perspiration, salivation; and mammary and seminal fluids can be named (Sutariya and Pathak 2014). For MNP, renal (Bourrinet et al. 2006) and hepatobiliary system (Pham 2018) have been described as two important clearance pathways. Depending on their characteristics, excretion time can be quite long, a property not usually considered in the short-termed studies prevailing in the literature. This was the case of silica-coated magnetic nanoparticles containing rhodamine B isothiocyanate, which were still found in several organs of mice such as liver, lungs, kidney, and spleen 4 weeks after injection (Kim et al. 2006). It has been proposed that excretion time is particularly slow for IONPs because iron would be incorporated to the body's iron pool upon degradation of the iron oxide core, the reason for which MNPs are classified as biocompatibles (Almeida et al. 2011).

Methods for In Vivo Toxicity Evaluation

There are at least four parameters that need to be measured to determine biocompatibility of NP: cytotoxicity, hemocompatibility, immune response, and acute toxicity (Sutariya and Pathak 2014). Cytotoxicity and hemocompatibility (induction of red blood cells lysis and coagulation studies) are usually assessed in vitro or ex vivo. Host's immune response may be evaluated through immunohistochemistry

or enzyme-linked immunosorbent assay (ELISA). Acute toxicity can be determined by histological evaluation, protein tissue extraction, gene expression, and measurement of damage markers in plasma (see Fig. 5). It should be noticed that compared to the in vitro research area, there is a clear lack of in vivo studies characterizing NP genotoxic effects, and they are mainly restricted to rodents. Among the most frequent methods used are comet assay in liver, lung, colon, bone marrow; and micronucleus test in blood or bone marrow (Bourrinet et al. 2006). The protocols to perform these techniques do not substantially differ when in vivo or in vitro models are used and therefore will not be further described. Readers are referred to the previous section.

1. *Blood analysis*

   Blood is often used to determine the presence of markers related to damage. Depending on the organs expected to be affected, a wide variety of molecules can be analyzed. Jia and colleagues injected neuropilin-1-targeted exosomes containing SPIONs and curcumin in BALB/c nude mice carrying gliomas (Jia 2018). Toxicity was evaluated by measuring the level of markers of cardiac (creatine kinase MB isoenzyme), hepatic (aspartate aminotransferase), and renal (serum creatinine) damage in serum 15 days after the treatment. In another study, IONPs coated with PEG or PEI were injected intravenously, and aspartate aminotransferase, alanine aminotransferase, blood urea nitrogen, total bilirubin, and creatinine levels were quantified in blood 7 days post-administration to evaluate hepatic and renal function (Feng et al. 2018b). Most values were in the normal range except for alanine aminotransferase, which returned to normality 14 days post-injection.
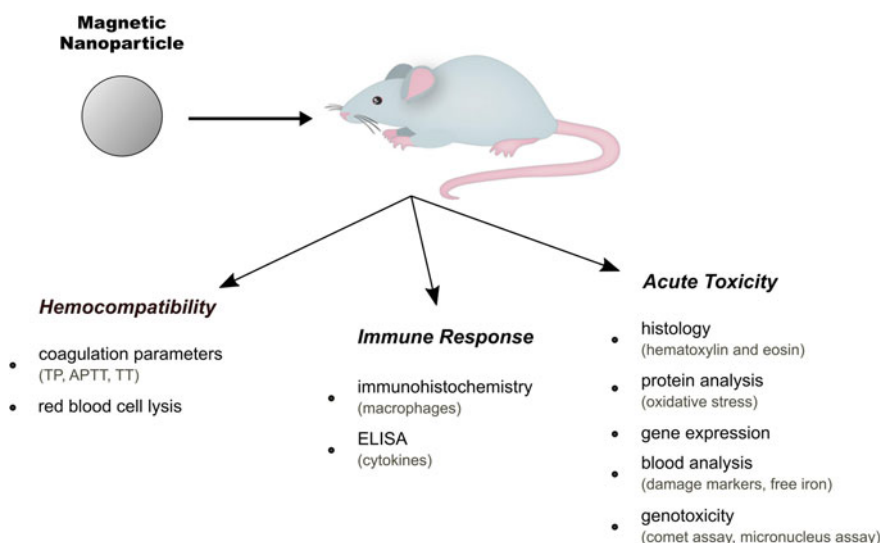

Fig. 5 Frequent assays and parameters evaluated when in vivo toxicity studies of nanoparticles are performed

Excessive tissue accumulation of free iron is known to cause toxicity (Weir et al. 1984; Barnham and Bush 2008). Quantification of iron in blood can be performed using ICP-MS. In one of these studies, iron concentration was measured 24 and 48 h following intravenous injection of citrate-stabilized IONPs in male athymic nude mice (Sharma et al. 2018). In this case, authors wanted to evaluate the effect of negatively (carboxymethyl dextran) or positively (PEG-PEI) coatings on biodistribution and concluded that nanoparticle clearance from blood circulation occurred within 24 h. On the contrary, in the study from Jain and colleagues, rats needed more than 3 weeks to recover normal content of iron in serum after oleic acid-Pluronic-coated IONP intravenous injection (Jain et al. 2008). In this case, a colorimetric method based on Fe(III) to Fe(II) reduction to measure iron content in serum was used. Once again, results appear to be highly dependent on NP physicochemical properties, biological model, and experimental design.

Plasma can also be separated from blood by centrifugation at 1500 g for 10 min to determine if coagulation parameters, typically prothrombin time, activated partial thromboplastin time, and fibrinogen, are affected (Zhu et al. 2008).

2. *Tissue analysis through histology and immunohistochemistry*

Histopathological examination has been used in tissue exposed to NP, such as lung, eyes, brain, liver, kidneys, heart, and spleen (Kumar et al. 2017). To perform this method, the animals are sacrificed after NP administration and organs are removed and fixed using 4% paraformaldehyde solution or 10% formalin. After dehydration by increasing alcohol concentration immersion, they are paraffin embedded and 4 µm thickness sectioned for hematoxylin and eosin (H&E) staining (Fischer et al. 2008) to visualize cellular morphology (see Fig. 6) or Prussian blue staining to detect ferric iron ions (Liu et al. 2010).

To perform H&E staining, the sections must be deparaffinized on a heating block followed by washing of xylene and rehydrated by immersing them successively for 5 min with agitation in xylene, 100% ethanol, and 70% ethanol, followed by 1 min in an appropriate buffer or water. Samples are then stained with a solution containing one or more cationic aluminum–hematein metal complex, subsequently termed hemalum. Hematein is generated by oxidation from hematoxylin, a colorless compound, and binds to chromatin conferring the characteristic blue color to cell nuclei. The nuclear staining is followed by counterstaining with an anionic solution of eosin Y dye, which colors eosinophilic structures in various shades of red, pink, and orange. Finally, samples are washed and dehydrated in 95 and 100% alcohol. Before visualization, alcohol can be extracted with xylene, and samples can be mounted. H&E staining is probably the most popular staining method used by pathologist in their daily work. However, important drawbacks of this technique include insufficient cytoplasmic differentiation and poor contrast between cytoplasmic and extracellular structures (Wittekind 2003).

Immunohistochemistry analysis can be also conducted to analyze colocalization of NP with immune system cells. If necessary, tissue must be deparaffinized. Positively charged slides must then be dehydrated in 100, 95, and 70% ethanol
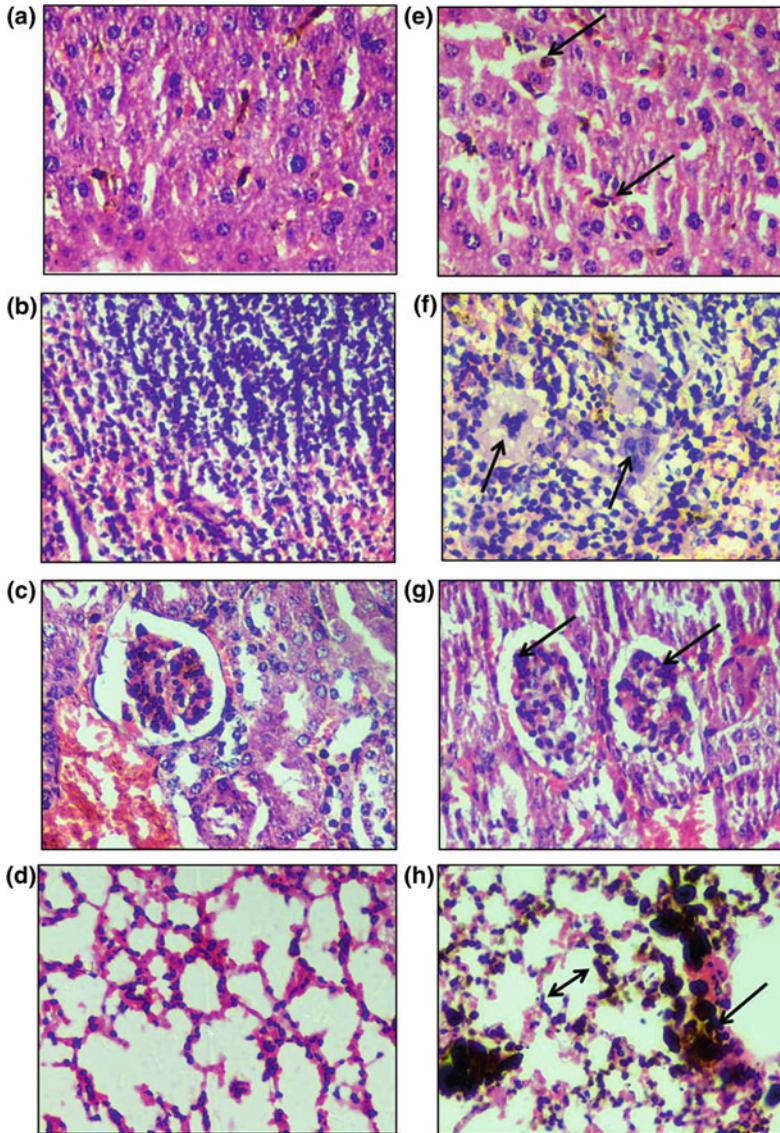
Fig. 6 Representative histological photomicrographs showing the untreated group of animals depicting normal liver (**a**), spleen (**b**), kidney (**c**), and lung (**d**). The pathology of the group of animals treated with PEGylated SPIONs at a dose of 500 mg/kg showing **e** section of the liver showing granular pigmentation in the kupffer cells (black arrow); **f** megakaryocyte hyperplasia in spleen (black arrow) and increased cellularity; **g** section of the kidney showing congestion in the glomerulus (black arrow); and **h** section of lung showing pigmentation in the alveolar sacks and widening of the interstitial walls (black arrow). Figure taken from Prabhu et al. (2015). Reprinted with permission of Springer Nature

followed by water. Then, heat-induced antigen retrieval must be performed, and samples must be incubated with an antibody targeting macrophages or monocytes (e.g., IBA-1, CD68, or F4/80 antibody). Finally, after incubation with secondary antibody, the slides must be developed with a peroxidase substrate, typically 3,3′-Diaminobenzidine (DAB). A counterstain with hematoxylin can also be carried out. Samples are visualized and photographed with bright-field microscopy.

Limitations of staining methods are associated with variation in results depending on fixatives, fixation temperature, and fixation time.

3. *Analysis of immune response through ELISA*

It is well established that organisms facing allergens may develop an anaphylactic reaction. Depending on the chemical nature of the molecule, hosts will produce antibodies or inflammatory responses. Studies in animals showed that immune responses can have phenotypical and behavioral manifestations, such as a hunched position, piloerection, slowing of movement, bronchospasm, respiratory arrest, and anaphylaxis (Gamboa and Leong 2013). Several parameters, like antibody titers and cytokine release, can also be measured in blood by ELISA (Chen et al. 2010). There are multiple ways to perform ELISA assays but all are based on the use of an enzyme bound to an immune reactant to specifically recognize a desired molecule (Schuurs and Van Weemen 1980). In the simplest strategy, named direct ELISA, the protein sample binds to the plate through absorption and an enzyme-conjugated antibody is added to detect the expected antigen by spectrophotometry. Another way to perform this method, termed sandwich ELISA, involves coating the plates with the antibodies to measure the amount of a specific antigen in the plasma (Wottrich et al. 2004). After sample addition, a secondary antibody is used to detect the captured molecule, and then a third enzyme-conjugated immunoglobulin is used to perform quantification. This is the case when cytokines, proteins that regulate function of immune cells and increase in response to inflammation, are measured. Typically detected proteins include IL1β, IL-8, tumor necrosis factor-a (TNF-a), and IL-6 (Wang et al. 2015).

Among common difficulties outstand false positives by inefficient blocking and inhibition of detection by non-specific serum factors.

4. *Detection of upregulation of stress-related molecules through microarrays*

Analysis of gene expression inside a tissue is one of the most sensitive methods for detecting molecules associated with cellular damage. This is done by lysing tissue samples, obtaining and purifying RNA, and performing PCR or microarrays. Microarrays consist of an arranged series of thousands of microscopic spots of oligonucleotides, each containing picomoles of a specific sequence used as a probe to assay. Through hybridization under high-stringency conditions, the presence of a complementary sequence in the sample can be measured (Sahu and Casciano 2009). Hybridization is usually detected and quantified by fluorescence-based detection of a fluorophore-labeled target to determine the relative abundance of each sequence in the sample. In one of these studies, Teeguarden and colleagues used a microarray to evaluate transcriptional regulation of inflammation markers in BALB/c mice exposed to SPIO by inhalation (Teeguarden et al.

2014). They found that NP led to an inflammatory response in the alveolar region characterized by interstitial inflammation, macrophage infiltration, and increased expression of CXCL2 and CCL3.

Microarrays have proven especially useful when expression of large number of genes needs to be analyzed at the same time, but results of special interest must be validated by real-time PCR. It should also be taken into consideration that variation in transcripts abundance will not necessarily have a direct translation into protein levels due to diverse mechanisms of regulation. Therefore, microarrays must be complemented with techniques measuring toxicity at protein level.

5. *Measurement of protein related to damage in target tissues*

Oxidative stress caused by MNP is considered to be one of the most important mechanisms of toxicity. This could be due to induction of reactive oxygen species and reactive nitrogen species, which react with biological molecules causing DNA damage, protein oxidation, lipids peroxidation, and impairing redox internal balance (Khanna et al. 2015). If repair mechanism cannot compensate, the final outcome for the cell will be necrosis or apoptosis. ROS-associated damage protein analysis can be done by sacrificing the animal, removing the organ of interest, and homogenizing the tissue to obtain proteins whose concentration or activity could be determined by different techniques. The classical procedure to identify and determine relative amounts of proteins, Western blotting, is not the first choice when tissue extracts must be analyzed, probably due to difficulties that antibody recognition has in complex samples. Rather, enzymatic reactions, usually coupled to colorimetric assays, are selected. This is the case for total glutathione, reduced glutathione, and oxidized disulfide, as well for activity of glutathione peroxidase, superoxide dismutase, and nitric oxide synthase (Zhu et al. 2008; Wang et al. 2009).

Conclusion and Future Perspectives

Research area on MNP has spread due to their attractiveness as theragnostic agents. They are generally associated with low toxicity and present high potential use for biomedical applications.

Although many reports evaluating in vivo toxicity of MNP can be found, there is still much to be standardized regarding proper routes and doses of administration, methodologies to follow, and relevant tissues to analyzed. Also, the temporal window in which toxicity should be examined in each metabolic step has not been clearly established, and a systematic approach to address these issues is missing. One of the reasons that interfere with reaching a common criterion regarding lines of action is that NPs are usually tailor-made. Consequently, studies differ in NP composition, chemical properties and biological models assayed, hindering comparisons. Another factor obscuring the possibility of drawing firm conclusions is that not all MNPs under the same name are identical; formulations can vary in purity, reactivity, surface

chemistry, and porosity. In this context, a common agreement regarding essential techniques for MNP characterization is urgently needed.

References

Abakumov MA et al (2018) Toxicity of iron oxide nanoparticles: size and coating effects. J Biochem Mol Toxicol 32:e22225

Adiseshaiah PP, Hall JB, McNeil SE (2010) Nanomaterial standards for efficacy and toxicity assessment. Wiley Interdiscip Rev Nanomed Nanobiotechnol 2:99–112

Aggarwal P, Hall JB, McLeland CB, Dobrovolskaia MA, McNeil SE (2009) Nanoparticle interaction with plasma proteins as it relates to particle biodistribution, biocompatibility and therapeutic efficacy. Adv Drug Deliv Rev 61:428–437

Ahamed M et al (2008) DNA damage response to different surface chemistry of silver nanoparticles in mammalian cells. Toxicol Appl Pharmacol 233:404–410

Ahamed M et al (2013) Iron oxide nanoparticle-induced oxidative stress and genotoxicity in human skin epithelial and lung epithelial cell lines. Curr Pharm Des 19:6681–6690

Al Faraj A, Shaik AP, Shaik AS (2014) Effect of surface coating on the biocompatibility and in vivo MRI detection of iron oxide nanoparticles after intrapulmonary administration. Nanotoxicology 5390:1–10

Alarifi S, Ali D, Alkahtani S, Alhader MS (2014) Iron oxide nanoparticles induce oxidative stress, DNA damage, and caspase activation in the human breast cancer cell line. Biol Trace Elem Res 159:416–424

Alberts B et al (2015) Molecular biology of the cell. Garland Sciense

Ali S, Rytting E (2014) Influences of nanomaterials on the barrier function of epithelial cells. In: Advances in experimental medicine and biology, vol 811, pp 45–54

Alivisatos AP (1996) Semiconductor clusters, nanocrystals, and quantum dots. Science (80–.) 271:933–937

Almeida JPM, Chen AL, Foster A, Drezek R (2011) Vivo biodistribution of nanoparticles. Nanomedicine 6:815–835

Amstad E, Textor M, Reimhult E (2011) Stabilization and functionalization of iron oxide nanoparticles for biomedical applications. Nanoscale 3:2819

Arami H, Khandhar A, Liggitt D, Krishnan KM (2015) In vivo delivery, pharmacokinetics, biodistribution and toxicity of iron oxide nanoparticles. Chem Soc Rev 44:8576–8607

Aranda A et al (2013) Dichloro-dihydro-fluorescein diacetate (DCFH-DA) assay: a quantitative method for oxidative stress assessment of nanoparticle-treated cells. Toxicol Vitr 27:954–963

Arbab AS et al (2003) Characterization of biophysical and metabolic properties of cells labeled with superparamagnetic iron oxide nanoparticles and transfection agent for cellular MR imaging. Radiology 229:838–846

Auffan M et al (2006) In vitro interactions between DMSA-coated maghemite nanoparticles and human fibroblasts: a physicochemical and cyto-genotoxical study. Environ Sci Technol 40:4367–4373

Auffan M et al (2009) Towards a definition of inorganic nanoparticles from an environmental, health and safety perspective. Nat Nanotechnol 4:634–641

Azqueta A, Arbillaga L, López de Cerain A (2015) Genotoxicity of nanoparticles. In: Sutariya Y, Pathak Y (eds) Biointeractions of nanomaterials. CRC Press, pp 353–363

Banerjee R et al (2010) Nanomedicine: magnetic nanoparticles and their biomedical applications. Curr Med Chem 17:3120–3141

Barick KC et al (2009) Novel and efficient MR active aqueous colloidal Fe_3O_4 nanoassemblies. J Mater Chem 19:7023

Barltrop JA, Owen TC, Cory AH, Cory JG (1991) 5-(3-carboxymethoxyphenyl)-2-(4,5-dimethylthiazolyl)-3-(4-sulfophenyl)tetrazolium, inner salt (MTS) and related analogs of 3-(4,5-dimethylthiazolyl)-2,5-diphenyltetrazolium bromide (MTT) reducing to purple water-soluble formazans As cell-viability indicators. Bioorg Med Chem Lett 1:611–614

Barnham KJ, Bush AI (2008) Metals in Alzheimer's and Parkinson's diseases. Curr Opin Chem Biol 12:222–228

Barry SE (2008) Challenges in the development of magnetic particles for therapeutic applications. Int J Hyperth 24:451–466

Beddoes CM, Case CP, Briscoe WH (2015) Understanding nanoparticle cellular entry: a physico-chemical perspective. Adv Colloid Interface Sci 218:48–68

Bell G et al (2019) Functionalised iron oxide nanoparticles for multimodal optoacoustic and magnetic resonance imaging. J Mater Chem B7:2212–2219

Benigni R, Bossa C (2011) Mechanisms of chemical carcinogenicity and mutagenicity: a review with implications for predictive toxicology. Chem Rev 111:2507–2536

Bernas T, Dobrucki J (2002) Mitochondrial and nonmitochondrial reduction of MTT: interaction of MTT with TMRE, JC-1, and NAO mitochondrial fluorescent probes. Cytometry 47:236–242

Berridge MV, Tan AS, McCoy KD, Wang RUI (1996) The biochemical and cellular basis of cell proliferation assays that use tetrazolium salts. Biochemica 4:14–19

Berridge MV, Herst PM, Tan AS (2005) Tetrazolium dyes as tools in cell biology: new insights into their cellular reduction. Biotechnol Annu Rev 11:127–152

Bhabra G et al (2009) Nanoparticles can cause DNA damage across a cellular barrier. Nat Nanotechnol 4:876–883

Bhatia SN, Ingber DE (2014) Microfluidic organs-on-chips. Nat Biotechnol. https://doi.org/10.1038/nbt.2989

Bhattacharya K et al (2012) Comparison of micro- and nanoscale Fe^{+3}–containing (hematite) particles for their toxicological properties in human lung cells in vitro. Toxicol Sci 126:173–182

Biehl P et al (2018) Synthesis, characterization, and applications of magnetic nanoparticles featuring polyzwitterionic coatings. Polymers 10:91

Blanco E, Shen H, Ferrari M (2015) Principles of nanoparticle design for overcoming biological barriers to drug delivery. Nat Biotechnol. https://doi.org/10.1038/nbt.3330

Bolognesi C, Fenech M (2013) Micronucleus assay in human cells: lymphocytes and buccal cells. In: Dhawan A, Bajpayee M (2013) Genotoxicity assessment: methods and protocols. Springer Science+Business Media, pp 191–208

Bonvin D, Bastiaansen JAM, Stuber M, Hofmann H, Mionić Ebersold M (2017) Folic acid on iron oxide nanoparticles: platform with high potential for simultaneous targeting, MRI detection and hyperthermia treatment of lymph node metastases of prostate cancer. Dalton Trans 46:12692–12704

Borenfreund E, Babich H, Martin-Alguacil N (1988) Comparisons of two in vitro cytotoxicity assays—the neutral red (NR) and tetrazolium MTT tests. Toxicol Vitr 2:1–6

Borm P et al (2006) Research strategies for safety evaluation of nanomaterials, Part V: role of dissolution in biological fate and effects of nanoscale particles. Toxicol Sci. https://doi.org/10.1093/toxsci/kfj084

Bouhifd M et al (2012) Automation of an in vitro cytotoxicity assay used to estimate starting doses in acute oral systemic toxicity tests. Food Chem Toxicol 50:2084–2096

Bourrinet P et al (2006) Preclinical safety and pharmacokinetic profile of ferumoxtran-10, an ultrasmall superparamagnetic iron oxide magnetic resonance contrast agent. Invest Radiol 41:313–324

Boverhof DR et al (2015) Comparative assessment of nanomaterial definitions and safety evaluation considerations. Regul Toxicol Pharmacol 73:137–150

Boyer C et al (2010) Anti-fouling magnetic nanoparticles for siRNA delivery. J Mater Chem 20:255–265

Bresgen N, Eckl P, Bresgen N, Eckl PM (2015) Oxidative stress and the homeodynamics of iron metabolism. Biomolecules 5:808–847

Briley-Saebo K et al (2004) Hepatic cellular distribution and degradation of iron oxide nanoparticles following single intravenous injection in rats: implications for magnetic resonance imaging. Cell Tissue Res 316:315–323

Buliaková B et al (2017) Surface-modified magnetite nanoparticles act as aneugen-like spindle poison. Nanomed Nanotechnol Biol Med 13:69–80\

Busquets M et al (2015a) Magnetic nanoparticles cross the blood-brain barrier: when physics rises to a challenge. Nanomaterials 5:2231–2248

Busquets M, Espargaró A, Sabaté R, Estelrich J (2015b) Magnetic nanoparticles cross the blood-brain barrier: when physics rises to a challenge. Nanomaterials. https://doi.org/10.3390/nano5042231

Buzea C, Pacheco II, Robbie K (2007) Nanomaterials and nanoparticles: sources and toxicity. Biointerphases 2:MR17–MR71

Cai H et al (2013) Facile hydrothermal synthesis and surface functionalization of polyethyleneimine-coated iron oxide nanoparticles for biomedical applications. ACS Appl Mater Interfaces 5:1722–1731

Candeias LP et al (1998) The catalysed NADH reduction of resazurin to resorufin. J Chem Soc Perkin Trans 20:2333–2334

Caro C et al (2019) Comprehensive toxicity assessment of PEGylated magnetic nanoparticles for in vivo applications. Colloids Surf B Biointerfaces. https://doi.org/10.1016/j.colsurfb.2019.01.051

Chen J et al (2009a) Cationic nanoparticles induce nanoscale disruption in living cell plasma membranes. J Phys Chem B 113:11179–11185

Chen Y-S, Hung Y-C, Liau I, Huang GS (2009b) Assessment of the in vivo toxicity of gold nanoparticles. Nanoscale Res Lett 4:858–864

Chen BA et al (2010) The effect of magnetic nanoparticles of Fe_3O_4 on immune function in normal ICR mice. Int J Nanomed 5:593–599

Chertok B, Cole AJ, David AE, Yang VC (2010) Comparison of electron spin resonance spectroscopy and inductively-coupled plasma optical emission spectroscopy for biodistribution analysis of iron-oxide nanoparticles. Mol Pharm 7:375–385

Child HW et al (2011) Working together: the combined application of a magnetic field and penetratin for the delivery of magnetic nanoparticles to cells in 3D. ACS Nano. https://doi.org/10.1021/nn202163v

Choi HS, Frangioni JV (2010) Nanoparticles for biomedical imaging: fundamentals of clinical translation. Mol Imaging 9:291–310

Choi HS et al (2007) Renal clearance of quantum dots. Nat Biotechnol 25:1165–1170

Choi S-J, Oh J-M, Choy J-H (2009) Toxicological effects of inorganic nanoparticles on human lung cancer A549 cells. J Inorg Biochem 103:463–471

Chonn A, Semple SC, Cullis PR (1992) Association of blood proteins with large unilamellar liposomes in vivo: relation to circulation lifetimes. J Biol Chem

Chouly C, Pouliquen D, Lucet I, Jeune JJ, Jallet P (1996) Development of superparamagnetic nanoparticles for MRI: effect of particle size, charge and surface nature on biodistribution. J Microencapsul 13:245–255

Chow A, Brown BD, Merad M (2011) Studying the mononuclear phagocyte system in the molecular age. Nat Rev Immunol 11:788–798

Chu M et al (2013) Near-infrared laser light mediated cancer therapy by photothermal effect of Fe_3O_4 magnetic nanoparticles. Biomaterials 34:4078–4088

Contini C, Schneemilch M, Gaisford S, Quirke N (2018) Nanoparticle–membrane interactions. J Exp Nanosci 13:62–81

Corbo C et al (2016) The impact of nanoparticle protein corona on cytotoxicity, immunotoxicity and target drug delivery. Nanomedicine 11:81–100

Cory AH, Owen TC, Barltrop JA, Cory JG (1991) Use of an aqueous soluble tetrazolium/formazan assay for cell growth assays in culture. Cancer Commun 3:207–212

Costa C et al (2015) In vitro cytotoxicity of superparamagnetic iron oxide nanoparticles on neuronal and glial cells. Evaluation of nanoparticle interference with viability tests. J Appl Toxicol 36:361–372

Costa EC, Gaspar VM, Marques JG, Coutinho P, Correia IJ (2013) Evaluation of nanoparticle uptake in co-culture cancer models. PLoS One 8:1–13

Countryman PI, Heddle JA (1976) The production of micronuclei from chromosome aberrations in irradiated cultures of human lymphocytes. Mutat Res 41

Cowie H et al (2015) Suitability of human and mammalian cells of different origin for the assessment of genotoxicity of metal and polymeric engineered nanoparticles. Nanotoxicology 9:57–65

Crisponi G et al (2017) Toxicity of nanoparticles: etiology and mechanisms. Antimicrob Nanoarchitectonics 511–546. https://doi.org/10.1016/b978-0-323-52733-0.00018-5

Czekanska EM (2011) Assessment of cell proliferation with resazurin-based fluorescent dye. In: Stoddart MJ (ed) Mammalian cell viability: methods and protocols. Methods in molecular biology, vol 740. Humana Press, pp 27–32. https://doi.org/10.1007/978-1-61779-108-6_5

Davies LC, Jenkins SJ, Allen JE, Taylor PR (2013) Tissue-resident macrophages. Nat Immunol 14:986–995

de Lima R et al (2013) Iron oxide nanoparticles show no toxicity in the comet assay in lymphocytes: a promising vehicle as a nitric oxide releasing nanocarrier in biomedical applications. J Phys Conf Ser 429:012021

De Matteis V (2017) Exposure to inorganic nanoparticles: routes of entry, immune response, biodistribution and in vitro/in vivo toxicity evaluation. Toxics 5

De Simone U et al (2018) Human 3D cultures as models for evaluating magnetic nanoparticle CNS cytotoxicity after short- and repeated long-term exposure. Int J Mol Sci 19

Debnath J, Muthuswamy SK, Brugge JS (2003) Morphogenesis and oncogenesis of MCF-10A mammary epithelial acini grown in three-dimensional basement membrane cultures. Methods. https://doi.org/10.1016/S1046-2023(03)00032-X

Decker T, Lohmann-Matthes M-L (1988) A quick and simple method for the quantitation of lactate dehydrogenase release in measurements of cellular cytotoxicity and tumor necrosis factor (TNF) activity. J Immunol Methods 115:61–69

Deng ZJ, Liang M, Monteiro M, Toth I, Minchin RF (2011) Nanoparticle-induced unfolding of fibrinogen promotes Mac-1 receptor activation and inflammation. Nat Nanotechnol 6:39–44

Dhawan A, Bajpayee M (eds) (2013) Genotoxicity assessment: methods and protocols. Methods in molecular biology, vol 1044. Humana Press

Doak SH et al (2009) Confounding experimental considerations in nanogenotoxicology. Mutagenesis 24:285–293

Doak SH, Liu Y, Chen C (2017) Genotoxicity and cancer. In: Fadeel B, Pietroiusti A, Shvedova AA (eds) Adverse effects of engineered nanomaterials: exposure, toxicology, and impact on human health, 2nd edn. Academic Press, pp 423–445. https://doi.org/10.1016/b978-0-12-809199-9.00018-5

Dobson J (2006) Magnetic micro- and nano-particle-based targeting for drug and gene delivery. Nanomedicine 1:31–37

Donaldson K, Poland CA (2013) Nanotoxicity: challenging the myth of nano-specific toxicity. Curr Opin Biotechnol 24:724–734

Douville NJ et al (2010) Fabrication of two-layered channel system with embedded electrodes to measure resistance across epithelial and endothelial barriers. Anal Chem. https://doi.org/10.1021/ac9029345

Eastmond DA, Pinkel D (1990) Detection of aneuploidy and aneuploidy-inducing agents in human lymphocytes using fluorescence in situ hybridization with chromosome-specific DNA probes. Mutat Res Mutagen Relat Subj 234:303–318

Elder A et al (2006) Translocation of inhaled ultrafine manganese oxide particles to the central nervous system. Environ Health Perspect 114:1172–1178

Evans SJ et al (2019) In vitro detection of in vitro secondary mechanisms of genotoxicity induced by engineered nanomaterials. Part Fibre Toxicol 16:1–14

Fadeel B (2015) Handbook of safety assessment of nanomaterials: from toxicological testing to personalized medicine. Pan Standford series on biomedical nanotechnology. doi:10.1017/CBO9781107415324.004

Fairbairn DW, Olive PL, O'Neill KL (1995) The comet assay: a comprehensive review. Mutat Res Genet Toxicol 339:37–59

Fang K et al (2016) Magnetofection based on superparamagnetic iron oxide nanoparticle-mediated low lncRNA HOTAIR expression decreases the proliferation and invasion of glioma stem cells. Int J Oncol 49:509–518

Fenech M (2000) The in vitro micronucleus technique. Mutat Res Mol Mech Mutagen 455:81–95

Fenech M, Morley AA (1985) Measurement of micronuclei in lymphocytes. Mutat Res Mutagen Relat Subj 147:29–36

Feng Q et al (2018a) Uptake, distribution, clearance, and toxicity of iron oxide nanoparticles with different sizes and coatings. Sci Rep 8:2082

Feng Q et al (2018b) Uptake, distribution, clearance, and toxicity of iron oxide nanoparticles with different sizes and coatings. Sci Rep 8:1–13

Fernández-Bertólez N et al (2018a) Neurotoxicity assessment of oleic acid-coated iron oxide nanoparticles in SH-SY5Y cells. Toxicology 406–407:81–91

Fernández-Bertólez N et al (2018b) Assessment of oxidative damage induced by iron oxide nanoparticles on different nervous system cells. Mutat Res Toxicol Environ Mutagen. https://doi.org/10.1016/J.MRGENTOX.2018.11.013

Fernández-Bertólez N et al (2018c) Toxicological assessment of silica-coated iron oxide nanoparticles in human astrocytes. Food Chem Toxicol 118:13–23

Fischer HC, Chan WC (2007) Nanotoxicity: the growing need for in vivo study. Curr Opin Biotechnol 18:565–571

Fischer D, Li Y, Ahlemeyer B, Krieglstein J, Kissel T (2003) In vitro cytotoxicity testing of polycations: influence of polymer structure on cell viability and hemolysis. Biomaterials 24:1121–1131

Fischer AH, Jacobson KA, Rose J, Zeller R (2008) Hematoxylin and eosin staining of tissueand cell sections. Cold Spring Harb Protoc 3:4986–4988

Foroozandeh P, Aziz AA (2018) Insight into cellular uptake and intracellular trafficking of nanoparticles. Nanoscale Res Lett 13:339

Friedrich J et al (2007) A reliable tool to determine cell viability in complex 3-D culture: the acid phosphatase assay. J Biomol Screen. https://doi.org/10.1177/1087057107306839

Friedrich J, Seidel C, Ebner R, Kunz-Schughart LA (2009) Spheroid-based drug screen: considerations and practical approach. Nat Protoc. https://doi.org/10.1038/nprot.2008.226

Fu X, Wang X, Zhou S, Zhang Y (2017) IONP-doped nanoparticles for highly effective NIR-controlled drug release and combination tumor therapy. Int J Nanomed 12:3751–3766

Fubini B, Ghiazza M, Fenoglio I (2010) Physico-chemical features of engineered nanoparticles relevant to their toxicity. Nanotoxicology 4:347–363

Gaharwar US, Meena R, Rajamani P (2017) Iron oxide nanoparticles induced cytotoxicity, oxidative stress and DNA damage in lymphocytes. J Appl Toxicol 37:1232–1244

Gamboa JM, Leong KW (2013) In vitro and in vivo models for the study of oral delivery of nanoparticles. Adv Drug Deliv Rev. https://doi.org/10.1016/j.addr.2013.01.003

Gangopadhyay S et al (1992) Magnetic properties of ultrafine iron particles. Phys Rev B 45:9778–9787

Garnett MC, Kallinteri P (2006) Nanomedicines and nanotoxicology: some physiological principles. Occup Med (Chic Ill) 56:307–311

Gilbert DF, Friedrich O (2017) Cell viability assays: methods and protocols. Methods in molecular biology, vol 1601. Humana Press

Gojova A et al (2007) Induction of inflammation in vascular endothelial cells by metal oxide nanoparticles: effect of particle composition. Environ Health Perspect 115:403–409

Gonzalez RJ, Tarloff JB (2001) Evaluation of hepatic subcellular fractions for Alamar blue and MTT reductase activity. Toxicol Vitr 15:257–259

Gonzalez L, Sanderson BJS, Kirsch-Volders M (2011) Adaptations of the in vitro MN assay for the genotoxicity assessment of nanomaterials. Mutagenesis 26:185–191

Gonzalez-Moragas L et al (2017) Toxicogenomics of iron oxide nanoparticles in the nematode *C. elegans*. *Nanotoxicology* 11:647–657

Goodman TT, Olive PL, Pun SH (2007) Increased nanoparticle penetration in collagenase-treated multicellular spheroids. Int J Nanomed

Goodman TT, Chee PN, Suzie HP (2008) 3-D tissue culture systems for the evaluation and optimization of nanoparticle-based drug carriers. Bioconjugate Chem. https://doi.org/10.1021/bc800233a

Gordon S, Martinez-Pomares L (2017) Physiological roles of macrophages. Pflugers Arch 469:365–374

Granot D, Shapiro EM (2011) Release activation of iron oxide nanoparticles: (REACTION) a novel environmentally sensitive MRI paradigm. Magn Reson Med 65:1253–1259

Gratton SEA et al (2008) The effect of particle design on cellular internalization pathways. Proc Natl Acad Sci 105:11613–11618

Graziano MJ, Jacobson-Kram D (2015) Genotoxicity and carcinogenicity testing of pharmaceuticals. Springer International Publishing

Gref R et al (1994) Biodegradable long-circulating polymeric nanospheres. Science 263:1600–1603

Greish K (2010) Enhanced permeability and retention (EPR) effect for anticancer nanomedicine drug targeting. In: Methods molecular biology, vol 624, pp 25–37

Grunwald DJ, Eisen JS (2002) Headwaters of the zebrafish—emergence of a new model vertebrate. Nat Rev Genet 3:711–717

Guarnieri D et al (2014) Transport across the cell-membrane dictates nanoparticle fate and toxicity: a new paradigm in nanotoxicology. Nanoscale 6:10264–10273

Guo S, Huang L (2011) Nanoparticles escaping RES and endosome: challenges for siRNA delivery for cancer therapy. J Nanomater 2011:1–12

Guo C, Sun L, Chen X, Zhang D (2013) Oxidative stress, mitochondrial damage and neurodegenerative diseases. Neural Regen Res 8:2003–2014

Guo Y, Wang W, Peng L, Zhang P (2015) Transferrin-conjugated doxorubicin-loaded lipid-coated nanoparticles for the targeting and therapy of lung cancer. Oncol Lett 9:1065–1072

Gustafson HH, Holt-Casper D, Grainger DW, Ghandehari H (2015) Nanoparticle uptake: the phagocyte problem. Nano Today 10:487–510

Halamoda Kenzaoui B, Chapuis Bernasconi C, Guney-Ayra S, Juillerat-Jeanneret L (2012) Induction of oxidative stress, lysosome activation and autophagy by nanoparticles in human brain-derived endothelial cells. Biochem J 441:813–821

Hamid R, Rotshteyn Y, Rabadi L, Parikh R, Bullock P (2004) Comparison of alamar blue and MTT assays for high through-put screening. Toxicol Vitr 18:703–710

Han D-W et al (2011) Subtle cytotoxicity and genotoxicity differences in superparamagnetic iron oxide nanoparticles coated with various functional groups. Int J Nanomed 6:3219

Hanot CC, Choi YS, Anani TB, Soundarrajan D, David AE (2015) Effects of iron-oxide nanoparticle surface chemistry on uptake kinetics and cytotoxicity in CHO-K1 cells. Int J Mol Sci 17

Harris G et al (2015) Iron oxide nanoparticle toxicity testing using high-throughput analysis and high-content imaging. Nanotoxicology 9:87–94

Haselsberger K, Peterson DC, Thomas DG, Darling JL (1996) Assay of anticancer drugs in tissue culture: comparison of a tetrazolium-based assay and a protein binding dye assay in short-term cultures derived from human malignant glioma. Anticancer Drugs 7:331–338

Heldin CH, Rubin K, Pietras K, Östman A (2004) High interstitial fluid pressure—an obstacle in cancer therapy. Nat Rev Cancer. https://doi.org/10.1038/nrc1456

Helmlinger G, Netti PA, Lichtenbeld HC, Melder RJ, Jain RK (1997) Solid stress inhibits the growth of multicellular tumor spheroids. Nat Biotechnol. https://doi.org/10.1038/nbt0897-778

Hirayama D, Iida T, Nakase H (2017) The phagocytic function of macrophage-enforcing innate immunity and tissue homeostasis. Int J Mol Sci 19

Hirsch V et al (2013) Surface charge of polymer coated SPIONs influences the serum protein adsorption, colloidal stability and subsequent cell interaction in vitro. Nanoscale 5:3723

Hong S et al (2004) Interaction of poly(amidoamine) dendrimers with supported lipid bilayers and cells: hole formation and the relation to transport. Bioconjug Chem 15:774–782

Hong S et al (2006) Interaction of polycationic polymers with supported lipid bilayers and cells: nanoscale hole formation and enhanced membrane permeability. Bioconjug Chem 17:728–734

Horváth S (1980) Cytotoxicity of drugs and diverse chemical agents to cell cultures. Toxicology 16:59–66

Hsiao J-K et al (2008) Macrophage physiological function after superparamagnetic iron oxide labeling. NMR Biomed 21:820–829

Huang Y-W, Wu C, Aronstam RS (2010) Toxicity of transition metal oxide nanoparticles: recent insights from in vitro studies. Materials 3:4842–4859

Huang X et al (2011a) The shape effect of mesoporous silica nanoparticles on biodistribution, clearance, and biocompatibility in vivo. ACS Nano 5:5390–5399

Huang H-C, Barua S, Sharma G, Dey SK, Rege K (2011b) Inorganic nanoparticles for cancer imaging and therapy. J Control Release 155:344–357

Huang Y, Mao K, Zhang B, Zhao Y (2017) Superparamagnetic iron oxide nanoparticles conjugated with folic acid for dual target-specific drug delivery and MRI in cancer theranostics. Mater Sci Eng C 70:763–771

Hume DA (2006) The mononuclear phagocyte system. Curr Opin Immunol 18:49–53

Hume DA, Irvine KM, Pridans C (2019) The mononuclear phagocyte system: the relationship between monocytes and macrophages. Trends Immunol 40:98–112

Huth S et al (2004) Insights into the mechanism of magnetofection using PEI-based magnetofectins for gene transfer. J Gene Med 6:923–936

Inglese J (2010) A practical guide to assay development and high-throughput screening in drug discovery. CRC Press

Ishiyama M, Shiga M, Sasamoto K, Mizoguchi M, He PG (1993) A new sulfonated tetrazolium salt that produces a highly water-soluble formazan dye. Chem Pharm Bull 41:1118–1122

ISO/TS 80004-1 (2015(en)) Nanotechnologies—vocabulary—Part 1: Core terms. Available at: https://www.iso.org/obp/ui/#iso:std:iso:ts:80004:-1:ed-2:v1:en. Accessed: 29 Mar 2019

Jain TK, Reddy MK, Morales MA, Leslie-Pelecky DL, Labhasetwar V (2008) Biodistribution, clearance, and biocompatibility of iron oxide magnetic nanoparticles in rats. Mol Pharm 5:316–327

Jain MR, Bandyopadhyay D, Sundar R (2018) Scientific and regulatory considerations in the development of in vitro techniques for toxicology. In Vitro Toxicol 165–185. https://doi.org/10.1016/b978-0-12-804667-8.00009-2

Jia G et al (2018) NRP-1 targeted and cargo-loaded exosomes facilitate simultaneous imaging and therapy of glioma in vitro and in vivo. Biomaterials 178

Jones DP (2002) Redox potential of GSH/GSSG couple: assay and biological significance. Methods Enzymol 348:93–112

Joris F et al (2016) The impact of species and cell type on the nanosafety profile of iron oxide nanoparticles in neural cells. J Nanobiotechnol 14:69

Jun Y, Seo J, Cheon J (2008) Nanoscaling laws of magnetic nanoparticles and their applicabilities in biomedical sciences. Acc Chem Res 41:179–189

Kain J, Karlsson HL, Moller L (2012) DNA damage induced by micro- and nanoparticles–interaction with FPG influences the detection of DNA oxidation in the comet assay. Mutagenesis 27:491–500

Kang H et al (2018) Theranostic nanosystems for targeted cancer therapy. Nano Today 23:59–72

Kansara K et al (2015) TiO$_2$ nanoparticles induce DNA double strand breaks and cell cycle arrest in human alveolar cells. Environ Mol Mutagen 56:204–217

Karlsson HL, Gustafsson J, Cronholm P, Möller L (2009) Size-dependent toxicity of metal oxide particles—a comparison between nano- and micrometer size. Toxicol Lett 188:112–118

Karlsson HL et al (2013) Cell membrane damage and protein interaction induced by copper containing nanoparticles—importance of the metal release process. Toxicology 313:59–69

Kenny PA et al (2007) The morphologies of breast cancer cell lines in three-dimensional assays correlate with their profiles of gene expression. Mol Oncol. https://doi.org/10.1016/j.molonc.2007.02.004

Khandhar AP, Ferguson RM, Simon JA, Krishnan KM (2012) Tailored magnetic nanoparticles for optimizing magnetic fluid hyperthermia. J Biomed Mater Res A 100:728–737

Khanna P, Ong C, Bay B, Baeg G (2015) Nanotoxicity: an interplay of oxidative stress. Inflamm Cell Death Nanomater 5:1163–1180

Kharazian B et al (2018) Bare surface of gold nanoparticle induces inflammation through unfolding of plasma fibrinogen. Sci Rep 8:12557

Kievit FM et al (2009) PEI-PEG-chitosan copolymer coated iron oxide nanoparticles for safe gene delivery: synthesis, complexation, and transfection. Adv Funct Mater 19:2244–2251

Kievit FM et al (2011) Doxorubicin loaded iron oxide nanoparticles overcome multidrug resistance in cancer in vitro. J Control Release 152:76–83

Kiliç G et al (2015) In vitro toxicity evaluation of silica-coated iron oxide nanoparticles in human SHSY5Y neuronal cells. Toxicol Res 5:235–247

Kim JS et al (2006) Toxicity and tissue distribution of magnetic nanoparticles in mice. Toxicol Sci 89:338–347

Kim T-H et al (2012) Size-dependent cellular toxicity of silver nanoparticles. J Biomed Mater Res Part A100A:1033–1043

Kim Y et al (2014) Probing nanoparticle translocation across the permeable endothelium in experimental atherosclerosis. Proc Natl Acad Sci. https://doi.org/10.1073/pnas.1322725111

Kircher MF, Mahmood U, King RS, Weissleder R, Josephson L (2003) A multimodal nanoparticle for preoperative magnetic resonance imaging and intraoperative optical brain tumor delineation. Cancer Res 63:8122–8125

Klein S, Sommer A, Distel LVR, Neuhuber W, Kryschi C (2012) Superparamagnetic iron oxide nanoparticles as radiosensitizer via enhanced reactive oxygen species formation. Biochem Biophys Res Commun 425:393–397

Koh JY, Choi DW (1987) Quantitative determination of glutamate mediated cortical neuronal injury in cell culture by lactate dehydrogenase efflux assay. J Neurosci Methods 20:83–90

Könczöl M et al (2011) Cytotoxicity and genotoxicity of size-fractionated iron oxide (magnetite) in A549 human lung epithelial cells: role of ROS, JNK, and NF-jB. Chem Res Toxicol 24:1460–1475

Kreyling WG et al (2009) Size dependence of the translocation of inhaled iridium and carbon nanoparticle aggregates from the lung of rats to the blood and secondary target organs. Inhal Toxicol 21:55–60

Kristensen BW, Noer H, Gramsbergen JB, Zimmer J, Noraberg J (2003) Colchicine induces apoptosis in organotypic hippocampal slice cultures. Brain Res. https://doi.org/10.1016/S0006-8993(02)04080-5

Kroll A, Pillukat MH, Hahn D, Schnekenburger J (2012) Interference of engineered nanoparticles with in vitro toxicity assays. Arch Toxicol 86:1123–1136

Kuhn SJ, Hallahan DE, Giorgio TD (2006) Characterization of superparamagnetic nanoparticle interactions with extracellular matrix in an in vitro system. Ann Biomed Eng. https://doi.org/10.1007/s10439-005-9004-5

Kumar A, Dhawan A (2013) Genotoxic and carcinogenic potential of engineered nanoparticles: an update. Arch Toxicol 87:1883–1900

Kumar V, Sharma N, Maitra SS (2017) In vitro and in vivo toxicity assessment of nanoparticles. Int Nano Lett 7:243–256

Kumar A, Aileen Senapati V, Dhawan A (2018) Protocols for in vitro and in vivo toxicity assessment of engineered nanoparticles. In: Dhawan A, Anderson D, Shanker R (eds) Nanotoxicology: experimental and computational perspectives (issues in toxicology No. 35). Royal Society of Chemistry, pp 94–132. https://doi.org/10.1039/9781782623922-00094

Kunzmann A et al (2011) Efficient internalization of silica-coated iron oxide nanoparticles of different sizes by primary human macrophages and dendritic cells. Toxicol Appl Pharmacol 253:81–93

Kupcsik L (2011) Estimation of cell number based on metabolic activity: the MTT reduction assay. In: Stoddart M (ed) Mammalian cell viability: methods and protocols. Methods in molecular biology, vol 740. Humana Press, pp 13–19. https://doi.org/10.1007/978-1-61779-108-6_3

Kurtz-Chalot A et al (2014) Adsorption at cell surface and cellular uptake of silica nanoparticles with different surface chemical functionalizations: impact on cytotoxicity. J Nanoparticle Res 16:2738

Kwon Y-S, Choi K-B, Lim H, Lee S, Lee J-J (2018) Preparation and characterization of alginate based-fluorescent magnetic nanoparticles for fluorescence/magnetic resonance multimodal imaging applications. Jpn J Appl Phys 57:06HE03

Langley G et al (2015) Lessons from toxicology: developing a 21st-century paradigm for medical research. Environ Health Perspect 123:A268–A272

Lartigue L et al (2012) Cooperative organization in iron oxide multi-core nanoparticles potentiates their efficiency as heating mediators and MRI contrast agents. ACS Nano 6:10935–10949

Lee MJE et al (2010) Rapid pharmacokinetic and biodistribution studies using cholorotoxin-conjugated iron oxide nanoparticles: a novel non-radioactive method. PLoS One 5:e9536

Lee C-M et al (2009a) SPION-loaded chitosan–linoleic acid nanoparticles to target hepatocytes. Int J Pharm 371:163–169

Lee J, Lilly D, Doty C, Podsiadlo P, Kotov N (2009b) In vitro toxicity testing of nanoparticles in 3D cell culture. Small. https://doi.org/10.1002/smll.200801788

Leroueil PR et al (2007) Nanoparticle interaction with biological membranes: does nanotechnology present a Janus face? Acc Chem Res 40:335–342

Levy M et al (2011) Long term in vivo biotransformation of iron oxide nanoparticles. Biomaterials 32:3988–3999

Li L et al (2015) Folic acid-conjugated superparamagnetic iron oxide nanoparticles for tumor-targeting MR imaging. Drug Deliv 1–8 (2015). https://doi.org/10.3109/10717544.2015.1006404

Li S-D, Huang L (2009) Nanoparticles evading the reticuloendothelial system: role of the supported bilayer. Biochim Biophys Acta 1788:2259–2266

Li J et al (2013) Facile one-pot synthesis of Fe_3O_4@Au composite nanoparticles for dual-mode MR/CT imaging applications. ACS Appl Mater Interfaces 5:10357–10366

Lindberg HK et al (2009) Genotoxicity of nanomaterials: DNA damage and micronuclei induced by carbon nanotubes and graphite nanofibres in human bronchial epithelial cells in vitro. Toxicol Lett 186:166–173

Ling D, Hyeon T (2013) Chemical design of biocompatible iron oxide nanoparticles for medical applications. Small 9:1450–1466

Liu H-L et al (2010) Magnetic resonance monitoring of focused ultrasound/magnetic nanoparticle targeting delivery of therapeutic agents to the brain. Proc Natl Acad Sci 107:15205–15210

Liu G et al (2011) N-Alkyl-PEI-functionalized iron oxide nanoclusters for efficient siRNA delivery. Small 7:2742–2749

Liu MC et al (2013) Electrofluidic pressure sensor embedded microfluidic device: a study of endothelial cells under hydrostatic pressure and shear stress combinations. Lab Chip. https://doi.org/10.1039/c3lc41414k

Liu Z et al (2016) Magnetic-dependent protein corona of tailor-made superparamagnetic iron oxides alters their biological behaviors. Nanoscale 8:7544–7555

Longmire M, Choyke PL, Kobayashi H (2008) Clearance properties of nano-sized particles and molecules as imaging agents: considerations and caveats. Nanomedicine 3:703–17

Lu A-H, Salabas EL, Schüth F (2007) Magnetic nanoparticles: synthesis, protection, functionaliza-tion, and application. Angew Chemie Int Ed 46:1222–1244

Lundin A, Hasenson M, Persson J, Pousette A (1986) Estimation of biomass in growing cell lines by ATP assay. Methods Enzymol 133:27–42

Lundqvist M et al (2017) The nanoparticle protein corona formed in human blood or human blood fractions. PLoS One 12:e0175871

Lundqvist M et al (2008) Nanoparticle size and surface properties determine the protein corona with possible implications for biological impacts. Proc Natl Acad Sci. https://doi.org/10.1073/pnas.0805135105

Luo C et al (2015) Superparamagnetic iron oxide nanoparticles exacerbate the risks of reactive oxygen species-mediated external stresses. Arch Toxicol 89:357–369

Ma HL, Xu YF, Qi XR, Maitani Y, Nagai T (2008) Superparamagnetic iron oxide nanoparticles stabilized by alginate: pharmacokinetics, tissue distribution, and applications in detecting liver cancers. Int J Pharm 354:217–226

Magdolenova Z et al (2014) Mechanisms of genotoxicity. A review of in vitro and in vivo studies with engineered nanoparticles. Nanotoxicology 8:233–278

Magdolenova Z et al (2015) Coating-dependent induction of cytotoxicity and genotoxicity of iron oxide nanoparticles. Nanotoxicology 9:44–56

Mahmoudi M et al (2011) Irreversible changes in protein conformation due to interaction with superparamagnetic iron oxide nanoparticles. Nanoscale 3:1127–1138

Mahmoudi M, Hofmann H, Rothen-Rutishauser B, Petri-Fink A (2012) Assessing the in vitro and in vivo toxicity of superparamagnetic iron oxide nanoparticles. Chem Rev 112:2323–2338

Malvindi MA et al (2014) Toxicity assessment of silica coated iron oxide nanoparticles and biocompatibility improvement by surface engineering. PLoS ONE 9:1–11

Manke A, Wang L, Rojanasakul Y (2013) Mechanisms of nanoparticle-induced oxidative stress and toxicity. Biomed Res Int 2013:1–15

Manshian BB et al (2018) Nanoparticle-induced inflammation can increase tumor malignancy. Acta Biomater 68:99–112

Marshall RR, Murphy M, Kirkland DJ, Bentley KS (1996) Fluorescence in situ hybridisation with chromosome-specific centromeric probes: a sensitive method to detect aneuploidy. Mutat Res Mol Mech Mutagen 372:233–245

McCaffrey TA, Agarwal LA, Weksler BB (1988) A rapid fluorometric DNA assay for the measurement of cell density and proliferation in vitro. Vitr Cell Dev Biol 24:247–252

McKelvey-Martin VJ et al (1993) The single cell gel electrophoresis assay (comet assay): a European review. Mutat Res Mol Mech Mutagen 288:47–63

Mejías R et al (2013) Long term biotransformation and toxicity of dimercaptosuccinic acid-coated magnetic nanoparticles support their use in biomedical applications. J Control Release 171:225–233

Miao X, Leng X, Zhang Q (2017) The current state of nanoparticle-induced macrophage polarization and reprogramming research. Int J Mol Sci 18

Miernicki M, Hofmann T, Eisenberger I, von der Kammer F, Praetorius A (2019) Legal and practical challenges in classifying nanomaterials according to regulatory definitions. Nat Nanotechnol 14:208–216

Mishra SK, Khushu S, Gangenahalli G (2018) Effects of iron oxide contrast agent in combi-nation with various transfection agents during mesenchymal stem cells labelling: An in vitro toxicological evaluation. Toxicol Vitr 50:179–189

Mitjans M, Nogueira-Librelotto DR, Vinardell MP, Nogueira-Librelotto DR, Vinardell MP (2018) Nanotoxicity In vitro: limitations of the main cytotoxicity assays. In: Kumar V, Dasgupta N, Ranjan S (eds) Nanotoxicology: toxicity evaluation, risk assessment and management. CRC Press, pp 171–192. https://doi.org/10.1201/b21545-8

Moghimi SM, Hunter AC, Andresen TL (2011) Factors controlling nanoparticle pharmacokinetics: an integrated analysis and perspective. Annu Rev Pharmacol Toxicol 52:481–503

Mok H et al (2010) pH-sensitive sirna nanovector for targeted gene silencing and cytotoxic effect in cancer cells. Mol Pharm 7:1930–1939

Mosmann T (1983) Rapid colorimetric assay for cellular growth and survival: application to proliferation and cytotoxicity assays. J Immunol Methods 65:55–63

Mueller-Klieser W (1987) Multicellular spheroids—a review on cellular aggregates in cancer research. J Cancer Res Clin Oncol. https://doi.org/10.1007/BF00391431

Mueller-Klieser W (2017) Three-dimensional cell cultures: from molecular mechanisms to clinical applications. Am J Physiol Physiol. https://doi.org/10.1152/ajpcell.1997.273.4.c1109

Mulder WJ et al (2007) Magnetic and fluorescent nanoparticles for multimodality imaging. Nanomedicine 2:307–324

Müller K et al (2007) Effect of ultrasmall superparamagnetic iron oxide nanoparticles (Ferumoxtran-10) on human monocyte-macrophages in vitro. Biomaterials 28:1629–1642

Müller E et al (2018) Magnetic nanoparticles interact and pass an in vitro co-culture blood-placenta barrier model. Nanomaterials 8:108

Nabiev I et al (2007) Nonfunctionalized nanocrystals can exploit a cell's active transport machinery delivering them to specific nuclear and cytoplasmic compartments. Nano Lett. https://doi.org/10.1021/NL0719832

Nachlas MM, Margulies SI, Goldberg JD, Seligman AM (1960) The determination of lactic dehydrogenase with a tetrazolium salt. Anal Biochem 1:317–326

Nakamura H, Watano S (2018) Direct permeation of nanoparticles across cell membrane: a review. KONA Powder Part J 35:49–65

Nakayama GR, Caton MC, Nova MP, Parandoosh Z (1997) Assessment of the Alamar Blue assay for cellular growth and viability in vitro. J Immunol Methods 204:205–208

Narayanan S et al (2012) Biocompatible magnetite/gold nanohybrid contrast agents via green chemistry for MRI and CT bioimaging. ACS Appl Mater Interfaces 4:251–260

Nederman T, Twentyman P (1984) Spheroids for studies of drug effects. In: Acker H, Carlsson J, Durand R, Sutherland RM (eds) Spheroids in cancer research: methods and perspectives, pp 84–102. Springer, Berlin. https://doi.org/10.1007/978-3-642-82340-4_5

Nel A, Xia T, Mädler L, Li N (2006) Toxic potential of materials at the nanolevel. Science (80–.) 311:622–627

Nel A, Xia T, Mädler L, Li N (2006b) Toxic potential of materials at the nanolevel. Science. https://doi.org/10.1126/science.1114397

Neri M et al (2007) Efficient in vitro labeling of human neural precursor cells with superparamagnetic iron oxide particles: relevance for in vivo cell tracking. Stem Cells. https://doi.org/10.1634/stemcells.2007-0251

Neuwelt EA et al (2009) Ultrasmall superparamagnetic iron oxides (USPIOs): a future alternative magnetic resonance (MR) contrast agent for patients at risk for nephrogenic systemic fibrosis (NSF)? Kidney Int 75:465–474

Nguyen VH, Lee B-J (2017) Protein corona: a new approach for nanomedicine design. Int J Nanomed 12:3137–3151

Nguyen TA, Yin TI, Reyes D, Urban GA (2013) Microfluidic chip with integrated electrical cell-impedance sensing for monitoring single cancer cell migration in three-dimensional matrixes. Anal Chem. https://doi.org/10.1021/ac402761s

Niles AL, Moravec RA, Riss TL (2008) Update on in vitro cytotoxicity assays for drug development. Expert Opin Drug Discov 3:655–670

Nima ZA et al (2019) Bioinspired magnetic nanoparticles as multimodal photoacoustic, photothermal and photomechanical contrast agents. Sci Rep 9:887

O'Brien J, Wilson I, Orton T, Pognan F (2000) Investigation of the Alamar Blue (resazurin) fluorescent dye for the assessment of mammalian cell cytotoxicity. Eur J Biochem 5426:5421–5426

O'Brien LE et al (2001) Rac1 orientates epithelial apical polarity through effects on basolateral laminin assembly. Nat Cell Biol. https://doi.org/10.1038/ncb0901-831

Oberdörster G et al (2004) Translocation of inhaled ultrafine particles to the brain. Inhal Toxicol 16:437–445

Oberdörster G, Oberdörster E, Oberdörster J (2005) Nanotoxicology: an emerging discipline evolving from studies of ultrafine particles. Environ Health Perspect 113:823–839

Oh N, Park JH (2014) Endocytosis and exocytosis of nanoparticles in mammalian cells. Int J Nanomed 9(Suppl 1):51

Oliveira H et al (2013) Magnetic field triggered drug release from polymersomes for cancer therapeutics. J Control Release 169:165–170

Ostling O, Johanson KJ (1984) Microelectrophoretic study of radiation-induced DNA damages in individual mammalian cells. Biochem Biophys Res Commun 123:291–298

Owens DE, Peppas NA (2006) Opsonization, biodistribution, and pharmacokinetics of polymeric nanoparticles. Int J Pharm 307:93–102

Palmer LS et al (1930) Milchuntersuchung. Fresenius' Zeitschrift für Anal Chemie 82:268–271

Pan DC et al (2018) Nanoparticle properties modulate their attachment and effect on carrier red blood cells. Sci Rep 8:1615

Pankhurst QA, Connolly J, Jones SK, Dobson J (2003) Applications of magnetic nanoparticles in biomedicine. J Phys D Appl Phys 36:R167–R181

Park E-J et al (2014) Magnetic iron oxide nanoparticles induce autophagy preceding apoptosis through mitochondrial damage and ER stress in RAW264.7 cells. Toxicol Vitr 28:1402–1412

Paul W, Sharma CP (2010) Inorganic nanoparticles for targeted drug delivery. Biointegr Med Implant Mater 204–235. https://doi.org/10.1533/9781845699802.2.204

Paull KD et al (1988) The synthesis of XTT: a new tetrazolium reagent that is bioreducible to a water-soluble formazan. J Heterocycl Chem 25:911–914

Perez RP, Godwin AK, Handel LM, Hamilton TC (1993) A comparison of clonogenic, microtetra-zolium and sulforhodamine B assays for determination of cisplatin cytotoxicity in human ovarian carcinoma cell lines. Eur J Cancer 29:395–399

Pham BTT et al (2018) Biodistribution and clearance of stable superparamagnetic maghemite iron oxide nanoparticles in mice following intraperitoneal administration. Int J Mol Sci 19

Pietroiusti A (2012) Health implications of engineered nanomaterials. Nanoscale 4:1231

Pietroiusti A, Campagnolo L, Fadeel B (2013) Interactions of engineered nanoparticles with organs protected by internal biological barriers. Small 9:1557–1572

Pincu M, Bass D, Norman A (1984) An improved micronuclear assay in lymphocytes. Mutat Res Lett 139:61–65

Pöttler M et al (2015) Genotoxity of superparamagnetic iron oxide nanoparticles in granulosa cells. Int J Mol Sci 16:26280–26290

Prabhakarpandian B et al (2008) Synthetic microvascular networks for quantitative analysis of particle adhesion. Biomed Microdev. https://doi.org/10.1007/s10544-008-9170-y

Prabhu S, Mutalik S, Rai S, Udupa N, Rao BSS (2015) PEGylation of superparamagnetic iron oxide nanoparticle for drug delivery applications with decreased toxicity: an in vivo study. J Nanoparticle Res 17

Präbst K, Engelhardt H, Ringgeler S, Hübner H (2017) Basic colorimetric proliferation assays: MTT, WST, and resazurin. In: Gilbert D, Friedrich O (eds) Cell viability assays: methods and protocols. Methods in molecular biology, vol 1601. Humana Press, New York, pp 1–17. https://doi.org/10.1007/978-1-4939-6960-9_1

Prosen L et al (2013) Magnetofection: a reproducible method for gene delivery to melanoma cells. Biomed Res Int 2013:209452

Qiao R et al (2012) Receptor-mediated delivery of magnetic nanoparticles across the blood-brain barrier. ACS Nano. https://doi.org/10.1021/nn300240p

Reddy ST et al (2007) Exploiting lymphatic transport and complement activation in nanoparticle vaccines. Nat Biotechnol 25:1159–1164

Reichel D, Tripathi M, Perez JM (2019) Biological effects of nanoparticles on macrophage polarization in the tumor microenvironment. Nanotheranostics 3:66–88

Repetto G, del Peso A, Zurita JL (2008) Neutral red uptake assay for the estimation of cell viability/cytotoxicity. Nat Protoc 3:1125–1131

Riss TL, Moravec RA (2006) Cell proliferation assays: improved homogeneous methods used to measure the number of cells in culture. In: Celis JE (ed) Cell biology: a laboratory handbook, vol 1. Elsevier Academic Press, pp 25–33

Riss TL, Moravec RA, O'Brien MA, Hawkins EM, Niles A (2006) Homogeneous multiwell assays for measuring cell viability, cytotoxicity and apoptosis. In: Minor L (ed) Handbook of assay development in drug discovery. Taylor & Francis Group, pp 385–406

Riss TL, Moravec RA, Niles AL (2010) Assay development for cell viability and apoptosis for high-throughput screening. In: Chen T (ed) A practical guide to assay development and high-throughput screening in drug discovery. Critical reviews in combinatorial chemistry. CRC Press, pp 99–122

Riss TL, Moravec RA, Niles AL (2011) Cytotoxicity testing: measuring viable cells, dead cells, and detecting mechanism of cell death. In: Stoddart M (ed) Mammalian cell viability: methods and protocols. Humana Press, pp 103–114. https://doi.org/10.1007/978-1-61779-108-6_12

Rivera Gil P, Oberdörster G, Elder A, Puntes V, Parak WJ (2010) Correlating physico-chemical with toxicological properties of nanoparticles: the present and the future. ACS Nano 4:5227–5231

Rizzo LY et al (2013) In vivo nanotoxicity testing using the zebrafish embryo assay. J Mater Chem B1:3918

Rodrigues RM et al (2013) Assessment of an automated in vitro basal cytotoxicity test system based on metabolically-competent cells. Toxicol Vitr 27:760–767

Rosano JM et al (2009) A physiologically realistic in vitro model of microvascular networks. Biomed Microdev. https://doi.org/10.1007/s10544-009-9322-8

Rubinstein LV et al (1990) Comparison of in vitro anticancer-drug-screening data generated with a tetrazolium assay versus a protein assay against a diverse panel of human tumor cell lines. J Natl Cancer Inst 82:1113–1118

Ruponen M, Ylä-Herttuala S, Urtti A (1999) Interactions of polymeric and liposomal gene delivery systems with extracellular glycosaminoglycans: physicochemical and transfection studies. Biochim Biophys Acta Biomembr. https://doi.org/10.1016/S0005-2736(98)00199-0

Sadeghi L, Tanwir F, Yousefi Babadi V (2015) In vitro toxity of iron oxide nanoparticle: oxidative damages on Hep G2 cells. Exp Toxicol Pathol 67:197–203

Sadiq R, Khan QM, Mobeen A, Hashmat AJ (2015) In vitro toxicological assessment of iron oxide, aluminium oxide and copper nanoparticles in prokaryotic and eukaryotic cell types. Drug Chem Toxicol 38:152–161

Sahu SC, Casciano DA (2009) Nanotoxicity: from in vivo and in vitro models to health risks. https://doi.org/10.1002/9780470747803

Sahu SC, Hayes AW (2017) Toxicity of nanomaterials found in human environment. Toxicol Res Appl 1:239784731772635

Salatin S, Dizaj SM, Khosroushahi AY (2015) Effect of the surface modification, size, and shape on cellular uptake of nanoparticles. Cell Biol Int 39:881–890

Same S, Aghanejad A, Nakhjavani SA, Barar J, Omidi Y (2016) Radiolabeled theranostics: magnetic and gold nanoparticles. Bioimpacts 6:169–181

Sargent LM et al (2009) Induction of aneuploidy by single-walled carbon nanotubes. Environ Mol Mutagen 50:708–717

Sayes CM, Reed KL, Warheit DB (2007) Assessing toxicology of fine and nanoparticles: comparing in vitro measurements to in vivo pulmonary toxicity profiles. Toxicol Sci 97:163–180

Schleich N et al (2013) Dual anticancer drug/superparamagnetic iron oxide-loaded PLGA-based nanoparticles for cancer therapy and magnetic resonance imaging. Int J Pharm 447:94–101

Schuurs AHWM, Van Weemen BK (1980) Enzyme-immunoassay: a powerful analytical tool. J Immunoassay 1:229–249

Scudiero DA et al (1988) Evaluation of a soluble tetrazolium/formazan assay for cell growth and drug sensitivity in culture using human and other tumor cell lines. Cancer Res 48:4827–4833

Seabra AB et al (2014) Preparation, characterization, cytotoxicity, and genotoxicity evaluations of thiolated- and S-nitrosated superparamagnetic iron oxide nanoparticles: Implications for cancer treatment. Chem Res Toxicol 27:1207–1218

Seo DY, Jin M, Ryu JC, Kim YJ (2017) Investigation of the genetic toxicity by dextran-coated superparamagnetic iron oxide nanoparticles (SPION) in HepG2 cells using the comet assay and cytokinesis-block micronucleus assay. Toxicol Environ Health Sci 9:23–29

Shah V et al (2013) Genotoxicity of different nanocarriers: possible modifications for the delivery of nucleic acids. Curr Drug Discov Technol 10:8–15

Shamir ER, Ewald AJ (2014) Three-dimensional organotypic culture: Experimental models of mammalian biology and disease. Nat Rev Mol Cell Biol. https://doi.org/10.1038/nrm3873

Shanavas A, Sasidharan S, Bahadur D, Srivastava R (2017) Magnetic core-shell hybrid nanoparticles for receptor targeted anti-cancer therapy and magnetic resonance imaging. J Colloid Interface Sci 486:112–120

Sharifi S et al (2012) Toxicity of nanomaterials. Chem Soc Rev 41:93

Sharkey J et al (2017) Functionalized superparamagnetic iron oxide nanoparticles provide highly efficient iron-labeling in macrophages for magnetic resonance–based detection in vivo. Cytotherapy 19:555–569

Sharma A et al (2018) Physical characterization and in vivo organ distribution of coated iron oxide nanoparticles. Sci Rep 8:1–12

Shaw J, Raja SO, Dasgupta AK (2014) Modulation of cytotoxic and genotoxic effects of nanoparticles in cancer cells by external magnetic field. Cancer Nanotechnol 5:2

Shi J et al (2012) Hemolytic properties of synthetic nano- and porous silica particles: the effect of surface properties and the protection by the plasma corona. Acta Biomater. https://doi.org/10.1016/j.actbio.2012.04.024

Shi J et al (2013) PEGylated fullerene/iron oxide nanocomposites for photodynamic therapy, targeted drug delivery and MR imaging. Biomaterials 34:9666–9677

Shi D, Mi G, Bhattacharya S, Nayar S, Webster TJ (2016) Optimizing superparamagnetic iron oxide nanoparticles as drug carriers using an in vitro blood–brain barrier model. Int J Nanomed. https://doi.org/10.2147/IJN.S108333

Shvedova AA, Kagan VE, Fadeel B (2010) Close encounters of the small kind: adverse effects of man-made materials interfacing with the nano-cosmos of biological systems. Annu Rev Pharmacol Toxicol 50:63–88

Shydlovska O et al (2017) Synthesis and comparative characteristics of biological activities of (La, Sr)MnO$_3$ and Fe$_3$O$_4$ nanoparticles. Eur J Nanomed 9:33–43

Sierra LM, Gaivão I (2014) Genotoxicity and DNA repair: a practical approach. Methods in pharmacology and toxicology. Humana Press

Singamaneni S, Bliznyuk VN, Binek C, Tsymbal EY (2011) Magnetic nanoparticles: recent advances in synthesis, self-assembly and applications. J Mater Chem 21:16819

Singh N et al (2017) Exposure to engineered nanomaterials: impact on DNA Repair Pathways. Int J Mol Sci 18

Singh NP, McCoy MT, Tice RR, Schneider EL (1988) A simple technique for quantitation of low levels of DNA damage in individual cells. Exp Cell Res 175:184–191

Singh N et al (2009) Nanogenotoxicology: the DNA damaging potential of engineered nanomaterials. Biomaterials 30:3891–3914

Singh N, Jenkins GJS, Asadi R, Doak SH (2010) Potential toxicity of superparamagnetic iron oxide nanoparticles (SPION). Nano Rev 1:5358

Sitbon G et al (2014) Multimodal Mn-doped I-III-VI quantum dots for near infrared fluorescence and magnetic resonance imaging: from synthesis to in vivo application. Nanoscale 6:9264–9272

Skehan P et al (1990) New colorimetric cytotoxicity assay for anticancer-drug screening. J Natl Cancer Inst 82:1107–1112

Soenen SJH, Nuytten N, De Meyer SF, De Smedt SC, De Cuyper M (2010) High intracellular iron oxide nanoparticle concentrations affect cellular cytoskeleton and focal adhesion kinase-mediated signaling. Small 6:832–842

Stafford S et al (2018) Multimodal magnetic-plasmonic nanoparticles for biomedical applications. Appl Sci 8:97

Stern ST, Adiseshaiah PP, Crist RM (2012) Autophagy and lysosomal dysfunction as emerging mechanisms of nanomaterial toxicity. Part Fibre Toxicol 9:20

Stevenson R, Hueber AJ, Hutton A, McInnes IB, Graham D (2011) Nanoparticles and inflammation. Sci World J 11:1300–1312

Stocke NA et al (2017) Toxicity evaluation of magnetic hyperthermia induced by remote actuation of magnetic nanoparticles in 3D micrometastasic tumor tissue analogs for triple negative breast cancer. Biomaterials. https://doi.org/10.1016/j.biomaterials.2016.12.019

Stoddart MJ (2011) Mammalian cell viability: methods and protocols. Methods in molecular biology, vol 740. Humana Press

Streuli CH, Bailey N, Bissell MJ (1991) Control of mammary epithelial differentiation: basement membrane induces tissue-specific gene expression in the absence of cell-cell interaction and morphological polarity. J Cell Biol. https://doi.org/10.1083/jcb.115.5.1383

Stroh A et al (2004) Iron oxide particles for molecular magnetic resonance imaging cause transient oxidative stress in rat macrophages. Free Radic Biol Med 36:976–984

Sun C et al (2008) Tumor-targeted drug delivery and MRI contrast enhancement by chlorotoxin-conjugated iron oxide nanoparticles. Nanomedicine 3:495–505

Sutariya VB et al (2015) Introduction—biointeractions of nanomaterials challenges and solutions. In: Sutariya VB, Pathak Y (eds) Biointeractions of nanomaterials, pp 1–48. CRC Press

Sutariya VB, Pathak Y (2014) Biointeractions of nanomaterials. Biointeractions of Nanomaterials. https://doi.org/10.1201/b17191

Sylvester PW (2011) Optimization of the tetrazolium dye (MTT) colorimetric assay for cellular growth and viability. In: Satyanarayanajois S (ed) Drug design and discovery: methods and protocols. Methods in molecular biology, vol 716. Humana Press, pp 157–168. https://doi.org/10.1007/978-1-61779-012-6_9

Tasso M et al (2015) Sulfobetaine-vinylimidazole block copolymers: a robust quantum dot surface chemistry expanding bioimaging's horizons. ACS Nano 9:11479–11489

Teeguarden JG et al (2014) Comparative iron oxide nanoparticle cellular dosimetry and response in mice by the inhalation and liquid cell culture exposure routes. Part Fibre Toxicol 11:1–18

Territo MC, Cline MJ (1975) Mononuclear phagocyte proliferation, maturation and function. Clin Haematol 4:685–703

Theumer A et al (2015) Superparamagnetic iron oxide nanoparticles exert different cytotoxic effects on cells grown in monolayer cell culture versus as multicellular spheroids. J Magn Magn Mater 380:27–33

Thorek DLJ, Tsourkas A (2008) Size, charge and concentration dependent uptake of iron oxide particles by non-phagocytic cells. Biomaterials 29:3583–3590

Thu MS et al (2009) Iron labeling and pre-clinical MRI visualization of therapeutic human neural stem cells in a murine glioma model. PLoS One 4:e7218

Tice RR et al (2000) Single cell gel/comet assay: guidelines for in vitro and in vivo genetic toxicology testing. Environ Mol Mutagen 35:206–221

Timmins NE, Nielsen LK (2007) Generation of multicellular tumor spheroids by the hanging-drop method. Tissue Eng. https://doi.org/10.1007/978-1-59745-443-8_8

Tominaga H et al (1999) A water-soluble tetrazolium salt useful for colorimetric cell viability assay. Anal Commun 36:47–50

Tomitaka A et al (2019) Surface-engineered multimodal magnetic nanoparticles to manage CNS diseases. Drug Discov Today 24:873–882

Tse BW-C et al (2015) PSMA-targeting iron oxide magnetic nanoparticles enhance MRI of preclinical prostate cancer. Nanomedicine 10:375–386

Turiel-Fernández D, Bettmer J, Montes-Bayón M (2018) Evaluation of the uptake, storage and cell effects of nano-iron in enterocyte-like cell models. J Trace Elem Med Biol 49:98–104

Twigg RS (1945) Oxidation-reduction aspects of resazurin. Nature 155:401–402

Vedantam P, Huang G, Tzeng TRJ (2013) Size-dependent cellular toxicity and uptake of commercial colloidal gold nanoparticles in DU-145 cells. Cancer Nanotechnol 4:13–20

Veiseh O et al (2009a) Specific targeting of brain tumors with an optical/magnetic resonance imaging nanoprobe across the blood-brain barrier. Cancer Res 69:6200–6207

Veiseh O et al (2009b) Specific targeting of brain tumors with an optical/magnetic resonance imaging nanoprobe across the blood-brain barrier. Cancer Res. https://doi.org/10.1158/0008-5472.CAN-09-1157

Vichai V, Kirtikara K (2006) Sulforhodamine B colorimetric assay for cytotoxicity screening. Nat Protoc 1:1112–1116

Vinci M et al (2012) Advances in establishment and analysis of three-dimensional tumor spheroid-based functional assays for target validation and drug evaluation. BMC Biol. https://doi.org/10.1186/1741-7007-10-29

Walkey CD, Chan WCW (2012) Understanding and controlling the interaction of nanomaterials with proteins in a physiological environment. Chem Soc Rev 41:2780–2799

Wan R et al (2017) Cobalt nanoparticles induce lung injury, DNA damage and mutations in mice. Part Fibre Toxicol 14:38

Wang B et al (2009) Neurotoxicity of low-dose repeatedly intranasal instillation of nano- and submicron-sized ferric oxide particles in mice. J Nanoparticle Res 11:41–53

Wang X et al (2012) Cancer stem cell labeling using poly(l-lysine)-modified iron oxide nanoparticles. Biomaterials. https://doi.org/10.1016/j.biomaterials.2012.01.058

Wang D et al (2014) Targeted iron-oxide nanoparticle for photodynamic therapy and imaging of head and neck cancer. ACS Nano 8:6620–6632

Wang Q et al (2015) Low toxicity and long circulation time of polyampholyte-coated magnetic nanoparticles for blood pool contrast. Sci Rep 5:1–8

Wang F, Salvati A, Boya P (2018) Lysosome-dependent cell death and deregulated autophagy induced by amine-modified polystyrene nanoparticles. Open Biol 8

Warren EAK, Payne CK (2015) Cellular binding of nanoparticles disrupts the membrane potential. RSC Adv 5:13660–13666

Wei Y et al (2016) Iron overload by superparamagnetic iron oxide nanoparticles is a high risk factor in cirrhosis by a systems toxicology assessment. Sci Rep 6:29110

Weir MP, Gibson JF, Peters TJ (1984) Haemosiderin and tissue damage. Cell Biochem Funct. https://doi.org/10.1002/cbf.290020402

Weselsky P (1871) Ueber die Azoverbindungen des Resorcins. Berichte der Dtsch Chem Gesellschaft 4:613–619

Węsierska-Gądek J, Gueorguieva M, Ranftler C, Zerza-Schnitzhofer G (2005) A new multiplex assay allowing simultaneous detection of the inhibition of cell proliferation and induction of cell death. J Cell Biochem 96:1–7

Wittekind D (2003) Traditional staining for routine diagnostic pathology including the role of tannic acid. 1. Value and limitations of the hematoxylin-eosin stain. Biotech Histochem 78:261–270

Wolff I, Müller P (2006) Micronuclei and comet assay. In: Celis JE (2006) Cell biology: a laboratory handbook, vol 1. Elsevier Academic Press, pp 325–331

Woolston C, Martin S (2011) Analysis of tumor and endothelial cell viability and survival using sulforhodamine B and clonogenic assays. In: Stoddart MJ (ed) Mammalian cell viability: methods and protocols. Methods in molecular biology, vol 740; Humana Press, pp 45–56. https://doi.org/10.1007/978-1-61779-108-6_7

Wottrich R, Diabate S, Krug HF (2004) Biological effects of ultrafine model particles in human macrophages and epithelial cells in mono- and co-culture. Int J Hyg Environ Heal 207:353–361

Wu Y et al (2009) Multiplexed assay panel of cytotoxicity in HK-2 cells for detection of renal proximal tubule injury potential of compounds. Toxicol Vitr 23:1170–1178

Wu K, Su D, Liu J, Saha R, Wang J-P (2018) Magnetic nanoparticles in nanomedicine

Xia T, Kovochich M, Liong M, Zink JI, Nel AE (2008) Cationic polystyrene nanosphere toxicity depends on cell-specific endocytic and mitochondrial injury pathways. ACS Nano 2:85–96

Xia T, Li N, Nel AE (2009) Potential health impact of nanoparticles. Annu Rev Public Health 30:137–150

Xie Y et al (2016) Size-dependent cytotoxicity of Fe_3O_4 nanoparticles induced by biphasic regulation of oxidative stress in different human hepatoma cells. Int J Nanomed 11:3557–3570

Xu S, Olenyuk BZ, Okamoto CT, Hamm-Alvarez SF (2013) Targeting receptor-mediated endocytotic pathways with nanoparticles: rationale and advances. Adv Drug Deliv Rev 65:121–138

Xuan S et al (2011) Synthesis of biocompatible, mesoporous Fe_3O_4 nano/microspheres with large surface area for magnetic resonance imaging and therapeutic applications. ACS Appl Mater Interfaces 3:237–244

Yallapu MM et al (2015) Implications of protein corona on physico-chemical and biological properties of magnetic nanoparticles. Biomaterials 46:1–12

Yang S-A, Choi S, Jeon SM, Yu J (2018) Silica nanoparticle stability in biological media revisited. Sci Rep 8:185

Yu W et al (2007) Formation of cysts by alveolar type II cells in three-dimensional culture reveals a novel mechanism for epithelial morphogenesis. Mol Biol Cell. https://doi.org/10.1091/mbc.e06-11-1052

Zanoni M et al (2016) 3D tumor spheroid models for in vitro therapeutic screening: a systematic approach to enhance the biological relevance of data obtained. Sci Rep. https://doi.org/10.1038/srep19103

Zelazna K, Rudnicka K, Tejs S (2011) In vitro micronucleus test assessment of polycyclic aromatic hydrocarbons. Environ Biotechnol 7

Zhang X-Q et al (2012a) Interactions of nanomaterials and biological systems: implications to personalized nanomedicine. Adv Drug Deliv Rev 64:1363

Zhang T et al (2012b) Evaluation on cytotoxicity and genotoxicity of the L-glutamic acid coated iron oxide nanoparticles. J Nanosci Nanotechnol 12:2866–2873

Zhang M, Xu C, Jiang L, Qin J (2018) A 3D human lung-on-a-chip model for nanotoxicity testing. Toxicol Res. https://doi.org/10.1039/c8tx00156a

Zhen X, Cheng P, Pu K (2019) Recent advances in cell membrane-camouflaged nanoparticles for cancer phototherapy. Small 15:1804105

Zheng X-C et al (2018) The theranostic efficiency of tumor-specific, pH-responsive, peptide-modified, liposome-containing paclitaxel and superparamagnetic iron oxide nanoparticles. Int J Nanomed 13:1495–1504

Zhu MT et al (2008) Comparative study of pulmonary responses to nano- and submicron-sized ferric oxide in rats. Toxicology 247:102–111

Zhu M-T et al (2011) Endothelial dysfunction and inflammation induced by iron oxide nanoparticle exposure: Risk factors for early atherosclerosis. Toxicol Lett 203:162–171

Zhu M et al (2013a) Physicochemical properties determine nanomaterial cellular uptake, transport, and fate. Acc Chem Res 46:622–631

Zhu L et al (2013b) Multifunctional pH-sensitive superparamagnetic iron-oxide nanocomposites for targeted drug delivery and MR imaging. J Control Rel 169:228–238

Zou P et al (2010) Superparamagnetic iron oxide nanotheranostics for targeted cancer cell imaging and pH-dependent intracellular drug release. Mol Pharm 7:1974–1984

Chapter 14
Persistence, Toxicity, and Biodegradation of Gold- and Iron Oxide-Based Nanoparticles in the Living Systems

Kanwal Akhtar, Yasir Javed, Naveed A. Shad, Navadeep Shrivastava and S. K. Sharma

Abstract Inorganic nanomaterials have been extensively investigated for several biological applications ranging from targeted drug delivery to cancer treatment and tissue engineering to in vivo imaging. Gold and iron oxide nanoparticles (IONPs) are important candidate of inorganic nanomaterials considering their non-toxic nature and relevant magnetic and optical properties. Most of the biomedical applications involve detailed tuning of surface charge and physiochemical properties. Understanding of pharmacokinetics of these nanoparticles is very important to elaborate on the distribution and fate in the living organism. Many factors including size distribution, charge, and plasma protein adsorption; coating molecules can tune effectively to monitor the biodistribution and pharmacokinetics of the gold- and iron oxide-based nanoparticles. This chapter reviews the crucial parameters that affect the biodistribution, fate, and toxicity of the inorganic nanoparticles in the biological systems.

Keywords Inorganic nanomaterials · Biomedical applications · Pharmacokinetics · Bio-distribution · Bio-degradation

Introduction

Nanomaterials are not only part of technical products but also play a major role in biomedicine and biotechnology branch. Combination of these two branches defines

K. Akhtar · Y. Javed (✉)
Magnetic Materials Laboratory, Department of Physics, University of Agriculture, University Main Rd., Faisalabad 38000, Pakistan
e-mail: myasi60@hotmail.com

N. A. Shad
Department of Physics, Government College University Faisalabad, Faisalabad, Pakistan

N. Shrivastava
Institute of Physics, Federal University of Goias, Goiania-GO, Brazil

S. K. Sharma
Department of Physics, Faculty of Science and Technology, The University of the West Indies, Saint Augustine, Trinidad and Tobago

most promising cross-disciplinary research developments. Nanomaterials especially inorganic nanoparticles have emerged as novel tools with enhanced pharmacokinetics, therapeutic efficacy, and biodistribution (Docter et al. 2015a; Setyawati et al. 2015; Webster 2013). These nanomaterials have applications in vascular imaging, drug delivery, gene delivery, cancer therapies, and contrast agents in bio-imaging purposes (Javed et al. 2017) because of low toxicity, biocompatibility, and high biodegradability (Docter et al. 2015b; Pautler and Brenner 2010; Riehemann et al. 2009). Recent advancement for enhancing their abilities to rationally manipulate the nanomaterials such as chemical, biological, and physical properties, open many possibilities in synthesizing new generation of nanomaterial-based probes. Development of IONPs shows considerable progress in clinical applications including hyperthermia, drug delivery, and in vitro low-cost diagnostics (Rizzo et al. 2013; Seeney et al. 2012; Wahajuddin 2012). Plasmonic properties of gold nanoparticles are extensively employed in photodynamic therapy, drug delivery, photothermal therapy, photoacoustic imaging, photodynamic therapy, and plasmonic sensing (Ferrari et al. 2009; Murday et al. 2009; Prabhu and Patravale 2012).

Despite the large-scale production of multifunctional nanomaterials, few of them have been accepted for the clinical use. Yet, many of iron oxide- and gold-based formulations have been under clinical trials of phase 3. Use of these nanoparticles in biomedical applications requires elaborative tuning for enhancement of their surface and physiochemical properties at the same time minimizing the toxicity effects (del Pino 2014; Ferrari et al. 2009; Luo et al. 2012). To address the biocompatibility and safety issues, potential toxicity of nanomaterials is a major concern for in vitro and in vivo biomedical applications (Fig. 14.1). Different parameters including coatings, diameter, shape, dose, and route of administration play crucial role in absorption, distribution, accumulations, biotransformation, and elimination of these nanoparticles (Colombo et al. 2012; Ding and Ma 2014; Helou et al. 2013). This chapter will review all possible crucial parameters, considering latest design strategies and biological barriers used to overcome them. A careful overview of persistence, toxicity, and biodegradation of gold- and iron oxide-based nanoparticles in relation to their designs are discussed.
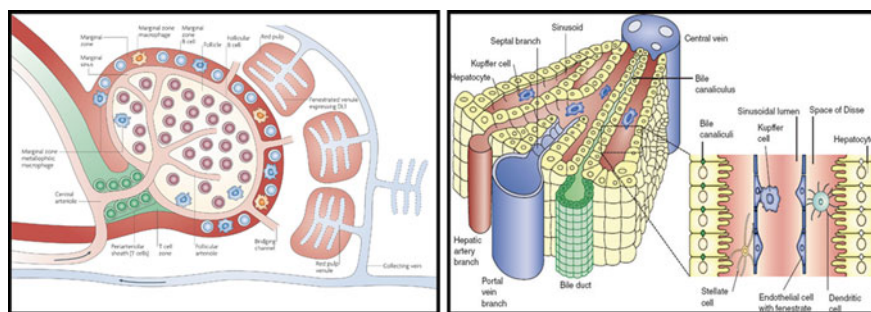

Fig. 14.1 Schematic anatomy of Spleen (left) and liver (right). Reprinted with permission from Pillai and Cariappa (2009) and Adams and Eksteen (2006)

In Vivo Fate and Distribution of Gold- and Iron Oxide-Based Nanomaterials as Tunable Tools Toward Biomedical Applications

In vivo biodistribution of inorganic nanoparticles (IONPs) is mainly concerned with the core material. Organic coatings are necessary to make these NPs more biocompatible and stable. Without organic coatings, these nanoparticles show accumulation and form complexes within biological environments (Wan et al. 2015). These complexes are composed of engineered surface coatings, compounds absorbed from biological environment and inorganic material. Conceptually, nanoparticles core is the basic functional physical property being used for specific applications such as fluorescent, plasmonic, and superparamagnetic. In biological environment, persistence of these physical properties is critical for theranostic efficiency of inorganic nanoparticles (Urban et al. 2018).

Primary Interaction of NPs with Biological Medium

Biotransformation of gold and IONPs (dissolution, aggregation, and degradation) might change their properties depending on the environment over time. Coatings on nanoparticles determine their physiochemical properties including biological identity, circulation, etc. Typical functionalization on inorganic nanoparticles includes ligand molecules such as peptides (Clarke et al. 2010), silica shells (Selvan et al. 2007), lipid micelles (Klapper et al. 2015), and lipoic acids (Clarke et al. 2010). Resulting properties such as hydrophobicity/hydrophilicity and charge are important for colloidal stability of prepared nanoparticles (NPs) (Parak et al. 2003; Pelaz et al. 2013; Rivera-Gil et al. 2012). Appropriate coatings of NPs not only prevent from accumulation but ensure the proper dispersion and interaction in the complex biological environment. Distinct surface coatings have intense impact on fate and biocompatibility of NPs including cellular uptake, cell adhesion, cell viability, lifetime, and biopersistence of mononuclear phagocyte system usually referred as reticuloendothelial system (Clarke et al. 2010; Fadeel et al. 2013). These coatings also help in functionalization through conjugation with the specific bioactive and targeting ligands for obtaining multifunctional NPs in the active targeting schemes (Lin et al. 2009; Shang et al. 2011).

Upon intravenous (IV) injection, NPs immediately expose to a complex environment, consequently, large number of ions and biomolecules including metabolites, sugars, lipids, and proteins start adsorbing on the surface of NPs by hydrogen bonding, electrostatic, van der Wall and/or hydrophilic/hydrophobic interactions. All these adsorption processes grow biomolecule corona on the surface of the nanoparticles (Kolosnjaj-Tabi et al. 2015; Zhang et al. 2010). This biomolecule/protein corona formation affects the physiochemical, physiological, and biological characteristics. This corona formation can be distinguished into hard and soft corona; hard corona
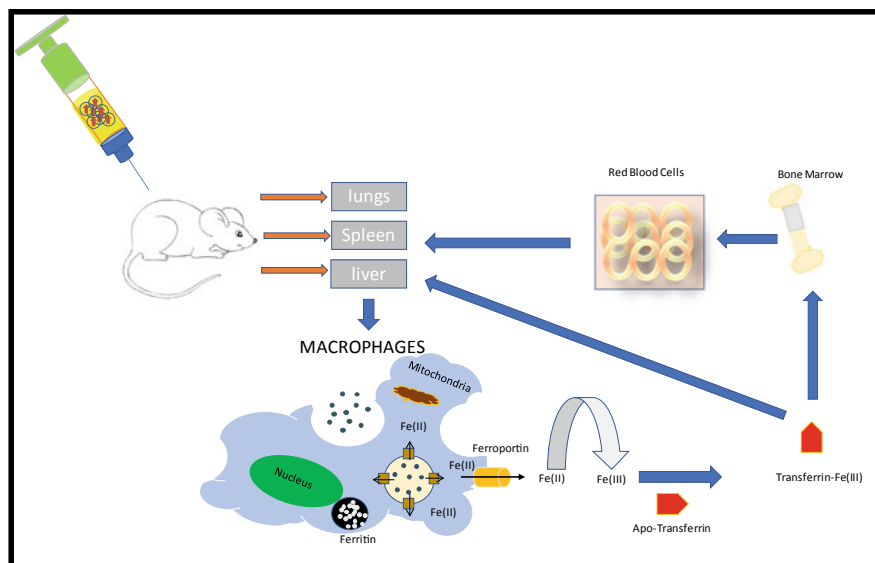
Fig. 14.2 Different possible processing routes that can metabolize the nanoparticles. Adapted with permission from Drakesmith and Prentice (2008)

is referred as long-lived protein signature on NPs (e.g., protein plasma signature on nanoparticles in blood), and soft corona can form on the hard corona because of rapid formation of transient layers of biomolecule through loose association (Carrillo-Carrión et al. 2014; Cedervall et al. 2007). Soft corona desorbs during biological purification processes. Protein corona is not related to interfaces between biological environment and NPs but it triggers initially the transformations of nanoparticles by altering their colloidal stability (Monopoli et al. 2012; Walkey and Chan 2012). Stabilizing effect of corona formation can be achieved through great control over charge, composition, steric stabilization, charge inhomogeneity, and destabilizing the impact produced by protein mediated bridging. Considering as colloids, physical properties of the synthesized nanoparticles need to be characterized for defining their hydrophobicity/hydrophilicity, aggregation, and surface charge (Tenzer et al. 2013; Xia et al. 2010). So, some biological identities involve molecules of the biological medium to adsorb at the surface of nanoparticles (Fig. 14.2). So, complete characterization of these nanoparticles dispersed in vivo is needed objectively.

In Vivo Exposure of Gold- and Iron Oxide-Based Nanomaterials

Accidental or intended in vivo exposure of NPs takes complex path in the body. NPs can face hostile conditions (i.e., local protein-based compositions and pH) in complex

biological environment (Di Corato et al. 2014; Kolosnjaj-Tabi et al. 2017; Lévy et al. 2012). At cell organelle level, tumor, stomach, or lysosomes/endosomes provide acidic environment. NPs are agglomerated inside these intracellular compartments where protein adsorption and pH affect aggregation-based modifications (i.e., optical and magnetic properties) and colloidal stability. Acidic behavior actively facilitates the corrosion of NPs core (i.e., superparamagnetic iron oxide and gold) which can be dissolved completely/partially by different mechanisms, i.e., dissolution, hydrolysis, degradation, etc. (Lévy et al. 2010; Soenen et al. 2015; Yang et al. 2012; Zeng et al. 2014). These enzymes can digest organic coatings around NPs as reported in the literature. Certain enzymes and proteins can adsorb on the surface of NPs and dynamically evolve the protein corona (Fig. 14.4). In vivo integrity, internalization, degradation, and clearance of these NPs are still challenging and need extensive investigation (Branca et al. 2015; Montenegro et al. 2013; Wang and Gu 2015).

In vivo fate of gold nanoparticles (AuNPs) and IONPs depends on different factors such as administered route, formation of protein corona, distribution inside the cardiovascular system, uptake by different cells, intracellular release, process and degradation (Fig. 14.3) (Levy et al. 2011). Zhang et al. investigated pharmacokinetics and biodistribution of polyethylene glycol-coated gold NPs. They injected these particles in mice suffering with A431 squamous tumors to evaluate the effects of anchoring ligand, colloidal stability, PEG (molecular weight), and particle size of NPs. Au NPs with mean size of 20 nm showed lowest uptake by reticuloendothelial system with slowest clearance rate (Zhang et al. 2009). Hillyer et al. studied the gastrointestinal uptake with distribution of colloidal gold NPs with mean diameter of 4, 10, 28, 58 nm through oral route of administration in mice. Small-sized colloidal gold
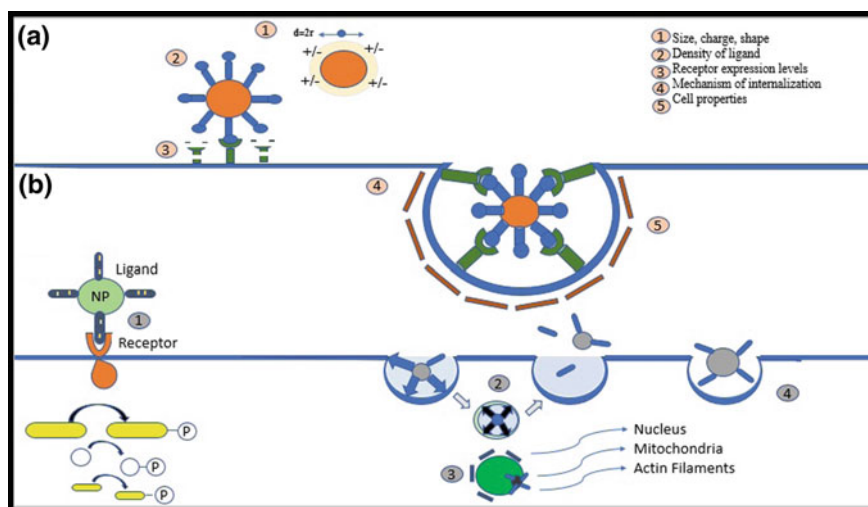

Fig. 14.3 Nanomaterials–cell interactions. **a** Factors affecting the interactions at the nanoparticles surface and **b** ligand functionalized nanoparticles interactions with cells. Reproduced from Saptarshi et al. (2013)
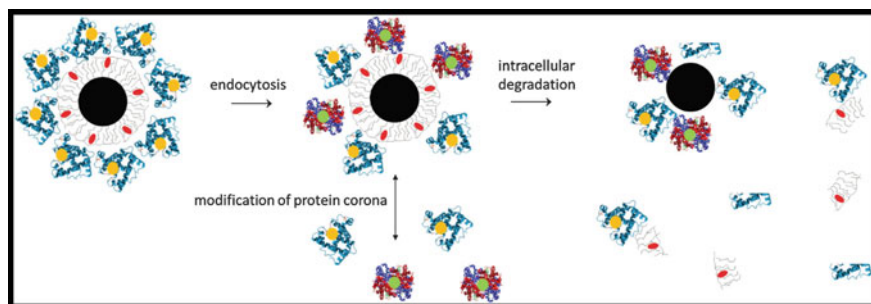
Fig. 14.4 Formation of protein corona on the nanoparticles' surface can change the biological identity and exchange of different proteins can happen. Inorganic core of the nanoparticles can metabolize in the microenvironment at later stages (Feliu et al. 2016)—Published by The Royal Society of Chemistry

NPs showed rapid uptake in gastrointestinal tract (Hillyer and Albrecht 2001). Hirn et al. studied the biodistribution of gold nanoparticles with opposite surface charges and different size ranges (1.4, 5, 18, 80 and 200 nm) through intravenous injection. Surface charge and size were the major contributor to determine the distribution of these particles. They observed higher accumulation rate with increased Au NPs size, 50% for 1.4 nm to >99% for 200 nm (Hirn et al. 2011) (Fig. 14.4).

Pharmacokinetics of Gold- and Iron Oxide-Based Nanomaterials

Gold and iron oxide NPs can be administrated in the body depending on the requirement of application through oral, intravenous, or inhalation pathways. Immune system of the body quickly responds to these NPs presence and tried to eliminate them effectively through metabolic, phagocytic, and degradation regardless of any biological barrier (including stability and gastric acidic pH) (Weissleder et al. 1990b). For elimination of these particles from the body, macrophages of spleen and liver play a critical role. In this section, we will focus on pharmacokinetic performance of gold and IONPs through different routes of administration (Arami et al. 2015).

Biodistribution of Nanomaterials Administered Through Different Routes of Administration

Cell culture investigations revealed that NPs can incorporate into all types of mammalian cells to some extent because of the non-specific uptake mechanisms. Behavior of NPs can affect the cellular uptake efficiency and their intracellular processing

because of partial/complete degradation or complete persistent in unaltered form (Hillaireau and Couvreur 2009). It is believed that mammalian cells can metabolize these NPs but this is not necessarily the case for all cells. Culture cells are either divided very fast or limited in their interactions and metabolisms. Interaction between in vivo tissues such as macrophages of mononuclear phagocyte system is much important in processing and clearance of NPs from the blood flow (Hillaireau and Couvreur 2009; Moore et al. 2000). However, other cells have limited capacity to uptake or process those nanoparticles. The clearance processes of nanoparticles depend on the immune system of any individual. Therefore, in vivo intracellular transfer, biodistribution, and degradation of gold and IONPs strongly depend on cell type and physiochemical properties of materials (Freund et al. 2012; Jones et al. 2013).

In peripheral vein, bolus injection seems the most promising and easy route for many biomedical applications. Through IV route of administration, NPs spread into right heart followed by lung capillaries to the left heart and finally to the arterial system which transfer NPs to the various parts of body. Under prevailing conditions, main fraction of the blood enters into spleen and liver, which possesses the great capacity to remove the xenobiotics from the bloodstream (Bargheer et al. 2015a; Carambia et al. 2015). Many studies have revealed the distribution of gold and IONPs; Balasubramanian et al. reported distribution and accumulation of gold NPs after 2 months of IV administration in spleen (8.4 ± 5.0–9.5 ± 6.4 ng/g) and liver (49.4 ± 50.4–72.2 ± 40.5 ng/g). In kidney and testis, significant accumulation of AuNPs was (up to 5.5 ± 2.5 ng/g) and (0.6 ± 0.1 ng/g), respectively (Balasubramanian et al. 2010). Weissleder et al. compared the hydrodynamic size of ultra-small superparamagnetic IONPs (20–30 nm) with first-generation IONPs (150 nm) and observed longer circulation time in rats of approximately 4 h 30 min (Weissleder et al. 1989). Dipolar/zwitterionic materials including poly (amino acids) and dopamine sulfonate, vinyl polymers (poly-vinylpyrrolidone) and polymers having heteroatoms (polyglycerol) are referred as best alternatives for polyethylene glycol. Results confirmed that NPs functionalized with such novel polymers have longer circulation time. Crosslinked IONPs were synthesized to prevent the weak bonding of hydroxyl groups with dextran coatings (Parween et al. 2013; Weissleder et al. 1989). Morais et al. reported gold NPs distribution with different coatings i.e. 3 pentapeptides and citrate after IV administration (0.6–1 mg Au/Kg) in rats. They reported that citrate coatings were removed up to 60% and deposited in the liver. In lungs, after 30 min of injection, 6% injected dose with decreased levels up to 0.7% within 24 h was reported. In spleen, gold level was 2.6%. However, after 24 h, the highest level of gold was reported in liver followed by blood and spleen (Morais et al. 2012). Bargheer et al. designed superparamagnetic IONPs-modified PEGylation with bi/mono-functional olyethylene amines oxide. They carried the in vitro model by albumin and transferrin (^{125}I-labeled) labeled proteins to study the exchange and bindings of corona proteins. Incubation of transferrin showed increased PEGylation grade, binding was diminished substantially without any difference between covalently bounded and adsorbed proteins. Particles labeled with ^{59}Fe/^{125}I were cleared within 30 min from the blood and appeared in large extent up to >90% in spleen and liver, whereas same results for

in vitro study revealed stability issues of hard corona formation with covalently bound or free proteins (Bargheer et al. 2015b). Wei et al. investigated the non-specific interactions of superparamagnetic IONPs coated with zwitterionic dopamine sulfonate ligand (ZDS) in HeLa cells and mice. ZDS-coated SPIONs retained their saturation magnetization value (M_s = 74 emu/g). They confirmed small non-specific in vitro uptake of ZDS-coated SPIONs in HeLa cancer cells and low serum proteins binding in mice (Wei et al. 2013).

Efficient uptake of gold and IONPs are usually done by endothelial cells like arteries, veins, and capillaries through different parts of body. Studies indicate the difference between peripheral endothelial cells and endothelial cells. Both showed different uptake of NPs due to their charge such as cationic NPs bind with peripheral endothelial cells while anionic NPs usually taken up by liver cells (Mahon et al. 2012). When injected through peritoneal cavity, they faced different situations. After passing from the visceral peritoneum, NPs move to the interstitium through blood vessels or lymph. Limited quantitative information is reported on cell processing efficacy through different in vivo administration routes (dermal, pulmonary, inhalation, and oral route) (Lunov et al. 2010; Sée et al. 2009). Sadauskas et al., studied the biodistribution of intratracheally administered gold nanoparticles with size 2, 40, and 100 nm in female adult mice. Reported distribution in mice after repeated dose of 2 nm gold NPs were 1.4–1.9% in liver, 40 nm gold NPs 0.1%, whereas 100 nm gold NPs were not detected (Sadauskas et al. 2009). Bargheer et al. reported the distribution of ^{51}Cr and ^{59}Fe labeled FeO$_x$ NPs through intestinal absorption in mice. ^{59}Fe showed significant absorption, whereas no absorption in case of 51Cr was observed. No degradation after 24 h was reported, and however, no fluorescent NPs were detected after 12 weeks which confirmed the substantial degradation of injected NPs (Bargheer et al. 2015a, b). Table 14.1 is showing different parameters of iron oxide-derived formulations.

Clearance Routes

Major clearance route for administrated NPs is mononuclear phagocytic system. Most of the NPs are taken up selectively by spleen and live (Xu et al. 2011). However, some reports confirmed the presence of administrated NPs in the lungs and other parts. Major clearance pathways for gold and IONPs are spleen and liver (Cui et al. 2013). These organs form monocyte macrophage and mononuclear phagocytic system (MPS) called reticuloendothelial system. MPS consists of macrophages (present in various organs, i.e., brain, bone marrow, liver, lymph nodes, and lung) and monocytes (circulate in blood). Mostly, hematopoietic stem cells consist of precursor macrophages cells in the bone marrow and released as monocytes in blood circulation (Peer et al. 2007). Through endothelium, circulating monocytes migrate to different tissues through differentiation based on their function phenotype and anatomical locations in large-sized subsets of macrophages. Major macrophages in lung, liver, interstitial tissues, and bones are alveolar macrophages, Kupffer cell, histiocytes,

Table 14.1 Blood half-life, charge and dose of different IONPs after injected in human/animal model

Name	Coating molecule	Model	Charge	Half-life	Dose (mg Fe/Kg)	References
SPIO (AMI25)	Dextran	Rats	NA	6 min	0.224	Weissleder et al. (1990a, b)
Amino-dextran SPIO-micromod	Dextran (20 KDa)	Mice	−4.95 to −0.77	5–60 min	4	Simberg et al. (2009)
Resovist (SHU 555 C)	Carboxy dextran	Rats	Anionic	56 ± 17	5.6	Frericks et al. (2009)
Ocean nanotech	Dextran + antibody	Mice	NA	7.5 h	NR	Tomanek et al. (2011)
Nanoworms	Cross-linked dextran (20 KDa)	Mice	NA	10 h	5	Wang et al. (2014)
Clariscan (NC100150)	PEG + starch	Humans	Anionic	3-4 h	3-4	Bachmann et al. (2002), Weishaupt et al. (1999)
VSOP-C184	Citrate coating	Rats	NA	21 ± 5 min	2.52	Wagner et al. (2002)

and osteoclasts, respectively (Melancon et al. 2009). All these macrophages clear the blood circulation from foreign bodies (i.e., viruses, gold/IONPS, old/abnormal cells, and bacteria) or pathogens through additional macrophages and phagocytosis (i.e., engulfing by following metabolism and degradation). Spleen and liver are blood filters that play a major role in the clearance process of gold and IONPs from blood circulation. These organs can eliminate only a fraction of NPs from bloodstream. However, excess of these NPs can accumulate in the macrophages of other rich tissues including adipose tissues and lung (Beckmann et al. 2009). Uptake mechanisms of IONPs through macrophages of spleen and liver are proceeded by phagocytosis, opsonization and recognition from macrophages. Accurate distribution of gold and IONPs demands detailed experimental studies (Weissleder et al. 1995). Van Beer et al. used different techniques to study the accurate liver distribution of dextran-coated ultra-small IONPs with core size (d_H = 30–35 nm, d_c = 5 nm) on rats. They reported maximum uptake of ferric ions (dose range = 15 mol Fe/Kg) by Kupffer cells after 1–4 h of administration. With the increased dosage rate (150 mmol Fe/kg), peak was observed after 8–24 h which revealed significantly changed liver contrast.

IONPs were distributed in interstitum and extracellular blood in spite of hepatocytes and Kupffer cells (Van Beers et al. 2001). Heinfield et al. injected the AuNPs through IV administration in mice and measured the biodistribution with atomic absorption. They reported low retention time in spleen and liver with high spatial resolution and unusual clarity from kidney. After 11–30 h post-injection of 10 mg Au/ml in blood, no sign of toxicity was observed (Hainfeld et al. 2006). Jong et al. injected gold NPs with mean diameter (10, 20, 100, and 250 nm) in rats intravenously. They sacrificed the rats after 24 h and determined the distribution of gold NPs in different organs. Clear difference in distribution based on particles size was observed. Small-sized gold NPs (10 nm) were detected in spleen, lung, kidney, brain, and liver. However, large particles were detected in spleen, liver, and blood (De Jong et al. 2008). Tate et al. reported the biodistribution of IONPs in different organs of mice after 14 and 580 days of post-injection. They confirmed the complete clearance after 580 days. This report only revealed the results after 14 and 580 days without any other time intervals, and that is why exact clearance time cannot be established (Tate et al. 2011).

Renal clearance is a non-phagocytizing pathway. If renal clearance is considered as appropriate clearance path, then through urine, large dosage of gold, and IONPs would be excreted. However, few reports on degraded gold and IONPs due to size constraints are present. Small coated molecules might be excreted through the renal pathway due to small biodegradation by-products and weak bonding (Alexis et al. 2008; Almeida et al. 2011). Liu et al. reported the renal clearance and physiological stability of glutathione-coated gold NPs with mean diameter of ($\sim$2.5 nm). They revealed the longer retention time (43.4 ± 6.6 min) in tumors with faster tissue clearance, which indicates enhanced retention and permeability effects. They reported half-lives for distribution and elimination as (5.4 ± 1.2 min) and (8.5 ± 2.1 min), respectively (Fig. 14.5) (Liu et al. 2013).

Parameters Affecting the Blood Clearance Pharmacokinetics

Hydrodynamic size: Biodistribution kinetics of IONPs can be determined by their hydrodynamic size. Effect of hydrodynamic size on the pharmacokinetics of gold and IONPs have been reported in the literature (Alexis et al. 2008; Almeida et al. 2011). Roohi et al. studied the decreased blood half-life from 50 to 3 min by increase of hydrodynamic size of IONPs from 20 to 85 nm, respectively (Roohi et al. 2012). Saebo and Wang confirmed that IONPs with hydrodynamic size of 4–100 nm accumulated quickly in spleen and live by macrophage phagocytosis and finally confined into spleen and liver (Briley-Saebo et al. 2011; Wang et al. 2001). Gupta et al. reported higher uptake rates of IONPs with hydrodynamic size ranges from 4 to 200 nm in spleen due to mechanical filtration through macrophage phagocytosis as compared to liver (Gupta and Wells 2004; Lan et al. 2012). Kunzmann and Fleige reported pinocytosis as major internalization path for dextran-coated IONPs with 20 nm hydrodynamic size. Internalization of larger IONPs was reported through
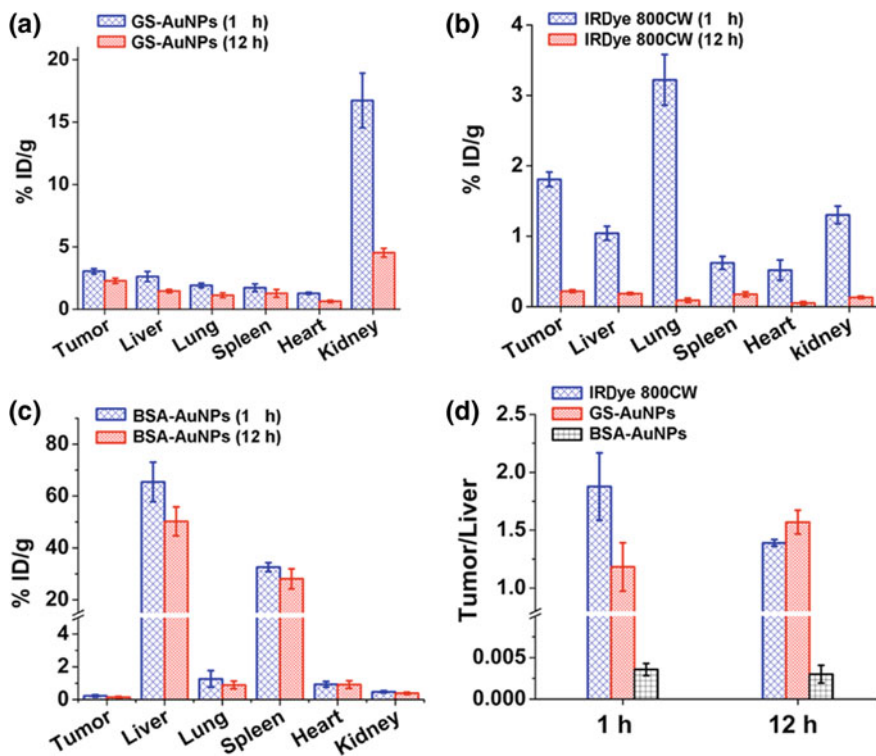
Fig. 14.5 Biodistribution of glutathione-coated gold NPs, IRdye 800CW and bovine serum albumin coated gold NPs after 1 and 12 h (**a**–**c**). **d** Comparison of three probe concentrations in tumor and liver after 1 and 12 h. Reprinted with permission from Liu et al. (2013). Copyright (2013) American Chemical Society

endocytosis. Internalized NPs transferred to lysosomes and finally eliminated from the body with hydrodynamic size of 10–15 nm through kidney (Kunzmann et al. 2011). Cho et al. reported higher concentration of PEG-coated gold NPs (4–13 nm) in blood for 24 h and clearance time was 7 days. However, large gold NPs showed less elimination phase and rapid take-up by spleen, mesenteric lymph, and liver within 30 min (Cho et al. 2010). (Chithrani, Lu and Jin) reported the endocytosis rate of 10^{-6} min^{-1} of spherical-shaped gold NPs with 50 nm hydrodynamic size (Albanese and Chan 2011). Sonavane et al. studied the effect of particle size (15, 50, 100 and 200 nm) on biodistribution of prepared colloidal gold nanoparticles through IV administration (1 g/kg) to mice. Higher distribution of small gold NPs (15 nm) in kidney, lung, and spleen was observed. However, gold NPs (15 and 50 nm) crossed the blood-brain barrier and it was evident from the presence of gold NPs in the brain (Sonavane et al. 2008).

Core size: Core size (d_c) plays the major role to determine the saturation magnetization and monitor the relaxation times (T_1, T_2, and T_2^*) of contrast agents for magnetic

resonance imaging. Tong et al. reported three times increase in relaxation rate (r_2) by increasing the core size of IONPs from 5 to 14 nm (Ferguson et al. 2015; Tong et al. 2010). Gu et al. demonstrated fast biodegradation rates of IONPs with core size (15–30 nm) in spleen and liver but also reported higher toxicity issues. Large crystal size has stronger dipole and magnetostatic interactions with each other which result in cluster core formation with large hydrodynamic sizes (Roca et al. 2009). Lou et al. reported shorter half-life due to splenic and hepatic filtration for nanoparticles with large hydrodynamic sizes (4–200 nm). Large Au and IONPs have low surface volume, which presented low physically and chemically available sites for conjugation of desired therapeutic biomolecules and polymer coatings (Lou et al. 2012). Ferreira et al. reported the functionalized gold nanoparticles with Gd^{3+} chelates which showed enhanced relaxivity (29 mM^{-1} s^{-1}, 30 MHz, 25 °C) (Ferreira et al. 2012). Yang et al. investigated different size gold nanoparticles for their pharmacokinetics in mice and observed longer accumulation time for larger particle sizes (Fig. 14.6) (Yang et al. 2016). Table 14.2 describes the effect of different gold formulations on toxicity and subcellular localization.

Zeta potential and surface charge: Charge on gold and IONPs surface depends directly on molecular structure of the coated materials. Positive charge leads toward
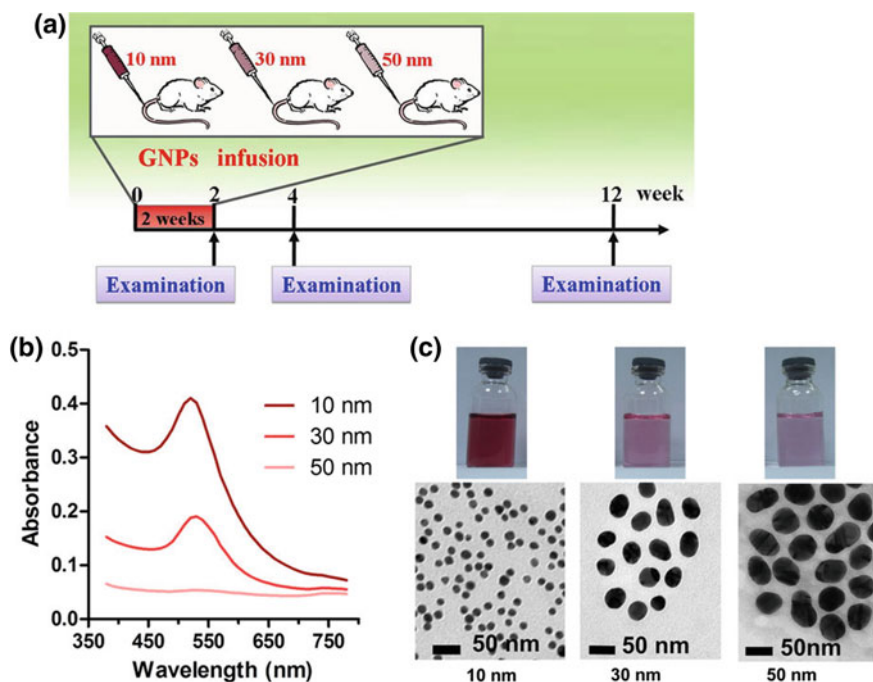

Fig. 14.6 Size-dependent studies of gold nanoparticles: **a** examination scheme; **b** absorption spectra of 19, 30, and 50 nm gold nanoparticles; and **c** suspension and images of different size gold nanoparticles. Reprinted from Yang et al. (2016)

Table 14.2 Subcellular localization of differed core-sized gold NPs modified from the literature (Levy et al. 2010)

Capping	Method	Core size of gold nanoparticles (nm)	Toxicity	Subcellular localization	References
DDPE	Ultrasound	100	Non-toxic	Endosomal	Soman et al. (2008)
2% Tat, 2% penetratin, 94% PEG, 2% NLS	CPP	16	Not reported	Nuclear and cytoplasmic	Nativo et al. (2008)
Sweet arrow peptide	CPP	12	Not reported	Endosomal	Pujals et al. (2009)
Tat peptide	CPP	2.8	Not reported	In nucleus and cytosolic around mitochondria	Berry (2008)
PEI	PEI	4	20-30% deaths	Some localized in nucleus and mainly in endosomal	Thomas and Klibanov (2003)
Phospholipids	Liposomes	1.4	Not reported	Lysosomes present near nuclear membranes	Chithrani et al. (2010)

attachment of large number of amine groups. However, carboxyl, sulfate, and hydroxyl groups contribute toward the negative charge. Functional groups at the NPs surfaces determine blood circulation time. Protein adsorption is also affected by the charge at the surface of nanoparticles (Mahmoudi et al. 2015). However, limited information is available regarding the role of functional groups on biodistribution and pharmacokinetics of gold- and iron-based NPs (Cole et al. 2011a). Huang et al. compared the zeta potential (+2 to 14 mV) of polyvinylpyrrolidone-coated IONPs accumulated in liver with Feridex (25 mV). They revealed the small liver uptake with large accumulation of positively charged IONPs (d_H = 118 nm) as compared to Feridex (d_H = 118 nm) (Huang et al. 2010).

Methods Used for Determining the Biodistribution and Pharmacokinetics of Iron- and Gold-Based Nanomaterials

Various methods are being used for the detection of low iron oxide and gold NPs concentrations (i.e., nanomoles per gram) in tissues of different organs and blood. These

methods can be classified roughly into magnetometry, imaging, and spectroscopy (Chertok et al. 2010). Imaging techniques, such as optical microscopy, transmission electron microscopy (TEM), magnetic particle imaging, and magnetic resonance imaging, are widely used for characterization of biodistribution of iron oxide- and gold-based nanomaterials. High-resolution TEM is useful technique to observe the distribution of IONPs and AuNPs in extracellular and intracellular regions of thin tissue slices (Giustini et al. 2011). TEM offers elemental and electron beam diffraction analysis, which can differentiate the encapsulated iron oxide in ferritins from crystalline superparamagnetic IONPs present. Consequently, TEM can provide detailed analysis of pharmacokinetics of gold and IONPs and recycle mechanisms (Torres Martin de Rosales et al. 2011). TEM requires electron transparent samples (thickness ~ 100 nm) and elaborative preparation methods. However, TEM can provide limited details of the specified region from the sample due to small field view. Many advanced techniques are being utilized for the quantification of nanomaterials (Hua et al. 2011; Levy et al. 2011). Recently, Abe et al. reported a non-destructive technique, X-ray scanning microscopy (XSAM), for elemental mapping of iron in mice, based on energy-dispersed fluorescent X-rays analysis in air, even when sample contains water (Abe et al. 2009). Histology is another cost-effective tissue analysis method which can provide the detailed information about the storage of these nanoparticles in larger tissue areas. Tissue sections are sometimes stained chemically with some suitable chemical agents such as Prussian blue for identification of gold and IONPs. Histopathological analysis through Prussian blue staining has some limitations, i.e., it can be beneficial for visualization of iron and gold ions but cannot detect nanoparticles before the degradation (Cole et al. 2011b). It cannot differentiate the endogenous iron oxide in different tissues from the one which administrated. For quantitative analysis, tissue sections (~100 to 200 mg) first dissolve in an acidic solution (1 mL, Aqua Regia). Then Prussian blue is added for absorbance measurements to quantify material in different organs (Maurizi et al. 2014). To study the peroxidase-mimicking activity of IONPs, another method is used in which peroxidase substrates are catalyzed, followed by oxidation to produce the color foci at the point of NPs accumulation in respective tissues. Zhuang et al. used this method for more accurate and highly sensitive quantification purposes and compared with Prussian blue staining method. They concluded higher sensitivity through magnetic NPs-peroxidase approach. They determined the distribution of magnetic NPs and clearance rata in different organs by quantifying those localized NPs in different organs. Higher sensitivity through magnetic NPs-peroxidase approach was reported (Zhuang et al. 2012). In addition to the traditionally used ex vivo imaging methods, in vivo imaging with MPI and MRI can also be used to study the biodistribution of these NPs. MRI is considered as non-destructive method for biodistribution of gold- and iron-based nanoparticles in the living organisms. In vivo tracking of IONPs through MRI with T_2 contrast has been used extensively but it is not suitable for higher concentrations of IONPs when localized in liver and spleen because T_2 signal saturates and produce the dark images, consequently, does not provide required information. Hoopes et al. used ultrashort T_2 MRI to produce the positive contrast with IONPs and cover the sensitivity issues of conventional MRI (Hoopes et al. 2012).

Real-time positive contrast micrographs can be obtained through MPI with iron and gold NPs. MPI shows the nonlinear magnetic response to AC applied magnetic field which induces the strong magnetic DC field gradient. MPI and MRI techniques can detect small concentration of gold and iron NPs up to nanograms per liter (Goodwill et al. 2012). Inductively coupled plasma atomic emission spectroscopy (ICP-AES) can also be used for chemical elemental analysis. In acid-digested tissues, ICP-AES can quantify the elemental iron with the concentration down to nanomoles per grams. However, the major limitation is its non-differentiating ability between endogenous and exogenous iron oxide nanomaterials (Gleich and Weizenecker 2005). Song et al. studied the gold contents from the enriched Gd (III)-polyvalvent Cy3-DNA-gold NPs in HeLa and NIH/3T3 cells through ICP-AES. They determined inductively coupled plasma mass spectroscopic ratio after cell internalization which remains constant for 24 h. It indicates no enzyme digestion activity of DNA-Gd^{III} @AuNP over long period of time (Song et al. 2009, 2012).

Fate and Biodegradation of Gold- and Iron Oxide-Based Nanoparticles

Degradation of Surface Coatings

Coating at the surface of nanoparticles provides them synthetic identity. However, in vivo stability of surface coatings is still challenging and need extensive studies. In vitro studies performed inside lysosomes/endosomes indicated release of polymer coatings from the NPs surface (Fadeel et al. 2013). The lysosomal/endo-cathepsin L enzyme separates one third part of the human protein and peptides conjugated with iron and gold NPs that show significant degradation in endosomal compartments (Sée et al. 2009). Lunov et al. reported degradation of carboxydextran shell formed at the superparamagnetic NPs core through a-glucosidase enzyme. Quantitative degradation through double labeling technique is reported in the literature (Lunov et al. 2010). Bargheer et al. studied the ^{125}I-labeled and ^{14}C-labeled covalently bounded peptide with the iron oxide ^{59}Fe-labeled core. They carried in vivo study by IV administration of ferucarbotran in mice which leads toward fast accumulation of iron in kidney and liver. They incorporated the ferucarbotran inside lysosomal vesicles contained α-glucosidase and confirmed the carboxydextran shell degradation from ferucarbotran particles (Bargheer et al. 2015b; Soenen et al. 2015). Distribution of radiolabeled NPs provides reliable and sensitive quantification in different parts of body. However, appropriate selection of isotopes is very critical. Many issues including role of enzymatic degradation in protein corona compositional exchange is still need to be unraveled (Bargheer et al. 2015a; Kreyling et al. 2015). Many in vitro studies suggested that lysosomal enzymes might digest original protein corona (PC) after intracellular incorporation. To detect such in situ modifications, many advanced

techniques such as fluorescence correlation spectroscopy and dynamic light scattering are applied for PC characterization of many biological liquid samples (Carambia et al. 2015; Lunov et al. 2010).

Degradation of Core

Ultimately, inorganic core of the NPs can be degraded. Recycling of inorganic part is important for the complete fate of the NMs in the body otherwise persistence can create different problems. Degradation of inorganic core highly depends on the composition of the material. FeO_X-based NPs are known as corrode and release metal ions (Soenen et al. 2015). However, AuNPs are considered more inert and stable against degradation. NPs can undergo structural alterations, and ligands (thiols) bind strongly with the gold surface and may pull out the gold atoms through ligand from the surface. Thiols are present in cells, such as glutathione, and so gold NPs dissolve slowly (Krüger et al. 2003; Paulsson et al. 2008). Nanocubes offered higher area ($6d^2$) and volume (d^3) for NPs having unit volume in contrast with the spherical NPs with area ($A = 4\pi(d/2)^2$) and volume ($V = (4\pi/3)(d/2)^3$), which lead toward the surface area equal to unity. Hence, cube NPs possess higher surface area as compared to spherical geometries for the same volume (Mejías et al. 2013). Lartigue and co-workers studied the degradation of amphiphilic coated iron oxide nanocubes and observed preferential degradation from the corner of the nanocubes due to inhomogeneous polymer functionalization (Fig. 14.7). They also observed the transfer of degraded iron species into ferritin proteins during in vivo studies. In another study, in our group based on iron oxide–gold hybrid nanostructures shows that iron oxide and gold have distinct degradation mechanisms and gold degraded at a longer time due to its inert nature in the biological environment (Fig. 14.8). Shape transitions are governed by thermodynamics of interaction of internalized NPs. Crystalline re-organization or degradation of inert NPs such as gold occurred to some extent. Superparamagnetic iron oxide (FeO_x)-based NPs are discussed here. Inductively coupled plasma mass spectroscopy is used for quantification of inorganic NPs cores and degradation residues in the body. In normal human, iron is present in hemoglobin, myoglobin, transferrin, and ferritin up to 65%, 4%, 0.1%, and 15–30%, respectively. Ferritins are present mainly in liver hepatocytes (Lévy et al. 2010). Mechanism of intracellular degradation of IONPs is much similar to ferritin. Protein shells dissolved first through lysosomal proteases and finally internalized IONPs released in acidic environment followed by rapid dissolution in lysosomes. Excess iron in the body can be stored in these apoferritins (empty ferritins) and/or can eliminate from the body through different releasing mechanisms. Functionalization and radiolabeling are common methods for tracking IONPs movements through different excretion routes (Lartigue et al. 2013). Bourrinet et al. labeled the dextran coating with $_{14}C$ tag and core of iron oxide with $_{56}Fe$, which showed faster clearance kinetics of dextran molecule as compared with core of iron (Bourrinet et al. 2006). Lamanna et al. reported the degradation and clearance rate of injected coated molecules after 56 days on a rat model up to 12.9% and 88.6% through feces and urine, respectively, whereas the administrated iron was excreted through urine and feces up to 21.8% and 16.8%, respectively (Arami et al. 2015; Feliu et al. 2016).
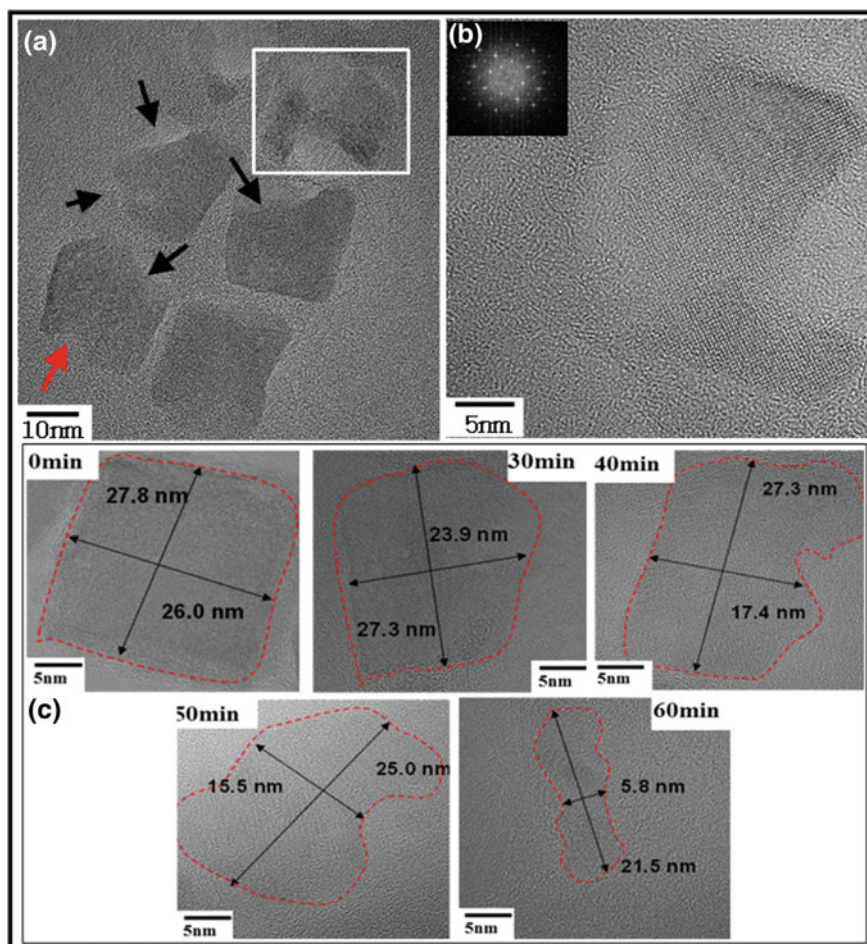
Fig. 14.7 Degradation of amphiphilic polymer-coated IONPs. **a** Thin layer of polymer at the corners make them more prone to degradation as compare to facets. **b** Residual nanoparticles maintain their original crystal structure. **c** From series of images at different time intervals (0–60 min) indicates the stochastic process of degradation. Reprinted with permission from Lartigue et al. (2013). Copyright (2013) American chemical society

Toxicity of Gold- and Iron Oxide-Based Nanoparticles

Toxicity of IONPs: IONPs are considered more safe, non-toxic, and biocompatible inorganic material. Reported lethal dose (LD-50) for uncoated IONPs is 300–600 mg Fe/Kg of the total body weight. However, this dose in case of dextran-coated IONPs, dextran used as biocompatible and stabilizing agent, can increase up to 2000–6000 mg Fe/Kg (Bourrinet et al. 2006; Tate et al. 2011). For carboxy dextran-coated IONPs, reported value of LD-50 was 30 mmol (Wada et al. 2001). However, more

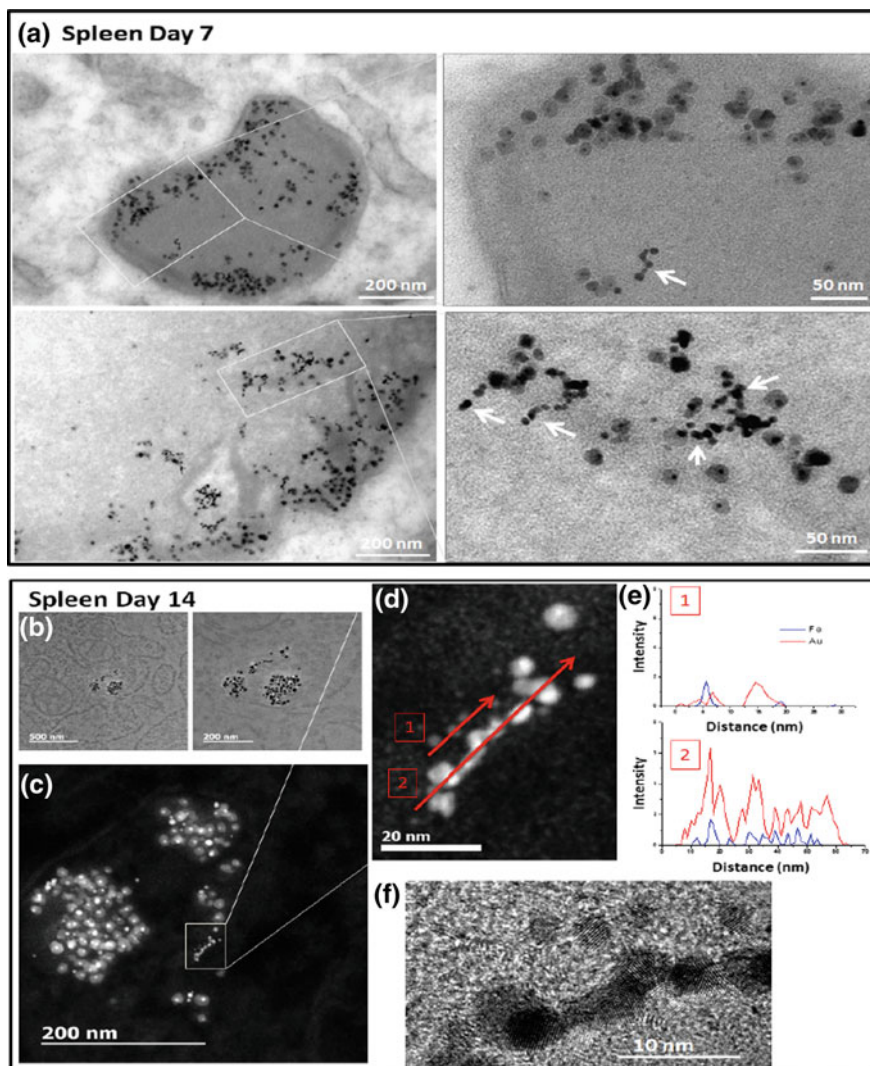**Fig. 14.8** Fate of gold–iron oxide dimers in vivo (Day 7 and Day 14 spleen). Distinct kinetics of gold moiety was observed (low biodegradability of gold) when compared with iron oxide. There was also the tendency of chain formation of gold nanoparticles after the corrosion of iron oxide part. Reprinted with permission from Kolosnjaj-Tabi et al. (2015). Copyright (2015) American chemical society

studies on the toxicity evaluation are needed for different types of fluorophores, polymers, radioactive tags, different synthetic capping agents (oleyl amine and oleic acid), and incorporated therapeutic molecules in different coating layers of the prepared IONPs. Long-term monitoring even for months or up to years are needed for in vivo evaluation of IONPS toxicities because degraded IONPs can circulate in the body for a longer duration (Gu et al. 2012). However, some ethical issues raised for carrying LD-50 measurements on animals. Traditional testing through LD-50 is not recommended by Food and Drug Administration, USA. Different pharmacokinetics and degradation rates of IONPs coatings and cores make studies more complicated. For example, Dextran-coated IONPs cleared from the body of rat after 56 days of administration, circulation of 80% injected IONPs were still reported as protein–iron complexes even after 84 days (Bourrinet et al. 2006; Yang et al. 2015). Jain et al. evaluated the toxicity followed by alkaline phosphatase, alanine aminotransferase, and aspartate aminotransferase tests on pluronic-coated IONPs with the hydrodynamic size (186–206 nm) in rats. They also reported the concentration of lipid hydroperoxide to evaluate the oxidative stress after IONPs administration. Minor transient changes of enzyme level in liver were reported for a period up to (6–24 h). Reduced oxidative stress in different types of tissues was also reported after 3 days (Jain et al. 2008). This was also confirmed by histological analysis, where no apparent abnormal changes were observed. Yang et al. analyzed changes in the gene expression inside liver of a mice after injected IONPs (hydrodynamic size = 14, 25, 34, 43 nm and core size = 10, 20, 30, 40 nm). After 1 and 7 days of injection, results showed that IONPs with small size (10 and 20 nm) might induce some changes in the susceptible genes (heme oxygenase 1, proprotein convertase subtilisin/kexin type 9) indicated some changes in the metabolic process and induce oxidative stress (Yang et al. 2015). Gu et al. evaluated in vivo toxicity of oleic acid capped monodispersed IONPs with hydrodynamic size of 5, 15, and 30 nm, which coated further with phospholipid PEG layer. Their hematology study revealed increased neutrophils after 24 h of administration that come back to normal level in next 30 days. Increased level of alkaline phosphatase and aspartate aminotransferase was observed due to shift of oleic acid molecules toward hepatocytes from liver macrophages (Fig. 14.9) (Gu et al. 2012). Monge-Fuentes et al. evaluated the toxicity of dimercaptosuccinic acid (DMSA)-coated IONPs in a group of monkeys (Monge-Fuentes et al. 2011). Previous studies on DMSA-coated IONPs preferentially confirmed the accumulation inside brain and lungs because of unknown mechanisms. No significant toxicity was observed in primate non-human models carried out for the period of 120 days (Mejías et al. 2011).

Clinical safety for human: Extensive clinical and preclinical research from the last two decades has been done for evaluation of possible side effects of administrated IONPS to humans. However, only formulation, silica-coated IONPs (i.e., Ferumoxsil) through oral route of administration and dextran-coated IONPs (i.e., Feridex or Ferumoxide, Feraheme or Fermoxytol, Resovist or Feraheme) through IV administration have been reached at clinical and preclinical trials. Toxicological profiles of IONPs with no side effects have been reported as clinically significant for standard pharmacological testing followed by oral or IV administration (McCormack
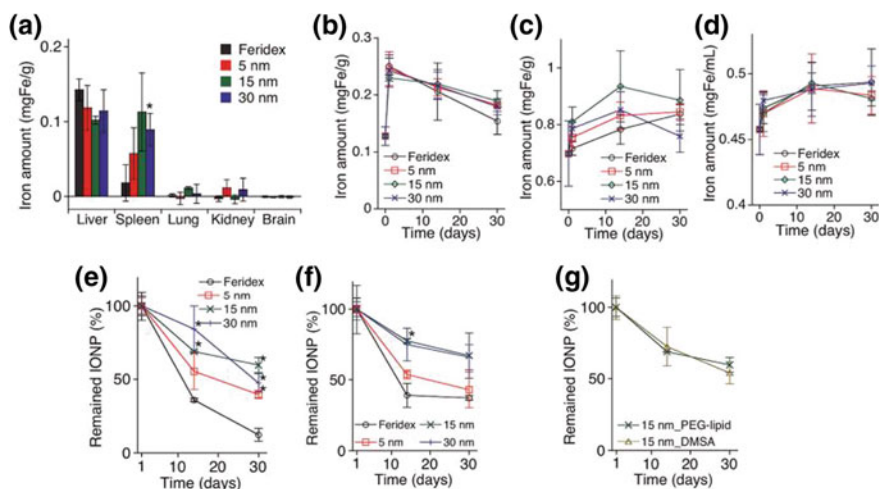
Fig. 14.9 In vivo pharmacokinetics of IONPs in mice **a** excess iron accumulation in different organs, liver, and spleen store more amount of iron as compare to other organs, **b–d** iron quantification by ICP-OES in liver, spleen, and blood, respectively, till one-month accumulation, **e–f** quantification of superparamagnetic/ferromagnetic ratio in liver and spleen as function of time, **g** quantification of superparamagnetic/ferromagnetic ratio in liver for different functionalization, PEG-lipid, and DMSA. Reprinted with permission from Gu et al. (2012). Copyright (2012) American Chemical Society

2012). Recently, Motoyama et al. studied the map of lymph node metastasis with fer-ucarbotran (Resovist) in 22 patients suffering from esophageal cancer and reported no side effects (Masselli and Gualdi 2012; Motoyama et al. 2012). In another study, Howarth et al. used dextran-coated IONPs for diagnosis of carotid inflammation in 20 patients and observed no toxicity (Howarth et al. 2009). For safety evaluation of Ferumoxtran-10, it was tested on group of 1777 adults, where they reported adverse effects such as pruritus, urticarial, headache, and back pain in 23.7% patients. Severe side effects (e.g., 2 cases of hypotension, skin rash, anaphylactic shock, decreased oxygen saturation, and chest pain) were detected in 0.42% patients (Bernd et al. 2009; Schiller et al. 2014). Due to undiluted IONPs, they reported one death by the bolus injection. Bolus IV administration is not recommended for IONPs. This results in the development of dextran-coated IONPs (Fereageme or Ferumoxytol) with lower molecular weight. The most recent clinical application of IONPs for the treatment of iron deficient chronic diseases is the approval of Ferahem or Ferumoxytol by US Food and Drug Administration (FDA) in June 2009. In 2012, IONPs with the name of Rienso gained European authorization (McCormack 2012). High-dose (510 mg one injection) tolerability and increased hemoglobin level in patients with the use of these products were reported (Lu et al. 2010). Most recent study performed on 396 patients in USA followed by 570, IV injections of IONPs revealed no severe side effects. In 22 patients, minor side effects (nasal congestion, headache, pruritus, chest discomfort, nausea, flushing, and myalgia) were reported (Lu et al. 2010). Hasan et al., reported

cerebral aneurysm due to early uptake of IONPs. In retrospective one-year study realized on 8666 US patients revealed some side effects [hypersensitivity (0.06%), loss of consciousness (0.03%), hypotension (0.12%), dyspnoea (0.05%), syncope (0.02%), anaphylactoid reaction (0.02%), unresponsive to stimuli (0.02%), and loss of consciousness (0.03%)] treated with IONPS (Hasan et al. 2012). Gastrointestinal effects (i.e., vomiting, diarrhea, nausea, abdominal pain, and constipation) were reported in 1562 US patients and some adverse effects in 7.9% patients during clinical study. However, long-term safety evaluation of IONPS is ambiguous and still under discussion (Hasan et al. 2012).

Toxicity of the gold nanoparticles: Particle size, shape and surface modifications of gold nanoparticles play a major role in controlling cellular localization, endocytosis effectiveness, and in vivo accumulation sites which is responsible for the cytotoxicity of gold nanoparticles. Ma et al. prepared gold nanoparticles with the diameter (10, 25, 50 nm). Large-sized gold nanoparticles (50 nm) were easily and efficiently taken up due to heavy dependence on the particle size (Schrand et al. 2010). Pan et al. reported the toxicity of gold nanoparticles (0.8–15 nm) with cell lines J774A1, L929, SKMel-28, and HeLa. Gold NPs with size (1.4 nm) showed more cytotoxicity with half-maximal inhibitory concentration (IC_{50}) values which range from (30 to 46 mmol/L). Lower IC_{50} values (250, 140, and 230 mmol/L) for the gold NPs with size of 0.8, 1.2 and 1.8 nm, respectively, were reported as compared to AuNP with 1.4 nm (Pan et al. 2007, 2009). Li et al. revealed faster internalization rate of spherical-shaped gold NPs followed by cube- and rod-like particles. Nangia et al. observed the damage by the translocation mechanism of functionalized gold NPs through cell membranes (Li and Rothberg 2004). They investigated the effect of different shapes by comparing high-index faceted shapes (pyramid and rice) with less faceted (cone and rod) shaped counterparts (Nangia and Sureshkumar 2012). Wang et al. investigated the toxicity of AuNPs of different shapes including sphere, polyhedron. and rod on zebrafish. They reported the higher toxicity effects of spherical AuNPs as compared to polyhedron- and rod-shaped particles. Polyhedron AuNPs elicited more lethality after storage as compared to other shaped NPs (Wang et al. 2016). Lipka et al. studied the kinetics after intratracheal and intravenous application of the modified gold nanoparticles with and without PEG coatings. Various gold contents in different organs and tissues were determined quantitively after 1 and 24 h. After vein tail injection of coated and naked AuNPs, accumulated contents were reported in the spleen and liver but after intratracheal administration majority of AuNPs were reported in the lungs. No change in translocation after intravenous administration toward circulation was observed after PEGylation of Au NPs. PEGylation of Au NPs (5 nm) greatly influenced the kinetics and uptake mechanism especially in spleen and liver. They also determined the prolonged time for blood circulation with PEG chains (Lipka et al. 2010).

Future Outcomes and Conclusion

Gold and IONPs possess safety factor with excellent biocompatibility due to their unique properties that can be optimized easily by tuning their distribution and size. Therefore, these NMs are usually considered as the most reliable candidates toward many biomedical applications such as cancer therapies (by separating stem cells labeling and malignant cells) and imaging purposes. Clinical success of gold- and iron oxide-based NPs mainly depends on short- and long-term tolerance ability in body, pharmacokinetics, and diagnostic or therapeutic functionality in the desired organs. Despite the comprehensive research done for the development of advanced instruments and characterization techniques from the last six decades, many questions are still unanswered regarding the effective and safe use of these prepared particles in different therapeutic and diagnostic applications. Various types of gold and IONPs have been prepared and functionalized by different types of coatings. However, only a few families of synthesized NPs have reached on clinical trials (Martin et al. 1955). In vivo performance of gold- and iron oxide-based nanoparticles significantly affected by hydrodynamic size, surface charge, core size, types of coatings, and polydispersity factors. However, experimental variations including human/animal models, route of administration, and characterization techniques for evaluation purposes are considered as influential factors. Establishment of the standard database is required for categorizing biodistribution, pharmacokinetics, and toxicity results to evaluate the required information in cost-effective and faster way. Same approach is needed for categorizing physical, chemical, and mechanical properties of a wide range of compounds and metallic alloys based on the parameters of complex processing and elemental compositions (Arami et al. 2015; Jia et al. 2017). Materials databases can be used as a key tool to address efficiently the clinical trials by providing valuable results. Effect of the additional parameters including rigidity, density, weight, mechanical flexibility, consistency, administrated dose, and molecular structure of gold/IONPs require to be studied.

References

Abe S, Kida I, Esaki M, Akasaka T, Uo M, Hosono T, Sato Y, Jeyadevan B, Kuboki Y, Morita M (2009) Biodistribution imaging of magnetic particles in mice: X-ray scanning analytical microscopy and magnetic resonance imaging. Bio-Med Mater Eng 19:213–220. https://doi.org/10.3233/bme-2009-0583

Adams DH, Eksteen B (2006) Aberrant homing of mucosal T cells and extra-intestinal manifestations of inflammatory bowel disease. Nat Rev Immunol 6:244–251. https://doi.org/10.1038/nri1784

Albanese A, Chan WC (2011) Effect of gold nanoparticle aggregation on cell uptake and toxicity. ACS Nano 5:5478–5489. https://doi.org/10.1021/nn2007496

Alexis F, Pridgen E, Molnar LK, Farokhzad OC (2008) Factors affecting the clearance and biodistribution of polymeric nanoparticles. Mol Pharm 5:505–515. https://doi.org/10.1021/mp800051m

Almeida JPM, Chen AL, Foster A, Drezek R (2011) In vivo biodistribution of nanoparticles. Nanomedicine 6:815–835. https://doi.org/10.2217/nnm.11.79

Arami H, Khandhar A, Liggitt D, Krishnan KM (2015) In vivo delivery, pharmacokinetics, biodistribution and toxicity of iron oxide nanoparticles. Chem Soc Rev 44:8576–8607. https://doi.org/10.1039/c5cs00541h

Bachmann R, Conrad R, Kreft B, Luzar O, Block W, Flacke S, Pauleit D, Träber F, Gieseke J, Saebo K (2002) Evaluation of a new ultrasmall superparamagnetic iron oxide contrast agent Clariscan®, (NC100150) for MRI of renal perfusion: experimental study in an animal model. J Magn Reson Imaging 16:190–195. https://doi.org/10.1002/jmri.10149

Balasubramanian SK, Jittiwat J, Manikandan J, Ong C-N, Liya EY, Ong W-Y (2010) Biodistribution of gold nanoparticles and gene expression changes in the liver and spleen after intravenous administration in rats. Biomaterials 31:2034–2042. https://doi.org/10.1016/j.biomaterials.2009.11.079

Bargheer D, Giemsa A, Freund B, Heine M, Waurisch C, Stachowski GM, Hickey SG, Eychmüller A, Heeren J, Nielsen P (2015a) The distribution and degradation of radiolabeled superparamagnetic iron oxide nanoparticles and quantum dots in mice. Beilstein J Nanotechnol 6:111. https://doi.org/10.3762/bjnano.6.11

Bargheer D, Nielsen J, Gébel G, Heine M, Salmen SC, Stauber R, Weller H, Heeren J, Nielsen P (2015b) The fate of a designed protein corona on nanoparticles in vitro and in vivo. Beilstein J Nanotechnol 6:36. https://doi.org/10.3762/bjnano.6.5

Beckmann N, Cannet C, Babin AL, Blé FX, Zurbruegg S, Kneuer R, Dousset V (2009) In vivo visualization of macrophage infiltration and activity in inflammation using magnetic resonance imaging. Wiley Interdisc Rev Nanomed Nanobiotechnol 1:272–298. https://doi.org/10.1002/wnan.16

Bernd H, De Kerviler E, Gaillard S, Bonnemain B (2009) Safety and tolerability of ultrasmall superparamagnetic iron oxide contrast agent: comprehensive analysis of a clinical development program. Invest Radiol 44:336–342. https://doi.org/10.1097/rli.0b013e3181a0068b

Berry C (2008) Intracellular delivery of nanoparticles via the HIV-1 tat peptide. https://doi.org/10.2217/17435889.3.3.357

Bourrinet P, Bengele HH, Bonnemain B, Dencausse A, Idee J-M, Jacobs PM, Lewis JM (2006) Preclinical safety and pharmacokinetic profile of ferumoxtran-10, an ultrasmall superparamagnetic iron oxide magnetic resonance contrast agent. Invest Radiol 41:313–324. https://doi.org/10.1097/01.rli.0000197669.80475.dd

Branca M, Marciello M, Ciuculescu-Pradines D, Respaud M, del Puerto Morales M, Serra R, Casanove M-J, Amiens C (2015) Towards MRI T2 contrast agents of increased efficiency. J Magn Magn Mater 377:348–353. https://doi.org/10.1016/j.jmmm.2014.10.086

Briley-Saebo KC, Cho YS, Shaw PX, Ryu SK, Mani V, Dickson S, Izadmehr E, Green S, Fayad ZA, Tsimikas S (2011) Targeted iron oxide particles for in vivo magnetic resonance detection of atherosclerotic lesions with antibodies directed to oxidation-specific epitopes. J Am Coll Cardiol 57:337–347. https://doi.org/10.1016/j.jacc.2010.09.023

Carambia A, Freund B, Schwinge D, Bruns OT, Salmen SC, Ittrich H, Reimer R, Heine M, Huber S, Waurisch C (2015) Nanoparticle-based autoantigen delivery to Treg-inducing liver sinusoidal endothelial cells enables control of autoimmunity in mice. J Hepatol 62:1349–1356. https://doi.org/10.1016/j.jhep.2015.01.006

Carrillo-Carrión C, Nazarenus M, Paradinas SS, Carregal-Romero S, Almendral MJ, Fuentes M, Pelaz B, del Pino P, Hussain I, Clift MJ (2014) Metal ions in the context of nanoparticles toward biological applications. Curr Opin Chem Eng 4:88–96. https://doi.org/10.1016/j.coche.2013.11.006

Cedervall T, Lynch I, Lindman S, Berggård T, Thulin E, Nilsson H, Dawson KA, Linse S (2007) Understanding the nanoparticle–protein corona using methods to quantify exchange rates and affinities of proteins for nanoparticles. Proc Natl Acad Sci 104:2050–2055. https://doi.org/10.1073/pnas.0608582104

Chertok B, Cole AJ, David AE, Yang VC (2010) Comparison of electron spin resonance spectroscopy and inductively-coupled plasma optical emission spectroscopy for biodistribution analysis of iron-oxide nanoparticles. Mol Pharm 7:375–385. https://doi.org/10.1021/mp900161h

Chithrani DB, Dunne M, Stewart J, Allen C, Jaffray DA (2010) Cellular uptake and transport of gold nanoparticles incorporated in a liposomal carrier. Nanomed Nanotechnol Biol Med 6:161–169. https://doi.org/10.1016/j.nano.2009.04.009

Cho W-S, Cho M, Jeong J, Choi M, Han BS, Shin H-S, Hong J, Chung BH, Jeong J, Cho M-H (2010) Size-dependent tissue kinetics of PEG-coated gold nanoparticles. Toxicol Appl Pharmacol 245:116–123. https://doi.org/10.1016/j.taap.2010.02.013

Clarke S, Pinaud F, Beutel O, You C, Piehler J, Dahan M (2010) Covalent monofunctionalization of peptide-coated quantum dots for single-molecule assays. Nano Lett 10:2147–2154. https://doi.org/10.1021/nl100825n

Cole AJ, David AE, Wang J, Galbán CJ, Hill HL, Yang VC (2011a) Polyethylene glycol modified, cross-linked starch-coated iron oxide nanoparticles for enhanced magnetic tumor targeting. Biomaterials 32:2183–2193. https://doi.org/10.1016/j.biomaterials.2010.11.040

Cole AJ, David AE, Wang J, Galbán CJ, Yang VC (2011b) Magnetic brain tumor targeting and biodistribution of long-circulating PEG-modified, cross-linked starch-coated iron oxide nanoparticles. Biomaterials 32:6291–6301. https://doi.org/10.1016/j.biomaterials.2011.05.024

Colombo M, Carregal-Romero S, Casula MF, Gutiérrez L, Morales MP, Böhm IB, Heverhagen JT, Prosperi D, Parak WJ (2012) Biological applications of magnetic nanoparticles. Chem Soc Rev 41:4306–4334. https://doi.org/10.1039/c2cs15337h

Cui X, Li Z, Zhong S, Wang B, Han Y, Wang H, Möhwald H (2013) A facile sonochemical route for the fabrication of magnetic protein microcapsules for targeted delivery. Chem-A Eur J 19:9485–9488. https://doi.org/10.1002/chem.201301302

De Jong WH, Hagens WI, Krystek P, Burger MC, Sips AJ, Geertsma RE (2008) Particle size-dependent organ distribution of gold nanoparticles after intravenous administration. Biomaterials 29:1912–1919. https://doi.org/10.1016/j.biomaterials.2007.12.037

del Pino P (2014) Tailoring the interplay between electromagnetic fields and nanomaterials toward applications in life sciences: a review. J Biomed Opt 19:101507. https://doi.org/10.1117/1.jbo.19.10.101507

Di Corato R, Espinosa A, Lartigue L, Tharaud M, Chat S, Pellegrino T, Ménager C, Gazeau F, Wilhelm C (2014) Magnetic hyperthermia efficiency in the cellular environment for different nanoparticle designs. Biomaterials 35:6400–6411. https://doi.org/10.1016/j.biomaterials.2014.04.036

Ding H-m, Ma Y-q (2014) Computer simulation of the role of protein corona in cellular delivery of nanoparticles. Biomaterials 35:8703–8710. https://doi.org/10.1016/j.biomaterials.2014.06.033

Docter D, Strieth S, Westmeier D, Hayden O, Gao M, Knauer SK, Stauber RH (2015a) No king without a crown–impact of the nanomaterial-protein corona on nanobiomedicine. Nanomedicine 10:503–519. https://doi.org/10.2217/nnm.14.184

Docter D, Westmeier D, Markiewicz M, Stolte S, Knauer S, Stauber R (2015b) The nanoparticle biomolecule corona: lessons learned–challenge accepted? Chem Soc Rev 44:6094–6121. https://doi.org/10.1039/c5cs00217f

Drakesmith H, Prentice A (2008) Viral infection and iron metabolism. Nat Rev Microbiol 6:541–552. https://doi.org/10.1038/nrmicro1930

Fadeel B, Feliu N, Vogt C, Abdelmonem AM, Parak WJ (2013) Bridge over troubled waters: understanding the synthetic and biological identities of engineered nanomaterials. Wiley Interdisc Rev Nanomed Nanobiotechnol 5:111–129. https://doi.org/10.1002/wnan.1206

Feliu N, Docter D, Heine M, del Pino P, Ashraf S, Kolosnjaj-Tabi J, Macchiarini P, Nielsen P, Alloyeau D, Gazeau F, Stauber RH, Parak WJ (2016) In vivo degeneration and the fate of inorganic nanoparticles. Chem Soc Rev 45:2440–2457. https://doi.org/10.1039/c5cs00699f

Ferguson RM, Khandhar AP, Kemp SJ, Arami H, Saritas EU, Croft LR, Konkle J, Goodwill PW, Halkola A, Rahmer J (2015) Magnetic particle imaging with tailored iron oxide nanoparticle tracers. IEEE Trans Med Imaging 34:1077–1084. https://doi.org/10.1109/tmi.2014.2375065

Ferrari M, Philibert M, Sanhai W (2009) Nanomedicine and society. Clin Pharmacol Ther 85:466–467. https://doi.org/10.1038/nbt1377

Ferreira M, Mousavi B, Ferreira P, Martins C, Helm L, Martins JA, Geraldes CF (2012) Gold nanoparticles functionalised with stable, fast water exchanging Gd 3+ chelates as high relaxivity contrast agents for MRI. Dalton Trans 41:5472–5475. https://doi.org/10.1039/c2dt30388d

Fricks BB, Wacker F, Loddenkemper C, Valdeig S, Hotz B, Wolf K-J, Misselwitz B, Kühl A, Hoffmann JC (2009) Magnetic resonance imaging of experimental inflammatory bowel disease: quantitative and qualitative analyses with histopathologic correlation in a rat model using the ultrasmall iron oxide SHU 555 C. Invest Radiol 44:23–30. https://doi.org/10.1097/rli.0b013e3181899025

Freund B, Tromsdorf UI, Bruns OT, Heine M, Giemsa A, Bartelt A, Salmen SC, Raabe N, Heeren J, Ittrich H (2012) A simple and widely applicable method to 59Fe-radiolabel monodisperse superparamagnetic iron oxide nanoparticles for in vivo quantification studies. ACS Nano 6:7318–7325. https://doi.org/10.1021/nn3024267

Giustini A, Ivkov R, Hoopes P (2011) Magnetic nanoparticle biodistribution following intratumoral administration. Nanotechnology 22:345101. https://doi.org/10.1088/0957-4484/22/34/345101

Gleich B, Weizenecker J (2005) Tomographic imaging using the nonlinear response of magnetic particles. Nature 435:1214. https://doi.org/10.1038/nature03808

Goodwill PW, Saritas EU, Croft LR, Kim TN, Krishnan KM, Schaffer DV, Conolly SM (2012) X-space MPI: magnetic nanoparticles for safe medical imaging. Adv Mater 24:3870–3877. https://doi.org/10.1002/adma.201200221

Gu L, Fang RH, Sailor MJ, Park J-H (2012) In vivo clearance and toxicity of monodisperse iron oxide nanocrystals. ACS Nano 6:4947–4954. https://doi.org/10.1021/nn300456z

Gupta AK, Wells S (2004) Surface-modified superparamagnetic nanoparticles for drug delivery: preparation, characterization, and cytotoxicity studies. IEEE Trans Nanobiosci 3:66–73. https://doi.org/10.1109/tnb.2003.820277

Hainfeld J, Slatkin D, Focella T, Smilowitz H (2006) Gold nanoparticles: a new X-ray contrast agent. Br J Radiol 79:248–253. https://doi.org/10.1259/bjr/13169882

Hasan D, Chalouhi N, Jabbour P, Dumont AS, Kung DK, Magnotta VA, Young WL, Hashimoto T, Winn HR, Heistad D (2012) Early change in ferumoxytol-enhanced magnetic resonance imaging signal suggests unstable human cerebral aneurysm: a pilot study. Stroke 43:3258–3265. https://doi.org/10.1161/strokeaha.112.673400

Helou M, Reisbeck M, Tedde SF, Richter L, Bär L, Bosch JJ, Stauber RH, Quandt E, Hayden O (2013) Time-of-flight magnetic flow cytometry in whole blood with integrated sample preparation. Lab Chip 13:1035–1038. https://doi.org/10.1039/c3lc41310a

Hillaireau H, Couvreur P (2009) Nanocarriers' entry into the cell: relevance to drug delivery. Cell Mol Life Sci 66:2873–2896. https://doi.org/10.1007/s00018-009-0053-z

Hillyer JF, Albrecht RM (2001) Gastrointestinal persorption and tissue distribution of differently sized colloidal gold nanoparticles. J Pharm Sci 90:1927–1936. https://doi.org/10.1002/jps.1143

Hirn S, Semmler-Behnke M, Schleh C, Wenk A, Lipka J, Schäffler M, Takenaka S, Möller W, Schmid G, Simon U (2011) Particle size-dependent and surface charge-dependent biodistribution of gold nanoparticles after intravenous administration. Eur J Pharm Biopharm 77:407–416. https://doi.org/10.1016/j.ejpb.2010.12.029

Hoopes PJ, Petryk AA, Gimi B, Giustini AJ, Weaver JB, Bischof J, Chamberlain R, Garwood M (2012) In vivo imaging and quantification of iron oxide nanoparticle uptake and biodistribution. In: Medical imaging 2012: biomedical applications in molecular, structural, and functional imaging. International society for optics and photonics, p 83170R. https://doi.org/10.1117/12.916097

Howarth S, Tang T, Trivedi R, Weerakkody R, U-King-Im J, Gaunt M, Boyle J, Li Z, Miller S, Graves M (2009) Utility of USPIO-enhanced MR imaging to identify inflammation and the fibrous cap: a comparison of symptomatic and asymptomatic individuals. Eur J Radiol 70:555–560. https://doi.org/10.1016/j.ejrad.2008.01.047

Hua M-Y, Liu H-L, Yang H-W, Chen P-Y, Tsai R-Y, Huang C-Y, Tseng I-C, Lyu L-A, Ma C-C, Tang H-J (2011) The effectiveness of a magnetic nanoparticle-based delivery system for BCNU in

the treatment of gliomas. Biomaterials 32:516–527. https://doi.org/10.1016/j.biomaterials.2010. 09.065

Huang J, Bu L, Xie J, Chen K, Cheng Z, Li X, Chen X (2010) Effects of nanoparticle size on cellular uptake and liver MRI with polyvinylpyrrolidone-coated iron oxide nanoparticles. ACS Nano 4:7151–7160. https://doi.org/10.1021/nn101643u

Jain TK, Reddy MK, Morales MA, Leslie-Pelecky DL, Labhasetwar V (2008) Biodistribution, clearance, and biocompatibility of iron oxide magnetic nanoparticles in rats. Mol Pharm 5:316– 327. https://doi.org/10.1021/mp7001285

Javed Y, Akhtar K, Anwar H, Jamil Y (2017) MRI based on iron oxide nanoparticles contrast agents: effect of oxidation state and architecture. J Nanopart Res 19:366. https://doi.org/10.1007/s11051-017-4045-x

Jia Y-P, Ma B-Y, Wei X-W, Qian Z-Y (2017) The in vitro and in vivo toxicity of gold nanoparticles. Chin Chem Lett 28:691–702. https://doi.org/10.1016/j.cclet.2017.01.021

Jones SW, Roberts RA, Robbins GR, Perry JL, Kai MP, Chen K, Bo T, Napier ME, Ting JP, DeSimone JM (2013) Nanoparticle clearance is governed by Th1/Th2 immunity and strain background. J Clin Investig 123:3061–3073. https://doi.org/10.1172/JCI66895

Klapper Y, Maffre P, Shang L, Ekdahl KN, Nilsson B, Hettler S, Dries M, Gerthsen D, Nienhaus GU (2015) Low affinity binding of plasma proteins to lipid-coated quantum dots as observed by in situ fluorescence correlation spectroscopy. Nanoscale 7:9980–9984. https://doi.org/10.1039/C5NR01694K

Kolosnjaj-Tabi J, Javed Y, Lartigue L, Volatron J, Elgrabli D, Marangon I, Pugliese G, Caron B, Figuerola A, Luciani N, Pellegrino T, Alloyeau D, Gazeau F (2015) The one year fate of iron oxide coated gold nanoparticles in mice. ACS Nano 9:7925–7939. https://doi.org/10.1021/acsnano.5b00042

Kolosnjaj-Tabi J, Volatron J, Gazeau F (2017) Basic principles of in vivo distribution, toxicity, and degradation of prospective inorganic nanoparticles for imaging. In: Design and applications of nanoparticles in biomedical imaging. Springer, pp 9–41. https://doi.org/10.1007/978-3-319-42169-8_2

Kreyling WG, Abdelmonem AM, Ali Z, Alves F, Geiser M, Haberl N, Hartmann R, Hirn S, De Aberasturi DJ, Kantner K (2015) In vivo integrity of polymer-coated gold nanoparticles. Nat Nanotechnol 10:619. https://doi.org/10.1038/nnano.2015.111

Krüger D, Rousseau R, Fuchs H, Marx D (2003) Towards "mechanochemistry": mechanically induced isomerizations of thiolate–gold clusters. Angew Chem Int Ed 42:2251–2253. https://doi.org/10.1002/anie.200351000

Kunzmann A, Andersson B, Thurnherr T, Krug H, Scheynius A, Fadeel B (2011) Toxicology of engineered nanomaterials: focus on biocompatibility, biodistribution and biodegradation. Biochim et Biophys Acta (BBA)-Gen Subj 1810:361–373. https://doi.org/10.1016/j.bbagen.2010.04.007

Lan Q, Hsiung CA, Matsuo K, Hong Y-C, Seow A, Wang Z, Hosgood HD III, Chen K, Wang J-C, Chatterjee N (2012) Genome-wide association analysis identifies new lung cancer susceptibility loci in never-smoking women in Asia. Nat Genet 44:1330. https://doi.org/10.1038/ng.2456

Lartigue L, Alloyeau D, Kolosnjaj-Tabi J, Javed Y, Guardia P, Riedinger A, Péchoux C, Pellegrino T, Wilhelm C, Gazeau F (2013) Biodegradation of iron oxide nanocubes: high-resolution in situ monitoring. ACS Nano 7:3939–3952. https://doi.org/10.1021/nn305719y

Levy R, Shaheen U, Cesbron Y, See V (2010) Gold nanoparticles delivery in mammalian live cells: a critical review. Nano Rev 1:4889. https://doi.org/10.3402/nano.v1i0.4889

Levy M, Luciani N, Alloyeau D, Elgrabli D, Deveaux V, Pechoux C, Chat S, Wang G, Vats N, Gendron F (2011) Long term in vivo biotransformation of iron oxide nanoparticles. Biomaterials 32:3988–3999. https://doi.org/10.1016/j.biomaterials.2011.02.031

Lévy M, Lagarde F, Maraloiu V-A, Blanchin M-G, Gendron F, Wilhelm C, Gazeau F (2010) Degradability of superparamagnetic nanoparticles in a model of intracellular environment: follow-up of magnetic, structural and chemical properties. Nanotechnology 21:395103. https://doi.org/10.1088/0957-4484/21/39/395103

Lévy M, Wilhelm C, Devaud M, Levitz P, Gazeau F (2012) How cellular processing of superparamagnetic nanoparticles affects their magnetic behavior and NMR relaxivity. Contrast Media Mol Imaging 7:373–383. https://doi.org/10.1002/cmmi.504

Li H, Rothberg L (2004) Colorimetric detection of DNA sequences based on electrostatic interactions with unmodified gold nanoparticles. Proc Natl Acad Sci USA 101:14036–14039. https://doi.org/10.1073/pnas.0406115101

Lin C-AJ, Yang T-Y, Lee C-H, Huang SH, Sperling RA, Zanella M, Li JK, Shen J-L, Wang H-H, Yeh H-I (2009) Synthesis, characterization, and bioconjugation of fluorescent gold nanoclusters toward biological labeling applications. ACS Nano 3:395–401. https://doi.org/10.1021/nn800632j

Lipka J, Semmler-Behnke M, Sperling RA, Wenk A, Takenaka S, Schleh C, Kissel T, Parak WJ, Kreyling WG (2010) Biodistribution of PEG-modified gold nanoparticles following intratracheal instillation and intravenous injection. Biomaterials 31:6574–6581. https://doi.org/10.1016/j.biomaterials.2010.05.009

Liu J, Yu M, Zhou C, Yang S, Ning X, Zheng J (2013) Passive tumor targeting of renal-clearable luminescent gold nanoparticles: long tumor retention and fast normal tissue clearance. J Am Chem Soc 135:4978–4981. https://doi.org/10.1021/ja401612x

Lou S, Ye J-y, Li K-q, Wu A (2012) A gold nanoparticle-based immunochromatographic assay: the influence of nanoparticulate size. Analyst 137:1174–1181. https://doi.org/10.1039/C2AN15844B

Lu M, Cohen MH, Rieves D, Pazdur R (2010) FDA report: ferumoxytol for intravenous iron therapy in adult patients with chronic kidney disease. Am J Hematol 85:315–319. https://doi.org/10.1002/ajh.21656

Lunov O, Syrovets T, Röcker C, Tron K, Nienhaus GU, Rasche V, Mailänder V, Landfester K, Simmet T (2010) Lysosomal degradation of the carboxydextran shell of coated superparamagnetic iron oxide nanoparticles and the fate of professional phagocytes. Biomaterials 31:9015–9022. https://doi.org/10.1016/j.biomaterials.2010.08.003

Luo Z, Cai K, Hu Y, Li J, Ding X, Zhang B, Xu D, Yang W, Liu P (2012) Redox-responsive molecular nanoreservoirs for controlled intracellular anticancer drug delivery based on magnetic nanoparticles. Adv Mater 24:431–435. https://doi.org/10.1002/adma.201103458

Mahmoudi M, Sheibani S, Milani AS, Rezaee F, Gauberti M, Dinarvand R, Vali H (2015) Crucial role of the protein corona for the specific targeting of nanoparticles. Nanomedicine 10:215–226. https://doi.org/10.2217/nnm.14.69

Mahon E, Hristov DR, Dawson KA (2012) Stabilising fluorescent silica nanoparticles against dissolution effects for biological studies. Chem Commun 48:7970–7972. https://doi.org/10.1039/C2CC34023B

Martin L, Bates C, Beresford C, Donaldson J, McDonald F, Dunlop D, Sheard P, London E, Twigg G (1955) The pharmacology of an iron-dextran intramuscular haematinic. Br J Pharmacol 10:375–382. https://doi.org/10.1111/j.1476-5381.1955.tb00887.x

Masselli G, Gualdi G (2012) MR imaging of the small bowel. Radiology 264:333–348. https://doi.org/10.1148/radiol.12111658

Maurizi L, Sakulkhu U, Gramoun A, Vallee J-P, Hofmann H (2014) A fast and reproducible method to quantify magnetic nanoparticle biodistribution. Analyst 139:1184–1191. https://doi.org/10.1039/C3AN02153J

McCormack PL (2012) Ferumoxytol. Drugs 72:2013–2022. https://doi.org/10.2165/11209880-000000000-00000

Mejías R, Pérez-Yagüe S, Gutiérrez L, Cabrera LI, Spada R, Acedo P, Serna CJ, Lázaro FJ, Villanueva Á, del Puerto Morales M (2011) Dimercaptosuccinic acid-coated magnetite nanoparticles for magnetically guided in vivo delivery of interferon gamma for cancer immunotherapy. Biomaterials 32:2938–2952. https://doi.org/10.1016/j.biomaterials.2011.01.008

Mejías R, Gutiérrez L, Salas G, Pérez-Yagüe S, Zotes TM, Lázaro FJ, Morales MP, Barber DF (2013) Long term biotransformation and toxicity of dimercaptosuccinic acid-coated magnetic nanoparticles support their use in biomedical applications. J Controlled Release 171:225–233. https://doi.org/10.1016/j.jconrel.2013.07.019

Melancon MP, Lu W, Li C (2009) Gold-based magneto/optical nanostructures: challenges for in vivo applications in cancer diagnostics and therapy. MRS Bull 34:415–421. https://doi.org/10.1557/mrs2009.117

Monge-Fuentes V, Garcia MP, Tavares MCH, Valois CR, Lima EC, Teixeira DS, Morais PC, Tomaz C, Azevedo RB (2011) Biodistribution and biocompatibility of DMSA-stabilized maghemite magnetic nanoparticles in nonhuman primates (Cebus spp.). Nanomedicine 6:1529–1544. https://doi.org/10.2217/nnm.11.47

Monopoli MP, Åberg C, Salvati A, Dawson KA (2012) Biomolecular coronas provide the biological identity of nanosized materials. Nat Nanotechnol 7:779. https://doi.org/10.1038/nnano.2012.207

Montenegro J-M, Grazu V, Sukhanova A, Agarwal S, Jesus M, Nabiev I, Greiner A, Parak WJ (2013) Controlled antibody/(bio-) conjugation of inorganic nanoparticles for targeted delivery. Adv Drug Deliv Rev 65:677–688. https://doi.org/10.1016/j.addr.2012.12.003

Moore A, Marecos E, Bogdanov A Jr, Weissleder R (2000) Tumoral distribution of long-circulating dextran-coated iron oxide nanoparticles in a rodent model. Radiology 214:568–574. https://doi.org/10.1148/radiology.214.2.r00fe19568

Morais T, Soares ME, Duarte JA, Soares L, Maia S, Gomes P, Pereira E, Fraga S, Carmo H, de Lourdes Bastos M (2012) Effect of surface coating on the biodistribution profile of gold nanoparticles in the rat. Eur J Pharm Biopharm 80:185–193. https://doi.org/10.1016/j.ejpb.2011.09.005

Motoyama S, Ishiyama K, Maruyama K, Narita K, Minamiya Y, Ogawa J-i (2012) Estimating the need for neck lymphadenectomy in submucosal esophageal cancer using superparamagnetic iron oxide-enhanced magnetic resonance imaging: clinical validation study. World J Surg 36:83–89. https://doi.org/10.1007/s00268-011-1322-1

Murday JS, Siegel RW, Stein J, Wright JF (2009) "Translational nanomedicine: status assessment and opportunities. Nanomed Nanotechnol Biol Med 5:251–273. https://doi.org/10.1016/j.nano.2009.06.001

Nangia S, Sureshkumar R (2012) Effects of nanoparticle charge and shape anisotropy on translocation through cell membranes. Langmuir 28:17666–17671

Nativo P, Prior IA, Brust M (2008) Uptake and intracellular fate of surface-modified gold nanoparticles. ACS Nano 2:1639–1644. https://doi.org/10.1021/nn800330a

Pan Y, Neuss S, Leifert A, Fischler M, Wen F, Simon U, Schmid G, Brandau W, Jahnen-Dechent W (2007) Size-dependent cytotoxicity of gold nanoparticles. Small 3:1941–1949. https://doi.org/10.1002/smll.200700378

Pan Y, Leifert A, Ruau D, Neuss S, Bornemann J, Schmid G, Brandau W, Simon U, Jahnen-Dechent W (2009) Gold nanoparticles of diameter 1.4 nm trigger necrosis by oxidative stress and mitochondrial damage. Small 5:2067–2076. https://doi.org/10.1002/smll.200900466

Parak WJ, Gerion D, Pellegrino T, Zanchet D, Micheel C, Williams SC, Boudreau R, Le Gros MA, Larabell CA, Alivisatos AP (2003) Biological applications of colloidal nanocrystals. Nanotechnology 14:R15. https://doi.org/10.1088/0957-4484/14/7/201

Parween S, Ali A, Chauhan VS (2013) Non-natural amino acids containing peptide-capped gold nanoparticles for drug delivery application. ACS Appl Mater Interfaces 5:6484–6493. https://doi.org/10.1021/am4017973

Paulsson M, Krag C, Frederiksen T, Brandbyge M (2008) Conductance of alkanedithiol single-molecule junctions: a molecular dynamics study. Nano Lett 9:117–121. https://doi.org/10.1021/nl802643h

Pautler M, Brenner S (2010) Nanomedicine: promises and challenges for the future of public health. Int J Nanomed 5:803. https://doi.org/10.2147/IJN.S13816

Peer D, Karp JM, Hong S, Farokhzad OC, Margalit R, Langer R (2007) Nanocarriers as an emerging platform for cancer therapy. Nat Nanotechnol 2:751. https://doi.org/10.1038/nnano.2007.387

Pelaz B, Charron G, Pfeiffer C, Zhao Y, De La Fuente JM, Liang XJ, Parak WJ, Del Pino P (2013) Interfacing engineered nanoparticles with biological systems: anticipating adverse nano–bio interactions. Small 9:1573–1584. https://doi.org/10.1002/smll.201201229

Pillai S, Cariappa A (2009) The follicular versus marginal zone B lymphocyte cell fate decision. Nat Rev Immunol 9:767–777. https://doi.org/10.1038/nri2656

Prabhu P, Patravale V (2012) The upcoming field of theranostic nanomedicine: an overview. J Biomed Nanotechnol 8:859–882. https://doi.org/10.1166/jbn.2012.1459

Pujals S, Bastús NG, Pereiro E, López-Iglesias C, Puntes VF, Kogan MJ, Giralt E (2009) Shuttling gold nanoparticles into tumoral cells with an amphipathic proline-rich peptide. ChemBioChem 10:1025–1031. https://doi.org/10.1002/cbic.200800843

Riehemann K, Schneider SW, Luger TA, Godin B, Ferrari M, Fuchs H (2009) Nanomedicine—challenge and perspectives. Angew Chem Int Ed 48:872–897. https://doi.org/10.1002/anie.200802585

Rivera-Gil P, Jimenez De Aberasturi D, Wulf V, Pelaz B, Del Pino P, Zhao Y, De La Fuente JM, Ruiz De Larramendi I, Rojo Tf, Liang X-J (2012) The challenge to relate the physicochemical properties of colloidal nanoparticles to their cytotoxicity. Acc Chem Res 46:743–749. https://doi.org/10.1021/ar300039j

Rizzo LY, Theek B, Storm G, Kiessling F, Lammers T (2013) Recent progress in nanomedicine: therapeutic, diagnostic and theranostic applications. Curr Opin Biotechnol 24:1159–1166. https://doi.org/10.2147/IJN.S30320

Roca AG, Veintemillas-Verdaguer S, Port M, Robic C, Serna CJ, Morales MP (2009) Effect of nanoparticle and aggregate size on the relaxometric properties of MR contrast agents based on high quality magnetite nanoparticles. J Phys Chem B 113:7033–7039. https://doi.org/10.1021/jp807820s

Roohi F, Lohrke J, Ide A, Schütz G, Dassler K (2012) Studying the effect of particle size and coating type on the blood kinetics of superparamagnetic iron oxide nanoparticles. Int J Nanomed 7:4447. https://doi.org/10.2147/IJN.S33120

Sadauskas E, Jacobsen NR, Danscher G, Stoltenberg M, Vogel U, Larsen A, Kreyling W, Wallin H (2009) Biodistribution of gold nanoparticles in mouse lung following intratracheal instillation. Chem Cent J 3:16. https://doi.org/10.1186/1752-153X-3-16

Saptarshi SR, Duschl A, Lopata AL (2013) Interaction of nanoparticles with proteins: relation to bio-reactivity of the nanoparticle. J Nanobiotechnol 11:26. https://doi.org/10.1186/1477-3155-11-26

Schiller B, Bhat P, Sharma A (2014) Safety and effectiveness of ferumoxytol in hemodialysis patients at 3 dialysis chains in the United States over a 12-month period. Clin Ther 36:70–83. https://doi.org/10.1016/j.clinthera.2013.09.028

Schrand AM, Rahman MF, Hussain SM, Schlager JJ, Smith DA, Syed AF (2010) Metal-based nanoparticles and their toxicity assessment. Wiley Interdisc Rev Nanomed Nanobiotechnol 2:544–568. https://doi.org/10.1002/wnan.103

Sée V, Free P, Cesbron Y, Nativo P, Shaheen U, Rigden DJ, Spiller DG, Fernig DG, White MR, Prior IA (2009) Cathepsin L digestion of nanobioconjugates upon endocytosis. ACS Nano 3:2461–2468. https://doi.org/10.1021/nn9006994

Seeney C, Ojwang JO, Weiss RD, Klostergaard J (2012) Magnetically vectored platforms for the targeted delivery of therapeutics to tumors: history and current status. Nanomedicine 7:289–299. https://doi.org/10.2217/nnm.11.183

Selvan S, Patra PK, Ang CY, Ying JY (2007) Synthesis of silica-coated semiconductor and magnetic quantum dots and their use in the imaging of live cells. Angew Chem 119:2500–2504. https://doi.org/10.1002/ange.200604245

Setyawati MI, Tay CY, Docter D, Stauber RH, Leong DT (2015) Understanding and exploiting nanoparticles' intimacy with the blood vessel and blood. Chem Soc Rev 44:8174–8199. https://doi.org/10.1039/C5CS00499C

Shang L, Azadfar N, Stockmar F, Send W, Trouillet V, Bruns M, Gerthsen D, Nienhaus GU (2011) One-pot synthesis of near-infrared fluorescent gold clusters for cellular fluorescence lifetime imaging. Small 7:2614–2620. https://doi.org/10.1002/smll.201100746

Simberg D, Park J-H, Karmali PP, Zhang W-M, Merkulov S, McCrae K, Bhatia SN, Sailor M, Ruoslahti E (2009) Differential proteomics analysis of the surface heterogeneity of dextran iron

oxide nanoparticles and the implications for their in vivo clearance. Biomaterials 30:3926–3933. https://doi.org/10.1016/j.biomaterials.2009.03.056

Soenen SJ, Parak WJ, Rejman J, Manshian B (2015) (Intra) cellular stability of inorganic nanoparticles: effects on cytotoxicity, particle functionality, and biomedical applications. Chem Rev 115:2109–2135. https://doi.org/10.1021/cr400714j

Soman N, Marsh J, Lanza G, Wickline S (2008) New mechanisms for non-porative ultrasound stimulation of cargo delivery to cell cytosol with targeted perfluorocarbon nanoparticles. Nanotechnology 19:185102. https://doi.org/10.1088/0957-4484/19/18/185102

Sonavane G, Tomoda K, Makino K (2008) Biodistribution of colloidal gold nanoparticles after intravenous administration: effect of particle size. Colloids Surf, B 66:274–280. https://doi.org/10.1016/j.colsurfb.2008.07.004

Song Y, Xu X, MacRenaris KW, Zhang XQ, Mirkin CA, Meade TJ (2009) Multimodal Gadolinium-enriched DNA–Gold nanoparticle conjugates for cellular imaging. Angew Chem Int Ed 48:9143–9147. https://doi.org/10.1002/anie.200904666

Song Y, Shi W, Chen W, Li X, Ma H (2012) Fluorescent carbon nanodots conjugated with folic acid for distinguishing folate-receptor-positive cancer cells from normal cells. J Mater Chem 22:12568–12573. https://doi.org/10.1039/C2JM31582C

Tate JA, Petryk AA, Giustini AJ, Hoopes Pj (2011) In vivo biodistribution of iron oxide nanoparticles: an overview. In: Energy-based treatment of tissue and assessment VI, 2011. International society for optics and photonics, p 790117. https://doi.org/10.1117/12.876414

Tenzer S, Docter D, Kuharev J, Musyanovych A, Fetz V, Hecht R, Schlenk F, Fischer D, Kiouptsi K, Reinhardt C (2013) Rapid formation of plasma protein corona critically affects nanoparticle pathophysiology. Nat Nanotechnol 8:772. https://doi.org/10.1038/nnano.2013.181

Thomas M, Klibanov A (2003) Non-viral gene therapy: polycation-mediated DNA delivery. Appl Microbiol Biotechnol 62:27–34. https://doi.org/10.1007/s00253-003-1321-8

Tomanek B, Iqbal U, Blasiak B, Abulrob A, Albaghdadi H, Matyas JR, Ponjevic D, Sutherland GR (2011) Evaluation of brain tumor vessels specific contrast agents for glioblastoma imaging. Neuro-Oncol 14:53–63. https://doi.org/10.1093/neuonc/nor183

Tong S, Hou S, Zheng Z, Zhou J, Bao G (2010) Coating optimization of superparamagnetic iron oxide nanoparticles for high T2 relaxivity. Nano Lett 10:4607–4613. https://doi.org/10.1021/nl102623x

Torres Martin de Rosales R, Tavaré R, Glaria A, Varma G, Protti A, Blower PJ (2011) "99mTc-bisphosphonate-iron oxide nanoparticle conjugates for dual-modality biomedical imaging. Bioconjug Chem 22:455–465. https://doi.org/10.1021/bc100483k

Urban DA, Milosevic AM, Bossert D, Crippa F, Moore TL, Geers C, Balog S, Rothen-Rutishauser B, Petri-Fink A (2018) Taylor dispersion of inorganic nanoparticles and comparison to dynamic light scattering and transmission electron microscopy. Colloid Interface Sci Commun 22:29–33. https://doi.org/10.1016/j.colcom.2017.12.001

Van Beers BE, Sempoux C, Materne R, Delos M, Smith AM (2001) Biodistribution of ultrasmall iron oxide particles in the rat liver. J Magn Reson Imaging 13:594–599. https://doi.org/10.1002/jmri.1083

Wada S, Yue L, Tazawa K, Furuta I, Nagae H, Takemori S, Minamimura T (2001) New local hyperthermia using dextran magnetite complex (DM) for oral cavity: experimental study in normal hamster tongue. Oral Dis 7:192–195. https://doi.org/10.1034/j.1601-0825.2001.70309.x

Wagner S, Schnorr J, Pilgrimm H, Hamm B, Taupitz M (2002) Monomer-coated very small superparamagnetic iron oxide particles as contrast medium for magnetic resonance imaging: preclinical in vivo characterization. Invest Radiol 37:167–177

Wahajuddin SA (2012) Superparamagnetic iron oxide nanoparticles: magnetic nanoplatforms as drug carriers. Int J Nanomed 7:3445. https://doi.org/10.2147/IJN.S30320

Walkey CD, Chan WC (2012) Understanding and controlling the interaction of nanomaterials with proteins in a physiological environment. Chem Soc Rev 41:2780–2799. https://doi.org/10.1039/C1CS15233E

Wan S, Kelly PM, Mahon E, Stöckmann H, Rudd PM, Caruso F, Dawson KA, Yan Y, Monopoli MP (2015) The "sweet" side of the protein corona: effects of glycosylation on nanoparticle–cell interactions. ACS Nano 9:2157–2166. https://doi.org/10.1021/nn506060q

Wang Y, Gu H (2015) Core–shell-type magnetic mesoporous silica nanocomposites for bioimaging and therapeutic agent delivery. Adv Mater 27:576–585. https://doi.org/10.1002/adma.201401124

Wang Y-XJ, Hussain SM, Krestin GP (2001) Superparamagnetic iron oxide contrast agents: physicochemical characteristics and applications in MR imaging. Eur Radiol 11:2319–2331. https://doi.org/10.1007/s003300100908

Wang G, Inturi S, Serkova NJ, Merkulov S, McCrae K, Russek SE, Banda NK, Simberg D (2014) High-relaxivity superparamagnetic iron oxide nanoworms with decreased immune recognition and long-circulating properties. ACS Nano 8:12437–12449. https://doi.org/10.1021/nn505126b

Wang Z, Xie D, Liu H, Bao Z, Wang Y (2016) Toxicity assessment of precise engineered gold nanoparticles with different shapes in zebrafish embryos. RSC Adv 6:33009–33013. https://doi.org/10.1039/C6RA00632A

Webster TJ (2013) Interview: nanomedicine: past, present and future. Nanomedicine 8:525–529. https://doi.org/10.2217/NNM.13.37

Wei H, Bruns OT, Chen O, Bawendi MG (2013) Compact zwitterion-coated iron oxide nanoparticles for in vitro and in vivo imaging. Integr Biol 5:108–114. https://doi.org/10.1039/C2IB20142A

Weishaupt D, Hilfiker PR, Schmidt M, Debatin JF (1999) Pulmonary hemorrhage: imaging with a new magnetic resonance blood pool agent in conjunction with breathheld three-dimensional magnetic resonance angiography. Cardiovasc Intervent Radiol 22:321–325. https://doi.org/10.1007/s002709900396

Weissleder Ra DD, Stark BL Engelstad, Bacon BR, Compton CC, White DL, Jacobs P, Lewis J (1989) Superparamagnetic iron oxide: pharmacokinetics and toxicity. Am J Roentgenol 152:167–173. https://doi.org/10.2214/ajr.152.1.167

Weissleder R, Elizondo G, Wittenberg J, Lee A, Josephson L, Brady T (1990a) Ultrasmall superparamagnetic iron oxide: an intravenous contrast agent for assessing lymph nodes with MR imaging. Radiology 175:494–498. https://doi.org/10.1148/radiology.175.2.2326475

Weissleder R, Elizondo G, Wittenberg J, Rabito C, Bengele H, Josephson L (1990b) Ultrasmall superparamagnetic iron oxide: characterization of a new class of contrast agents for MR imaging. Radiology 175:489–493. https://doi.org/10.1148/radiology.175.2.2326474

Weissleder R, Bogdanov A, Neuwelt EA, Papisov M (1995) Long-circulating iron oxides for MR imaging. Adv Drug Deliv Rev 16:321–334. https://doi.org/10.1016/0169-409X(95)00033-4

Xia X-R, Monteiro-Riviere NA, Riviere JE (2010) An index for characterization of nanomaterials in biological systems. Nat Nanotechnol 5:671. https://doi.org/10.1038/nnano.2010.164

Xu H, Cheng L, Wang C, Ma X, Li Y, Liu Z (2011) Polymer encapsulated upconversion nanoparticle/iron oxide nanocomposites for multimodal imaging and magnetic targeted drug delivery. Biomaterials 32:9364–9373. https://doi.org/10.1016/j.biomaterials.2011.08.053

Yang H-W, Hua M-Y, Liu H-L, Tsai R-Y, Chuang C-K, Chu P-C, Wu P-Y, Chang Y-H, Chuang H-C, Yu K-J (2012) Cooperative dual-activity targeted nanomedicine for specific and effective prostate cancer therapy. ACS Nano 6:1795–1805. https://doi.org/10.1021/nn2048526

Yang L, Kuang H, Zhang W, Aguilar ZP, Xiong Y, Lai W, Xu H, Wei H (2015) Size dependent biodistribution and toxicokinetics of iron oxide magnetic nanoparticles in mice. Nanoscale 7:625–636. https://doi.org/10.1039/C4NR05061D

Yang C, Tian A, Li Z (2016) Reversible cardiac hypertrophy induced by PEG-coated gold nanoparticles in mice. Sci Rep 6:20203. https://doi.org/10.1038/srep20203

Zeng J, Jing L, Hou Y, Jiao M, Qiao R, Jia Q, Liu C, Fang F, Lei H, Gao M (2014) Anchoring group effects of surface ligands on magnetic properties of Fe3O4 nanoparticles: towards high performance MRI contrast agents. Adv Mater 26:2694–2698. https://doi.org/10.1002/adma.201304744

Zhang G, Yang Z, Lu W, Zhang R, Huang Q, Tian M, Li L, Liang D, Li C (2009) Influence of anchoring ligands and particle size on the colloidal stability and in vivo biodistribution of

polyethylene glycol-coated gold nanoparticles in tumor-xenografted mice. Biomaterials 30:1928–1936. https://doi.org/10.1016/j.biomaterials.2008.12.038

Zhang F, Ali Z, Amin F, Feltz A, Oheim M, Parak WJ (2010) Ion and pH sensing with colloidal nanoparticles: influence of surface charge on sensing and colloidal properties. ChemPhysChem 11:730–735. https://doi.org/10.1002/cphc.200900849

Zhuang J, Fan K, Gao L, Lu D, Feng J, Yang D, Gu N, Zhang Y, Liang M, Yan X (2012) Ex vivo detection of iron oxide magnetic nanoparticles in mice using their intrinsic peroxidase-mimicking activity. Mol Pharm 9:1983–1989. https://doi.org/10.1021/mp300033a

Chapter 15
Multiple Myeloma: Role of Magnetic Nanoparticles

Raghvendra A. Bohara and Priyanaka Singh

Abstract With rapid progress in nanomedicine, magnetic nanoparticles (MNPs) have been proved as a promising theranostics tool in biomedical applications including diagnostic imaging, drug delivery, and novel therapeutics. Multiple myeloma is a hematological malignancy with relapse rate greater than 90%. Limitations in the treatment of MM are the serious side effects caused by drugs used in chemotherapy. The emphasis in cancer treatment has shifted from cytotoxic, non-specific chemotherapies to molecularly targeted and rationally designed therapies showing greater efficacy with fewer side effects. Nanomedicine may help to address these issues and a revolutionary treatment. Here, we explained brief insights of MM, the key pathways that play a vital role in the development of the disease and the role of magnetic nanoparticles in the diagnosis and treatment of the MM.

Keywords Magnetic nanoparticles · Multiple myeloma · Targeted drug delivery · Novel therapy

Introduction

Multiple myeloma (MM) is an abnormal malignancy of plasma cell, characterized by diminished immune surveillance mechanism, such as altered antibody production, crookedness of T cell and natural killer cell proliferation and activation, disordering of antigen presentation processes, and upregulation of cell cycle checkpoints and immunosuppressive mediators. MM is also signified by increased production of abnormal immunoglobulins which require tertiary folding in the endoplasmic reticulum (Ghobrial et al. 2019; Saunders 2005; Usmani and Chiosis 2011). MM cells activate varieties of signaling cascades by reacting with the microenvironment of different cells like endothelial cells, bone marrow stromal cells (BMSCs) and

R. A. Bohara (✉) · P. Singh
Centre for Interdisciplinary Research, D. Y. Patil University, Kolhapur, M.S., India
e-mail: raghvendrabohara@gmail.com

R. A. Bohara
CÚRAM, SFI, Center for Research in Medical Devices, National University of Ireland Galway, Ireland, Galway, Ireland

by secretion of different cytokines like autocrine, interleukin 6 (IL 6), insulin-like growth factor (IGF), vascular endothelial growth factor (VEGF) or paracrine cytokine secretions. These activated signaling cascades result into uncontrolled growth, proliferation and develop resistance to apoptosis (Ramakrishnan and D'Souza 2016; Gertz and Vincent Rajkumar 2014). The symptoms with multiple myeloma are generally non-specific and last for an extended period of time. These include fatigue, bone pain, anemia, renal diseases, hypercalcemia, lytic bone lesions, thrombocytopenia, and hypogammaglobulinemia. Components related to a poorer prognosis include: Age (normally strikes people with older age), people with prior family history, overweight, gender (male is more receptive to this disease than female) and race (African American are more susceptible to this disease when compared to white Americans) (Fairfield et al. 2016; Morgan et al. 2012; Siegel et al. 2019). MM is an incurable cancer that strikes over 24,000 people every year in USA and is the second most common hematologic malignancy there and responsible for nearly 11,000 deaths per year. It accounts for nearly 1% of all malignant tumor and represents about 10% of hematologic malignancies (Musto and Montefusco 2016; Ghosh et al. 2018). It has double probability of affecting blacks than white for which the reasons are not known properly. It is primarily said to be a disease of older people affecting individuals of age of 50 and above (Huang et al. 1999). Regardless of various advances in the past two decades, MM is supposed to be fatal disease as it is developing resistance to new drugs within a short period of time during therapy. This highlights the importance of the recognition of new targets and understanding of clonal heterogeneity as there is advancement in new treatment strategies that will help to patient in better treatment (Wong and Comenzo 2015).

Difficulties Associated with Proper Diagnosis of MM

To support MM patients, there are clinical practices which are used such as bone marrow biopsies, blood biological markers, and various imaging modalities.

(a) **Bone marrow biopsies**:

Diagnosis by bone marrow analysis is one of the standard methods. It detects morphologies and involvement of bone marrow by plasma cells. Bone marrow aspirate (BMA) observation evaluates plasma cells that can be differentiated into mature, immature and plasmablastic (Štifter et al. 2010). It is a painful technique often used to detect stages of diseases. Bone marrow samples can be tested for further characterization of status of disease that include immunohostochemistry and flow cytometry which identify monoclonal plasma cells that represent CD38, CD138, and CD56 antigens and cytoplasmic kappa or lambda light chain. Chromosomal abnormality can be detected by using fluorescence in situ hybridization (FISH). Previously mentioned techniques have limitations that occur by the sampling from a single focus of bony pelvis that can give rise to false negative results.

(b) **Blood sampling**:

As compared with bone marrow biopsy, blood sampling technique is less-invasive method that can provide equivalent information as bone marrow biopsy technique. Circulating tumor cells (CTCs) and circulating cell-free DNA (cfDNA) in blood samples are detected as they can provide genetic profile of MM and can detect treatment responses with cancer relapses. In serological diagnosis and to detect stages of MM measurements of M-protein, albumin, and beta-2 microglobulin are detected. Serum free light chain (SFLC) test measures the amount of FLCs in blood. Unstable amount and ratio of kappa or lambda light chains confirms the MM. Higher level of kappa or lambda is related to higher amount of active myeloma cells in the body.

(c) **Imaging Biomarkers**:

The extent of bone disease can be assessed accurately by PET/CT or MRI scans. MRI scans are useful in suspected MM to detect focal bone marrow lesions. These methods lack specificity because of intrinsic limitations of existing contrast agents. These agents are not specifically targeted to tumor cells (Detappe et al. 2018).

In MM therapy, novel agents like bortezomib, thalidomide, and lenalidomide have been used. It was reported that their activity enhanced survival rate from 2 to 3 years to an average of 7 years in the USA by changing treatment patterns when these drugs were combined with older drugs (dexamethasone, cyclophosphamide, and alkylating agents). Newly diagnosed MM patients, with the availability of better drugs on an average, have a survival hope of more than 10 years according to accessible population registries (Kyle and Rajkumar 2011; Richardson et al. 2011; Bensinger et al. 2010; Larocca et al. 2017; Pantani et al. 2016; Alexanian et al. 2013). In the last few years, combination therapy was extensively used and proved to be quite successful. This therapy uses multiple techniques that improve anti-cancerous activity and reduces dose and minimizes side effect. It is widely reported that MM patients as well as monoclonal gammopathy of undetermined significance (MGUS) suffer from cytogenetic abnormalities. Hence, such alterations are not supposed to confirm disease progression. But, secondary alterations such as Ras/Raf mutations, NF-κB mutations, and c-Myc alterations occur in progression of MM disease not in MGUS patients. Moreover, MM cells interact with cells in the microenvironment such as marrow stromal cells (BMSCs) or endothelial cells and activate different signaling cascades through autocrine or paracrine secretion that result into uncontrolled growth, proliferation, and resistance to apoptosis. Hence, it is crucial to study such signaling pathways that can give better understanding of pathophysiology of MM and can help to develop targeted therapies that in turn will increase the efficiency of existing therapeutic perspectives. Here, we are explaining these signaling routes in MM and emerging therapies targeting these irregulars signaling incidents that initialize in MM patients (Fig. 15.1).

(A) **NF-kB Pathway**

In unstimulated cells, the NF-kB proteins are continuing to cling in the cytoplasm by proteins called inhibitory kB (IkB), while in case of MM, after proper stimuli, such
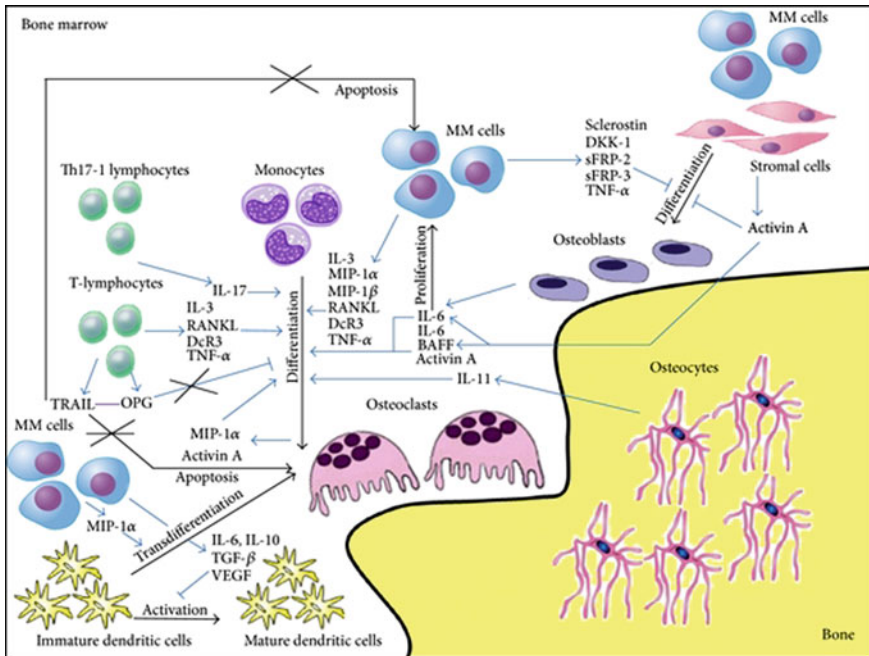
Fig. 15.1 Interaction between bone cells and bone marrow microenvironment cells in promoting both malignant plasma cell survival and bone lesions in MM patients. Myeloma cells can directly support osteoclast formation and activity as well as inhibit osteoblast differentiation by releasing numerous cytokines. Moreover, other molecules can be secreted by bone cells and other cells interacting with each other in the bone microenvironment, thus supporting both the progression of MM tumor burden and the development of MM bone disease. Figure taken from Oranger (2013) from Hindawi Publication

as secretion of BAFF, APRIL by BMSCs, or TNF—α secretion by MM cells, the expression of BAFFR, TNFR, BCMA, and TAKI on the MM cell surface proliferated, that results into activation of the canonical and non-canonical NF-kB pathways. NF-kB is a crucial and prominent signaling pathway that nurtures MM cell survival and resistance to apoptosis.

(B) The Ras/Raf/Mek/Erk Pathway

The Ras/Raf/Mek/Erk pathways get triggered in MM through the process that includes activating mutations and elevated levels of cytokines such as vascular endothelial growth factor (VEGF) and insulin-like growth factor (IGF) in the tumor microenvironment. It is well known that Ras mutations are a negative factor in MM.

(C) P13K/Akt/mTOR Pathway

The P13K/Akt/mTOR pathway is leading signaling cascade that encourages the development and viability of various cancers including MM. This route is a typical signal transduction pathway which commences through the association of cytokines

with cell surface receptors. There are few cytokines (IGF, IL6, VEGF, IL-1β, SDF1) that can activate the P13K/Akt/mTOR pathway (30).

(D) **Other Signaling Pathways in MM**

It is widely known that Jak2/Stat3 signaling cascade stimulates the proliferations and survival of MM cells. IL 6 also stimulates the Jak2/Stat3 pathway, which then resulted into increased levels of anti-apoptotic Bcl-XI and McII, thereby promoting MM cells persistence and resistance to dexamethasone (Ramakrishnan and D'Souza 2016). The role of Dickkopf-related protein 1 (DKK1) in the Wnt signaling pathways is also noticeable success. Lenalidomide targets MM maturation by prompting apoptosis through G1 growth arrest as well as interrupting the adhesion of tumor cells to adherent stroma, preventing the release of growth-promoting cytokines and obstructing angiogenesis. In a similar manner, the first in class proteasome inhibitor bortezomib targets MM in the context of both the cortical bone and bone marrow (Richardson et al. 2011). Explaining most appropriate combination strategies and correlating companion diagnostics that will conduct clinical decisions are needed to target relapsed or refractory MM in order to enhance disease growth, survival and quality of life for patients. Elotuzumab is a sophisticated monoclonal antibody that targets signaling lymphocytic activation molecule (SALMF7), approved by the US Food and Drug Administration (FDA) in 2015 and the European Medicines Agency in 2016 for the treatment of MM. SLAMF7 shows its expression in normal and malignant plasma cells and has limited expression on natural killer (NK) cells. Experimental authentication indicates that elotuzumab shows anti-myeloma activity through antibody-dependent cell mediated cytotoxicity, boosting NK cells cytotoxicity and disturbing adhesion of MM cells to bone marrow stem cells (BMSCs) (Chen et al. 2017; Larocca et al. 2017; Agarwal and Mahadevan 2013).

Lenalidomide with dexamethasone is also used for patients with RRMM. Despite the fact that this combination exhibits very high level of efficacy, it further worsens the hypercoagulable state that coexists within myeloma. Thromboprophylactic regimen requires careful selection and if warfarin is chosen, assiduous monitoring is required to ensure it will be clinically effective (Rushworth et al. 2012). Supporting these exceptional advances in therapeutics and their impact on prognosis are important laboratory discoveries, which depicted the key role of the bone marrow microenvironment in relation to the growth, survival and resistance of MM. New chemical agents are also in development on the basis of understanding other signaling pathways and molecular mechanisms like tumor necrosis factor-α, proteasome and MARKs. It has been found that post all the above-mentioned drug therapies, there are some side effect been seen in some of the patients from some selective drugs. Some of the problems associated with these therapies are cardiovascular disease, thrombotic risk, Stevens-Johnson syndrome, tumor lysis syndrome (Rushworth et al. 2012; Alexanian et al. 2013; Li et al. 2017; Kenealy et al. 2006).

Nanomedicine and Magnetic Nanoparticles

Nanomedicine term is used when nanotechnology is applied in medicine. Nanomedicine can overcome limitations of previously mentioned criteria used for MM diagnosis and therapy. The advancement in novel nanomedicine has increased over past decade that have wide range of applications as molecular diagnostic agents, drug delivery agents and in vivo gene editing tools (Lammers et al. 2012). It is widely reported that as compared with small molecules or antibody conjugates nanoparticles possess unique properties such as high surface area to volume ratio, varieties in size and shape that enhances drug and imaging agent's incorporation, tissue specific delivery and controlled release of drugs (Fig. 15.2).

Nanoparticles used for in vivo applications range from 5 to 200 nm in size and can be categorized into two groups: (i) Organic-based nanoparticles (e.g., carbon nanotubes, dendrimers, micelles), (ii) Inorganic-based nanoparticles (e.g., quantum dots, NPs with other metallic components). The selection of nanoparticles depends upon the desired application. For example, inorganic nanoparticles which incorporate metals such as supra-paramagnetic iron oxide are used for magnetic resonance imaging (MRI) of biomolecular targets that gives high resolution and translational in vivo imaging for single cell tracking (Detappe et al. 2018).

Nowadays, application of nanotechnology in cancer treatment has attracted much attention that leads into emergence of cancer nanotechnology which is a field of interdisciplinary research. This field has received a great interest in USA as several centers for cancer nanotechnology have launched since 2004. In Europe also number of groups is active in research of cancer nanotechnology. Nowadays, it has become possible to tackle cancer and to specify therapies by designing personalized treatments. Clinical labs extensively use nanotechnology-based assays and also detect tumor markers of individual patient. Simultaneously, scientists formulate the nanoparticles by using same biomarkers that found in patients tumor that carry specific genetic drug designed for interaction with biomarker protein related to tumor (Shamsi et al. 2018; Zhou et al. 2016; Firer and Gellerman 2012). Cancer biomarkers include mutant genes, RNAs, proteins, lipids, and carbohydrates. They alter their expression as per biological change and clinical outcome. Most of the nanoparticles get deposited in tumor cells due to high permeation of blood vessels and defected angiogenesis. Tumor cells are characterized by dysfunctional lymphatic drainage that retain nanoparticles in tumor for a long time enough to allow release of drug (Kemp et al. 2016).

The major challenge to use of nanoparticles in MM is the development of material that has specific biological affinity for them and should interact with them in their natural in vivo microenvironment (Tzakos et al. 2013).

The use of magnetic microparticles and MNPs for the delivery of chemotherapeutics started in 1976 when Zimmermann and Pilwat employed magnetic erythrocytes for the delivery of cytotoxic drugs. However, MNPs were used for the initial time in animal models by Lubbe et al. who tested epirubicin-loaded MNPs targeting pancreatic cancer. To elevate the targeting efficiency further and to increase the specific
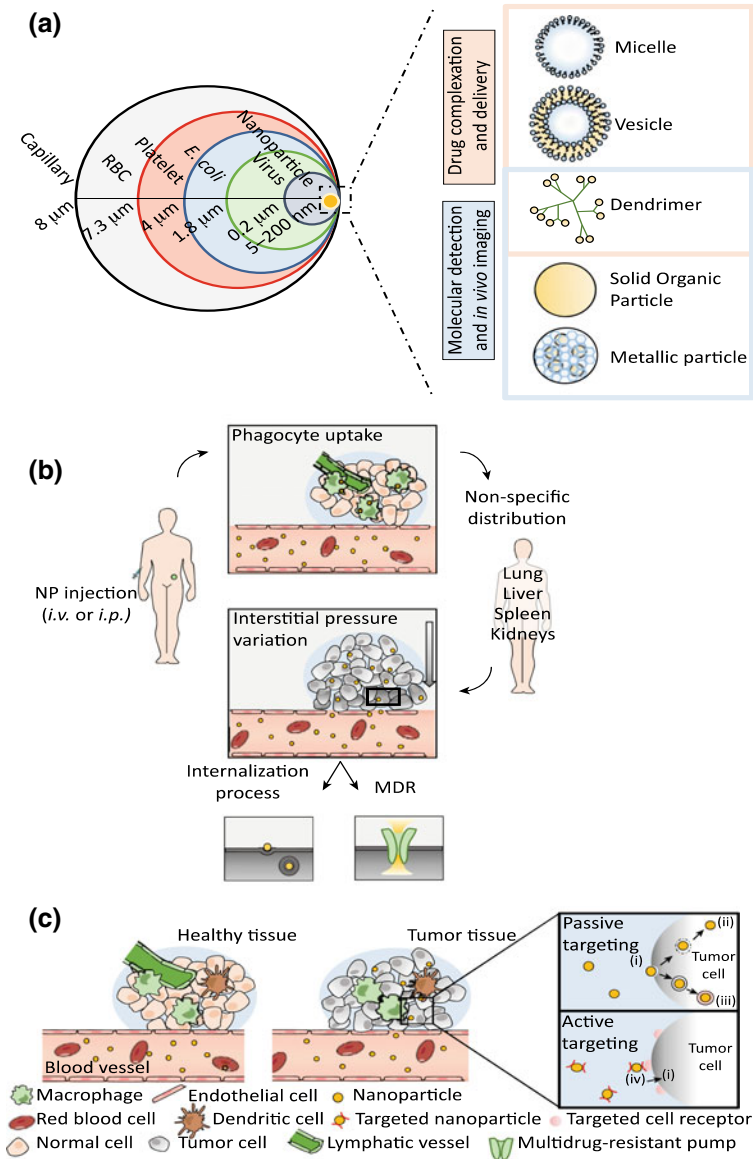
◄**Fig. 15.2 a** Multiple nanoparticle-based constructs have been generated from various starting materials, yielding agents with unique architectures and differential capabilities for molecular detection, in vivo imaging, and/or drug complexation and delivery. **b** Upon intravenous (IV) or intraperitoneal (IP) injection, which are the most common modes of systemic administration, nanoparticles carrying drugs and/or imaging agents will circulate in the blood stream and accumulate in tumor sites, predominantly via a passive targeting mechanism. There, they may interact with multiple cell types, be internalized via different processes, and encounter intracellular resistant mechanisms. **c** Differences between the vasculature of healthy tissues and tumors are predominantly due to active angiogenesis by the latter, which helps to address the increased nutritional and metabolic demands of rapidly dividing and malignant cells and which may enable enhanced accumulation of nanoparticles. Once in the perivascular spaces of tumors, nanoparticles may nonspecifically interact with tumor cells and be taken up by (i) endocytosis. Intracellularly, nanoparticles may achieve (ii) endosomal escape or experience (iii) fusion with endolysosomes that can lead to their degradation, to damage of their payloads, and/or to their retrafficking to outside the cell. In actively targeted nanoparticles, specific biomolecular features may enable preferential interactions with a cellular components and/or specific binding to various cell types within the tumor microenvironment. In this schematic, molecularly oriented targeting moieties (depicted in red on the surfaces of the nanoparticles) can be engineered to bind (iv) antigens on the surfaces of cells in order to affect their intratumoral cellular tropism. These actively targeted nanoparticles may then be internalized through receptor-mediated endocytosis or via other cellular uptake pathways utilized by passively targeted nanoparticles. (Abbreviations: MDR, multidrug resistant; NP, nanoparticle; RBC, red blood cell from Trends in Molecular Medicine, June 2018, Vol. 24, No. 6). Figure taken from Detappe et al. (2018). Reprinted with permission (Permission applied) from Cell Press

assembly of MNPs at the target site, several efforts have been made to attach targeting ligands (Shamsi et al. 2018; Zhou et al. 2016; Firer and Gellerman 2012). Materials normally used for magnetic drug delivery contain metal or metal oxide nanoparticles, such as superparamagnetic iron oxide nanoparticles (SPIONs). SPIONs contains an iron oxide core, commonly coated with organic material like fatty acids, polysaccharides or polymers to enhance colloidal stability and to avert separation into particles and carrier medium (Fig. 15.3). The magnetic properties of SPIONs let the remote control of their accumulation by means of an outer magnetic field. Association of SPIONs with drugs, in conjugation with an external magnetic field (designated as "magnetic drug targeting"), has additionally emerged as a propitious strategy of drug delivery (Tietze et al. 2015; Huang et al. 2016).

Magnetic Nanoparticles (MNPs): Biodistribution, Pharmacokinetics, and Toxicity

Magnetic nanoparticles have gained much more attention worldwide for their biomedical applications such as magnetic resonance imaging (MRI), cell separation, cellular labeling, tissue repair, and disease therapeutic agents. In vivo application of magnetic nanoparticles mainly depends upon their passive transport to desired target via blood stream (Tzakos et al. 2013; Kemp et al. 2016). The pharmacokinetics of MNPs depends mainly on hydrodynamic size, charge and surface chemistry. MNPs
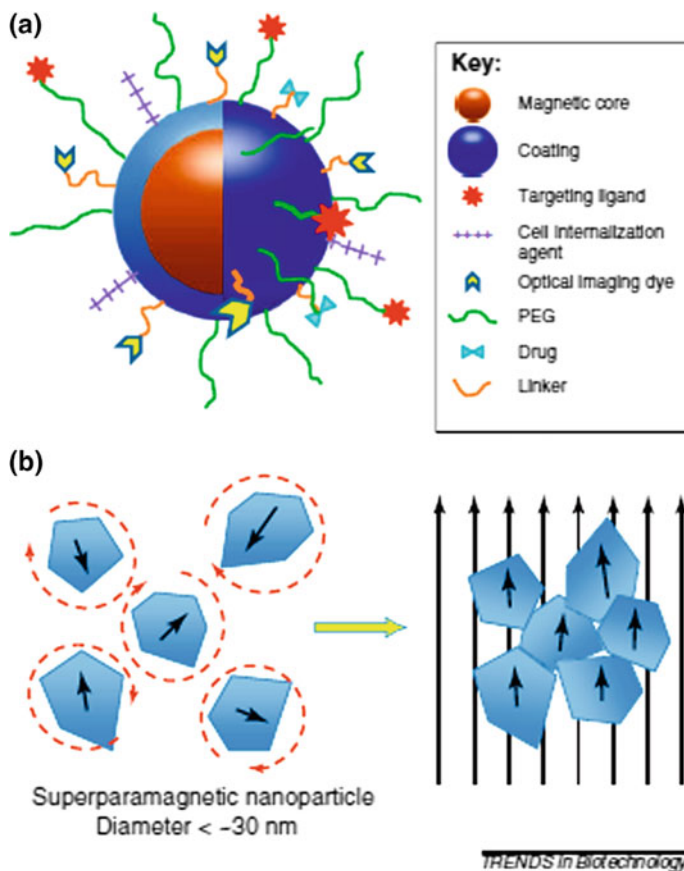
Fig. 15.3 a Schematic representation of the "core–shell" structure of MNPs and multi-functional surface decoration. MNPs consist of a magnetic iron oxide core coated with a biocompatible material (e.g., polysaccharide, lipid, protein, small silane linkers, etc.). Functional groups on the surface of coatings are often used to link ligands for molecular targeting, cellular internalization, optical imaging, enhanced plasma residence and/or therapy. The variety of moieties that decorate the MNP surface imparts the nanoparticle with its multi-functional, theranostic character. **b** Illustration of superparamagnetic MNP response to applied magnetic fields. MNPs comprise rotating crystals that align with the direction of an applied magnetic field. Crystal reorientation provides the high magnetic susceptibility and saturation magnetization observed for this material. The circular dashed lines around the superparamagnetic nanoparticles on the left illustrate the randomization of their orientation, due to temperature effects, in the absence of a magnetic field. Figure taken from Cole et al. (2011). Reprinted with permission (Permission applied) from Elsevier

of 10–100 nm are assumed to be suitable for intravenous (IV) administration, because nanoparticles >200 nm acquired to be filter mechanically and by phagocytosis in the spleen, and nanoparticles <10 nm are quickly cleared by renal filtration.

Furthermore, opsonization and dispersion of nanoparticles by the reticuloendothelial system (RES) can be circumvented by providing a layering of cationic polymers

or hydrophilic polymers such as PEG. Particle size, surface charge, and coating are important factors that affect the biodistribution, pharmacokinetics, and toxicity of MNPs. The coating to MNPs reduces their uptake in reticuloendothelial system (RES) organs and allows long time blood circulation which is an important factor in biomedical application like drug delivery, therapy, and imaging.

Additionally, the toxicity of MNPs linked with the oxidation state because magnetite effortlessly undergoes oxidation to form maghemite. Although the toxicity of MNPs can be declined by coating MNPs, veiling the oxidative sites therefore, making the reduced activity of MNPs and so ultimately reducing the risk of DNA damage (Zhou et al. 2016).

Targeting MNPs to Tumors

Careful targeting of MNPs to the required site is an important criteria for effective therapeutic application and to diminish toxic effect on tissue. MNPs can be targeted to the tumor site by two ways (Fig. 15.4).
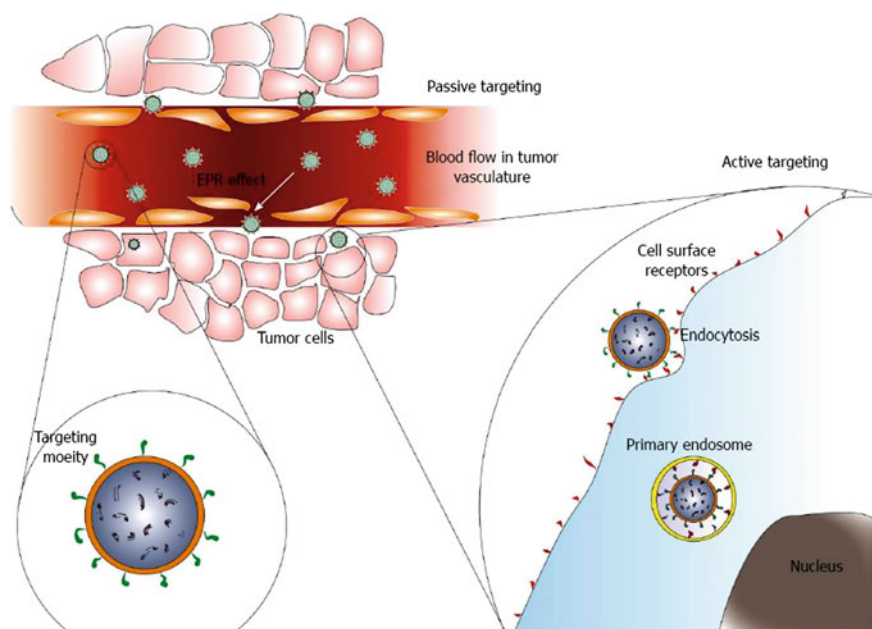

Fig. 15.4 Illustration of the mechanism of MNP-based drug delivery systems. Taking tumor as an example, MNP-based drug carriers may reach the tumor tissue via the EPR effect due to leaky vasculature, and facilitate active targeting to tumor cells through the conjugated targeting ligands interacting with cellular receptors. Figure taken from Varshosaz and Farzan (2015). Published by Baishideng Publishing

Passive Targeting

In the cancer treatment, the delivery of MNPs to affected tissues take place by enhanced permeability and retention (EPR) effect. EPR effect describes enhanced permeability of tumor vasculature that allows macromolecules, lipids and NPs circulating in blood to forcely pass out through the leaky tumor blood vessel and then enters in interstitial spaces of tumor cells. Lack of lymphatic drainage in tumor retains MNPs within tumor by preventing NPs to get back into circulation. So, administered nanoparticles get accumulated in the tumor tissues that result in passive targeting of tumor without targeting ligands.

Active Targeting

Magnetic nanoparticles targets tumor site actively by using some ligands that are particular for the surface receptors present on the tumor cells that helps in enhancement of tumor residence time of the MNPs, which is expanded by the EPR effect. There are different types of targeting ligands which includes peptides, proteins or antibodies, small molecules like folate, etc. (Cole et al. 2011).

Magnetic Triggered Drug Release in MNPs

The magnetic property of iron containing nanoparticles gets influenced by the nature of the iron oxide core (e.g., magnetite) and the size (Huang et al. 2016). A ferromagnetic material like iron oxide contains atoms with strong magnetic dipoles, where the individual magnetic moments prone to be coupled leading to sub domain structures with a single magnetic moment (weiss domain). When there is the absence of an external field, the individual weiss domains of material are ordered randomly, leading to zero net magnetization. When an outer magnetic field is utilized, the magnetic moments of the weiss domain will moderately align along with this field, guiding to a single large magnetic domain with a very high net magnetization. These kinds of particles are designated as superparamagnetic and are extensively applied in biomedical research. Generally, the difference between two groups of these particles are made according to their diameter: ultrasmall superparamagnetic iron oxide particles (USPIOs) are smaller than 50 nm, while superparamagnetic iron oxide particles (SPIOs) are larger than 50 nm (Soenen and De Cuyper 2010; Cole et al. 2011). Table 15.1 discusses the key nanomedicine in MM.

In MM, the combination of magnetic hyperthermia treatment by using MNPs and controlled drug release from MNPs by heat to trigger drug release are used. Magnetic hyperthermia treatment mainly depends upon the heat produced by magnetic nanoparticles under changing magnetic field (ACMF). MNPs must heat the tumor to a temperature which is necessary to destroy the tumor cells (above 42.5 °C). The ACMF of amplitude (H) and frequency (f) of the field, less than 5×10^9 A/m/s is

Table 15.1 Preclinical FDA approved nanomedicines in MM (Copied from Trends in Molecular Medicine, June 2018, Vol. 24, No. 6)

Nanotechnology platform	Active pharmaceutical ingredient(s)	Injection method	In vivo tumor model	Tumor site implantation	References
Albumin NP	Rapamycin and perifosine	IV	MM.1S	Subcutaneous xenograft	[126]
VLA4-micelle NP	Doxorubicin	IV	NCI-H929	Subcutaneous xenograft	[146]
PEI NP	pExp5A plasmid	IV	KAS-6/1; RPMI-8226	Subcutaneous xenograft	[147]
PEI NP	elF5 siRNA	IV	KAS-6/1; RPMI-8226	Subcutaneous xenograft	[147]
Silica NP	Snake venom	i.t./IV	OPM2; U266	Subcutaneous xenograft	[148–150]
Oleic acid-coated iron oxide NP	Paclitaxel	IV	U266; MMJN3	Subcutaneous xenograft	[151]
VL4-liposome	Carfilzomib	IV	NCI-H929	Subcutaneous xenograft	[120]
PEG-liposome	Bortezomib	IV	NCI-H929	Subcutaneous xenograft	[120]
PEG-PCL NP	Carfilzomib	IV	NCI-H929	Subcutaneous xenograft	[127]
PEG-liposome	Doxorubicin and carfilzomib	IV	NCI-H929	Subcutaneous xenograft	[127]
DMSA-Fe_3O_4 NP	Bortezomib	IV	RPMI-8226	Subcutaneous xenograft	[152]
DMSA-Fe_3O_4 NP	Paclitaxel	IV	RPMI-8226	Subcutaneous xenograft	[153]
PEG-liposome	RU 58668	IV	RPMI-8226	Subcutaneous xenograft	[154]
Nanocolloid	Camptothecin	IV	MPC-11	Subcutaneous xenograft	[155]
αvβ-PEG-liposome	MYC prodrug inhibitor	IV	5TGM1	Orthotopic xenograft	[123]
Alendronate-PEG PLGA NP	Bortezomib	IV	MM.1S	Orthotopic xenograft	[121]
Chitosane NP	Bortezomib	IV	MM.1S	Orthotopic xenograft	[125]
Micelle NP	Titanocene	IV	MM.1S	Orthotopic xenograft	[124]

Table taken from Detappe et al. (2018). Reprinted with permission (Permission applied) from Cell Press

considered harmless. In clinical applications, MNPs are designed with high ACMF-to-heat conversion which is followed by specific absorption rate (SAR). To increase SAR, the composition of MNPs should be controlled. Magnetite (Fe_3O_4) is more promising material because of its low toxicity and high saturation magnetization. Clustering of MNPs increase magnetic moment and possess high SAR and Ms than single MNP. Hence, clusters of MNPs provide enhanced SAR without release of harmful elements. According to several studies, MHT can hamper the growth of tumor, but it cannot cure completely. This concludes that MHT cannot kill the cancer cells. Chemotherapy also cannot kill cancer cells and shows serious side effects. So combination of MHT and chemotherapy may minimize the problem in treatment that produce the synergistic effects as: (i) MHT increases the space between the cells by shrinkage of the cells that allow anticancer drug to disperse throughout the tumor and destroy cancer cell, (ii) heat released by MNPs under ACMF triggers the drug release from NPs that prevents anticancer drug to leave tumor and minimizes side effects and (iii) MHT increases the effect of anticancer drug that destroy cancer cells. When heat is used as a trigger for drug release, the drug carriers should retain their load at body temperature (~37 °C) and drug release in heated tumor at therapeutic temperature for hyperthermia (42.5–45 °C). ACMF heating has advantages over conventional heating methods: (i) ACMF gets penetrated deeply in tissues and heat tumors without affecting normal hypodermal tissues; (ii) easy regulation of tumor temperature by adjusting H and f. So, ACMF is a favorable trigger for drug release (Hayashi et al. 2014).

Other Nanoparticles

Based on the preparation method, nanocapsules, nanospheres and nanoparticles can be designed with controlled properties to enhance encapsulation and delivery and also to reduce cytotoxicity. Among the various types of nanoparticles utilized iron oxide, nanoparticles (IONPs), quantum dots (QDs), carbon nanotubes (CNT), gold nanoparticles are extensively studied.

Quantum Dots (QDs)

QDs are practically spherical semiconductor nanocrystals which contain elements from periodic groups ll–Vl or lll–V ranging of size in the middle of 2 and 10 nm. In recent years, unique properties of QDs attracted much more attention in the biomedical field for the application in real-time tissue imaging (bioimaging), diagnostics, single molecule probes, and drug delivery. However, there is challenge of low biological specificity and poorly controlled biodistribution to target tissues. The biodistribution of QD shows inadequate clearance from real-time in vivo (Wagner et al. 2019).

Carbon Nanotubes

Carbon nanotubes are a new form of carbon that can be seen as a single or multiple

graphene sheets (single vs multiwalled CNTs) rolled into a tube with a diameter of several nanometers, but up to one mm in length. For medical purposes, the key benefits of CNTs are their potential to efficiently cross biological barriers according to nanosyringe model and their extremely good conductivity which enables electrical stimulation to neuronal pathways.

Nanometer-Sized Gold Nanoparticles

These are small as compared to the wavelength of visible light and when the light has a frequency close to that of the surface plasmon (the natural oscillation of an electron gas inside a given nanosphere) then the surface plasmon absorbs energy. These particles can be utilized for biomedical purposes, mainly in the field of cancer research for tumor detection and laser induces therapy (Wang et al. 2010).

Key Learning

Development of more personalized therapy in MM could be one of the safest and most prominent options in the treatment. The key pathways that play a vital role give clear understanding to target them so as to have better control on the disease's progression. The formulations of advanced nanomedicine that achieve these objectives are critically reliant on the development of methods to actively target MM cells.

References

Agarwal A, Mahadevan D (2013) Novel targeted therapies and combinations for the treatment of multiple myeloma. Cardiovasc Hematol Disord-Drug Targets 13(1):2–15. https://doi.org/10.2174/1871529x11313010002

Alexanian R, Delasalle K, Wang M (2013) High frequencies of response after limited primary therapy for multiple myeloma. Clin Lymphoma Myeloma Leuk 13(2):119–122. https://doi.org/10.1016/j.clml.2012.11.008

Bensinger WI, Jagannath S, Vescio R, Camacho E, Wolf J, Irwin D et al (2010) Phase 2 study of two sequential three-drug combinations containing bortezomib, cyclophosphamide and dexamethasone, followed by bortezomib, thalidomide and dexamethasone as frontline therapy for multiple myeloma. Br J Haematol 148(4):562–568. https://doi.org/10.1111/j.1365-2141.2009.07981.x

Chen WC, Kanate AS, Craig M, Petros WP, Hazlehurst LA (2017) Emerging combination therapies for the management of multiple myeloma: the role of elotuzumab. Cancer Manag Res 9:307–314. https://doi.org/10.2147/CMAR.S117477

Cole AJ, Yang VC, David AE (2011) Cancer theranostics: the rise of targeted magnetic nanoparticles. Trends Biotechnol 29(7):323–332. https://doi.org/10.1016/j.tibtech.2011.03.001

Detappe A, Bustoros M, Mouhieddine TH, Ghoroghchian PP (2018) Advancements in nanomedicine for multiple myeloma. Trends Mol Med 24(6):560–574. https://doi.org/10.1016/j.molmed.2018.04.005

Fairfield H, Falank C, Avery L, Reagan MR (2016) Multiple myeloma in the marrow: pathogenesis and treatments. Ann N Y Acad Sci 1364(1):32–51. https://doi.org/10.1111/nyas.13038

Firer MA, Gellerman G (2012) Targeted drug delivery for cancer therapy: the other side of antibodies. J Hematol Oncol 5(1):1. https://doi.org/10.1186/1756-8722-5-70

Gertz MA, Vincent Rajkumar S (2014) Multiple myeloma: diagnosis and treatment. Multiple Myeloma Diagn Treat 91(1):1–311. https://doi.org/10.1007/978-1-4614-8520-9

Ghobrial I, Cruz CH, Garfall A, Shah N, Munshi N, Kaufman J, et al (2019) Immunotherapy in multiple myeloma: accelerating on the path to the patient. Clin Lymphoma, Myeloma and Leuk. https://doi.org/10.1016/j.clml.2019.02.004

Ghosh A, Mailankody S, Giralt SA, Landgren CO, Smith EL, Brentjens RJ (2018) CAR T cell therapy for multiple myeloma: where are we now and where are we headed? Leuk Lymphoma 59(9):2056–2067. https://doi.org/10.1080/10428194.2017.1393668

Hayashi K, Nakamura M, Miki H, Ozaki S, Abe M, Matsumoto T, Sakamoto W, Yogo T, Ishimura K (2014) Magnetically responsive smart nanoparticles for cancer treatment with a combination of magnetic hyperthermia and remote-control drug release. Theranostics 4(8):834–844. https://doi.org/10.7150/thno.9199

Huang Y-W, Hamilton A, Arnuk OJ, Chaftari P, Chemaly R (1999) Current drug therapy for multiple myeloma. Drugs 57(4):485–506. https://doi.org/10.2165/00003495-199957040-00004

Huang J, Li Y, Orza A, Lu Q, Guo P, Wang L, et al (2016) Magnetic nanoparticle facilitated drug delivery for cancer therapy with targeted and image-guided approaches. Adv Funct Mater 26(22):3818–3836. https://doi.org/10.1002/adfm.201504185

Kemp JA, Shim MS, Heo CY, Kwon YJ (2016) "Combo" nanomedicine: co-delivery of multi-modal therapeutics for efficient, targeted, and safe cancer therapy. Adv Drug Deliv Rev 98:3–18. https://doi.org/10.1016/j.addr.2015.10.019

Kenealy MK, Prince HM, Hönemann D (2006) Tumor lysis syndrome early after treatment with bortezomib for multiple myeloma. Pharmacotherapy 26(8 I):1205–1206. https://doi.org/10.1592/phco.26.8.1205

Kyle RA, Rajkumar SV (2011) ASH 50th anniversary review multiple myeloma. Bone 111(6):2962–2972

Lammers T, Kiessling F, Hennink WE, Storm G (2012) Drug targeting to tumors: principles, pitfalls and (pre-) clinical progress. J Controlled Release 161(2):175–187. https://doi.org/10.1016/j.jconrel.2011.09.063

Larocca A, Mina R, Gay F, Bringhen S, Boccadoro M (2017) Emerging drugs and combinations to treat multiple myeloma. Oncotarget 8(36):60656–60672. https://doi.org/10.18632/oncotarget.19269

Li W, Garcia D, Cornell RF, Gailani D, Laubach J, Maglio ME, et al (2017) Cardiovascular and thrombotic complications of novel multiple myeloma therapies: a review. JAMA Oncol 3(7):980–988. http://doi.org/10.1001/jamaoncol.2016.3350

Morgan GJ, Walker BA, Davies FE (2012) The genetic architecture of multiple myeloma. Nat Rev Cancer 12(5):335–348. https://doi.org/10.1038/nrc3257

Musto P, Montefusco V (2016) Are maintenance and continuous therapies indicated for every patient with multiple myeloma? Exp Rev Hematol 9(8):743–751. https://doi.org/10.1080/17474086.2016.1196127

Oranger A, Carbone C, Izzo M, Grano M (2013) Cellular mechanisms of multiple myeloma bone disease. Clin Dev Immunol 29:2013

Pantani L, Brioli A, Tacchetti P, Zannetti BA, Mancuso K, Rocchi S et al (2016) Current and emerging triplet combination therapies for relapsed and refractory multiple myeloma. Exp Rev Hematol 9(3):315–323. http://doi.org/10.1586/17474086.2016.1127754

Ramakrishnan V, D'Souza A (2016) Signaling pathways and emerging therapies in multiple myeloma. Curr Hematol Malignancy Rep 11(2):156–164. https://doi.org/10.1007/s11899-016-0315-4

Richardson PG, Laubach J, Mitsiades CS, Schlossman R, Hideshima T, Redman K, et al (2011) Managing multiple myeloma: the emerging role of novel therapies and adapting combination treatment for higher risk settings. Br J Haematol 154(6):755–762. http://doi.org/10.1111/j.1365-2141.2011.08791.x

Rushworth GF, Leslie SJ, Forsyth P, Vincent C (2012) Evidence-based case report: multiple thrombotic episodes associated with lenalidomide and dexamethasone therapy for multiple myeloma. Ther Adv Drug Saf 3(3):115–122. https://doi.org/10.1177/2042098611433773

Saunders G (2005) Overview of drug therapy for multiple myeloma. J Oncol Pharm Pract 11(3):83–100. https://doi.org/10.1191/1078155205jp160oa

Shamsi M, Sedaghatkish A, Dejam M, Saghafian M, Mohammadi M, Sanati-Nezhad A (2018) Magnetically assisted intraperitoneal drug delivery for cancer chemotherapy. Drug Deliv 25(1):846–861. https://doi.org/10.1080/10717544.2018.1455764

Siegel RL, Miller KD, Jemal A (2019) Cancer statistics, 2019. CA Cancer J Clin 69(1):7–34. https://doi.org/10.3322/caac.21551

Soenen SJ, De Cuyper M (2010) Assessing iron oxide nanoparticle toxicity in vitro: current status and future prospects. Nanomedicine 5(8):1261–1275. http://doi.org/10.2217/nnm.10.106

Štifter S, Babarovic V, Valkovic T, Bekafigo IS, Štemberger C, Načinovic N, Lucin K, Jonjić N (2010) Combined evaluation of bone marrow aspirate and biopsy is superior in the prognosis of multiplemyeloma. Diagn Pathol 5(30):1–7. http://www.diagnosticpathology.org/content/5/1/30

Tietze R, Zaloga J, Unterweger H, Lyer S, Friedrich RP, Janko C et al (2015) Magnetic nanoparticle-based drug delivery for cancer therapy. Biochem Biophys Res Commun 468(3):463–470. http://doi.org/10.1016/j.bbrc.2015.08.022

Tzakos AG, Briasoulis E, Thalhammer T, Jäger W, Apostolopoulos V (2013) Novel oncology therapeutics: targeted drug delivery for cancer. J Drug Deliv 2013:1–5. https://doi.org/10.1155/2013/918304

Usmani SZ, Chiosis G (2011) HSP90 inhibitors as therapy for multiple myeloma. Clin Lymphoma, Myeloma Leuk 11(Suppl.1):S77–S81. https://doi.org/10.1016/j.clml.2011.03.027

Varshosaz J, Farzan M (2015) Nanoparticles for targeted delivery of therapeutics and small interfering RNAs in hepatocellular carcinoma. World J Gastroenterol 21(42):12022

Wagner A, Knipe J, Orive G, Peppas N (2019) Quantum dots in biomedical applications. Acta Biomater 94:44–63. https://doi.org/10.1016/j.actbio.2019.05.022

Wang M, Thanou M (2010) Targeting nanoparticles to cancer. Pharmacol Res 62:90–99. http://doi.org/10.1016/j.phrs.2010.03.005

Wong SW, Comenzo RL (2015) CD38 monoclonal antibody therapies for multiple myeloma. Clin Lymphoma Myeloma Leuk 15(11):635–645. https://doi.org/10.1016/j.clml.2015.07.642

Ying E, Hwang HM (2010) In vitro evaluation of the cytotoxicity of iron oxide nanoparticles with different coatings and different sizes in A3 human T lymphocytes. Sci Total Environ 408(20):4475–4481. https://doi.org/10.1016/j.scitotenv.2010.07.025

Zhou Y, Wang R, Teng Z, Wang Z, Hu B, Kolios M et al (2016) Magnetic nanoparticle-promoted droplet vaporization for in vivo stimuli-responsive cancer theranostics. NPG Asia Mater 8(9):e313–e318. http://doi.org/10.1038/am.2016.146